


# The metamorphic and anatexis history of Archaean metapelitic granulites from the South Marginal Zone, Limpopo Belt, South Africa

by

Gautier Nicoli

*Dissertation presented for the joint-Degree of Doctor of  
Geology at the University of Stellenbosch, South Africa and  
Université Jean Monnet, France*



Promoters:

Prof. Gary Stevens

Prof. Jean-François Moyen

Faculty of Science

Faculté des Sciences

Department of Earth Sciences

Laboratoire Magmas et Volcans

Stellenbosch University

Université Jean-Monnet, Saint-Étienne

March 2015

# Declaration

By submitting this dissertation electronically, I declare that the entirety of the work contained therein is my own, original work, that I am the sole author thereof (save to the extent explicitly otherwise stated), that reproduction and publication thereof by Stellenbosch University will not infringe any third party rights and that I have not previously in its entirety or in part submitted it for obtaining any qualification.

Signature: .....

G. Nicoli

Date: ..... 2014/12/01 .....

Copyright © 2015 Stellenbosch University  
All rights reserved.

# Dedications

*To my grandfather Achille*

“Los errores tienen casi siempre un carácter sagrado. Nunca intentéis corregirlos. Al contrario: lo que procede es racionalizarlos, compenetrarse con aquellos integralmente. Después, os será posible sublimarlos”.

Savaldor Dalí

“Todo lo que puedas imaginar es real”.

Pablo Picasso

“Chaque chose que nous voyons en cache une autre, nous désirons toujours voir ce qui est caché par ce que nous voyons”.

René Magritte

# Abstract

Anatexis is the first step in granite genesis. Partial melting in the lower crust may produce leucocratic features of unusual chemical compositions, very different from the final products of crustal differentiation. Therefore, the links that exist between some migmatites and crustal-derived granites can be ambiguous.

This study is an investigation of the anatexis history of a high-grade terrain: the Southern Marginal Zone of the Limpopo Belt (SMZ), north to the Kaapvaal Craton in South Africa. The work involved an integrated field, metamorphic, geochemical and geochronological study of the metasedimentary granulites from two separate quarries in the northern zone of the Southern Marginal Zone, the Bandelierkop quarry and the Brakspruit quarry, where Neoproterozoic high-grade partial melting features can be observed.

The project has aimed to address two main issues: (1) to accurately constrain the pressure-temperature conditions and the age of the metamorphic episode in the SMZ, with implication for the geodynamic processes near the end of the Proterozoic, (2) to investigate the fluid-absent partial melting reactions that control formation of K<sub>2</sub>O-poor leucosomes and to understand the chemical relationships in the system source-leucosome-melt-S-type granite.

The *P-T-t* record retained in the Bandelierkop Formation metapelites, constrained by phase equilibria modelling as well as zircon LA-ICP-MS geochronology, gives an insight into crustal differentiation processes in the lower crust. Rocks in both quarries indicate high-temperature metamorphism episodes with peak conditions of 840-860 °C and 9-11 kbar at *c.* 2.71 Ga with formation of leucosomes (L1) during the prograde path. Minor leucocratic features (L2) were produced during decompression to 6-7 kbar. The end of the metamorphic event is marked by the granulites/amphibolites facies transition (< 640 °C) at *c.* 2.68 Ga. The maximum deposit age for the detrital zircons in the metapelites (*c.* 2.73 Ga) indicates a rapid burial process ( $\sim 0.17 \text{ cm.y}^{-1}$ ). Those evidences strongly support that the Southern Marginal Zone contains sediments deposited in an active margin

during convergence, and that the metapelites were metamorphosed and partially melted as a consequence of continental collision along the northern margin of the Kaapvaal Craton at *c.* 2.7 Ga.

The leucocratic features generated along this *P-T-t* path display an unusual chemistry with low K<sub>2</sub>O and FeO+MgO content and high CaO content. The combination of field observations, chemical mapping and geochemical analyses leads to the conclusion the major part of the leucosomes (L1) crystallized prior to syn-peak of metamorphism concurrent with melt extraction from the source.

This study documents the details of leucosomes formation using field observations in the Southern Marginal Zone and numerical modelling. This work demonstrates that the formation of K<sub>2</sub>O-poor leucosome in the metasedimentary lower crust is controlled by the difference in volume of equilibration and heterogeneities within the migmatites. The partial melting of the source coupled with melt loss and water diffusivity within the melt transfer site is a potential mechanism to explain the chemical link in the sytem residuum–melt–S-type granite.

# Opsomming

Anateksis is die eerste stap in granietgenese. Meganismes wat in die onderste kors aan die werk is, is verantwoordelik vir korsdifferensiasie en bepaal die chemiese samestelling van die graniet.

Hierdie studie het 'n ondersoek behels van die anatektiese geskiedenis van 'n ho egraadse terrein: die suidelike randstreek van die Limpopo-gordel, noord van die Kaapvaal-kraton in Suid-Afrika. Die werk het 'n geïntegreerde veld-, metamorfiese, geochemiese en geochronologiese studie van die metasedimentêre granuliete van twee afsonderlike groewe in die noordelike sone van die suidelike randstreek (SRS), die Bandelierkop-groef en die Brakspruit-groef, waar Neoaargiese ho egraadse gedeeltelike smeltkenmerke waargeneem kan word, ingesluit.

Die projek was gerig op die ondersoek van twee belangrike kwessies: (1) om die druk-temperatuurtoestande en die ouderdom van die metamorfiese episode in die SRS akkuraat te beheer, met implikasie vir die geodinamiese prosesse naby die einde van die Argeïkum, en (2) om die reaksies onder gedeeltelik gesmelte toestande wat die vorming van migmatiete beheer, te ondersoek en die chemiese verwantskappe in die stelsel bron - leukosoom - smelt - S-tipe graniet te begryp.

Die P-T-t-rekord wat in die Bandelierkop-formasie metapeliete behoue is, ingeperk deur modellering van fase-ekwilibria asook sirkoon LA-ICP-MS-geochronologie, gee insig in korsdifferensiasieprosesse in die onderste kors. Rotse in albei groewe dui op metamorfiese episodes teen hoër temperature met piektoestande van 840-860 °C en 9-11 kbar teen ongeveer 2.71 Ga met vorming van leukosome (L1) gedurende die progradeerpad. Geringe leukokratiese eienskappe (L2) het tydens dekompresie tot 6-7 kbar ontstaan. Die einde van die metamorfiese voorval word gekenmerk deur die fasiesoorgang van granuliete / amfiboliete (<640 °C) by ongeveer 2.68 Ga. Die maksimum afsettingsouderdom vir die detritale sirkone in die metapeliete (ongeveer 2.73 Ga) dui op 'n snelle begrawingsproses ( $\sim 0.17 \text{ cm.y}^{-1}$ ). Daardie bewyse bied sterk ondersteuning daarvoor dat die SRS sedimente bevat wat gedurende konvergensie in 'n aktiewe rand afgeset is, en dat die metapeliete

gemetamorfoseer en gedeeltelik gesmelt het as gevolg van kontinentbotsing langs die noordelike rand van die Kaapvaal-kraton teen ongeveer 2.7 Ga.

Die leukokratiese eienskappe wat langs hierdie P-T-t-pad opgewek word, toon 'n ongewone chemiese samestelling met lae  $K_2O$  en  $FeO+MgO$ -inhoud en hoë  $CaO$ -inhoud. Die kombinasie van veldwaarnemings, chemiese kartering en geochemiese ontledings lei tot die gevolgtrekking dat die grootste deel van die leukosome (L1) gekristalliseer het voor die syn-piek van metamorfisme tesame met smeltekstraksie van die bron. Hierdie studie het die besonderhede van leukosoomformasie met behulp van veldwaarnemings in die SRS en numeriese modellering opgeteken. Hierdie werk toon aan dat korsdifferensiasie in die metasedimentêre onderste kors deur 'n ander volume van ekwilibrasie en heterogeniteit in die migmatiet beheer word. Die gedeeltelike smelting van die bron gepaard met smeltverlies en waterdiffusiwiteit tot in die smeltoordragterrein is 'n potensiële meganisme om die chemiese skakel in die stelsel residuum-smelt-S-tipe graniet te verklaar.

# Résumé

Les processus d'anatéxie représentent la première étapes dans la génèse des granites. La fusion partielle de la croûte inférieure peut produire des structures leucocrates à signatures chimiques particulières, très différentes. Par conséquent le lien qui existe entre certaines migmatites et les granites crûstaux peut être ambigu.

Ce projet de thèse est une étude de l'évolution des processus d'anatéxie au sein des métapelites de la formation de Bandelierkop dans le Zone Marginale Sud de la Ceinture du Limpopo en Afrique du Sud. Ce travail comprend une étude complète du métamorphisme, de la géochimie et de la géochronologie des paragneiss granulitiques de deux carrières dans la zone nord de la Zone Marginal Sud, la carrière de Bandelierkop et la carrière de Brakspruit, où la fusion partielle d'une croûte néoarchéenne peut être observée.

Le projet a pour but de répondre à deux problématiques principales: (1) contraindre de manière précise les conditions et l'âge de l'épisode métamorphique de la Zone Marginale Sud, avec ce que cela implique pour la géodynamique archéenne, (2) comprendre les réactions de fusion partielle en absence de fluide et leur contrôle sur la chimie des migmatites et le liens qui existent entre les leucosomes, la source, le liquide de fusion et les granites de type S.

Les informations  $P$ - $T$ - $t$  enregistrées dans les métapelites de la formation de Bandelierkop, contraintes par des diagrammes d'équilibre de phase ainsi que de la géochronologie sur zircon, donnent une idée sur les processus de différenciation crustale dans la croûte inférieure. Les roches des deux carrières enregistrent les conditions de pic de métamorphisme de 840-860 °C et 9-11 kbar à *c.* 2.71 Ga. Cet épisode est accompagné d'une production importante de leucosome (L1). Des leucosomes de seconde génération (L2) sont produits pendant la décompression à 6-7 kbar. La fin de l'épisode métamorphique est marquée par la transition granulites/amphibolites (< 640 °C) à *c.* 2.68 Ga. L'âge de dépôt maximum (*c.* 2.73 Ga) des zircons détritiques dans les métapelites indique un enfouissement rapide ( $\sim 0.17 \text{ cm.y}^{-1}$ ). L'ensemble des ces données montre que la Zone Marginale Sud contient des sédiments déposés dans des conditions de marge active durant un phénomène de



convergence. Les métapelites ont par conséquent subi leur métamorphisme et leur fusion partielle durant une collision continentale le long de la marge nord du craton du Kaapvaal à *c.* 2.7 Ga.

Les formations leucocrates générées le long du trajet *P-T-t* possèdent une signature géochimique spécifique caractérisée par une teneur en  $K_2O$  et  $FeO+MgO$  faible et une teneur élevée en  $CaO$ . La combinaison des observations de terrains, de la cartographie chimique et des analyses géochimiques permet de conclure que la majeure partie des leucosomes (L1) cristallisent avant le pic de métamorphisme après extraction du liquide de la source. En s'appuyant sur le laboratoire naturel qu'est la Zone Marginale Sud et utilisant une approche modélisatrice, cette étude présente les détails de la formation des leucosomes.

Ce travail démontre que la formation de leucosomes pauvres en potassium dans les sédiments de la croûte inférieure et les processus qui contrôlent la chimie du résidu et des granites de type S sont les différences des volumes d'équilibration et l'hétérogénéité de la source couplées avec des pertes de liquide et diffusion de l'eau dans les structures d'anatexis.

# Acknowledgements

Firstly, I would like to express my sincere gratitude to my supervisors, Gary Stevens and Jean-François Moyen, who gave me this incredible opportunity to undertake this project under their supervision, who always supported me along the way and to whom I am greatly indebted. Thanks to them I have discovered the magical wonders of South Africa, the snowy winters of Saint-Etienne and I have been where no geologist has gone before.

I wish to thank all the people who have taken part in my research, for their advices and the long brainstorming sessions we had together: Jeanne Taylor, Oscar Laurent, Ian Buick, Armin Zeh, Adrien Vezinet and Dirk Frei.

Very special thanks goes to Arnaud “Perple\_X” Villaros for the endless discussions on thermodynamic modelling.

Thank you to Lucie Tajčmanová, Mark Caddick and John Clemens for spending time reading and commenting my work.

I thank all the staff members from Stellenbosch University who have assisted me with my analytical work: Cynthia Sanchez-Garido, Riana Rossouw, Anton du Plessis, Madeleine Frazenburg. Thank you to Mr. Du Toit for giving us access to his quarry and to the Lianga Lodge staff members for being so welcoming.

Because I am not a huge fan of bureaucracy, I would like to express my gratitude to the people who have helped me with all the administrative issues and who have made my life easier: Dorothy Stevens, Loxie Conradie, Jean-Yves Cottin, George Oliver, Bertrand Moine and Alekandra Roychoudhury.

Thank you to my parents and family for their many years of support, wherever I was and whatever rock I was crushing. I know I never really managed to make you clearly understand what my work is about, but hopefully this thesis will give you a better answer.

I cannot express the full extent of my gratitude to my south African “family” who has made my stay in Stellenbosch an unforgettable experience: Andrea, Andries, Arnie, Capucine, Carlo, Cynthia, Duncan, Kathryn, Leonardo, Marina, Raimund, Shawn, Stephan, Stephan, Theo and Tolene.

Thank you to the Saint-Etienne Postgrade Research Unit: Adrien “Coupe dâEurope”, Bogdana “Miaou”, Gaelle “Gagou”, Simon “the Elder” and Simon “the Younger”. And the old team back in 2011: Antoine, Luc-Serge and Sylvain.

At last but not least, I wish to thank my friends who have supported me emotionally and physically for all these years: Alex, Benjamin, Clémentine, Geoffrey, Laura, Léa, Marion, Morgane, Quentin Sylvain and Sébastien.

And thanks to many other people that I forgot to mention above.

This research was carried out as part of the France-South Africa scientific collaboration and was supported by South African National Research Foundation (NRF) funding to Gary Stevens via the SARChI program, as well as through a PhD bursary I was granted for the duration of my studies, and a Centre de la Recherche Scientifique (CNRS) funding.

# Contents

Declaration	i
Dedications	ii
Abstract	iii
Opsomming	v
Résumé	vii
Acknowledgements	ix
Contents	xi
List of Figures	xiii
List of Tables	xvi
<b>1 General introduction</b>	<b>1</b>
1.1 Partial melting and leucosome formation . . . . .	2
1.2 The Southern Marginal Zone of the Limpopo Belt, South Africa . . . . .	8
1.3 Structure of the thesis . . . . .	10
<b>2 The SMZ: a geological controversy</b>	<b>19</b>
<b>3 Constrain the P-T-t evolution of the SMZ</b>	<b>31</b>
<b>4 Partial melting, melt loss and water diffusivity: the formation of K<sub>2</sub>O-poor leucosome</b>	<b>59</b>
<b>5 Synthesis, discussion and conclusion</b>	<b>115</b>
5.1 Metamorphic study on the Bandelierkop Formation metapelites . . . . .	115
5.2 Partial melting processes and crustal differentiation . . . . .	121

<i>CONTENTS</i>	<b>xii</b>
5.3 General conclusion . . . . .	124
<b>Appendices</b>	<b>128</b>
<b>A Glossary</b>	<b>129</b>
<b>B Analytical techniques and numerical modelling</b>	<b>132</b>
B.1 Analytical techniques . . . . .	132
B.2 Thermodynamic modelling . . . . .	133
<b>C Whole rock and trace elements chemistry</b>	<b>137</b>
<b>D Mineral Chemistry</b>	<b>144</b>
<b>E U-Pb zircon analyses</b>	<b>168</b>
<b>F Abstracts to conferences</b>	<b>181</b>

# List of Figures

1.1	Schematic representation of partial melting in the lower crust and granite genesis	3
1.2	Influence of the source chemistry on the chemistry of the melt . . . . .	4
1.3	Main melting reactions in the lower crust . . . . .	6
1.4	Harker diagram leucosome - S-type granite - glass inclusion . . . . .	7
1.5	General view Limpopo Belt . . . . .	9
1.6	SMZ and northern edge of the Kaapvaal Craton . . . . .	11
5.1	Evolution of the Pietersburg Block between 2800 Ma and 2650 Ma . . . . .	118
5.2	Orogenic settings . . . . .	119
5.3	Gravimetric map . . . . .	120
5.4	K <sub>2</sub> O-poor leucosomes formation and crustal differentiation . . . . .	123
A.1	Granites petrogenesis and origins . . . . .	129
B.1	Standard normalization P-XRF . . . . .	134

## List of Figures in attached publications

2.1	Bandelierkop Quarry outcrop and thin section	22
2.2	<i>P-T</i> evolution Bandelierkop Quarry	23
2.3	Comparison <i>a-x</i> models	24
2.4	TTG compositions	28
2.5	Granitoids Matok pluton	29
3.1	Map of the SMZ and Kaapvaal Craton	34
3.2	Compilation <i>P-T</i> paths SMZ	36
3.3	Brakspruit Quarry outcrop	37
3.4	Brakspruit Quarry thin sections	38
3.5	Brakspruit Quarry thin sections - details	40
3.6	Ternary plots metasedimentary rocks Brakspruit Quarry	41
3.7	Compositions garnet, biotite and plagioclase	45
3.8	T-H <sub>2</sub> O pseudosection	45
3.9	P-Fe <sup>2+</sup> O <sup>3</sup> pseudosection	46
3.10	<i>P-T</i> pseudosection fo M5 sample	47
3.11	<i>P-T</i> pseudosection for DT04B sample	49
3.12	<i>P-T</i> pseudosection for GMr sample	50
3.13	<i>P-T</i> pseudosection for DT14 sample	51
3.14	<i>P-T</i> pseudosectionmelt reintegrated	52
3.15	Compilation P-T pseudosection	53
3.16	U-Pb concordia plots	54
3.17	<i>P-T-t</i> path	55

## LIST OF FIGURES

xv

4.1	Map of the SMZ	63
4.2	Bandelierkop Quarry outcrop	66
4.3	Bandelierkop Quarry outcrop details	67
4.4	Bandelierkop Quarry thin sections	68
4.5	Bandelierkop Quarry thin section details	71
4.6	Leucosome chemistry, experimental melts and S-type granite chemistry	74
4.7	<i>P-T</i> pseudosection for the metapelite Bandelierkop Quarry	76
4.8	Melt-reintegrated pseudosection	77
4.9	U–Pb concordia plots	78
4.10	Plagioclase compositions and numerical model of leucosome formation	82
4.11	Leucosome formation via “disequilibrium” mechanism	84
4.12	Map of the SMZ	92
4.13	<i>P-T</i> path for the SMZ and partial melting reactions	93
4.14	Brakspruit Quarry leucosomes	95
4.15	Brakspruit Quarry metasedimentary rocks thin sections	96
4.16	Leucosome composition compared to melts, Grt, Pl and Qtz chemistry	97
4.18	P-XRF analyses (outcrop maps)	98
4.19	P-XRF analyses (traverses)	99
4.20	Brakspruit Quarry leucosome thin sections	101
4.21	Tomography in garnet-bearing leucosome samples	102
4.22	Garnet and plagioclase chemistry	102
4.23	$a_{H_2O}$ in the melt transfer site	103
4.24	Influence of water diffusivity in the melt	103
4.25	Formation of the leucosome in a closed system	105
4.26	Formation of the leucosome in an open system	106
4.27	Formation and evolution of the leucosomes	107
4.28	Comparison P-XRF <i>vs.</i> XRF analyses	111



# List of Tables

C.1	Leucosome and metasedimentary rocks chemistry Bandelierkop Quarry . . . . .	139
C.2	Leucosomes chemistry Brakspruit Quarry . . . . .	141
C.3	Metasedimentary rocks chemistry Brakspruit Quarry . . . . .	143
D.1	Garnet chemistry metasedimentary rocks Bandelierkop Quarry . . . . .	145
D.2	Garnet chemistry leucosomes Bandelierkop Quarry . . . . .	146
D.3	Plagioclase chemistry stromatic leucosomes Bandelierkop Quarry . . . . .	147
D.4	Plagioclase chemistry deformed leucosomes Bandelierkop Quarry . . . . .	148
D.5	Plagioclase chemistry metasedimentary rocks Bandelierkop Quarry . . . . .	149
D.6	K-feldspar chemistry metasedimentary rocks, stromatic and nebulitic leucosomes Bandelierkop Quarry . . . . .	150
D.7	Cordierite chemistry metasedimentary rocks and stromatic leucosomes Bandelierkop Quarry . . . . .	151
D.8	Orthopyroxene chemistry metasedimentary rocks, stromatic and nebulitic leucosomes Bandelierkop Quarry . . . . .	152
D.9	Orthoamphibole chemistry metasedimentary rocks, stromatic and nebulitic leucosomes Bandelierkop Quarry . . . . .	153
D.10	Biotite chemistry stromatic leucosomes Bandelierkop Quarry . . . . .	154
D.11	Biotite chemistry nebulitic leucosomes Bandelierkop Quarry . . . . .	155
D.12	Biotite chemistry metasedimentary rocks Bandelierkop Quarry . . . . .	156
D.13	Biotite chemistry metasedimentary rocks Bandelierkop Quarry . . . . .	157
D.14	Garnet chemistry metasedimentary rocks Brakspruit Quarry . . . . .	158
D.15	Biotite chemistry metasedimentary rocks Brakspruit Quarry . . . . .	159
D.16	Cordierite chemistry metasedimentary rocks Brakspruit Quarry . . . . .	160
D.17	Orthopyroxene chemistry metasedimentary rocks Brakspruit Quarry . . . . .	161
D.18	Plagioclase chemistry metasedimentary rocks Brakspruit Quarry . . . . .	162
D.19	K-feldspar chemistry metasedimentary rocks Brakspruit Quarry . . . . .	163
D.20	Rutile and ilmenite chemistry metasedimentary rocks Brakspruit Quarry . . . . .	164
D.21	Garnet chemistry leucosomes Brakspruit Quarry . . . . .	165

D.22 Biotite chemistry leucosomes Brakspruit Quarry . . . . .	166
D.23 Plagioclase and K-feldspar chemistry leucosomes Brakspruit Quarry . . . . .	167
E.1 U-Th-Pb geochronologic data for metamorphic zircon rim in stromatic leucosome in the Bandelierkop Quarry . . . . .	170
E.2 U-Th-Pb geochronologic data for metamorphic zircon rim in nebulitic leucosome in the Bandelierkop Quarry . . . . .	172
E.3 U-Th-Pb geochronologic data for detrital zircon in metapelite in the Brakspruit Quarry . . . . .	176
E.4 U-Th-Pb geochronologic data for metamorphic zircon in leucosomes in the Brakspruit Quarry . . . . .	178
E.5 U-Th-Pb geochronologic data for zircon in the pegmatite in the Brakspruit Quarry . . . . .	180

## List of Tables in attached publications

3.1	Compositions metasedimentary rocks Brakspruit Quarry	41
3.2	Mineral composition for M5 sample	42
3.3	Mineral composition for DT04B sample	43
3.4	Mineral composition for DT14 sample	44
3.5	Mineral composition for Ogn sample	44
4.1	Rock compositions Bandelierkop Quarry	73
4.2	U-Pb zircon ages L1 leucosome	79
4.3	U-Pb zircon ages L1 leucosome	81
4.4	Partial melting modelling results	90
4.5	Rock compositions Brakspruit Quarry	112
4.6	Garnet composition in the Brakspruit quarry rocks	113
4.7	Plagioclase composition in the Brakspruit quarry rocks	114

# Chapter 1

## General introduction

## 1.1 Partial melting and leucosome formation

The question of the origin and the significance of leucosomes<sup>1</sup> in anatectic terrains is an old and still debated issue (Johannes, 1988; Watt *et al.*, 1996; Braun & Kreigsman, 2001; Kreigsman, 2001; Mengel *et al.*, 2001; White *et al.*, 2004, 2010). The nub of the problem can be summarized as follows: *“It might... appear somewhat strange to combine a... review of migmatite and their rather complex origin with the so-called “granite-problem”...however, many problems are shared by both groups, and a close inspection of the one encompasses some insight into the other”* (Mehnert, 1968). In other words, migmatites and granites should be considered as two complementary objects. Therefore, the study of the formation of leucosomes must be understood within the boundaries of the SLG (source-leucosome-granite) system.

Over the years it has been established that crustal differentiation and granite genesis generally occur within the simplified following sequence: melting, melt segregation and extraction, magma ascent to upper crustal level and magma emplacement (Brown, 2004). In the anatectic zone, melt segregates from solid residue and migrates, forming magma composed of melt with a variable proportions of entrained material (peritectic phases, xenoliths and/or restites). Bons *et al.* (2004, 2009) suggested segregation and melt extraction follow a more evolved stepwise non-continuous model that allows magma ascent by isolated batches linking small melt volumes (leucosomes) to largest structures (batholiths). Thus, crustal differentiation is achieved through partial melting and segregation of felsic melt batches from a more mafic residue. As a result magma fractions that crystallize after migration at shallower levels contribute to a more evolved upper crust, whereas the deep crust becomes more refractory and usually displays evidence of the partial melting episodes (Fig. 1.1).

Experimental studies (e.g. Vielzeuf & Holloway, 1988; Patiño-Douce & Johnston, 1991; Montel & Vielzeuf, 1997; Stevens *et al.*, 1997; Patiño-Douce & Harris, 1998; Piekerling & Johnston, 1998) provide strong evidence of the kind of processes that may take place in the source. It has been recognized that the nature of the incongruent melting reaction in the source exerts a strong control on magma chemistry by determining both melt chemistry and the mineral assemblages most likely to be entrained along with the melt in the anatectic network (Stevens *et al.*, 2007, Clemens *et al.*, 2011; Clemens & Stevens 2012). It has been acknowledge that different sources and different regional settings lead to different types of magma (Fig. 1.2): Tholeiitic to peralkaline granitoids (M-type and A-type) occur in ocean spreading and continental rifting settings. In subduction/collision settings,

---

<sup>1</sup>Principal terms used in this manuscript are explained in the Appendix A: Glossary

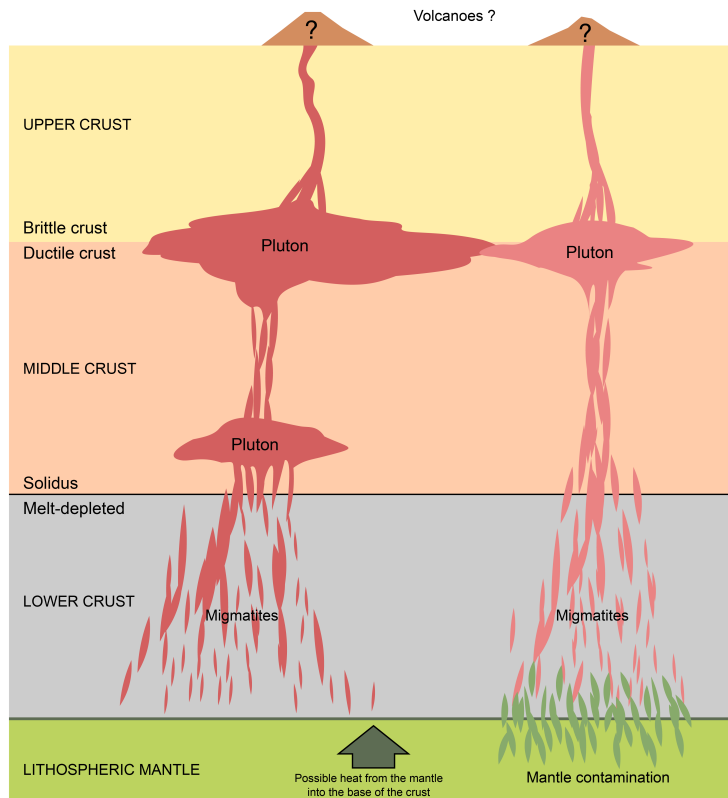


Figure 1.1: Schematic representation of partial melting in the lower crust and granite genesis. Partial melting occurs at crustal level where temperatures exceed the solidus, which results in the formation of migmatitic pockets, dykes and/or network. Melt is formed on grain boundaries and segregates to melt transfer sites. Magma accumulates to form plutonic intrusions in upper crustal level (at different depths?), which might lead to volcanic activity at the surface. Mantle-derived melt (e.g. underplating) may interact with the lower crust (extra heating source or magma mingling). Modified after Sawyer *et al.*, 2011

metaluminous and calc-alkaline granitoids (I-type) are the product of anatexis in a crustal source of intermediate composition (Clemens *et al.*, 2011) or from the differentiation of basaltic-melts injected in the lower crust (Annen *et al.*, 2006). In continental collision settings partial melting typically occurs at granulite facies  $P$ - $T$  conditions (Sawyer *et al.*, 2010). The deep continental crust is in a fluid absent state (Le Breton *et al.*, 1988; Vielzeuf *et al.*, 1990; Skjerlie *et al.*, 1993; Stevens & Clemens, 1993; Stevens *et al.*, 2007, Villaros 2009). Under this condition major melt production in metasedimentary rocks generally occurs at temperatures above 800 °C via the incongruent melting of mica or amphibole to produce peraluminous to metaluminous granitic melts. Crustal differentiation leads to the formation of S-type and I-type granites (Chapell & White, 1974, 1983; Barbarin, 1999).

In the lower crust, migmatites (or anatexites) display at different scales (terrain, outcrop, hand-size sample, mineral) evidence of the mechanisms responsible for the partial melting of the lower crust. They can present different degrees of partial melting from metatexitic migmatites (< 50 % leucocratic material) to diatexitic migmatites (> 50 % leucocratic material) (Sawyer, 2010) and they comprise at least two distinct petrographic components. One of these parts must have formed by partial melting of the source ma-

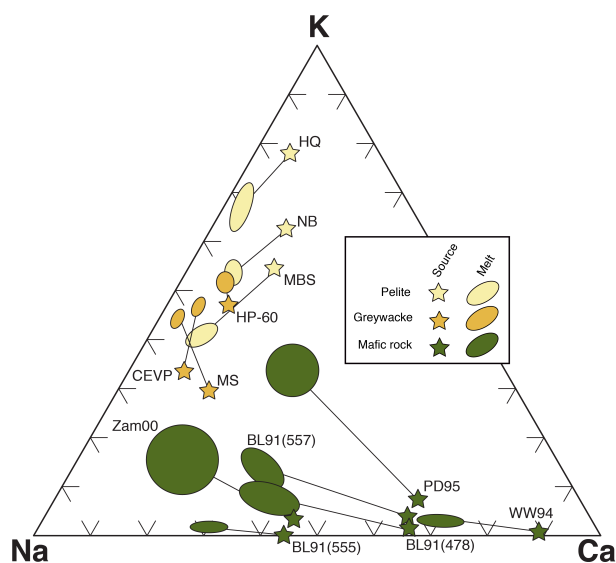


Figure 1.2: Influence of the source chemistry on the chemistry of the melt, After Moyen (2011). Stars: source composition; ellipses: average melt compositions. Pelitic sources. HQ: Patiño-Douce & Johnston (1991); NB: Stevens *et al.* (1997); MBS: Patiño-Douce & Harris (1998). Greywacke sources. CEVP: Montel & Vielzeuf (1997); HP-60 Pickering & Johnston (1998); MS. Mafic sources. PDB95: Patiño-Douce & Beard (1995); BL91: Beard & Lofgren (1991); WW94: Wolf & Wyllie (1994); Zam00: Zamora (2000).

terial<sup>2</sup>. In many locations (Ancient Gneiss Complex, Swaziland: Taylor & Stevens 2010; Bohemian Massif, Czech Republic: Hasalová *et al.*, 2008; Racek *et al.*, 2008; Fosdick Complex, West Antarctica: Korhonen *et al.*, 2010a, b; Limpopo Belt: Stevens & van Reenen, 1992a,b; Opatica Subprovince, Québec: Holness & Sawyer, 2008; Morfin *et al.*, 2013, 2014; Sawyer, 2010; St. Malo, France: MiLord *et al.*, 2001; Moine Supergroup, NW Scotland, Cutts *et al.*, 2010; Turku Area, Finland: Mengel *et al.*, 2001) the leucocratic part of the migmatite has been interpreted as an evidence of former melt network. But does this network represent melt trapped in the source? Does the chemistry of the leucosome match the chemistry of the melt or the chemistry of the granite?

Despite several hypotheses regarding what leucosomes may represent (Johannes, 1988; Watt *et al.*, 1996; Braun & Kreigsman, 2001; Kreigsman, 2001; Mengel *et al.*, 2001; White *et al.*, 2004, 2010), the chemical bonds in the SLG system are still poorly understood. In the context of this study, I particularly focused on the chemical relationship within the SLG system of a crustal-derived granite. As it has been previously explained, in order to understand the chemistry of the leucosome, we need to understand the chemistry of the granite. Three main scenarios have been suggested to explain the relationships between the source and S-type granite:

(1) The chemistry of granites is mainly controlled by the chemistry of the source (Patiño-Douce, 1999). Consequently, the heterogeneity of the granitoids reflects the heterogeneity of the source. S-type peraluminous leucogranites represent pure crustal melt produced by dehydration of mica-rich metasediments during orogenic belt formation. Therefore, the differences existing between each type of granite in the S-type granite suite reflects the

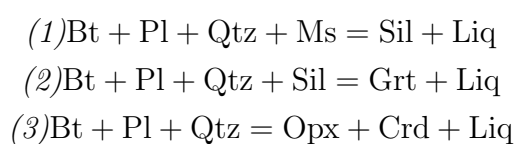
<sup>2</sup>see Appendix A: Glossary

nature of the source material and the depth at which the melting took place.

(2) Restite unmixing model: the chemistry of granites is controlled by residual source material. Chappell (1984) and Chappell *et al.* (1987) considered that partial melting in the crust produces a granitic melt in equilibrium with the residuum. The composition of a rock formed this way will be a function of the composition of the melt and the composition of the restite. Many of the granites contain a significant amount of crystals that did not crystallize from the melt, but are a residue from partial melting of the source rocks or originate from the conduit (Vernon *et al.*, 1988; Vernon, 2007). This hypothesis might be used to estimate the compositions of the source rocks but it generally plays only a subordinate role compared to other differentiation mechanisms (Clemens, 2003). The most plausible and generally accepted explanation for the high-grade metasedimentary enclaves in S-type granites described by Chappell *et al.* (1984) is that they represent mid-crustal amphibolitic xenoliths; restitic enclaves are often absent (Clemens, 2003).

(3) The chemistry of granites is controlled by peritectic crystals carried within the melt (Stevens *et al.*, 2007; Clemens *et al.*, 2011). Stevens *et al.*, 2007 demonstrated that the proportion of entrained peritectic products controls the compositional variations in the granites. This may explain the chemical link between granitoid bodies and their sources and it provides a very tight correlation between Ti and maficity (total iron and magnesium content and expressed as atomic Fe + Mg) that is inherent to almost all granitic magmas (Stevens *et al.*, 2007). The peritectic entrainment model has been proposed to explain the nature of leucosomes as melt transfer site in Swaziland (Taylor & Stevens, 2010), Spain (Bartoli *et al.*, 2013a) and Namibia (Diener *et al.*, 2014). Therefore granites might arise as a mixture of melt and peritectic assemblages produced by incongruent melting reactions.

The peritectic phases entrainment model seems to be the more plausible and the more complete scenario capable to explain the chemical link within the SLG system. In partially melted granulitic metasedimentary terrain, petrographic evidences along with relevant fluid-absent partial melting experiments (e.g. Vielzeuf & Holloway, 1988; Patiño Douce & Johnston, 1991; Montel & Vielzeuf, 1997; Stevens *et al.*, 1997; Patiño Douce & Harris, 1998; Pickering & Johnston, 1998) indicate the melt is produced via incongruent melting of mica (i.e. muscovite and mainly biotite) and might produce a significant amount of peritectic phases. Simplified partial melting reaction in the source material can be represented as follows (Fig. 1.3):





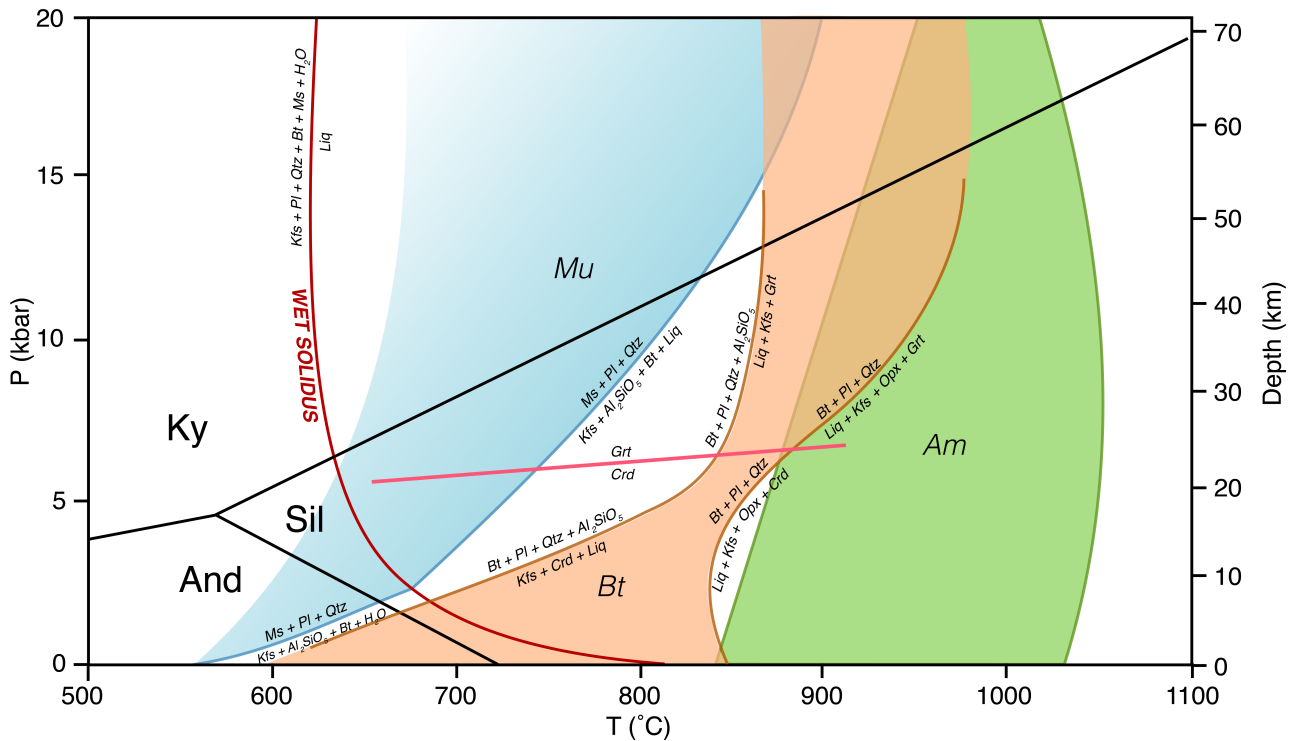


Figure 1.3: Main melting reactions in the lower crust. The biotite breakdown reaction usually produces important quantities of melt. For rocks with an amphibolitic protolith, the melting occurs at higher temperature via hornblende breakdown (Vielzeuf & Holloway, 1988; Patiño-Douce & Johnston, 1991; Montel & Vielzeuf, 1997; Stevens *et al.*, 1997; Patiño-Douce & Harris, 1998; Piekering & Johnston, 1998; Sawyer *et al.*, 2011)

Melting by muscovite breakdown may occur without the assistance of the biotite:  $\text{Pl} + \text{Qtz} + \text{Ms} = \text{Sil} + \text{Liq}$  (Storre, 1972; Storre & Karotke 1972; Harris *et al.*, 1995). K-feldspar may also be part of the products of the reaction, depending of the  $\text{K}_2\text{O}/\text{H}_2\text{O}$  ratio in the hydrous phases (Carrington & Watt, 1995).

The presence of peritectic crystals such as garnet, orthopyroxene, cordierite and in smaller proportion sillimanite, is a good indicator of the partial melting steps the rocks have been through (e.g. Stevens & Van Reenen, 1992a,b; Srogi *et al.*, 1993; Johnson *et al.*, 2003). The load of peritectic phases within the leucocratic features and the mafic residuum depends on the degree of partial melting reactions. The more efficient the melting reaction is, the more peritectic phases will be produced. In some granulitic terrains, the abundance and the preservation of peritectic assemblages in the source strongly argues for melt production followed by melt loss subsequent to magma segregation into the leucosomes (e.g. White & Powell, 2002, 2010; Brown, 2004; White *et al.*, 2004).

Consequently, the peritectic phase entrainment model may explain the chemical links within the SLG system. However, in some geological settings where partial melting occurs via biotite incongruent melting, the leucosome chemistry poorly matches the chemistry of the preserved melt inclusions and the S-type granite (Fig. 1.4). The leucosomes are

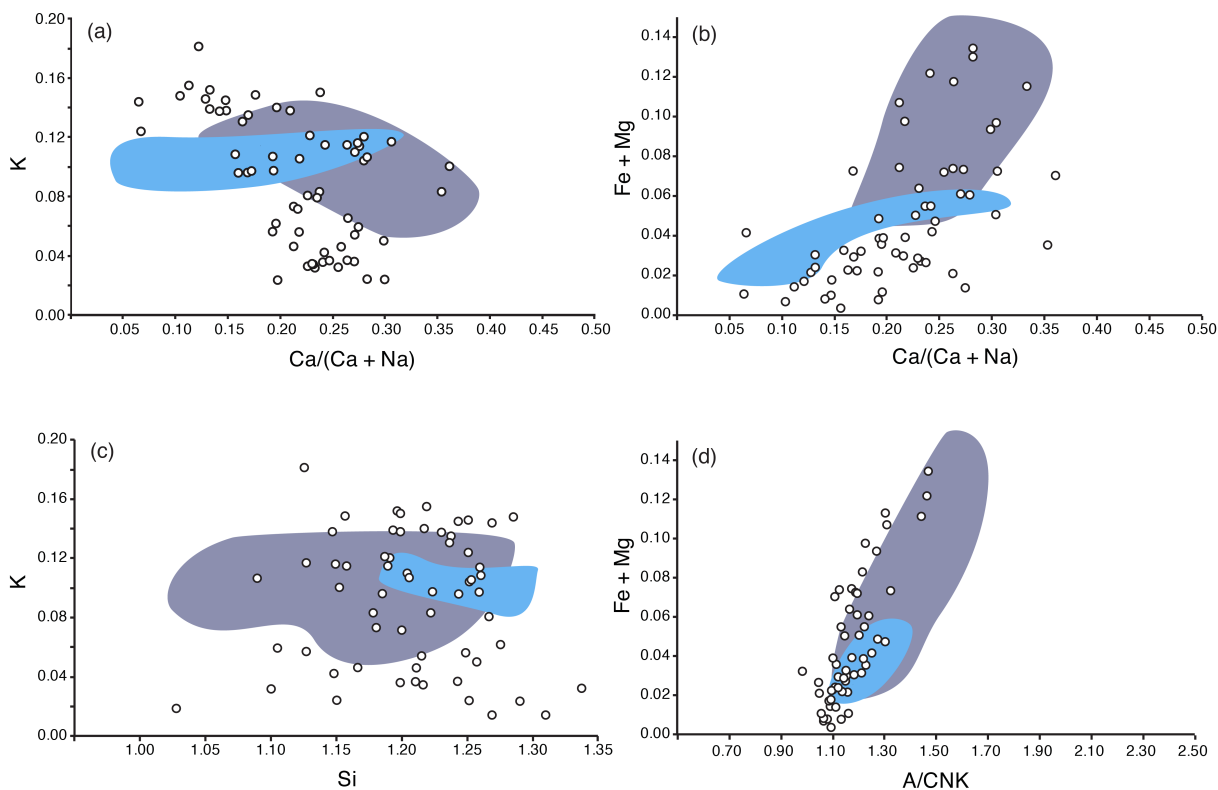


Figure 1.4: (a-d) Compositions of granulite facies leucosomes compiled from the literature (unit in mol). Leucosomes are from metasedimentary migmatites (white dots) where partial melting is well constrained and known to have occurred through biotite incongruent melting under fluid-absent conditions. The leucosomes are compared with natural glass compositions (light blue area) (both homogenized melt inclusions and glass inclusions in peritectic phases from natural migmatites, generated between 700 and 860 °C and 5-8 kbar; Acosta-Vigil *et al.*, 2007; Ferrero *et al.*, 2012; Bartoli *et al.*, 2013b) and the compositions of Cape Granite Suite S-type rocks (dark blue area) (Scheepers, 1990; Scheepers & Poujol, 2002; Scheepers & Armstrong, 2002).

markedly  $K_2O$ -depleted, and  $FeO + MgO$  and  $CaO$ -enriched whereas melt inclusions and S-type granites display higher  $K_2O$  and  $FeO + MgO$  values and are less rich in  $CaO$  (e.g. Torres-Roldan, 1983; Barbey *et al.*, 1990; Sawyer *et al.*, 1999; Chavagnac *et al.*, 2001; Mengel *et al.*, 2001; Martignole & Martelat, 2003; Taylor & Stevens, 2010). Hence, leucosomes are not just crystallized melt within the source and there is still an important chemical mismatch between the generated melt from the source, the leucosomes and the S-type granite.

These observations highlight the outstanding issues of the nature of the leucosomes, their significance and how they form. Peritectic assemblages have an important influence on granite chemistry (Clemens & Stevens, 2012). They might explain some chemical differences (maficity, titanium content) among the source, the leucosomes and the magma.

However, peritectic assemblages fail to explain the lack of potassium and the high calcium content of the leucosomes. Therefore, the chemical signature of K<sub>2</sub>O-poor leucosomes must be influenced by the mechanisms triggering their crystallization. Leucosomes are defined as a quartz and plagioclase rich cumulate formed within sites of melt accumulation. Their composition has or has not been modified by the extraction of a fraction of the melt phase (Sawyer, 1987; Brown, 2002; Waters, 1988; Kriegsman & Hensen, 1988). The redistribution of H<sub>2</sub>O and K<sub>2</sub>O back to the residuum (White & Powell 2002, 2010) subsequent to cooling also has a direct influence on the leucosome chemistry. If H<sub>2</sub>O diffuses back to the residuum it produces a distinct rehydrated selvage in the wall rock that would explain the anhydrous character of the leucosome. However, based on petrographic ground and phase equilibria modelling, recent works (Mengel *et al.*, 2001; Guernina & Sawyer, 2003; Martignole & Martelat, 2003; Yakymchuk & Brown, 2014) argue that melt loss occurs prior to peak metamorphism conditions. In such a scenario the leucocratic features are “high grade” felsic objects forming in the melt transfer site. This challenging hypothesis implies finding new mechanisms to explain the crystallization of leucosomes during the heating of the whole terrain.

## 1.2 The Southern Marginal Zone of the Limpopo Belt, South Africa

In order to investigate how the leucosomes form and what consequences their formation has on crustal differentiation, I studied the anatectic features exposed in the *c.* 2.7 Ga old granulites of the Southern Marginal Zone (SMZ) of the Limpopo Belt, South Africa. The Limpopo Belt is an E-W trending, 300 km x 500 km high-grade metamorphic terrain located along the South Africa-Zimbabwe-Botswana borders. It separates the Zimbabwe Craton (North) from the Kaapvaal craton (South) (Fig. 1.5). MacGregor (1953) was the first to establish the appellation Limpopo Orogenic Belt. The Limpopo Belt is subdivided into three distinct zones (Cox *et al.*, 1965) delimited by major shear zones: a Central Zone (CZ) and two marginal zones, the Northern Marginal Zone (NMZ) and the Southern Marginal Zone (SMZ). The Central Zone (CZ) has a polymetamorphic history, with both an older, 3.2-3.1 Ga, (Holzer *et al.*, 1998) and a younger, *c.* 2.0 Ga granulite facies overprint (Kreissig *et al.*, 2001; Buick *et al.*, 2006; Zeh *et al.*, 2010). In contrast, the NMZ and SMZ are considered to have undergone a single metamorphic event and to constitute the reworked, high-grade equivalent of the granite-greenstone succession of the adjacent cratons (van Reenen *et al.*, 1992).

The SMZ consists of a variety of grey granitoid gneisses (i.e. Baviaanskloof Gneisses), with inter-layered bodies of metasedimentary granulites and metamafic to meta-ultramafic

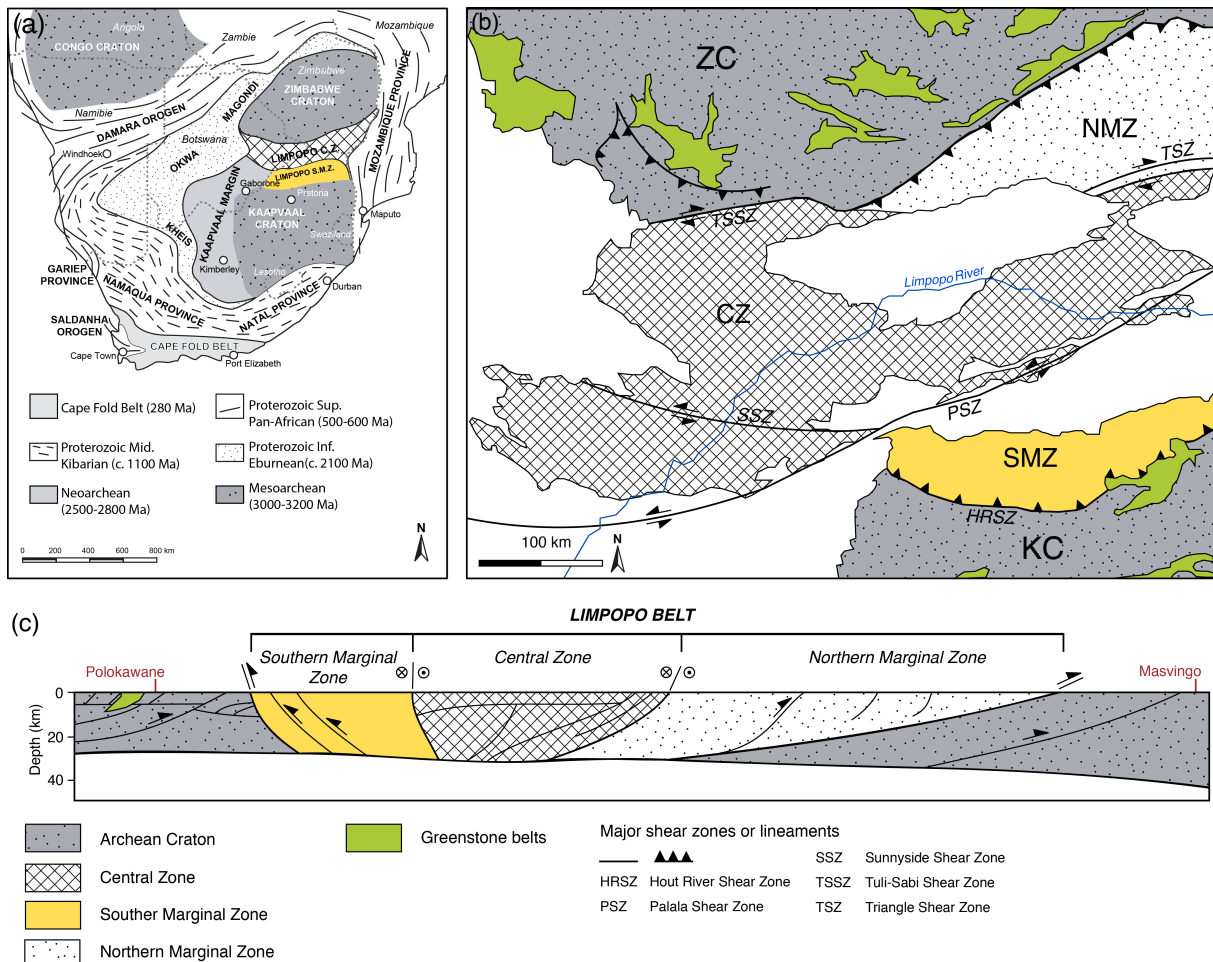


Figure 1.5: (a) Overview of the South Africa and adjacent countries geology after Norman & Whitfield (2006). The Limpopo Belt separates the Kaapvaal Craton (KZ) from the Zimbabwe Craton (ZC). (b) The Limpopo Belt is organized in three distinct zones: the Central Zone (CZ) and two marginal zones, the Northern Marginal Zone (NMZ) and the Southern Marginal Zone (SMZ). Each zone is separated from each other by major shear zones. (c) S-N Seismic profile through the Limpopo Belt. Modified after Durrheim *et al.* (1992).

rocks (i.e. the Bandelierkop Formation) (Du Toit *et al.*, 1983) (Fig. 1.6). The Bandelierkop Formation is interpreted as dismembered and metamorphosed greenstone belt lithologies and the Baviaanskloof Gneiss is interpreted as the metamorphosed trondhjemites and tonalites from the Kaapvaal basement (e.g. Roering *et al.*, 1992a; Van Reenen *et al.*, 1992). The SMZ has undergone a granulite facies metamorphic event at *c.* 2.7 Ga. To the north, the Palala Shear Zone separating the SMZ from the CZ records *c.* 2.0 Ga strike-slip sense of motion (Kreissig *et al.*, 2000, Holzer *et al.*, 1998), consequently, the two blocks may have followed different histories prior to *c.* 2.0 Ga. To the south, the Hout River Shear Zone (HRSZ) defines a seismic reflector (Roering *et al.*, 1992a) between the SMZ and the Kaapvaal craton which has been interpreted to be the consequence of

long-lived N-S oriented tectonic forces (Fig. 1.5). The general consensus is that the SMZ preserved evidence of collision between the Kaapvaal and Zimbabwe cratons (or an exotic block) at *c.* 2.7 Ga (van Reenen *et al.*, 1992; Kreissig *et al.*, 2000; Poujol *et al.*, 2003; Khoza *et al.*, 2013; Laurent *et al.*, 2014). Thus, it has been argued that the SMZ lithologies provide support for the hypothesis that lateral tectonics already operated on Earth in the Neoproterozoic.

The metamorphic history of SMZ provides insight into one of the oldest preserved continental collision zones. These well-exposed granulites represent an exceptional window into the lower crust. They offer a unique natural laboratory where anatexis mechanisms can be directly observed and quantified. The metasedimentary granulites of the Bandelierkop Formation have undergone partial melting via a large range of biotite incongruent melting reactions (see reactions above), resulting in the formation of migmatites (Stevens & Van Reenen, 1992a). A zone of retrogressed granulites, equilibrated at amphibolitic conditions, is developed in the SMZ to the north of the HRSZ, defining an orthoamphibole isograd (Van Reenen, 1986). It has been argued that the amphibolite facies rocks resulted most likely from the interaction with melts produced by partial melting of the granulitic metapelites (Stevens, 1997). Therefore, the hydrated zone represents an area of the SMZ that would have retained much of the original volume of the *in situ* melt, whilst the granulite facies area represents a domain which lost most of the melt formed during the metamorphic episode.

### 1.3 Structure of the thesis

In light of these observations, in this thesis I attempt to contribute to the state of knowledge on the evolution of the Limpopo Belt - SMZ and on the formation of K<sub>2</sub>O-poor leucosomes, by investigating the metamorphism and anatexis history of the metasedimentary granulites from SMZ. I hereby present the work in three parts through the compilation of three published, one accepted manuscripts and one manuscript in preparation generated during the course of my PhD, and which can be summarised as follows:

(1) In the first two manuscripts (comments) I discuss the validity of the *P-T* estimates published in the area, the validity of the UHT metamorphic episode (Belyanin *et al.*, 2012) as well as the geodynamic model suggested by Rajesh *et al.* (2014). These two comments prepare the ground for further investigations of the geodynamic setting and partial melting processes in the area.

(2) The third manuscript presents the *P-T-t* evolution of the Bandelierkop Formation

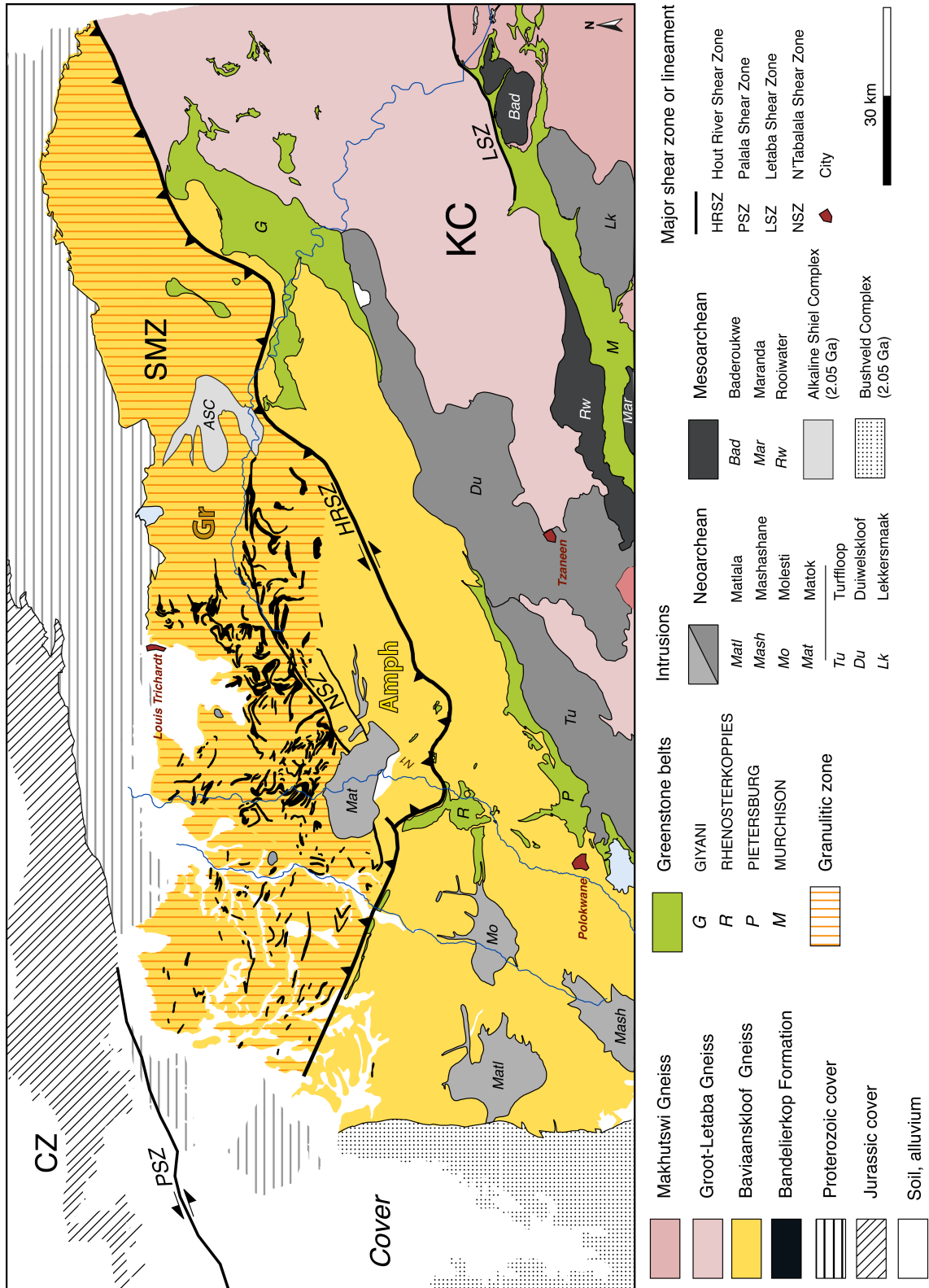


Figure 1.6: Detailed map of the Southern Marginal Zone (SMZ) of the Limpopo Belt and adjacent units. The dashed area in the Baviaanskloof Gneisses represents the classic boundaries of the SMZ. The terrain is equilibrated in granulitic conditions except for the area between the N'tabalala Shear Zone and the Hout River Shear Zone, which is a retrogressed amphibolitic domain.

metapelites. In this paper I constrained the  $P$ - $T$  conditions by using phase equilibria modelling. Metasedimentary rocks were buried to  $852.5 \pm 7.5$  °C and  $11.1 \pm 1.3$  kbar ( $\sim 35$  km). Preserved granulitic and amphibolitic assemblages indicates that peak metamorphism was followed by rapid decompression to 7.0 kbar, further followed by cooling to  $< 650$  °C. U-Pb zircons ages on detrital ( $2733 \pm 13$  Ma), metamorphic zircons ( $2713 \pm 8$  Ma) and zircon in crosscutting pegmatite ( $2680 \pm 6$  Ma) provide a very well framed time window for the whole episode. The findings of this paper strongly argue for fast ( $\sim 50$  Ma from burial to exhumation), modern plate tectonic-like mechanism during the Neoproterozoic.

(3) In the fourth and fifth manuscripts, I investigate the chemical processes that lead to the formation of  $K_2O$ -poor leucosomes. In these manuscripts, field evidences coupled with numerical modelling strongly argue for the formation of the leucosome being driven by the heterogeneity of the source and the changes in the volume of equilibrium. In consequence, this brings up new hypothesis on how crustal differentiation and granite genesis may occur.

## REFERENCES

- Acosta-Vigil, A., London, D. & Morgan VI, G.B. 2006. Experiments on the kinetics of partial melting of a leucogranite at 200 MPa H<sub>2</sub>O and 690-800°C: compositional variability of melt during the onset of H<sub>2</sub>O-saturated crustal anatexis. *Contributions to Mineralogy and Petrology*, **151**, 539-557.
- Annen, C., Blundy, J. D. & Sparks, R. S. J., 2006. The sources of granitic melt in Deep Hot Zones. *Transactions of the Royal Society of Edinburgh: Earth Sciences*, **97**, 297-309.
- Barbarin, B., 1999. A review of the relationships between granitoid types, their origins and their geodynamic environments. *Lithos*, **46**, 605-626.
- Barbey, P., Macaudiere, J. & Nzenti, J.P., 1990. High-pressure dehydration melting of metapelites: evidence from the migmatites of Yaounde (Cameroon). *Journal of Petrology*, **31**, 401-427.
- Bartoli, O., Cesare, B. & Poli, S., 2013a. Recovering the composition of melt and the fluid regime at the onset of crustal anatexis and S-type granite formation. *Geology*, **41**, 115-118.
- Bartoli, O., Tajčmanová, L., Cesare, B. Acosta-Vigil, A., 2013b. Phase equilibria constraints on melting of stromatic migmatites from Ronda (S. Spain): insights on the formation of peritectic garnet. *Journal of Metamorphic Geology*, **31**, 775-789.
- Beard, J. B. & Lofren, G. E., 1991. Dehydration Melting and Water-Saturated Melting of Basaltic and Andesitic Greenstones and Amphibolites at 1, 3, and 6.9 kb. *Journal of Petrology*, **32**, 365-401.
- Belyanin, G.A., Rajesh, H.M., Sajeev, K. & Van Reenen, D.D., 2012. Ultrahigh-temperature metamorphism from an unusual corundum+orthopyroxene intergrowth bearing Al-Mg granulite from the Southern Marginal Zone, Limpopo Complex, South Africa. *Contributions to Mineralogy and Petrology*, **164**, 457-475.
- Bons, P.D., Becker, J.K., Elburg, M.A. & Urtson, K., 2009. Granite formation: Stepwise accumulation of melt or connected networks? *Earth and Environmental Science Transactions of the Royal Society of Edinburgh*, **100**, 105-115.
- Bons, P.A., Druguet, E., Hamann, I., Carreras, J. & Passchier, C.W., 2004. Apparent boudinage in dykes. *Journal of Structural Geology*, **26**, 625-636.
- Braun, I. & Kriegsman, L.M., 2001. Partial melting in crustal xenoliths and anatectic migmatites: a comparison. *Physics and Chemistry of the Earth, Part A: Solid Earth and Geodesy*, **26**, 261-266.
- Brown, M., 2002. Retrograde processes in migmatites and granulites revisited. *Journal of Metamorphic Geology*, **20**, 25-40.
- Brown, M., 2004. The mechanism of melt extraction from lower continental crust of orogens. *Geological Society of America*, **289**, 35-48.
- Buick, I.S., Hermann, J., Williams, I.S., Gibson, R.L. & Rubatto, D., 2006. A SHRIMP U-Pb and LA-ICP-MS trace element study of the petrogenesis of garnet-cordierite-orthoamphibole gneisses from the Central Zone of the Limpopo Belt, South Africa. *Lithos*, **88**, 150-172.
- Carrington, D. P. & Watt, G. R., 1995. A geochemical and experimental study of the role of K-feldspar during water-undersaturated melting of metapelites. *Chemical Geology*, **122**, 59-76.
- Chappell, B.W., 1984. Source rocks of I- and S-type granites in the Lachlan Fold Belt, southeastern Australia Phil. Trans. *Royal Society of London*, **10**, 693-707.
- Chappell, B.W. & White, A. J. R., 1974. Two contrasting granite types, *Pacific Geology*, **8**, 173-174.
- Chappell, B.W., White, A.J.R. & Wyborn, D., 1987. The Importance of Residual Source Material (Restite) in Granite Petrogenesis. *Journal of Petrology*, **28**, 1111-1138.
- Chavagnac, V., Kramers, J.D., Neagler, T.F. & Holzer, L., 2001. The behaviour of Nd and Pb isotopes during 2.0 Ga migmatization in paragneisses of the Central Zone of the Limpopo Belt (South



Africa and Botswana). *Precambrian Research*, **112**, 51-86.

Clemens, J.D., 2003. S-type granitic magmas—petrogenetic issues, models and evidence. *Earth-Science Reviews*, **61**, 1-18.

Clemens, J.D. & Stevens, G., 2012. What controls chemical variation in granitic magmas? *Lithos*, **134-135**, 317-329.

Cutts, K.A., Kinny, P.D., Strachan, R.A., Hand, M., Kelsey, D.E., Emery, M., Friend, C.R.L. & Leslie, A.G., 2010. Three metamorphic events recorded in a single garnet: Integrated phase modelling, in situ LA-ICPMS and SIMS geochronology from the Moine Supergroup, NW Scotland. *Journal of Metamorphic Geology*, **28**, 249-267.

Diener, J. F., White, R. W. & Hudson, T. J., 2014. Melt production, redistribution and accumulation in mid-crustal source rocks, with implications for crustal-scale melt transfer. *Lithos*, **200**, 212-225.

Durrheim, R.J. & Green, R.W.E., 1992. A seismic refraction investigation of the Archaean Kaapvaal Craton, South Africa, using mine tremors as the energy source. *Geophysical Journal International*, **108**, 812-832.

Du Toit, M.C., Van Reenen, D.D. & Roering, C., 1983. Some aspects of the geology, structure and metamorphism of the Southern Marginal Zone of the Limpopo metamorphic complex. *Geological Society of South Africa, Special Publications*, **8**, 121-142.

Ferrero, S., Bartoli, O. & Cesare, B., 2012. Microstructures of melt inclusions in anatexitic metasedimentary rocks. *Journal of Metamorphic Geology*, **30**, 303-322.

Guernina, S. & Sawyer, E.W. 2003. Large-scale melt-depletion in granulite terranes: an example from the Archean Ashuanipi Subprovince of Quebec. *Journal of Metamorphic Geology*, **21**, 181-201.

Harris, N., Ayres, M. & Massey, J., 1995. Geochemistry of granitic melts produced during the incongruent melting of muscovite: implications for the extraction of Himalayan leucogranite magmas. *Journal of Geophysical Research: Solid Earth*, **100**, 15767-15777.

Hasalová, P., Schumann, K., Lexa, O., típska, P., Hroudá, F., Ulrich, S., Haloda, J. & Týcová, 2008. Origin of migmatites by deformation-enhanced melt infiltration of orthogneiss: a new model based on quantitative microstructural analysis. *Journal of Metamorphic Geology*, **26**, 29-53.

Holness, M.B. & Sawyer, E.W., On the Pseudomorphing of Melt-filled Pores During the Crystallization of Migmatites. *Journal of Petrology*, **49**, 1343-1363.

Holzer, L., Frei, R., Barton, J.M. & Kramers, J.D., 1998. Unravelling the record of successive high grade events in the Central Zone of the Limpopo Belt using Pb single phase dating of metamorphic minerals. *Precambrian Research*, **87**, 87-115.

Johannes, W., 1988. What controls partial melting in migmatites? *Journal of Metamorphic Geology*, **6**, 451-465. Johnson, T.E., Hudson, N.F.C. & Droop, G.T.R., 2003. Evidence for a genetic granite-migmatite link in the Dalradian of NE Scotland. *The Geological Society of London*, **20**, 447-457.

Khoza, D., Jones, A.G., Muller, M.R., Evans, R.L., Webb, S.J. & Miensopust, M., 2013. Tectonic model of the Limpopo belt: Constraints from magnetotelluric data. *Precambrian Research*, **226**, 143-156.

Korhonen, F. J., Saito, S., Brown, M., Siddoway, C.S. & Day, J.M., 2010. Multiple Generations of Granite in the Fosdick Mountains, Marie Byrd Land, West Antarctica: Implications for Polyphase Intracrustal Differentiation in a Continental Margin Setting. *Journal of Petrology*, **51**, 627-670.

Kriegsman, L.M., 2001. Partial melting, partial melt extraction and partial back reaction in anatexitic migmatites. *Lithos*, **56**, 75-96

Kriegsman, L.M. & Hensen, B.J., 1998. Back reaction between restite and melt: implications for geothermobarometry and pressure-temperature paths. *Geology*, **26**, 1111-1114.

Kreissig, K., Holzer, L., Frei, R., Villa, I.M., Kramers, J.D., Kroner, A., Smit, C.A. & Van Reenen, D.D., 2001. Geochronology of the Hout River Shear Zone and the metamorphism in the Southern Marginal Zone of the Limpopo Belt, Southern Africa. *Preambrian Research*, **109**, 145-173.

Kreissig, K., Nagler, T.F., Kramers, J.D., Van Reenen, D.D. & Smit C.A., 2000. An isotopic and geochemical study of the northern Kaapvaal Craton and the Southern Marginal Zone of the Limpopo Belt: are they juxtaposed terranes? *Lithos*, **50**, 1-25.

Kretz, R., 1983. Symbols for rock-forming minerals. *American Mineralogist*, **68**, 277-279.

Laurent, O., Rapopo, M., Stevens, G., Moyen, J-F., Martin, H., Doucelance, R. & Bosq, A. 2014. Constraining petrogenesis of Mg-K and F-K granitoids and implications for post-collisional magmatism: Case study from the late-Archean Matok pluton (Pietersburg, South Africa). *Lithos*, **197**, 131-149.

Le Breton, N. & Thompson, A. B., 1988. Fluid-absent (dehydration) melting of biotite in metapelites in the early stages of crustal anatexis. *Contributions to Mineralogy and Petrology*, **99**, 226-237.

MacGregor, A.M, 1953. Precambrian formations of tropical southern Africa. *International Geological Congress Algiers*, **19**, 39-50.

Martignole, J. & Martelat J-E., 2003. Regional-scale Grenvillian-age UHT metamorphism in the Mollendo-Camana block (basement of the Peruvian Andes). *Journal of Metamorphic Geology*, **21**, 99-120.

Mehnert, K. R., 1968. Migmatites and Origin of Granitic Rocks. Elsevier Pub., University of California, 394 pp.

Mengel, K., Richter, M. & Johanne, W., 2001. Leucosome-forming small-scale geochemical processes in the metapelitic migmatites of the Turku area, Finland. *Lithos*, **5**, 47-73.

Milord, I., Sawyer, E.W. & Brown, G., 2001. Formation of Diatexite Migmatite and Granite Magma during Anatexis of Semi-pelitic Metasedimentary Rocks: an Example from St. Malo, France. *Journal of Petrology*, **42**, 487-505.

Montel, J.M. & Vielzeuf, D., 1997. Partial melting of metagreywackes. 2. Compositions of minerals and melts. *Contribution to Mineral and Petrology*, **128**, 176-196.

Morfin, S., Sawyer, E.W. & Bandyayera, D., 2014. The geochemical signature of a felsic injection complex in the continental crust: Opanica Subprovince, Quebec. *Lithos*, **196-197**, 339-355.

Morfin, S., Sawyer, E.W. & Bandyayera, D., 2013. Large volumes of anatectic melt retrained in granulite facies migmatites: an injection complex in northern Quebec. *Lithos*, **168-169**, 200-218.

Moyen, J-F., 2011. The composite Archean grey gneisses: Petrological significance, and evidences for a non-unique tectonic setting for Archean crustal growth. *Lithos*, **123**, 21-36.

Norman, N. & G. Whitfield, G., 2006, Geological journeys – a traveller's guide to South Africa's rocks and landforms, 320 pp., Struik publishers, Cape Town.

Patiño Douce, A.E., 1999. What do experiments tell us about the relative contributions of crust and mantle to the origin of granitic magmas? *The Geological Society of London*, **168**, 55-75.

Patiño Douce, A.E. & Beard, J.S., 1995. Dehydration melting of biotite gneiss and quartz amphibolite from 3 to 15 kbar. *Journal of Petrology*, **36**, 707-738.

Patiño Douce, A.E. & Beard, J.S., 1996. Effects of P, f(O<sub>2</sub>) and Mg/Fe ratio on dehydration melting of model metagreywackes. *Journal of Petrology*, **37**, 999-1024.

Patiño Douce, A.E. & Harris, N., 1998. Experimental constraints on Himalayan anatexis. *Journal of Petrology*, **39**, 689-710.

Patiño Douce, A.E. & Johnston, A.D., 1991. Phase equilibria and melt productivity in the pelitic system: implications for the origin of peraluminous granitoids and aluminous granites. *Contribution to Mineralogy and Petrology*, **107**, 202-218.

Pickering, J.M. & Johnston, A.D., 1998. Fluid-absent melting behavior of two-mica metapelite: experimental constraints on the origin of black hills granite. *Journal of Petrology*, **39**, 1797-1894.

Poujol, M., Robb, L.J., Anhaeusser, C.R. & Gericke, B., 2003. A review of the geochronological constraints on the evolution of the Kaapvaal Craton, South Africa. *Precambrian Research*, **127**, 181-213.

Racek, M., típska, P., Pitra, P., Schulmann, K. & Lexa, O., 2006. Metamorphic record of burial and exhumation of orogenic lower and middle crust: a new tectonothermal model for the Drosendorf window (Bohemian Massif, Austria). *Mineralogy and Petrology*, **86**, 221-251.

Rajesh, H.M., Santosh, M., Wan, Y., Lui, D., Lui, S.J. & Belyanin, G.A., 2014. Ultrahigh temperature granulites and magnesian charnockites: Evidence for Neoproterozoic accretion along the northern margin of the Kaapvaal Craton. *Precambrian Research*, **246**, 150-159.

Roering, C., Van Reenen, D.D., De Wit, M., Smit, C.A., De Beer, J. & Van Schalkwyk J.F., 1992a. Structural, geological and metamorphic significance of the Kaapvaal craton, Limpopo belt contact. *Precambrian Research*, **55**, 69-80.

Sawyer, E.W., 1987. The role of partial melting and fractional crystallization in determining discordant migmatite leucosome compositions. *Journal of Petrology*, **28**, 445-473.

Sawyer, E.W., 1999. Criteria for the recognition of partial melting. *Physics and Chemistry of the Earth, Part A: Solid earth and Geodesy*, **24**, 269-279.

Sawyer, E.W., 2010. Migmatites formed by water-fluxed partial melting of a leucogranodiorite protolith: Microstructures in the residual rocks and source of the fluid. *Lithos*, **116**, 273-286.

Sawyer, E.W., Cesare, B. & Brown, M., 2011. When the Continental Crust Melts. *Elements*, **7**, 229-234.

Skjerlie, K. P., Douce, A. E. P. Johnston, A. D., 1993. Fluid absent melting of a layered crustal protolith: implications for the generation of anatectic granites. *Contributions to Mineralogy and Petrology*, **114**, 365-378.

Srogi, L., Wagner, M.E. & Lutz, T.M., 1993. Dehydration partial melting and disequilibrium in the granulite-facies Wilmington Complex, Pennsylvania-Delaware Piedmont. *American journal of Science*, **293**, 405-462

Stevens, G., 1997. Melting, carbonic fluids and water recycling in the deep crust: an example from the Limpopo Belt, South Africa. *Journal of Metamorphic Geology*, **15**, 141-154.

Stevens, G., Clemens, J.D. & Droop, G.T.R., 1997. Melt production during granulite-facies anatexis: experimental data from primitive metasedimentary protoliths. *Contribution to Mineralogy and Petrology*, **128**, 352-370.

Stevens, G. & Clemens, J. D., 1993. Fluid-absent melting and the roles of fluids in the lithosphere: a slanted summary? *Chemical Geology*, **108**, 1-17.

Stevens, G. & Van Reenen, D.D., 1992a. Partial melting and the origin of metapelitic granulites in the Southern Marginal Zone of the Limpopo Belt, South Africa. *Precambrian Research*, **55**, 303-319.

Stevens, G. & Van Reenen, D.D., 1992b. Constraints on the form of the P-T loop in the Southern Marginal Zone of the Limpopo Belt, South Africa. *Precambrian Research*, **55**, 279-296.

Stevens, G., Villaros, A. & Moyon, J-F., 2000. Selective peritectic garnet entrainment as the origin of geochemical diversity in S-type granites. *Geology*, **35**, 9-12.

Storre, B., 1972. Dry melting of muscovite + quartz in the range  $P = 7$  kb to  $P = 20$  kb. *Contributions to Mineralogy and Petrology*, **37**, 87-89.

Storre, B. & Karotke, E., 1972. Experimental data on melting reactions of muscovite + quartz in the system  $K_2O-Al_2O_3-SiO_2-H_2O$  to 20 kb water pressure. *Contributions to Mineralogy and Petrology*, **36**, 343-345.

Taylor, J. & Stevens, G., 2010. Selective entrainment of peritectic garnet into S-type granitic magmas: Evidence from Archaean mid-crustal anatectites. *Lithos*, **120**, 277-292.

Torres-Roldan, R.L., 1983. Fractionated melting of metapelite and further crystal-melt equilibria. The example of the Blanca Unit Migmatite Complex, north of Estepona (southern Spain). *Tectonophysics*, **96**, 95-123.

Van Reenen, D.D., 1986. Hydration of cordierite and hypersthene and a description of the retrograde orthoamphibole isograd in the Limpopo Belt, South Africa. *American Mineralogist*, **71**, 900-915.

Van Reenen, D.D., Roering, C., Ashwal L.D. & de Wit, M.J., 1992. Regional geological setting of the Limpopo Belt. *Precambrian Research*, **55**, 1-5.

Vernon, R. H., 2007. Problems in identifying restite in S-type granites of southeastern Australia, with speculations on sources of magma and enclaves. *The Canadian Mineralogist*, **45**, 147-178. Vernon, R. H., Etheridge, M. A. & Wall, V. J., 1988. Shape and microstructure of microgranitoid enclaves: indicators of magma mingling and flow. *Lithos*, **22**, 1-11.

Vielzeuf, D. & Holloway, J.R., 1988. Experimental determination of the fluid-absent melting reactions in the pelitic system. *Contribution to Mineralogy and Petrology*, **98**, 257-276.

Vielzeuf, D., Clemens, J. D., Pin, C. & Moinet, E., 1990. Granites, granulites, and crustal differentiation. In *Granulites and crustal evolution*, Springer Netherlands, 59-85.

Villaros, A., 2009. The Petrogenesis of S-type Granites: Example of the Cape Granite Suite, PhD thesis, Stellenbosch University, pp. 225

Villaros, A., Buick, I.S. & Stevens, G. 2012. Isotopic variations in S-type granites: an inheritance from a heterogeneous source? *Contribution to Mineralogy and Petrology*, **163**, 243-257.

Villaros, A., Stevens, G., Moyon, J-F. & Buick, I.S., 2009. The trace element compositions of S-type granites: evidence for disequilibrium melting and accessory phase entrainment in the source. *Contributions to Mineralogy and Petrology*, **158**, 543-561.

Villaseca, C., Downes, H., Pin, H. & Barbero, L. 1999. Nature and Composition of the Lower Crust in Central Spain and the Granulite-Granite Linkage: Inference from Granulitic Xenoliths. *Journal of Petrology*, **40**, 1465-1496.

Waters, D.J., 1988. Partial melting and the formation of granulite-facies assemblages in Namaqualand, South Africa. *Journal of Metamorphic Geology*, **6**, 387-404.

Watt, G.R., Burns, I.M. & Graham, G.A., 1996, Chemical characteristics of migmatites accessory phase distribution and evidences for fast melt segregation rates. *Contributions to Mineralogy and Petrology*, **125**, 100-111

White, A. J. R. & Chappell, B. W., 1983. Granitoid types and their distribution in the Lachlan Fold Belt, southeastern Australia. *Geological Society of America*, **159**, 21-34.

White, R.W. & Powell, R., 2010. Retrograde melt-residue interaction and the formation of near-anhydrous leucosomes in migmatites. *Journal of Metamorphic Geology*, **28**, 579-597.

White, R.W., Powell, R. & Clarke, G.L., 2002. The interpretation of reaction textures in Fe-rich metapelite granulites of the Musgrave Block, central Australia: constraints from mineral equilibria calculations in the system K<sub>2</sub>O-FeO-MgO-Al<sub>2</sub>O<sub>3</sub>-SiO<sub>2</sub>-H<sub>2</sub>O-TiO<sub>2</sub>-Fe<sub>2</sub>O<sub>3</sub>. *Journal of Metamorphic Geology*, **20**, 41-55.

White, R.W., Powell, R. & Clarke, G.L., 2004. Prograde Metamorphic Assemblage Evolution during Partial Melting of Metasedimentary Rocks at Low Pressures: Migmatites from Mt Stafford, Central Australia. *Journal of Petrology*, **44**, 1937-1960.

Wolf, M. B. & Wyllie, P. J., 1994. Dehydration-melting of amphibolite at 10 kbar: the effects of temperature and time. *Contribution to Mineralogy and Petrology*. **115**, 369-383.

Yakymchuk, C. & Brown, M., 2014. Consequences of open-system melting in tectonics. *Journal Geological Society*, **171**, 21-40.

Zamora, D., 2000. Fusion de la croûte océanique subductée: approche expérimentale et géochimique. University Thesis Université Blaise Pascal, Clermont-Ferrand, pp. 314.

Zeh, A., Gerdes, A., Barton Jr, J. & Klemd, R., 2010. U–Th–Pb and Lu–Hf systematics of zircon from TTGâs, leucosomes, metaâanorthosites and quartziteâs of the Limpopo Belt (South Africa): Constraints for the formation, recycling and metamorphism of Palaeoarchean crust. *Precambrian Research*, **179**, 50-68.

## Chapter 2

### The SMZ: a geological controversy

## Presentation of the publications

These papers<sup>1,2</sup>, first and second authored by Gautier Nicoli, were accepted for publication in the journals of Contributions to Mineralogy and Petrology and Precambrian Research. The following aspects of the research were done independently by Gautier Nicoli while receiving standard supervision by his supervisors Gary Stevens and Jean-François Moyen: (i) mineral equilibria modelling in Theriak-Domino and PerpleX; (ii) writing of the manuscript.

**Gautier Nicoli<sup>a,b</sup>**

**Gary Stevens<sup>a</sup>**

**Jean-François Moyen<sup>b</sup>**

**Ian Buick<sup>a</sup>**

**Oscar Laurent<sup>c</sup>**

**Armin Zeh<sup>c</sup>**

**Adrien Vezinet<sup>a,b</sup>**

a: Center for Crustal Petrology, Department of Earth Sciences, Stellenbosch University, Private Bag X1, Matieland 7602, South Africa

b: UMR 6524 CNRS Université Jean-Monnet, 23 rue du Dr Michelon, 42023 Saint-Etienne, France

c: Institut für Geowissenschaften, Fachinheit Mineralogie, Johann Wolfgang Goethe Universität, Altenhofallee 1, D-60438 Frankfurt am Main, Germany

---

<sup>1</sup>Nicoli, G., Stevens, S., Buick, I.S. & Moyen J-F. 2014. A comment on Ultrahigh-temperature metamorphism from an unusual corundum + orthopyroxene intergrowth bearing Al-Mg granulite from the Southern Marginal Zone, Limpopo Complex, South Africa by Belyanin et al. Contributions to Mineralogy and Petrology, 167:1022. doi.org/10.1007/s00410-014-1022-6

<sup>2</sup>Laurent, O., Nicoli, G., Zeh, A., Stevens, G. Moyen, J-F. & Vezinet, A., 2014. Comment on “Ultrahigh temperature granulites and magnesian charnockites: Evidence for the Neoproterozoic accretion along the northern margin of the Kaapvaal craton” by Rajesh et al. Precambrian Research, doi.org/10.1016/j.precamres.2014.07.010

## A comment on ultrahigh-temperature metamorphism from an unusual corundum + orthopyroxene intergrowth bearing Al–Mg granulite from the Southern Marginal Zone, Limpopo Complex, South Africa, by Belyanin et al.

Gautier Nicoli · Gary Stevens · Ian Buick · J.-F. Moyen

Received: 16 November 2012 / Accepted: 23 May 2014  
© Springer-Verlag Berlin Heidelberg 2014

Studies on the Southern Marginal Zone (SMZ) of the Limpopo Belt have generally concluded that this terrain was affected by a single granulite-facies metamorphic event at 2.67–2.66 Ga (Kröner et al. 2000; Kreissig et al. 2000; Zeh et al. 2005; Elington and Armstrong 2004; Stevens and Van Reenen 1992a, b; Barton and van Reenen 1992; Barton et al. 1992; Van den Berg and Huizenga 2001; Rigby et al. 2008), with peak metamorphic conditions of 7.5–9.5 kbar and 800–850 °C. In their recent paper, Belyanin et al. (2012) propose an ultrahigh-temperature (UHT) metamorphic event in the SMZ, with peak metamorphic conditions in excess of 1,000 °C at approximately 12 kbar. Similar conclusions were proposed by earlier work on the same rock (Belyanin et al. 2010). The proposed UHT conditions are based on Al-rich orthopyroxene and ternary feldspar thermometry using reintegrated feldspar compositions. This evidence is derived from a single outcrop containing unusual aluminous layers within metasedimentary granulites, although Tsunogae et al.

(2004) used Al-in-orthopyroxene and ternary feldspar thermometry to argue for a peak metamorphic temperature of >950 °C from more representative metapelitic granulites of the Bandelierkop formation. Both these studies have proposed that UHT metamorphism affected the SMZ generally and thus that the relevant PT path of all rocks traversed UHT conditions.

This interpretation is problematic because it is difficult to reconcile with the partial melting history of the rocks and with the peak metamorphic assemblage in most rocks. In essence, both the metasedimentary granulites of the Bandelierkop formation and the trondhjemitic to tonalitic Bavianskloof gray gneisses contain a significant proportion of biotite, which defines a syn-peak metamorphic fabric (Fig. 1). Within the metasediments of the Bandelierkop formation, compositional banding at the outcrop scale (Fig. 1) exists that is considered to represent primary differences in composition between different sedimentary units (van Reenen 1983). Anatexis of these rocks has occurred via three reactions (Stevens and van Reenen 1992a):  $Ms + Qtz + Pl = Sil + Melt$ ;  $Bt + Sil + Qtz + Pl = Grt + Melt$ ; and  $Bt + Qtz + Pl = Opx + Crd + Melt$ . The first two reactions exhausted muscovite and sillimanite, respectively, while the third reaction had just begun to occur in the chemically most favorable rocks at the conditions of peak metamorphism. Pseudosection modeling of metapelitic granulites from the Bandelierkop quarry, which have undergone anatexis and that represent restitic, melt-depleted compositions, indicates that biotite in such rocks would not have survived temperatures significantly above 900 °C and that the mineral compositions in such rocks are consistent with peak metamorphic temperatures of 820–860 °C at 8–10 kbar (Fig. 2). At the peak metamorphic conditions proposed by Belyanin et al. (2012), these restitic granulites would have become

---

Communicated by T. L. Grove.

---

G. Nicoli (✉) · G. Stevens · I. Buick  
Department of Earth Sciences, Centre for Crustal Petrology,  
Stellenbosch University, Private Bag X1, Matieland 7602,  
South Africa  
e-mail: gnicoli@sun.ac.za

G. Stevens  
e-mail: gs@sun.ac.za

I. Buick  
e-mail: ibuick@sun.ac.za

J.-F. Moyen  
UMR 6524 CNRS, Université Jean-Monnet,  
23 rue du Dr Michelon, 42023 Saint-Étienne, France  
e-mail: jean-francois.moyen@univ-st-etienne.fr



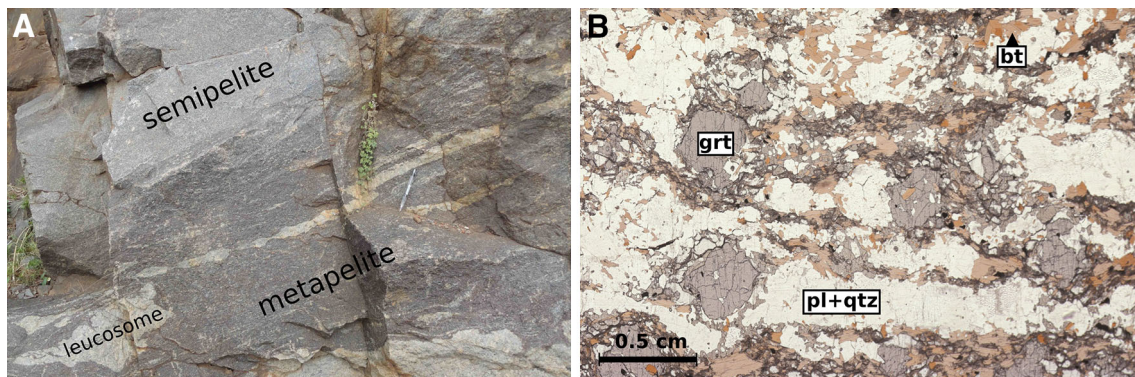


**Fig. 1** **a** Bandelierkop quarry outcrop. The main foliation is defined by biotite, the orientation of leucosomes, as well as contacts between different varieties on metasedimentary gneisses (metapelite/semipelite) that are interpreted to represent original sedimentary layering. **b** Thin section of typical  $\text{Al}_2\text{O}_3$ -rich metapelite, developed as residuum after the extraction of melt to form large (meter) stromatic

leucosome, from the Bandelierkop quarry. The fabric is defined by the preferred orientation of biotite and the quartzofeldspathic banding. In this relatively aluminous rock, Crd and Opx are part of the high-temperature, decompression-induced retrograde assemblage. Mineral abbreviations after Kretz (1983)

partially melted rocks consisting of some 50–70 % melt and a garnet-dominated residuum (Fig 2). Thus, had such temperatures been attained, the metasedimentary rocks of the Bandelierkop formation, which occur as bodies throughout the SMZ, would have been transformed into residuum-rich, diatextitic, peraluminous dioritic to granodioritic plutons, with no preservation of primary sedimentary contacts. All biotite in the SMZ would have to be retrograde. The finding that biotite stability in typical SMZ metapelitic granulites is limited to approximately 870 to 900 °C is compatible with experimental investigations of biotite partial melting in metapelites and metagraywackes (Vielzeuf and Holloway 1988; Patinõ Douce and Johnston 1991; Montel and Vielzeuf 1997; Stevens and Clemens 1993; Patinõ Douce and Harris 1998; Pickering and Johnston 1998), including experiments on compositions designed to directly investigate anatexis in the SMZ (Stevens et al. 1997). It is also compatible with the findings of a great many metamorphic studies in metapsammites and metapelites, which have predicted biotite to be completely consumed by anatectic reactions as temperatures approach ~900 °C (e.g., Taylor et al. 2010; Stevens and van Reenen 1992a; Carson et al. 1997; White et al. 2003).

The anatectic consequences of general UHT metamorphism in the SMZ would also have impacted on the typically biotite-bearing, trondhjemitic Baviaanskloof gneisses, which constitute the most abundant rock type in the SMZ. Experiments on the fluid-absent partial melting of such rocks indicate that biotite will be exhausted by 900 °C at 10 kbar (Singh and Johannes 1996) and that at higher temperature, the dominant ferromagnesian mineral in the rock would be orthopyroxene. This is not compatible with the appearance of the Baviaanskloof gneiss. These rocks are banded gray gneisses with biotite defining the foliation.

The rocks typically contain minor stromatic leucosomes (typically 2–10 cm thick), and in these, minor peritectic orthopyroxene exists in some outcrops, but is absent in others. Within the general outcrop, biotite is always more volumetrically abundant than orthopyroxene, by at least a factor of 10. These characteristics are consistent with incipient biotite fluid-absent melting via the reaction:  $\text{Bt} + \text{Qtz} + \text{Pl} = \text{Opx} + \text{Melt}$ . Appropriate experiments suggest a temperature of 840 to 850 °C as the peak metamorphic temperature for these rocks.

Thus, UHT metamorphism in the SMZ is impossible because the rocks contain abundant biotite at the peak of metamorphism and do not record the obvious macroscopic evidence consistent with the whole terrain being 40–85 % melt that would have been produced by such metamorphism. Consequently, it is necessary to seek alternative explanations for the assemblages and mineral chemistries documented by Belyanin et al. (2012).

In general, the assemblages documented by Belyanin et al. (2012) occur as fine-grained ( $\mu\text{m}$  scale) intergrowths of minerals. These intergrowths occur as rims around a much more coarse-grained granulite-facies assemblage, or interstitial to this assemblage. The very small crystal sizes are extremely unusual for assemblages proposed to have formed at >1,000 °C in a long-lived, regional metamorphic event. There are two explanations that may reconcile these UHT assemblages with the overwhelming evidence in support of peak metamorphic temperatures in the general SMZ not exceeding 900 °C. The first of these is the possibility that the UHT rocks represent local heating. The hypothesis that this might have occurred via magma transfer does not appear to fit the field evidence and the fact that evidence for UHT has been proposed from two different types of rocks in two different localities (Belyanin

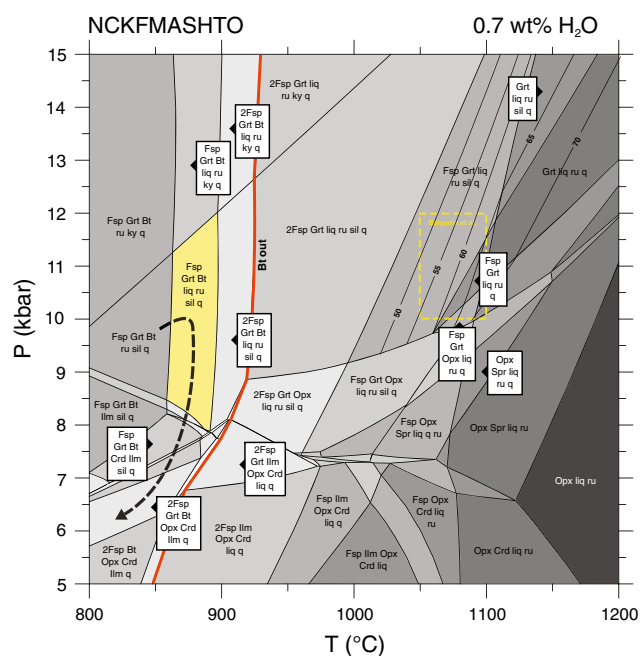


**Fig. 2** A PT pseudosection for a typical granulite-facies metapelite from the Southern Marginal Zone (Bandelierkop quarry outcrop). The peak metamorphic assemblage in this rock is: Grt + Qtz + Melt + Pl + Bt + sil + ru (Melt: 0–1 vol%). The rock composition is: SiO<sub>2</sub>: 58.85 wt%, TiO<sub>2</sub>: 0.98 wt%, Al<sub>2</sub>O<sub>3</sub>: 19.08 wt%, FeO: 7.88 wt%, MnO: 0.1 wt%, MgO: 7.06 wt%, CaO: 1.49 wt%, Na<sub>2</sub>O: 1.34 wt%, K<sub>2</sub>O: 2.38 wt%. Fe<sub>2</sub>O<sub>3</sub> and H<sub>2</sub>O have been estimated using Perple\_X T-X section at 9 kbar. The value chosen for Fe<sub>2</sub>O<sub>3</sub> and H<sub>2</sub>O were 0.02 and 0.7 wt%, respectively. Phase equilibria modeling was undertaken in the chemical system NCKFMASHTO using THERIAK-DOMINO software (de Capitani and Petrakakis 2010), in combination with the updated HoPomelt dataset that includes silicate melt and A–X models by Baldwin et al. (2005), White et al. (2007) and Holland and Powell (1998). The arrow represents the retrograde path proposed for the SMZ consistent with the ones modeled by Stevens and van Reenen (1992a,b), Van Reenen (1983). The dashed-line box represents the peak of metamorphism proposed by Belyanin et al. (2012). Isopleths for melt proportion (vol%) have been plotted in the area of interest. Mineral abbreviations are after Kretz (1983). An equivalent PT pseudosection has been calculated with Perple\_X to investigate the impact of Biot(TCC) (Tajcmanová et al. 2009) or TiBio(WPH) (White et al. 2007) on biotite stability. Both of these models produce a similar biotite-out temperature to that achieved in the THERIAK-DOMINO modeling

et al. 2012; Tsunogae et al. 2004). Shear heating of such discrete small domains in the ductile, partially melted crust would appear to be impossible (Camacho et al. 2001). The second alternative is that the UHT finding is incorrect. We consider this to be a much more likely possibility for the reasons outlined below.

The UHT assemblages: Fine-grained intergrowths and symplectites of high-grade metamorphic minerals developed as rims on a preexisting coarse-grained assemblage are typically the consequence of reaction between phases, commonly as a consequence of changing volume of equilibration, due to decreasing PT conditions and/or melt

loss (Waters 2001). The assemblages cited by Belyanin et al. 2012 generally only have UHT significance if quartz is part of the assemblage. In the case of the intergrowths in question, it is highly doubtful whether this is the case.

Ternary feldspar thermometry: Belyanin et al. (2012) observe perthite and antiperthite in the granulites. From the images presented, these appear to be part of the coarser-grained granulite-facies assemblage. Thus, they are overprinted by the symplectic assemblages alleged to constitute a case for UHT. It is doubtful that parts the rock texture developed at different times could both constitute a valid case for equilibration under peak metamorphic conditions. Belyanin et al. (2012) reintegrate the feldspar compositions in order to apply ternary feldspar thermometry (Fuhrman and Lindsley 1988). The application of this thermometer is based on the hypothesis that a ternary feldspar was stable at peak metamorphic conditions and that the intergrowths observed in thin section are the results of exsolution. Exsolution is crystallographically controlled. Thus, it is feasible that the calculated or measured integrated feldspar compositions are variable with orientation relative to the plane of the thin section. Additionally, the compositional variation of feldspar with temperature is controlled by many parameters, such as silica and water activity. In partially melted rocks that very likely underwent melt loss during high-temperature metamorphism, these parameters are not constant during metamorphic evolution. Additionally, the co-precipitation of plagioclase and alkali-feldspar during the cooling may produce textures that are similar to exsolution features, and the concurrent crystallization of two feldspars may be expected during the crystallization of a granitic melt fraction. Therefore, ternary feldspar thermometry should be handled with care, and the results will always be open to question if inconsistent with more conclusive and simpler estimates of metamorphic temperature, as is the case in this example.

Al in Opx: Al-in-Opx thermometry in UHT quartz-bearing granulite-facies rocks is a very useful tool for constraining temperature, commonly providing accurate temperature estimates for peak temperature in UHT rocks equilibrated in the temperature range between 1,000 and 1,100 °C (Guiraud et al. 1996; Ouzegane et al. 2003; Shaw and Arima 1998). In such rocks, temperature is the only parameter that controls the content of Al<sub>2</sub>O<sub>3</sub> in Opx. However, when the rock becomes quartz deficient, the silica content of the system has a direct influence on the partitioning of Al<sub>2</sub>O<sub>3</sub> into Opx (Kelsey 2007; Kelsey et al. 2003). As a consequence, Al-in-Opx thermometry cannot be used to constrain peak temperature for quartz under saturated rocks. Belyanin et al. (2012) use such thermometry on Opx crystals produced in the Al<sub>2</sub>O<sub>3</sub>-rich (38.70 wt%) SiO<sub>2</sub>-depleted (37.72 wt%) layer. Therefore, the temperatures are likely to be an overestimate and

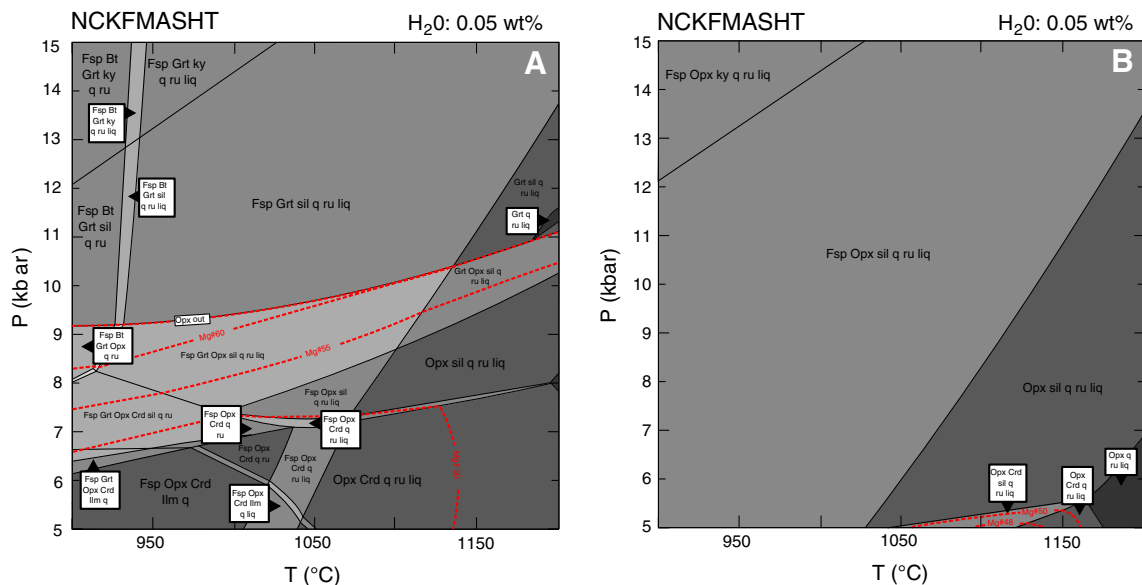


**Fig. 3** Pseudosections for the Si-rich layer of Belyanin et al. (2010) in the chemical system NCKFMASHT calculated using Perple\_X. The rock composition is: SiO<sub>2</sub>: 61.51 wt%, TiO<sub>2</sub>: 0.21 wt%, Al<sub>2</sub>O<sub>3</sub>: 16.72 wt%, FeO: 9.74 wt%, MgO: 10.15 wt%, CaO: 0.12 wt%, Na<sub>2</sub>O: 0.25 wt%, K<sub>2</sub>O: 1.21 wt%, with H<sub>2</sub>O content assumed at 0.05 wt% from the restitic character of the rock. Both phase diagrams use hp04ver.dat and solut\_09.dat (Holland and Powell 1998). Solid-solution models used to establish pseudosection A are: TiBio(WPH) (White et al. 2007), Oxp (HP), melt(HP) (Holland and Powell 2001; White et al. 2001), hCrD (Thompson and Hovis 1979), Gt(WPH)

(Holland and Powell 2003) and feldspar (Fuhrman and Lindsley 1988). Solid-solution models used to establish pseudosection B are identical except for using Opx(stx) and Grt(stx) (Stixrude and Lithgow-Bertelloni 2005) in place of Opx(HP) and Gt(WPH). In both cases, orthopyroxene Mg# isopleths have been plotted. In the analysis of metamorphic conditions conducted by Belyanin et al. (2010), Mg# in Opx is important in determining the peak temperature condition, yet this parameter has been heavily influenced by an inappropriate combination of solid-solution models and thermodynamic dataset

cannot reliably reflect the peak metamorphic temperature. Interestingly, the study by Tsunogae et al. (2004) also produced high Al-in-Opx temperatures for individual Opx crystals in quartz-bearing rocks where the majority of Opx crystals produced peak estimates in the 850 °C range via this method. In the SMZ metapelitic granulites, Opx is produced near peak metamorphic conditions by both melting reactions that consume biotite, quartz and plagioclase, and by garnet decompression reactions that consume garnet and quartz (Stevens and van Reenen 1992b):  $Grt + Qtz = Crd + Opx$ . Thus, quartz-Opx coexistence cannot be assumed, and particularly in the case of decompression reactions occurring once melt has left the assemblage, it is very likely that some garnet breaks down in the absence of quartz. This produces spinel crystals in association with the cordierite and Opx replacing garnet. We suggest that the anomalous Al-in-Opx temperatures consistent with UHT conditions from individual crystals within quartz-bearing SMZ rocks with general Al-in-Opx temperatures that are consistent with the presence of peak metamorphic biotite are produced by transient quartz-absent conditions in local domains in rocks within which garnet was breaking down by decompression reactions.

Phase diagram modeling remains the best option to constrain peak metamorphism conditions (Prakash and

Sharma 2008; Kelsey et al. 2003) in partially melted granulites. However, Belyanin et al. (2012) do not provide enough information about their modeling for it to be tested completely. They base their calculation on KFMASHT and NCKFMASHT systems, but do not provide precise information about the bulk rock water content, Fe<sub>2</sub>O<sub>3</sub> content, nor the thermodynamic datafile used in the calculations. This last point is particularly problematic because the solid-solution models used appear to be incompatible with the thermodynamic datafile implied by the inclusion of melt in their assemblages. Melt-present assemblage implies the use of a Holland and Powell thermodynamic dataset. However, the A–X models used for garnet and orthopyroxene by Belyanin et al. (2012) are only appropriate for use with the Stixrude and Lithgow-Bertelloni (2005) thermodynamic dataset, which is designed for constraining rock behavior under mantle  $P$ – $T$  conditions. Figure 3 replicates this apparent mistake for one of the compositions studied by Belyanin et al. (2012) and illustrates the magnitude of the shift in assemblage fields and mineral compositional isopleths that may result.

In conclusion, no mechanism has been identified to generate local substantial temperature excursions in the SMZ granulites, and the mineral associations and mineral chemistries that have been used to propose the UHT

evolution are all subject to significant uncertainty or misinterpretation. The proposed UHT conditions are completely inconsistent with the widespread preservation of biotite through the peak metamorphic event and the fact that the anatectic features, mineral assemblages and mineral compositions in almost all rocks from the granulite zone are consistent with a peak metamorphic temperature in the region of 850 °C. Consequently, we regard the notion of UHT metamorphism in the SMZ as both unsupported by the evidence and impossible in the regional context.

## References

- Baldwin JA, Powell R, Brown M, Moraes RA, Fuck RA (2005) Modelling of mineral equilibria in ultrahigh-temperature metamorphic rocks from the Anápolis–Itaçu Complex, central Brazil. *J Metamorph Geol* 23:511–532. doi:[10.1111/j.1525-1314.2005.00591.x](https://doi.org/10.1111/j.1525-1314.2005.00591.x)
- Barton JM, Van Reenen DD (1992) When was the Limpopo Orogeny? *Precambrian Res* 55:7–16. doi:[10.1016/0301-9268\(92\)90010-L](https://doi.org/10.1016/0301-9268(92)90010-L)
- Barton JM, Doig R, Smith CB, Bohlender F, Van Reenen DD (1992) Isotopic and REE characteristics of the intrusive charnoenderbite and enderbite geographically associated with the Matok Pluton, Limpopo belt, Southern Africa. *Precambrian Res* 55:451–567. doi:[10.1016/0301-9268\(92\)90039-Q](https://doi.org/10.1016/0301-9268(92)90039-Q)
- Belyanin GA, Rajesh HM, van Reenen DD, Mouri H (2010) Corundum + orthopyroxene ± spinel intergrowths in an ultrahigh-temperature Al–Mg granulite from the Southern Marginal Zone, Limpopo Belt, South Africa. *Am Mineral* 95:196–199. doi:[10.2138/am.2010.3383](https://doi.org/10.2138/am.2010.3383)
- Belyanin GA, Rajesh HM, Sajeev K, van Reenen DD (2012) Ultrahigh-temperature metamorphism from an unusual corundum + orthopyroxene intergrowth bearing Al–Mg granulite from the Southern Marginal Zone, Limpopo Complex, South Africa. *Contrib Mineral Petrol* 164:457–475. doi:[10.1007/s00410-012-0747-3](https://doi.org/10.1007/s00410-012-0747-3)
- Camacho A, McDougall I, Armstrong R, Braun J (2001) Evidence for shear heating, Musgrave Block, Central Australia. *J Struct Geol* 23:1007–1013. doi:[10.1016/S0191-8141\(00\)00172-3](https://doi.org/10.1016/S0191-8141(00)00172-3)
- Carson CJ, Powell R, Wilson CJL, Dirks PHGM (1997) Partial melting during tectonic exhumation of a granulite terrane: an example from the Larsemann Hills, East Antarctica. *J Metamorph Geol* 15:105–126. doi:[10.1111/j.1525-1314.1997.00059.x](https://doi.org/10.1111/j.1525-1314.1997.00059.x)
- De Capitani C, Petrakakis K (2010) The computation of equilibrium assemblage diagrams with Theriak/Domino software. *Am Miner* 95:1006–1016. doi:[10.2138/am.2010.3354](https://doi.org/10.2138/am.2010.3354)
- Elington BM, Armstrong EA (2004) The Kaapvaal Craton and adjacent orogens, southern Africa: a geochronological database and overview of the geological development of the craton. *S Afr J Geol* 10:13–32. doi:[10.2113/107.1-2.13](https://doi.org/10.2113/107.1-2.13)
- Fuhrman ML, Lindsley DH (1988) Ternary-feldspar modeling and thermometry. *Am Mineral* 73:201–215
- Guiraud M, Kienast JR, Ouzegane K (1996) Corundum–quartz bearing assemblage in the Ihouhaouene area (In Ouzal, Algeria). *J Metamorph Geol* 14:755–761. doi:[10.1111/j.1525-1314.1996.00046.x](https://doi.org/10.1111/j.1525-1314.1996.00046.x)
- Holland TJB, Powell R (1998) An internally consistent thermodynamic data set for phases of petrological interest. *J Metamorph Geol* 16:309–343. doi:[10.1111/j.1525-1314.1998.00140.x](https://doi.org/10.1111/j.1525-1314.1998.00140.x)
- Holland T, Powell R (2001) Calculation of phase relations involving haplogranitic melts using an internally consistent thermodynamic dataset. *J Petrol* 42:673–683. doi:[10.1093/ptrology/42.4.673](https://doi.org/10.1093/ptrology/42.4.673)
- Holland T, Powell R (2003) Activity–composition relations for phase in petrological calculations: an asymmetric multicomponent formulation. *Contrib Mineral Petrol* 10:395–406. doi:[10.1007/s00410-003-0464-z](https://doi.org/10.1007/s00410-003-0464-z)
- Kelsey DE (2007) On ultrahigh-temperature crustal metamorphism. *Gondwana Res*. doi:[10.1016/j.gr.2007.06.001](https://doi.org/10.1016/j.gr.2007.06.001)
- Kelsey DE, White RW, Powell R (2003) Orthopyroxene–sillimanite–quartz assemblages; distribution, petrology, quantitative P–T–X constraints and P–T paths. *J Metamorph Geol* 21:439–453. doi:[10.1046/j.1525-1314.2003.00456.x](https://doi.org/10.1046/j.1525-1314.2003.00456.x)
- Kreissig K, Nägler TF, Kramers JD, van Reenen DD, Smit CA (2000) An isotopic and geochemical study of the northern Kaapvaal Craton and the Southern Marginal Zone of the Limpopo Belt: are they juxtaposed terranes? *Lithos* 50:1–25. doi:[10.1016/S0024-4937\(99\)00037-7](https://doi.org/10.1016/S0024-4937(99)00037-7)
- Kretz R (1983) Symbols for rock-forming minerals. *Am Mineral* 68:277–279
- Kröner A, Jaekel P, Brandl G (2000) Single zircon ages for felsic to intermediate rocks from the Pietersburg and Giyani greenstone belts and bordering granitoid orthogneisses, northern Kaapvaal Craton, South Africa. *J Afr Earth Sci* 30:773–793. doi:[10.1016/S0899-5362\(00\)00052-X](https://doi.org/10.1016/S0899-5362(00)00052-X)
- Montel JM, Vielzeuf D (1997) Partial melting of metagreywackes. 2. Compositions of minerals and melts. *Contrib Mineral Petrol* 128:176–196. doi:[10.1007/s004100050302](https://doi.org/10.1007/s004100050302)
- Ouzegane K, Guiraud M, Kienast JR (2003) Prograde and retrograde evolution in high-temperature corundum granulites (FMAS and KFMASH systems) from In Ouzal Terrane (NW Hoggar, Algeria). *J Petrol* 44:517–545. doi:[10.1093/ptrology/44.3.517](https://doi.org/10.1093/ptrology/44.3.517)
- Patinõ Douce AE, Harris N (1998) Experimental constraints on Himalayan anatexis. *J Petrol* 39:689–710. doi:[10.1093/ptrology/39.4.689](https://doi.org/10.1093/ptrology/39.4.689)
- Patinõ Douce AE, Johnston AD (1991) Phase equilibria and melt productivity in the pelitic system: implications for the origin of peraluminous granulites and aluminous granites. *Contrib Mineral Petrol* 107:202–218. doi:[10.1007/BF00310707](https://doi.org/10.1007/BF00310707)
- Pickering JM, Johnston AD (1998) Fluid-absent melting behavior of two-mica metapelite: experimental constraints on the origin of Black Hills granite. *J Petrol* 39:1797–1894. doi:[10.1093/ptrology/39.10.1787](https://doi.org/10.1093/ptrology/39.10.1787)
- Prakash D, Sharma IN (2008) Reaction textures and metamorphic evolution of quartz-free granulites from Namlekonda (Karimnagar), Andhra Pradesh, Southern India. *Int Geol Rev* 50:1008–1020
- Rigby M, Mouri H, Brandl G (2008) A review of the pressure–temperature–time evolution of the Limpopo Belt: constraints for a tectonic model. *J Afr Earth Sci* 50:120–132. doi:[10.1016/j.jafrearsci.2007.09.010](https://doi.org/10.1016/j.jafrearsci.2007.09.010)
- Shaw RK, Arima M (1998) A corundum–quartz assemblage from the Eastern Ghats Granulite Belt, India: evidence for high P–T metamorphism? *J Metamorph Geol* 16:189–196. doi:[10.1111/j.1525-1314.1998.00073.x](https://doi.org/10.1111/j.1525-1314.1998.00073.x)
- Singh J, Johannes W (1996) Dehydration melting of tonalites, Part II. Composition of melts and solids. *Contrib Mineral Petrol* 125:26–40. doi:[10.1007/s004100050204](https://doi.org/10.1007/s004100050204)
- Stevens G, Clemens JD (1993) Fluid-absent melting and the roles of fluids in the lithosphere: a slanted summary? *Chem Geol* 108:1–17. doi:[10.1016/0009-2541\(93\)90314-9](https://doi.org/10.1016/0009-2541(93)90314-9)
- Stevens G, van Reenen DD (1992a) Partial melting and the origin of metapelitic granulites in the Southern Marginal Zone of the Limpopo Belt. *S Afr Precambrian Res* 55:303–319. doi:[10.1016/0301-9268\(92\)90030-R](https://doi.org/10.1016/0301-9268(92)90030-R)
- Stevens G, van Reenen DD (1992b) Constraints on the form of the P–T loop in the Southern Marginal Zone of the Limpopo Belt.

- S Afr Precambrian Res 55:279–296. doi:[10.1016/0301-9268\(92\)90028-M](https://doi.org/10.1016/0301-9268(92)90028-M)
- Stevens G, Clemens JD, Droop GTR (1997) Melt production during granulite-facies anatexis: experimental data from primitive metasedimentary protoliths. *Contrib Mineral Petrol* 128:352–370. doi:[10.1007/s004100050314](https://doi.org/10.1007/s004100050314)
- Stixrude L, Lithgow-Bertelloni C (2005) Thermodynamics of mantle minerals I: physical properties. *Geophys J Int* 162:610–632. doi:[10.1111/j.1365-246X.2005.02642.x](https://doi.org/10.1111/j.1365-246X.2005.02642.x)
- Tajcmanová L, Connolly JAD, Cesare B (2009) A thermodynamic model for titanium and ferric iron solution in biotite. *J Metamorph Geol* 27:153–165. doi:[10.1111/j.1525-1314.2009.00812.x](https://doi.org/10.1111/j.1525-1314.2009.00812.x)
- Taylor J, Stevens G, Armstrong R, Kisters AFM (2010) Granulite facies anatexis in the Ancient Gneiss Complex, Swaziland, at 2.73 Ga: mid-crustal metamorphic evidence for mantle heating of the Kaapvaal craton during Ventersdorp magmatism. *Precambrian Res* 177:88–102. doi:[10.1016/j.precamres.2009.11.005](https://doi.org/10.1016/j.precamres.2009.11.005)
- Thompson JB, Hovis GL (1979) Entropy of mixing in sanidine. *Am Mineral* 64:57–65. <http://hdl.handle.net/10385/1098>
- Tsunogae T, Miyano T, van Reenen DD, Smit CA (2004) Ultrahigh temperature metamorphism of the Southern Marginal Zone of the Archaean Limpopo Belt, South Africa. *J Mineral Petrol Sci* 99:213–224. doi:[10.2465/jmps.99.213](https://doi.org/10.2465/jmps.99.213)
- Van den Berg R, Huizenga JM (2001) Fluids in granulites of the Southern Marginal Zone of the Limpopo belt, South Africa. *Contrib Mineral Petrol* 141:529–545. doi:[10.1007/s004100100249](https://doi.org/10.1007/s004100100249)
- Van Reenen DD (1983) Cordierite + garnet + hypersthene + biotite-bearing assemblages as a function of changing metamorphic conditions in the Southern Marginal Zone of the Limpopo metamorphic complex. *S Afr Geol Soc S Afr Spec Publ* 8:143–167
- Vielzeuf D, Holloway JR (1988) Experimental determination of the fluid-absent melting reactions in the pelitic system. *Contrib Mineral Petrol* 98:257–276. doi:[10.1007/BF00375178](https://doi.org/10.1007/BF00375178)
- Waters DJ (2001) The significance of prograde and retrograde quartz bearing intergrowth microstructures in partially melted granulite-facies rocks. *Lithos* 56:97–110. doi:[10.1016/S0024-4937\(00\)00061-X](https://doi.org/10.1016/S0024-4937(00)00061-X)
- White RW, Powell R, Holland TJB (2001) Calculation of partial melting equilibria in the system Na<sub>2</sub>O–CaO–K<sub>2</sub>O–FeO–MgO–Al<sub>2</sub>O<sub>3</sub>–SiO<sub>2</sub>–H<sub>2</sub>O (NCKFMASH). *J Metamorph Geol* 19:139–153. doi:[10.1046/j.0263-4929.2000.00303.x](https://doi.org/10.1046/j.0263-4929.2000.00303.x)
- White RW, Powell R, Clarke GL (2003) Prograde metamorphic assemblage evolution during partial melting of metasedimentary rocks at low pressures: migmatites from Mt Stafford, Central Australia. *J Petrol* 44:1937–1960. doi:[10.1093/petrology/egg065](https://doi.org/10.1093/petrology/egg065)
- White RW, Powell R, Holland TJB (2007) Progress relating to calculation of partial melting equilibria for metapelite. *J Metamorph Geol* 25:511–527. doi:[10.1111/j.1525-1314.2007.00711.x](https://doi.org/10.1111/j.1525-1314.2007.00711.x)
- Zeh A, Holland TJB, Klemd R (2005) Phase relationships in grunerite–garnet bearing amphibolites in the system CFMASH, with applications to metamorphic rocks from the Central Zone of the Limpopo Belt, South Africa. *J Metamorph Geol* 23:1–17. doi:[10.1111/j.1525-1314.2005.00554.x](https://doi.org/10.1111/j.1525-1314.2005.00554.x)



ELSEVIER

Contents lists available at [ScienceDirect](http://ScienceDirect)

Precambrian Research

journal homepage: [www.elsevier.com/locate/precamres](http://www.elsevier.com/locate/precamres)

## Commentary

## Comment on “Ultrahigh temperature granulites and magnesian charnockites: Evidence for the Neoproterozoic accretion along the northern margin of the Kaapvaal craton” by Rajesh et al.

O. Laurent<sup>a,\*</sup>, G. Nicoli<sup>b,c</sup>, A. Zeh<sup>a</sup>, G. Stevens<sup>b</sup>, J.-F. Moyen<sup>c</sup>, A. Vezinet<sup>c,b</sup><sup>a</sup> Institut für Geowissenschaften, Fachinheit Mineralogie, Johann Wolfgang Goethe Universität, Altenhöferallee 1, D-60438 Frankfurt am Main, Germany<sup>b</sup> Centre for Crustal Petrology, Department of Earth Sciences, Stellenbosch University, Private Bag X1, Matieland 7602, South Africa<sup>c</sup> UMR 6524-CNRS-IRD, Université Jean-Monnet, 23 rue du Dr. Michelon, 42023 Saint-Étienne, France

## ARTICLE INFO

## Article history:

Received 15 May 2014

Accepted 14 July 2014

Available online xxx

## 1. Introduction

Over the years, the Southern Marginal Zone (SMZ) of the Limpopo mobile belt has been intensively studied, as it potentially results from one of the oldest continent–continent collision on Earth. Indeed, the general consensus about the evolution of this terrane is that it underwent a single tectono–metamorphic event at ~2.7 Ga, ascribed to collision between the Kaapvaal and Zimbabwe Cratons (Barton et al., 2006; Eglington and Armstrong, 2004; Kröner et al., 2000; Kreissig et al., 2001; Roering et al., 1992; Rigby et al., 2008; Stevens and van Reenen, 1992a,b; Zeh et al., 2009). The study of the Limpopo belt, and in particular the SMZ, is therefore of primary interest to unravel the tectonic regimes that prevailed back in the late–Archean and their evolution throughout Earth history.

In a recent contribution, Rajesh et al. (2014) proposed a new “out-of-the-box” interpretation of the geological record in the SMZ, which would represent a micro–continent accreted to the northern margin of the Kaapvaal Craton during the Neoproterozoic at 2.72 Ga. The key element on which this interpretation is based is the spatial and temporal association of ultra–high temperature (UHT) granulites and magnesian charnockites, which would be a criterion to identify subduction and collision settings in Precambrian terranes. To demonstrate the occurrence of both rock types in the SMZ, Rajesh et al. (2014) provide (1) new zircon U–Pb ages of 2.72 Ga, obtained from metamorphic zircon overgrowths in proposed UHT metamorphic rocks, and (2) a new interpretation of major–element data from the spatially associated Matok pluton,

originally produced by Bohlender (1992), to reflect a magmatic arc setting at the time of intrusion.

This new interpretation, however, is in conflict with previous models and other published data, which strongly support that (1) the SMZ underwent metamorphism at “normal” granulite facies temperatures of 850–875 °C, with the preservation of a substantial volume of peak metamorphic biotite in most rocks; (2) granitoids of the Matok pluton were not generated within an arc setting but rather during the post–collisional stage of the ca. 2.72 Ga orogeny, as testified by both their age (~2.68 Ga) and chemical compositions; (3) the SMZ represent reworked material of the adjacent and overthrust Pieterburg Block, and thus cannot have been an isolated terrane prior to amalgamation with the Kaapvaal Craton.

## 2. UHT metamorphism

A detailed comment on the occurrence of UHT metamorphism proposed by Belyanin et al. (2012) and Rajesh et al. (2014) was provided by Nicoli et al. (2014); the reader is referred to this work for further details, only the key points being repeated here. The *P–T* estimates suggested by Belyanin et al. (2012) and Rajesh et al. (2014) (i.e. ~1000 °C and ~12 kbar) are inconsistent with both field observations and experimental studies. The detailed metamorphic analysis provided by Taylor et al. (2014) clearly demonstrates that the presence of peak metamorphic biotite in the Bandelierkop formation metapelites is inconsistent with peak metamorphic temperatures in excess of 900 °C. This is in agreement with earlier metamorphic studies (e.g. Stevens and van Reenen, 1992a,b), more recent conclusions from phase equilibrium modelling (Koizumi et al., 2014), as well as a very large body of experimental data on partial melting of biotite-bearing metasediments (e.g. Montel

\* Corresponding author. Tel.: +49 69 798 40133.

E-mail addresses: [laurent@em.uni-frankfurt.de](mailto:laurent@em.uni-frankfurt.de), [oscarlaurent86@gmail.com](mailto:oscarlaurent86@gmail.com) (O. Laurent).<http://dx.doi.org/10.1016/j.precamres.2014.07.010>

0301-9268/© 2014 Elsevier B.V. All rights reserved.

and Vielzeuf, 1997; Patiño Douce and Harris, 1998; Patiño Douce and Johnston, 1991; Pickering and Johnston, 1998; Stevens et al., 1997; Vielzeuf and Holloway, 1988) arguing for a temperature peak around fluid-absent biotite breakdown partial melting conditions, i.e. 820–870 °C.

In addition to these considerations about the peak temperature attained by the SMZ, it is important to note that Rajesh et al. (2014) provide no metamorphic analysis for the two dated samples (i.e. DR-19C and DR-20). Therefore, it is not clear whether the obtained metamorphic ages documented by Rajesh et al. (2014) actually reflect peak metamorphism, and if so, if the dated samples underwent the same  $P$ – $T$  conditions as the sample used for the metamorphic study (i.e. DR-19A).

### 3. Geochemical signature of the Matok pluton

#### 3.1. Terminology issues

Rajesh et al. (2014) suggest that the ~2.68 Ga granitoids of the Matok pluton are “magnesian charnockites”, a family of rocks supposedly formed in subduction settings (Frost and Frost, 2008; Rajesh, 2012), being compositionally similar to arc magmas. In this context, it must be noted that the “charnockite” appellation used by Rajesh et al. (2014) is incorrect, because it should (strictly speaking) only be used for orthopyroxene-bearing granites (Frost and Frost, 2008). However, the Matok pluton is a composite intrusion, made up of different magmatic rocks having a wide range of silica contents ( $\text{SiO}_2 = 55$ – $70$  wt.%; Laurent et al., 2014 and Fig. 5f–g of Rajesh et al., 2014), i.e. not only granites. This misuse is confusing, as Bohlen et al. (1992) clearly demonstrated that there are at least two different generations of orthopyroxene-bearing rocks in the SMZ, namely (1) metamorphic charnockites (sensu stricto), in which orthopyroxene is the dominant mafic phase and formed at the expense of biotite, presumably during dehydration melting, for example in the Baviaanskloof TTG gneisses; and (2) a suite of so-called “charnockitic rocks” (jotunites, enderbites and charnoenderbites), restricted to the Matok pluton and igneous in origin. These latter contain orthopyroxene in places, but always much less than clinopyroxene, and both phases are completely absent in the more felsic rocks (Bohlen et al., 1992; Laurent et al., 2014; Rapopo,

2010). Therefore, it is likely that several, if not most, of the samples plotted by Rajesh et al. (2014) in their discrimination diagrams are not charnockites at all, and probably not even orthopyroxene-bearing.

#### 3.2. Matok granitoids are not similar to arc magmas

Apart from the terminology issue, the geochemical arguments used by Rajesh et al. (2014) to discriminate the geodynamic setting of the “Matok charnockites” are also problematic. Indeed, the interpretation of magmatic arc affinity solely relies on the use of a few major-element data. In fact, many previous studies clearly showed that “subduction signatures” are commonly equivocal, even when trace element systematics are considered (e.g. Bédard, 2006; Rollinson, 2009; Willbold et al., 2009). The “magnesian” signature used by Rajesh (2012) and Rajesh et al. (2014) as a smoking gun to reflect a subduction origin is therefore not unambiguous, and could also characterize magmas formed in very different geodynamic environments. To support the magmatic arc setting, Rajesh et al. (2014) argue that the “Matok charnockites” formed by dehydration melting of amphibolites, in a roughly similar process to that proposed for the formation of Archean TTGs (e.g. Moyen and Martin, 2012 and references therein). However, Archean TTGs, although mostly magnesian in character, can be generated in a wide range of geodynamic environments (Fig. 1), not necessarily requiring a convergent plate margin (Moyen, 2011; Moyen and Martin, 2012).

In addition, the magnesian signature of the Matok “charnockites” is not that obvious. It is clear in Fig. 5f of Rajesh et al. (2014) that their samples are richer in Fe than typical charnockites from the Northern Marginal Zone (NMZ), several of them straddling the boundary between magnesian and ferroan groups defined by Frost et al. (2001). Moreover, the diagram presented in Fig. 5h of Rajesh et al. (2014) also shows that the Matok granitoids follow a very distinctive trend with respect to the NMZ ones, characterized by lower  $\text{Al}_2\text{O}_3/\text{CaO}$  ratios. These two characteristics (high Fe and low Al contents) have been recently highlighted by Laurent et al. (2014), who conducted a detailed petrogenetic study of the Matok granitoids on the basis of major-, trace element and Sm–Nd isotope geochemistry as well as geochemical modelling. In contrast to the suggestion made by Rajesh et al.

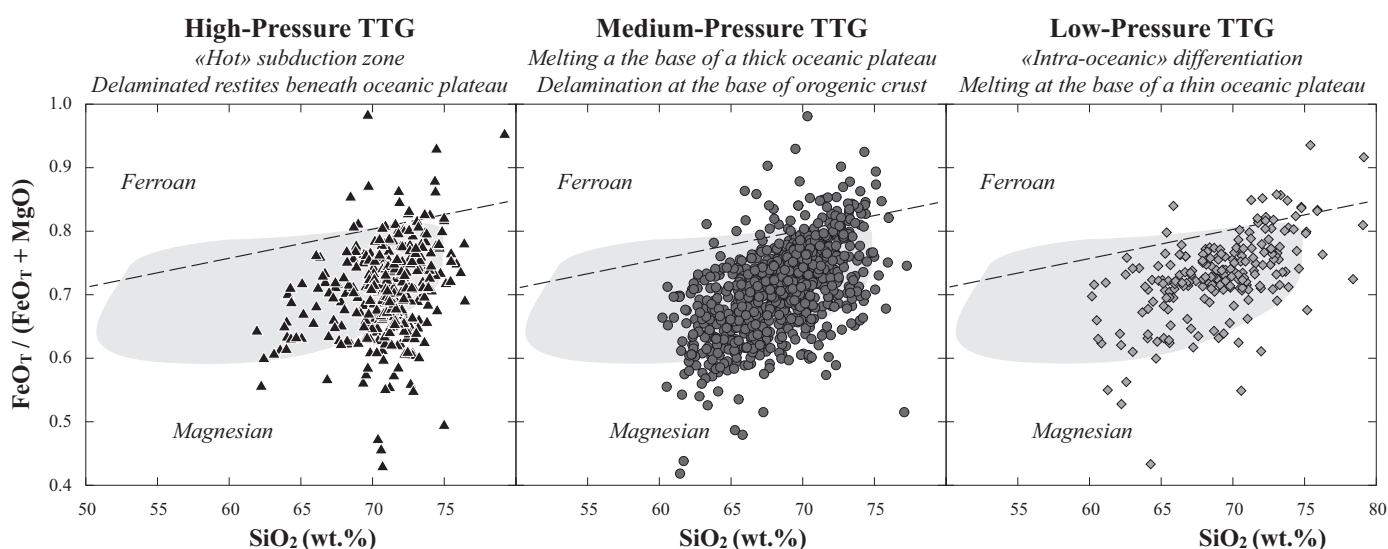


**Fig. 1.**  $\text{FeO}_T/(\text{FeO}_T + \text{MgO})$  vs.  $\text{SiO}_2$  diagram of Frost et al. (2001) presenting the composition of representative samples of the three groups of sodic TTGs defined by Moyen (2011). As specified on the top of each plot, these different groups can form in contrasted geodynamic environments, implying convergent plate settings, but also intraplate or even divergent ones (e.g. intra-oceanic differentiation at a mid-ocean ridge – see Moyen, 2011 for details and discussion). More than 90% of TTGs are magnesian, regardless the petrogenetic group they belong to and thus the geodynamic setting in which they formed. The light grey field represents the field of “magnesian charnockites” defined by Rajesh (2012).

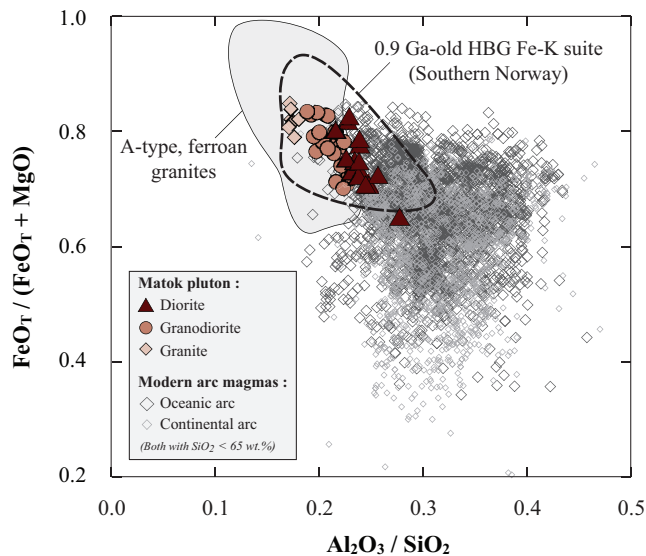


**Fig. 2.**  $\text{FeO}_t/(\text{FeO}_t + \text{MgO})$  vs.  $\text{Al}_2\text{O}_3/\text{SiO}_2$  diagram where the whole-rock compositions of granitoids from the Matok pluton (data from Laurent et al., 2014) are reported, together with that of the Proterozoic “ferro-potassic” Hornblende–Biotite–Granitoid suite of southern Norway (data from Bogaerts et al., 2003 and Vander Auwera et al., 2007) as well as typical A-type, Fe-rich granites and modern subduction-related magmas from both continental and oceanic arcs (>5000 samples from the GEOROC database). In average and at similar  $\text{SiO}_2$  contents (<65 wt.%), rocks from the Matok pluton clearly show higher  $\text{FeO}_t/(\text{FeO}_t + \text{MgO})$  and lower  $\text{Al}_2\text{O}_3/\text{SiO}_2$  than arc magmas.

(2014), Laurent et al. (2014) concluded that the Matok granitoids are akin to “ferro-potassic” suites, very common in Proterozoic terranes (e.g. Duchesne et al., 2010; Ferré et al., 1998; Peucat et al., 2005; Vander Auwera et al., 2011) and intermediate in composition between (1) Al-, Mg-rich sanukitoids and (2) Al-poor, Fe-rich anorthosite–mangerite–charnockite–granite (AMCG) suites. This intermediate composition is well illustrated in the  $\text{FeO}_t/(\text{FeO}_t + \text{MgO})$  vs.  $\text{Al}_2\text{O}_3/\text{SiO}_2$  diagram of Fig. 2. This diagram also shows unequivocally that the Matok granitoids are globally more ferroan and less aluminous than modern, classical arc magmas from both oceanic and continental convergent margins (Fig. 2).

#### 4. Geodynamic model

The geodynamic model proposed by Rajesh et al. (2014) is that the SMZ was a microcontinent, which was accreted to the northern margin of the Kaapvaal Craton by ~2.72 Ga at the latest, after a period of north-verging subduction. This interpretation, however, suffers two major problems:

- (1) This model is in conflict with the fact that the Matok pluton (suggested to be subduction related) intruded at ~2.68 Ga (U–Pb age data of Barton et al., 1992; Laurent et al., 2013; Zeh et al., 2009), whereas terrane collision happened at 2.71–2.72 Ga, as indicated by U–Pb ages of metamorphic zircons obtained from granulite-facies rocks of the SMZ (Rajesh et al., 2014; Taylor et al., 2014). Furthermore, field observations and additional age data from the Hout River Shear Zone indicate that uplift and southward thrusting of the SMZ granulites over the Pietersburg block started prior to the intrusion of the Matok pluton, i.e. around 2.70 Ga (Kreissig et al., 2001; Laurent et al., 2013). In summary, the Matok pluton is clearly 10–30 Ma younger than the inferred age of collision, such that it cannot be related to subduction and rather represents a typical post-collisional intrusion as recently proposed by Laurent et al. (2014).

- (2) Accretion of the SMZ as an individual microterrane to the northern edge of the Kaapvaal Craton is also at odds with previous studies based on Hf–Sr–Nd–Pb isotopes (e.g. Barton et al., 1992, 2006; Kreissig et al., 2000; Zeh and Gerdes, 2012; Zeh et al., 2009). These data unequivocally show that the SMZ and the adjacent rocks of the Pietersburg block actually belong to the same crustal domain. Specifically, the SMZ results from internal reworking of the Pietersburg block crust owing to continental collision at 2.72 Ga (Laurent et al., 2014; Zeh et al., 2009, 2013), with a northward-located terrane that could be represented by the Central Zone of the Limpopo belt. Internal reworking is for instance supported by Pb isotopic data indicating similarly low  $\mu$ -values ( $^{238}\text{U}/^{204}\text{Pb}$ ) of  $\leq 10$  for all rocks of the Northern Kaapvaal Craton (including the SMZ), which are very different to the high- $\mu$  rocks exposed in the Central Zone of the Limpopo belt and the Zimbabwe Craton, both having values  $\geq 11.5$  (Barton et al., 2006). Combined age and Hf isotope data also support that all granitoids of the northern Kaapvaal Craton, including the SMZ, formed by reworking of a single crustal component, which derived from a depleted mantle source between 3.3 and 3.0 Ga (e.g. Zeh and Gerdes, 2012; Zeh et al., 2009, 2013). Ortho- and paragneisses from both the SMZ and the Pietersburg block also show undistinguishable Nd model ages (2.9–3.2 Ga), as well as similar major- and trace-element systematics (Kreissig et al., 2000). It is worthwhile noting, in addition, that detrital zircon grains in the metasedimentary samples investigated by Rajesh et al. (2014) yield ages of ~3.40, ~3.33, 3.00–2.95 and 2.85–2.75 Ga. These ages actually correspond to the main magmatic episodes in the Pietersburg block (Laurent et al., 2013; Zeh et al., 2009). The youngest ages (2.85–2.75 Ga) are typical for granite emplacement (Turloop batholith and associated intrusions; Henderson et al., 2000; Kröner et al., 2000; Laurent et al., 2013; Zeh et al., 2009), whereas all ages  $\geq 2.95$  Ga are that of the Pietersburg TTGs (Kröner et al., 2000; Laurent et al., 2013; Zeh et al., 2009) and are also recorded by detrital zircons from low- to medium grade metasedimentary rocks of the Murchison and Pietersburg greenstone belts (Zeh and Gerdes, 2012; Zeh et al., 2013). All lines of evidence therefore support that rocks of the SMZ and the Pietersburg block belong to the same crustal domain, but underwent contrasted  $P$ – $T$  evolution during the ~2.72 Ga collision event.

#### 5. Conclusion

The recent contribution by Rajesh et al. (2014) proposes a new geodynamic model for the evolution of the SMZ of the Limpopo belt and the Kaapvaal Craton in the Neoproterozoic, implying that both terranes were amalgamated at ~2.72 Ga as a result of north-verging subduction and subsequent collision. The main supporting evidence for such a model is the spatial and temporal association of UHT granulites in one hand, and subduction-related magmatic rocks referred to as “magnesian charnockites” on the other hand. However, their arguments to support both (1) UHT metamorphic conditions in the SMZ; and (2) a subduction-related origin for the Matok granitoids are unreasonable and/or equivocal. Moreover, this new geodynamic model does not fit at all with the results of a great deal of previous studies in the area, and must therefore be regarded with some criticism.

Nevertheless, we believe that the data presented by Rajesh et al. (2014), especially their new U–Pb ages on detrital zircons from the SMZ, provide valuable information regarding (1) the timing of granulite-facies metamorphism and continental collision in this terrane; and (2) the provenance of the studied metasediments. These new data must be reconsidered in the scope of ongoing work



about the evolution of the Pietersburg block and the SMZ during the Neoproterozoic.

## References

- Barton Jr., J.M., Doig, R., Smith, C.B., Bohlender, F., van Reenen, D.D., 1992. Isotopic and REE characteristics of the intrusive charnoerbite and enderbite geographically associated with the Matok pluton, Limpopo belt, southern Africa. *Precambrian Res.* 55 (1–4), 451–467.
- Barton Jr., J.M., Klemm, R., Zeh, A., 2006. The Limpopo belt: a result of Archean to Proterozoic, Turkestan-type orogenesis? *Geological Society of America Special Paper* 405, 315–332.
- Bédard, J.H., 2006. A catalytic delamination-driven model for coupled genesis of Archean crust and sub-continental lithospheric mantle. *Geochim. Cosmochim. Acta* 70 (5), 1188–1214.
- Belyanin, G.A., Rajesh, H.M., Sajeev, K., van Reenen, D.D., 2012. Ultrahigh-temperature metamorphism from an unusual corundum + orthopyroxene intergrowth bearing Al-Mg granulite from the Southern Marginal Zone, Limpopo Complex, South Africa. *Contrib. Mineral. Petrol.* 164, 457–475.
- Bogaerts, M., Scailliet, B., Liégeois, J.-P., Vander Auwera, J., 2003. Petrology and geochemistry of the Lyngdal granodiorite (Southern Norway) and the role of fractional crystallization in the genesis of Proterozoic ferro-potassic A-type granites. *Precambrian Res.* 124, 149–184.
- Bohlender, F., 1992. Igneous and metamorphic charnockitic rocks associated with the Matok pluton and their significance in the Limpopo orogeny. Ph.D. thesis, Rand Afrikaans University, Johannesburg, South Africa.
- Bohlender, F., Van Reenen, D.D., Barton Jr., J.M., 1992. Evidence for metamorphic and igneous charnockites in the Southern Marginal Zone of the Limpopo belt. *Precambrian Res.* 55 (1–4), 429–449.
- Duchesne, J.C., Martin, H., Baginski, B., Wiszniewska, J., Vander Auwera, J., 2010. The origin of ferroan-potassic A-type granitoids: the case of the hornblende-biotite granite suite of the Mesoproterozoic Mazury complex, northeastern Poland. *Can. Mineral.* 48 (4), 947–968.
- Eglington, B.M., Armstrong, R.A., 2004. The Kaapvaal Craton and adjacent orogens, southern Africa: a geochronological database and overview of the geological development of the craton. *S. Afr. J. Geol.* 107, 13–32.
- Ferré, E.C., Caby, R., Peucat, J.J., Capdevila, R., Monié, P., 1998. Pan-African, post-collisional, ferro-potassic granite and quartz-monzonite plutons of Eastern Nigeria. *Lithos* 45, 255–279.
- Frost, B.R., Barnes, C.G., Collins, W.J., Arculus, R.J., Ellis, D.J., Frost, C.D., 2001. A geochemical classification for granitic rocks. *J. Petrol.* 42, 2033–2048.
- Frost, B.R., Frost, C.D., 2008. On charnockites. *Gondwana Res.* 13, 30–44.
- Henderson, D.R., Long, L.E., Barton Jr., J.M., 2000. Isotopic ages and chemical and isotopic composition of the Archean Turfloop Batholith, Pietersburg granite-greenstone terrane, Kaapvaal Craton, South Africa. *S. Afr. J. Geol.* 103 (1), 38–46.
- Koizumi, T., Tsunogae, T., van Reenen, D.D., 2014. Fluid evolution of partially retrogressed metapelites from the Southern Marginal Zone of the Neoproterozoic Limpopo Complex, South Africa: evidence from phase equilibrium modelling. *Precambrian Res.*, <http://dx.doi.org/10.1016/j.precamres.2014.04.017>.
- Kreissig, K., Holzer, L., Frei, R., Villa, I.M., Kramers, J.D., Smit, C.A., van Reenen, D.D., 2001. Geochronology of the Hout River Shear Zone and the metamorphism in the Southern Marginal Zone of the Limpopo belt, Southern Africa. *Precambrian Res.* 109, 145–173.
- Kreissig, K., Nagler, T.F., Kramers, J.D., Van Reenen, D.D., Smit, C.A., 2000. An isotopic and geochemical study of the Kaapvaal Craton and the Southern Marginal Zone of the Limpopo belt: are they juxtaposed terranes? *Lithos* 50, 1–25.
- Kröner, A., Jaekel, P., Brandl, G., 2000. Single zircon ages for felsic to intermediate rocks from the Pietersburg and Giyani greenstone belts and bordering granulite orthogneisses, northern Kaapvaal Craton, South Africa. *J. Afr. Earth Sci.* 30 (4), 773–793.
- Laurent, O., Paquette, J.-L., Martin, H., Doucelance, R., Moyen, J.-F., 2013. LA-ICP-MS dating of zircons from Meso- and Neoproterozoic granitoids of the Pietersburg block (South Africa): crustal evolution at the northern margin of the Kaapvaal craton. *Precambrian Res.* 230, 209–226.
- Laurent, O., Raposo, M., Stevens, G., Moyen, J.-F., Martin, H., Doucelance, R., Bosq, C., 2014. Contrasting petrogenesis of Mg-K and Fe-K granitoids and implications for post-collisional magmatism: case study from the late-Archean Matok pluton (Pietersburg block, South Africa). *Lithos* 196, 131–149.
- Montel, J.M., Vielzeuf, D., 1997. Partial melting of metagreywackes. 2. Compositions of minerals and melts. *Contrib. Mineral. Petrol.* 128, 176–196.
- Moyen, J.-F., 2011. The composite Archean grey gneisses: petrological significance, and evidence for a non-unique tectonic setting for Archean crustal growth. *Lithos* 123, 21–36.
- Moyen, J.-F., Martin, H., 2012. Forty years of TTG research. *Lithos* 148, 312–336.
- Nicoli, G., Stevens, S., Buick, I.S., Moyen, J.-F., 2014. A comment on “Ultrahigh-temperature metamorphism from an unusual corundum+orthopyroxene intergrowth bearing Al-Mg granulite from the Southern Marginal Zone, Limpopo Complex, South Africa” by Belyanin et al. *Contrib. Mineral. Petrol.* 167, 1022, <http://dx.doi.org/10.1007/s00410-014-1022-6>.
- Patiño Douce, A.E., Harris, N., 1998. Experimental constraints on Himalayan anatexis. *J. Petrol.* 39, 689–710.
- Patiño Douce, A.E., Johnston, A.D., 1991. Phase equilibria and melt productivity in the pelitic system: implications for the origin of peraluminous granitoids and aluminous granites. *Contrib. Mineral. Petrol.* 107, 202–218.
- Pickering, J.M., Johnston, A.D., 1998. Fluid-absent melting behavior of two-mica metapelite: experimental constraints on the origin of Black Hills granite. *J. Petrol.* 39, 1797–1894.
- Peucat, J.J., Capdevila, R., Drareni, A., Mahdjoub, Y., Kahouri, M., 2005. The Eglab massif in the West African Craton (Algeria), an original segment of the Eburnean orogenic belt: petrology, geochemistry and geochronology. *Precambrian Res.* 136, 309–352.
- Rajesh, H.M., 2012. A geochemical perspective on the episodic charnockite magmatism in peninsular India. *Geosci. Front.* 3, 773–788.
- Rajesh, H.M., Santosh, M., Wan, Y., Liu, D., Liu, S.J., Belyanin, G.A., 2014. Ultrahigh temperature granulites and magnesian charnockites: evidence for Neoproterozoic accretion along the northern margin of the Kaapvaal Craton. *Precambrian Res.* 246, 150–159.
- Raposo, M., (MSc. thesis) 2010. Petrogenesis of the Matok pluton, South Africa: implications on the heat source that induced regional metamorphism in the Southern Marginal Zone of the Limpopo belt. University of Stellenbosch, South Africa.
- Rigby, M., Mouri, H., Brandl, G., 2008. A review of the pressure-temperature-time evolution of the Limpopo belt: constraints for a tectonic model. *J. Afr. Earth Sci.* 50 (2–4), 120–132.
- Roering, C., van Reenen, D.D., Smit, C.A., Barton, J.M., de Beer, J.H., de Wit, M.J., Stettler, E.H., van Schalkwyk, J.F., Stevens, G., Pretorius, S., 1992. Tectonic model for the evolution of the Limpopo belt. *Precambrian Res.* 55, 539–552.
- Rollinson, H., 2009. New models for the genesis of plagiogranites in the Oman ophiolite. *Lithos* 112 (3–4), 603–614.
- Stevens, G., Clemens, J.D., Droop, G.T.R., 1997. Melt production during granulite-facies anatexis: experimental data from primitive metasedimentary protoliths. *Contrib. Mineral. Petrol.* 128, 352–370.
- Stevens, G., van Reenen, D.D., 1992a. Partial melting and the origin of metapelitic granulites in the Southern Marginal zone of the Limpopo belt, South Africa. *Precambrian Res.* 55, 303–319.
- Stevens, G., van Reenen, D.D., 1992b. Constraints on the form of the P-T loop in the Southern Marginal zone of the Limpopo belt, South Africa. *Precambrian Res.* 55, 279–296.
- Taylor, J., Nicoli, G., Stevens, G., Frei, D., Moyen, J.-F., 2014. The processes that control leucosome compositions in metasedimentary granulites: perspectives from the Southern Marginal Zone migmatites, Limpopo belt, South Africa. *J. Metamorph. Geol.*, <http://dx.doi.org/10.1111/jmg.12087>.
- Vander Auwera, J., Bogaerts, M., Bolle, O., Longhi, J., 2007. Genesis of intermediate igneous rocks at the end of the Sveconorwegian (Grenvillian) orogeny (S Norway) and their contribution to intracrustal differentiation. *Contrib. Mineral. Petrol.* 156, 721–743.
- Vander Auwera, J., Bolle, O., Bingen, B., Liégeois, J.-P., Bogaerts, M., Duchesne, J.-C., de Waele, B., Longhi, J., 2011. Sveconorwegian massif-type anorthosites and related granulites result from post-collisional melting of a continental arc root. *Earth Sci. Rev.* 107, 375–397.
- Vielzeuf, D., Holloway, J.R., 1988. Experimental determination of the fluid-absent melting reactions in the pelitic system. *Contrib. Mineral. Petrol.* 98, 257–276.
- Willbold, M., Hegner, E., Stracke, A., Rocholl, A., 2009. Continental geochemical signatures in dacites from Island and implications for models of early Archean crust formation. *Earth Planet. Sci. Lett.* 279 (1–2), 44–52.
- Zeh, A., Gerdes, A., 2012. U-Pb and Hf isotope record of detrital zircons from gold-bearing sediments of the Pietersburg Greenstone belt (South Africa) – is there a common provenance with the Witwatersrand Basin? *Precambrian Res.* 204–205, 46–56.
- Zeh, A., Gerdes, A., Barton Jr., J.M., 2009. Archean accretion and crustal evolution of the Kalahari Craton – the Zircon Age and Hf Isotope Record of Granitic Rocks from Barberton/Swaziland to the Francistown Arc. *J. Petrol.* 50, 933–966.
- Zeh, A., Jaguin, J., Poujol, M., Boulvais, P., Block, S., Paquette, J.-L., 2013. Juvenile crust formation in the northeastern Kaapvaal Craton at 2.97 Ga – implications for Archean terrane accretion, and the source of the Pietersburg gold. *Precambrian Res.* 233, 20–43.

## Chapter 3

# Constrain the P-T-t evolution of the SMZ

## Presentation of the publications

This paper<sup>1</sup>, first authored by Gautier Nicoli, was accepted for publication in the *Journals of Metamorphic Geology*. The following aspects of the research were done independently by Gautier Nicoli while receiving standard supervision by his supervisors Gary Stevens and Jean-François Moyen: (i) fieldwork and sampling; (ii) zircon separation, and preparation of zircon for LA–SF–ICP–MS dating; (iii) acquisition of mineral chemical data on the SEM and zircon U–Pb data on the LA–SF–ICP–MS; (iv) mineral equilibria modelling in Theriak-Domino and PerpleX; (v) writing of the manuscript. Zircon U–Pb LA–SF–ICP–MS data reduction was done by Dirk Frei.

**Gautier Nicoli<sup>a,b</sup>**

**Gary Stevens<sup>a</sup>**

**Jean-François Moyen<sup>b</sup>**

**Dirk Frei<sup>a</sup>**

a: Center for Crustal Petrology, Department of Earth Sciences, Stellenbosch University, Private Bag X1, Matieland 7602, South Africa

b: UMR 6524 CNRS & Université Jean-Monnet, 23 rue du Dr Michelon, 42023 Saint-Etienne, France

---

<sup>1</sup>Nicoli, G., Stevens, S., Moyen, J-F. & Frei, D.. 2014. Rapid evolution from sediment to anatectic granulite in an Archean continental collision zone: The example of the Bandelierkop Formation metapelites, Southern Marginal Zone, Limpopo Complex, South Africa. *Journal of Metamorphic Geology*, doi: 10.1111/jmg.12116

# Rapid evolution from sediment to anatectic granulite in an Archean continental collision zone: the example of the Bandelierkop Formation metapelites, South Marginal Zone, Limpopo Belt, South Africa

G. NICOLI,<sup>1,2</sup> G. STEVENS,<sup>1</sup> J.-F. MOYEN<sup>2</sup> AND D. FREI<sup>1</sup>

<sup>1</sup>Centre for Crustal Petrology, Department of Earth Sciences, Stellenbosch University, Private Bag X1, Matieland 7602, South Africa ([gnicoli@sun.ac.za](mailto:gnicoli@sun.ac.za))

<sup>2</sup>UMR 6524 CNRS & Université Jean Monnet, 23 rue du Dr Michelon, 42023 Saint-Etienne, France

**ABSTRACT** The metamorphic history of the Southern Marginal Zone (SMZ) of the Limpopo Belt, South Africa, possibly provides insight into one of the oldest preserved continental collision zones. The SMZ consists of granitoid gneisses (the Baviaanskloof Gneiss) and subordinate, infolded metasedimentary, metamafic and meta-ultramafic lithologies (the Bandelierkop Formation) and is regarded as the *c.* 2700 Ma granulite facies reworked equivalent of the Kaapvaal craton basement. The granulite facies metamorphism is proposed to have occurred in response to collision between the Kaapvaal and Zimbabwe cratons. Previous studies have proposed a wide variety of *P–T* loops for the granulites, with considerable discrepancy in both the shapes of the retrograde paths and the magnitude of the peak *P–T* conditions. To date, the form of the prograde path and the timing of the onset of metamorphism remain unknown. This study has used a range of different metasedimentary rocks from a large migmatitic quarry outcrop to better constrain the metamorphic history and the timing of metamorphism in the SMZ. Detrital zircon ages reveal that the protoliths to the metasedimentary rocks were deposited subsequent to  $2733 \pm 13$  Ma. Peak metamorphic conditions of  $852.5 \pm 7.5$  °C and  $11.1 \pm 1.3$  kbar were attained at  $2713 \pm 8$  Ma. The clockwise *P–T* path is characterized by heating in the sillimanite field along a *P–T* trajectory which approximately parallels the kyanite to sillimanite transition, followed by near-isothermal decompression at peak temperature and near-isobaric cooling at  $\sim 6.0$  kbar. These results support several important conclusions. First, the sedimentary rocks from the Bandelierkop Formation are not the equivalent of any of the greenstone belt sedimentary successions on the Kaapvaal craton, as has been previously proposed. Rather, they post-date the formation of the Dominion and Witwatersrand successions on the Kaapvaal craton. From the age distribution of detrital zircon, they appear to have received significant input from various origins. Consequently, at *c.* 2730 Ma, the Baviaanskloof Gneiss most likely acted as basement onto which the sedimentary succession represented by the Bandelierkop Formation metapelites was deposited. Second, the rocks of the SMZ underwent rapid evolution from sediment to granulite facies anatexis, with a burial rate of  $\sim 0.17$  cm yr<sup>-1</sup>. Peak metamorphism was followed by an isothermal decompression to  $787.5 \pm 32.5$  °C and  $6.7 \pm 0.5$  kbar and isobaric cooling to amphibolite facies conditions, below 640 °C prior to  $2680 \pm 6$  Ma. This age for the end of the high-grade metamorphic event is marked by the intrusion of crosscutting, undeformed pegmatites that are within error the same age as the crosscutting Matok intrusion ( $2686 \pm 7$  Ma). Collectively, the burial rate of the sedimentary rocks, the shape of the *P–T* path, the burial of the rocks to in excess of 30 km depth and the post-peak metamorphic rapid decompression argue strongly that the SMZ contains sediments deposited along an active margin during lateral convergence, and that the SMZ was metamorphosed as a consequence of continental collision along the northern margin of the Kaapvaal craton at *c.* 2700 Ma.

**Key words:** Archean orogen; granulite; phase equilibria modelling; *P–T–t* path; zircon dating.

## INTRODUCTION

The metamorphic record represents a powerful tool for understanding both present-day and ancient geodynamic processes and has considerable potential to

contribute to our understanding of Archean geodynamic processes. Well-constrained *P–T–t* paths exist for specific metamorphic events within major Archean provinces such as the Superior Province, Canada (Easton, 2000; Valli *et al.*, 2004; Benn, 2006;

Percival & Helmstaedt, 2006) and Yilgarn craton, Australia (Goleby *et al.*, 2004; Goscombe *et al.*, 2009). The addition of seismic profiles through the crust in these areas (Drummond *et al.*, 2000; Ludden & Hynes, 2000) provides strong evidence supporting the idea that horizontal tectonic processes resulted in the successive lateral accretion of individual blocks or volcanic arcs at *c.* 2700 Ma (Sawyer & Benn, 1993; Jackson & Cruden, 1995; Myers, 1995). In South Africa, the Kaapvaal craton also possesses a strong metamorphic-structural grain that is well exposed along the Eastern Mpumalanga escarpment (Poujol *et al.*, 2003; Diener *et al.*, 2005; Moyen *et al.*, 2006; Stevens & Moyen, 2007; Block *et al.*, 2013). From the south to the north, this portion of the craton is organized into domains of 3550–3100 Ma gneissic granitoid rocks that were assembled within the interval 3230–2880 Ma (Eglington & Armstrong, 2004; Schmitz *et al.*, 2004; Schoene *et al.*, 2008). The individual domains are commonly delimited by E–W-trending greenstone belts, typically metamorphosed under greenschist to amphibolite facies conditions. The northern boundary of the craton is defined by the granulite facies Limpopo Belt, where the Southern Marginal Zone (SMZ) of the Limpopo Belt is directly in contact with the northern edge of the Kaapvaal craton along the Hout River Shear Zone (HRSZ; Roering *et al.*, 1992a) (Fig. 1a). This sequence of Archean rocks has been interpreted to be the consequence of long-lived N–S-directed tectonic forces and the general consensus is that the SMZ preserves the evidence of collision between the Kaapvaal

and Zimbabwe cratons at *c.* 2.7 Ga (Van Reenen *et al.*, 1992; Kreissig *et al.*, 2000; Poujol *et al.*, 2003; Khoza *et al.*, 2013; Laurent *et al.*, 2014). Thus, it has been argued that these rocks provide support for the hypothesis that lateral tectonics operated on Earth in the Neoproterozoic.

However, despite many studies on the geology of the Limpopo Belt, it is still difficult to precisely constrain the geodynamic history that has shaped the belt. It has been demonstrated that the Central Zone (CZ) of the belt has a polymetamorphic history, with both an older, 3.2–3.1 Ga (Holzer *et al.*, 1998) and a younger, *c.* 2.0 Ga granulite facies overprint (Kreissig *et al.*, 2001; Buick *et al.*, 2006; Zeh *et al.*, 2010); neither of which are recorded by the rocks of the SMZ. The SMZ experienced a single granulite facies metamorphic event at *c.* 2.7 Ga. In addition, the contact between the CZ and the SMZ records a *c.* 2.0 Ga strike-slip sense of motion (Holzer *et al.*, 1998; Kreissig *et al.*, 2000), which makes the *c.* 2.7 Ga spatial relationships between the two blocks unclear. Consequently, both blocks may have followed different histories prior to *c.* 2.0 Ga. The current *P–T* information available from the SMZ is inadequate to properly constrain the causative tectonic processes behind the *c.* 2.7 Ga metamorphic event. There are several reasons for this. First, the published metamorphic constraints generally only use exchange thermobarometry, with the added complication that the works published by Perchuk *et al.* (2000, 2006) combine mineral compositions that are from the same thin section, but where the textural association of the

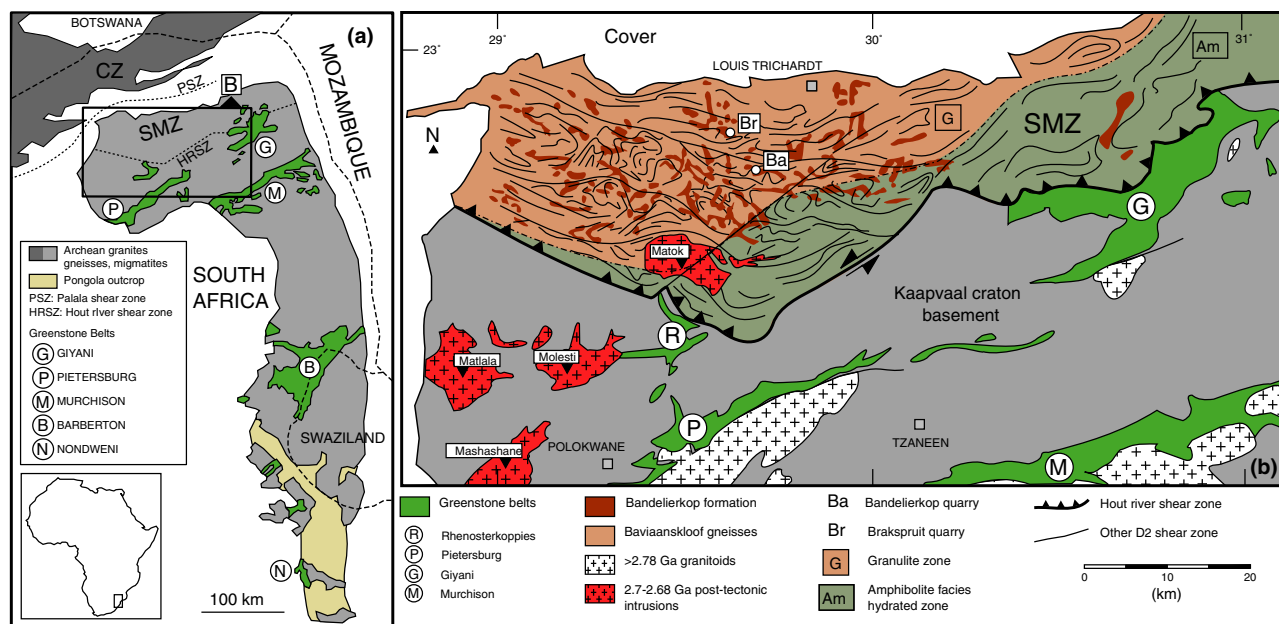


**Fig. 1.** (a) Kaapvaal craton overview. (b) The Limpopo Belt is subdivided into three zones: the Central Zone (CZ), the Northern Marginal Zone (NMZ) and the Southern Marginal Zone (SMZ). It separates the Zimbabwe craton (north) from the Kaapvaal craton (south). The map shows the geology of the SMZ (modified after Stevens, 1997) and the location of Brakspruit quarry (Br) and Bandelierkop quarry (Ba).

minerals is undefined. This is generally a questionable strategy, but doubly so in rocks such as these with multiple generations of some of the important ferromagnesian phases (e.g. Van Reenen *et al.*, 1987; Stevens & Van Reenen, 1992a; Nicoli *et al.*, 2014; Taylor *et al.*, 2014). Second, as discussed in more detail below, the published  $P$ – $T$  loops from rocks that are closely spatially associated and similar in terms of mineral assemblages and textures are sufficiently different that they are unlikely to all be correct. Last, as a consequence of the focus on exchange thermobarometry, no information is available on the prograde metamorphic history. Consequently, the  $P$ – $T$ – $t$  evolution of the SMZ granulites is relatively poorly constrained and there is no information available on the duration of the prograde path, although post- and syn-metamorphic intrusions provide some constraints on the timing of the retrograde path (see section below). This paper seeks to contribute to the understanding of how the SMZ granulites formed in two different ways: First, through better constraining the metamorphic evolution of the SMZ by investigating an exceptionally well-exposed quarry in which fresh migmatitic, metapsammitic and metapelitic granulites of variable compositions are accessible in three-dimensional exposure. The extent of exposure and the range of metasedimentary rock compositions available far exceed any other known locality in the SMZ. This range of rock types will aid in achieving a more tightly constrained metamorphic evolution than currently exists. In addition, U–Pb geochronology on detrital and metamorphic zircon within the metasedimentary rocks will provide information on the timing of sedimentation and metamorphism as well as a maximum constraint on the duration of burial and prograde metamorphism.

## REGIONAL SETTING AND PREVIOUS METAMORPHIC WORKS IN THE SMZ

The SMZ is a complex terrane that predominantly consists of a variety of grey granitoid gneisses (i.e. Baviaanskloof Gneiss), with bodies of metasedimentary granulites and metamafic and meta-ultramafic rocks (i.e. the Bandelierkop Formation), included within the gneisses (Fig. 1b) (Du Toit *et al.*, 1983). These rocks are proposed to represent the granulite facies reworked equivalent of the Kaapvaal craton basement. Thus, the Bandelierkop Formation is proposed to represent dismembered and metamorphosed greenstone belt lithologies, while the Baviaanskloof Gneiss is interpreted to represent the granulite facies-metamorphosed trondhjemites and tonalites of the Kaapvaal craton basement (e.g. Roering *et al.*, 1992a; Van Reenen *et al.*, 1992). The metasedimentary granulites of the Bandelierkop Formation have undergone partial melting via a range of biotite-incongruent melting reactions resulting in the formation of migmatites (Stevens & Van Reenen, 1992a;

Taylor *et al.*, 2014). The SMZ is separated from the Kaapvaal craton by the HRSZ along which the granulites have been thrust over the amphibolite to greenschist facies rocks of the northern Kaapvaal craton (Roering *et al.*, 1992a; Kreissig *et al.*, 2001). A zone of amphibolite facies rocks is developed in the SMZ to the north of the HRSZ, defining an orthoamphibole isograd at the contact between these rocks and the granulites (Van Reenen, 1986). This has been interpreted in different ways: Van Reenen (1986) proposed retrogression of the granulites by  $H_2O$ – $CO_2$ -dominated fluids, which infiltrated the granulites along the HRSZ; Vennemann & Smith (1992) proposed that layer-scale variations in carbon isotope ratios within the graphitic metasedimentary rocks ruled out reaction with an externally derived  $CO_2$ -rich fluid and proposed instead a prograde orthoamphibole isograd; Stevens (1997) argued on petrographic grounds that the amphibolite facies rocks likely resulted from interaction of graphite-bearing granulites with an internally derived mixed fluid that was produced when water derived from crystallizing melts underwent reaction with graphite in the metasedimentary rocks. In this interpretation, the hydrated zone represents an area of the SMZ which retained much of the original volume of *in situ* melt, while the area which preserves a granulite facies assemblage represents a domain which lost most of the melt formed at peak metamorphism.

Through the years, a number of  $P$ – $T$  paths of different shapes have been proposed for the SMZ (Fig. 2). Several suggested paths are characterized by clockwise  $P$ – $T$  evolution with peaks of pressure in the range of 8.0–11.0 kbar, followed by isothermal decompression at high temperature (780–880 °C), with cooling to below 650 °C at 6.0–7.0 kbar (paths 1 and 2 in Fig. 2) (Van Reenen, 1983; Van Reenen *et al.*, 1987; Roering *et al.*, 1992a; Stevens & Van Reenen, 1992b; Taylor *et al.*, 2014). These paths are consistent with burial to the approximate base of continental crust of normal thickness as a consequence of collision, prograde heating of the deeply buried rocks due to re-establishment of the disrupted geotherm, isostatic rebound of the crust and tectonic denudation of the mountain belt resulting in exhumation and thrusting of the granulites over the Kaapvaal craton, followed by cooling in the mid-crust (Roering *et al.*, 1992a; Smit *et al.*, 1992; Smit & Van Reenen, 1997). As an alternative explanation for this  $P$ – $T$  evolution, Gerya *et al.* (2000) suggested exhumation of the granulite facies rocks by gravitational redistribution processes that do not require continental collision mechanism. Perchuk *et al.* (2000) published a fundamentally different  $P$ – $T$  evolution involving decompression coupled with cooling from 850 °C at 7.5 kbar to 600 °C at 4.5 kbar (Fig. 2). This  $P$ – $T$  path is inconsistent with the common occurrence of retrograde kyanite identified by Van Reenen *et al.* (1987) and Stevens (1997). However, if

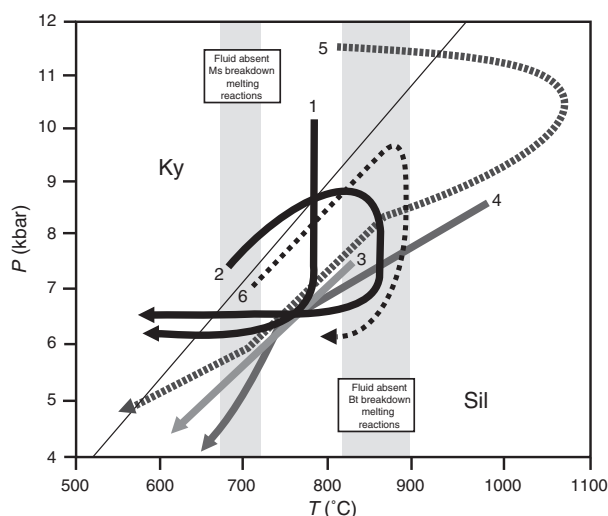


**Fig. 2.** Compilation of the published  $P$ - $T$  paths for the Southern Marginal Zone of the Limpopo Belt. 1. Van Reenen (1983); 2. Stevens & Van Reenen (1992b); 3. Perchuk *et al.* (2000); 4. Tsunogae *et al.* (2004); 5. Belyanin *et al.* (2012); 6. Taylor *et al.* (2014). The information on experimental constraints on biotite and muscovite stability that is provided for reference is from Vielzeuf & Holloway (1988); Patiño Douce & Johnston (1991); Montel & Vielzeuf (1997); Stevens *et al.* (1997); Patiño Douce & Harris (1998); Pickering & Johnston (1998). Consequently, the shaded bands represent the range in upper temperature limits for these minerals across a broad range of metasedimentary bulk compositions.

interpreted in a tectonic context, the path would record simultaneous cooling and decompression during thrusting of the granulites over the Kaapvaal craton. Belyanin *et al.* (2010, 2012) and Tsunogae *et al.* (2004) proposed an ultra-high temperature (UHT) metamorphic event in the SMZ, with peak metamorphic conditions in excess of 1000 °C at ~12.0 kbar (Belyanin *et al.*, 2012) (Fig. 2). However, as detailed by Nicoli *et al.* (2014), such UHT metamorphism in the SMZ is completely inconsistent with the common preservation of peak metamorphic biotite in both the Baviaanskloof Gneiss and the Bandelierkop Formation metapelites.

The timing of peak metamorphism in the SMZ is indicated by the  $^{207}\text{Pb}/^{206}\text{Pb}$  age of  $2691 \pm 7$  Ma, obtained by U-Pb in monazite from SHRIMP analyses from a migmatitic metapelite from the Bandelierkop quarry (Kreissig *et al.*, 2001). In addition, the age of the late to post-tectonic Matok Intrusive Complex has been constrained by a number of studies. Barton *et al.* (1992) presented a U-Pb zircon age of  $2665 \pm 2$  Ma for the intrusion of the Matok complex, an age that is in good agreement with the U-Pb monazite age of  $2663 \pm 4$  Ma described by Kreissig *et al.* (2001). A somewhat older U-Pb zircon age of  $2686 \pm 7$  Ma is also reported by Laurent *et al.* (2013). Taylor *et al.* (2014) reported ages of  $2714 \pm 6.4$  and  $2713 \pm 5.4$  Ma in the Bandelierkop quarry leuco-

somes, interpreted to be the age of peak metamorphism. Collectively, these results provide a well-constrained time window for peak metamorphism and the timing of high- $T$  exhumation. The fact that the Matok Intrusive Complex cuts across the orthoamphibole isograd (Van Reenen, 1986) indicates that the terrane had cooled to <650 °C at the time of the Matok intrusion. Thus, this portion of the retrograde path lasted less than *c.* 20 Ma. The granulites documented in this study are exposed in a quarry, referred to as the Brakspruit quarry by Van den Berg & Huizenga (2001), located ~15 km northeast of Bandelierkop in the northern granulite facies domain of the SMZ. The extremely fresh exposure of the quarry, with a length of 150 m and width of 50 m, is quite exceptional and provides outcrops containing a large range of different metapelitic rock compositions, along with leucocratic material derived from the anatexis of the metasedimentary rocks.

## PETROGRAPHY

One of the main characteristics of the Brakspruit quarry is the occurrence of a large variety of different metasedimentary rock compositions and the fact that many of these rocks contain features consistent with *in situ* anatexis. The geochemical diversity within the metasedimentary rocks at the Brakspruit quarry locality is considerably higher than in the Bandelierkop quarry, which was first studied in detail by Stevens & Van Reenen (1992a,b). The granulite facies paragneisses of the Brakspruit quarry can be classified according to their mineralogy and bulk-rock chemistry (cf. Whole rock and mineral chemistry). They are organized into a steeply dipping layered sequence, with individual rock compositions defining layers that vary in thickness from a few cm to ~2 m (Fig. 3). The transitions between different layers are characterized by changes in the mineralogy of the rocks, as well as by their colour and the presence of leucocratic features. The compositional banding of the rocks is interpreted to represent original lithological layering ( $S_0$ ) that has been transposed into the metamorphic fabric ( $S_1$ ). This layer parallel fabric has also accommodated melt segregation and possible upward migration of melt, and consequently many of the leucosomes are also layer parallel (Fig. 3). The metapelitic rocks from the Brakspruit quarry host a significant amount of leucocratic material. The high CaO and low  $\text{K}_2\text{O}$  content of the leucosomes, as well as the fact that they are produced in conjunction with new generations of high-grade ferromagnesian minerals, is consistent with the veins representing Ca-plagioclase and quartz-dominated residuum, from which melt has been lost, after biotite-dehydration partial melting in the metasedimentary rocks (Taylor *et al.*, 2014). The largest volume of this material occurs as garnet-bearing deformed leucosome veins of variable thickness (from <1 to >50 cm) within the

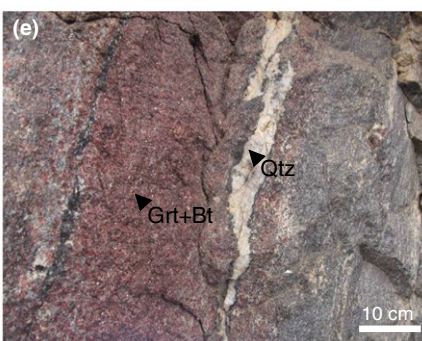
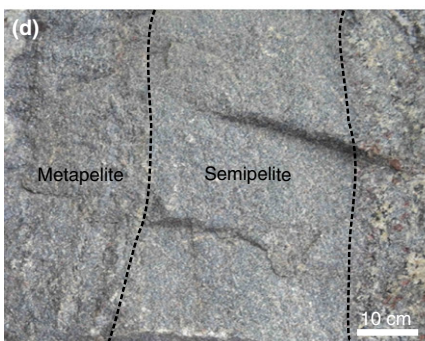
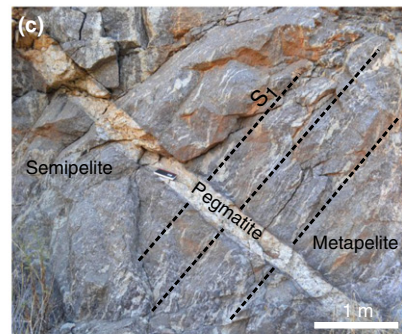
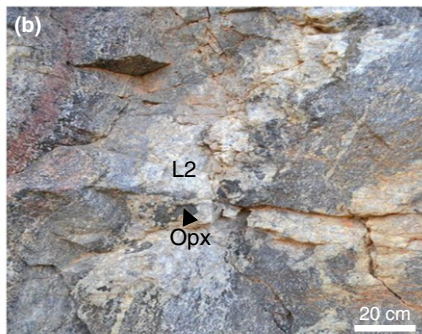
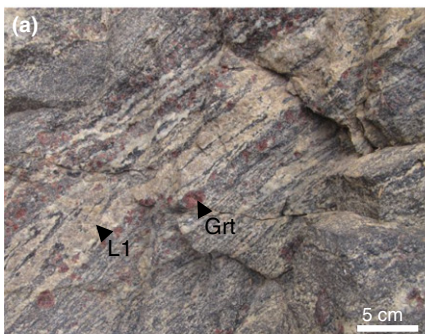
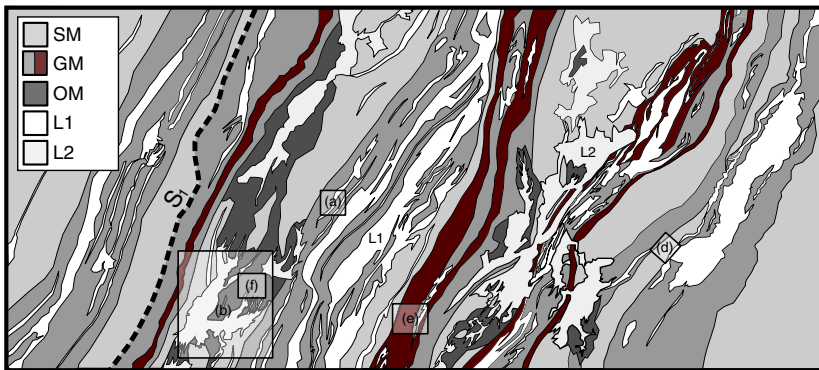


**Fig. 3.** Field photographs from the Brakspruit quarry. Panoramic view (top) and interpretation (middle) of the northern face of the quarry, showing the relationship between metapelite and semipelite layers, stromatic leucosomes and patch leucosomes. The main fabric ( $S_1$ ) is defined by the alternating bands of semipelite (SM) and metapelite (GM), both of which host deformed leucocratic veins. (a) Metapelite hosting L1 garnet-bearing stromatic leucosome (GM). (b) L2 orthopyroxene-bearing patch. (c) Late crosscutting pegmatite (perpendicular to the northern face of the quarry). (d) Semipelite (SM). (e) Garnet restite metapelite layer (GDM) hosting a deformed quartz vein edged by blocky orthopyroxene. (f) Orthopyroxene-bearing metapelite (OM).

metapelite (Fig. 3a). A second generation of orthopyroxene-bearing leucosome occurs as patches and overprints the main foliation and the first leucosome generation (Fig. 3b). The quarry also hosts two discrete undeformed, coarse-grained, crosscutting pegmatite dykes (Fig. 3c) that are mainly composed of quartz, plagioclase and K-feldspar along with cm-sized biotite crystals.

We distinguish three kinds of metasedimentary rocks based on the presence or absence of garnet and/or cordierite. Semipelite (SM) is the most abundant rock in the quarry (Fig. 3d) and is a light-grey medium-grained, banded gneiss that is characterized by the granulite facies assemblage  $\text{Grt} + \text{Pl} + \text{Qtz} + \text{Rt} + \text{Ilm} \pm \text{Bt} \pm \text{Opx}$  and minor K-feldspar (mineral abbreviations after Kretz, 1983) (Fig. 4a,b).



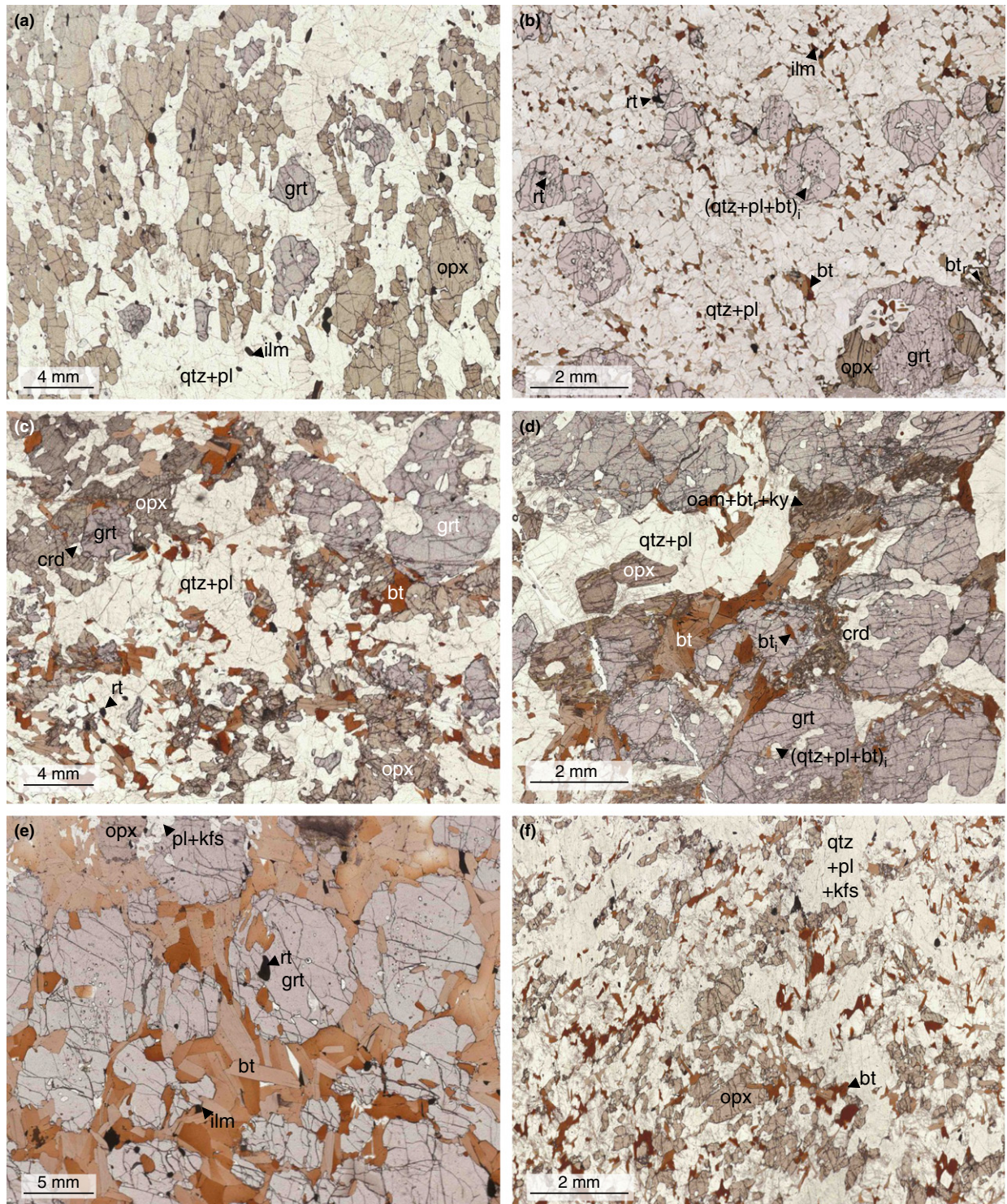


**Fig. 4.** Petrography of the Brakspuit quarry gneisses. (a) Scanned thin section of an orthopyroxene-rich SM sample with foliation marked by the alternating bands of orthopyroxene and quartz + plagioclase. (b) Scanned thin section of the sample M5 (SM) showing the rock texture, which includes evidence of orthopyroxene having nucleated around garnet. The biotite defines a light fabric parallel to the main fabric in the quarry. (c) Thin section showing the main granulite facies microtexture of the metapelitic gneiss GM (DT04B), with biotite defining a very light fabric. This rock, away from the leucosome, is not affected by fluid-present retrograde reactions. (d) The primary and secondary textural features of the GM metapelites with biotite + kyanite + orthoamphibole formed as secondary textures, with acicular arrangement of the kyanite, which replaces cordierite that forms part of the primary granulite texture. (e) Scanned thin section showing the main microtextural features of the metapelitic gneiss GDM. (f) Textural features in the scanned thin section of the orthopyroxene–metapelite OM. i, inclusion; r, retrograde.

Cordierite and aluminosilicate minerals are absent from SM and the mode of garnet varies from 0 to 25 vol.%. Orthopyroxene is always present but its proportion varies. The garnet is considered to be predominantly peritectic in origin, having arisen through fluid-absent biotite melting reactions and generally presents a poikiloblastic character with inclusions of quartz, biotite and plagioclase. It is important to note that the garnet in all rocks is unaffected by retrograde hydration reactions. As a consequence of the absence of aluminosilicates in the rock, as well as the relatively low proportion of biotite, the SM was less fertile for melting than some of the other rock types in the quarry at the conditions of peak metamorphism. In some samples, the banding is prominently marked by alternating domains rich in orthopyroxene and quartz (Fig. 4a). A very small proportion of orthopyroxene is affected by retrogression and the resultant quartz and biotite intergrowths which replace orthopyroxene are restricted to a very small volume of the rock (Fig. 4b). Idioblastic garnet with a crystal size of  $<10\ \mu\text{m}$  grain size is occasionally found associated with these small domains of retrogression. Sample M5 used for phase equilibria modelling presents all the characteristics of the SM group with the mineral assemblage Grt + Pl + Bt + Opx + Qtz + Ilm and minor K-feldspar (Fig. 4b). Rutile is found as inclusion in the garnet and in the matrix. In this sample, orthopyroxene is not found as crystals in the matrix but occurs exclusively in corona structures around garnet.

Metapelite is the other dominant rock type in the quarry, which has undergone substantial *in situ* partial melting (Fig. 3). Garnet-metapelite (GM) represents ~30% of the quarry outcrops. The characteristic metamorphic assemblage is Grt + Pl + Bt + Qtz + Opx  $\pm$  Crd  $\pm$  Kfs  $\pm$  Ilm  $\pm$  Rt. The mineral proportions are extremely variable between different layers reflecting the large range in bulk compositions. In general terms, these rocks correspond to the garnet-cordierite gneiss and cordierite gneiss described from the Bandelierkop quarry by Van Reenen (1983) and Stevens & Van Reenen (1992a). The metapelites can be distinguished from one another by their different modal proportions of garnet. As for the SM, the garnet has a peritectic origin, as is indicated by its poikiloblastic character and the presence of quartz, biotite, plagioclase inclusions and minor sillimanite. Sample DT04B is a typical example of the GM (Fig. 3a). It is a dark-grey, medium- to coarse-grained porphyroblastic restitic metapelite, characterized by the assemblage Grt + Opx + Pl + Bt + Qtz + Crd + Rt and minor K-feldspar (Fig. 4c). Biotite defines a weak peak metamorphic fabric. Garnet crystals are xenoblastic and are ~1 mm in size and contain small inclusions of biotite, quartz, plagioclase and sillimanite. The garnet is generally partially replaced by cordierite and/or orthopyroxene (Fig. 5a). The K-feldspar occurs occasionally

as small exolutions within plagioclase (Fig. 5b). The main mineral assemblage reflects granulite facies conditions. However, for samples collected close to the edge of stromatic leucosomes, some of the GM samples host small domains within which a retrograde assemblage is developed. These areas of re-equilibration affect only very small domains (typically  $200 \times 200\ \mu\text{m}$ ) within the sample that are characterized by the assemblage Grt + Bt + Pl + Qtz + Pl + Rt  $\pm$  Oam + Ky (Figs 4d & 5c). Consequently, the peak metamorphic assemblage is well preserved in the bulk of such samples. In the small domains of retrograde amphibolite facies re-equilibration, orthopyroxene is partially replaced by a second generation of biotite that is intergrown with quartz, while cordierite is partly replaced by orthoamphibole needles, which are intergrown with kyanite (Figs 4d & 5c). This intergrowth replaces the cordierite crystals from the crystal edge inwards. A second generation of idioblastic garnet crystals that are  $<10\ \mu\text{m}$  size is associated with these domains and replaces the aluminosilicate-bearing assemblages (Fig. 5c). Identical retrograde textures and assemblages have been described for metapelites from other areas in the SMZ (Stevens, 1997). Garnet-dominated metapelite (GDM) occurs as a minor rock type in the quarry (Fig. 3e). It is a coarse-grained, granoblastic metapelite that occurs as garnet porphyroblast-rich layers. Sample DT14 is the only GDM sample that has been analysed in detail. The bulk of the rock is made of Grt ( $>50\ \text{vol.}\%$ ) + Bt + Pl + Opx  $\pm$  Qtz  $\pm$  Ilm  $\pm$  Kfs (Fig. 4e). The idioblastic garnet crystals ( $>5\ \text{mm}$  in size) are lightly zoned with regard to inclusion density and have a core rich in inclusions of biotite, quartz and plagioclase and minor sillimanite (Fig. 5d). The presence of biotite, plagioclase and quartz inclusions reflects a peritectic origin for the garnet. Interstitial orthopyroxene occurs with low abundance between the garnet porphyroblasts. A small proportion of this orthopyroxene has been retrogressed to intergrowths of biotite and quartz. Quartz is present in very low proportions. Rutile occurs as inclusion in the garnet and ilmenite is present in the matrix.

The final metasedimentary lithology is the orthopyroxene-rich metapelite (OM) (Fig. 3f). It represents ~5% of the outcrop, and is a dark-grey, coarse-grained rock characterized by the absence of garnet and the assemblage Opx + Pl + Qtz + Bt + Ilm (Fig. 4f). It is strongly associated with the patchy orthopyroxene-bearing leucosomes that overprint the dominant foliation (Fig. 3b). OM corresponds to the pegmatoidal metapelite described by Stevens & Van Reenen (1992a) in the Bandelierkop quarry. The orthopyroxene occurs as porphyroblasts in excess of 1 cm size, as well as smaller crystals within the matrix of the rock (Fig. 4f). Orthopyroxene crystals contain inclusions of quartz and biotite, reflecting a peritectic origin. While the OM is in general characterized by a lack of foliation, in some small domains

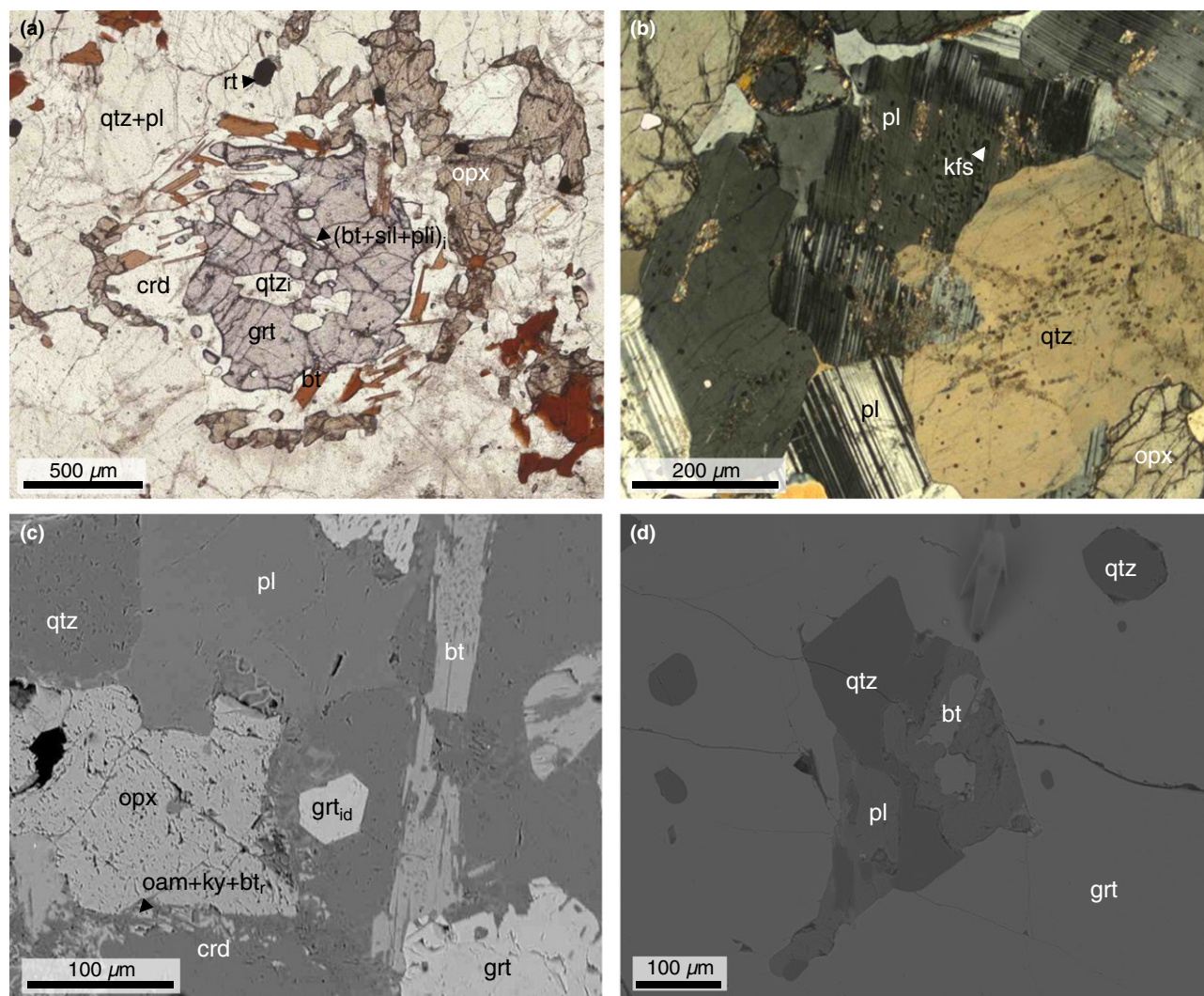


**Fig. 5.** Details of selected metamorphic textures in the Brakspruit quarry metasedimentary rocks. (a) Well preserved granulite facies assemblage in GM metapelite showing a decompression feature: garnet is rimmed by cordierite and orthopyroxene. (b) K-feldspar exsolution in plagioclase in GM metapelite. (c) SEM backscattered electron image showing the restricted development of the retrograde (oam + ky + bt<sub>r</sub>) assemblage in GM showing idioblastic garnet (grt<sub>id</sub>). (d) SEM backscattered electron image from GDM showing a micro-granite inclusion in garnet that is interpreted to represent a recrystallized melt inclusion. The inclusion consists of plagioclase, quartz and biotite.

a ghost fabric remains which is in alignment with the general foliation in the quarry. In these areas, less recrystallization has occurred during the breakdown of biotite to produce the large orthopyroxene crystals.

## WHOLE ROCK AND MINERAL CHEMISTRY

### Whole-rock chemistry

Representative bulk compositions are presented in Table 1 (the analytical methods are described in Appendix S1). The metasedimentary rocks from the Brakspruit quarry display a large range of concentrations for Al<sub>2</sub>O<sub>3</sub>, Fe<sub>2</sub>O<sub>3T</sub>, MgO, CaO, Na<sub>2</sub>O and K<sub>2</sub>O (Fig. 6). Samples M5, DT04B, DT14 and Ogn

are representative of the four different metasedimentary rock varieties exposed in the quarry, SM, GM, GDM and OM respectively. The compositions of relevant experimental starting materials such as shale and greywacke (Vielzeuf & Holloway, 1988; Patiño Douce & Johnston, 1991; Vielzeuf & Montel, 1994; Patiño Douce & Beard, 1995, 1996; Stevens *et al.*, 1997) have been added in order to show possible protolith compositions. The general depletion in Al and K compared to the experimental starting materials, as well as the presence of abundant garnet, orthopyroxene and cordierite indicates that if the rock had a mica-rich protolith it must have lost melt (Taylor *et al.*, 2014) and is restitic in character. M5 is more sodic and less rich in K and ferromagnesian components than the other rock types. Its relatively high Al

**Table 1.** Bulk-rock major compositions of leucosomes and metasedimentary rocks from the Brakspruit quarry expressed in wt%. Total iron as Fe<sub>2</sub>O<sub>3</sub>.

Rock type Sample	SM M6	SM M5	OM Ogn	GM DT04B	GM DT10B	GDM GRT2	GDM DT14	L1 DT09	L1 DT08A	L2 DT03A
SiO <sub>2</sub>	63.93	65.08	54.74	55.77	50.87	51.57	39.41	74.29	69.42	70.52
TiO <sub>2</sub>	0.78	0.58	0.86	0.85	0.83	1.10	1.43	0.02	0.01	0.25
Al <sub>2</sub> O <sub>3</sub>	12.82	14.49	12.69	15.11	16.38	16.68	18.43	15.00	17.85	15.25
Fe <sub>2</sub> O <sub>3T</sub>	9.06	9.05	12.20	11.82	12.43	16.26	25.00	0.65	0.26	1.88
MnO	0.13	0.10	0.12	0.11	0.22	0.16	0.22	0.03	0.01	0.03
MgO	6.67	4.50	10.99	11.35	11.86	9.72	11.43	0.41	0.16	1.97
CaO	2.04	1.80	3.03	2.05	2.20	1.47	1.07	3.44	2.90	3.57
Na <sub>2</sub> O	2.10	2.38	2.05	1.26	2.17	0.80	0.22	3.81	5.55	3.42
K <sub>2</sub> O	1.36	1.37	1.02	1.33	1.57	1.63	2.26	0.48	1.61	0.83
P <sub>2</sub> O <sub>5</sub>	0.05	0.06	0.05	0.02	0.05	0.06	0.04	0.03	0.04	0.06
LOI	0.10	0.06	0.00	0.40	0.33	0.00	0.00	0.42	0.74	0.77
Total	99.05	99.48	97.75	100.07	98.90	99.47	99.50	98.59	98.55	98.55
Mg#	0.34	0.31	0.41	0.43	0.40	0.29	0.29	0.30	0.30	0.42
A/CNK	1.86	2.07	1.73	2.78	2.23	3.75	3.75	1.49	1.30	1.54

content reflects the presence of a large amount of feldspar in the mineral assemblage. DT04B, DT14 and Ogn are characterized by a high ferromagnesian content and a large range of K values. This directly reflects variations in the abundance of biotite in the different rocks. In order to facilitate the modelling of the retrograde path, quantitative EDS analyses were performed on areas of sample DT04B that had been re-equilibrated to retrograde amphibolite grade assemblages. The average composition of these areas is considered to represent the bulk composition within which the retrograde assemblage equilibrated. This composition is represented by GMr in Fig. 6.

### Mineral chemistry

Representative mineral analyses are presented in Tables 2–5 (see method in Appendix S1). The calcu-

lated end-member concentrations and ratios discussed below are  $X_{alm}$ ,  $X_{pyp}$ ,  $X_{spss}$  and  $X_{grs}$  for garnet, Mg# for garnet, cordierite and orthopyroxene,  $\gamma(opx)$  for orthopyroxene,  $X_{an}$  for plagioclase and Ti the titanium content in biotite. These are defined as follows:  $X_{alm} = Fe/(Fe + Mg + Mn + Ca)$ ,  $X_{pyp} = Mg/(Fe + Mg + Mn + Ca)$ ,  $X_{spss} = Mn/(Fe + Mg + Mn + Ca)$ ,  $X_{grs} = Ca/(Fe + Mg + Mn + Ca)$ ,  $Mg\# = Mg^{2+}/(Fe^{2+} + Mg^{2+})$ ,  $\gamma(opx) = Al^{4+} + Si^{4+} - 2$ ,  $X_{an} = Ca/(Ca + Na + K)$ .

Garnet in SM, GM and GDM is almandine-rich and does not display any significant zoning. Typical compositional ranges for garnet in the three rock types are SM:  $X_{alm}$  0.50–0.58,  $X_{pyp}$  0.34–0.45,  $X_{spss} \sim 0.01$ ,  $X_{grs}$  0.02–0.05; GM:  $X_{alm}$  0.54–0.60,  $X_{pyp}$  0.31–0.40,  $X_{spss} \sim 0.01$ ,  $X_{grs}$  0.03–0.05; GDM:  $X_{alm}$  0.56–0.58,  $X_{pyp}$  0.34–0.40,  $X_{spss} \sim 0.01$ ,  $X_{grs}$  0.02–0.05 and Mg# 0.45–0.48 (SM), 0.37–0.48 (GM), 0.36–0.43 (GDM). The small idioblastic garnet in GM displays slightly

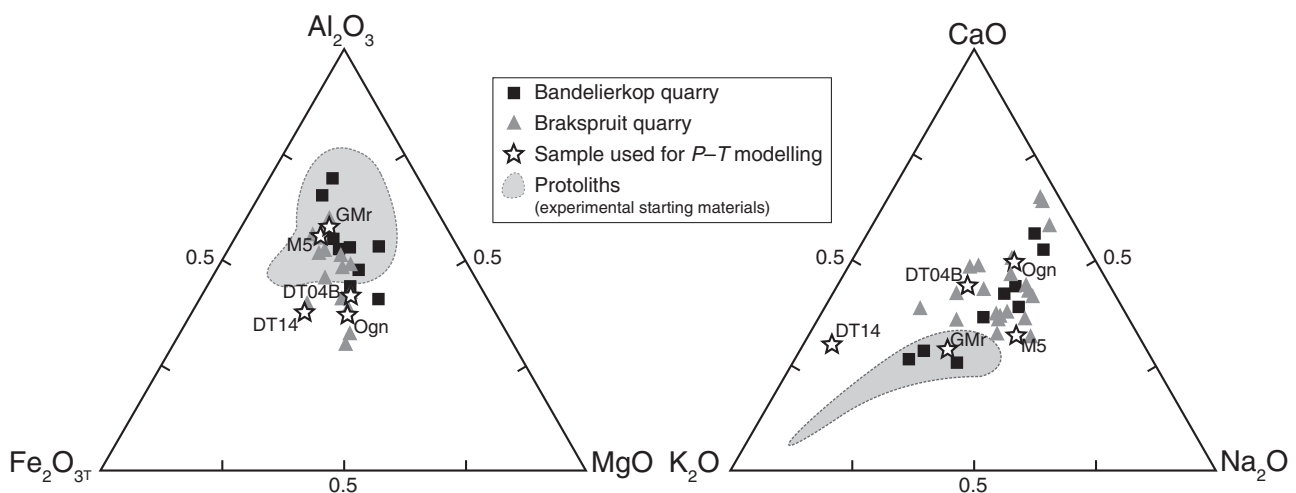


**Fig. 6.** Al<sub>2</sub>O<sub>3</sub>–Fe<sub>2</sub>O<sub>3T</sub>–MgO and CaO–K<sub>2</sub>O–Na<sub>2</sub>O ternary plots for the metasediments. M5, DT04B, DT14 and Ogn represent the samples investigated in detail in this study. GMr represents the small domain of DT04B that was re-equilibrated to amphibolite facies conditions. Bandelierkop Formation metasedimentary rock compositions from Stevens & Van Reenen (1992a,b) and Taylor *et al.* (2014). Relevant experimental starting materials compilation after Patiño Douce & Johnston (1991), Patiño-Douce & Beard (1995), Stevens *et al.* (1997), Vielzeuf & Holloway (1988) and Vielzeuf & Montel (1994).

**Table 2.** Representative scanning electron microscopy data for the M5 sample. Cation compositions include a stoichiometric estimate of Fe<sup>3+</sup> after Droop (1987).

<i>n</i>	Grt <sub>core</sub> 9	Grt <sub>rim</sub> 9	Grt <sub>euhedral</sub> 6	Pl <sub>inclusion</sub> 5	Pl <sub>matrix</sub> 6	Kfs 4	Bt <sub>matrix</sub> 10	Bt <sub>inclusion</sub> 5	Opx 16	Rt 2	Ilm 1
SiO <sub>2</sub>	39.11	39.00	39.30	62.19	63.31	65.71	37.56	38.75	49.76	0.47	0.34
TiO <sub>2</sub>	0.00	0.00	0.00	–	–	–	5.90	4.07	0.00	96.05	54.50
Al <sub>2</sub> O <sub>3</sub>	22.37	22.09	22.26	23.82	23.14	18.15	15.82	16.68	7.48	0.00	0.00
Cr <sub>2</sub> O <sub>3</sub>	0.00	0.00	0.00	–	–	–	0.31	0.24	0.00	0.98	0.30
FeO <sub>T</sub>	25.27	25.38	27.77	0.32	0.00	0.00	12.55	8.66	20.39	1.67	44.22
MnO	0.46	0.36	0.56	–	–	–	0.00	0.00	–	0.00	0.77
MgO	11.66	11.77	9.90	–	–	–	14.99	18.24	22.35	–	–
CaO	1.21	0.68	1.77	5.91	5.23	0.00	–	–	–	–	0.54
Na <sub>2</sub> O	–	–	–	7.95	8.39	0.78	0.00	0.29	–	–	–
K <sub>2</sub> O	–	–	–	0.30	0.21	15.20	9.94	9.15	–	–	–
Total	100.08	99.30	101.57	100.49	100.28	99.84	97.07	96.09	99.99	99.17	100.67
ox	12.00	12.00	12.00	8.00	8.00	8.00	24.00	24.00	6.00	2.00	3.00
Si	2.96	2.98	2.93	2.76	2.81	3.04	5.95	6.04	1.83	0.01	0.01
Ti	0.00	0.00	0.00	0.00	0.00	0.00	0.70	0.48	0.00	0.96	1.03
Al	2.00	1.99	1.96	1.25	1.21	0.99	2.95	3.07	0.32	0.00	0.00
Cr	0.00	0.00	0.00	0.00	0.00	0.00	0.04	0.03	0.00	0.01	0.01
Fe <sup>3+</sup>	0.08	0.06	0.18	0.00	0.00	0.00	–	–	0.02	0.00	0.00
Fe <sup>2+</sup>	1.52	1.56	1.56	0.01	0.00	0.00	1.66	1.13	0.60	0.02	0.93
Mn <sup>2+</sup>	0.03	0.02	0.04	0.00	0.00	0.00	0.00	0.00	0.00	0.00	0.02
Mg	1.32	1.34	1.10	0.00	0.00	0.00	3.54	4.24	1.22	0.00	0.00
Ca	0.10	0.06	0.14	0.28	0.25	0.00	0.00	0.00	0.00	0.00	0.01
Na	0.00	0.00	0.00	0.68	0.72	0.07	0.00	0.09	0.00	0.00	0.00
K	0.00	0.00	0.00	0.02	0.01	0.90	2.01	1.82	0.00	0.00	0.00
Total	8.00	8.00	7.90	5.00	5.00	5.00	16.85	16.89	4.00	1.00	2.00
X <sub>alm</sub>	0.51	0.52	0.55	–	–	–	–	–	–	–	–
X <sub>pyp</sub>	0.44	0.45	0.39	–	–	–	–	–	–	–	–
X <sub>spss</sub>	0.01	0.01	0.01	–	–	–	–	–	–	–	–
X <sub>grs</sub>	0.03	0.02	0.05	–	–	–	–	–	–	–	–
Mg#	0.46	0.46	0.41	–	–	–	0.68	0.79	0.67	–	–
X <sub>an</sub>	–	–	–	0.29	0.25	0.00	–	–	–	–	–
y(opx)	–	–	–	–	–	–	–	–	0.15	–	–

Mean values given, *n* = number of analyses used to define the mean.

different compositions;  $X_{alm}$  0.53–0.54,  $X_{pyp}$  0.38–0.41,  $X_{spss}$  ~0.01,  $X_{grs}$  0.02–0.4 and Mg# 0.41 (Fig. 7a).

Biotite inclusions in garnet show Mg# values of 0.75–0.79 (SM), 0.56–0.69 (GM), 0.60–0.62 (GDM) and 0.60–0.65 (OM). Ti in the biotite inclusions is slightly lower than Ti in the matrix biotite but varies from sample to sample (Fig. 7b). Two generations of biotite exist in the matrix of the metapelites: a predominant peak assemblage biotite characterized by Mg# values of 0.67–0.70 (SM), 0.71–0.74 (GM) and 0.68–0.70 (GDM), and Ti values of 0.60–0.70; and a retrograde biotite associated with kyanite, quartz and orthoamphibole replacement of cordierite, with Mg# and Ti of 0.68–0.70, 0.60–0.62 (SM), 0.70–0.72, 0.40–0.60 (GM) and 0.67–0.70, 0.58–0.63 (GDM). The OM samples display a different biotite composition with no distinction between matrix biotite and inclusion biotite. Mg# values vary between 0.63 and 0.65 and Ti values vary between 0.70 and 0.80.

Matrix plagioclase is unzoned and displays  $X_{an}$  values of 0.22–0.24 (SM), 0.31–0.34 (GM), 0.27–0.29 (GDM) and 0.45–0.50 (OM) (Fig. 7c). Plagioclase inclusions in garnet have  $X_{an}$  values of 0.27–0.28 (SM), 0.40–0.45 (GM) and 0.39–0.44 (GDM).

Orthopyroxene is unzoned. It displays Mg# values of 0.66–0.68 (SM), 0.64–0.67 (GM), 0.63–0.65 (GDM) and 0.64–0.65 (OM). The corresponding *y* (opx) values are 0.14–0.15, 0.09–0.13, 0.12–0.15 and 0.07–0.11 respectively.

Cordierite is a common mineral in the GM metapelite but is absent in SM and OM samples. Cordierite is found in the matrix in GM with a blocky texture (Mg# 0.85–0.86).

## P–T MODELLING

Phase equilibria modelling was undertaken in the chemical system MnO–Na<sub>2</sub>O–CaO–K<sub>2</sub>O–FeO–MgO–Al<sub>2</sub>O<sub>3</sub>–SiO<sub>2</sub>–H<sub>2</sub>O–TiO<sub>2</sub>–O<sub>2</sub> (MnNCKFMASHTO) using Theriak/Domino software (De Capitani & Petrakakis, 2010), in combination with the updated Holland & Powell (1998) data set that includes silicate melt. The following *a*–*x* models were used: garnet, biotite (White *et al.*, 2005), feldspar (Holland & Powell, 2003), orthopyroxene (White *et al.*, 2002), cordierite, chlorite (Holland & Powell, 1998), ilmenite (White *et al.*, 2000, 2005), muscovite (Coggon & Holland, 2002), orthoamphibole (Diener & Powell, 2012), spinel (White *et al.*, 2000) and melt (White *et al.*, 2007). Pseudosections were calculated using the bulk compositions of garnet-bearing samples M5 (SM), DT04B (GM) and DT14 (GDM), over the same range of temperatures and pressures previously investigated by Taylor *et al.* (2014) on the metapelite exposures at the Bandelierkop quarry. Mn is included as it has an influence on the stability of garnet in the lower pressure portion of its stability range. For the purpose of modelling such restitic compositions, we followed the

**Table 3.** Representative scanning electron microscopy data for the DT04B sample. Cation compositions include a stoichiometric estimate of Fe<sup>3+</sup> after Droop (1987) and Tindle & Webb (1994) for the amphibole.

<i>n</i>	Gr <sub>core</sub> 8	Gr <sub>rim</sub> 8	Gr <sub>ehedral</sub> 6	Pl <sub>matrix</sub> 5	Pl <sub>inclusion</sub> 6	Kfs 4	Bt <sub>matrix</sub> 9	Bt <sub>inclusion_grt</sub> 2	Bt <sub>inclusion_opx</sub> 2	Bt <sub>retro</sub> 5	Opx 15	Crd 11	Oam 2	Rt <sub>matrix</sub> 6	Rt <sub>inclusion</sub> 2
SiO <sub>2</sub>	39.12	38.58	39.30	60.82	57.94	65.28	37.64	37.91	36.97	37.97	50.06	50.77	50.61	0.50	0.21
TiO <sub>2</sub>	0.00	0.00	0.00	–	–	–	5.02	4.81	4.92	5.14	0.13	–	0.00	98.04	97.86
Al <sub>2</sub> O <sub>3</sub>	22.33	22.20	22.26	24.18	26.30	17.70	15.59	15.89	15.40	16.31	5.52	33.85	4.09	0.00	0.00
Cr <sub>2</sub> O <sub>3</sub>	0.00	0.00	0.00	–	–	–	0.00	0.00	0.00	0.00	0.30	–	0.00	–	–
FeO <sub>T</sub>	24.78	27.93	27.77	0.00	0.00	0.00	11.35	11.03	11.97	11.35	21.62	2.94	19.50	0.68	0.47
MnO	0.71	0.68	0.56	–	–	–	0.00	0.00	0.00	0.00	–	–	0.00	0.00	0.00
MgO	11.81	9.29	9.90	–	–	–	15.88	15.83	15.18	15.80	21.45	11.44	23.01	0.00	0.00
CaO	1.05	1.53	1.77	6.53	8.98	0.17	–	–	–	–	0.00	–	0.50	–	–
Na <sub>2</sub> O	–	–	–	7.41	6.44	0.63	0.18	0.00	0.00	0.00	–	–	0.10	0.00	0.00
K <sub>2</sub> O	–	–	–	0.32	0.25	15.45	9.72	9.75	9.68	9.46	–	0.00	0.00	0.00	0.00
Total	99.80	100.22	101.57	99.27	99.90	99.23	95.38	95.22	96.10	96.01	99.07	99.00	97.80	99.22	98.54
ox	12.00	12.00	12.00	8.00	8.00	8.00	24.00	24.00	24.00	24.00	6.00	18.00	23.00	2.00	2.00
Si	2.97	2.96	2.93	2.72	2.60	3.03	6.03	6.06	6.02	6.01	1.87	5.07	7.12	0.01	0.00
Ti	0.00	0.00	0.00	0.00	0.00	0.00	0.60	0.58	0.60	0.61	0.00	0.00	0.68	0.99	0.99
Al	2.00	2.01	1.96	1.28	1.39	0.97	2.94	2.99	2.96	3.04	0.24	3.98	0.00	0.00	0.00
Cr	0.00	0.00	0.00	0.00	0.00	0.00	0.00	0.00	0.00	0.00	0.01	0.00	0.00	0.00	0.00
Fe <sup>3+</sup>	0.07	0.06	0.18	–	–	–	–	–	–	–	–	–	1.05	–	–
Fe <sup>2+</sup>	1.50	1.73	1.56	0.00	0.00	0.00	1.52	1.47	1.63	1.50	0.68	0.25	1.25	0.01	0.01
Mn <sup>2+</sup>	0.05	0.04	0.04	0.00	0.00	0.00	0.00	0.00	0.00	0.00	0.00	0.00	0.00	0.00	0.00
Mg	1.33	1.06	1.10	0.00	0.00	0.00	3.79	3.77	3.69	3.73	1.20	1.70	4.83	0.00	0.00
Ca	0.09	0.13	0.14	0.31	0.43	0.01	0.00	0.00	0.00	0.00	0.00	0.00	0.08	0.00	0.00
Na	0.00	0.00	0.00	0.64	0.56	0.06	0.06	0.05	0.00	0.00	0.00	0.00	0.03	0.00	0.00
K	0.00	0.00	0.00	0.02	0.01	0.91	1.98	1.99	2.01	1.91	0.00	0.00	0.00	0.00	0.00
Total	8.00	8.00	7.90	4.97	4.99	4.97	16.92	16.91	16.90	16.81	4.00	11.00	15.03	1.00	1.00
X <sub>alm</sub>	0.51	0.58	0.55	–	–	–	–	–	–	–	–	–	–	–	–
X <sub>pyr</sub>	0.45	0.36	0.39	–	–	–	–	–	–	–	–	–	–	–	–
X <sub>spss</sub>	0.02	0.01	0.01	–	–	–	–	–	–	–	–	–	–	–	–
X <sub>grs</sub>	0.03	0.04	0.05	–	–	–	–	–	–	–	–	–	–	–	–
Mg#	0.47	0.38	0.41	–	–	–	0.71	0.72	0.69	0.71	0.64	0.87	0.79	–	–
X <sub>an</sub>	–	–	–	0.32	0.43	0.01	–	–	–	–	–	–	–	–	–
y(opx)	–	–	–	–	–	–	–	–	–	–	0.12	–	–	–	–

Mean values given, *n* = number of analyses used to define the mean.

methodology used by Taylor *et al.* (2014) on other metasedimentary rocks from the Bandelierkop Formation, which assumes that the preservation of the dry, granulite facies assemblages in the rocks was a consequence of melt loss at or shortly prior to peak metamorphic conditions (e.g. White & Powell, 2002; Taylor *et al.*, 2014). Although modelling using a melt-depleted bulk composition does not allow the prograde evolution of the rock to be constrained, it does permit investigation of the phase equilibria from the moment when melt was lost from the system. Following this approach and within rocks that have retained insufficient melt to allow for a significant degree of retrograde reaction, only the stability of the peak metamorphic assemblage and a small portion of the high-*T* retrograde path can be investigated. It is important to note that following this approach, the modelled rocks retain the granulite facies assemblage existing after decompression. The reconstructed melt-present, pre-decompression assemblage is inferred by removing from the assemblage the phases related to decompression (i.e. orthopyroxene and/or cordierite). The growth of peritectic garnet can be investigated by the melt reintegration method (White *et al.*, 2004).

The Fe<sub>2</sub>O<sub>3</sub> wt% and H<sub>2</sub>O wt% in the bulk composition were set using reconnaissance modelling on *P*–*X* and *T*–*X* pseudosections (Figs 8 & 9). The

purpose of this was to constrain Fe<sub>2</sub>O<sub>3</sub> wt% and H<sub>2</sub>O wt% to values consistent with the formation of the observed metamorphic assemblage as well as estimated abundance of minerals in the sample at peak metamorphism. The choice of bulk-rock H<sub>2</sub>O content was based on the hypothesis of partial melting driven by fluid-absent biotite reaction and nearly complete melt loss from the restitic granulites. Therefore, H<sub>2</sub>O values were chosen to be consistent with a modal abundance of melt at peak metamorphic condition between 0 and 10 vol.% and the absence of phases that, in the relevant rocks, occur only as decompression-related textures replacing garnet (e.g. cordierite and orthopyroxene) (Fig. 8). The value chosen for Fe<sup>3+</sup> concentration (Fig. 9) determines the pressure of the transition area between rutile and ilmenite and thus influences the minimum pressure represented by the peak assemblage. Consequently, the Fe<sup>3+</sup> concentration was chosen by considering the nature of the oxide phases (rutile and/or ilmenite both as inclusions) at *P*–*T* conditions where X<sub>alm</sub> garnet isopleths match the measured values in the preserved granulite assemblage field.

Scanned thin sections and software program ImageJ (Rasband, 1997–2012) were used to determine modes of garnet, orthopyroxene, cordierite and plagioclase in the samples.

**Table 4.** Representative mineral compositions measured using EDX on an SEM for sample DT14. Cation compositions include a stoichiometric estimate of Fe<sup>3+</sup> after Droop (1987).

<i>n</i>	Grt <sub>core</sub> 18	Grt <sub>rim</sub> 18	Pl <sub>matrix</sub> 7	Pl <sub>inclusion</sub> 3	Kfs 5	Bt <sub>matrix</sub> 9	Bt <sub>inclusion</sub> 3	Bt <sub>retro</sub> 3	Opx 10	Ilm 2	Rt 5
SiO <sub>2</sub>	38.78	38.17	61.51	57.82	65.05	35.90	38.08	40.59	50.17	0.85	0.00
TiO <sub>2</sub>	0.00	0.00	–	–	–	5.38	0.61	5.24	0.00	49.63	99.25
Al <sub>2</sub> O <sub>3</sub>	22.32	21.67	23.78	25.76	18.19	15.45	19.36	15.48	6.97	0.30	0.00
Cr <sub>2</sub> O <sub>3</sub>	0.00	0.00	–	–	–	0.41	0.00	0.00	0.17	–	–
FeOT	26.32	27.73	0.00	0.18	0.00	11.79	9.01	11.45	22.01	49.10	0.52
MnO	0.35	0.32	–	–	–	0.00	0.00	0.00	–	0.21	0.00
MgO	10.86	10.07	–	–	–	13.98	20.05	14.75	21.22	0.52	0.00
CaO	1.60	1.19	6.10	8.75	0.00	–	–	–	0.00	–	–
Na <sub>2</sub> O	–	–	7.77	6.43	0.66	0.20	0.00	0.00	–	–	–
K <sub>2</sub> O	–	–	0.44	0.12	15.26	9.62	7.98	9.47	–	0.14	0.00
Total	100.24	99.14	99.60	99.07	99.16	92.72	95.08	96.98	100.54	100.75	99.77
ox	12.00	12.00	8.00	8.00	8.00	24.00	24.00	24.00	15.00	3.00	2.00
Si	2.95	2.95	2.75	2.62	3.03	5.95	5.94	6.32	1.85	0.02	0.00
Ti	0.00	0.00	0.00	0.00	0.00	0.67	0.07	0.61	0.00	0.92	1.00
Al	2.00	1.97	1.25	1.38	1.00	3.02	3.56	2.84	0.30	0.01	0.00
Cr	0.00	0.00	0.00	0.00	0.00	0.05	0.00	0.00	0.01	–	–
Fe <sup>3+</sup>	0.11	0.12	–	–	–	–	–	–	0.00	0.10	–
Fe <sup>2+</sup>	1.56	1.67	0.00	0.01	0.00	1.64	1.18	1.49	0.68	0.91	0.01
Mn <sup>2+</sup>	0.02	0.02	0.00	0.00	0.00	0.00	0.00	0.00	0.00	0.00	0.00
Mg	1.23	1.16	0.00	0.00	0.00	3.46	4.67	3.43	1.17	0.02	0.00
Ca	0.13	0.10	0.29	0.43	0.00	0.00	–	–	0.00	–	–
Na	0.00	0.00	0.67	0.57	0.06	0.06	0.00	0.00	0.00	–	–
K	0.00	0.00	0.02	0.01	0.91	2.04	1.59	1.88	0.00	0.00	0.00
Total	8.00	8.00	5.00	5.00	5.00	16.89	17.00	16.58	4.00	2.00	1.00
X <sub>alm</sub>	0.53	0.57	–	–	–	–	–	–	–	–	–
X <sub>pyp</sub>	0.42	0.39	–	–	–	–	–	–	–	–	–
X <sub>spss</sub>	0.01	0.01	–	–	–	–	–	–	–	–	–
X <sub>grs</sub>	0.04	0.03	–	–	–	–	–	–	–	–	–
Mg#	0.44	0.41	–	–	–	0.68	0.80	0.70	0.63	–	–
X <sub>an</sub>	–	–	29.27	42.50	0.00	–	–	–	–	–	–
y(opx)	–	–	–	–	–	–	–	–	0.15	–	–

Mean values given, *n* = number of analyses used to define the mean.**Table 5.** Representative mineral compositions measured using EDX on an SEM for sample Ogn. Cation compositions include a stoichiometric estimate of Fe<sup>3+</sup> after Droop (1987).

<i>n</i>	Pl 12	Kfs 5	Bt <sub>matrix</sub> 6	Bt <sub>inclusion</sub> 2	Opx <sub>core</sub> 10	Opx <sub>rim</sub> 10	Ilm 4
SiO <sub>2</sub>	57.62	65.02	37.49	38.87	50.78	51.26	0.23
TiO <sub>2</sub>	–	–	6.34	6.12	0.00	0.00	49.90
Al <sub>2</sub> O <sub>3</sub>	27.95	18.15	15.39	14.80	4.89	4.75	0.00
Cr <sub>2</sub> O <sub>3</sub>	–	–	1.10	–	0.29	0.33	0.50
FeO <sub>T</sub>	0.00	0.00	14.14	12.77	21.67	21.51	47.24
MnO	–	–	0.00	0.18	–	–	1.16
MgO	–	–	13.71	14.42	21.32	21.77	–
CaO	10.13	0.31	–	–	–	–	–
Na <sub>2</sub> O	5.91	0.37	–	0.00	0.14	0.15	0.09
K <sub>2</sub> O	0.26	16.23	9.92	10.16	–	–	–
Total	101.87	100.08	98.08	97.32	99.10	99.78	99.11
ox	8.00	8.00	24.00	24.00	6.00	6.00	3.00
Si	2.54	3.02	5.93	6.04	1.90	1.90	0.00
Ti	0.00	0.00	0.76	0.72	0.00	0.00	0.82
Al	1.45	0.98	2.87	2.89	0.22	0.21	0.00
Cr	0.00	0.00	0.14	0.00	0.01	0.01	0.01
Fe <sup>3+</sup>	–	–	–	–	0.00	0.00	0.61
Fe <sup>2+</sup>	0.00	0.00	1.87	1.79	0.68	0.67	0.26
Mn <sup>2+</sup>	0.00	0.00	0.00	0.02	0.00	0.00	0.02
Mg	0.00	0.00	3.23	3.34	1.19	1.21	0.00
Ca	0.48	0.02	0.00	0.00	0.01	0.01	0.00
Na	0.51	0.03	0.00	0.00	0.00	0.00	0.02
K	0.01	0.95	2.00	2.01	0.00	0.00	0.25
Total	5.00	4.99	16.81	16.81	4.00	4.00	2.00
Mg#	–	–	0.63	0.65	0.64	0.64	–
X <sub>an</sub>	47.95	1.53	–	–	–	–	–
y(opx)	–	–	–	–	0.12	0.11	–

Mean values given, *n* = number of analyses used to define the mean.**Sample M5**

Pseudosection modelling following the method described above is useful in constraining the *P–T* conditions of equilibration of the high-*P* peak assemblage, Grt + Bt + Pl + Qtz + Rt + Kfs + Melt, to between 815–870 °C and 7.0–13.0 kbar (Fig. 10a). The amount of melt present in the peak metamorphic assemblage is <4 vol.% (Fig. 10b). The preserved granulite facies assemblage Grt + Opx + Bt + Pl + Qtz + Kfs + Rt + Ilm is stable between 700–825 °C and 5.25–7.0 kbar (Fig. 10a). In this field, the garnet mode is 15–20 vol.%, plagioclase mode ~30% and orthopyroxene mode <5 vol.% (Fig. 10c–e). In thin section, garnet and orthopyroxene make up ~15 and ~5 vol.% respectively. The ferromagnesian portion of the mineral assemblage becomes enriched in orthopyroxene, while the mode of garnet decreases. This behaviour is interpreted to explain the nucleation texture of orthopyroxene around garnet. The sillimanite-in reaction line at ~5.0 kbar delimits the low-*P* boundary of the preserved granulite assemblage. There is a good match between the measured Mg# for garnet (0.45–0.48), orthopyroxene (0.66–0.68) and X<sub>an</sub> in plagioclase (0.22–0.29) and the calculated isopleths of composition for these minerals within the preserved granulite assemblage field (garnet Mg#: 0.46–0.48; orthopyroxene Mg#: 0.64–0.66;

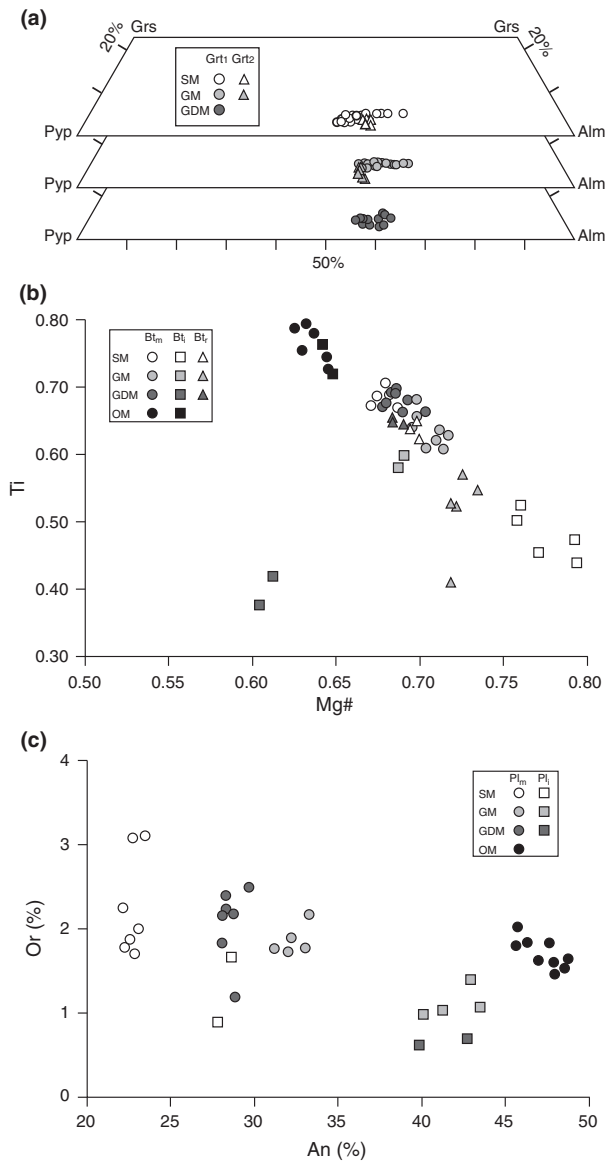


**Fig. 7.** Mineral chemistry for the SM, GM, GDM and OM rock groups. (a) Grs–Alm–Pyr garnet diagram. Grt1: the peritectic garnet; Grt2: retrograde idioblastic garnet. (b) Titanium content in biotite as a function of Mg#. Bt<sub>m</sub>, biotite in the matrix; Bt<sub>i</sub>, biotite that occurs as inclusions in garnet or orthopyroxene; Bt<sub>r</sub>, biotite developed in retrograde textures. (c) Plagioclase composition. Pl<sub>m</sub>, plagioclase in the matrix; Pl<sub>i</sub>, plagioclase formed as inclusions in garnet.

and plagioclase  $X_{an}$ : 0.24–0.28) (Fig. 10c–e). The isopleths help to constrain the likely  $P$ – $T$  conditions of equilibration of the assemblage to 740–820 °C and 5.25–6.5 kbar.

#### Sample DT04B

$P$ – $T$  pseudosection modelling constrains the stability of the peak metamorphic assemblage Grt + Pl + Bt + Opx + Qtz + Rt + Melt to between 835 and 875 °C at 7.25–13.0 kbar (Fig. 11a). Within this  $P$ – $T$  field,

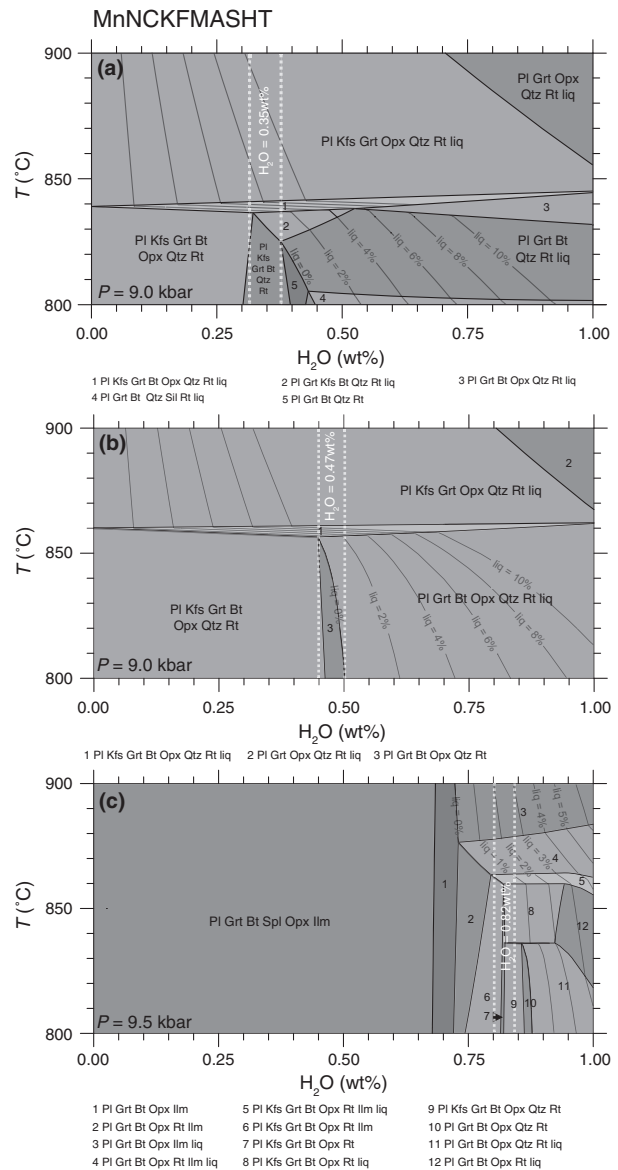


**Fig. 8.** The  $T$ – $X$  pseudosections used in determining the  $H_2O$  content of the peak assemblage in the granulites.  $H_2O$  content was determined through consideration of the amount of melt present in the peak assemblage (liq < 10 vol.%), the occurrence and disappearance of some phases (Sil, Crd, Kfs, Qtz and Opx) and the biotite breakdown reaction happening between 820 and 870 °C. Water on the  $x$ -axis varies from 0 to 1 wt%. (a)  $T$ – $H_2O$  pseudosection for sample M5 at 9.0 kbar. Water content for peak assemblage (Pl + Kfs + Grt + Bt + Qtz + Rt + liq) is estimated at 0.35 wt% (< 2 vol.%) where Sil is not stable. (b)  $T$ – $H_2O$  pseudosection for sample DT04B at 9.0 kbar. Water content for peak assemblage (Pl + Kfs + Grt + Opx + Bt + Qtz + Rt + liq) is estimated at 0.47 wt% (< 10 vol.%). (c)  $T$ – $H_2O$  pseudosection for sample DT14 at 9.5 kbar. Water content for peak assemblage (Pl + Kfs + Grt + Opx + Bt + Qtz + Rt + Ilm + liq) is estimated at 0.82 wt% (< 5 vol.%) where biotite breaks down between 840 and 860 °C.

the melt proportion is below 2 vol.% (Fig. 11b). The preserved granulite assemblage Grt + Opx + Crd + Pl + Kfs + Bt + Qtz + Rt is stable between 700–845 °C



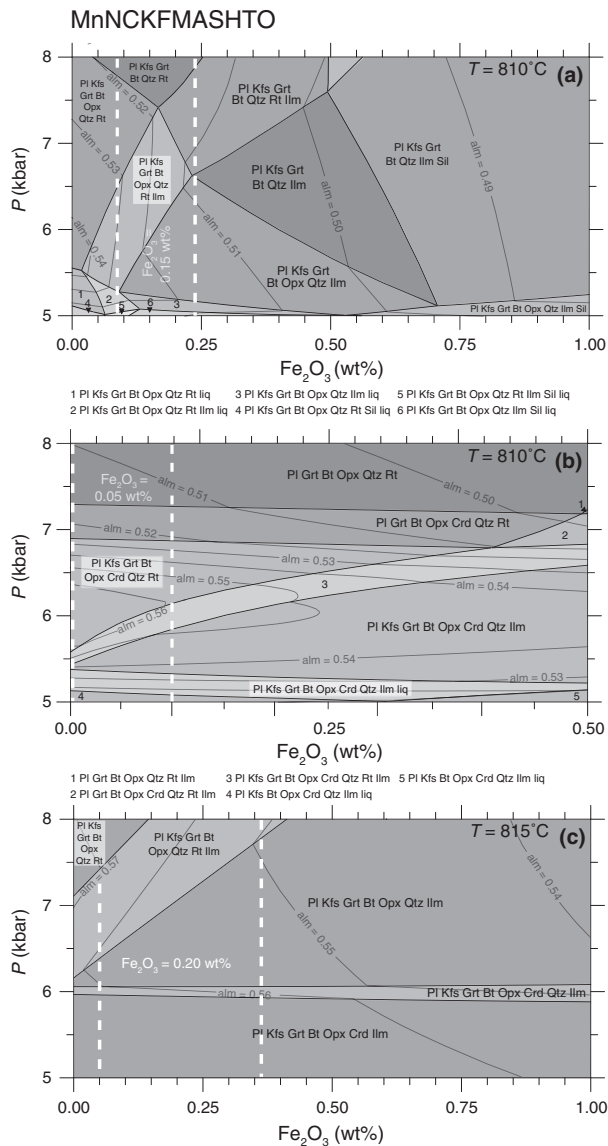


**Fig. 9.**  $P$ - $X$  pseudosections used for determination of  $\text{Fe}_2\text{O}_3$  content of the rocks.  $\text{Fe}^{3+}$  was determined using  $X_{\text{alm}}$  isopleths on the pseudosections in conjunction with the observed compositions of the peritectic garnet at the preserved granulite facies conditions, as well as the nature (Rt and/or Ilm) of the oxide at the peak metamorphic conditions (i.e. in inclusion in garnet or orthopyroxene) and in the preserved granulite assemblage (i.e. in the matrix).  $\text{Fe}_2\text{O}_3$  on the  $x$ -axis varies from 0 to 1 wt% or 0.5 wt%. (a)  $P$ - $\text{Fe}_2\text{O}_3$  for sample M5 at 810 °C.  $\text{Fe}^{3+}$  is estimated at 0.15 wt% as ( $X_{\text{alm}} = 0.51$ – $0.53$ ) with Rt and Ilm in the matrix. (b)  $P$ - $\text{Fe}_2\text{O}_3$  for sample DT04B at 810 °C.  $\text{Fe}^{3+}$  is estimated at 0.05 wt% as ( $X_{\text{alm}} = 0.54$ – $0.56$ ) with Rt in the matrix. (c)  $P$ - $\text{Fe}_2\text{O}_3$  for sample DT14 at 815 °C.  $\text{Fe}^{3+}$  is estimated at 0.20 wt% as ( $X_{\text{alm}} = 0.55$ – $0.57$ ) with Ilm in the matrix.

and 5.0–7.4 kbar (Fig. 11a). Within this field (Fig. 11c–e), garnet (5–20 vol.%), cordierite (0–15 vol.%) and orthopyroxene (25–35 vol.%) modes are consistent with estimates of mineral proportions in thin section (garnet: ~10 vol.%; cordierite:

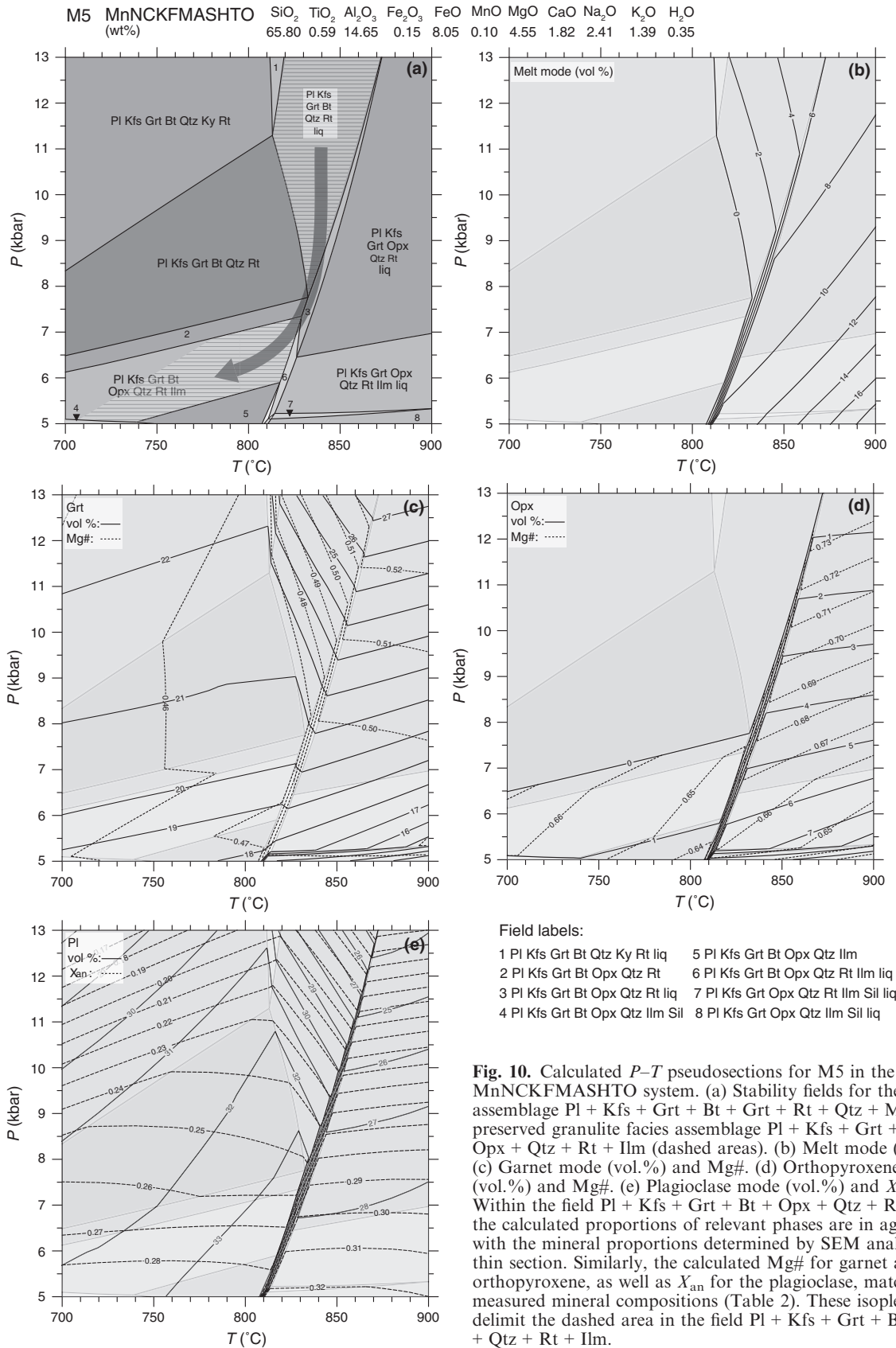
~5 vol.%; orthopyroxene: ~30 vol.%). The low- $P$  boundary of the preserved assemblage field is delimited by the ilmenite-in reaction line. Modes of orthopyroxene and cordierite increase with decompression through the preserved assemblage field, with a corresponding decrease in garnet proportion. This is reflected in thin section by the presence of cordierite and orthopyroxene corona around garnet. The Mg# values measured in garnet (0.38–0.47), orthopyroxene (0.64–0.69) and cordierite (0.84–0.87) fit with the Mg# isopleths calculated for the preserved assemblage field (garnet Mg#: 0.42–0.48; orthopyroxene Mg#: 0.62–0.68; and cordierite Mg#: 0.84–0.86) (Fig. 11c–e). The use of these calculated mineral isopleths helps to narrow down the likely  $P$ - $T$  conditions of equilibration of the preserved granulite facies assemblage to 725–845 °C and 5.8–7.4 kbar.

### Sample GMr

The small domains of retrograde assemblage development in the DT04B sample are potentially useful in constraining parts of the retrograde  $P$ - $T$  evolution. The relevant bulk composition has been determined by electron beam analysis, as described in the Whole-rock chemistry section (Fig. 12). The  $\text{H}_2\text{O}$  content of the retrograde domain has been determined via a  $T$ - $X_{\text{H}_2\text{O}}$  pseudosection, to allow the coexistence of orthoamphibole and kyanite. This is consistent with the textural characteristics of the retrograde domains. GMr is characterized by the assemblage Grt + Bt + Pl + Qtz + Rt  $\pm$  Oam  $\pm$  Ky (Fig. 10). This assemblage is stable between below 640 °C and 4.0–6.5 kbar. The low- $P$  boundary for this field is delimited by the ilmenite-in reaction line (Fig. 12).

### Sample DT14

The peak metamorphic assemblage is defined by Grt + Opx + Bt + Pl + Kfs + Rt + Melt, which has a field of stability between 830–860 °C and 8.75–12.5 kbar (Fig. 13a). Within this field, the mode of melt is <1 vol.% (Fig. 13b). The preserved garnet-rich granulite facies assemblage, Grt + Opx + Pl + Bt + Qtz + Ilm + Kfs, is stable between 700–830 °C and 5.6–8.75 kbar (Fig. 13a). The measured garnet mode in thin section (50–60 vol.%) matches with the calculated garnet mode (55–60 vol.%) for the preserved assemblage field (Fig. 13c–e). The low- $P$  boundary for this field is delimited by the cordierite-in reaction line. The occurrence of quartz in the recorded assemblage field reflects the partial consumption of orthopyroxene, with the presence of melt, along the retrograde path by the modelled reaction  $\text{Opx} + \text{Melt} = \text{Qtz} + \text{Bt}$ . In thin section, the garnet and the orthopyroxene display Mg# of 0.36–0.43 and 0.63–0.65 respectively; and the plagioclase is characterized by an  $X_{\text{an}}$  value of 0.28–0.29. There is a good fit with these values and the values calculated in the pseudo-



section (garnet Mg#: 0.39–0.41; orthopyroxene Mg#: 0.62–0.64; and plagioclase  $X_{an}$ : 0.24–0.34) (Fig. 13c–e). The combination of these isopleths helps to narrow down the field of equilibration of the preserved assemblage to 710–825 °C and 6.2–7.7 kbar.

### Prograde path

The prograde path can be investigated by reintegrating melt back into the melt-depleted bulk composition of the restitic granulites. This was achieved using the method of White *et al.* (2004) by reintegrating step by step, with decreasing temperature, the melt composition predicted to be in equilibrium with the restitic rock. We applied melt reintegration step methods to the two main lithologies of SM (M5) and metapelite (DT04B).

The pseudosection modelling of the melt-reintegrated semipelitic (M5) bulk-composition predicts that muscovite was present just below the wet solidus, with the subsolidus assemblage Pl + Bt + Ms + Qtz + Ilm ± Grt and H<sub>2</sub>O (<0.5 vol.%) stable at 650 °C and 6.0–9.5 kbar (Fig. 14a). On crossing the wet solidus, the rock undergoes muscovite breakdown (650 °C) followed by the onset of biotite melting at ~725–750 °C, as is indicated by the increase in melt mode. A small amount of K-feldspar is formed as a consequence of muscovite breakdown but its amount remains very low (<5 vol.%). As the temperature and the pressure increase towards peak metamorphic conditions (dashed area in Fig. 11a), the modes of melt and garnet increase (Fig. 14b) due to the formation of peritectic garnet and melt by fluid-absent melting reactions. Garnet mode at peak metamorphic conditions (~12 vol.%) matches the garnet mode observed in thin sections (10–15 vol.%). Melt mode reaches 14–24 vol.% at peak conditions.

The pseudosection modelling of the melt-reintegrated metapelitic (DT04B) bulk composition predicts that muscovite and sillimanite were present just below the wet solidus in the pre-melting assemblage Grt + Pl + Bt + Ms + Qtz + Sil and H<sub>2</sub>O (<0.5 vol.%) at 650 ± 20 °C and 6.5 ± 0.5 kbar (Fig. 14c). The maximum pressure for the pre-melting assemblage is given by the occurrence of sillimanite-in inclusions in garnet. Below 10.0 kbar, on crossing the wet solidus, muscovite breaks down (670 °C) followed by the onset of biotite melting at ~800 °C, as is indicated by the increase in melt mode. A small amount of K-feldspar is formed as a consequence of muscovite breakdown, but its amount remains very low (<5 vol.%). As the temperature and the pressure increase towards peak metamorphic conditions (dashed area in Fig. 14c), garnet mode increases along with the mode of melt (Fig. 14d), due to the formation of peritectic phases during fluid-absent partial melting reactions. The garnet mode at peak metamorphic conditions (10–14 vol.%) matches that

observed in thin sections (~10 vol.%). Melt mode reaches 24–38 vol.% at peak conditions.

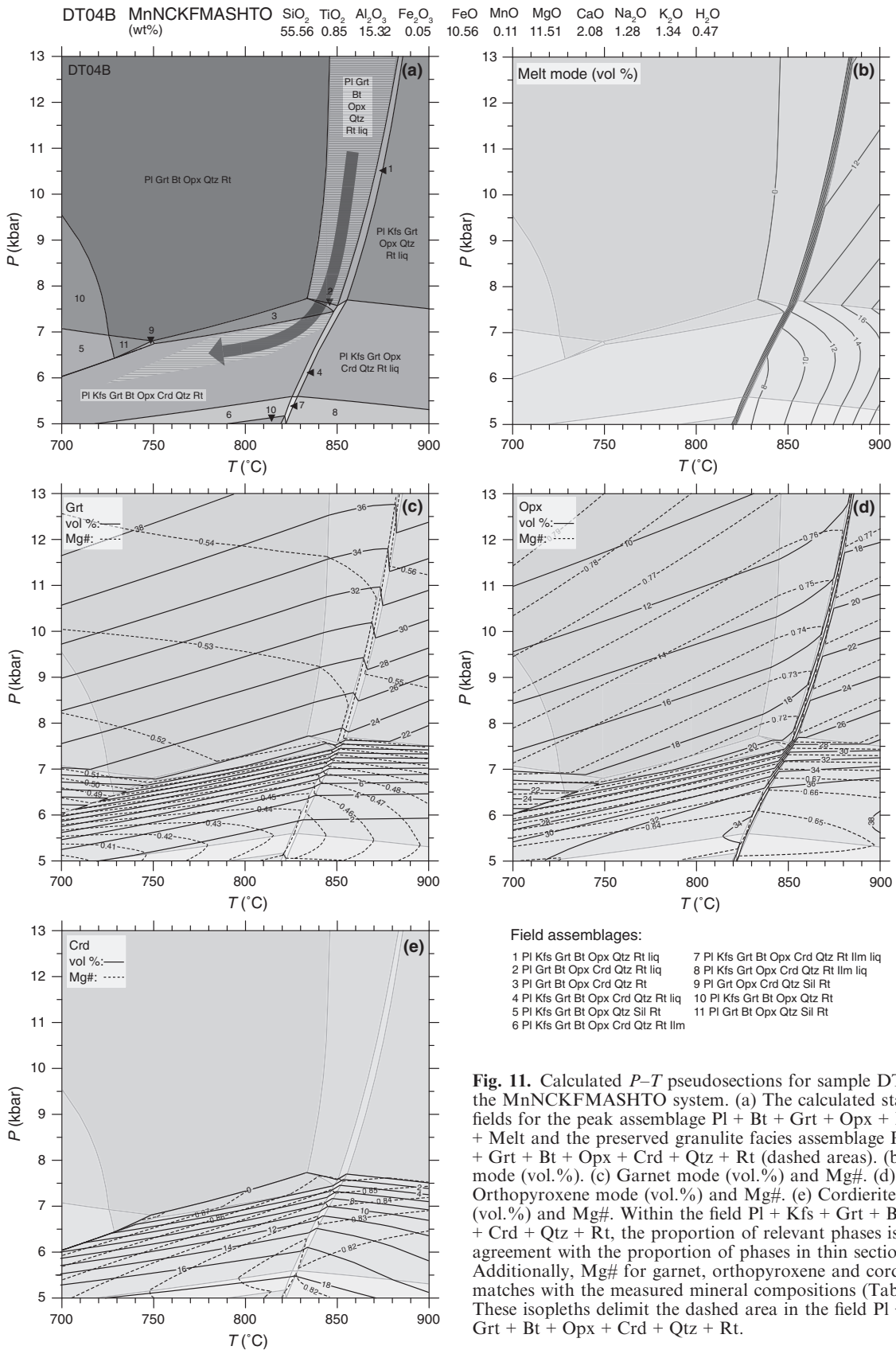
The combination of the two pseudosections indicates pre-melting conditions of 625–670 °C and 6.0–6.75 kbar. The resultant prograde paths constrained by sample M5 and DT04B agree with the *P–T* path determined by previous studies on the metasedimentary rocks exposed at the Bandelierkop quarry (Stevens & Van Reenen, 1992a,b; Taylor *et al.*, 2014). The pre-melting assemblage is stable for *P–T* conditions allowing the presence of sillimanite in aluminosilicate-bearing pre-anatexis metapelites of the Bandelierkop Formation (Stevens & Van Reenen, 1992a,b; Taylor *et al.*, 2014).

### *P–T* path

Rocks used in this study come from the same continuous locality. As they share the same degree of deformation and no major structural breaks are observed within the outcrop, the rocks exposed at the Brakspruit quarry are all interpreted to have experienced the same *P–T* evolution. Consequently, all the pseudosections are combined to obtain an accurate estimate of the peak to high-*T* retrograde portion of the *P–T* path (Fig. 15) followed by the portion of the SMZ. The melt-reintegrated pseudosections provide information on the prograde path with the relevant subsolidus conditions constrained to 625–670 °C and 6.0–6.75 kbar. In addition, the melt-reintegrated modelling allows the development of their peritectic mineral assemblage and melt production to be evaluated. Garnet proportion increases from <1 to ~15 vol.% along the prograde path, which is consistent with its poikiloblastic character observed in the samples (Taylor *et al.*, 2014; this study). It is also consistent with relevant experimental studies (Vielzeuf & Holloway, 1988; Patiño Douce & Johnston, 1991; Montel & Vielzeuf, 1997; Stevens *et al.*, 1997; Patiño Douce & Harris, 1998; Pickering & Johnston, 1998) that indicate garnet growth and increase in melt volume after biotite starts breaking down at ~800 °C. Peak conditions are 852.5 ± 7.5 °C and 11.1 ± 1.3 kbar. The different preserved granulite facies assemblages overlap at 787.5 ± 32.5 °C and 6.7 ± 0.5 kbar. Thus, rocks from the Brakspruit quarry have undergone isothermal decompression of 2.5–6.1 kbar. Then, thanks to preserved small retrograde amphibolite facies assemblages, it can be demonstrated that the rocks cooled to temperatures below 640 °C at a pressure of 5.25 ± 1.25 kbar.

### GEOCHRONOLOGY

In an attempt to constrain the duration of the prograde and retrograde portion of the metamorphic episode, cores and/or rims of zircon were analysed in different samples. The age spectrum derived from the



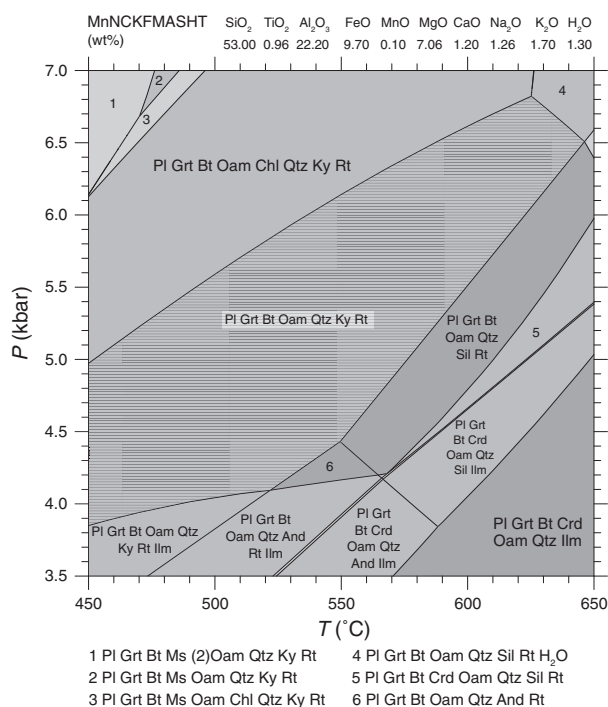


**Fig. 12.** Calculated  $P$ - $T$  pseudosection for the GMr composition. An average of the compositions of four  $\sim 0.1$  cm<sup>2</sup> sized domains characterized by retrograde assemblages gives the following composition: SiO<sub>2</sub>:  $53.0 \pm 2.86$  wt%; TiO<sub>2</sub>:  $0.96 \pm 0.27$  wt%; Al<sub>2</sub>O<sub>3</sub>:  $22.2 \pm 5.44$  wt%; FeO<sub>T</sub>:  $9.70 \pm 1.25$  wt%; MnO:  $0.1 \pm 0.05$  wt%; MgO:  $7.06 \pm 0.54$  wt%; CaO:  $1.2 \pm 0.75$  wt%; Na<sub>2</sub>O:  $1.26 \pm 0.57$  wt%; K<sub>2</sub>O:  $1.70 \pm 0.32$  wt%; H<sub>2</sub>O:  $1.30$  wt%. The pseudosection displays the retrograde assemblage to Pl + Bt + Grt + Qtz + Ky + Oam + Rt assemblage (dashed area) at a temperature of  $<640$  °C and pressure of 4.0–7.0 kbar.

cores of detrital zircon in metapelite provides a minimum age constraint for the deposition of the sediments of the Bandelierkop Formation. Analyses of zircon rims from the first generation of leucosome samples provide an age estimate for peak metamorphism. Zircon analyses from the crosscutting pegmatite provide a minimum age estimate for the end of deformation in the Brakspruit locality (see method in Appendix S1). Closure temperature for Pb-U-Th in zircon exceeds 900 °C (Lee *et al.*, 1997), therefore the age estimates are considered to reflect the zircon crystallization age.

#### Detrital zircon

Zircon crystals extracted from the metapelites (M2) of the Brakspruit quarry are typically 50–150  $\mu$ m in size, and rounded in shape. Cathodoluminescence (CL) imaging of their internal structure shows euhedral oscillatory-zoned core domains, with the zoning in the cores truncated by the abraded surface and with an overgrowth rim. LA-ICP-MS analyses of core domains (110 spots) show that they have relatively high Th/U ratios, i.e. Th/U = 0.2–1.78. In spot

analyses of the cores, 47 are  $\geq 90\%$  concordant and define a continuous trend from *c.* 3300 to *c.* 2700 Ma (Fig. 16a). These data yield a maximum <sup>207</sup>Pb/<sup>206</sup>Pb depositional age of  $2733 \pm 13$  Ma. The remaining data are  $<90\%$  concordant and were therefore not utilized. The narrow zircon rims do not allow accurate determination of the metamorphic age. Th/U ratios were used to remove any potentially mixed core-rim analyses (low Th/U ratio) from the data set to improve age calculation on the detrital zircon ages.

#### Metamorphic zircon

Zircon grains extracted from the garnet-bearing deformed leucosomes (L1b) vary between 100 and 300  $\mu$ m in size and have rounded shapes. CL imaging of their internal structure shows euhedral, oscillatory-zoned core domains, which are truncated and overgrown by large unzoned rim domains. Th/U ratios in the rim domains are 0.02–0.08. Of 48 spot analyses of the rims, 40 are  $>95\%$  concordant (Fig. 16b). The concordia ages for the metamorphic rims are  $2713 \pm 8$  Ma giving an accurate estimate of the age of peak metamorphism. The remaining  $<90\%$  concordant data are excluded from age calculation. Three core spots have been analysed and display concordant <sup>207</sup>Pb/<sup>206</sup>Pb ages of  $2754 \pm 34$ ,  $2769 \pm 35$  and  $2848 \pm 34$  Ma.

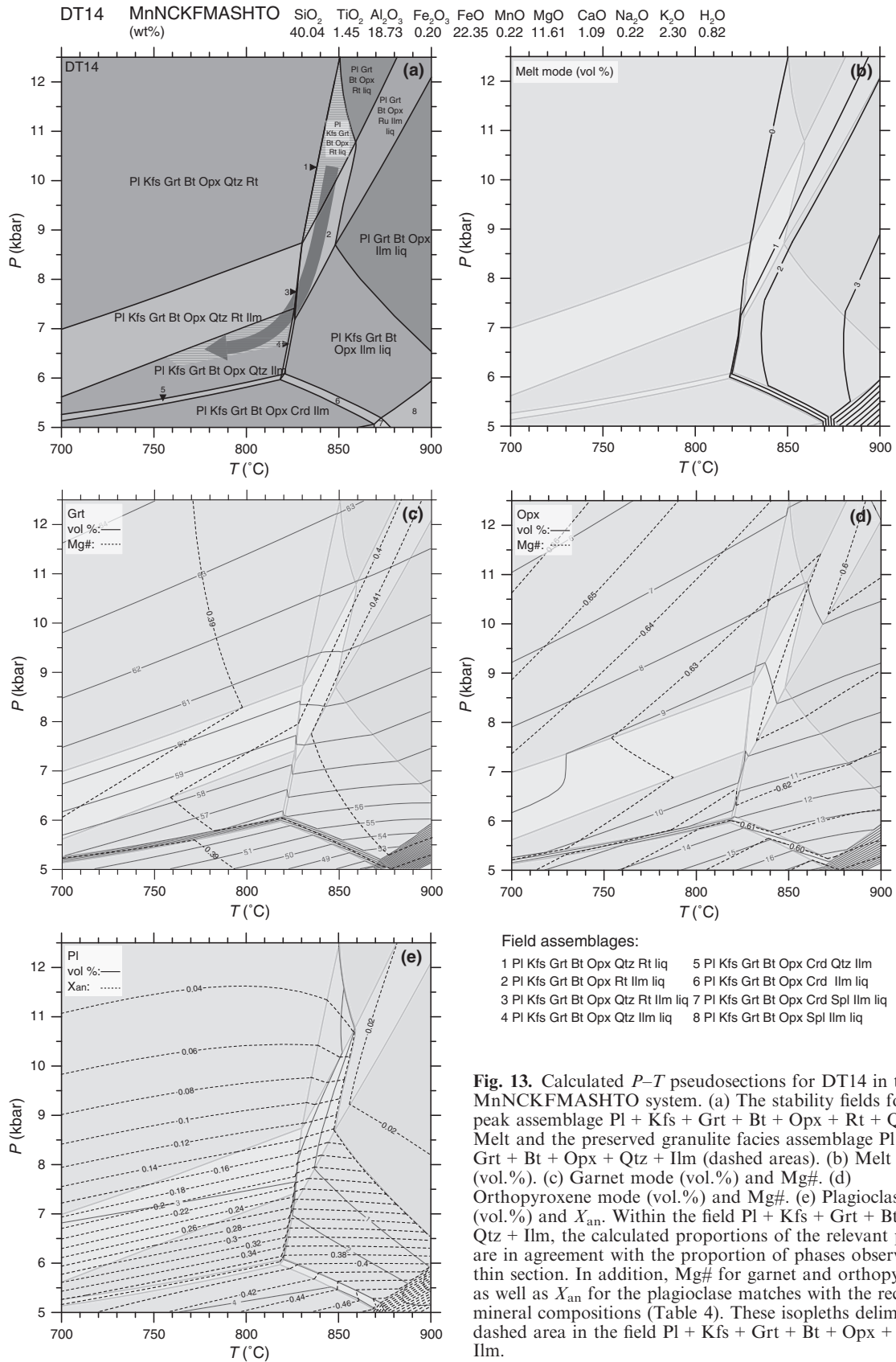
#### Zircon in the pegmatite

Zircon grains extracted from the pegmatite (Peg1) are 200–500  $\mu$ m in size, and are elongated and idioblastic in shape. CL imaging of the internal structure of the zircon shows continuous euhedral oscillatory zoning. LA-ICP-MS analyses have relatively low Th/U ratios, i.e. Th/U = 0.17–0.88. Fifty-eight spot analyses ( $>90\%$  concordant) were performed (Fig. 16c). The upper intersect with the Concordia gives an age of  $2680 \pm 6$  Ma. The lower intercept gives an age of  $32 \pm 260$  Ma and does not have any geological significance.

## DISCUSSION

#### High-resolution peak $P$ - $T$ constraints for the SMZ

Using pseudosection analysis of several different rock types, the peak metamorphic conditions experienced by the rocks of the Brakspruit quarry were determined to be within the range  $852.5 \pm 7.5$  °C and  $11.1 \pm 1.3$  kbar (Fig. 15). This estimate appears to be robust, as there is good agreement with the less precise peak  $P$ - $T$  estimate of Taylor *et al.* (2014) for the rocks of the Bandelierkop quarry, i.e. 820–890 °C and 8.0–12.0 kbar. There is also a good fit between the predicted  $P$ - $T$  conditions of equilibration and the petrographic and field evidences for partial melting



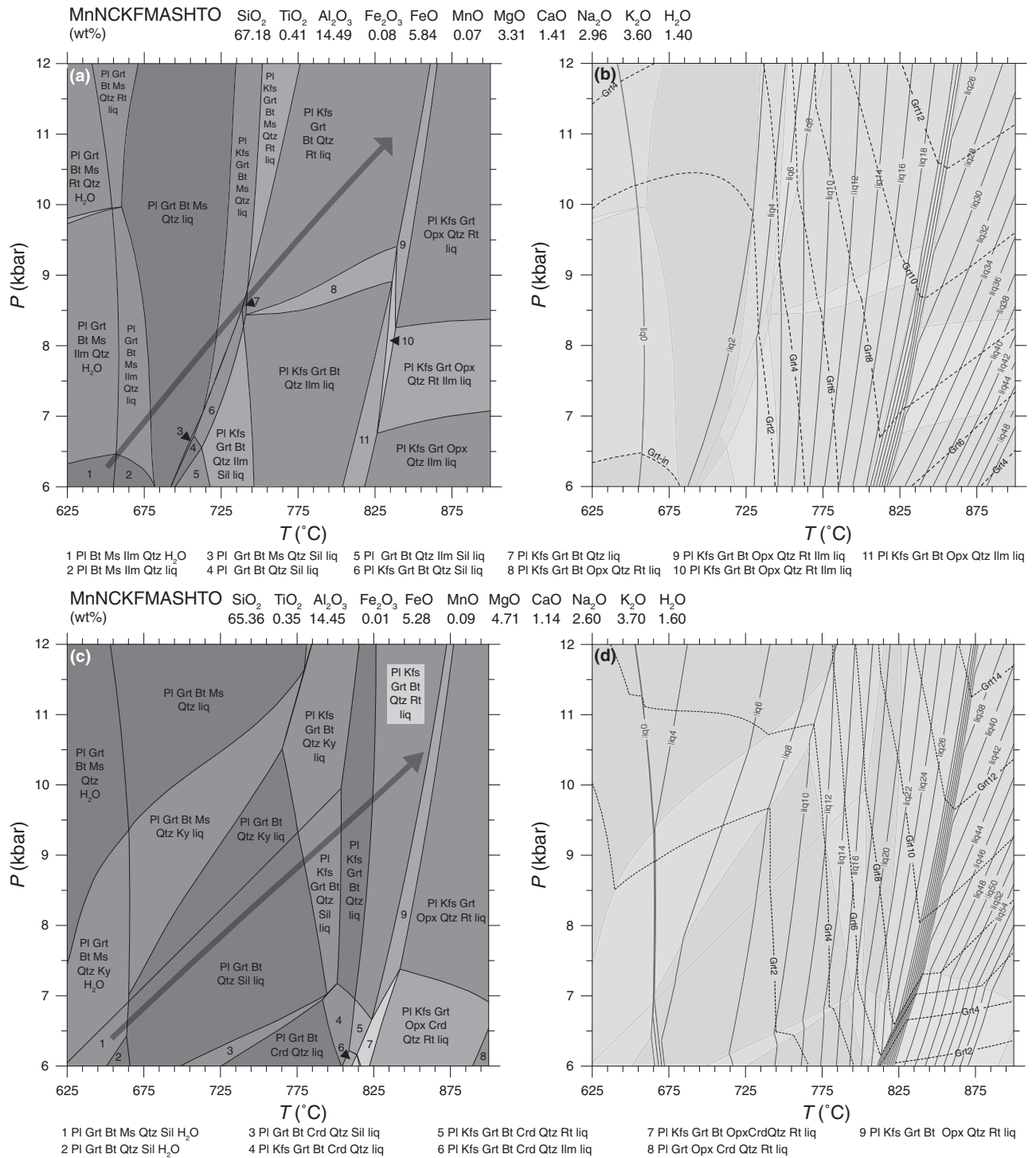


**Fig. 14.** Melt-reintegrated  $P$ - $T$  pseudosection for samples M5 (a, b) and DT04B (c, d) (method by White *et al.*, 2004). (a) The arrow shows the prograde path from the subsolidus assemblage, PI + Bt + Ms + Qtz + H<sub>2</sub>O ± Grt, towards peak metamorphism, PI + Kfs + Grt + Bt + Rt + Qtz + Melt (dashed area). This path goes through aluminium phase (Sil, Ky and Crd) free fields. (b) Melt (liq) and garnet (Grt) modes (vol.%). (c) The arrow shows the prograde path from the subsolidus assemblage, PI + Bt + Ms + Qtz + Sil + H<sub>2</sub>O towards peak metamorphism, PI + Kfs + Grt + Bt + Rt + Qtz + Melt (dashed area). As no inclusion of kyanite has been found in the garnet, this path does not cross the Sil/Ky reaction line. (d) Melt (liq) and garnet (Grt) modes (vol.%).

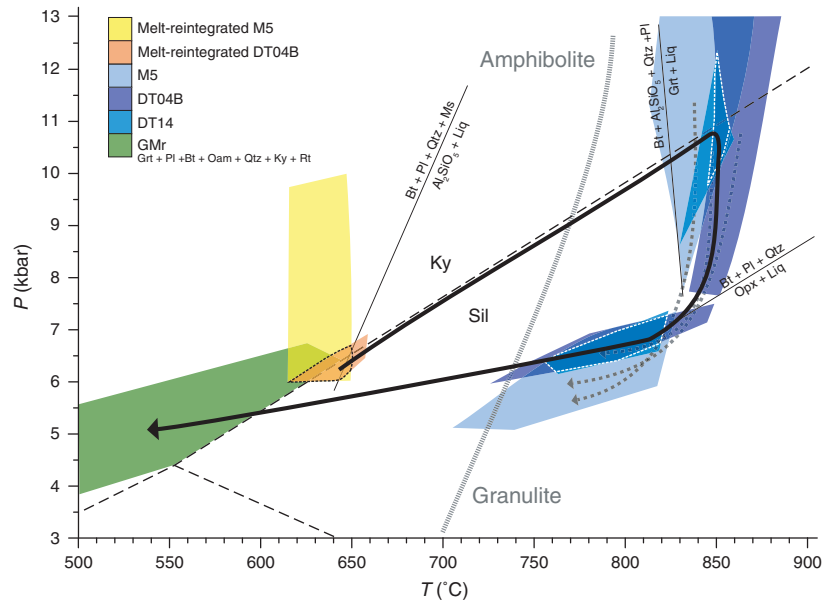


**Fig. 15.**  $P$ - $T$  path for metasedimentary rocks from the Brakspruit quarry. Compilation of the prograde, peak metamorphic conditions, preserved granulite facies and retrograde  $P$ - $T$  conditions from Figs 10, 11, 12, 13 and 14. Reaction curves after partial melting experiments (Vielzeuf & Holloway, 1988; Patiño Douce & Johnston, 1991; Montel & Vielzeuf, 1997).

of the rocks.  $Bt + Sil + Qtz + Pl$  stability has been exceeded in all rocks; while in some rocks the availability of quartz and aluminosilicate has limited the progress of the incongruent biotite melting reaction. Comparison with the behaviour of biotite in relevant experimental studies (Vielzeuf & Holloway, 1988; Patiño Douce & Johnston, 1991; Montel & Vielzeuf, 1997; Stevens *et al.*, 1997; Patiño Douce & Harris, 1998; Pickering & Johnston, 1998) suggests that the temperature bracket for peak metamorphic condition is probably  $\pm 10$  °C, with a temperature not exceeding 900 °C, which is in good agreement with the preservation of peak metamorphic biotite in the rock. The pressure peak is constrained by the presence of a small fraction of melt, the nature of the titanium oxide phase and the absence of cordierite in the mineral assemblage. Combination of several pseudosections helps to narrow down the pressure bracket to  $\pm 1.3$  kbar. The preserved granulite facies assemblages are defined by the presence of cordierite and/or orthopyroxene. Within the calculated  $P$ - $T$  stability fields for the preserved granulite facies assemblages, garnet, orthopyroxene and cordierite  $Mg\#$  isopleths as well as  $X_{an}$  in plagioclase help to narrow down the field of equilibration to  $787.5 \pm 32.5$  °C and  $6.7 \pm 0.5$  kbar. Consequently, this indicates a  $4.3 \pm 1.8$  kbar of near-isothermal decompression between peak pressure and that of equilibration of the preserved granulite facies assemblage. This relatively precise constraint on the amount of decompression is made possible by the fact that the rocks have retained sufficient melt to have undergone minor retrogression on cooling, typically by reactions that have consumed cordierite and to a lesser degree, orthopyroxene. This has been demonstrated in this study (cf. Petrography) and previous works (Stevens, 1997; Taylor *et al.*, 2014).

#### $P$ - $T$ - $t$ loop for the SMZ

The combination of U-Pb dating on zircon from the leucosomes, metapelites and pegmatite, with the metamorphic constraints discussed above, results in a well-constrained high-grade  $P$ - $T$ - $t$  path for the granulite grade portion of the SMZ that hosts the Brakspruit quarry (Fig. 17). Peak metamorphism and partial melting recorded in the SMZ anatectites has been dated at  $2713 \pm 8$  Ma (Taylor *et al.*, 2014; this study). The age of peak metamorphism for the Bavianskloof Gneiss, which hosts the Bandelierkop Formation, of *c.* 2720 Ma (Retief *et al.*, 1990), matches with the results obtained on the Brakspruit metasedimentary rocks and confirms that both units shared a common metamorphic history. Kreissig *et al.* (2001) determined an age of metamorphism for leucocratic features of  $2691 \pm 7$  Ma via U-Pb dating of two monazite crystals. In comparison, this study has obtained ages from over 40 zircon crystals. The data support a zircon crystallization age of  $2713 \pm 8$  Ma. The relatively small discrepancy between these ages may be a consequence of the fact that the much larger data set of near-concordant analyses in this study provides a more precise determination of the actual age of high-grade metamorphism. However, it is also important to consider that zircon in leucosomes typically crystallizes close to peak temperature, while monazite typically crystallizes at lower temperature conditions (Parrish, 1990; Lee *et al.*, 1997). After peak metamorphism, the rocks of the SMZ underwent isothermal decompression followed by isobaric cooling to retrograde amphibolite facies conditions. The Kreissig *et al.* (2001) age of  $2691 \pm 7$  Ma on the monazite in the Bandelierkop quarry leucosomes can be linked to the formation of the retrograde assemblage and the crystallization of the last drops of melt



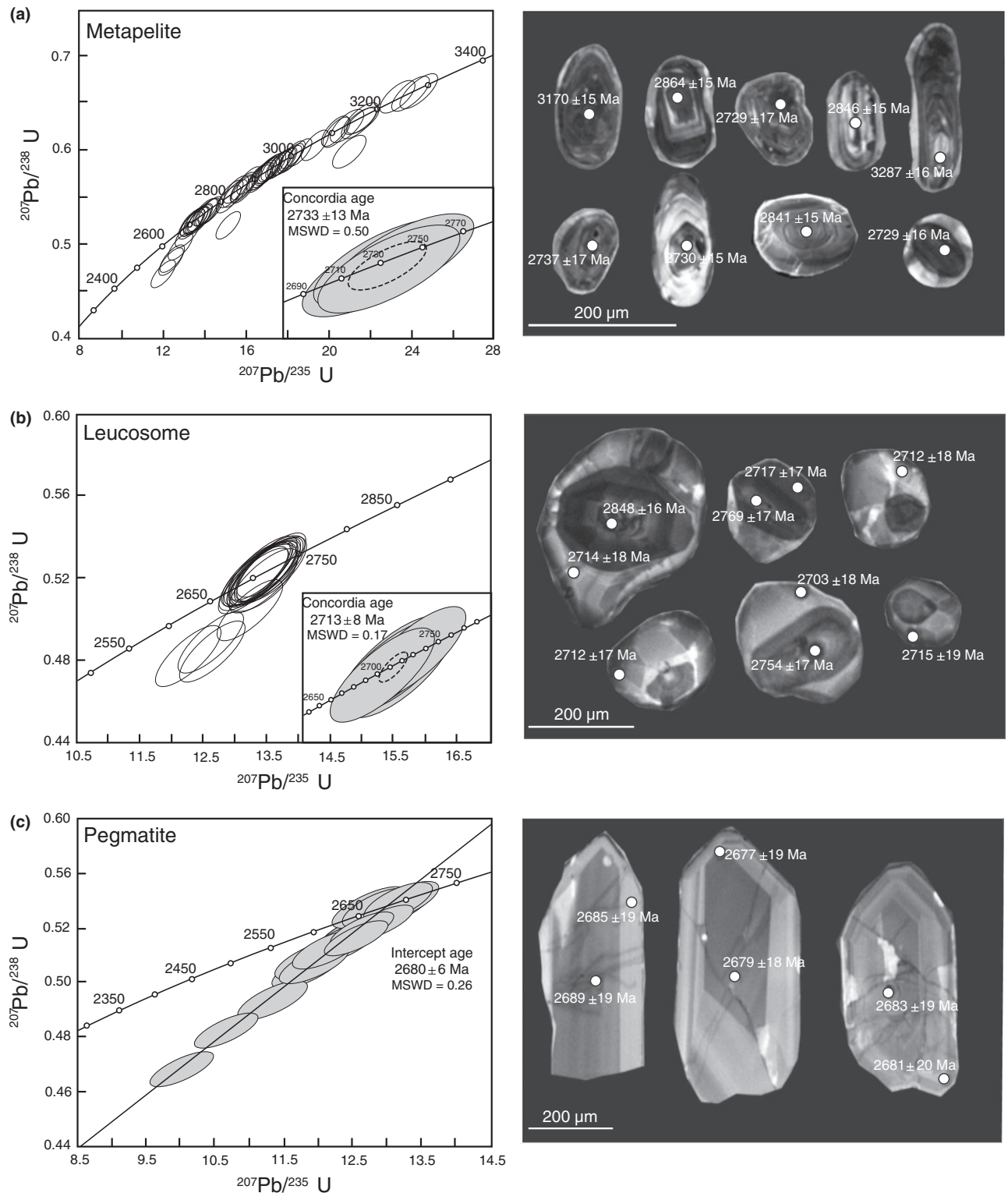


**Fig. 16.** U–Pb concordia plots and representative CL images for the zircon crystals analysed in this study. (a) Detrital zircon from metapelite M2. (b) Zircon from concordant leucosome L1b. (c) Zircon from pegmatite Peg1. Data-point error ellipses are shown at  $2\sigma$ . The full LA–ICP–MS U/Pb zircon data set used for calculation can be found in Tables S1–S3.

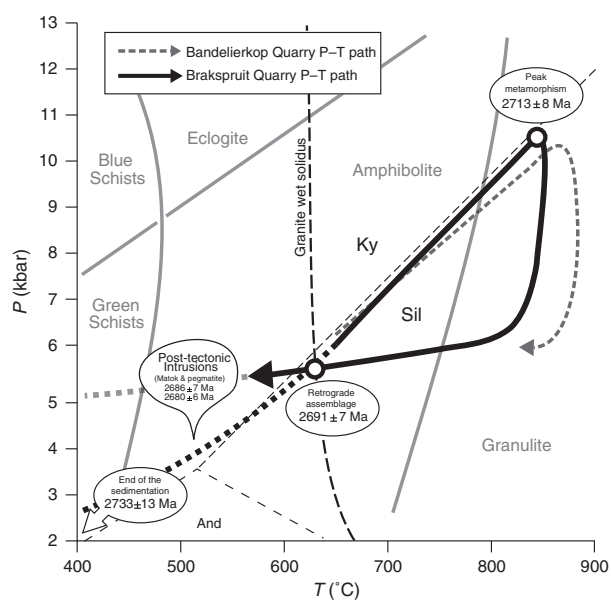


**Fig. 17.**  $P$ - $T$ - $t$  path for the SMZ metasedimentary rocks.  $P$ - $T$  path by Taylor *et al.* (2014) for the metapelites of the Bandelierkop quarry has been added for comparison. Matok age after Laurent *et al.* (2013). Retrograde age after Kreissig *et al.* (2001).

in the system when the rocks crossed the granite wet solidus (Fig. 17). Therefore, it brackets the speed of the exhumation + cooling event to  $\sim 0.7$  mm yr $^{-1}$ . The end of the penetrative deformation event at the Brakspruit quarry is indicated by the intrusion of late undeformed pegmatites at  $2680 \pm 6$  Ma (Fig. 17). This finding is consistent with the emplacement of the post-tectonic Matok body at  $2686 \pm 7$  Ma (Laurent *et al.*, 2013).

### The SMZ: record of an active margin, not simply reworked Kaapvaal craton rocks

Over the years, there have been many models applied to the SMZ as a means to explain the Limpopo orogenic episode: the Neoproterozoic Himalayan type model with accretion of several terranes responsible for crustal thickening (Roering *et al.*, 1992b; Aikman *et al.*, 2008), the transpressive collisional event and the uplift of the CZ model (Schaller *et al.*, 1999), the terranes accretion model (Barton *et al.*, 2006) and the more recent continent–continent collision model involving slab break-off (Khoza *et al.*, 2013; Laurent *et al.*, 2014). In addition, Gerya *et al.* (2000) suggested an alternative process to lateral accretion by proposing gravitational instability to generate the granulite facies rocks. Most of these models try to explain the formation of the Limpopo Belt as a single geological object in contact with the surrounding cratons. In this study, there is strong evidence that the SMZ is not only part of the Kaapvaal craton but contains evidence for an active margin setting.

The SMZ appears to include reworked Kaapvaal craton basement Baviaanskloof gneisses (Kreissig *et al.*, 2000), mafic/ultramafic rocks of unknown affinity and clastic sedimentary rocks, deriving from source rocks whose ages range between *c.* 3300 and *c.* 2730 Ma. This implies that the sediments from the Bandelierkop Formation metasedimentary rocks are not the equivalent of any of the greenstone belt sedimentary successions on the Kaapvaal craton. This wide spectrum of ages, with the majority of zircon crystals indicating source rocks younger than *c.* 3000 Ma, is very different to what could be predicted for sediments formed through erosion of the northern Kaapvaal craton. In this portion of the craton, ages range between 3.5 and 3.0 Ga, with a big peak at *c.* 3.1 Ga (Zeh *et al.*, 2013). Therefore, it is likely that the sediments were derived from another source such as the block colliding with the Kaapvaal craton or non-preserved volcanic arcs that would constitute a large sedimentary discharge along the northern boundary of the Kaapvaal craton.

The  $P$ - $T$ - $t$  path modelled for the rocks from the Brakspruit quarry is similar to the  $P$ - $T$  path modelled for the Bandelierkop quarry (Taylor *et al.*, 2014), some 15 km to the south. Consequently, it appears reasonable to propose that the  $P$ - $T$  path followed by the rocks at these two quarry exposures may be applicable to the whole SMZ (Fig. 17). The burial rate of the Bandelierkop Formation metasedimentary rocks is well constrained to  $\sim 0.17$  cm yr $^{-1}$  by their maximum sedimentation age ( $2733 \pm 13$  Ma) combined with the age and  $P$ - $T$  conditions of peak metamorphism ( $10.8 \pm 1.6$  kbar at  $2713 \pm 8$  Ma) (Fig. 17). Thus, the SMZ underwent metamorphism equivalent to lower crust conditions (35 km depth,  $\sim 11.0$  kbar) followed by an isothermal decompression and an isobaric cooling in less than 35 Ma. As the current thickness of the continental crust in the SMZ is  $\sim 30$  km (Roering *et al.*, 1992a), this implies that the thickness of the crust is likely to have exceeded 60 km at *c.* 2713 Ma. Collectively, these findings strongly argue for a double thickening of the crust at *c.* 2.7 Ga (Ellis, 1987). In such a scenario, the amount of radiogenic material in the crustal pile (Andreoli *et al.*, 2011) would have been sufficient to produce the heat responsible for the metamorphic episode.

Deposition of sediments on the northern part of the Kaapvaal craton, fast burial (10–20 Ma), double thickening of the crust and isothermal decompression strongly argue in favour of a convergence zone culminating in continental collision along the northern margin of the Kaapvaal craton at *c.* 2.7 Ga with the SMZ interpreted to be the active margin in an important orogenic system.

### CONCLUSIONS

The SMZ of the Limpopo Belt represents the northern margin of the Kaapvaal craton, metamorphosed

and deformed during the late Archean *c.* 2.7 Ga. At this time, sedimentary rocks formed from active margin detritus were deposited on the Kaapvaal craton basement and subsequently buried and metamorphosed to granulite facies grade and partially exhumed in an *c.* 35 Ma period. This study demonstrates the existence of an active continental convergence domain. These findings combined with previous studies strongly argue for the presence of lateral shortening and present look-alike modern orogenic mechanisms in the Neoproterozoic.

## ACKNOWLEDGEMENTS

The authors thank Prof. A. Kister, Dr K. Cutts and Dr G. Mahéo for discussion and advice, as the editor Dr D. Robinson, Dr P. Horváth and the anonymous reviewers for their helpful comments. We also acknowledge the owner of the Brakspruit quarry for allowing us access to his property. This work was carried out as part of the France–South Africa scientific collaboration and was supported by a National Research Foundation (South Africa) grant and Centre National de la Recherche Scientifique (France) funding. G. Stevens and G. Nicoli acknowledge PhD bursary support to G. Nicoli via the SARChI programme.

## REFERENCES

- Aikman, A.B., Harrison, T.M. & Lin, D., 2008. Evidence for early (>44 Ma) Himalayan crustal thickening, Tethyan Himalaya, southeastern Tibet. *Earth and Planetary Science Letters*, **274**, 14–23.
- Andreoli, M.A.G., Brandl, G., Kramer, J.D. & Mouri, H., 2011. Intracrustal radioactivity as an important heat source for Neoproterozoic metamorphism in the Central Zone of the Limpopo Complex. In: *Origin and Evolution of Precambrian High-grade Gneiss Terranes, with Special Emphasis on the Limpopo Complex of Southern Africa* (eds Van Reenen, D.D., Kramers, J.D., McCourt, S. & Perchuk, L.L.), vol. 207, pp. 143–161. Geological Society of America Memoir.
- Barton, J.M., Doig, R., Smith, C.B., Bohlender, F. & Van Reenen, D.D., 1992. Isotopic and REE characteristics of the intrusive charnoenderbite and enderbite geographically associated with the Matok Pluton, Limpopo belt, Southern Africa. *Precambrian Research*, **55**, 451–567.
- Barton, J.M., Klemd, R. & Zeh, A., 2006. The Limpopo Belt: a result of Archean to Proterozoic, Turkeic-type orogenesis? *Geological Society of America, Special Publication*, **405**, 315–332.
- Belyanin, G.A., Rajesh, H.M., Van Reenen, D.D. & Mouri, H., 2010. Corundum + orthopyroxene + spinel intergrowths in an ultrahigh-temperature Al–Mg granulite from the Southern Marginal Zone, Limpopo Belt, South Africa. *American Mineralogist*, **95**, 196–199.
- Belyanin, G.A., Rajesh, H.M., Sajeev, K. & Van Reenen, D.D., 2012. Ultrahigh-temperature metamorphism from an unusual corundum+orthopyroxene intergrowth bearing Al–Mg granulite from the Southern Marginal Zone, Limpopo Complex, South Africa. *Contributions to Mineralogy and Petrology*, **164**, 457–475.
- Benn, K., 2006. Tectonic delamination of the lower crust during Late Archean collision of the Abitibi–Opatica and Pontiac terranes, Superior Province, Canada. *Geophysical Monograph Series, Archean Geodynamics and Environments*, **164**, 267–282.
- Block, S., Moyon, J.-F., Zeh, A., Poujol, M., Jaguin, J. & Paquette, J.-L., 2013. The Murchison Greenstone Belt, South Africa: accreted slivers with contrasting metamorphic conditions. *Precambrian Research*, **227**, 77–98.
- Buick, I.S., Hermann, J., Williams, I.S., Gibson, R.L. & Rubatto, D., 2006. A SHRIMP U–Pb and LA–ICP–MS trace element study of the petrogenesis of garnet–cordierite–orthopyroxene gneisses from the Central Zone of the Limpopo Belt, South Africa. *Lithos*, **88**, 150–172.
- Coggon, R. & Holland, T.J.B., 2002. Mixing properties of phengitic micas and revised garnet–phengite thermobarometers. *Journal of Metamorphic Geology*, **20**, 683–696.
- De Capitani, C. & Petrakakis, K., 2010. The computation of equilibrium assemblage diagrams with Theriak/Domino software. *American Mineralogist*, **95**, 1006–1016.
- Diener, J.F.A. & Powell, R., 2012. Revised activity–composition models for clinopyroxene and amphibole. *Journal of Metamorphic Geology*, **20**, 131–142.
- Diener, J.F.A., Stevens, S., Kister, A.F.M. & Poujol, M., 2005. Metamorphism and exhumation of the basal parts of the Barberton greenstone belt, South Africa: constraining the rates of Mesoproterozoic tectonism. *Precambrian Research*, **143**, 87–112.
- Droop, G.T.R., 1987. A general equation for Fe<sup>3+</sup> concentrations in ferromagnesian silicates and oxides from microprobe analyses, using stoichiometric criteria. *Mineralogical Magazine*, **51**, 431–435.
- Drummond, B.J., Goleby, B.R. & Swager, C.P., 2000. Crustal signature of Late Archean tectonic episodes in the Yilgarn craton, Western Australia: evidence from deep seismic sounding. *Tectonophysics*, **329**, 193–221.
- Du Toit, M.C., Van Reenen, D.D. & Roering, C., 1983. Some aspects of the geology, structure and metamorphism of the Southern Marginal Zone of the Limpopo metamorphic complex. *Geological Society of South Africa, Special Publications*, **8**, 121–142.
- Easton, R.M., 2000. Metamorphism of the Canadian Shield, Ontario, Canada. I. The Superior Province. *The Canadian Mineralogist*, **38**, 287–317.
- Eglington, B.M. & Armstrong, R.A., 2004. The Kaapvaal Craton adjacent orogens, southern Africa: a geochronological database and overview of the geological development of the craton. *South African Journal of Geology*, **107**, 13–32.
- Ellis, D.J., 1987. Origin and evolution of granulites in normal and thickened crust. *Geology*, **15**, 167–170.
- Frei, D. & Gerdes, A., 2009. Precise and accurate in situ U–Pb dating of zircon with high sample throughput by automated LA–SF–ICP–MS. *Chemical Geology*, **261**, 261–270.
- Gerdes, A. & Zeh, A., 2006. Combined U–Pb and Hf isotope LA–(MC)–ICP–MS analyses of detrital zircons: comparison with SHRIMP and new constraints for the provenance and age of an Armorican metasediment in Central Germany. *Earth and Planetary Science Letters*, **249**, 47–61.
- Gerya, T.V., Perchuk, L.L., Van Reenen, D.D. & Smit, C.A., 2000. Two-dimensional numerical modelling of pressure–temperature–time paths for the exhumation of some granulite facies terrains in the Precambrian. *Journal of Geodynamics*, **30**, 17–35.
- Goleby, B.R., Blewett, R.S., Korsch, R.J. et al., 2004. Deep seismic reflection profiling in the Archean northeastern Yilgarn Craton, Western Australia: implications for crustal architecture and mineral potential. *Tectonophysics*, **388**, 119–133.
- Goscombe, B., Blewett, R.S., Czarnota, K., Groenewald, P.B. & Maas, R., 2009. *Metamorphic Evolution and Integrated Terrane Analysis of the Eastern Yilgarn Craton: Rationale*,

- Methods, Outcomes and Interpretation*. Geoscience Australia, Canberra. Record 2009/23.
- Holland, T.J.B. & Powell, R., 1998. An internally consistent thermodynamic data set for phases of petrological interest. *Journal of Metamorphic Geology*, **16**, 309–343.
- Holland, T. & Powell, R., 2003. Activity–composition relations for phases in petrological calculations: an asymmetric multi-component formulation. *Contributions to Mineralogy and Petrology*, **145**, 492–501.
- Holzer, L., Frei, R., Barton, J.M. & Kramers, J.D., 1998. Unravelling the record of successive high grade events in the Central Zone of the Limpopo Belt using Pb single phase dating of metamorphic minerals. *Precambrian Research*, **87**, 87–115.
- Jackson, S.L. & Cruden, A.R., 1995. Formation of the Abitibi greenstone belt by arc-trench migration. *Geological Society of America*, **23**, 471–474.
- Khoza, D., Jones, A.G., Muller, M.R., Evans, R.L., Webb, S.J. & Miensoopust, M., 2013. Tectonic model of the Limpopo belt: constraints from magnetotelluric data. *Precambrian Research*, **226**, 143–156.
- Kreissig, K., Nagler, T.F., Kramers, J.D., Van Reenen, D.D. & Smit, C.A., 2000. An isotopic and geochemical study of the northern Kaapvaal Craton and the Southern Marginal Zone of the Limpopo Belt: are they juxtaposed terranes? *Lithos*, **50**, 1–25.
- Kreissig, K., Holzer, L., Frei, R. *et al.*, 2001. Geochronology of the Hout River Shear Zone and the metamorphism in the Southern Marginal Zone of the Limpopo Belt, Southern Africa. *Precambrian Research*, **109**, 145–173.
- Kretz, R., 1983. Symbols for rock-forming minerals. *American Mineralogist*, **68**, 277–279.
- Laurent, O., Paquette, J.-L., Martin, H., Doucelance, R. & Moyon, J.-F., 2013. LA–ICP–MS dating of zircons from Meso- and Neoproterozoic granitoids of the Pietersburg block (South Africa): crustal evolution at the northern margin of the Kaapvaal craton. *Precambrian Research*, **230**, 209–226.
- Laurent, O., Rapopo, M., Stevens, G. *et al.*, 2014. Constraining petrogenesis of Mg–K and Fe–K granitoids and implications for post-collisional magmatism: case study from the late-Archean Matok pluton (Pietersburg, South Africa). *Lithos*, **197**, 131–149.
- Lee, J.K., Williams, I.S. & Ellis, D.J., 1997. Pb, U and Th diffusion in natural zircon. *Letters to Nature*, **390**, 159–162.
- Ludden, J. & Hynes, A., 2000. The Lithoprobe Abitibi–Grenville transect: two billion years of crust formation and recycling in the Precambrian Shield of Canada. *Canadian Journal of Earth Sciences*, **37**, 459–476.
- Ludwig, K.R., 2003. *Isoplot/Ex version 3.00: A Geochronological Toolkit for Microsoft Excel*. Berkeley Geochronology Center, Berkeley, CA.
- Mattey, J.M., 2010. Analysis of the decay constants of the  $^{235}\text{U}$  and  $^{238}\text{U}$  multi-step CA–TIMS measurements of closed-system natural zircon samples. *Chemical Geology*, **275**, 186–198.
- Montel, J.M. & Vielzeuf, D., 1997. Partial melting of meta-greywackes. 2. Compositions of minerals and melts. *Contributions to Mineralogy and Petrology*, **128**, 176–196.
- Moyon, J.-F., Stevens, G. & Kister, A.F.M., 2006. Record of mid-Archean subduction from metamorphism in the Barberton terrain, South Africa. *Nature*, **442**, 559–562.
- Myers, J.S., 1995. The generation and assembly of an Archean supercontinent: evidence from the Yilgarn craton, Western Australia. In: *Early Precambrian Processes* (eds Coward, M.P. & Ries, A.C.), *Geological Society of London, Special Publication*, **95**, 143–154.
- Nasdala, L., Hofmeister, W., Norberg, N. *et al.*, 2008. Zircon M257 – a homogeneous natural reference material for the ion microprobe U–Pb analysis of zircon. *Geostandards and Geoanalytical Research*, **32**, 247–265.
- Nicoli, G., Stevens, S., Buick, I.S. & Moyon, J.-F. 2014. A comment on ultrahigh-temperature metamorphism from an unusual corundum+orthopyroxene intergrowth bearing Al–Mg granulite from the Southern Marginal Zone, Limpopo Complex, South Africa by Belyanin *et al.* *Contributions to Mineralogy and Petrology*, **167**, 1022.
- Parrish, R.R., 1990. U–Pb dating of monazite and its application to geological problems. *Revue canadienne des sciences de la Terre*, **7**, 1431–1450.
- Patiño Douce, A.E. & Beard, J.S., 1995. Dehydration-melting of biotite gneiss and quartz amphibolite from 3 to 15 kbar. *Journal of Petrology*, **36**, 707–738.
- Patiño Douce, A.E. & Beard, J.S., 1996. Effects of P,  $f(\text{O}_2)$  and Mg/Fe ratio on dehydration melting of model meta-greywackes. *Journal of Petrology*, **37**, 999–1024.
- Patiño Douce, A.E. & Harris, N., 1998. Experimental constraints on Himalayan anatexis. *Journal of Petrology*, **39**, 689–710.
- Patiño Douce, A.E. & Johnston, A.D., 1991. Phase equilibria and melt productivity in the pelitic system: implications for the origin of peraluminous granitoids and aluminous granites. *Contributions to Mineralogy and Petrology*, **107**, 202–218.
- Perchuk, L.L., Gerya, T.V., Van Reenen, D.D., Smit, C.A. & Krotov, A.V., 2000. P–T path and tectonic evolution of shear zones separating high-grade terrains from cratons: example from Kola Peninsula (Russia) and Limpopo Region (South Africa). *Mineralogy and Petrology*, **69**, 109–142.
- Perchuk, L.L., Gerya, T.V., Van Reenen, D.D. & Smit, C.A., 2006. P–T paths and problems of high-temperature poly-metamorphism. *Petrology*, **14**, 117–153.
- Percival, J.A. & Helmstaedt, H., 2006. The Western Superior Province Lithoprobe and NATMAP transects: introduction and summary. *Canadian Journal of Earth Sciences*, **43**, 743–747.
- Pickering, J.M. & Johnston, A.D., 1998. Fluid-absent melting behavior of two-mica metapelite: experimental constraints on the origin of black hills granite. *Journal of Petrology*, **39**, 1797–1894.
- Poujol, M., Robb, L.J., Anhaeusser, C.R. & Gericke, B., 2003. A review of the geochronological constraints on the evolution of the Kaapvaal Craton, South Africa. *Precambrian Research*, **127**, 181–213.
- Rasband, W.S., 1997–2012. ImageJ. U.S. National Institutes of Health, Bethesda, MD. Available at: <http://imagej.nih.gov/ij/> (last accessed on February 2014).
- Retief, E.A., Compston, W., Armstrong, R.A. & Williams, I.S., 1990. Characteristics and preliminary U–Pb ages of zircons from Limpopo Belt lithologies. In: *Extended Abstracts, Limpopo Workshop*, pp. 95–99. Rand Afrikaans University, Johannesburg, South Africa.
- Roering, C., Van Reenen, D.D., de Wit, M., Smit, C.A., De Beer, J. & Van Schalkwyk, J.F., 1992a. Structural, geological and metamorphic significance of the Kaapvaal craton, Limpopo belt contact. *Precambrian Research*, **55**, 69–80.
- Roering, C., Van Reenen, D.D., Smit, C.A. *et al.*, 1992b. Tectonic model for the evolution of the Limpopo Belt. *Precambrian Research*, **55**, 539–552.
- Sawyer, E.W. & Benn, K., 1993. Structure of the high-grade Opatica Belt and adjacent low-grade Abitibi Subprovince, Canada: an Archean mountain front. *Journal of Structural Geology*, **15**, 1443–1458.
- Schaller, M., Steiner, O., Studer, I., Holzer, L. & Herwegh, M., 1999. Exhumation of Limpopo Central Zone granulites and dextral continent-scale transcurrent movement at 2.0 Ga along the Palala Shear Zone, Northern Province, South Africa. *Precambrian Research*, **96**, 263–288.
- Schmitz, M.D., Bowning, S.M., de Wit, M.J. & Gartz, V., 2004. Subduction and terrane collision stabilize the western Kaapvaal craton tectosphere 2.9 billion years ago. *Earth and Planetary Science Letters*, **222**, 363–376.
- Schoene, B., de Wit, M.J. & Bowning, S.A., 2008. Mesoarchean assembly and stabilization of the eastern Kaapvaal

- craton: a structural-thermochronological perspective. *Tectonics*, **27**, 1–27.
- Sláma, J., Kosler, J., Condon, D.J. et al., 2008. Plesovice zircon – a new natural reference material for U–Pb and Hf isotopic microanalysis. *Chemical Geology*, **249**, 1–35.
- Smit, C.A. & Van Reenen, D.D., 1997. Deep crustal shear zone, high-grade tectonites, and associated metasomatic alteration in the Limpopo Belt, South Africa: implications for deep crustal processes. *Journal of Geology*, **106**, 37–57.
- Smit, C.A., Roering, C. & Van Reenen, D.D., 1992. The structural framework of the Southern Marginal Zone of the Limpopo Belt, South Africa. *Precambrian Research*, **55**, 51–67.
- Stevens, G., 1997. Melting, carbonic fluids and water recycling in the deep crust: an example from the Limpopo Belt, South Africa. *Journal of Metamorphic Geology*, **15**, 141–154.
- Stevens, G. & Moyen, J.-F., 2007. Metamorphism in the Barberton Granite Greenstone Terrain: a record of Paleoproterozoic accretion. In: *Earth's Oldest Rocks* (eds Van Kranendonk, M.J., Smithies, R.S. & Bennett, V.C.), *Developments in Precambrian Geology*, **15**, 669–698.
- Stevens, G. & Van Reenen, D.D., 1992a. Partial melting and the origin of metapelitic granulites in the Southern Marginal Zone of the Limpopo Belt, South Africa. *Precambrian Research*, **55**, 303–319.
- Stevens, G. & Van Reenen, D.D., 1992b. Constraints on the form of the *P–T* loop in the Southern Marginal Zone of the Limpopo Belt, South Africa. *Precambrian Research*, **55**, 279–296.
- Stevens, G., Clemens, J.D. & Droop, G.T.R., 1997. Melt production during granulite-facies anatexis: experimental data from primitive metasedimentary protoliths. *Contributions to Mineralogy and Petrology*, **128**, 352–370.
- Taylor, J., Nicoli, G., Stevens, G., Frei, D. & Moyen, J.-F., 2014. The processes that control leucosome compositions in metasedimentary granulites: perspectives from the Southern Marginal Zone migmatites, Limpopo Belt, South Africa. *Journal of Metamorphic Geology*, **32**, 713–742.
- Tindle, A.G. & Webb, P.C., 1994. Probe-AMPH – a spreadsheet program to classify microprobe-derived amphibole analyses. *Computers and Geosciences*, **20**, 1201–1228.
- Tsunogae, T., Miyano, T., Van Reenen, D.D. & Smit, C.A., 2004. Ultrahigh temperature metamorphism of the Southern Marginal Zone of the Archean Limpopo Belt, South Africa. *Journal of Mineralogical and Petrological Sciences*, **99**, 213–224.
- Valli, F., Guillot, S. & Hattori, K.H., 2004. Source and tectono-metamorphic evolution of mafic and pelitic metasedimentary rocks from the central Quetico metasedimentary belt, Archean Superior Province of Canada. *Precambrian Research*, **132**, 155–177.
- Van den Berg, R. & Huizenga, J., 2001. Fluids in granulites of the Southern Marginal Zone of the Limpopo Belt, South Africa. *Contributions to Mineralogy and Petrology*, **141**, 529–545.
- Van Reenen, D.D., 1983. Cordierite + garnet + hypersthene + biotite-bearing assemblages as a function of changing metamorphic conditions in the Southern Marginal Zone of the Limpopo metamorphic complex, South Africa. *Geological Society of South Africa, Special Publication*, **8**, 143–167.
- Van Reenen, D.D., 1986. Hydration of cordierite and hypersthene and a description of the retrograde orthoamphibole isograd in the Limpopo Belt, South Africa. *American Mineralogist*, **71**, 900–915.
- Van Reenen, D.D., Barton, J.M., Roering, C., Smit, C.A. & Van Schalkwyk, J.F., 1987. Deep crustal response to continental collision: the Limpopo belt of southern Africa. *Geology*, **15**, 11–14.
- Van Reenen, D.D., Roering, C., Ashwal, L.D. & de Wit, M.J., 1992. Regional geological setting of the Limpopo Belt. *Precambrian Research*, **55**, 1–5.
- Vennemann, T.W. & Smith, H.S., 1992. Stable isotope profile across the orthoamphibole isograd in the Southern Marginal Zone of the Limpopo Belt, South Africa. *Precambrian Research*, **55**, 365–397.
- Vielzeuf, D. & Holloway, J.R., 1988. Experimental determination of the fluid-absent melting reactions in the pelitic system. *Contributions to Mineralogy and Petrology*, **98**, 257–276.
- Vielzeuf, D. & Montel, J.-M., 1994. Partial melting of greynwacks. 1. Fluid-absent experiments and phase relationships. *Contributions to Mineralogy and Petrology*, **117**, 375–393.
- White, R.W. & Powell, R., 2002. Melt loss and the preservation of granulite facies mineral assemblages. *Journal of Metamorphic Geology*, **20**, 621–632.
- White, R.W., Powell, R., Holland, T.J.B. & Worley, B.A., 2000. The effect of TiO<sub>2</sub> and Fe<sub>2</sub>O<sub>3</sub> on metapelitic assemblages at greenschist and amphibolite facies conditions: mineral equilibria calculations in the system K<sub>2</sub>O–FeO–MgO–Al<sub>2</sub>O<sub>3</sub>–SiO<sub>2</sub>–H<sub>2</sub>O–TiO<sub>2</sub>–Fe<sub>2</sub>O<sub>3</sub>. *Journal of Metamorphic Geology*, **18**, 497–511.
- White, R.W., Powell, R. & Clarke, G.L., 2002. The interpretation of reaction textures in Fe-rich metapelite granulites of the Musgrave Block, central Australia: constraints from mineral equilibria calculations in the system K<sub>2</sub>O–FeO–MgO–Al<sub>2</sub>O<sub>3</sub>–SiO<sub>2</sub>–H<sub>2</sub>O–TiO<sub>2</sub>–Fe<sub>2</sub>O<sub>3</sub>. *Journal of Metamorphic Geology*, **20**, 41–55.
- White, R.W., Powell, R. & Clarke, G.L., 2004. Prograde metamorphic assemblage evolution during partial melting of metasedimentary rocks at low pressures: migmatites from Mt Stafford, Central Australia. *Journal of Petrology*, **44**, 1937–1960.
- White, R.W., Pomroy, N.E. & Powell, R., 2005. An in situ metatextite-diatextite transition in upper amphibolite facies rocks from Broken Hill, Australia. *Journal of Metamorphic Geology*, **23**, 579–602.
- White, R.W., Powell, R. & Holland, T.J.B., 2007. Progress relating to calculation of partial melting equilibria for metapelites. *Journal of Metamorphic Geology*, **25**, 511–527.
- Zeh, A., Gerdes, A., Barton, J. & Klemd, R., 2010. U–Th–Pb and Lu–Hf systematics of zircon from TTG's, leucosomes, meta-anorthosites and quartzites of the Limpopo Belt (South Africa): constraints for the formation, recycling and metamorphism of Palaeoproterozoic crust. *Precambrian Research*, **179**, 50–68.
- Zeh, A., Jaguin, J., Poujol, M., Boulvais, P., Block, S. & Paquette, J.-L., 2013. Juvenile crust formation in the northeastern Kaapvaal Craton at 2.97 Ga – implication for Archean terrane accretion, and source of the Pietersburg gold. *Precambrian Research*, **233**, 20–43.

## SUPPORTING INFORMATION

Additional Supporting Information may be found in the online version of this article at the publisher's web site:

**Appendix S1.** Analytical Methods.

**Table S1.** LA–SF–ICP–MS U–Th–Pb dating methodology.

**Table S2.** U–Th–Pb geochronological data for detrital zircon in metapelite.

**Table S3.** U–Th–Pb geochronological data for metamorphic zircon in leucosomes.

**Table S4.** U–Th–Pb geochronological data for zircon in the pegmatite.

Received 27 March 2014; revision accepted 31 October 2014.

## Chapter 4

Partial melting, melt loss and water diffusivity: the formation of K<sub>2</sub>O-poor leucosome

## Presentation of the publications

These papers<sup>1,2</sup> first and second authored by Gautier Nicoli, were accepted for publication in the Journals of Metamorphic Geology and in preparation for submission in Earth and Planetary Science Letters. The following aspects of the research were done independently by Gautier Nicoli and Jeanne Taylor while receiving standard supervision by his supervisors Gary Stevens and Jean-François Moyen: (i) fieldwork and sampling; (ii) zircon separation, and preparation of zircon for LA–SF–ICP–MS dating; (iii) acquisition of mineral chemical data on the SEM and zircon U–Pb data on the LA–SF–ICP–MS; (iv) mineral equilibria and trace elements modelling in Theriak-Domino and Perple\_X; (v) writing of the manuscript. Zircon U–Pb LA–SF–ICP–MS data reduction was done by Dirk Frei.

Gautier Nicoli<sup>a,b</sup>

Gary Stevens<sup>a</sup>

Jean-François Moyen<sup>b</sup>

Jeanne Taylor<sup>a,c</sup>

Dirk Frei<sup>a</sup>

a: Center for Crustal Petrology, Department of Earth Sciences, Stellenbosch University, Private Bag X1, Matieland 7602, South Africa

b: UMR 6524 CNRS Université Jean-Monnet, 23 rue du Dr Michelon, 42023 Saint-Etienne, France

c: Institut für Geowissenschaften, Fachinheit Mineralogie, Johann Wolfgang Goethe Universität, Altenhoferallee 1, D-60438 Frankfurt am Main, Germany

---

<sup>1</sup>Taylor, J., Nicoli, G., Stevens, S., Frei, D. & Moyen J-F. 2014. The processes that control leucosome compositions in metasedimentary granulites: perspectives from the Southern Marginal Zone migmatites, Limpopo Belt. *Journal of Metamorphic Geology*, 37, 713-742. doi.org/10.1111/jmg.12087

<sup>2</sup>Nicoli, G., Moyen, J-F. & Stevens, G. In prep. The formation of  $K_2O$ -poor leucosomes in the granulitic lower crust: key to crustal differentiation processes. Example from the Southern Marginal Zone of the Limpopo Belt, South Africa.

# The processes that control leucosome compositions in metasedimentary granulites: perspectives from the Southern Marginal Zone migmatites, Limpopo Belt, South Africa

J. TAYLOR,<sup>1,\*</sup> G. NICOLI,<sup>1,2</sup> G. STEVENS,<sup>1</sup> D. FREI<sup>1</sup> AND J.-F. MOYEN<sup>2</sup>

<sup>1</sup>Department of Earth Sciences, Centre for Crustal Petrology, Stellenbosch University, Private Bag X1, Matieland 7602, South Africa ([gs@sun.ac.za](mailto:gs@sun.ac.za))

<sup>2</sup>UMR 6524 CNRS & Université Jean-Monnet, 23 rue du Dr Michelon, 42023 Saint-Etienne, France

\*Present address: Institut für Geowissenschaften, Fachinheit Mineralogie, Johann Wolfgang Goethe Universität, Altenhöferallee 1, D-60438 Frankfurt am Main, Germany

**ABSTRACT** Anatexis of metapelitic rocks at the Bandelierkop Quarry (BQ) locality in the Southern Marginal Zone of the Limpopo Belt occurred via muscovite and biotite breakdown reactions which, in order of increasing temperature, can be modelled as: (1) Muscovite + quartz + plagioclase = sillimanite + melt; (2) Biotite + sillimanite + quartz + plagioclase = garnet + melt; (3) Biotite + quartz + plagioclase = orthopyroxene ± cordierite ± garnet + melt. Reactions 1 and 2 produced stromatic leucosomes, which underwent solid-state deformation before the formation of undeformed nebulitic leucosomes by reaction 3. The zircon U–Pb ages for both leucosomes are within error identical. Thus, the melt or magma formed by the first two reactions segregated and formed mechanically solid stromatic veins whilst temperature was increasing. As might be predicted from the deformational history and sequence of melting reactions, the compositions of the stromatic leucosomes depart markedly from those of melts from metapelitic sources. Despite having similar Si contents to melts, the leucosomes are strongly K-depleted, have Ca:Na ratios similar to the residua from which their magmas segregated and are characterized by a strong positive Eu anomaly, whilst the associated residua has no pronounced Eu anomaly. In addition, within the leucosomes and their wall rocks, peritectic garnet and orthopyroxene are very well preserved. This collective evidence suggests that melt loss from the stromatic leucosome structures whilst the rocks were still undergoing heating is the dominant process that shaped the chemistry of these leucosomes and produced solid leucosomes. Two alternative scenarios are evaluated as generalized petrogenetic models for producing Si-rich, yet markedly K-depleted and Ca-enriched leucosomes from metapelitic sources. The first process involves the mechanical concentration of entrained peritectic plagioclase and garnet in the leucosomes. In this scenario, the volume of quartz in the leucosome must reflect the remaining melt fraction with resultant positive correlation between Si and K in the leucosomes. No such correlation exists in the BQ leucosomes and in similar leucosomes from elsewhere. Consequently, we suggest disequilibrium congruent melting of plagioclase in the source and consequential crystallization of peritectic plagioclase in the melt transfer and accumulation structures rather than at the sites of biotite melting. This induces coprecipitation of quartz in the structures by increasing SiO<sub>2</sub> content of the melt. This process is characterized by an absence of plagioclase-induced fractionation of Eu on melting, and the formation of Eu-enriched, quartz + plagioclase + garnet leucosomes. From these findings, we argue that melt leaves the source rapidly and that the leucosomes form incrementally as melt or magma leaving the source dumps its disequilibrium Ca load, as well as quartz and entrained ferromagnesian peritectic minerals, in sites of magma accumulation and escape. This is consistent with evidence from S-type granites suggesting rapid magma transfer from source to high level plutons. These findings also suggest that leucosomes of this type should be regarded as constituting part of the residuum from partial melting.

**Key words:** disequilibrium melting; leucosome compositions; melt compositions; partial melting; peritectic minerals.

## INTRODUCTION

Field and petrographic evidence from migmatitic metapelitic and semipelitic granulites indicates muscovite and biotite fluid-absent melting reactions to be the

main melt-generating reactions in such rocks. This is in good agreement with the findings of fluid-absent partial melting experiments using similar, fertile sedimentary starting materials (e.g. Vielzeuf & Holloway, 1988; Patinō Douce & Johnston, 1991; Montel &



Vielzeuf, 1997; Stevens *et al.*, 1997; Patinõ Douce & Harris, 1998; Pickering & Johnston, 1998) and phase equilibria modelling (e.g. White *et al.*, 2001; Korhonen *et al.*, 2010; Yakymchuk & Brown, 2013). The common production of peritectic sillimanite, garnet, cordierite and orthopyroxene in conjunction with the leucosomes in metasedimentary granulites allows for the identification of the incongruent melting reactions and, in some cases, a sequence of melting reactions can be identified (e.g. Stevens & Van Reenen, 1992a,b; Srogi *et al.*, 1993; Johnson *et al.*, 2003). Moreover, the preservation of a substantial proportion of the peritectic assemblage, both within residua-rich zones adjacent to leucosomes and within leucosomes, argues strongly for melt loss subsequent to melt or magma segregation into the leucosomes (e.g. White & Powell, 2002, 2010; White *et al.*, 2004). Consequently, it might be expected that leucosome compositions should differ from those of high-*T* anatectic melts produced in experiments, or preserved as natural glass inclusions within peritectic minerals (e.g. Bartoli *et al.*, 2013). Indeed, there are many examples from natural migmatite terranes where partial melting is known to have occurred through biotite incongruent melting; yet, the leucosomes are markedly K<sub>2</sub>O-depleted, and FeO + MgO and CaO-enriched (e.g. Torres-Roldan, 1983; Barbey *et al.*, 1990; Sawyer *et al.*, 1999; Chavagnac *et al.*, 2001; Mengel *et al.*, 2001; Martignole & Martelat, 2003; Taylor & Stevens, 2010).

Two different mechanisms have been proposed to account for this behaviour. The first involves melt loss from the leucosome structures following crystallization of minerals such as plagioclase and garnet (e.g. Sawyer, 1987; Brown, 2002). The second involves redistribution of K<sub>2</sub>O and H<sub>2</sub>O from the segregated melt back into residue-rich domains of the rock-mass. This results in a distinct, re-hydrated mafic selvage along the margins of leucosomes (e.g. Waters, 1988; Kriegsman & Hensen, 1998; Brown, 2002). White & Powell (2010) have argued that melt loss from the leucosomes, followed by long-range diffusion of the more mobile components H<sub>2</sub>O, K<sub>2</sub>O and Na<sub>2</sub>O along chemical potential gradients, established between the leucosome and the residue upon cooling, are important in producing the near-anhydrous mineral assemblages that are typical of leucosomes in granulite facies rocks. Importantly, the scenario proposed by White & Powell (2010) allows for melt loss soon after anatexis, with long-term residency of only a minor melt fraction. This is in agreement with evidence from S-type granites, which arise through the partial melting of such sediments, where the preservation of xenocrystic zircon in zirconium-undersaturated granites indicates that, at least in some cases, magma segregation, ascent and cooling are sufficiently rapid that zircon crystals remain undissolved in such magmas. Time periods in the order of thousands of years are implied (e.g. Villaros

*et al.*, 2009). On the other hand, long-term melt residency in the crust has been proposed in the Tibet plateau (e.g. Alsdorf & Nelson, 1999), as well as in many 'hot orogens' (e.g. Vanderhaeghe, 2009), with an important mechanical role for melt in weakening the crust and determining the retrograde pressure–temperature (*P–T*) evolution of rocks (e.g. Gapais *et al.*, 2009). Consequently, it is important to understand the significance of leucosome features for melt residency in the high-grade metamorphic crust as this has major tectonic implications.

The metapelitic granulites of the Southern Marginal Zone (SMZ) of the Limpopo Belt in South Africa represent a unique opportunity to study the processes of S-type granite magma generation and segregation in the granulite facies source. Previous studies have demonstrated that these rocks underwent granulite facies metamorphism at pressures close to 10 kbar (e.g. Van Reenen *et al.*, 1987; Stevens & Van Reenen, 1992b) and that anatexis involved a sequence of muscovite and biotite fluid-absent melting reactions, but that the resultant leucosomes are markedly K<sub>2</sub>O-depleted (Stevens & Van Reenen, 1992a). The current work documents the salient metamorphic and geochemical features of these migmatites, with the aim of gaining insights into the lower-crustal anatectic processes that have shaped the leucosome compositions preserved in the rocks, thereby contributing to our understanding of the processes that control differentiation of the continental crust.

## REGIONAL SETTING AND PREVIOUS WORK

The Limpopo Belt is an E–W trending, high-grade metamorphic terrane situated along the South Africa–Zimbabwe–Botswana borders (Fig. 1). The belt is bounded by the Zimbabwe Craton to the north and the Kaapvaal Craton to the south. It is internally subdivided into three distinct zones by major shear zones: a Central Zone (CZ), a Northern Marginal Zone (NMZ) and SMZ. The CZ is an epicontinental, polymetamorphic, exotic crustal block that has experienced a number of granulite facies metamorphic events during the Mesoarchean, Neoproterozoic and Palaeoproterozoic (Holzer *et al.*, 1998; Zeh *et al.*, 2005; Millonig *et al.*, 2008). In contrast, the NMZ and SMZ are considered to constitute the reworked, high-grade equivalents of the granite–greenstone successions of the adjacent cratons, with the SMZ having been metamorphosed during a single, major Neoproterozoic granulite facies event (Du Toit *et al.*, 1983; Van Reenen *et al.*, 1990; Stevens & Van Reenen, 1992a,b; Kreissig *et al.*, 2001).

The geology of the SMZ is dominated by the Baviaansklouf Gneiss, a migmatized, tonalitic to trondhjemitic grey gneisses, which includes the volumetrically subordinate mafic/ultramafic and metasedimentary units of the Bandelierkop Formation (Fig. 1)

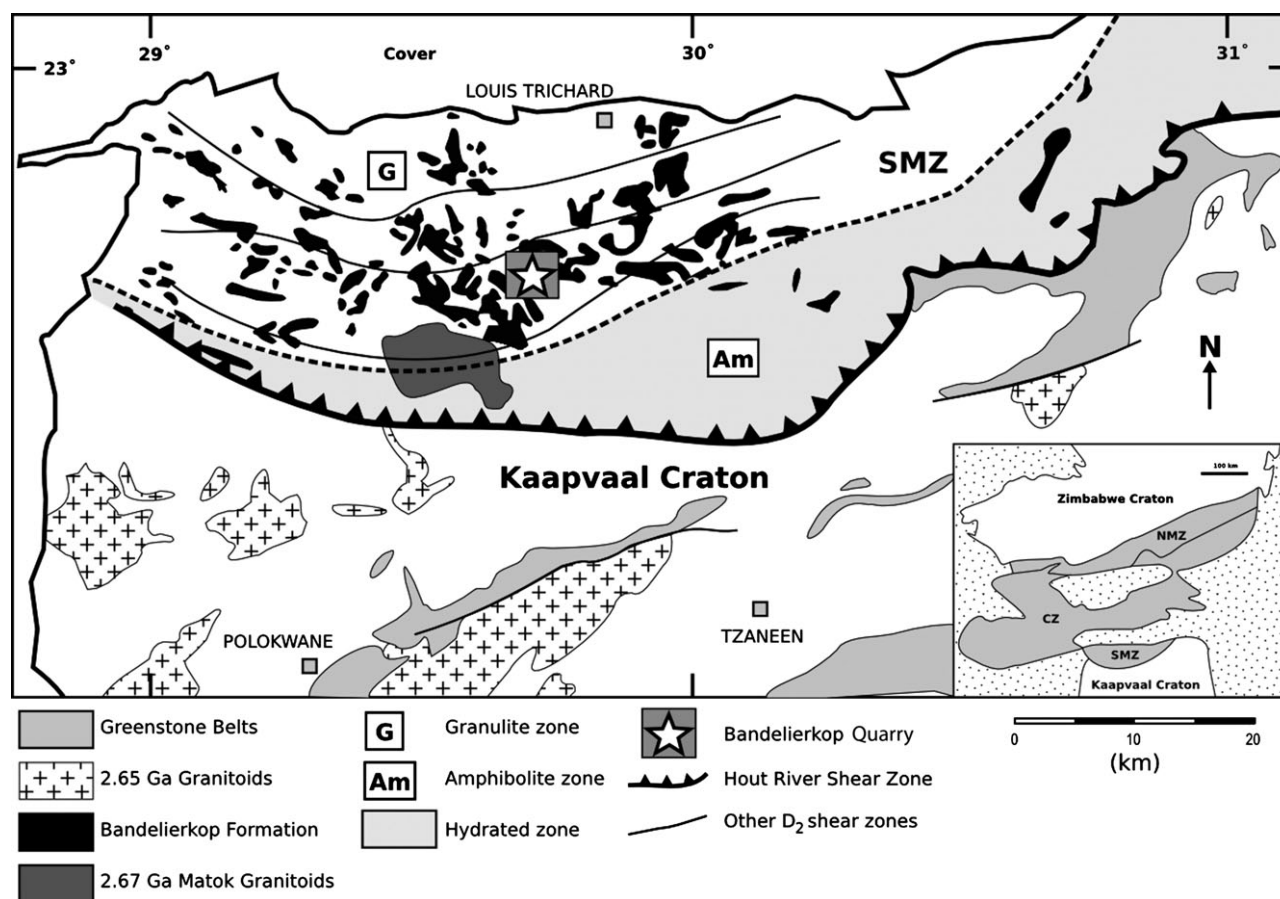


**Fig. 1.** The Limpopo Belt is subdivided into three zones: the Central Zone (CZ), the Northern Marginal Zone (NMZ) and the Southern Marginal Zone (SMZ). It separates the Zimbabwe Craton to the north from the Kaapvaal Craton to the south. The map shows the geology of the SMZ, modified after Stevens (1997). The star indicates the position of the Bandelierkop Quarry sample locality of the present study.

(Du Toit *et al.*, 1983). The tectonic boundaries of the SMZ are defined by E–W trending, crustal-scale shear zones that dip steeply to the north (Roering *et al.*, 1992). These include the Palala Shear Zone, which forms the northern boundary with the CZ; and the Hout River Shear Zone (HRSZ), which forms the southern boundary between the SMZ and low-grade rocks of the Kaapvaal Craton (Fig. 1). The SMZ is further divided into two subzones: a northern, high-grade granulite zone, and a southern zone of amphibolite facies rehydrated granulites, separated by a well-defined retrograde orthoamphibole isograd (Van Reenen, 1986).

Previous studies that have investigated the metamorphism of SMZ metasedimentary rocks have proposed a clockwise  $P$ – $T$  evolution for the rocks, which involved mid- to lower-crustal burial, prograde heating accompanied by *in situ* anatexis, isothermal decompression at high temperature, followed by a period of isobaric cooling (e.g. Van Reenen *et al.*, 1987, 1988; Stevens & Van Reenen, 1992a,b). Isothermal decompression in the SMZ is proposed to have coin-

ceded with SW-directed thrusting and exhumation of the high-grade rocks of the SMZ over the lower grade rocks of the Kaapvaal Craton along the HRSZ (Smit *et al.*, 1992; Smit & Van Reenen, 1997). The timing of this exhumation event is indicated by the age of synkinematically grown garnet, staurolite and kyanite, dated at *c.* 2690 Ma via Pb step-leaching (Kreissig *et al.*, 2001), from the Giyani Greenstone Belt in the footwall to the HRSZ. This corresponds closely with the  $^{207}\text{Pb}/^{206}\text{Pb}$  age of  $2691 \pm 7$  Ma, obtained by U–Pb geochronology on monazite separates from a migmatitic metapelite from the Bandelierkop Quarry (BQ) in the SMZ (Kreissig *et al.*, 2001). The late- to post-tectonic intrusion of parts of the HRSZ at 2670–2690 Ma by charnoenderbites of the Matok Intrusive Complex provides a constraint on the timing of high- $T$  exhumation of the SMZ (Barton *et al.*, 1992; Laurent *et al.*, 2013). Hence, the general consensus is that the SMZ represents the granulite facies root of a Neoproterozoic orogeny that resulted from a continental collision event between the Kaapvaal and Zimbabwe Cratons at *c.* 2.7 Ga (Van Reenen *et al.*, 1987; De Wit

*et al.*, 1992). The regional, high-grade fabric and pervasive folding related to the orogeny is extensively developed throughout the SMZ and coaxial with the E–W trend of the Limpopo Belt (Smit *et al.*, 1992).

The Bandelierkop Formation metasedimentary rocks from the granulite zone of the SMZ preserve typical granulite facies assemblages comprised of garnet, orthopyroxene, Ti-rich biotite, plagioclase, quartz, cordierite, sillimanite and kyanite. These rocks show features consistent with biotite incongruent melting in all areas where they are exposed. This is evidenced by the generation of new ferromagnesian peritectic phases associated with several generations of anatectic leucosomes. In contrast, the biotite-bearing, Baviaanskloof grey gneisses of the granulite zone have generally not melted to the same degree as the metasedimentary rocks. The widespread hydration of migmatites that were formerly at granulite grade, south of the orthoamphibole isograd, has been described in detail by Van Reenen (1986) and Stevens (1997). These authors identified a chronological sequence of retrograde hydration reactions that are similar in rocks both north and south of the isograd, but which are much more extensively developed at the isograd and in the zone of hydration. In these outcrops, cordierite and orthopyroxene have been almost entirely removed from the assemblage due to replacement by coarse-grained intergrowths of biotite, kyanite and orthoamphibole.

Recently, ultra high-temperature metamorphic conditions, in excess of 1000 °C at 10–12 kbar, have been proposed for the SMZ (Belyanin *et al.*, 2012). The latter is difficult to reconcile with the findings of a substantial number of previous works (e.g. Van Reenen, 1983; Stevens & Van Reenen, 1992a,b), which have documented the widespread existence of peak metamorphic biotite in rocks that would have become biotite deficient at the conditions proposed by Belyanin *et al.* (2012). For this reason it is very unlikely that the SMZ experienced regional peak metamorphic temperatures in excess of 900 °C.

#### ANALYTICAL METHODS

All the analyses reported in this manuscript were conducted at the Central Analytical Facility at Stellenbosch University. Additional details of equipment and standard operating conditions are available at [www.sun.ac.za/caf](http://www.sun.ac.za/caf).

#### XRF for bulk-rock major elements

Samples were crushed to a fine powder using a jaw crusher and tungsten carbide swing mill prior to the preparation of fused discs for major element and trace analysis. Glass discs were prepared for XRF analysis using 10 g of high-purity trace element and rare earth element (REE) free flux ( $\text{LiBO}_2 = 32.83\%$ ;

$\text{Li}_2\text{B}_4\text{O}_7 = 66.67\%$ ;  $\text{LiI} = 0.50\%$ ) mixed with 1 g of the rock sample. Whole-rock major element compositions were determined by XRF spectrometry on a PANalytical Axios Wavelength Dispersive spectrometer. The spectrometer is fitted with an Rh tube and with the following analysing crystals: LIF200, LIF220, LIF420, PE and PX1. The instrument is fitted with a gas-flow proportional counter and a scintillation detector. The gas-flow proportional counter uses an argon (90%), methane (10%) gas mixture. Major elements were analysed on a fused glass disc at 50 kV and 50 mA tube operating conditions. Matrix effects in the samples were corrected for by applying theoretical alpha factors and measured line overlap factors to the raw intensities measured with the SuperQ PANalytical software. Control standards that were used in the calibration procedures for major element analyses were NIM-G (Granite from the Council for Mineral Technology, South Africa) and BHVO-1 (Basalt from the United States Geological Survey, Reston). For standards of known composition analysed as unknowns, typical deviation from the reference value is less than 1% relative for major elements present at a concentration of greater than 1 wt%.

#### ICPMS for bulk-rock trace elements

Fused glass discs were prepared by an automatic Claisse M4 Gas Fusion instrument using ultrapure Claisse Flux (66.67%  $\text{Li}_2\text{B}_4\text{O}_7$ ; 32.83%  $\text{LiBO}_2$ ; 0.50%  $\text{LiI}$ ) and a sample to flux ratio of 1:10. The discs were analysed for trace element concentration using a New Wave 213 nm laser connected to an Agilent 7500ce ICP-MS. The analyses used a 142  $\mu\text{m}$  spot size, a frequency of 10 Hz and ~100 mJ energy. Ablation was performed in He gas at a flow rate of 0.9 l  $\text{min}^{-1}$  and the He stream was mixed with argon (0.9 l  $\text{min}^{-1}$ ) directly before introduction into the ICP plasma. The data reported in this study represent an average of four ablation spots. Trace element concentrations were quantified using NIST 612 for calibration and the wt%  $\text{SiO}_2$  value from XRF measurement as the internal standard, using standard-sample bracketing. The calibration standard was run every 12 samples. A quality control standard was run in the beginning of the sequence as well as with the calibration standards throughout. BCR-2 or BHVO 2G, both basaltic glass, certified reference standards produced by USGS (Dr S. Wilson, Denver, CO), was used for this purpose. A fusion control standard from certified basaltic reference material (BCR-2, also from USGS) was also analysed at the beginning of each sequence to verify the effective ablation of the fused material. Data were processed using Glitter software distributed by Access Macquarie Ltd. (Macquarie University, NSW). Analytical accuracy is typically better than 5% relative.

### SEM EDS analysis of major element mineral chemistry

Mineral major element compositions were analysed using a LEO 1430VP Scanning Electron Microscope. Textures were studied in backscattered electron mode and mineral compositions quantified by energy dispersive X-ray analysis using an Oxford Instruments<sup>®</sup> 133 keV ED X-ray detector and Oxford INCA software. Beam conditions during the quantitative analyses were 20 kV accelerating voltage and 1.5 nA probe current, with a working distance of 15 mm and specimen beam current of  $-4.0$  nA. X-ray counts were typically  $\sim 7000$  cps, and the counting time was 50 s live-time. Analyses were quantified using natural mineral standards. Analysis of silicate mineral standards as unknowns indicates that analytical accuracy using this set-up is considerably better than 1% relative.

### U–Pb zircon geochronology

Zircon U–Pb age data were acquired by laser ablation–single collector–magnetic sectorfield–inductively coupled plasma–mass spectrometry (LA–SF–ICP–MS) employing a Thermo Finnigan Element2 mass spectrometer coupled to a NewWave UP213 laser ablation system. All age data presented here were obtained by single spot analyses with a spot diameter of  $30\ \mu\text{m}$  and a crater depth of  $\sim 15\text{--}20\ \mu\text{m}$ . The methods employed for analysis and data processing are described in detail by Gerdes & Zeh (2006) and Frei & Gerdes (2009). For quality control, the Plešovice (Sláma *et al.*, 2008) and M127 (Nasdala *et al.*, 2008; Mattinson, 2010) zircon reference materials were analysed, and the results were consistently in excellent agreement with the published ID–TIMS ages. Full analytical details and the results for all quality control materials analysed are reported in Table S1. The calculation of weighted mean and concordia ages and plotting of concordia diagrams were performed using Isoplot/Ex 3.0 (Ludwig, 2003).

### ROCK TYPES AND FIELD RELATIONSHIPS

The granulites documented in this study are located in the BQ, 3 km west of Bandelierkop village between Polokwane and Louis Trichardt, in the northern granulite zone of the SMZ (Fig. 1). This particular location has been the focus of previous investigations by Stevens & Van Reenen (1992a,b). The current work examines rocks described before from within the quarry, as well as pavement outcrops exposed around the quarry, which have recently become accessible due to substantial clearance of bush during the erection of electricity pylons in the area. Within these outcrops, a variety of different migmatite lithologies can be distinguished on the grounds of mineralogy, as well as the timing of leucosome formation relative to the dominant phase of

deformation in the rocks (Stevens & Van Reenen, 1992a,b).

### Metasedimentary rocks

#### *Semipelites*

This rock type occurs as light-grey, medium-grained, granoblastic rock layers (Fig. 2a) characterized by the mineral assemblage garnet + orthopyroxene + plagioclase + biotite + quartz. A distinguishing feature of the semipelites is the absence of cordierite and aluminium silicates from the metamorphic assemblage, as well as the fact that this rock type contains little *in situ*, stromatic leucosome material. In places, nebulitic orthopyroxene + garnet-bearing leucosomes and associated, coarse-grained orthopyroxene-bearing residua (see below) are developed as disseminated patches within semipelitic layers (Fig. 2a), where they destroy a pre-existing, moderate foliation in the rocks.

#### *Metapelitic residua*

This rock type occurs as grey-brown, medium- to coarse-grained, strongly deformed rock layers characterized by the mineral assemblage garnet + orthopyroxene + cordierite + plagioclase + biotite + quartz (Fig. 2a,b). In contrast to the semipelites, metapelites host abundant *in situ*, centimetre to metre-scale, garnet + sillimanite-bearing stromatic leucosomes (see below) (Fig. 2a), and therefore have an overall metatextitic structure (Sawyer, 2008). In addition, metapelites host rare orthopyroxene + cordierite + garnet-bearing nebulitic leucosomes and associated, coarse-grained orthopyroxene-bearing residua, which disrupt the pre-existing foliation in the metapelites (Fig. 3a).

A sub-variety of this rock type occurs as undeformed, medium- to coarse-grained, garnet-porphyroblast-rich layers and lenses in pavements exposed immediately to the SE of the quarry (Fig. 2c). The latter, which are referred to as garnet-bearing residua, contain up to 50 vol.% garnet, as well as quartz + plagioclase + orthopyroxene + cordierite  $\pm$  biotite, and host both stromatic garnet-bearing (but sillimanite-free) (Fig. 2c) and nebulitic orthopyroxene-bearing leucosomes (Fig. 3c).

#### *Coarse-grained orthopyroxene-bearing residua*

This rock type constitutes coarse-grained, undeformed, orthopyroxene-dominated domains that occur exclusively as disseminated patches within metapelite and semipelite layers and are intimately associated with the development of nebulitic leucosomes (Fig. 3b) (see below). In the semipelites, these coarse-grained domains are characterized by the assemblage orthopyroxene + garnet + plagioclase +

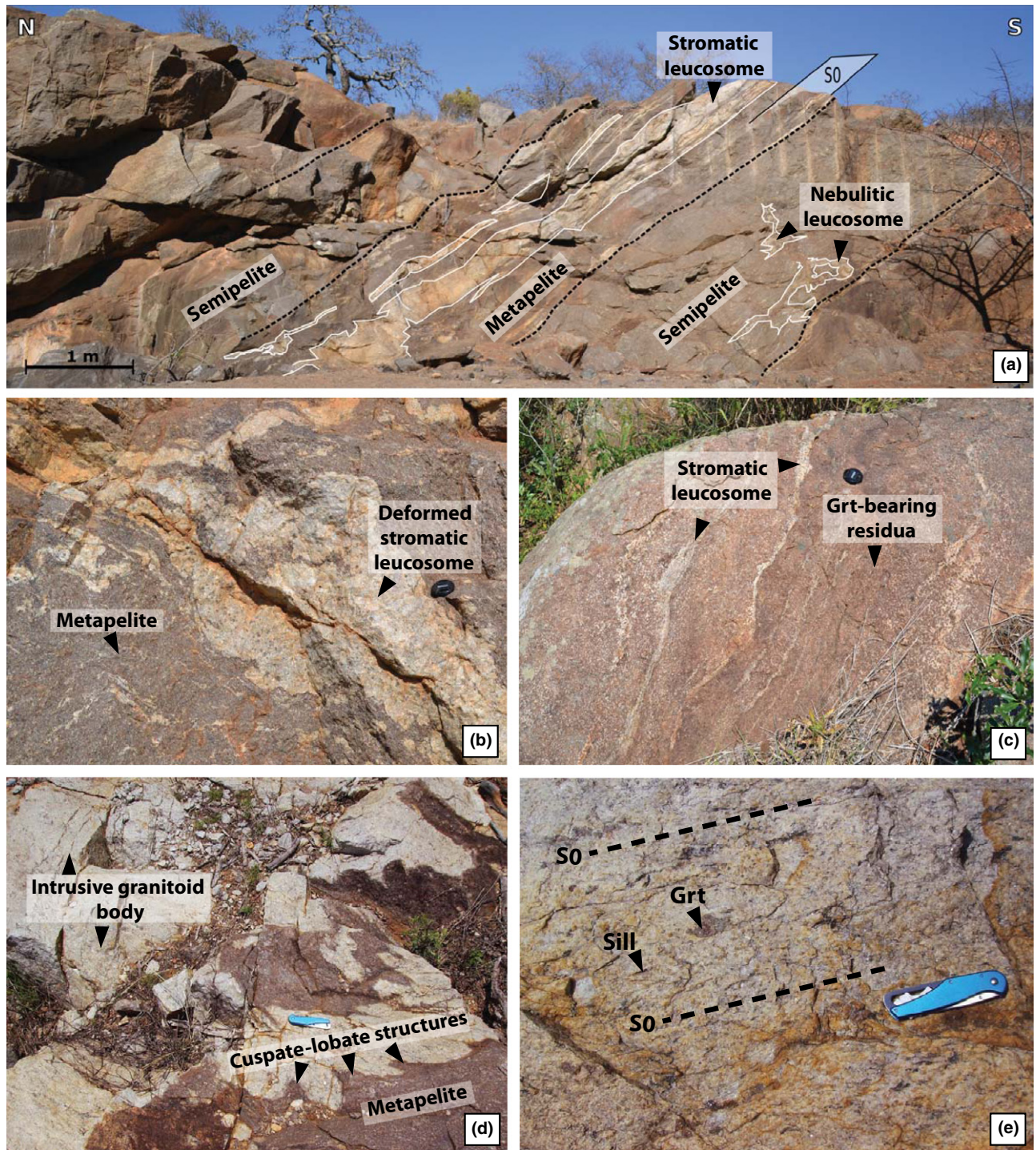


**Fig. 2.** Rock types and field relationships of the BQ migmatites. (a) Panoramic view of the western face of the Bandelierkop Quarry, showing the relationship between metapelitic and semipelitic layers, and the stromatic and nebulitic leucosomes, which they host. (b) Metapelite hosting a folded and boudinaged stromatic leucosome. (c) Garnet-bearing residua hosting garnet-bearing stromatic leucosomes. (d) Small intrusive granitoid body displaying cusped-lobate flame-structures at the contact with its host metapelite. (e) An internal fabric in a stromatic leucosome defined by aligned sillimanite laths, and stretched quartz and feldspar crystals. S0 is the dominant  $\pm$  E-W trending foliation in the BQ. See 8 cm camera lens cover and pocketknife for scale.

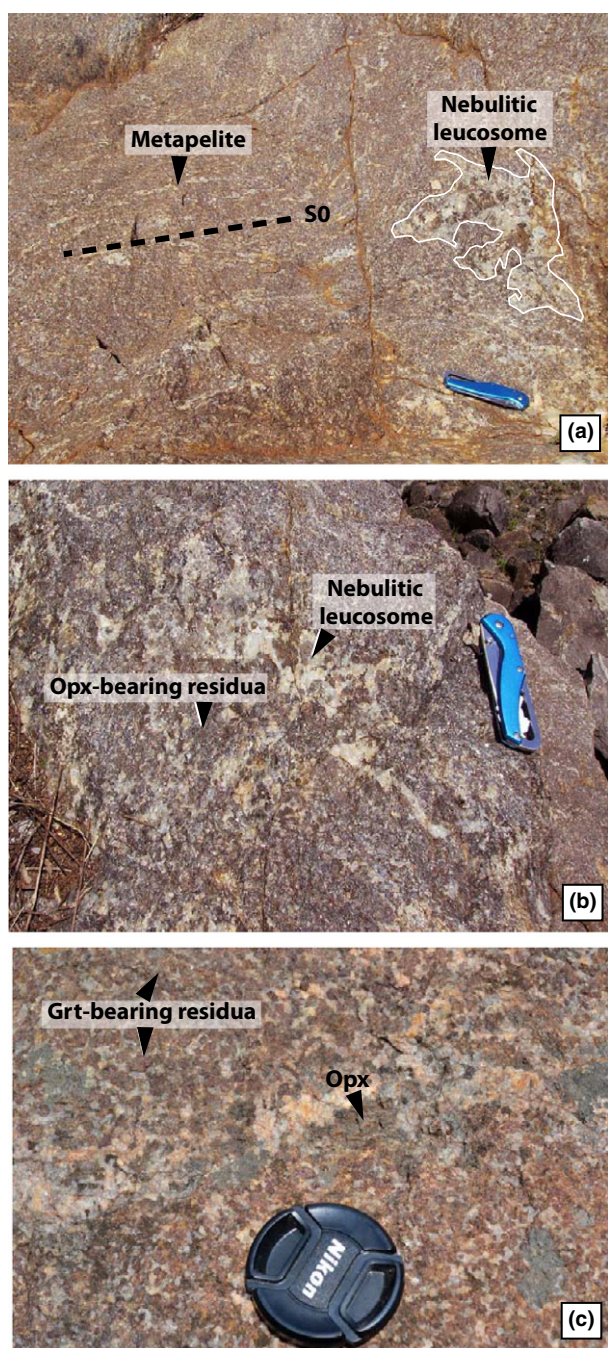


**Fig. 3.** Details of the coarse-grained orthopyroxene-bearing residua and associated nebulitic leucosomes (mineral abbreviations after Kretz, 1983). (a) An undeformed nebulitic leucosome, which cross-cuts the dominant S0 fabric in the surrounding metapelites. (b) Coarse-grained orthopyroxene-bearing residua hosting a nebulitic leucosome. (c) Garnet-bearing residua hosting an orthopyroxene-bearing nebulitic leucosome. See 8 cm camera lens cover and pocketknife for scale.

quartz + biotite, while in the metapelites, equivalent domains additionally contain cordierite, and garnet is subordinate.

## Anatectic leucosomes

### *Stromatic leucosomes*

Leucosomes of this variety all contain garnet (and sillimanite), but never contain orthopyroxene as a peritectic phase. They occur as deformed veins of variable thickness (from a few centimetres to a few metres) within metapelites and the garnet-bearing residua, where they are concordant with the layering and foliation in the host rocks (Fig. 2a–c). The veins are dominated by medium- to coarse-grained quartz + plagioclase + garnet ± sillimanite, with minor K-feldspar. The presence of 5–20 mm-sized, euhedral laths of sillimanite in metapelite-hosted stromatic leucosomes, as well as garnet (which occasionally contains inclusions of sillimanite) indicates generation of these leucosomes via two sequential partial melting reactions: muscovite + quartz + plagioclase = sillimanite + melt, and biotite + sillimanite + quartz + plagioclase = garnet + melt (Stevens & Van Reenen, 1992a,b).

Metapelite-hosted stromatic leucosomes display pervasive, solid-state deformation features. In addition to being boudinaged and folded about the foliation planes in the host rocks (Fig. 2b), an internal fabric in the leucosomes is defined by aligned sillimanite, and stretched quartz and feldspar crystals (Fig. 2e). Along their contacts with their host, cusped-lobate structures (Ramsay & Huber, 1987) are developed with fold axes that are concordant with the foliation in the bounding metapelites (Fig. 2d). These cusped-lobate structures, as well as boudinaging of the leucosomes, indicate higher competency in the leucosomes relative to the metapelites at the time of the deformation.

### *Nebulitic leucosomes*

Nebulitic leucosomes are considerably less voluminous in the BQ than stromatic leucosomes. As described above, they occur as disseminated, leucocratic patches within coarse-grained orthopyroxene-bearing residua (Fig. 3a,b) and in the garnet-bearing residua (Fig. 3c). These leucosomes are dominated by large, blocky orthopyroxene crystals, as well as coarse-grained quartz + plagioclase + biotite + garnet ± cordierite (depending on whether they are hosted by semipelites or metapelites), indicating their generation via the partial melting reaction biotite + quartz + plagioclase = orthopyroxene + garnet ± cordierite + melt (Stevens & Van Reenen, 1992a). Unlike the stromatic leucosomes, nebulitic leucosomes are undeformed and cross-cut the foliation in the host metapelites or semipelites (Fig. 3a). Hence, their formation is interpreted to post-date the main phase of deformation in the BQ (Stevens & Van Reenen, 1992a).

*Small intrusive granitoid*

In addition to the leucosomes described above, which show clear evidence for *in situ* anatexis (in the form of bounding residua rich in the peritectic phases that also occur in the leucosomes), a small, intrusive, albeit deformed granitoid body occurs in the eastern domain of the BQ (Fig. 2d). The granitoid is mineralogically very similar to garnet + sillimanite-bearing stromatic leucosomes, except for the fact that it contains a significantly higher proportion of K-feldspar. This rock is therefore interpreted to have formed by the same partial melting reactions that produced the stromatic leucosomes, but, in this case, represents a magma that probably accumulated and intruded at a level above its source layers.

**PETROGRAPHY AND MINERAL CHEMISTRY**

In this section, we report the compositions of all major minerals, from lithologies that are central to constraining the *P–T* conditions of metamorphism and the development of a petrogenetic model for leucosome formation. A comprehensive data set of mineral compositions from the BQ migmatites is given in Table S2.

**Metasedimentary rocks***Semipelites*

Semipelites contain 2–4 mm-sized garnet poikiloblasts set in a matrix of moderately foliated biotite, subordinate orthopyroxene and granoblastic plagioclase and quartz. Garnet poikiloblasts host abundant plagioclase and quartz, as well as rare rutile inclusions. The garnet crystals have embayed margins where they are rimmed by orthopyroxene + plagioclase, and occasionally biotite. In the semipelites, there is minor replacement of orthopyroxene by fine-grained biotite and orthoamphibole (see ‘crystallization–hydration’ reactions below).

*Metapelitic residua*

Metapelites contain 2–5 mm-sized garnet porphyroblasts that are set in a matrix of strongly foliated biotite, as well as cordierite, orthopyroxene, plagioclase and quartz (Fig. 4a). The garnet displays flat major element zonation profiles with Mg# ranges [ $100 \times \text{Mg}/(\text{Mg} + \text{Fe}^{2+})$ ] of 38–42 in the cores and 37–41 in the rims, and corresponding  $X_{\text{Sps}}$  [ $\text{Mn}/(\text{Fe}^{2+} + \text{Mn} + \text{Mg} + \text{Ca})$ ] ranges of 0.01–0.02, and  $X_{\text{Grs}}$  [ $\text{Ca}/(\text{Fe}^{2+} + \text{Mn} + \text{Mg} + \text{Ca})$ ] ranges of 0.04–0.05. The porphyroblasts host abundant euhedral plagioclase ( $X_{\text{An}}$  [ $\text{Ca}/(\text{Ca} + \text{Na} + \text{K})$ ] = 0.35–0.47) and rounded quartz inclusions, as well as rounded biotite (Mg# = 72–77,  $\text{TiO}_2$  4.2–4.7 wt%), rutile and occasionally sillimanite inclusions (Fig. 4b). The garnet

has embayed margins where it is rimmed, and partially replaced by symplectic intergrowths of orthopyroxene (Mg# = 63–68) and cordierite (Mg# = 84–85) (Fig. 4a–c). Biotite in the matrix (Mg# = 71–74,  $\text{TiO}_2$  4.1–5.3 wt%) defines the foliation in the rocks. A subordinate proportion of biotite, which is similar in composition, rims cordierite and orthopyroxene, where it is associated with the ‘crystallization–hydration’ textures described below. Matrix plagioclase (1–2 mm-sized crystals) is slightly zoned, with  $X_{\text{An}}$  = 0.29–0.30 in the cores, increasing gradually (~100–200  $\mu\text{m}$  from the crystal edge) to  $X_{\text{An}}$  = 0.35 at the rims. K-feldspar ( $X_{\text{San}}$  = 90) occurs exclusively as exsolved blebs in antiperthitic plagioclase. Common accessory phases in the matrix of the metapelites include ilmenite, zircon and monazite.

A characteristic feature of the metapelites from the BQ is the preservation of mineral textural associations that indicate late-stage retrogression of orthopyroxene and cordierite, either as a result of chemical interaction with crystallizing *in situ* melt or interaction with a grain-boundary fluid. These reactions, referred to as ‘crystallization–hydration’ reactions by Stevens (1997), are indicated by relatively minor replacement of orthopyroxene by biotite and quartz (Fig. 4a), as well as more widespread replacement of cordierite along its grain boundaries by fine-grained, fibrous intergrowths of biotite, kyanite, orthoamphibole and quartz (Fig. 4c).

Garnet porphyroblasts in the garnet-bearing residua are 2–5 mm in size (Fig. 4d) and unzoned in terms of their major element chemistry (Mg# = 41–44,  $X_{\text{Sps}}$  = 0.01 and  $X_{\text{Grs}}$  = 0.03–0.05). The garnet hosts euhedral plagioclase ( $X_{\text{An}}$  = 0.34–0.36), rounded quartz, biotite (Mg# = 81–84,  $\text{TiO}_2$  2.1–4.0 wt%) and rutile inclusions. The garnet porphyroblasts are rimmed and partially replaced by orthopyroxene (Mg# = 65–70) and cordierite (Mg# = 88–89) symplectite coronas (Fig. 4d). The matrix of the garnet-bearing residua is dominated by plagioclase + quartz. Plagioclase crystals (300–500  $\mu\text{m}$  grains) are slightly zoned, with  $X_{\text{An}}$  = 0.34–0.35 in the cores, increasing to  $X_{\text{An}}$  = 0.37–0.39 within 50–150  $\mu\text{m}$  from the crystal edge. Biotite is largely absent from the rock matrix, except for very minor biotite (Mg# = 78–80,  $\text{TiO}_2$  3.2–3.8 wt%) rimming orthopyroxene and cordierite in identical ‘crystallization–hydration’ textures to those seen in the metapelites.

*Coarse-grained orthopyroxene-bearing residua*

The orthopyroxene-bearing residuum investigated in this study occurs within a metapelitic host layer. It is characterized by the presence of both coarse-grained, blocky orthopyroxene (1–3 mm-sized grains), as well as finer-grained orthopyroxene + cordierite symplectic intergrowths that appear to form pseudomorphic clusters after garnet (Fig. 4e). The two textural

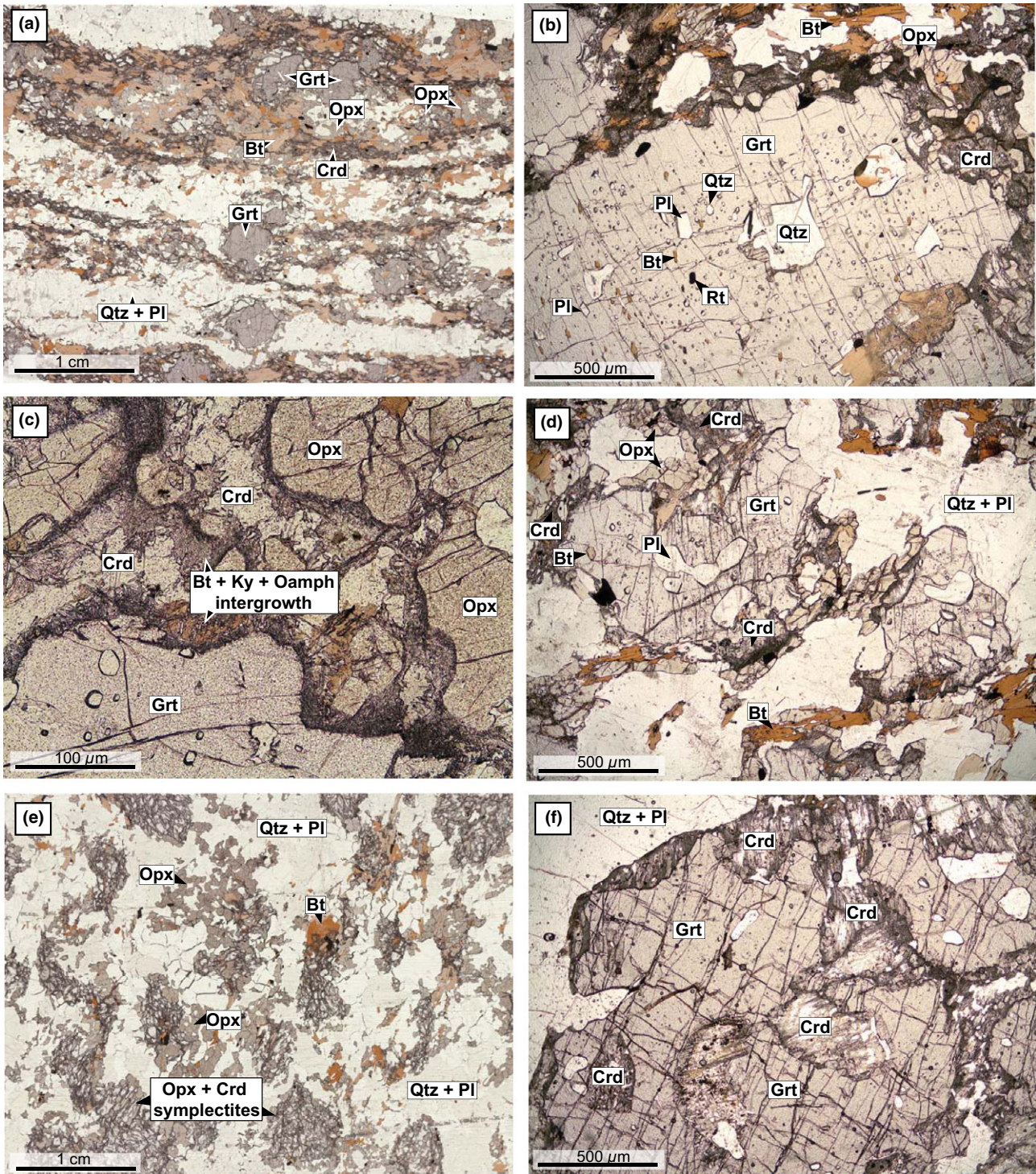


**Fig. 4.** Photomicrographs. (a) Scanned thin section showing the microtextural features of a metapelite. (b) A garnet crystal within a metapelite selvage to a stromatic leucosome, hosting euhedral plagioclase, rounded quartz, biotite, rutile and, occasionally, sillimanite inclusions. (c) Garnet crystals within metapelites are rimmed and partially replaced by symplectic intergrowths of orthopyroxene and cordierite; late-stage retrogression of cordierite rims has formed fine-grained, fibrous intergrowths of biotite, kyanite, orthoamphibole and quartz. (d) Garnet within garnet-bearing residua is rimmed by symplectic orthopyroxene and cordierite. (e) Orthopyroxene-bearing residua containing coarse-grained orthopyroxene, and orthopyroxene-cordierite symplectic intergrowths that form pseudomorphic clusters after garnet. (f) Garnet crystals within metre-scale stromatic leucosomes are partially replaced by cordierite.



varieties of orthopyroxene are, however, chemically indistinguishable from one another (Mg# = 65–66). Cordierite in the symplectite also displays a narrow compositional range (Mg# = 88–89). Occasionally, plagioclase is present as inclusions in orthopyroxene ( $X_{An} = 0.32–0.33$ ). The matrix of the orthopyroxene-bearing residuum is composed of granoblastic plagioclase + quartz. Matrix plagioclase (1.5–2 mm-sized crystals) is zoned, ranging in composition from  $X_{An} = 0.27–0.31$  in the cores to  $X_{An} = 0.33–0.35$  within 100  $\mu\text{m}$  from the crystal edge. Minor biotite (Mg# = 71–76,  $\text{TiO}_2$  3.2–3.8 wt%) occurs as coarse-grained biotite rimming orthopyroxene, or as fine-grained intergrowths with Ky + Oam + Qtz replacing cordierite.

### Anatectic leucosomes

#### *Stromatic leucosomes and the small intrusive granitoid*

Stromatic leucosomes that are  $\leq 15$  cm-wide contain 1–5 mm garnet porphyroblasts, which are compositionally and texturally similar to garnet in the metapelites and garnet-bearing residua. Garnet in the metapelite-hosted stromatic leucosomes is unzoned in terms of its major element chemistry (Mg# = 39–41,  $X_{Sps} = 0.02–0.03$  and  $X_{Grs} = 0.02–0.07$ ). The garnet hosts euhedral plagioclase ( $X_{An} = 0.33–0.39$ ), rounded quartz, biotite (Mg# = 76–77,  $\text{TiO}_2$  3.9–4.1 wt%), rutile and, occasionally, sillimanite inclusions. Garnet in the garnet-bearing residua-hosted stromatic leucosomes is inclusion-poor, and displays minor chemical zoning with Mg# = 43–45,  $X_{Sps} = 0.01$  and  $X_{Grs} = 0.03–0.05$  in the cores, and Mg# = 40–42,  $X_{Sps} = 0.01$  and  $X_{Grs} = 0.05$  within 20–100  $\mu\text{m}$  from the rims. Garnet within larger stromatic leucosomes (1–2 m-wide veins) is coarse-grained (typically 5–20 mm) (Fig. 4f), inclusion-poor and displays minor chemical zoning with Mg# = 36–37,  $X_{Sps} = 0.01–0.02$  and  $X_{Grs} = 0.02$  in the cores, and Mg# = 32–35,  $X_{Sps} = 0.02$  and  $X_{Grs} = 0.03–0.04$  within 20–100  $\mu\text{m}$  from the rims. The intrusive granitoid body in the eastern domain of the quarry contains two textural varieties of garnet. The first, subordinate variety is restricted to the margins of the structure, and resembles garnet hosted within metre-scale stromatic leucosomes, displaying similar retrogression features (see below). The second, dominant variety of garnet occurs as 0.3–2 mm, subhedral to rounded poikiloblasts, which contain rounded to lobate quartz inclusions, and show no evidence of retrogression (Fig. 5a). The two varieties of garnet are chemically indistinguishable from one another, with Mg# = 33–35,  $X_{Sps} = 0.0–0.02$  and  $X_{Grs} = 0.02$  in the cores, and Mg# = 28–33,  $X_{Sps} = 0.0–0.01$  and  $X_{Grs} = 0.02$  within 20  $\mu\text{m}$  from the rims. The majority of the garnet in the stromatic leucosomes has embayed margins where it is rimmed and partially replaced by cordierite (Mg# = 84–89) (Fig. 4f). The

cordierite rims are in turn altered to fine-grained, fibrous intergrowths of kyanite + biotite (Mg# = 77–84,  $\text{TiO}_2$  0.0 wt%) + quartz, analogous to the ‘crystallization–hydration’ textures seen in the metasedimentary residua.

Plagioclase and quartz dominate the matrix of the leucosomes. Plagioclase (2–5 mm-sized) crystals in the small-scale stromatic leucosomes show minor zoning, with  $X_{An} = 0.28–0.31$  in the cores, increasing gradually ( $\sim 100–200 \mu\text{m}$  from the crystal edge) to  $X_{An} = 0.31–0.35$  at the rims. K-feldspar ( $X_{San} = 0.91–0.95$ ) in these structures occurs exclusively as exsolved blebs in antiperthitic plagioclase. Plagioclase (3–5 mm-sized) crystals in metre-scale stromatic leucosomes are slightly zoned, with  $X_{An} = 0.20–0.21$  in the cores, increasing gradually ( $\sim 100–200 \mu\text{m}$  from the crystal edge) to  $X_{An} = 0.22–0.24$  at the rims. Although K-feldspar ( $X_{San} = 82–94$ ) forms a larger constituent of the metre-scale stromatic leucosomes, it is still a minor phase, occurring either as exsolved blebs in antiperthite (Fig. 5b), or as narrow interstitial films around individual plagioclase and quartz grains (Fig. 5c). The intrusive granitoid body contains plagioclase (1–2 mm-sized crystals) with  $X_{An} = 0.15–0.16$  in the cores; some plagioclase grains are slightly zoned, either increasing or decreasing gradually ( $\sim 50–100 \mu\text{m}$  from the crystal edge) to  $X_{An} = 0.10–0.17$  at the rims. K-feldspar ( $X_{San} = 88–89$ ) in the structure is present as discrete crystals of microperthite, or as abundant exsolution blebs in antiperthitic plagioclase (Fig. 5d).

Coarse-grained, blocky sillimanite is present in all of the metapelite-hosted stromatic leucosomes and the intrusive granitoid body as aligned, 5–20 mm, pristinely preserved laths (Fig. 5b). Plagioclase and quartz (and K-feldspar where present) are elongated in the direction of the foliation. These crystals exhibit micro-deformation features such as subgrain formation and lobate grain boundaries (Fig. 5b,d), which are consistent with extensive subsolidus recrystallization by grain-boundary migration, a typical feature of quartz and plagioclase deformed at high temperature (Rosenberg & Stunitz, 2003). Occasionally, plagioclase forms myrmekitic intergrowths with quartz (Fig. 5d).

#### *Nebulitic leucosomes*

Nebulitic leucosomes investigated in this study are intimately associated with coarse-grained orthopyroxene-bearing residua, with the leucocratic material commonly forming an interconnected network around the coarse-grained ferromagnesian minerals (Fig. 3b). Consequently, aspects of the petrography described below also relate to the residuum. The nebulitic leucosomes are dominated by 1–3 cm-sized, euhedral orthopyroxene crystals that are unzoned in terms of their major element chemistry (Mg# = 71–75), and contain plagioclase ( $X_{An} = 0.32$ ), rounded

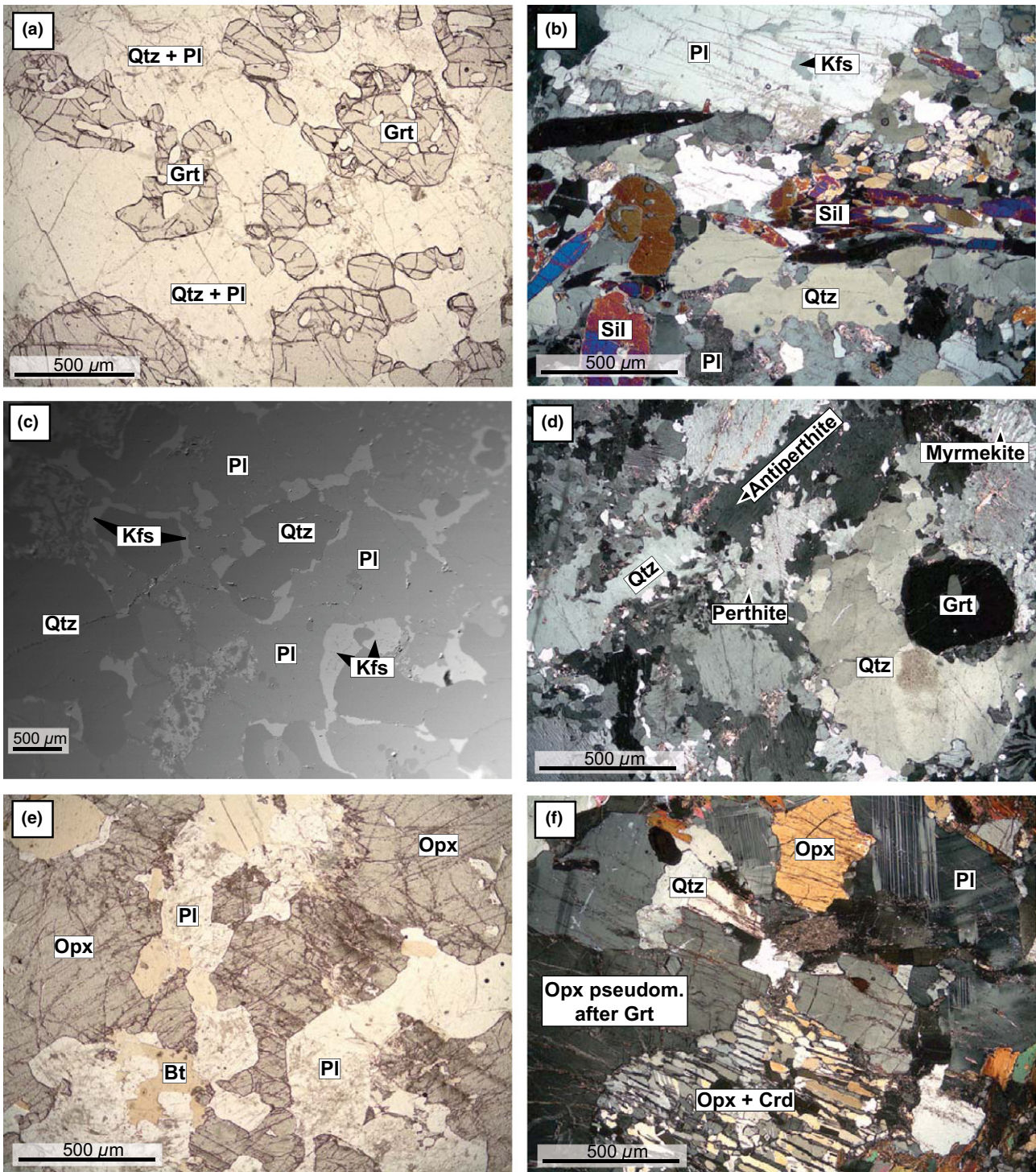


**Fig. 5.** Photomicrographs. (a) Garnet crystals within the small intrusive granitoid body lack cordierite replacement features, and occur as pristine, subhedral to rounded poikiloblasts that form clusters towards the centre of the structure. (b) Petrographic features of a deformed stromatic leucosome. (c) Interstitial films of K-feldspar around individual plagioclase and quartz crystals in a metre-scale stromatic leucosome. (d) Solid-state deformation features in the small intrusive granitoid including the formation of subgrains and lobate interphase grain boundaries in feldspar and quartz. (e) Coarse-grained, euhedral orthopyroxene and undeformed plagioclase and quartz crystals in a nebulitic leucosome. (f) Coarse-grained cordierite, as well as fine-grained orthopyroxene + cordierite symplectitic intergrowths around a large, blocky orthopyroxene crystal pseudomorphing garnet in a nebulitic leucosome.

biotite (Mg# = 78–80, TiO<sub>2</sub> 2.9–3.1 wt%) and rutile inclusions (Fig. 5e). A second, chemically similar generation of orthopyroxene (Mg# = 69–74) is present as fine-grained orthopyroxene + cordierite symplectic intergrowths where these minerals have partially replaced a large former garnet crystal, which is now pseudomorphed by orthopyroxene (Fig. 5f). Occasionally, cordierite occurs as coarse-grained, euhedral crystals in the matrix of the leucosomes (Mg# = 87–88).

Blocky orthopyroxene and cordierite crystals in the nebulitic leucosomes are separated by coats of plagioclase and quartz (Fig. 5e). Plagioclase (1–6 mm-sized crystals) are weakly zoned, ranging in composition from  $X_{An} = 0.29–0.31$  in the cores to  $X_{An} = 0.33–0.34$  within 50–200  $\mu\text{m}$  from the crystal edge. K-feldspar is absent from the nebulitic leucosomes. In addition, plagioclase and quartz lack microstructures indicative of pervasive solid-state deformation. Euhedral to subhedral plagioclase crystals commonly exhibit smooth, sharp inter- and intraphase grain boundaries with neighbouring orthopyroxene, plagioclase and quartz grains (Fig. 5e,f). Minor biotite (Mg# = 78–80, TiO<sub>2</sub> 2.2–3.1 wt%) occurs as coarse-grained biotite rimming orthopyroxene, or as fine-grained intergrowths with Ky + Oam + Qtz replacing cordierite.

## BULK-ROCK CHEMISTRY

Bulk-rock major and trace element compositions of representative leucosomes and metasedimentary rocks from the BQ are presented in Table 1. Due to the difficulty in separating nebulitic leucosomes from their coarse-grained orthopyroxene-bearing residua, bulk compositions for these leucosomes could not be determined.

Semipelites from the BQ are characterized by relatively high SiO<sub>2</sub> contents (66.6 wt%) and low A/CNK (atomic Al<sub>2</sub>/(Ca + Na<sub>2</sub> + K<sub>2</sub>)) values (1.21). Mg# [100 × atomic Mg/(Mg + Fe<sup>2+</sup>)] values (53) are low relative to typical metapelites of the Bandelierkop Formation (Table 1). Metapelites and coarse-grained orthopyroxene-bearing residua are characterized by relatively low SiO<sub>2</sub> contents (56.8 and 58.8 wt%; Table 1), high Mg# (62 & 71) values and intermediate A/CNK values (2.56 & 1.9). The garnet-bearing residua has intermediate SiO<sub>2</sub> (61.2) and Mg# (56) concentrations, and very high A/CNK values (4.93). This variation in bulk-rock Mg# among the metasedimentary lithologies in the BQ is thought to be the primary control on the different mineral assemblages developed in the rocks, with the lower Mg# semipelites lacking cordierite production at any stage during its peak and retrograde metamorphic evolution (Hensen & Green, 1973; Van Reenen, 1983).

Metapelite-hosted, garnet + sillimanite-bearing stromatic leucosomes have peraluminous compositions

with high SiO<sub>2</sub> contents (73.3–75.8 wt%), A/CNK values between 1.16 and 1.44 (typical A/CNK values for S-type granite are 1.10–1.30; Chappell & White, 1974), high CaO contents (2.0–3.5 wt%) and low K<sub>2</sub>O (0.9–1.3 wt%) concentrations (Table 1) (Fig. 6). The small intrusive granitoid also has high SiO<sub>2</sub> contents (71.9–77.3 wt%) and high A/CNK values (1.19–1.49); however, compared with the stromatic leucosomes, it has slightly higher K<sub>2</sub>O (1.8–3.6 wt%) and lower CaO concentrations (1.3–1.5 wt%). Although the intrusive granitoid more closely approximates a 'regular' leucogranitic composition, K<sub>2</sub>O in this structure is still too low to represent a pure melt (Fig. 6). Figure 6 illustrates that granulite facies leucosomes from many migmatite terranes fall outside the compositional range expected of high-*T* anatectic melts developed from appropriate source compositions. Such leucosomes tend to be K-depleted, and/or have Ca/(Ca + Na) ratios and Fe + Mg contents that are significantly higher than those of experimental and natural anatectic glasses (Fig. 6a,b; e.g. Torres-Roldan, 1983; Barbey *et al.*, 1990; Sawyer *et al.*, 1999; Chavagnac *et al.*, 2001; Mengel *et al.*, 2001; Martignole & Martelat, 2003; Taylor & Stevens, 2010). These leucosomes define negative K trends, and positive Fe + Mg trends with increasing Ca/(Ca + Na). Note that some of the leucosomes from the current study have the lowest K contents and highest Ca/(Ca + Na) ratios in the data set. Despite this, these leucosomes have Si concentrations in the range of melts (Fig. 6c). A/CNK concentrations in the BQ leucosomes do not seem to be positively correlated with increasing Fe + Mg (Fig. 6d).

Figure 6e presents chondrite-normalized REE patterns of representative metapelites, metapelite-hosted stromatic leucosomes and the intrusive granitoid from the BQ. An average REE pattern for S-type granite is plotted for reference (Cape Peninsula Granite Compilation, Villarros, 2009). S-type granites are characterized by high total REE contents, negative Eu anomalies and overall flat REE slopes. Stromatic leucosomes and the intrusive granitoid from the BQ are depleted in heavy (H)REE relative to light (L)REE, such that, whilst their LREE are only slightly lower than the reference S-type granite compositions, their HREE are markedly lower than S-type granites. The stromatic leucosomes and the intrusive body all have large positive Eu anomalies. In contrast, the metapelitic residua from which the leucosomes formed are characterized by relatively high total HREE concentrations, flat HREE slopes and do not display a marked Eu anomaly. It is important to note that there are no systematic differences in the REE patterns of small, centimetre-scale stromatic leucosomes compared with large, metre-scale stromatic leucosomes, or the intrusive granitoid body.

**Table 1.** Bulk-rock major and trace element compositions of leucosomes and metasedimentary rocks from the Bandelierkop Quarry expressed in wt% and ppm.

Rock type: Sample:	Stromatic leucosomes			Small intrusive granitoid			Metasedimentary rocks			
	L2a	L2b	L2-t	L3a	L3d	BD-C5	Semipelite	Metapelite	Grt-bearing residua	Opx-bearing residua
SiO <sub>2</sub>	73.3	75.8	75.1	73.5	77.3	71.9	66.6	56.8	61.2	58.8
TiO <sub>2</sub>	0.0	0.0	0.0	0.1	0.1	0.1	0.5	1.0	0.7	0.7
Al <sub>2</sub> O <sub>3</sub>	16.4	14.7	15.8	15.9	14.1	15.6	16.2	19.1	14.9	15.7
FeOT	0.5	1.1	0.1	0.9	0.6	0.2	4.9	7.9	12.0	6.9
MnO	0.0	0.0	0.0	0.0	0.0	0.0	0.1	0.1	0.1	0.1
MgO	0.5	0.9	0.1	0.2	0.2	0.1	3.1	7.1	8.4	9.6
CaO	3.5	3.1	2.0	1.3	1.4	1.5	4.2	1.5	1.3	2.0
Na <sub>2</sub> O	4.1	3.4	3.7	3.7	4.0	4.0	3.0	1.3	0.2	2.1
K <sub>2</sub> O	1.0	0.9	1.3	2.0	1.8	3.6	0.7	2.4	0.3	1.1
P <sub>2</sub> O <sub>5</sub>	0.1	0.1	0.0	0.1	0.1	0.1	0.1	0.0	0.0	0.0
LOI	0.2	0.4	0.6	0.4	0.3	0.6	0.3	0.5	0.0	0.3
Total	99.7	100.5	98.6	98.2	99.9	97.6	100.4	98.7	99.4	98.6
Ca/(Na + Ca)	0.32	0.34	0.23	0.16	0.17	0.17	0.43	0.38	0.75	0.35
Mg#	64	60	46	30	37	54	53	62	56	71
K/Na	0.16	0.17	0.23	0.36	0.30	0.60	0.16	1.16	0.92	0.35
A <sub>1</sub> /CNK	1.16	1.20	1.44	1.49	1.28	1.19	1.21	2.56	4.93	1.90
V	10	17	7.4	4.9	5.0	7.2	92	307	192	211
Cr	21	36	4.6	7.5	5.4	16	101	1624	1051	1966
Co	121	122	98	166	177	94	103	127	137	158
Ni	10	33	14	4.6	4.3	16	71	622	446	810
Cu	32	39	4.3	13	98	1.7	32	143	60	45
Zn	14	22	9.7	16	19	15	58	141	72	82
Rb	14	14	8.9	20	21	55	26	116	17	40
Sr	430	352	420	406	488	553	446	292	48	160
Y	2.0	2.4	0.65	1.9	1.4	0.43	12	19	15	17
Zr	69	41	22	22	24	44	135	120	78	114
Nb	0.50	0.42	0.05	0.92	2.3	0.21	4.5	5.9	3.8	4.6
Cs	1.4	1.5	0.09	0.08	0.12	0.12	2.8	3.6	1.3	4.7
Ba	216	244	762	1513	1199	3270	200	724	148	331
Hf	2.0	1.2	0.71	0.81	0.89	1.1	3.6	3.5	2.4	3.4
Pb	18	16	19	19	18	17	10	6.8	2.5	6.1
Th	0.23	0.75	0.18	2.1	2.7	1.1	2.5	0.75	2.0	1.8
U	0.37	0.53	0.12	0.42	0.25	0.32	0.70	0.16	0.32	0.35
Sc	5.0	6.5	2.0	6.6	6.0	2.3	15	43	31	36
La	9.8	8.9	10	8.6	12	10	21	13	11	12
Ce	20	20	21	18	25	21	43	25	24	26
Pr	1.9	2.1	2.0	1.8	2.5	2.1	5.4	2.9	3.1	3.1
Nd	6.5	7.4	6.4	6.1	8.7	7.1	22	11	12	12
Sm	1.1	1.3	1.0	1.1	1.6	1.1	3.9	2.2	3.0	2.7
Eu	1.1	0.94	0.90	0.67	0.67	0.95	1.3	0.93	0.33	0.94
Gd	0.77	0.83	0.43	0.71	0.97	0.65	3.2	2.9	3.0	2.9
Tb	0.08	0.08	0.02	0.09	0.10	0.05	0.44	0.51	0.48	0.44
Dy	0.45	0.37	0.14	0.38	0.37	0.14	2.6	3.5	3.0	3.1
Ho	0.08	0.08	0.02	0.07	0.05	0.02	0.46	0.79	0.63	0.65
Er	0.21	0.23	0.06	0.23	0.13	0.04	1.3	2.3	1.8	2.1
Tm	0.03	0.04	0.01	0.02	0.02	0.01	0.19	0.38	0.25	0.27
Yb	0.20	0.25	0.05	0.17	0.09	0.04	1.1	2.6	1.7	2.0
Lu	0.02	0.03	0.01	0.02	0.02	0.01	0.15	0.41	0.25	0.30
Rb/Sr	0.03	0.04	0.02	0.05	0.04	0.10	0.06	0.40	0.35	0.25
Eu/Eu*	3.5	2.6	3.5	2.2	1.5	3.1	1.1	1.1	0.3	1.0
ΣHREE	1.8	1.9	0.74	1.7	1.8	0.95	9.4	13	11	12
La <sub>N</sub> /LYb <sub>N</sub>	34	24	145	34	87	162	14	3.4	4.3	4.2

Total iron as FeO.

## PHASE EQUILIBRIA MODELLING: CONSTRAINTS ON THE CONDITIONS OF ANATEXIS

### Constraints on the peak and retrograde evolution

Phase equilibria modelling was undertaken in the chemical system Na<sub>2</sub>O–CaO–K<sub>2</sub>O–FeO–MgO–Al<sub>2</sub>O<sub>3</sub>–SiO<sub>2</sub>–H<sub>2</sub>O–TiO<sub>2</sub>–O<sub>2</sub> (NCKFMASHTO) using Theriak/Domino software (de Capitani & Petrakakis, 2010), in combination with the up-dated, tc2td.exe converted Holland & Powell (1998) database created

by D. Tinkham, and the following solution models: garnet, biotite (White *et al.*, 2007); cordierite (Holland & Powell, 1998); orthopyroxene, melt (White *et al.*, 2002); feldspar (Holland & Powell, 2003); muscovite (Coggon & Holland, 2002); and ilmenite (White *et al.*, 2000). Pseudosections were calculated using the bulk composition of a representative metapelite from the BQ (SiO<sub>2</sub> 56.8, TiO<sub>2</sub> 1.0, Al<sub>2</sub>O<sub>3</sub> 19.1, FeO 7.7, MgO 7.1, CaO 1.5, Na<sub>2</sub>O 1.3, K<sub>2</sub>O 2.4). For the purpose of modelling such a restitic bulk composition, it was assumed that the preservation of the dry, granulite facies assemblage in the rock was a consequence of

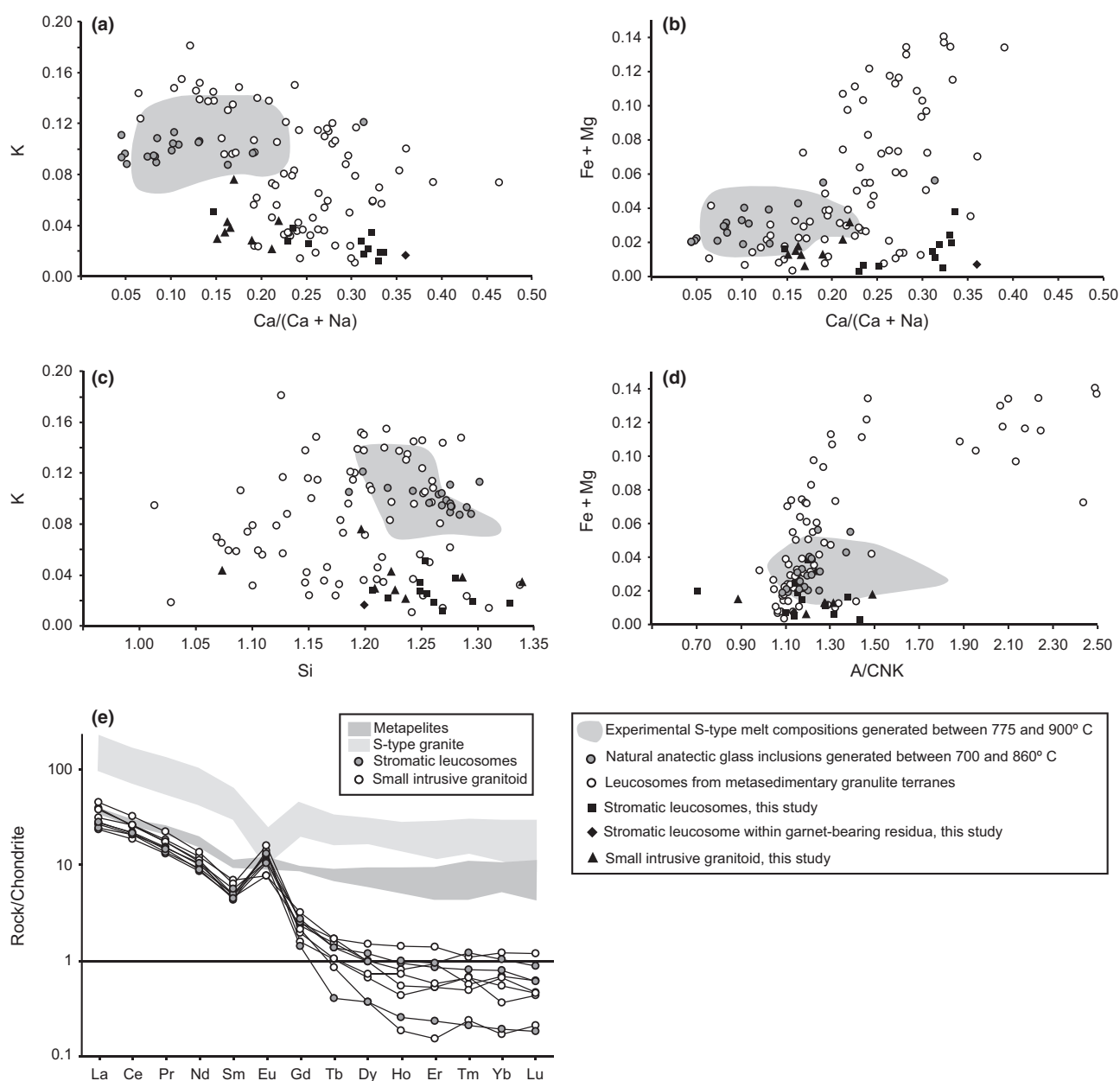


**Fig. 6.** (a–d) The compositions of BQ leucosomes compared with fluid-absent experimental glass compositions, produced from a wide range of metasedimentary starting materials between 775 and <900 °C and 1–15 kbar (Vielzeuf & Holloway, 1988; Patiño Douce & Johnston, 1991; Patiño Douce & Beard, 1996; Montel & Vielzeuf, 1997; Stevens *et al.*, 1997; Pickering & Johnston, 1998; Patiño Douce & Harris, 1998), as well as natural glass compositions (both homogenized melt inclusions and glassy inclusions in peritectic phases from natural migmatites, generated between 700 and 860 °C and 5–8 kbar; Acosta-Vigil *et al.*, 2007; Ferrero *et al.*, 2012; Bartoli *et al.*, 2013). Also shown for comparison are granulite facies leucosome compositions compiled from the literature. This compilation only includes leucosomes from metasedimentary migmatites, where partial melting is well constrained and known to have occurred through biotite incongruent melting under fluid-absent conditions (at >750 to 900 °C and 4–12 kbar), so as to avoid any complications related to partial melting of amphibolite facies, or ultra-high-*T* (UHT) rocks. Bulk-rock major element compositions (100 wt% normalized) are plotted as atomic Ca/(Ca + Na), K, Si and Fe + Mg. (e) Chondrite-normalized (Taylor & McLennan, 1985) REE plots of the stromatic garnet + sillimanite-bearing leucosomes and intrusive granite body compared with those of their source metapelites, and S-type granites (Villars, 2009).

melt loss at approximately peak metamorphic conditions (e.g. White & Powell, 2002). Although modelling using a melt-depleted bulk composition does not allow the prograde evolution of the rock to be con-

strained, it does permit investigation of the likely peak and high-*T* retrograde evolution of the rock.

Reconnaissance modelling involved the calculation of  $P - X_{\text{Fe}_2\text{O}_3}$  and  $T - X_{\text{H}_2\text{O}}$  pseudosections at a range

of temperature and pressure conditions. The aim was to investigate the dependence of the mineral equilibria on bulk-rock  $\text{Fe}_2\text{O}_3$  and  $\text{H}_2\text{O}$  content, and to constrain these parameters in the bulk composition to values consistent with the formation of the observed peak metamorphic assemblage and the estimated model abundance of garnet in the sample. For the modelled metapelite, the chosen bulk- $\text{Fe}_2\text{O}_3$  content was 0.22 wt%. As partial melting involved biotite breakdown in a fluid-absent system, bulk- $\text{H}_2\text{O}$  content choices were based on the predicted modal abundance of melt remaining in the rock after melt loss at peak metamorphic conditions (4–5 vol.%), as well as the modal abundance of garnet. The bulk- $\text{H}_2\text{O}$  content was chosen at 0.75 wt%. Scanned images of polished rock slabs and the software program ImageJ (Rasband, 1997–2012) were used to calculate the modes of garnet and orthopyroxene in the sample.

The relict petrographic features of the BQ metapelites and the stromatic leucosomes which they host (see the section dealing with petrography) allow for the inference of the peak metamorphic assemblage in the rocks: garnet + sillimanite + plagioclase + biotite + quartz + rutile + melt.  $P$ – $T$  modelling of the melt-depleted metapelitic bulk composition constrains the stability of this assemblage to between 820 and 890 °C at 8–12 kbar (diagonal line shaded field in Fig. 7a). The volume of melt predicted to have remained in the rock after melt loss at peak conditions is close to 4 vol.% (Fig. 7b), and the mode of garnet  $\pm 20$  vol.% (Fig. 7c). Textural evidence in the rock indicates subsequent replacement of garnet by symplectic intergrowths of orthopyroxene and cordierite (Fig. 4a,c). Modelling shows that this corresponded to a period of near-isothermal decompression, involving evolution through fields where first cordierite, and then orthopyroxene became stable in the assemblage at the expense of garnet. Along this segment of the  $P$ – $T$  path, garnet modes decrease correspondingly from 20 to 2–12 vol.% at low pressure (Fig. 7c), consistent with the calculated 4–8 vol.% of garnet in the rock; and orthopyroxene and cordierite modes increase from 0–10 vol.%, to 0–30 vol.% respectively (Fig. 7d,e). Given the lack of major element zonation in the garnet, it is assumed that the garnet remained open to diffusion and equilibration throughout this period of the rock's evolution, precluding the formation of smaller chemical subdomains in the rock.

Following decompression, the metapelite is predicted to cross the solidus (thick solid black line in Fig. 7a) at  $\pm 870$  °C at 6.5 kbar, preserving the observed mineral assemblage in the rock garnet + orthopyroxene + cordierite + plagioclase + biotite + quartz + Ilm + (Kfs) (diamond shaded field in Fig. 7a). Contouring Fig. 7c for garnet compositional isopleths shows that the measured garnet compositions in this sample ( $\text{Mg}\# = 38$ –42) intersect the solidus at 860–870 °C at  $\pm 6$  kbar.

### Constraints on the prograde evolution

To investigate prograde metamorphism in the BQ metapelites prior to melt loss, it was necessary to re-integrate melt back into the dry, restitic bulk composition of the modelled metapelite. This was done following the step-by-step approach of White *et al.* (2004).

Pseudosection modelling of the melt-reintegrated metapelitic bulk composition ( $\text{SiO}_2$  65.12,  $\text{TiO}_2$  0.64,  $\text{Al}_2\text{O}_3$  17.45,  $\text{Fe}_2\text{O}_3$  0.01, FeO 4.95, MgO 4.20, CaO 1.10,  $\text{Na}_2\text{O}$  2.06,  $\text{K}_2\text{O}$  4.74,  $\text{H}_2\text{O}$  2.40) indicates that muscovite coexisted with biotite just below the wet solidus at  $\pm 675$  °C (Fig. 8a). Given the mineralogy of the stromatic leucosomes, melting is assumed to have begun in the sillimanite stability field, at  $< 7$  kbar. As melting progressed with increasing  $P$ – $T$ , between the wet solidus and the muscovite-out reaction, some 15 vol.% melt (dashed lines in Fig. 8a) was produced in conjunction with peritectic sillimanite via the simplified model reaction, muscovite + quartz + plagioclase = sillimanite + melt. Although K-feldspar formed part of the peritectic assemblage produced by muscovite melting, across this  $P$ – $T$  window, modes of K-feldspar remained low (2–4 vol.%). With further increase in  $P$ – $T$ , garnet is predicted to enter the assemblage at  $\pm 820$  °C, which corresponded to a rapid increase in melt modes from 25 vol.%, to between 45 and 50 vol.% at the conditions of inferred peak metamorphism, at 875–890 °C and 9–10 kbar (white dashed box in Fig. 8a). Across this  $P$ – $T$  interval, incongruent melting of biotite and sillimanite occurred via the simplified model reaction biotite + sillimanite + quartz + plagioclase = garnet + melt.

The sequence of melting reactions constrained by the modelling in Fig. 8a is in line with the melting reactions predicted from the mineralogy of the stromatic leucosomes and the metapelitic residua, and shows that, prior to melt loss, the metapelites may have contributed as much as 45–50 vol.% melt to the stromatic leucosomes. To compare these melt volumes to the proportion of leucocratic features currently preserved in the BQ, analysis of the ratio of metapelitic residua to stromatic leucosome was performed using ImageJ software (Rasband, 1997–2012) on the main wall of the quarry, in a section that is approximately perpendicular to the foliation and approximately parallel to the lineation (Fig. 8b). Figure 8b shows that the stromatic leucosomes typically represent 1–15% of the combined leucosome: metapelitic host layer, whilst melt, at the peak of metamorphism comprised 35–45 vol.%, relative to residuum. Thus, even allowing for a reasonable degree of volume reduction on crystallization of the melt, there is a substantial mismatch between predicted melt volumes and the amount of stromatic leucosome preserved in the outcrop, suggesting melt loss from these structures.

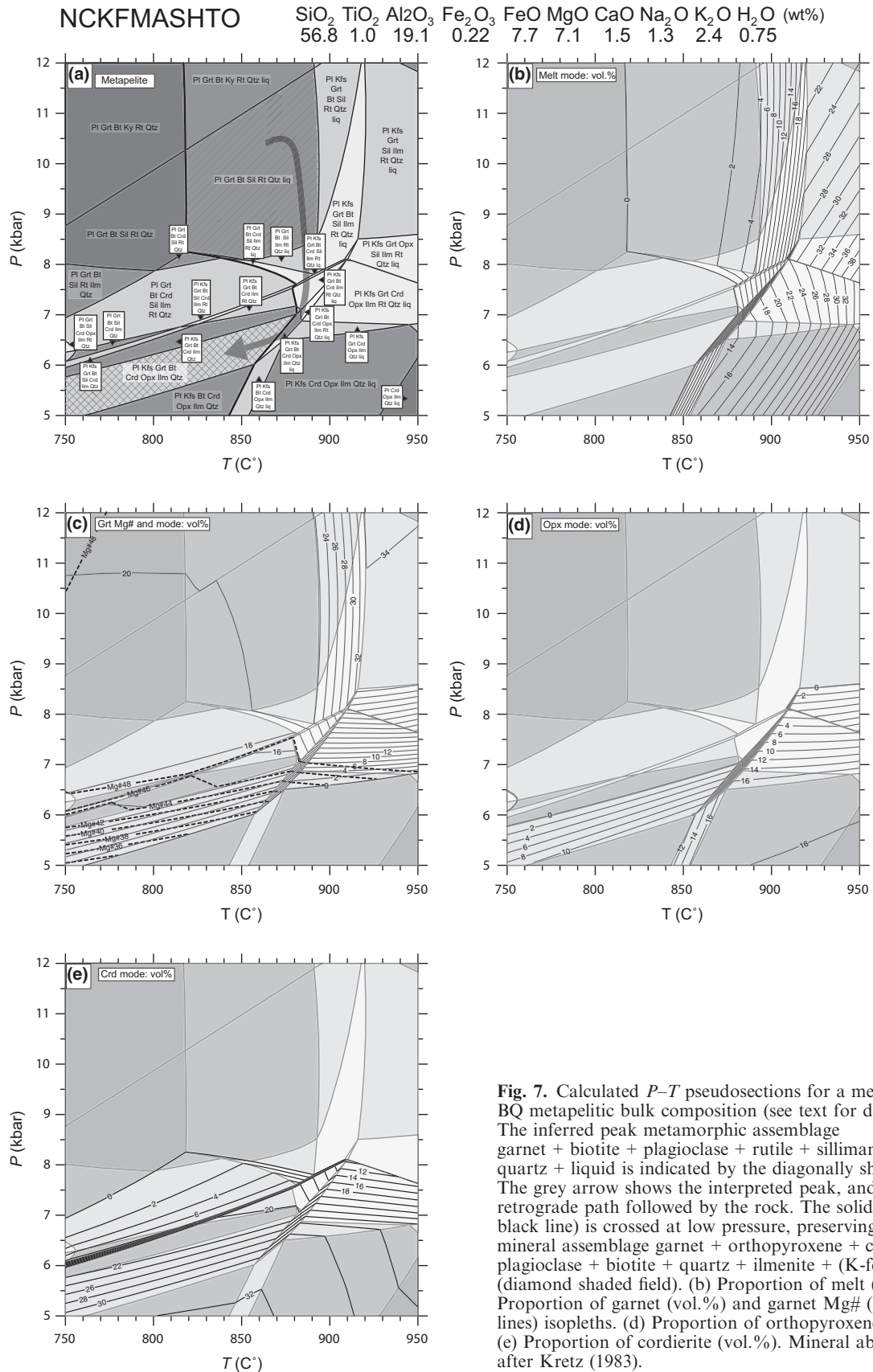


**Fig. 7.** Calculated  $P$ - $T$  pseudosections for a melt-depleted BQ metapelite bulk composition (see text for details). (a) The inferred peak metamorphic assemblage garnet + biotite + plagioclase + rutile + sillimanite + quartz + liquid is indicated by the diagonally shaded field. The grey arrow shows the interpreted peak, and high- $T$  retrograde path followed by the rock. The solidus (thick black line) is crossed at low pressure, preserving the mineral assemblage garnet + orthopyroxene + cordierite + plagioclase + biotite + quartz + ilmenite + (K-feldspar) (diamond shaded field). (b) Proportion of melt (vol.%). (c) Proportion of garnet (vol.%) and garnet Mg# (dashed lines) isopleths. (d) Proportion of orthopyroxene (vol.%). (e) Proportion of cordierite (vol.%). Mineral abbreviations after Kretz (1983).

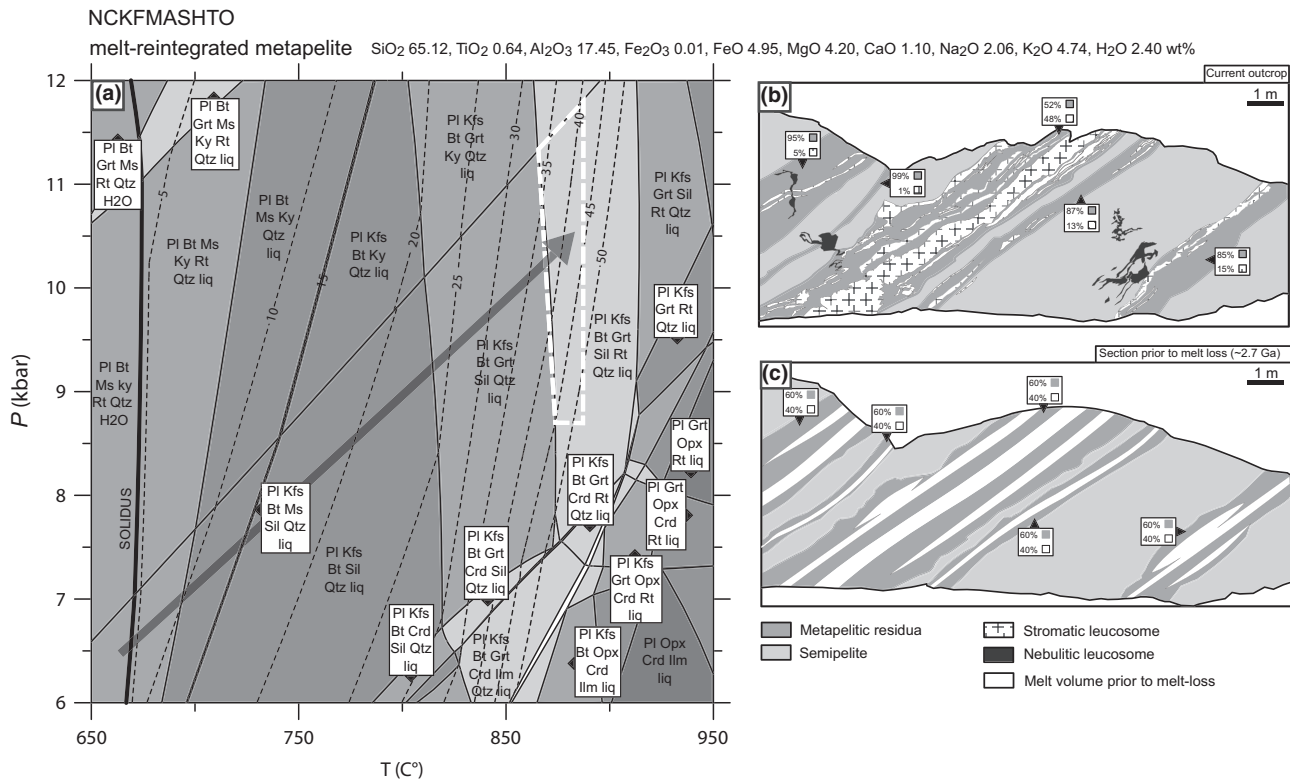


**Fig. 8.** The results of melt reintegration modelling of the same BQ metapelite composition shown in Fig. 7. (a) The melt-reintegrated pseudosection created following the approach of White *et al.* (2004). This illustrates that the maximum pressure during prograde evolution between 675 and 740 °C, when muscovite melted out, could not have exceeded between 7.5 and 8.5 kbar. Dashed lines represent modes of melt in vol.%. The inferred conditions for peak metamorphism are indicated by the white dashed box. (b) An illustration of the stromatic leucosome:metapelite residua proportions in the vertical outcrop section portrayed in Fig. 2. This section is close to perpendicular to the strike of the leucosomes and consequently provides a reasonable reflection of the true width of the layers. Note that there is some relief in the outcrop in the vicinity of the largest leucosome layer, which somewhat overestimates the proportion of this layer. The leucosome:residuum ratios indicated were calculated from image analysis of photographs. The nebulitic leucosomes were not considered in this calculation and are only included in the diagram so as to illustrate their proportions relative to the stromatic leucosomes. (c) A schematic illustration of the likely (60:40) residuum:leucosome proportions that would have existed in the panel of rocks depicted in (b) at the conditions of peak metamorphism. This assumes that the leucosome structures contained only melt and had not entrained any crystals from the source. It demonstrates, albeit in a simplistic way, that the material in the exposed leucosomes represents a significant volume of ~40% relative to the amount of melt generated within the outcrop, and that many of the layers have lost at least half the melt generated by the dominant melting reactions.

## GEOCHRONOLOGY

### Stromatic leucosome

Zircon extracted from a metapelite-hosted stromatic leucosome from the BQ (sample L2a) is 100–200  $\mu\text{m}$  in size, and oval to ‘soccer ball’ shaped. Cathodoluminescence (CL) imaging of the internal structures of the zircon shows that it is characterized by euhedral, oscillatory zoned core domains, which are truncated and overgrown by broad, faintly oscillatory zoned rim domains (Fig. 9b). LA-SF-ICP-MS analyses of the zircon core domains show that they have relatively high Th/U ratios, i.e. Th/U = 0.22–0.81. Twenty spot analyses of the cores were performed, and the data are presented in Table 2. Although these data are between 90% and 101% concordant, they display a scatter in

$^{207}\text{Pb}/^{206}\text{Pb}$  spot ages ranging from  $2925 \pm 37$  Ma to  $2828 \pm 26$  Ma, which precludes a single weighted mean  $^{207}\text{Pb}/^{206}\text{Pb}$  age from being calculated. Analyses of the zircon rim domains show that they have relatively low Th/U ratios, i.e. Th/U = 0.01–0.18. Forty-seven spot analyses of the rims were performed, and the data are plotted in Fig. 9a and presented in Table 2. Thirty-eight of these analyses are  $\geq 95\%$  concordant, and yield a weighted mean  $^{207}\text{Pb}/^{206}\text{Pb}$  age of  $2714 \pm 6$  Ma (95% c.l., MSWD = 1.5) (Fig. 8a; Table 2). The remaining data are  $< 95\%$  concordant and do not have the same  $^{207}\text{Pb}/^{206}\text{Pb}$  equal within analytical uncertainty, and were therefore excluded from the above weighted mean  $^{207}\text{Pb}/^{206}\text{Pb}$  age calculation. Twenty-seven analyses are  $\geq 99\%$  concordant, and yield a concordant age of  $2716 \pm 7$  Ma (95% c.l., MSWD = 0.33) (Fig. 9a).



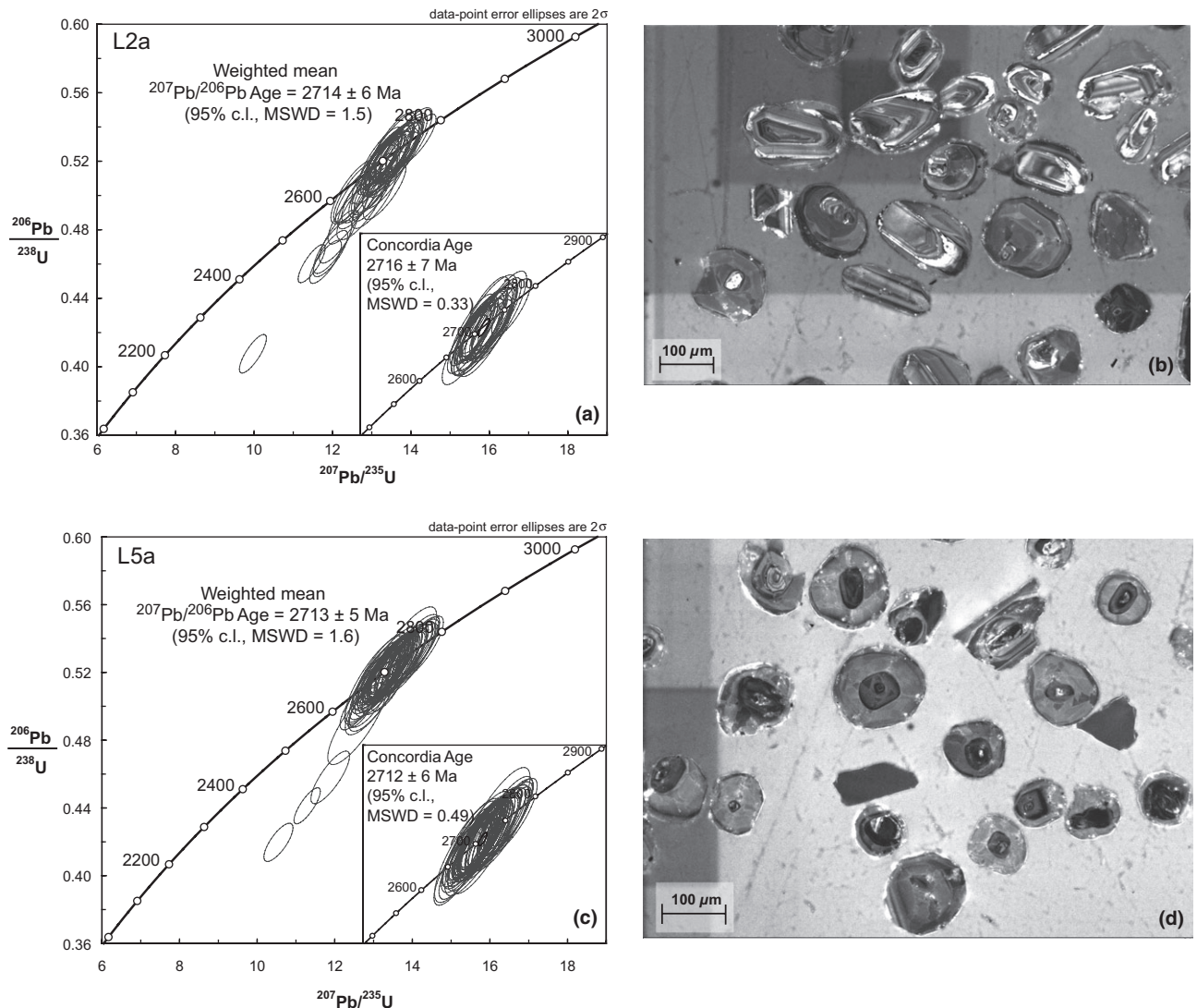


**Fig. 9.** U–Pb concordia plots. (a, b) Zircon from a stromatic leucosome, sample L2a. (c, d) Zircon from a nebulitic leucosome, sample L5a. Calculated weighted mean or concordia ages are reported at the 95% confidence level. Data-point error ellipses are shown at  $2\sigma$ .

### Nebulitic leucosome

Zircon extracted from a nebulitic leucosome from the BQ is 75–150  $\mu\text{m}$  in size, and has rounded grain shapes. Zircon from this leucosome variety is very similar to zircon from the stromatic leucosome L2a in CL, except that the oscillatory zoned core domains are smaller, and in some cases almost entirely obliterated by the growth of broad, CL-bright rim domains (Fig. 9d). The small size of the cores did not allow for accurate spot analysis by LA-SF-ICP-MS. However, analyses of the zircon rim domains show that they are characterized by low Th/U ratios, i.e. Th/U = 0.00–0.25. Sixty-five spot analyses of the rim domains were performed, and the data are plotted in Fig. 9c and presented in Table 3. Sixty of these analyses are  $\geq 95\%$  concordant, and

yield a weighted mean  $^{207}\text{Pb}/^{206}\text{Pb}$  age of  $2713 \pm 5$  Ma (95% c.l., MSWD = 1.6). The remaining data are  $< 95\%$  concordant and do not have the same  $^{207}\text{Pb}/^{206}\text{Pb}$  equal within analytical uncertainty, and were therefore excluded from the above weighted mean  $^{207}\text{Pb}/^{206}\text{Pb}$  age calculation. Fifty-three analyses are  $\geq 99\%$  concordant, yielding a concordant age of  $2712 \pm 6$  Ma (95% c.l., MSWD = 0.49) (Fig. 9c).

## DISCUSSION

### Melting reactions, melt compositions and melt: residuum proportions

Anatexis in the SMZ metasedimentary migmatites is well constrained by several different lines of evidence.

Table 2. U–Pb age data produced by LA-SF-ICP-MS dating of zircon from a stromatolite leucosome from the BQ sample L2a.

Sample	Domain	Analysis zircon sample	Ratios										Ages (Ma)				Conc. %		
			U (ppm) <sup>a</sup>	Pb (ppm) <sup>a</sup>	Th (U) <sup>a</sup>	<sup>207</sup> Pb/ <sup>235</sup> U <sup>b</sup>	2 $\sigma^d$	<sup>206</sup> Pb/ <sup>238</sup> U <sup>b</sup>	2 $\sigma^d$	rho <sup>c</sup>	<sup>207</sup> Pb/ <sup>206</sup> Pb <sup>e</sup>	2 $\sigma^d$	<sup>207</sup> Pb/ <sup>235</sup> U	2 $\sigma$	<sup>206</sup> Pb/ <sup>238</sup> U	2 $\sigma$		<sup>207</sup> Pb/ <sup>206</sup> Pb	2 $\sigma$
L2a	Core	035	220	124	0.31	15.90	0.52	0.564	0.015	0.83	0.204	0.004	2871	93	2883	62	2862	29	101
L2a	Core	007	195	111	0.47	16.31	0.47	0.568	0.014	0.83	0.208	0.003	2895	84	2901	56	2892	26	100
L2a	Core	041	314	174	0.35	15.25	0.43	0.552	0.013	0.82	0.200	0.003	2831	81	2836	53	2828	26	100
L2a	Core	029	147	84	0.37	16.71	0.36	0.574	0.016	0.83	0.211	0.004	2918	98	2922	65	2916	30	100
L2a	Core	048	259	146	0.44	16.16	0.44	0.565	0.013	0.81	0.207	0.003	2886	79	2889	52	2884	26	100
L2a	Core	013	132	75	0.31	16.05	0.46	0.564	0.013	0.83	0.207	0.003	2880	83	2882	55	2879	26	100
L2a	Core	010	208	119	0.45	16.57	0.45	0.571	0.013	0.83	0.211	0.004	2910	80	2911	53	2910	25	100
L2a	Core	089	221	124	0.53	16.03	0.51	0.563	0.014	0.80	0.207	0.004	2879	92	2879	59	2879	31	100
L2a	Core	048	227	130	0.36	16.58	0.47	0.570	0.013	0.82	0.211	0.003	2911	82	2910	54	2911	26	100
L2a	Core	034	296	166	0.31	15.85	0.41	0.560	0.012	0.82	0.205	0.003	2868	74	2866	49	2869	24	100
L2a	Core	050	412	230	0.31	15.70	0.40	0.558	0.012	0.81	0.204	0.003	2859	73	2856	48	2860	24	100
L2a	Core	009	172	97	0.34	16.06	0.55	0.563	0.016	0.83	0.207	0.004	2880	98	2878	66	2882	30	100
L2a	Core	103	81	46	0.32	16.66	0.67	0.570	0.018	0.81	0.212	0.005	2916	117	2909	76	2920	38	100
L2a	Core	085	136	75	0.56	16.09	0.65	0.549	0.018	0.82	0.213	0.005	2882	117	2822	76	2925	37	96
L2a	Core	087	107	56	0.32	14.70	0.55	0.520	0.016	0.81	0.205	0.005	2796	104	2698	67	2868	35	94
L2a	Core	059	240	123	0.81	14.38	0.41	0.515	0.012	0.81	0.203	0.003	2775	79	2677	51	2848	27	94
L2a	Core	065	71	37	0.55	15.18	0.58	0.524	0.017	0.82	0.210	0.005	2827	109	2717	70	2906	35	94
L2a	Core	027	258	132	0.79	14.91	0.47	0.510	0.013	0.83	0.212	0.004	2809	88	2658	56	2920	28	91
L2a	Core	067	141	69	0.55	13.90	0.45	0.491	0.013	0.81	0.205	0.004	2743	89	2574	56	2870	31	90
L2a	Rim	040	204	108	0.07	13.52	0.48	0.530	0.015	0.82	0.185	0.004	2716	97	2739	65	2699	33	101
L2a	Rim	012	225	117	0.11	13.23	0.45	0.522	0.015	0.82	0.184	0.004	2696	91	2708	62	2687	31	101
L2a	Rim	039	207	108	0.08	13.30	0.40	0.522	0.013	0.82	0.188	0.003	2731	84	2734	57	2729	28	100
L2a	Rim	033	251	131	0.08	13.40	0.38	0.524	0.012	0.82	0.186	0.003	2708	76	2714	51	2704	26	100
L2a	Rim	091	239	125	0.08	13.54	0.45	0.525	0.014	0.80	0.187	0.004	2718	91	2722	59	2715	33	100
L2a	Rim	011	166	88	0.06	13.72	0.42	0.528	0.013	0.82	0.188	0.003	2731	84	2734	57	2729	28	100
L2a	Rim	016	194	101	0.10	13.29	0.39	0.521	0.012	0.82	0.185	0.003	2701	79	2703	53	2699	27	100
L2a	Rim	054	325	170	0.07	13.52	0.45	0.525	0.014	0.82	0.187	0.004	2716	91	2718	61	2715	32	100
L2a	Rim	090	157	82	0.08	13.51	0.65	0.524	0.020	0.82	0.187	0.005	2716	130	2718	87	2715	45	100
L2a	Rim	015	283	147	0.10	13.23	0.37	0.519	0.012	0.82	0.185	0.003	2696	75	2697	50	2695	26	100
L2a	Rim	049	217	115	0.09	13.82	0.49	0.529	0.015	0.82	0.189	0.004	2737	97	2738	65	2737	33	100
L2a	Rim	014	221	115	0.08	13.38	0.38	0.522	0.012	0.82	0.186	0.003	2707	76	2707	51	2707	26	100
L2a	Rim	008	167	87	0.15	13.49	0.46	0.523	0.015	0.83	0.187	0.004	2714	92	2714	62	2715	31	100
L2a	Rim	047	138	73	0.19	13.85	0.57	0.529	0.018	0.82	0.190	0.004	2740	112	2739	75	2740	38	100
L2a	Rim	036	187	99	0.10	13.77	0.46	0.528	0.014	0.82	0.189	0.004	2734	91	2733	61	2735	31	100
L2a	Rim	053	216	112	0.09	13.15	0.44	0.518	0.014	0.82	0.184	0.004	2691	89	2689	59	2692	31	100
L2a	Rim	028	219	116	0.06	13.84	0.38	0.529	0.012	0.82	0.190	0.003	2739	76	2736	51	2741	26	100
L2a	Rim	088	130	69	0.09	13.63	0.47	0.525	0.015	0.80	0.188	0.004	2724	94	2720	62	2727	34	100
L2a	Rim	077	214	111	0.07	13.36	0.53	0.520	0.017	0.81	0.186	0.004	2705	107	2700	71	2709	37	100
L2a	Rim	052	309	165	0.02	14.17	0.39	0.533	0.012	0.81	0.193	0.003	2761	75	2755	49	2766	26	100
L2a	Rim	037	214	113	0.11	13.74	0.44	0.526	0.014	0.82	0.190	0.003	2732	88	2723	59	2739	30	99
L2a	Rim	055	205	107	0.07	13.42	0.47	0.520	0.015	0.82	0.187	0.004	2710	94	2698	63	2719	33	99
L2a	Rim	081	169	88	0.15	13.37	0.43	0.519	0.013	0.80	0.187	0.004	2706	87	2694	57	2716	32	99
L2a	Rim	096	129	67	0.18	13.39	0.50	0.518	0.016	0.80	0.187	0.004	2708	102	2693	66	2719	37	99
L2a	Rim	102	139	71	0.13	13.05	0.45	0.512	0.014	0.79	0.185	0.004	2683	94	2666	60	2696	35	99
L2a	Rim	060	130	67	0.11	13.54	0.52	0.519	0.016	0.82	0.189	0.004	2718	105	2696	70	2735	36	99
L2a	Rim	078	238	124	0.01	13.69	0.41	0.522	0.013	0.80	0.190	0.003	2729	82	2706	53	2746	30	99
L2a	Rim	094	95	48	0.12	12.54	0.47	0.502	0.015	0.80	0.181	0.004	2646	100	2623	65	2663	37	98
L2a	Rim	079	113	57	0.09	12.56	0.44	0.501	0.014	0.80	0.182	0.004	2647	92	2620	60	2669	34	98
L2a	Rim	093	162	81	0.10	12.60	0.42	0.500	0.013	0.79	0.183	0.004	2650	89	2613	57	2679	33	98
L2a	Rim	106	119	60	0.05	13.07	0.48	0.507	0.015	0.79	0.187	0.004	2685	99	2644	63	2716	36	97
L2a	Rim	086	150	76	0.08	13.09	0.44	0.507	0.014	0.80	0.187	0.004	2686	90	2643	58	2719	33	97
L2a	Rim	107	139	70	0.08	12.80	0.47	0.502	0.014	0.79	0.185	0.004	2665	97	2621	62	2699	36	97
L2a	Rim	099	141	71	0.11	12.97	0.45	0.504	0.014	0.79	0.187	0.004	2677	92	2631	59	2712	34	97

Table 2. (Continued)

Sample	Domain	Analysis zircon sample	U (ppm) <sup>a</sup>	Pb (ppm) <sup>a</sup>	Th/U <sup>a</sup>	Ratios				Ages (Ma)				Conc. %					
						<sup>207</sup> Pb/ <sup>235</sup> U <sup>b</sup>	<sup>206</sup> Pb/ <sup>238</sup> U <sup>b</sup>	2 $\sigma^d$	rho <sup>c</sup>	<sup>207</sup> Pb/ <sup>206</sup> Pb <sup>e</sup>	2 $\sigma^d$	<sup>207</sup> Pb/ <sup>235</sup> U	2 $\sigma$		<sup>206</sup> Pb/ <sup>238</sup> U	2 $\sigma$	<sup>207</sup> Pb/ <sup>206</sup> Pb	2 $\sigma$	
L2a	Rim	100	170	86	0.11	13.31	0.45	0.509	0.014	0.79	0.190	0.004	2702	91	2652	58	2740	34	97
L2a	Rim	104	149	74	0.09	12.67	0.44	0.497	0.014	0.79	0.185	0.004	2656	92	2602	59	2697	35	96
L2a	Rim	038	190	95	0.04	13.03	0.41	0.501	0.013	0.82	0.189	0.003	2682	85	2618	56	2730	30	96
L2a	Rim	101	83	41	0.06	12.74	0.51	0.494	0.016	0.80	0.187	0.005	2661	107	2587	69	2718	39	95
L2a	Rim	068	134	66	0.10	12.39	0.41	0.488	0.013	0.81	0.184	0.004	2634	88	2561	57	2692	32	95
L2a	Rim	066	100	50	0.06	13.07	0.46	0.498	0.014	0.81	0.190	0.004	2684	95	2607	62	2743	34	95
L2a	Rim	062	133	67	0.35	13.33	0.44	0.503	0.014	0.81	0.192	0.004	2703	90	2625	58	2763	31	95
L2a	Rim	063	128	61	0.09	12.16	0.40	0.476	0.013	0.81	0.185	0.004	2617	86	2510	56	2700	32	93
L2a	Rim	061	122	57	0.13	12.00	0.40	0.470	0.013	0.81	0.185	0.004	2605	87	2484	56	2701	32	92
L2a	Rim	042	604	278	0.01	11.47	0.28	0.460	0.009	0.81	0.181	0.003	2562	63	2441	40	2660	24	92
L2a	Rim	092	358	167	0.03	11.95	0.36	0.466	0.011	0.79	0.186	0.003	2600	78	2466	49	2707	30	91
L2a	Rim	080	467	216	0.04	11.82	0.33	0.461	0.010	0.79	0.186	0.003	2590	73	2445	45	2706	28	90
L2a	Rim	064	487	199	0.02	9.97	0.28	0.408	0.009	0.80	0.177	0.003	2432	69	2204	42	2629	28	84

<sup>a</sup>U and Pb concentrations and Th/U ratios are calculated relative to GJ-1 reference zircon.<sup>b</sup>Corrected for background and within-run Pb/U fractionation and normalized to reference zircon GJ-1 (ID-TIMS values/measured value); <sup>207</sup>Pb/<sup>235</sup>U calculated using (<sup>207</sup>Pb/<sup>206</sup>Pb)/(<sup>238</sup>U/<sup>206</sup>Pb) × 1/137.888.<sup>c</sup>Rho is the error correlation defined as the quotient of the propagated errors of the <sup>206</sup>Pb/<sup>238</sup>U and <sup>207</sup>Pb/<sup>235</sup>U ratio.<sup>d</sup>Quadratic addition of within-run errors (2 SD) and daily reproducibility of GJ-1 (2 SD).<sup>e</sup>Corrected for mass-bias by normalizing to GJ-1 reference zircon (-0.6 per atomic mass unit) and common Pb using the model Pb composition of Stacey & Kramers (1975).

The mineralogy of the leucosomes and the metasedimentary residua hosting the leucosomes allows for the identification of the melting reactions with confidence, i.e. in simplified form and in order of occurrence: muscovite + quartz + plagioclase = sillimanite + melt; biotite + sillimanite + quartz + plagioclase = garnet + melt and biotite + quartz + plagioclase = orthopyroxene + garnet ± cordierite + melt. These are in good agreement with experimental findings using comparable starting materials (e.g. Stevens *et al.*, 1997). Consequently, the melt compositions that would be produced by anatexis of the BQ metasedimentary rocks are well constrained by the compositions of experimental melts developed in relevant metapelitic bulk compositions, and from the compositions of natural melt inclusions recorded in peritectic phases from metasedimentary granulites (Fig. 6). As illustrated by the geochemical comparison presented in Fig. 6, the BQ leucosomes depart in several important ways from the compositions of the melts that were likely to have been involved in their formation. The leucosomes have lower K than relevant melt compositions; they have higher Ca/(Ca + Na) ratios, whilst A/CNK and Si values are similar to those of melts. These characteristics are not unique to the BQ leucosomes and are shared by granulite facies leucosomes from a number of different migmatite terranes (Fig. 6).

Pseudosection modelling of melt reintegration into the metapelitic residuum supports the sequence of melting reactions predicted from the mineralogy of the stromatic leucosomes and the metapelitic residuum (Fig. 8). Muscovite coexists with biotite below the wet solidus. Between this solidus and muscovite-out, some 15 vol.% of melt is produced in conjunction with peritectic sillimanite. This reaction is interpreted to contribute sillimanite-bearing magma to the stromatic leucosomes, and to produce sillimanite in the metapelitic residuum to these leucosomes. Subsequent biotite incongruent melting at higher temperature via the reaction biotite + sillimanite + quartz + plagioclase = garnet + melt is interpreted to have consumed sillimanite in the residuum, resulting in relict sillimanite inclusions in peritectic garnet, and contributed further magma, including peritectic garnet, to the leucosomes. By the peak of metamorphism, at ±875–890 °C and 9–10 kbar, the metapelitic residuum is predicted to have contributed ~45 to 50 vol.% melt to the stromatic leucosomes. Analysis of the ratio of metapelitic residuum to leucosome in the area of the BQ where the stromatic leucosomes are well exposed indicates that these zones have lost at least half of the melt that accumulated in such sites (Fig. 8). However, it must be considered that such modelling provides a minimum estimate of melt loss due to the possibility of magma, which includes crystals segregating from the source. The leucosome to residuum proportions in the quarry also demonstrate that the volume of melt produced from the

**Table 3.** U–Pb age data produced by LA-SF-ICP-MS dating of zircon from a nebular leucosome from the BQ, sample L5a.

Sample	Analysis zircon sample	U (ppm) <sup>a</sup>	Pb (ppm) <sup>a</sup>	Th/U <sup>a</sup>	Ratios				Ages (Ma)				Conc. %				
					<sup>207</sup> Pb/ <sup>235</sup> U <sup>b</sup>	<sup>206</sup> Pb/ <sup>238</sup> U <sup>b</sup>	2 $\sigma^d$	rho <sup>c</sup>	<sup>207</sup> Pb/ <sup>206</sup> Pb <sup>c</sup>	2 $\sigma^d$	<sup>207</sup> Pb/ <sup>235</sup> U	2 $\sigma$		<sup>206</sup> Pb/ <sup>238</sup> U	2 $\sigma$	<sup>207</sup> Pb/ <sup>206</sup> Pb	2 $\sigma$
L5a	028	135	72	0.14	13.73	0.530	0.73	0.83	0.188	0.006	2731	145	2742	98	2724	48	101
L5a	039	202	106	0.02	13.39	0.524	0.40	0.81	0.185	0.003	2708	81	2715	53	2702	29	100
L5a	066	142	74	0.10	13.18	0.520	0.58	0.81	0.184	0.005	2693	118	2700	79	2687	42	100
L5a	107	221	116	0.02	13.38	0.445	0.44	0.77	0.185	0.004	2702	90	2714	57	2702	35	100
L5a	038	269	142	0.04	13.60	0.527	0.44	0.81	0.187	0.004	2722	90	2729	59	2718	31	100
L5a	034	212	111	0.04	13.49	0.525	0.50	0.82	0.186	0.004	2714	101	2720	68	2710	35	100
L5a	101	278	146	0.02	13.42	0.524	0.46	0.78	0.186	0.004	2710	91	2715	57	2706	34	100
L5a	105	137	73	0.10	14.01	0.533	0.56	0.79	0.190	0.005	2750	111	2756	71	2746	40	100
L5a	063	103	54	0.15	13.10	0.518	0.46	0.81	0.183	0.004	2687	94	2692	62	2683	34	100
L5a	077	92	48	0.21	13.34	0.522	0.48	0.80	0.185	0.004	2704	96	2709	63	2701	35	100
L5a	102	91	48	0.12	13.44	0.524	0.51	0.79	0.186	0.004	2711	103	2714	67	2708	38	100
L5a	049	104	54	0.18	13.47	0.524	0.50	0.81	0.186	0.004	2713	100	2717	67	2711	35	100
L5a	054	111	58	0.19	13.46	0.522	0.46	0.81	0.185	0.004	2704	94	2707	62	2702	33	100
L5a	025	109	57	0.18	13.34	0.524	0.47	0.82	0.186	0.004	2712	94	2715	63	2710	33	100
L5a	033	152	81	0.06	14.09	0.534	0.50	0.82	0.191	0.004	2756	98	2758	65	2755	33	100
L5a	078	104	55	0.21	13.39	0.522	0.51	0.80	0.186	0.004	2708	103	2709	68	2706	37	100
L5a	053	216	114	0.03	13.88	0.530	0.42	0.80	0.190	0.003	2742	83	2743	55	2741	30	100
L5a	041	131	69	0.16	13.75	0.528	0.54	0.82	0.189	0.004	2733	107	2733	72	2733	37	100
L5a	046	365	193	0.10	13.88	0.37	0.530	0.80	0.190	0.003	2741	73	2742	47	2741	26	100
L5a	068	124	65	0.15	13.44	0.523	0.46	0.80	0.186	0.004	2711	93	2711	61	2711	33	100
L5a	062	102	54	0.22	14.09	0.533	0.48	0.81	0.192	0.004	2756	95	2756	62	2756	33	100
L5a	047	155	81	0.05	13.22	0.519	0.42	0.81	0.185	0.003	2696	85	2696	56	2696	30	100
L5a	080	128	68	0.10	13.95	0.47	0.531	0.79	0.191	0.004	2747	92	2747	59	2747	33	100
L5a	009	101	52	0.19	13.05	0.516	0.64	0.83	0.183	0.005	2683	131	2683	89	2684	45	100
L5a	088	122	63	0.19	13.11	0.517	0.56	0.80	0.184	0.005	2688	114	2688	75	2688	41	100
L5a	085	161	83	0.00	12.96	0.42	0.515	0.79	0.183	0.004	2677	87	2676	56	2678	33	100
L5a	104	195	101	0.15	13.13	0.517	0.44	0.77	0.184	0.004	2689	89	2688	56	2690	35	100
L5a	026	139	73	0.26	13.65	0.526	0.50	0.82	0.188	0.004	2725	99	2724	66	2726	34	100
L5a	060	159	83	0.12	13.24	0.519	0.42	0.80	0.185	0.004	2697	86	2695	56	2698	31	100
L5a	013	115	60	0.19	13.63	0.51	0.51	0.82	0.188	0.004	2725	102	2723	68	2726	35	100
L5a	090	401	209	0.00	13.33	0.521	0.41	0.82	0.186	0.004	2703	83	2701	53	2705	32	100
L5a	035	229	123	0.01	14.16	0.534	0.40	0.81	0.192	0.003	2761	78	2758	51	2762	27	100
L5a	050	348	182	0.02	13.41	0.522	0.39	0.80	0.186	0.003	2709	80	2707	52	2711	29	100
L5a	064	128	68	0.18	14.17	0.51	0.534	0.81	0.192	0.004	2761	100	2759	65	2763	34	100
L5a	011	95	50	0.21	13.34	0.520	0.67	0.83	0.186	0.005	2704	135	2701	91	2706	46	100
L5a	012	333	174	0.01	13.50	0.523	0.39	0.81	0.187	0.003	2715	78	2711	51	2718	27	100
L5a	067	180	93	0.06	13.19	0.518	0.40	0.81	0.185	0.003	2693	82	2689	53	2696	30	100
L5a	065	409	211	0.19	13.05	0.515	0.35	0.78	0.184	0.003	2683	73	2679	47	2686	28	100
L5a	079	174	91	0.05	13.53	0.523	0.53	0.80	0.188	0.004	2717	107	2713	70	2720	38	100
L5a	100	112	60	0.12	13.97	0.530	0.53	0.79	0.191	0.004	2748	104	2743	67	2751	38	100
L5a	051	110	57	0.21	13.35	0.520	0.50	0.81	0.186	0.004	2705	102	2700	67	2708	36	100
L5a	008	129	68	0.20	13.48	0.522	0.53	0.82	0.187	0.004	2714	106	2709	71	2718	36	100
L5a	055	101	52	0.18	13.13	0.516	0.45	0.81	0.184	0.004	2689	92	2683	61	2693	33	100
L5a	061	119	63	0.13	13.89	0.528	0.57	0.82	0.191	0.005	2742	113	2735	75	2748	39	100
L5a	040	94	50	0.19	13.73	0.526	0.52	0.82	0.189	0.004	2731	103	2724	69	2737	35	100
L5a	037	222	117	0.04	13.78	0.48	0.48	0.82	0.190	0.004	2735	95	2726	63	2741	33	99
L5a	106	141	73	0.14	13.29	0.518	0.45	0.77	0.186	0.004	2700	92	2691	58	2707	35	99
L5a	091	543	280	0.02	13.15	0.516	0.37	0.76	0.185	0.003	2690	76	2681	47	2697	30	99
L5a	086	328	170	0.01	13.37	0.519	0.39	0.77	0.187	0.003	2706	78	2695	49	2714	30	99
L5a	016	133	68	0.08	13.03	0.54	0.54	0.82	0.184	0.004	2682	110	2671	74	2690	38	99
L5a	010	100	52	0.20	13.45	0.519	0.61	0.83	0.188	0.005	2712	124	2695	83	2725	42	99
L5a	093	123	63	0.08	13.15	0.513	0.45	0.79	0.186	0.004	2690	93	2671	59	2705	35	99
L5a	094	88	45	0.20	12.84	0.508	0.48	0.79	0.183	0.004	2668	100	2647	64	2684	37	99
L5a	087	248	127	0.02	13.14	0.512	0.40	0.78	0.186	0.004	2690	82	2666	52	2708	31	98

Table 3. (Continued)

Sample	Analysis zircon sample	U (ppm) <sup>a</sup>	Pb (ppm) <sup>a</sup>	Th/U <sup>a</sup>	Ratios				Ages (Ma)				Conc. %				
					<sup>207</sup> Pb/ <sup>235</sup> U <sup>b</sup>	<sup>206</sup> Pb/ <sup>238</sup> U <sup>b</sup>	2 $\sigma^d$	rho <sup>e</sup>	<sup>207</sup> Pb/ <sup>206</sup> Pb <sup>c</sup>	2 $\sigma^d$	<sup>207</sup> Pb/ <sup>235</sup> U	2 $\sigma$		<sup>206</sup> Pb/ <sup>238</sup> U	2 $\sigma$	<sup>207</sup> Pb/ <sup>206</sup> Pb	2 $\sigma$
L5a	029	456	236	0.23	13.57	0.518	0.33	0.80	0.190	0.003	2720	67	2692	43	2742	24	98
L5a	081	189	95	0.02	12.61	0.501	0.39	0.78	0.183	0.003	2651	81	2617	52	2677	31	98
L5a	092	191	97	0.06	12.98	0.505	0.58	0.80	0.186	0.005	2678	119	2636	77	2710	43	97
L5a	099	123	62	0.12	12.99	0.512	0.51	0.79	0.187	0.004	2679	105	2633	67	2714	39	97
L5a	103	258	130	0.18	12.87	0.502	0.40	0.77	0.186	0.004	2670	84	2624	52	2706	33	97
L5a	007	506	253	0.02	12.71	0.499	0.31	0.80	0.185	0.003	2659	64	2610	42	2696	23	97
L5a	036	587	299	0.17	13.35	0.509	0.32	0.79	0.190	0.003	2704	65	2652	42	2744	24	97
L5a	052	108	53	0.19	12.58	0.490	0.62	0.82	0.186	0.005	2648	130	2570	85	2709	46	95
L5a	042	178	82	0.20	11.88	0.441	0.41	0.81	0.188	0.004	2595	89	2431	56	2726	33	89
L5a	015	483	213	0.25	11.29	0.441	0.28	0.80	0.186	0.003	2547	63	2356	39	2703	24	87
L5a	098	587	246	0.03	10.55	0.420	0.31	0.76	0.182	0.003	2484	72	2259	42	2674	31	84

<sup>a</sup>U and Pb concentrations and Th/U ratios are calculated relative to GJ-1 reference zircon.<sup>b</sup>Corrected for background and within-run Pb/U fractionation and normalized to reference zircon GJ-1 (ID-TIMS values/measured value); <sup>207</sup>Pb/<sup>235</sup>U calculated using (<sup>207</sup>Pb/<sup>206</sup>Pb)/(<sup>238</sup>U/<sup>206</sup>Pb × 1/137.88).<sup>c</sup>Rho is the error correlation defined as the quotient of the propagated errors of the <sup>206</sup>Pb/<sup>238</sup>U and <sup>207</sup>Pb/<sup>235</sup>U ratio.<sup>d</sup>Quadratic addition of within-run errors (2 SD) and daily reproducibility of GJ-1 (2 SD).<sup>e</sup>Corrected for mass-bias by normalizing to GJ-1 reference zircon (−0.6 per atomic mass unit) and common Pb using the model Pb composition of Stacey & Kramers (1975).

exposed rocks substantially exceeds the volume of the leucosomes. Consequently, the anatectic features documented in this study are consistent with an *in situ* anatectic process, and the addition of peraluminous magmas derived from deeper metasedimentary sources is not required.

Three separate lines of evidence suggest that the BQ stromatic leucosomes did not acquire their very low K, high Ca/(Ca + Na) character solely through the cooling driven processes currently invoked to explain such phenomena: i.e. the redistribution of K<sub>2</sub>O + H<sub>2</sub>O back into the residuum, or the loss of melt following partial crystallization of the leucosomes. Each of these is dealt with in detail below.

#### Deformation of the stromatic v. nebulitic leucosomes

The stromatic leucosomes of the BQ, as well as the small intrusive granitoid which is mineralogically and geochemically very similar to these leucosomes, carry a strong solid-state fabric. Indeed, the defining features of the margins of these leucosomes in horizontal pavement outcrops that are approximately perpendicular to the foliation are pinch and swell structures developed as a result of foliation-parallel stretching. As noted by Bons *et al.* (2004), such features may also be produced by the expansion and collapse of magma sheets. Within the context of the stromatic leucosomes, expansion and collapse induced by melt accumulation and upward migration is to be expected. However, the existence of cusped-lobate flame-structures, indicating higher competency in the leucosomes relative to the bounding metapelitic residuum (Fig. 2), clearly indicates that these structures were produced by penetrative deformation acting on both the metapelitic residuum and the leucosome, and that the leucosome was solid during the deformation. In contrast, the development of nebulitic leucosomes, and associated coarse-grained orthopyroxene-bearing residua, clearly cross-cut the foliation in the metapelites and the stromatic leucosomes which they host (Fig. 3). Petrographic evidence confirms the deformed nature of the stromatic leucosomes, v. the lack of solid-state deformation features in the nebulitic leucosomes. Importantly, on a macroscopic scale, the foliation in the metapelites does not bend or wrap around the coarse-grained nebulitic leucosomes + residua (Fig. 3a). Hence, the lack of foliation in these structures cannot simply be a consequence of strain partitioning away from such domains. There is little potential ambiguity in this interpretation, as strain partitioning around competent structures usually leads to an increase in strain at the interface between the deforming matrix and the more competent structure. No such increase in strain towards the margins of the orthopyroxene-bearing residua is observed. All of the above strongly suggest that the stromatic leucosomes formed, solidified and deformed prior to the formation of the neb-

ulitic leucosomes. Despite the fact that the formation of the leucosomes was separated by a regional deformation event, their U–Pb zircon ages are within error identical. The interpretation therefore follows that the anatexis reactions observed in the BQ metasedimentary rocks occurred during a single metamorphic event at  $\sim 2.71 \pm 0.005$  Ga, and that the stromatic leucosomes must have become rheologically solid whilst the SMZ was undergoing prograde heating.

#### *Preservation of the peritectic assemblage in leucosomes and residua*

In migmatitic granulites where no melt loss occurred, the potential exists for complete replacement of the anhydrous peritectic assemblage, developed by incongruent melting of muscovite and biotite, during cooling and crystallization of the melt. White & Powell (2010) have demonstrated how the chemical potential gradients that develop between leucosome and residuum upon cooling can lead to the preferential replacement of anhydrous ferromagnesian minerals in the residua by hydrous phases such as biotite and subsequent preservation of these minerals in the leucosome. While this process may enhance the preservation of peritectic minerals in leucosomes, the degree of replacement of these minerals in the residuum should be proportional to the amount of melt that is retained in the system. In evaluating the importance of  $K_2O$  redistribution back into the residuum in shaping the compositions of the BQ leucosomes, it is therefore important to consider the degree of replacement of garnet, cordierite and orthopyroxene by biotite, in all of the BQ lithologies. In the stromatic leucosomes and granitoid, there is virtually no replacement of peritectic garnet by biotite, nor significant replacement of orthopyroxene in the nebulitic leucosomes (Fig. 5); sillimanite in the stromatic leucosomes similarly shows no replacement by muscovite. Crystallization–hydration reactions are well documented in the SMZ (e.g. Stevens & Van Reenen, 1992b; Stevens, 1997), and have occurred to some degree in both the metapelitic residua and the coarse-grained orthopyroxene-bearing residua at the BQ. However, these hydration reactions did not result in the widespread replacement of garnet, and only relatively minor replacement of orthopyroxene by biotite. The main focus of the hydration reactions in the BQ is cordierite. In all samples of residuum examined in this study, cordierite is replaced by biotite and kyanite, including cordierite that occurs as a symplectic intergrowth with orthopyroxene after garnet, indicating that these reactions occurred after decompression. For the purposes of this study, the important information related to these retrograde assemblages is that they replace a relatively small percentage of the anhydrous ferromagnesian mineralogy of the residuum, and took place after decompression and after deformation of the stromatic leucosomes, i.e. following the peak of metamorphism.

In conclusion, substantial melt loss from all of the BQ migmatite lithologies is implied by (i) the absence of comprehensive replacement of ferromagnesian minerals by biotite, and sillimanite by muscovite in the stromatic leucosomes; (ii) the fact that relatively minor replacement of cordierite and orthopyroxene has occurred in the residua to the leucosomes; and that (iii) these reactions took place in the kyanite stability field after decompression, and considerable cooling of the granulites. Thus, although retrograde ‘crystallization–hydration’ reactions must have depleted leucosome  $K_2O$ -content to some degree, at the BQ, such reactions played a subordinate role to melt loss in creating the leucosome chemistry. The observed ‘crystallization–hydration’ reaction textures at the BQ most likely record an increase in  $H_2O$  and  $K_2O$  activity which coincided with crystallization of a very small fraction of melt that had remained in the leucosome structures.

#### *The compositions of the leucosomes*

The possibility that the chemistry of the BQ leucosomes resulted from partial crystallization of melt in the leucosome structures, prior to melt loss, can also be assessed by consideration of the bulk compositions of the leucosomes. Given that Ca and Na are almost completely contained within plagioclase in peraluminous granitoid rocks, the Ca:Na ratios of experimental melts from metapelitic sources are a reasonable proxy for the average plagioclase composition that would be produced on complete crystallization of the melt. Figure 10a,b shows the plagioclase core compositions present in the various leucosome varieties and metapelitic residua from the BQ, as well as the plagioclase composition present in the starting material of the biotite melting experiments of Stevens *et al.* (1997) (black star in Fig. 10a). The melt composition produced from biotite fluid-absent melting in a metapelitic composition at 900 °C and 10 kbar is also indicated (white star in Fig. 10a; Stevens *et al.*, 1997). As the starting plagioclase in the experiment was similar in composition to the plagioclase in the metapelitic residuum from the BQ, and the experimental melt was produced at 900 °C, the Ab:An ratio of the melt produced in the experiment should provide a minimum estimate of this ratio in melts produced by the same reaction in the BQ. Simple lever-rule considerations indicate that the plagioclase from the BQ leucosomes with the lowest Ab:An ratios could only be produced by <10% crystallization of the experimental melt composition. Such a figure is inconsistent with the ratio of leucosome to residuum preserved in the BQ. The low Ab:An ratio of the leucosome plagioclase relative to those of likely melt compositions also presents a further compelling argument against such leucosomes attaining their compositions via diffusive redistribution of  $K_2O$  and  $H_2O$  back into the residuum; and, that the leucosome

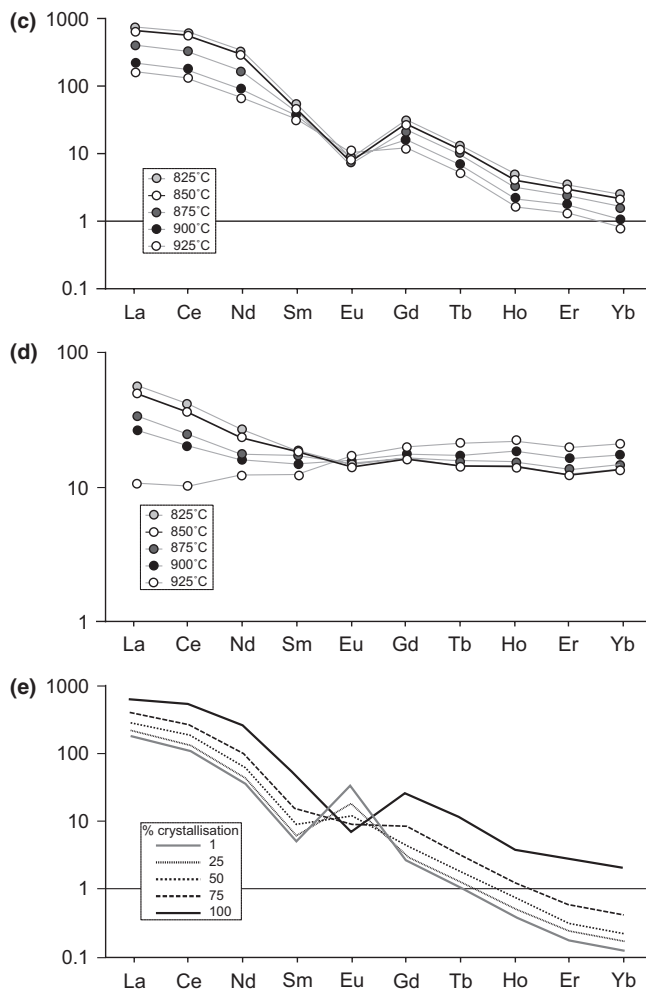
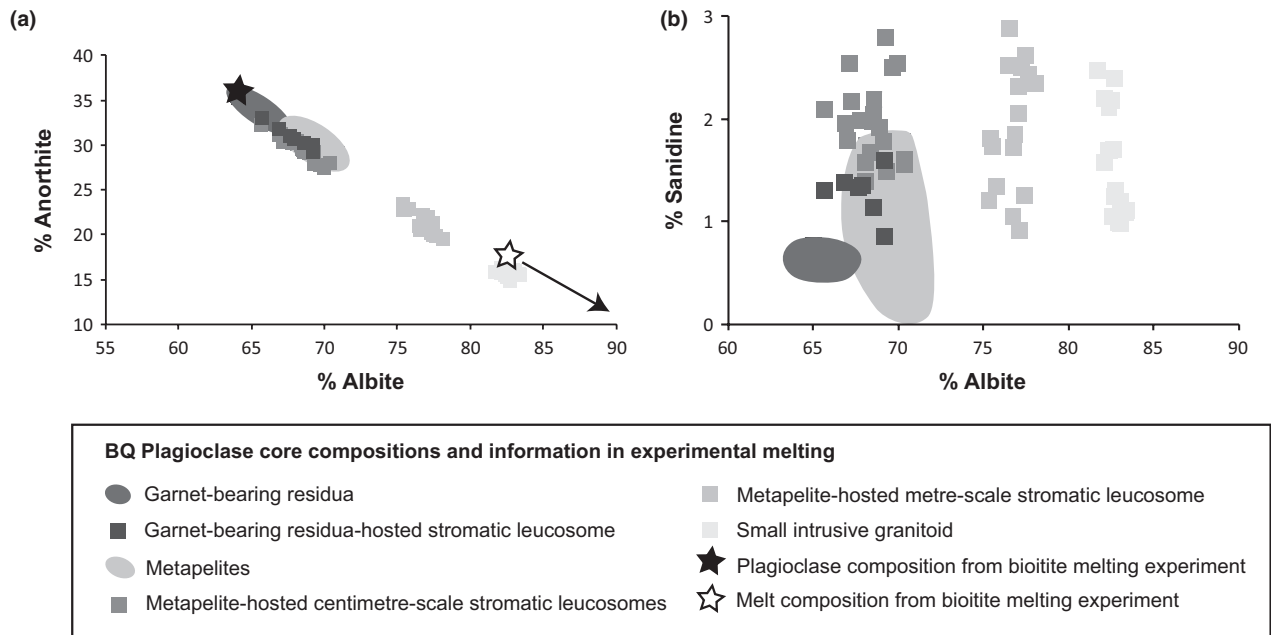


**Fig. 10.** (a, b) The composition of plagioclase in the leucosomes and residual metapelitic rocks. Note that plagioclase in the leucosomes often has Ab:An ratios similar to those of the residual rocks. Despite this, the plagioclase in the leucosomes has slightly but significantly different K contents, confirming that the leucosome plagioclase in these cases does not represent plagioclase entrained from the source. The experimental information presented is from Stevens *et al.* (1997), composition NBS. In these experiments, plagioclase of the composition indicated by the black star melted at 900 °C and 10 kbar with quartz + biotite to produce a melt with the composition of the white star. As the plagioclase in the starting material was as calcic as plagioclase in the residuum at the BQ, the white star represents a minimum estimate for Ab:An ratio in the BQ melts produced by this reaction. This illustrates with near certainty that the BQ leucosomes did not acquire their low K characteristics simply by loss of K to the residuum. If this was the case, their Ab:An ratios would have been >83. (c–e) Chondrite-normalized (Taylor & McLennan, 1985) REE modelling using the partition coefficients provided in the Appendix, and the mineral proportions from a melt-reintegrated pseudosection constructed as described in the Appendix. (c) The REE patterns of the melts produced by equilibrium batch melting at different temperatures. (d) The REE patterns of the residua produced by complete melt segregation after equilibrium batch melting at different temperatures. (e) The REE patterns of hypothetical crystal cumulates formed from the melt produced by equilibrium batch melting at 850 °C. The model assumes complete separation of the remaining melt from the crystal cumulate.

compositions are shaped by a process which changes Ca:Na ratio substantially from that which would have been created through complete crystallization of the melt.

Modelling of the REE compositions of the melts produced by equilibrium incongruent melting of biotite in the BQ metapelites (details of the modelling are presented in Appendix 1) suggests that the melts would be characterized by negative Eu anomalies (Fig. 10c). This is a consequence of the flat REE profile over Eu in the metapelites, and the fact that plagioclase forms a significant constituent of the residuum. Consequently, formation of the strong positive Eu anomaly in the leucosomes by accumulation of early-formed plagioclase and quartz would require that the leucosomes represent the products of <10% crystallization prior to melt loss (Fig. 10e). As documented above, the proportion of residua developed in association with the stromatic leucosomes is not sufficiently large to suggest 90% melt loss, following the crystallization of 10% cumulate quartz and plagioclase in the leucosomes.

The remainder of the discussion explores potential mechanisms to produce plagioclase and quartz within the leucosome structures where magma had accumulated or through which magma was migrating, whilst the BQ rocks were undergoing high-*T*, prograde metamorphism.

### The melting process and leucosome chemistry

In rocks from many magmatic environments, plagioclase major and trace element zonation confirms that diffusion rates in plagioclase are sufficiently slow to prevent diffusional equilibration within individual plagioclase crystals during magma crystallization (e.g. Vance, 1962). Similarly, Sr variation in granite magmas has been interpreted to reflect isotopic disequilibrium controlled by slow diffusion in plagioclase during anatexis (Farina & Stevens, 2011). Partial melting experiments using plagioclase-bearing starting materials with average crystal sizes as small as 5  $\mu\text{m}$  confirm that over time intervals of 10–20 days, plagioclase cores with the original starting composition remain in the partially molten rock (Johannes & Koepke, 2001). Thus, it is plausible that during granulite facies anatexis, individual plagioclase crystals in the millimetre to centimetre size range do not completely equilibrate. However, such granulites are unlikely to record disequilibrium melting processes at the crystal scale. This is due to the typically protracted periods of post-anatectic residency at high temperature; the inevitable re-crystallization of the high temperature plagioclase during cooling to exsolve K-feldspar; as well as the crystallization of new plagioclase (amongst other minerals) due to decreasing garnet mode in response to decompression (as evidenced in the rim compositions of plagioclase from the BQ residua and leucosomes, for instance).

Evidence of disequilibrium melting can, however, be found in the form of bulk-rock chemistry. For example, Del Moro *et al.* (2000) proposed disequilibrium melting to account for the trace element behaviour in the K<sub>2</sub>O-poor, positive Eu anomaly leucosomes of the Serre Massif, Italy. They suggested that the formation of the leucosomes is due to successive disequilibrium melting episodes involving principally plagioclase and quartz.

In the case of the BQ rocks, where melting occurred through the incongruent melting of biotite at high temperature, there would appear to be two different ways in which disequilibrium involving plagioclase could occur. Both would have the potential to produce low K<sub>2</sub>O leucosomes that are characterized by strong positive Eu anomalies relative to their sources, and that would become rheologically solid whilst the rocks are still undergoing heating. Both processes recognize that it is the outermost zones of the plagioclase crystals most likely to be involved in the melting reaction. As depicted in Fig. 11a, in the first case only the outer zone of the plagioclase crystals in the source melt incongruently, precipitating a CaO-enriched peritectic plagioclase, with a significant volume of the original plagioclase remaining inaccessible due to diffusional constraints, and thus unreactive. In this scenario, the CaO-rich peritectic plagioclase is largely entrained to the segregating magma, along with sillimanite and garnet (in the case of the BQ), and is deposited in the sites of magma accumulation and migration to form the leucosomes. Melt loss from the leucosomes is assumed to be sufficiently effective, that despite the fact that the source continues to produce melt, the leucosome structures become rheologically solid even as the melting reaction proceeds. Consequently, the chemistry of the leucosomes will reflect the volume and proportions of peritectic minerals precipitated in these sites, as well as the amount of melt which remains to crystallize in the sites. As quartz and K-feldspar will not be entrained phases, but are rather phases that will crystallize directly from the melt, the quartz and K-feldspar modes should correlate positively. This is not the case in the BQ leucosomes (Fig. 6c) as the leucosomes are characterized by Si contents that are comparable to melt compositions, yet are very K-depleted relative to such melts.

The second possibility, as depicted in Fig. 11b, is that the outer reactive zones of the plagioclase crystals in the source melt congruently as a result of sluggish diffusion, with no production of a more CaO-rich peritectic plagioclase at the site of the melting reaction. Such a disequilibrium process would produce a higher than equilibrium amount of CaO in the melt, with recovery from this state possibly only occurring after melt has segregated into the structures that host the leucosomes. This process would be characterized by a lack of plagioclase-induced Eu fractionation on melt formation and segregation,



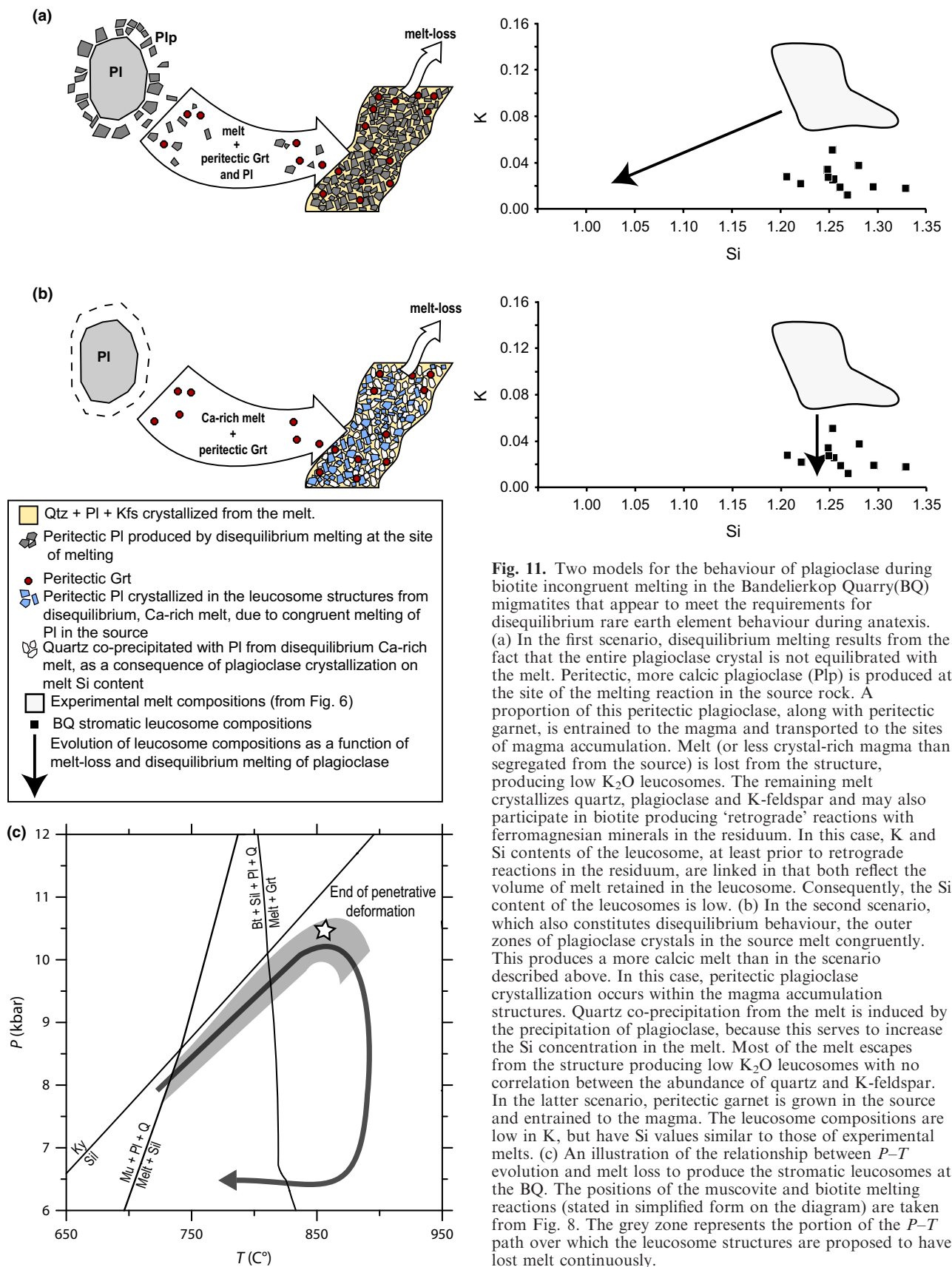


**Fig. 11.** Two models for the behaviour of plagioclase during biotite incongruent melting in the Bandelierkop Quarry (BQ) migmatites that appear to meet the requirements for disequilibrium rare earth element behaviour during anatexis. (a) In the first scenario, disequilibrium melting results from the fact that the entire plagioclase crystal is not equilibrated with the melt. Peritectic, more calcic plagioclase (Plp) is produced at the site of the melting reaction in the source rock. A proportion of this peritectic plagioclase, along with peritectic garnet, is entrained to the magma and transported to the sites of magma accumulation. Melt (or less crystal-rich magma than segregated from the source) is lost from the structure, producing low  $K_2O$  leucosomes. The remaining melt crystallizes quartz, plagioclase and K-feldspar and may also participate in biotite producing 'retrograde' reactions with ferromagnesian minerals in the residuum. In this case, K and Si contents of the leucosome, at least prior to retrograde reactions in the residuum, are linked in that both reflect the volume of melt retained in the leucosome. Consequently, the Si content of the leucosomes is low. (b) In the second scenario, which also constitutes disequilibrium behaviour, the outer zones of plagioclase crystals in the source melt congruently. This produces a more calcic melt than in the scenario described above. In this case, peritectic plagioclase crystallization occurs within the magma accumulation structures. Quartz co-precipitation from the melt is induced by the precipitation of plagioclase, because this serves to increase the Si concentration in the melt. Most of the melt escapes from the structure producing low  $K_2O$  leucosomes with no correlation between the abundance of quartz and K-feldspar. In the latter scenario, peritectic garnet is grown in the source and entrained to the magma. The leucosome compositions are low in K, but have Si values similar to those of experimental melts. (c) An illustration of the relationship between  $P-T$  evolution and melt loss to produce the stromatic leucosomes at the BQ. The positions of the muscovite and biotite melting reactions (stated in simplified form on the diagram) are taken from Fig. 8. The grey zone represents the portion of the  $P-T$  path over which the leucosome structures are proposed to have lost melt continuously.

with the crystallization of relatively CaO-rich plagioclase in the leucosome structures. The precipitation of plagioclase is likely to induce co-precipitation of quartz due to the influence of plagioclase crystallization on melt SiO<sub>2</sub> content. The latter model for disequilibrium melting of plagioclase, which would have occurred simultaneously with magma segregation, would appear to fit best with the entire spectrum of field, textural and chemical data from the BQ presented in this study. In Fig. 11a, garnet entrainment to the magma segregating from the source is proposed to occur via the processes described by Taylor & Stevens (2010). Thus, different behaviour is proposed for garnet and plagioclase. These differences in behaviour are proposed to be a consequence of the fact that melt compositions appear less 'elastic' for Fe and Mg solubility than for Ca and Al solubility, as well as the fact that plagioclase is a major reactant in the melting reaction.

### The nebulitic leucosomes

This study has not examined the petrogenesis of the BQ nebulitic leucosomes in detail, other than identifying the melting reaction involved in their formation. The key reason for this is the difficulty of separating nebulitic leucosomes from their residuum, which has prevented the acquisition of bulk compositions for this leucosome generation. In addition, the volume of rock which has experienced this melting reaction is relatively low, and the reaction followed the production of voluminous zones of melt-depleted residua by muscovite and biotite + sillimanite melting reactions. Thus, the balance between melt loss and K<sub>2</sub>O-depletion through retrograde reaction with the residuum, both that which is directly associated with the formation of the leucosome and that produced by earlier anatexis, is much more difficult to assess in the case of the nebulitic leucosomes.

### CONCLUSIONS

The findings of this study argue that in the case of fluid-absent granulite facies anatexis, the melt may leave the source, in geological terms, virtually instantaneously; that preserved leucosome volumes significantly underestimate the volume of melt lost from such rocks; and that individual leucosome volumes most likely do not represent the cumulative volume of melt or magma, which flowed through the leucosome structures. In this study, we make a strong case that the leucosome structures represent sites of magma accumulation that lost melt and underwent solid-state deformation, while the rocks were undergoing heating, and that the processes that control their chemistry therefore have to be different from the mainly retrograde processes that are usually evoked to explain aspects of granulite facies leucosome chemistry. Instead, the markedly low K and

high Ca/(Ca + Na) ratio of leucosomes at the BQ are proposed to have formed by disequilibrium melting, involving congruent melting of plagioclase, and subsequent recovery crystallization of plagioclase within the sites of melt migration. Thus, we propose that the chemistry of the leucosomes is controlled by the amount of plagioclase crystallization induced by the disequilibrium melting of plagioclase; the amount of co-precipitation of quartz induced by plagioclase crystallization; the amount of entrained peritectic ferromagnesian minerals that precipitate in the leucosome structures; and the amount of melt that remained in the structure. Reactions producing biotite in the residua from which the melts segregated must have further depleted leucosome K-content to some degree, but at the BQ, such reactions played a subordinate role to melt loss in creating the leucosome chemistry. Thus, in the BQ, the combination of the leucosome compositions, coupled with the high proportion of preserved anhydrous ferromagnesian minerals in the residuum to the leucosomes, indicates that very low proportions of melt remained in the leucosomes. In combination, these findings suggest that leucosomes form incrementally as the melting reactions proceed. Melt leaving the source, essentially as it forms, dumps its disequilibrium plagioclase load, as well as co-precipitated quartz and entrained ferromagnesian peritectic minerals, in sites of melt transfer. Consequently, we interpret leucosomes to essentially be comprised of residua, and that the presence of a significant volume of leucosome material of this type in the deep crust does not indicate that crustal differentiation was inefficient. In addition, the presence of such leucosome material in the lower crust does not indicate that melt was present for long periods.

### ACKNOWLEDGEMENTS

T. Johnson, B. Cesare, J. Diener and D. White are thanked for their constructive and helpful reviews. This study was made possible by support from the South African Research Chairs Initiative (SARChI) of the National Research Foundation to GS.

### REFERENCES

- Acosta-Vigil, A., Cesare, B., London, D. & Morgan, G.B., 2007. Microstructures and composition of melt inclusions in a crustal anatectic environment, represented by metapelitic enclaves within El Hoyazo dacites, SE Spain. *Chemical Geology*, **235**, 450–465.
- Als Dorf, D. & Nelson, D., 1999. Tibetan satellite magnetic low: evidence for widespread melt in the Tibetan crust? *Geology*, **27**, 943–946.
- Barbey, P., Macaudiere, J. & Nzenti, J.P., 1990. High-pressure dehydration melting of metapelites: evidence from the migmatites of Yaounde (Cameroon). *Journal of Petrology*, **31**, 401–427.
- Bartoli, O., Cesare, B., Poli, S. *et al.*, 2013. Recovering the composition of melt and the fluid regime at the onset of

- crustal anatexis and S-type granite formation. *Geology*, **41**, 115–118.
- Barton, J.M., Doig, R., Smith, C.B., Bohlender, F. & Van Reenen, D.D., 1992. Isotopic and REE characteristics of the intrusive charnoenderbite and enderbite geographically associated with the Matok Pluton, Limpopo belt, Southern Africa. *Precambrian Research*, **55**, 451–567.
- Belyanin, G.A., Rajesh, H.M., Sajeev, K. & Van Reenen, D.D., 2012. Ultrahigh-temperature metamorphism from an unusual corundum+orthopyroxene intergrowth bearing Al-Mg granulite from the Southern Marginal Zone, Limpopo Complex, South Africa. *Contributions to Mineralogy and Petrology*, **164**, 457–475.
- Bons, P.A., Druguet, E., Hamann, I., Carreras, J. & Passchier, C.W., 2004. Apparent boudinage in dykes. *Journal of Structural Geology*, **26**, 625–636.
- Brown, M., 2002. Retrograde processes in migmatites and granulites revisited. *Journal of Metamorphic Geology*, **20**, 25–40.
- de Capitani, C. & Petrakakis, K., 2010. The computation of equilibrium assemblage diagrams with Theriak/Domino software. *American Mineralogist*, **95**, 1006–1016.
- Chappell, B.W. & White, A.J.R., 1974. Two contrasting granite types. *Pacific Geology*, **8**, 173–174.
- Chavagnac, V., Kramers, J.D., Nägler, T.F. & Holzer, L., 2001. The behaviour of Nd and Pb isotopes during 2.0 Ga migmatization in paragneisses of the Central Zone of the Limpopo Belt (South Africa and Botswana). *Precambrian Research*, **112**, 51–86.
- Coggon, R. & Holland, T.J.B., 2002. Mixing properties of phengitic micas and revised garnet-phengite thermobarometers. *Journal of Metamorphic Geology*, **20**, 683–696.
- De Wit, M.J., Van Reenen, D.D. & Roering, C., 1992. Geologic observations across a tectono-metamorphic boundary in the Babangu area, Giyani (Sutherland) greenstone belt, South Africa. *Precambrian Research*, **55**, 111–122.
- Del Moro, A., Fornelli, A. & Piccarreta, G., 2000. Disequilibrium melting in granulite-facies metasedimentary rocks of the Northern Serre (Calabria-Southern Italy). *Mineralogy and Petrology*, **70**, 89–104.
- Du Toit, M.C., Van Reenen, D.D. & Roering, C., 1983. Some aspects of the geology, structure and metamorphism of the Southern Marginal Zone of the Limpopo metamorphic complex. *Geological Society of South Africa, Special Publications*, **8**, 121–142.
- Farina, F. & Stevens, G., 2011. Source controlled  $^{87}\text{Sr}/^{86}\text{Sr}$  isotope variability in granitic magmas: the inevitable consequence of mineral-scale isotopic disequilibrium in the protolith. *Lithos*, **122**, 189–200.
- Ferrero, S., Bartoli, O., Cesare, B. *et al.*, 2012. Microstructures of melt inclusions in anatectic metasedimentary rocks. *Journal of Metamorphic Geology*, **30**, 303–322.
- Frei, D. & Gerdes, A., 2009. Precise and accurate in situ U-Pb dating of zircon with high sample throughput by automated LA-SF-ICP-MS. *Chemical Geology*, **261**, 261–270.
- Gapais, D., Cagnard, F., Gueydan, F., Barbey, P. & Ballèvre, M., 2009. Mountain building and exhumation processes through time: inferences from nature and models. *Terra Nova*, **21**, 188–194.
- Gerdes, A. & Zeh, A., 2006. Combined U-Pb and Hf isotope LA-(MC)-ICP-MS analysis of detrital zircons: comparison with SHRIMP and new constraints for the provenance and age of an Armorican metasediment in Central Germany. *Earth and Planetary Science Letters*, **249**, 47–61.
- Hensen, B.J. & Green, D.H., 1973. Experimental study of the stability of cordierite and garnet in pelitic compositions at high pressures and temperatures. *Contributions to Mineralogy and Petrology*, **38**, 151–166.
- Holland, T.J.B. & Powell, R., 1998. An internally consistent thermodynamic data set for phases of petrological interest. *Journal of Metamorphic Geology*, **16**, 309–343.
- Holland, T. & Powell, R., 2003. Activity-composition relations for phases in petrological calculations: an asymmetric multi-component formulation. *Contributions to Mineralogy and Petrology*, **145**, 492–501.
- Holzer, L., Frei, R., Barton, J.M. & Kramers, J.D., 1998. Unravelling the record of successive high grade events in the Central Zone of the Limpopo Belt using Pb single phase dating of metamorphic minerals. *Precambrian Research*, **87**, 87–115.
- Johannes, W. & Koepke, J., 2001. Incomplete reaction of plagioclase in experimental dehydration melting of amphibolite. *Australian Journal of Earth Sciences*, **48**, 581–590.
- Johnson, T.E., Gibson, R.L., Brown, M., Buick, I.S. & Cartwright, I., 2003. Partial melting of metapelitic rocks beneath the Bushveld Complex, South Africa. *Journal of Petrology*, **44**, 789–813.
- Korhonen, F.J., Saito, S., Brown, M. & Siddoway, C.S., 2010. Modeling multiple melt loss events in the evolution of an active continental margin. *Lithos*, **116**, 230–248.
- Kreissig, K., Nägler, T.F., Kramers, J.D., Van Reenen, D.D. & Smit, C.A., 2001. An isotopic and geochemical study of the northern Kaapvaal Craton and the Southern Marginal Zone of the Limpopo Belt: are they juxtaposed terranes? *Lithos*, **50**, 1–25.
- Kretz, R., 1983. Symbols for rock-forming minerals. *American Mineralogist*, **68**, 277–279.
- Kriegsman, L.M. & Hensen, B.J., 1998. Back reaction between restite and melt: implications for geothermobarometry and pressure-temperature paths. *Geology*, **26**, 1111–1114.
- Laurent, O., Paquette, J.L., Martin, H., Doucelance, R. & Moyen, J.F., 2013. LA-ICP-MS dating of zircons from Meso- and Neoproterozoic granitoids of the Pietersburg block (South Africa): crustal evolution at the northern margin of the Kaapvaal craton. *Precambrian Research*, **230**, 209–226.
- Ludwig, K.R., 2003. *Isoplot/Ex version 3.00: A Geochronological Toolkit for Microsoft Excel*. Berkeley Geochronology Center, Berkeley, CA.
- Martignole, J. & Martelat, J.-E., 2003. Regional-scale Grenvillian-age UHT metamorphism in the Mollendo-Camana block (basement of the Peruvian Andes). *Journal of Metamorphic Geology*, **21**, 99–120.
- Mattison, J.M., 2010. Analysis of the decay constants of the  $^{235}\text{U}$  and  $^{238}\text{U}$  multi-step CA-TIMS measurements of closed-system natural zircon samples. *Chemical Geology*, **275**, 186–198.
- Mengel, K., Richter, M. & Johanne, W., 2001. Leucosome-forming small-scale geochemical processes in the metapelitic migmatites of the Turku area, Finland. *Lithos*, **5**, 47–73.
- Millonig, L., Zeh, A., Gerdes, A. & Klemd, R., 2008. Neoproterozoic high-grade metamorphism in the Central Zone of the Limpopo Belt (South Africa): combined petrological and geochronological evidence from the Bulai pluton. *Lithos*, **103**, 333–351.
- Montel, J.M. & Vielzeuf, D., 1997. Partial melting of metagreywackes. 2. Compositions of minerals and melts. *Contributions to Mineralogy and Petrology*, **128**, 176–196.
- Nasdala, L., Hofmeister, W., Norberg, N. *et al.*, 2008. Zircon M257 – a homogeneous natural reference material for the ion microprobe U-Pb analysis of zircon. *Geostandards and Geoanalytical Research*, **32**, 247–265.
- Otamendi, J.E. & Patinõ Douce, A.E., 2001. Partial melting of aluminous metagreywackes in the northern Sierra de Comechingones, Central Argentina. *Journal of Petrology*, **42**, 1751–1772.
- Patinõ Douce, A.E. & Beard, J.S., 1996. Effects of P, f (O<sub>2</sub>) and Mg/Fe ratio on dehydration-melting of model metagreywackes. *Journal of Petrology*, **37**, 999–1024.
- Patinõ Douce, A.E. & Harris, N., 1998. Experimental constraints on Himalayan anatexis. *Journal of Petrology*, **39**, 689–710.

- Patinô Douce, A.E. & Johnston, A.D., 1991. Phase equilibria and melt productivity in the pelitic system: implications for the origin of peraluminous granitoids and aluminous granites. *Contributions to Mineralogy and Petrology*, **107**, 202–218.
- Pickering, J.M. & Johnston, A.D., 1998. Fluid-absent melting behavior of two-mica metapelite: experimental constraints on the origin of black hills granite. *Journal of Petrology*, **39**, 1797–1894.
- Ramsay, J.G. & Huber, M.I., 1987. *The Techniques of Modern Structural Geology, Vol. 2: Folds and Fractures*. Academic Press, London, 700 pp.
- Rasband, W.S., 1997–2012. *ImageJ*. U.S. National Institutes of Health, Bethesda, MA. Available at: <http://imagej.nih.gov/ij/> (last accessed on January 2014)
- Roering, C., Van Reenen, D.D., De Wit, M., Smit, C.A., De Beer, J. & Van Schalkwyk, J.F., 1992. Structural, geological and metamorphic significance of the Kaapvaal craton, Limpopo belt contact. *Precambrian Research*, **55**, 69–80.
- Rosenberg, C.L. & Stunitz, H., 2003. Deformation and crystallization of plagioclase along a temperature gradient: an example from the Bergell tonalite. *Journal of Structural Geology*, **25**, 389–408.
- Sawyer, E.W., 1987. The role of partial melting and fractional crystallization in determining discordant migmatite leucosome compositions. *Journal of Petrology*, **28**, 445–473.
- Sawyer, E.W., 2008. *Atlas of Migmatites*. The Canadian Mineralogist Special Publication 9. Mineralogical Association of Canada, Quebec City, 386 pp.
- Sawyer, E.W., Dombrowski, C. & Collins, W.J., 1999. Movement of melt during synchronous regional deformation and granulite-facies anatexis, an example from the Wuluma Hills, central Australia. *Geological Society of London Special Publications*, **168**, 221–237.
- Slama, J., Kosler, J., Condon, D.J. *et al.*, 2008. Plesovice zircon – a new natural reference material for U-Pb and Hf isotopic microanalysis. *Chemical Geology*, **249**, 1–35.
- Smit, C.A. & Van Reenen, D.D., 1997. Deep crustal shear zone, high-grade tectonites, and associated metasomatic alteration in the Limpopo Belt, South Africa: implication for the deep crustal processes. *Journal of Geology*, **106**, 37–57.
- Smit, C.A., Roering, C. & Van Reenen, D.D., 1992. The structural framework of the Southern Marginal Zone of the Limpopo Belt, South Africa. *Precambrian Research*, **55**, 51–67.
- Srogi, L., Wagner, M.A. & Lutz, T.M., 1993. Dehydration partial melting and disequilibrium in the granulite-facies Wilmington Complex, Pennsylvania-Delaware Piedmont. *American Journal of Science*, **293**, 405–462.
- Stacey, J.S. & Kramers, J.D., 1975. Approximation of terrestrial lead isotope evolution by a 2-Stage Model. *Earth and Planetary Science Letters*, **26**, 207–221.
- Stevens, G., 1997. Melting, carbonic fluids and water recycling in the deep crust: an example from the Limpopo Belt, South Africa. *Journal of Metamorphic Geology*, **15**, 141–154.
- Stevens, G. & Van Reenen, D.D., 1992a. Partial melting and the origin of metapelitic granulites in the Southern Marginal Zone of the Limpopo Belt, South Africa. *Precambrian Research*, **55**, 303–319.
- Stevens, G. & Van Reenen, D.D., 1992b. Constraints on the form of the *P-T* loop in the Southern Marginal Zone of the Limpopo Belt, South Africa. *Precambrian Research*, **55**, 279–296.
- Stevens, G., Clemens, J.D. & Droop, G.T.R., 1997. Melt production during granulite-facies anatexis: experimental data from primitive metasedimentary protoliths. *Contributions to Mineralogy and Petrology*, **128**, 352–370.
- Taylor, S.R. & McLennan, S.M., 1985. *The Continental Crust: Its Composition and Evolution*. Blackwell, Oxford, 312 pp.
- Taylor, J. & Stevens, G., 2010. Selective entrainment of peritectic garnet into S-type granitic magmas: evidence from Archaean mid-crustal anatectites. *Lithos*, **120**, 277–292.
- Torres-Roldan, R.L., 1983. Fractionated melting of metapelite and further crystal-melt equilibria. The example of the Blanca Unit Migmatite Complex, north of Estepona (southern Spain). *Tectonophysics*, **96**, 95–123.
- Van Reenen, D.D., 1983. Cordierite + garnet + hypersthene + biotite-bearing assemblages as a function of changing metamorphic conditions in the Southern Marginal Zone of the Limpopo metamorphic complex, South Africa. In: *The Limpopo Belt* (eds Van Biljon, W.J. & Legg, J.H.), *Geological Society of South Africa Special Publication*, **8**, 143–167.
- Van Reenen, D.D., 1986. Hydration of cordierite and hypersthene and a description of the retrograde orthoamphibole isograd in the Limpopo Belt, South Africa. *American Mineralogist*, **71**, 900–915.
- Van Reenen, D.D., Barton, J.M., Roering, C., Smit, C.A. & Van Schalkwyk, J.F., 1987. Deep crustal response to continental collision: the Limpopo belt of southern Africa. *Geology*, **15**, 11–14.
- Van Reenen, D.D., Roering, C., Smit, C.A., Van Schalkwyk, J.F. & Barton, J.M., 1988. Evolution of the northern high-grade margin of the Kaapvaal craton, South Africa. *Journal of Geology*, **96**, 548–559.
- Van Reenen, D.D., Roering, C., Brandl, G., Smit, C.A. & Barton, J.M., 1990. The granulite-facies rocks of the Limpopo belt, southern Africa. In: *Granulites and Crustal Evolution* (eds Vielzeuf, D. & Vidal, P.), pp. 257–289. NATO ASI series C Mathematical and Physical Sciences, Volume **311**, Kluwer Acad. Publ., Dordrecht
- Vance, J.A., 1962. Zoning in igneous plagioclase; normal and oscillatory zoning. *American Journal of Science*, **260**, 746–760.
- Vanderhaeghe, O., 2009. Migmatites, granites and orogeny: flow modes of partially-molten rocks and magmas associated with melt/solid segregation in orogenic belts. *Tectonophysics*, **477**, 119–134.
- Vielzeuf, D. & Holloway, J.R., 1988. Experimental determination of the fluid-absent melting reactions in the pelitic system. *Contributions to Mineralogy and Petrology*, **98**, 257–276.
- Villars, A., 2009. *The Petrogenesis of S-type Granite Example of the Cape Granite*. Unpublished PhD thesis, Stellenbosch University, South Africa.
- Villars, A., Stevens, G., Moyen, J.-F. & Buick, I.S., 2009. The trace element compositions of S-type granites: evidence for disequilibrium melting and accessory phase entrainment in the source. *Contributions to Mineralogy and Petrology*, **158**, 543–561.
- Waters, D.J., 1988. Partial melting and the formation of granulite facies assemblages in Namaqualand, South Africa. *Journal of Metamorphic Geology*, **6**, 387–404.
- White, R.W. & Powell, R., 2002. Melt loss and the preservation of granulite facies mineral assemblages. *Journal of Metamorphic Geology*, **20**, 621–632.
- White, R.W. & Powell, R., 2010. Retrograde melt–residue interaction and the formation of near-anhydrous leucosomes in migmatites. *Journal of Metamorphic Geology*, **28**, 579–597.
- White, R.W., Powell, R., Holland, T.J.B. & Worley, B.A., 2000. The effect of TiO<sub>2</sub> and Fe<sub>2</sub>O<sub>3</sub> on metapelitic assemblages at greenschist and amphibolite facies conditions: mineral equilibria calculations in the system K<sub>2</sub>O–FeO–MgO–Al<sub>2</sub>O<sub>3</sub>–SiO<sub>2</sub>–H<sub>2</sub>O–TiO<sub>2</sub>–Fe<sub>2</sub>O<sub>3</sub>. *Journal of Metamorphic Geology*, **18**, 497–511.
- White, R.W., Powell, R. & Holland, T.J.B., 2001. Calculation of partial melting equilibria in the system Na<sub>2</sub>O–CaO–K<sub>2</sub>O–FeO–MgO–Al<sub>2</sub>O<sub>3</sub>–SiO<sub>2</sub>–H<sub>2</sub>O. *Journal of Metamorphic Geology*, **19**, 139–153.
- White, R.W., Powell, R. & Clarke, G.L., 2002. The interpretation of reaction textures in Fe-rich metapelite granulites of the Musgrave Block, central Australia: constraints from mineral equilibria calculations in the system K<sub>2</sub>O–FeO–MgO–

- Al<sub>2</sub>O<sub>3</sub>-SiO<sub>2</sub>-H<sub>2</sub>O-TiO<sub>2</sub>-Fe<sub>2</sub>O<sub>3</sub>. *Journal of Metamorphic Geology*, **20**, 41–55.
- White, R.W., Powell, R. & Clarke, G.L., 2004. Prograde metamorphic assemblage evolution during partial melting of metasedimentary rocks at low pressures: migmatites from Mt Stafford, Central Australia. *Journal of Petrology*, **44**, 1937–1960.
- White, R.W., Powell, R. & Holland, T.J.B., 2007. Progress relating to calculation of partial melting equilibria for metapelites. *Journal of Metamorphic Geology*, **25**, 511–527.
- Yakymchuk, C. & Brown, M., 2013. Consequences of open-system melting in tectonics. *Journal of the Geological Society of London*, **171**, 21–40.
- Zeh, A., Holland, T.J.B. & Klemd, R., 2005. Phase relationships in grunerite-garnet bearing amphibolites in the system CFMASH, with applications to metamorphic rocks from the Central Zone of the Limpopo Belt, South Africa. *Journal of Metamorphic Geology*, **23**, 1–17.

## SUPPORTING INFORMATION

Additional Supporting Information may be found in the online version of this article at the publisher's web site:

**Table S1.** LA-SF-ICP-MS U–Th–Pb dating methodology.

**Table S2.** Mineral compositions from the BQ leucosomes and metasedimentary rocks.

## APPENDIX 1

Modelling of leucosome chemistry as a function of magma segregation and melt loss was modelled using a granitic magma reintegration approach. This approach was followed so that the trace element

composition of the melt-reintegrated source could be readily calculated, with the only assumption being that the Bandelierkop Quarry (BQ) metapelitic residua lost S-type magma similar in composition to the granite used. A typical S-type granite composition from the Peninsula Pluton (Villaros *et al.*, 2009) was reintegrated into a metapelitic residuum composition from the BQ. *T*-*X* pseudosection modelling at 8.5 kbar indicated that a mixture of 71.2% of the BQ metapelite, and 28.8% of the S-type granite (with the resultant composition in wt% (BQ1): SiO<sub>2</sub> = 61.13; TiO<sub>2</sub> = 0.88; Al<sub>2</sub>O<sub>3</sub> = 18.29; FeO = 6.87; MgO = 5.77; Na<sub>2</sub>O = 1.48; CaO = 1.59; K<sub>2</sub>O = 2.95; H<sub>2</sub>O = 1.05), predicts muscovite breakdown at ~700 °C, to yield 1–2.5 vol.% melt, followed by biotite + sillimanite breakdown at 850–875 °C, to produce a significant volume of melt (~40 vol.%). This sequence of melting reactions, and the volume of peritectic sillimanite and garnet produced, closely matches the evidence from the magma-depleted metapelites bounding the stromatic leucosomes in the BQ.

Using the mineral proportions predicted by the *P*-*T* pseudosection along the 9 kbar isobar (Table 4), and the partition coefficients from Villaros *et al.* (2009) and Otamendi & Patinõ Douce (2001), we were able to generate REE patterns for melt, residuum and leucosome during batch melting and fractional crystallization processes, shown in Fig. 10c–e.

Received 2 April 2013; revision accepted 14 March 2014.

**Table 4.** Phase proportions, partition coefficients between mineral and melt, as well as plagioclase compositions used to model leucosome REE compositions: Partition coefficients for plagioclase, quartz, biotite, ilmenite and garnet are from Villaros *et al.* (2009), that used for K-feldspar is from Otamendi & Patinõ Douce (2001). The partition coefficients for sillimanite and rutile are not relevant to the outcome of the modeling.

<i>T</i> (°C)	Liq (vol.%)	Pl (vol.%)	Ksp (vol.%)	Qtz (vol.%)	Bt (vol.%)	Ilm (vol.%)	Grt (vol.%)	Sil (vol.%)	ru (vol.%)	Ab (%)	An (%)
750	0.67	21.78	–	34.3	26.91	0.35	8.49	7.5	–	67.22	32.77
775	0.96	21.65	–	34.31	26.79	0.28	8.73	7.28	–	66.99	32.99
800	1.38	21.5	–	34.2	26.63	0.21	9.03	7.05	–	66.79	33.20
825	2.05	21.33	–	33.9	26.37	0.13	9.4	6.83	–	66.49	33.50
850	3.41	21.00	–	33.26	25.71	0.06	10.02	6.55	–	66.17	33.81
875	9.67	18.68	2.57	29.73	20.24	0.17	13.34	5.61	–	63.80	36.18
900	23.01	14.23	7.29	22.41	9.1	0.57	19.68	3.7	–	58.21	41.78
925	37.74	10.23	8.84	14.95	–	–	25.81	1.38	0.6	53.95	46.03
950	44.73	9.77	5.65	12.93	–	–	25.44	0.88	0.59	54.10	45.88

Kd mineral/melt	Liq	Pl	Kfs	Qtz	Bt	Ilm	Grt	Sil	Rt
La	–	0.3	0.08	0.012	0.012	7.1	0.0	–	–
Ce	–	0.21	0.04	0.006	0.006	7.8	0.1	–	–
Nd	–	0.14	0.00	0.009	0.009	7.6	0.4	–	–
Sm	–	0.11	0.03	0.008	1.00	7.5	0.9	–	–
Eu	–	5.00	2.32	0.03	2.645	2.5	1.2	–	–
Gd	–	0.1	0.00	0.007	0.6	1.00	4.00	–	–
Tb	–	0.09	0.00	0.007	0.87	6.5	9.00	–	–
Ho	–	0.1	0.00	0.01	0.16	20.00	32.00	–	–
Er	–	0.06	0.00	0.011	0.41	0.01	38.00	–	–
Yb	–	0.06	0.04	0.012	0.32	4.1	60.00	–	–

Mineral proportions obtained from *Perple\_X* pseudosection at 8.5 kbar.

# The formation of K<sub>2</sub>O-poor leucosomes in the granulitic lower crust: key to crustal differentiation processes. Example from the Southern Marginal Zone of the Limpopo Belt, South Africa.

G. Nicoli<sup>a,b\*</sup>, J-F. Moyen<sup>b</sup>, G. Stevens<sup>a</sup>

<sup>a</sup>Centre for Crustal Petrology, Department of Earth Sciences, Stellenbosch University, Private Bag X1, Matieland 7602, South Africa; telephone (+27) 21 808 3219; fax (+27) 21 808 3129

<sup>b</sup>UMR 6524 CNRS & Université Jean Monnet, 23 rue du Dr Michelon, 42023 Saint-Etienne, France.

\*Corresponding author [gnicoli@sun.ac.za](mailto:gnicoli@sun.ac.za)

Short title: K<sub>2</sub>O-poor Leucosome formation

**ABSTRACT** The formation of migmatites in the Bandelierkop Formation of the Southern Marginal Zone of the Limpopo belt occurs via fluid-absent biotite incongruent melting. These reactions produce cm- to m-scale, K<sub>2</sub>O-poor stromatic leucosomes. The source material possesses different scale of heterogeneity and displays many different steps of leucosome formation. The leucosome chemistry is different from experimental melt chemistry as well as S-type granite chemistry. Both of which have higher K<sub>2</sub>O and FeO + MgO contents and a lower CaO content than the leucosome. This compositional mismatch has been interpreted to reflect processes affecting the leucosome after its formation. However, field-based XRF chemical profiles across the leucosome and its hosting gneiss do not show substantial K<sub>2</sub>O enrichment in the wall rock. In addition, leucosome formed by biotite breakdown partial melting is shown to have become rheologically solid prior peak metamorphic conditions. Moreover, The peritectic assemblage is well preserved in zones of residua adjacent to the leucosome. Constraints on the *P-T-t* evolution of the Southern Marginal Zone indicate that the leucosome forms during the prograde history of the rocks, while the terrain is heating up. To achieve its specific chemistry, we showed the formation of K<sub>2</sub>O-poor is controlled by two major mechanisms: changes in volume of equilibration and water diffusivity in the melt transfer site. These types of mechanisms have an important implication on our understanding of crustal differentiation.

**Key words:** SMZ; Leucosome; volume of equilibration, water diffusivity, crustal differentiation

## 1. Introduction

The processes that link crustal anatexis and granite magmatism are generally considered to occur in the following sequence: 1. partial melting of a fertile source, 2. Segregation of individual melt batches and stepwise accumulation in low-pressure sites. 3. Collection of leucocratic magma pockets to form wider transfer zone. 4. Draining of the magma out of the source, 4. Granite emplacement in upper crustal levels (Bons *et al.*, 2009; Kisters *et al.*, 2009). Thus, crustal differentiation is achieved through incongruent partial melting and the segregation of a felsic melt from a more mafic residuum. Magmas that crystallize after migration to shallower levels contribute to a more evolved upper crust, whereas the deep crust becomes more refractory. Partial melting typically occurs in a fluid absent state at the temperatures between 800 and 900 °C via the incongruent melting of micas and amphiboles (Clemens & Vielzeuf, 1987; Johannes, 1988; Le Breton *et al.*, 1988; Vielzeuf *et al.*, 1990; Skjervlie *et al.*, 1993; Stevens & Clemens, 1993).

In granulite facies migmatites, the volume of leucosome is often seen as representative of the volume of melt produced during crustal anatexis (Sawyer, 1987). However, in several examples, significant chemical differences exist between the leucosome and the granite. This point is most readily illustrated with the example of metasedimentary granulites and S-type granites; as detailed in many migmatitic terranes (Whitney & Irving, 1994; Del Moro, 2000; Johannes *et al.*, 2003; Taylor *et al.*, 2014). The leucosomes are often interpreted to represent the melt fraction that failed to escape the source (Sederholm, 1967; Mehnert, 1968; Sawyer, 2001; Vanderhaeghe, 2009). Hence the common view of migmatites as “failed granites”. However, if considered as such, the proportion of leucocratic material in some granulitic outcrops is too voluminous (> 40 % of the

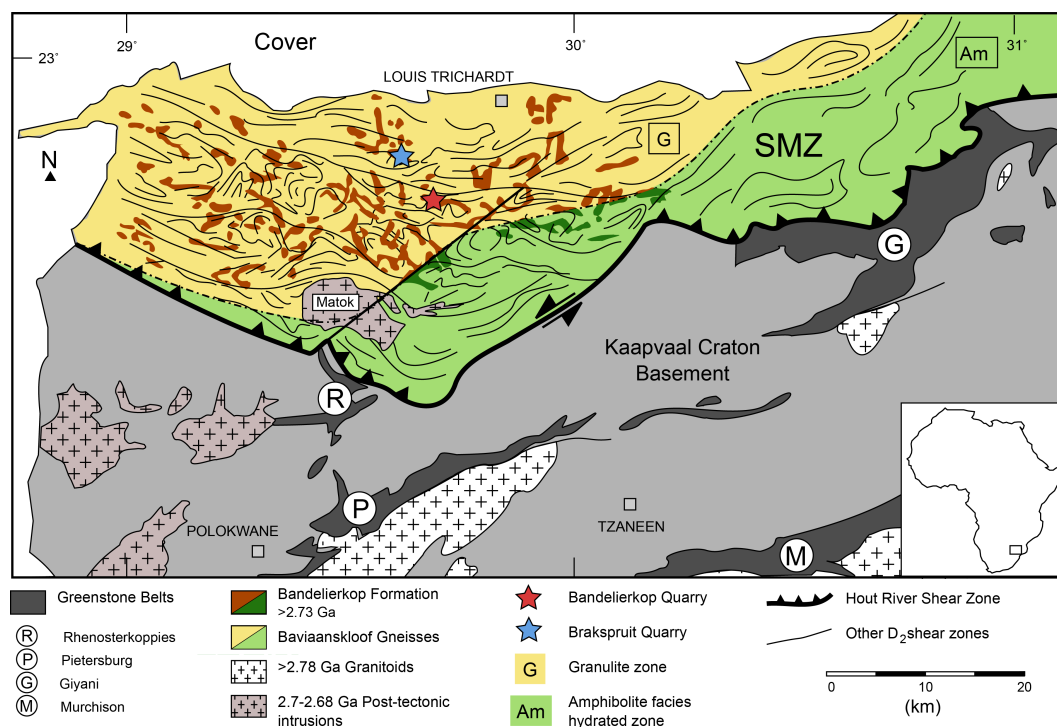


Figure 1: Map of the Southern Marginal Zone of the Limpopo Belt (modified after Nicoli *et al.*, 2014a). The Hout River Shear Zone (HRSZ) separates the Kaapvaal craton (South) from the SMZ (North). The two stars show the location of the quarries studied in this work.

outcrop) for the crustal differentiation being even efficient. In addition, in these particular anatectic terrains, the chemistry of the leucosome is a poor match with S-type granite composition and experimental melt chemistry. Those are characterized by markedly higher K<sub>2</sub>O and FeO + MgO contents and a lower CaO contents than the leucosome.

Therefore, the formation of K<sub>2</sub>O-leucosome is likely to represent a key step in the source-leucosome-granite (SLG) system formation. Consequently it is important to identify the real nature of the leucosome and the mechanisms through which it forms. To find elements of answer, we have access to several objects: (1) the final product (S-type granite) sometimes containing granulitic xenoliths (Montel *et al.*, 1992; Villaseca *et al.*, 1999); (2) experimental petrology on mica breakdown fluid-absent partial melting (e.g. Vielzeuf & Holloway, 1988; Patiño Douce & Johnston, 1991; Montel & Vielzeuf, 1997; Stevens *et al.*, 1997; Patiño Douce & Harris, 1998; Piekerling & Johnston, 1998); (3) and the preserved lower crustal metasedimentary source and its anatectic network (Stevens & van Reenen, 1992a; Hasalová *et al.*, 2008; Racek *et al.*, 2008; Cesare *et al.*, 2009; Taylor *et al.*, 2010, 2014).

In the processes that shape the leucosome chemistry, the general view is that a fraction of the melt leaves the structure after cooling of the terrain (Sawyer, 1987; Brown, 2002; Waters, 1988; Kriegsman & Hensen, 1988). In this scenario, the part of the melt that failed to escape will crystallize in the melt transfer site and a part of its chemistry will be achieved via diffusion of H<sub>2</sub>O and K<sub>2</sub>O back to the wall rock (Fourcade *et al.*, 1992; Kriegsman, 2001). This mechanism is characterized by the formation of a rehydrated selvage containing retrograde phases (biotite and amphibole). However recent works (Mengel *et al.*, 2001; Guernina & Sawyer, 2003; Martignole & Martelat, 2003; Taylor *et al.*, 2014; Yakymchuck & Brown, 2014) based on field observations and phase equilibria modeling strongly argued for melt loss prior to peak metamorphic conditions, ruling out the hypothesis of a back reaction mechanism during the cooling of the terrain. In this case, the anatectic features represent the fossilized print of the plumbing system through which the magma was transferred to upper crustal levels. Major melt production and draining would have occurred along the prograde path, leaving behind a felsic-rich residuum (i.e. leucosome). This challenging hypothesis implies to find new mechanisms to explain the crystallization of the K<sub>2</sub>O-poor leucosome while the whole terrain is heating up.

The Southern Marginal Zone (SMZ) of the Limpopo Belt in South Africa offers a good natural laboratory where anatexis processes can be directly observed and quantified in the field. It is a *c.* 2.7 Ga old granulitic terrain and represents an exceptional window into the lower crust. The *P-T-t* path followed by the metasedimentary rocks has been precisely constrained. Studies by Nicoli *et al.* (2014a) and Taylor *et al.* (2014) indicate the metasedimentary rocks from the SMZ were buried to  $\sim 10$  kbar ( $\sim 35$  km depth) and 870 °C. Under these conditions, fluid-absent partial melting produces leucosomes strongly associated with the mafic residuum and characterized by low K<sub>2</sub>O and high CaO contents. Taylor *et al.* (2014) suggested, based on field observations, mineral and whole rock chemistry, that the leucosome chemical signature is achieved by disequilibrium mechanism at the scale of the sample involving only a sub-part of the textural assemblage. Then melt escapes the melt transfer site subsequent to melt segregation and plagioclase, quartz and in less proportion garnet precipitate from the melt during the prograde history of the rock. The model provided by Taylor *et al.* (2014) fits both experimental data (Johannes & Koepke, 2001; Acosta-Vigil & London, 2006) and field observations. Using such hypothesis along side with the well-constrained *P-T-t* history of the metasedimentary rocks from Brakspruit quarry (Nicoli *et al.*, 2014a), this paper tries to solve important issues that will lead to a better understanding of crustal differentiation mechanisms. Firstly, we investigated the leucosome and the mafic residuum chemical signatures using standard techniques and new field mapping and tomography tools, which help to understand the repartition of different phases and elements inside the anatexitic features and their wall rock at the scale of the outcrop. Thereafter, we ran chemical models using thermodynamically constrained software to investigate the effect of full-rock system (“equilibrium”) *v.* sub-rock system (“disequilibrium”) processes, melt loss and H<sub>2</sub>O diffusivity on the chemistry of the leucosome. The combination of field observations and chemical modeling helped to explain the formation of the K<sub>2</sub>O-leucosomes.

## 2. Geological setting and previous works

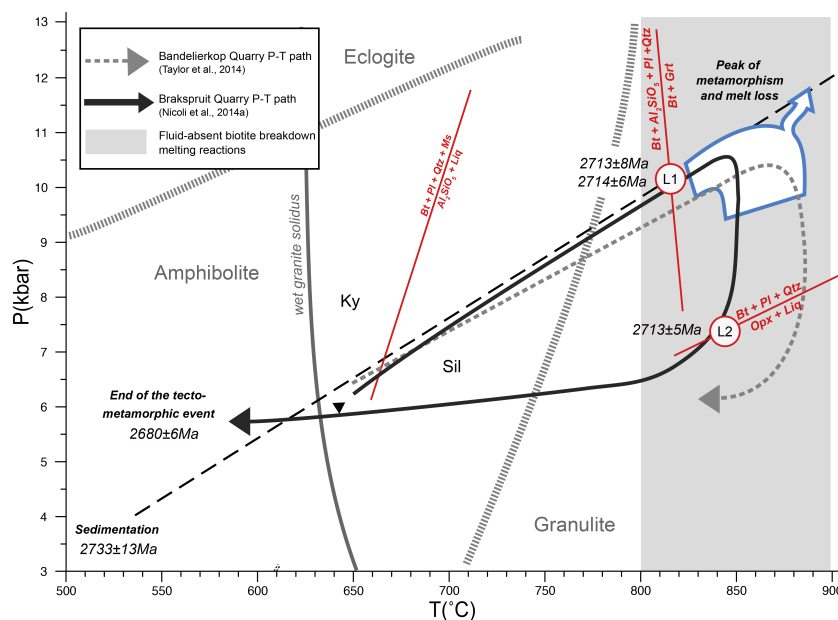


Figure 2: *P-T-t* path followed by the metasedimentary rocks determined by phase equilibria modeling on the metapelites of the Bandelierkop and the Brakspruit quarries (Nicoli *et al.*, 2014a, Taylor *et al.*, 2014). The information on biotite stability and reaction curves after Vielzeuf Holloway, (1988); Patiño Douce & Johnston, (1991); Montel Vielzeuf, (1997); Stevens *et al.*, (1997); Patiño Douce & Harris, (1998); Pickering & Johnston, (1998). Abbreviations after Kretz (1983). Main biotite and muscovite breakdown reactions have been highlighted.

The Southern Marginal Zone (SMZ) is commonly acknowledged as one of the three parts of the Limpopo Mobile Belt (Van Reenen *et al.*, 1992), the two other units being the Northern Marginal Zone (NMZ) and the Central Zone (CZ). The Hout River Shear Zone (HRSZ) (Fig.1) separates the SMZ from the Kaapvaal craton. The main lithologies present in the SMZ consist of light to dark grey granitoid gneisses, the Baviaanskloof gneiss, infolded with the Bandelierkop formation. The Bandelierkop formation mainly includes mafic and ultramafic rocks along with clastic sediments. The metasedimentary rocks underwent a single granulite facies metamorphic event at *c.* 2.71 Ga (Nicoli *et al.*, 2014a; Taylor *et al.*, 2014).

Accurate phase equilibria modeling have been made on two well-exposed locations in the SMZ, the



Bandelierkop quarry and the Brakspruit quarry (Fig.1). Peak metamorphic conditions in both locations are  $880 \pm 10^\circ\text{C}$ ,  $10 \pm 2$  kbar and  $852.5 \pm 7.5^\circ\text{C}$ ,  $11.1 \pm 1.3$  kbar respectively. Compositional banding, abundance of peak metamorphic biotite and well-preserved granulitic assemblages indicate metamorphism in the SMZ does not exceed  $900^\circ\text{C}$  (Nicoli *et al.*, 2014a,b) (Fig. 2). The maximum age of sedimentation  $2733 \pm 13$  Ma, relative to the peak metamorphic age (*c.* 2.713 Ma) indicates a burial rate of  $\sim 0.17$  cm.y<sup>-1</sup>. The shape of the *P-T* path and the fast burial rate (e.g. Nicoli *et al.*, 2014a; Taylor *et al.*, 2014), strongly argue for the SMZ containing sediments deposited in an active margin during a convergence episode, and metamorphosed as a consequence of continental collision along the northern margin of the Kaapvaal craton at *c.* 2.7 Ga. Late undeformed cross-cutting pegmatites at  $2680 \pm 6$  Ma (Nicoli *et al.*, 2014a) and the intrusion of the Matok Igneous Complex at  $2686 \pm 7$  Ma (Laurent *et al.*, 2013) indicate the end of this tectometamorphic event (Fig. 2).

As documented by Stevens & van Reneen (1992a), Kreissig *et al.* (2001), Taylor *et al.* (2014), the metapelitic rocks of the Bandelierkop formation have undergone anatexis via muscovite and biotite breakdown reactions. These reactions can be modeled as: (1)  $\text{Ms} + \text{Qtz} + \text{Pl} = \text{Sil} + \text{Melt}$ ; (2)  $\text{Bt} + \text{Sil} + \text{Qtz} + \text{Pl} = \text{Grt} + \text{Melt}$ ; (3)  $\text{Bt} + \text{Qtz} + \text{Pl} = \text{Opx} \pm \text{Crd} \pm \text{Grt} + \text{Melt}$ . Reactions (1) and (2) produced stromatic and deformed leucosomes (L1), which have undergone near solid-state deformation before the formation of undeformed nebulitic leucosomes (L2) (reaction 3) (Taylor *et al.*, 2014). Using mineral chemistry, textural assemblages and melt-reintegrated pseudosection modeling (White *et al.*, 2004), Taylor *et al.* (2014) demonstrated that the melting reactions in the Bandelierkop Formation metasedimentary rocks produced more than enough melt to generate large leucosomes veins as it is observed in the Bandelierkop and Brakspruit localities. It also indicates these structures lost a significant amount of melt. In the Brakspruit quarry, partial melting of the semipelite and metapelite would have produced 15-35 vol.% of melt (Nicoli *et al.*, 2014a), which is more than the average leucosome volume ( $\sim 10\%$  of the outcrop).

Taylor *et al.* (2014) showed that in the Bandelierkop quarry, the leucosome chemistry mismatches the relevant experimental melt compositions and S-type granite compositions as they are depleted in K and have Ca/Na ratios similar to one in the source rock. The leucosome also displays a strong positive Eu anomaly whereas the metapelitic residuum has no pronounced Eu anomaly. Mineral assemblages in the leucosome and the metapelite do not show any strong evidence of rehydration and peritectic garnet and orthopyroxene are very well preserved. Collectively, these pieces of evidence argue for major melt loss through the magma transfer site towards upper levels and crystallization of the leucosome during the prograde history of the rocks. Taylor *et al.* (2014) combined observations from migmatitic terrains (Korhonen *et al.*, 2010; Sawyer *et al.*, 1999; Del Moro *et al.*, 2000) and experimental data (Johannes & Koepke, 2001; Acosta-Vigil & London, 2006) to suggest that only a fraction of the entire textural assemblage takes part to the melting reaction. The incomplete consumption of biotite and plagioclase in the dehydration melting reaction intervenes as a potential mechanism able to produce low K<sub>2</sub>O leucosomes with strong positive Eu anomalies. In the first scenario, the plagioclase melts incongruently, which produces a more calcic peritectic plagioclase at the site of the melting reaction in the source rock. A proportion of this peritectic plagioclase is entrained to the melt transfer site. As a consequence, Si and K in the leucosome reflect the volume of melt remaining in the leucosome and should correlate positively. This correlation is not observed in the SMZ leucosomes. In the second scenario, Taylor *et al.* (2014) suggested the outer zone of the plagioclase melts congruently producing an An-molecule rich melt with as a consequence, crystallization of peritectic plagioclase in the melt transfer site. This would induce co-precipitation of quartz by increasing SiO<sub>2</sub> content of the melt and it would result the formation of Eu-enriched, quartz + plagioclase + garnet leucosomes while the terrain is still heating up.

To understand the origin of K<sub>2</sub>O-poor leucosome, we based our study on the anatectites of the Brakspruit quarry located approximately 15 km north-west of Bandelierkop (Nicoli *et al.*, 2014a). The extremely well-exposed quarry, with a length of 150 m and width of 50 m, is quite exceptional and provides outcrops containing a large range of metapelitic rock compositions, along with different leucocratic materials derived from fluid-absent partial melting reactions.

### 3. Analytical methods

The chemistry of migmatites is highly scale dependent and it should not be simply approximated to the average composition at the scale of one outcrop or one hand specimen. Processes that happen at one scale may or may not reflect processes that happen at lower or higher scales. Hence the notion of “equilibrium” *v.*



Figure 3: Field photos of the Brakspuit quarry anatectites. (a) Early partial melting step with formation of small leucocratic pockets and peritectic garnet in a metapelite. (b) Deformed leucosomes (L1) and alternation of metapelite and semipelite defining the main metamorphic fabric  $S_1$ . (c) Large L1 garnet-bearing leucosome (see details Fig. 9). (d) Large boudinage features in L1 leucosome within the metapelite layers. (e) L2 leucosome (patch) cross-cutting the main fabric  $S_1$ ; top view.

“disequilibrium”. The mechanism that involves melting of the outer zone of the plagioclase can be seen as a disequilibrium mechanism at the scale of the outcrop as it involves only a sub-part of the whole system. However, at a microscopic scale, the textural assemblage in which the process takes place represents a small equilibrium domain. Thus, the notion of “equilibrium” and “disequilibrium” may get too confusing to describe the mechanisms responsible for the K<sub>2</sub>O-poor leucosome formation. To avoid such issue, we will use instead in the rest of this study the notion of full-system and sub-system. In the following section we present different analytical techniques that allow the investigation of the chemistry of the migmatites from the scale of the outcrop to the scale of the mineral.

### 3.1 Outcrop scale: Portable XRF analyzes

The use of Portable X-ray fluorescence (P-XRF) analyzes is a way to instantly investigate the chemistry of a partially melted terrain (see appendix A.1). This technique is capable to provide quick semi-quantitative chemical data by a non-destructive and *in situ* method. It provides, for design purposes, parameters that represent a realistic evaluation of the composition of the rocks at the scale of the outcrop.

Such method has limitations. The size of the analyzed area, the grain size of the rock and the non-detection

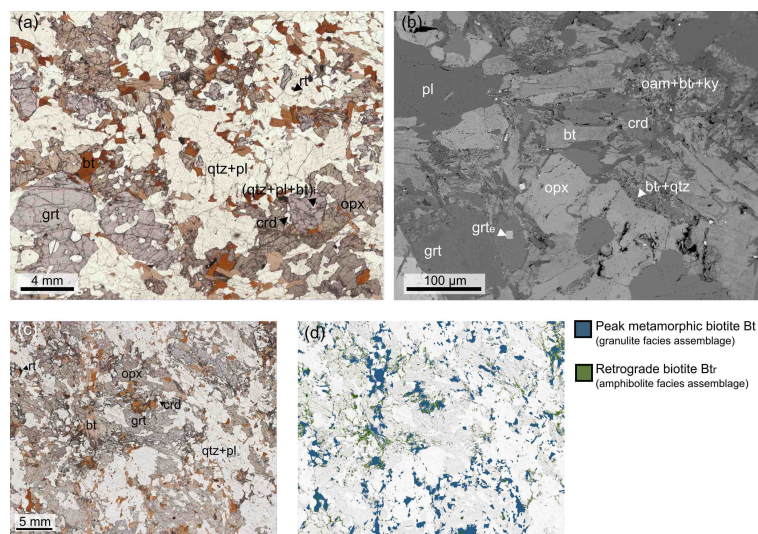


Figure 4: Petrography of the Brakspuit quarry metapelites. (a) Thin section showing the main granulitic textural assemblage in the metapelitic gneiss GM1. This rock, not in direct contact with the leucosome, is not affected by fluid-present retrograde reactions. (b) SEM backscattered electron image showing the restricted development of the retrograde Oam + Ky + Btr assemblage consuming the cordierite and Btr + Qtz consuming the orthopyroxene. The slide also shows small idioblastic garnet (grt<sub>id</sub>). (c-d) Image analyzes using ImageJ software (Rasband, 1997-2002) of the a thin section from the wall rock showing the proportion of peak metamorphic biotite (Bt) and retrogressed biotite (Btr)

of light elements, e.g. sodium, are the main issues the user has to deal with (Potts *et al.*, 1997). Despite these inconveniences, P-XRF analyzes have already been used successfully on geological samples, (Boyle, 2000; Zurfluh *et al.*, 2011) and add great value to complete our understanding of leucosome and mafic residuum chemistry. Benchmark calibrations have been determined using correlations between XRF analyzes from the whole rock in the laboratory and average P-XRF analyzes on medium-grain rock sample (Joseph, 2013) (Appendix A.1).

The P-XRF can generate a chemical overview of a meter-size section of the outcrop. In the case of the Bandelierkop formation anatectites, it highlights the repartition of the chemical elements between the leucocratic feature and its wall rock. Because the edge of the structure is easily identifiable on the field, we deployed the P-XRF on ten L1 stromatic and deformed leucosomes of different sizes. To optimize the result, the locations where the technique was applied have been chosen regarding good accessibility, fresh exposure and a relatively flat surface. A grid is deployed on the part of the outcrop to analyze. Potts *et al.* (1997) P-XRF analyzes on granite indicate the number of determinations that need to be averaged to estimate the bulk composition with a 5% to 10% standard deviation of the mean is  $\sim 10$  analyzes. Assuming the chemical variation occurs across strike the leucosome, we averaged the values to produce a more realistic chemical traverse through the leucosome. The P-XRF was run for 60 seconds (2x30s) per reading for each node. The Main filter (40 kV, 50 μA) and the Low filter (20kv, 100A) were used to measure the quantitative abundance of Si, Al, Fe, Mg, Ca and K in the rock.

### 3.2 Hand-sample scale: Tomography

Migmatites are 3-dimensional objects. Some of the leucosome samples collected on the field have been cut in a 3x3x5 cm<sup>3</sup> volume in order to be analyzed with the Phoenix VTOMEX L240 CT scanner. This method highlights the density of the different phases within the leucocratic veins. NF180 x-ray inspection of the sample generates a series of files, which are assembled with Volume Graphics VGStudio Max 2.1 to generate a 3D view of the sample. The resulting data are reconstructed to create a cross-sectional image of the object in a plane or a 3D environment. A more detailed summary of the CT scanner and its applications to geological materials is provided by Ketcham & Carlson (2001). The technique is entirely non-destructive, leaving samples available for other analyzes after scanning.

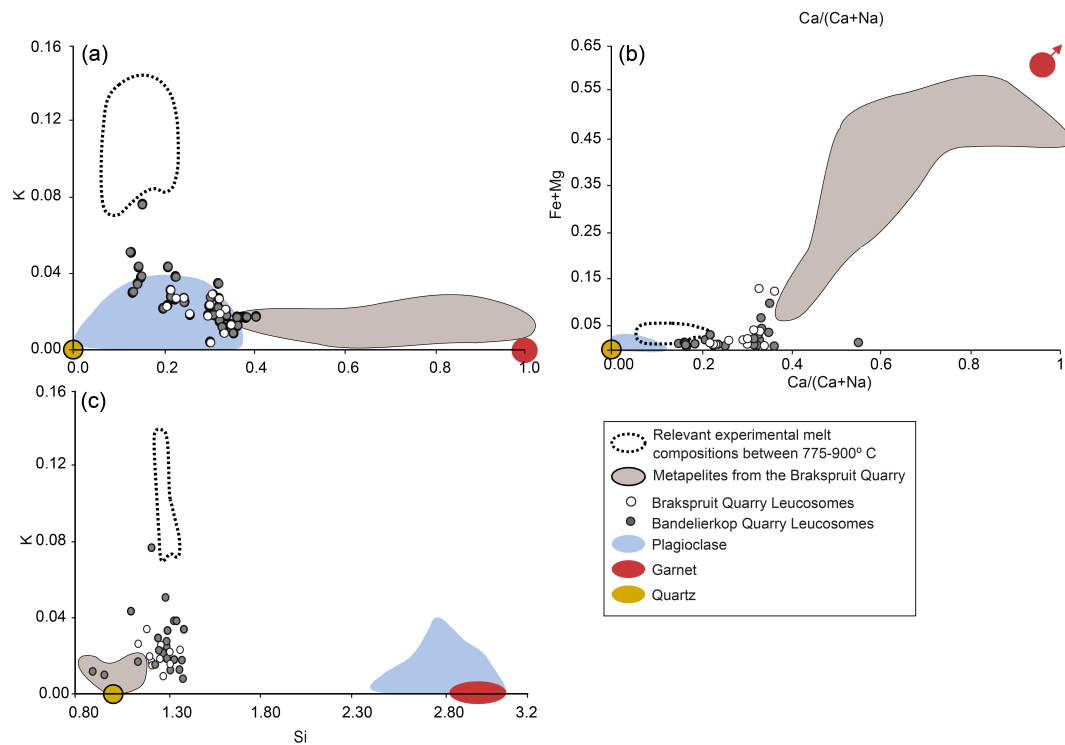


Figure 5: (a-c) The bulk compositions (i.e. at the scale of the hand-size specimen) of the Brakspruit quarry and Bandelierkop quarry (Taylor *et al.*, 2014) leucosomes compared with garnet, plagioclase and quartz chemistry from the leucosomes, fluid-absent experimental glass compositions, produced from a wide range of metasedimentary starting materials between 775 and < 900 ° C and 10-15 kbar (Vielzeuf & Holloway, 1988; Patiño-Douce & Johnston, 1991; Patiño-Douce & Beard, 1996; Montel & Vielzeuf, 1997; Stevens *et al.*, 1997; Pickering & Johnston, 1998; Patiño-Douce & Harris, 1998). Bulk-rock major element compositions (100 wt% normalized) are plotted as atomic  $Ca/(Ca + Na)$ , K, Si and Fe + Mg.

### 3.3 Mineral scale: mineral chemistry

Samples from the leucosomes analyzed with the P-XRF as well as other leucosomes have been collected to get more precisions on the bulk rock chemistry via XRF analyzes in the laboratory (Table 1) (see method in Appendix A.2). Leucosomes are mainly composed of quartz and plagioclase. The abundance of garnet within the structure is variable. In anatectic features with large garnet porphyroblast, several samples have been collected to identify the effect of the garnet content on the rock chemistry.

Representative mineral SEM analyzes for garnet and plagioclase in the leucosome and the wall rock are presented Tables 2 and 3 (see method in Appendix A.3). Analyzes for other phases are available in the supplementary information (Table S1). Mineral chemistry for the metasedimentary rocks have been described in detail by Nicoli *et al.* (2014a). The calculated end-members concentrations and ratios discussed below are  $X_{alm}$ ,  $X_{pyp}$ ,  $X_{spss}$ ,  $X_{grs}$  for garnet, Mg# for orthopyroxene and  $X_{an}$ ,  $X_{ab}$ ,  $X_{or}$  for plagioclase. These are defined as follows:  $X_{alm} = Fe/(Fe + Mg + Mn + Ca)$ ,  $X_{pyp} = Mg/(Fe + Mg + Mn + Ca)$ ,  $X_{spss} = Mn/(Fe + Mg + Mn + Ca)$ ,  $X_{grs} = Ca/(Fe + Mg + Mn + Ca)$ ,  $Mg\# = Mg^{2+}/(Fe^{2+} + Mg^{2+})$ ,  $X_{an} = Ca/(Ca + Na + K)$ ,  $X_{ab} = Na/(Ca + Na + K)$ ,  $X_{or} = K/(Ca + Na + K)$ .

## 4. Petrological and chemical organization of migmatites

### 4.1 Metasedimentary rock

The metasedimentary rocks of the Brakspruit quarry are characterized by a low K<sub>2</sub>O content (0.9–1.5 wt%). SiO<sub>2</sub> (50.0–67.0 wt%) and FeO + MgO (11–32 wt%) contents are highly variable. The metasedimentary rocks have been classified into three main lithologies regarding their composition and their textural assemblage

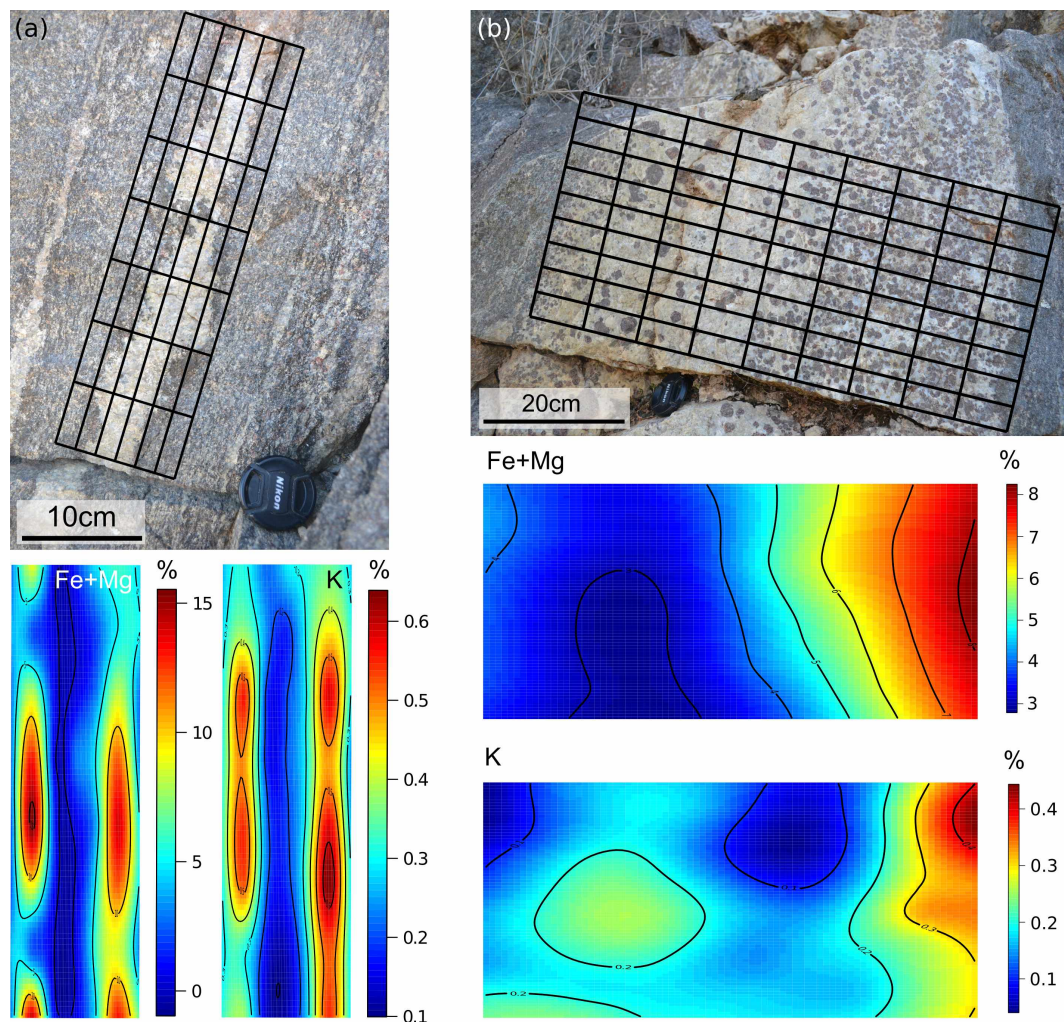


Figure 6: Portable XRF analyzes on L1 leucosomes. (a) Field photo showing the display of the analytical grid. (b) Repartition of Fe+Mg and K (%) in the leucosome and the wall rock. (c) Field photo showing the display of the analytical grid on the garnet-bearing leucosome. (d) Mapping of Fe+Mg and K (%) in the leucosome and the wall rock. In that particular case, the repartition of garnet influences the mapping of the ferromagnesian signature.

(Nicoli *et al.*, 2014a) (Fig. 3a,b): (1) the metapelite hosting the large stromatic leucosomes (GM) is a dark-grey, medium- to coarse-grained porphyroblastic restitic metapelite, characterized by the assemblage Grt + Opx + Pl + Bt + Qtz  $\pm$  Crd  $\pm$  Al<sub>2</sub>SiO<sub>5</sub>  $\pm$  Ilm  $\pm$  Rt and minor K-feldspar (Fig. 4a); (2) the semipelite (SM) characterized by the granulite assemblage Grt + Opx + Pl + Bt + Qtz  $\pm$  Ilm and a lack of aluminium silicate phases; (3) the orthopyroxene-bearing metapelite (OM) characterized by the assemblage Opx + Pl + Bt + Qtz  $\pm$  Kfs and absence of garnet. OM is linked to the nebulitic leucosomes. Phase equilibria modeling and melt-reintegrated pseudosections (White *et al.*, 2004) have been calculated for SM and GM compositions (Nicoli *et al.*, in press) and show the garnet and orthopyroxene are peritectic mineral and result from biotite breakdown partial melting reactions. The garnet and orthopyroxene do not present evidence of rehydration reactions. Therefore, the main preserved mineral assemblage reflects granulite facies conditions. However, in the wall rock of the anatectic veins, there are some micro-domains ( $\sim 100 \mu\text{m} \times \sim 100 \mu\text{m}$ ) reequilibrated to amphibolite facies conditions (Nicoli *et al.*, 2014a) (Fig. 4b). The proportion of biotite associated with the retrograde assemblage compared to the peak metamorphic biotite in the wall rock of the leucosome is very low (<5%) (Fig. 4c,d). Despite the melting episode, the metasedimentary rocks retained their original compositional banding (i.e. alternation of lithologies at the outcrop scale) and in some case the pre-metamorphic foliation in the metatextitic migmatite (Nicoli *et al.*, 2014a; Taylor *et al.*, 2014; Stevens & van Reenen, 1992b).

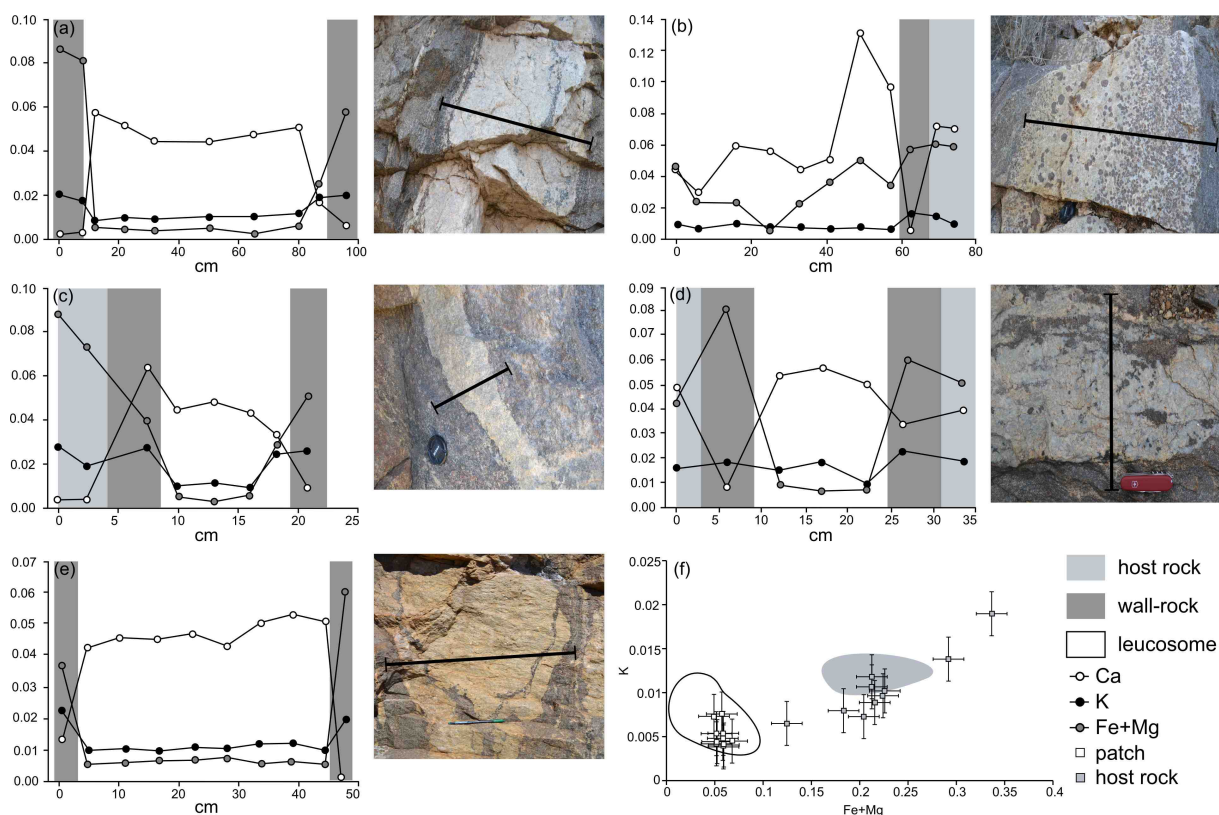


Figure 7: (a–e) Average profile through different L1 leucosomes showing that the anatectic features do not display any core/edge zoning in potassium, calcium or ferromagnesian elements (unit: atomic). (a) Metric-scale leucocratic and its selvage. (b) Garnet-bearing metric-scale leucosome and its selvage and host rock. (c,d) cm-scale leucosomes with their selvage and host rock. (e) Metric-scale boudinaged leucosome and its selvage. (f) P-XRF analyzes (spots) for L2 structures and their wall rocks. Average L1 values are plotted for comparison.

#### 4.2 Stromatic and deformed leucosome (L1)

The L1 leucosomes within metapelites represent the main anatectic feature in the quarry (Fig. 3b–d). These leucosomes are stromatic and deformed veins of variable thickness (from 1 cm to ~ 1 m) within the metapelites. They display boudinage and flame structures, which indicate they have undergone solid-state deformation. L1 leucosomes are concordant with the dominant foliation (Fig. 3b–d). They are characterized by a high silica content (72–79 wt%) and low potassium and ferromagnesium (FeO + MgO) content (respectively 0.89–1.30 wt% and 0.2–3.6 wt%) (Fig. 5).

Geochemical mapping (Fig. 6a–c) shows that independently of their size, L1 leucosomes are depleted in K and Fe+Mg compared to the wall rock. Importantly, the leucosomes do not display any zoning profile in their internal structure (Fig. 6b–d). On the other hand, the adjacent melanosomes is richer in K and Fe+Mg than the leucosomes. For leucosomes containing a large proportion of peritectic garnet, the chemical content is directly influenced by the repartition of the garnet inside the leucocratic structure. The metapelite-leucosome-metapelite traverses (Fig. 7a–e) show K and Fe+Mg contents increase towards the edge of the leucosomes. The selvage is also characterized by a lack of Ca (< 0.03 mol). On the other hand, the leucosomes are characterized by low, flat K and Fe+Mg profiles (< 0.02 mol) and a high; flat Ca profile (> 0.05 mol). High calcium concentrations are reached in the garnet layers parallel to edge of the leucosomes.

The L1 leucosomes usually contain 1–40 mm size garnet porphyroblasts. They are characterized by the assemblage Grt + Pl + Qtz ± Ilm ± Rt with minor K-feldspar, sillimanite and biotite. Quartz and plagioclase grains constitute > 95% of the leucosomes. Plagioclase occurs as cm-size grain and can contain

K-feldspar exsolutions (Fig. 8a). Garnet distribution within L1 leucosomes is well organized. The garnets are segregated along planes parallel to the edge of the leucosomes (Fig. 9). The garnet in L1 leucosomes is well preserved and does not display any evidence of hydrated retrograde reaction.

The L1 leucosomes were separated into two categories based on the abundance, size and texture of the garnet: (1) Small-scale (cm to dm) leucosomes hosting inclusion-free small size (< 0.5 cm) peritectic garnets, euhedral plagioclase, rounded quartz and minor rutile or ilmenite (Fig. 8b). In these leucosomes the garnet occurs as clusters in planes parallel to the edge of the leucosome (Fig. 9a-c). These leucosomes generally show a diffuse contact with the wall rock (2) Metric-scale leucosomes with the same mineral assemblage than small-scale leucosome but they might present a sharper contact with the hosting rock (Fig. 3c,d). Garnets are coarser-grained, > 1 cm size and more poikilitic (Fig. 8c), with core sometimes rich in quartz inclusion with a large free-inclusion rim (Fig. 8d; 9d-f). The garnet may occasionally show a thin cordierite corona.

The garnet in the small stromatic leucosomes does not display any major elements zonation profile ( $X_{alm}$  0.54–0.67,  $X_{pyr}$  0.25–0.40,  $X_{spss}$  0.02–0.05,  $X_{grs}$  0.03). The outer zone of the garnet (< 20  $\mu$ m) garnet is lightly enriched in Mn (Fig. 10a). In the large anatectic feature, the garnet shows a more pronounced core/rim zoning with a relatively Ca-rich core (rim:  $X_{alm}$  0.63,  $X_{pyr}$  0.32,  $X_{spss}$   $\sim$  0.01,  $X_{grs}$  0.03; core:  $X_{alm}$  0.56,  $X_{pyr}$  0.38,  $X_{spss}$   $\sim$  0.01,  $X_{grs}$  0.06) (Fig. 10b). The plagioclase displays a slightly different chemical pattern in small and large leucosomes. Plagioclases from the cm to dm leucosomes have a composition close to ones found in the metapelite ( $X_{an}$  0.30–0.34,  $X_{ab}$  0.60–0.65,  $X_{or}$  0.02–0.07). The plagioclase in large leucocratic structures shows a higher Na<sub>2</sub>O and K<sub>2</sub>O content ( $X_{an}$   $\sim$  0.20,  $X_{ab}$  0.75–0.80,  $X_{or}$  0.01–0.03) (Fig. 10c,d).

#### 4.3 Nebulitic leucosome (L2)

The second type of leucosome is a cm-size undeformed, crosscutting orthopyroxene-bearing nebulitic leucosome (L2) associated with OM (Fig. 3e). The volume of these features is largely inferior to the volume of L1 leucosomes. L2 are found indifferently in metapelite and semipelite. The mineral assemblage is Opx + Pl + Qtz + Ilm and minor garnet, biotite and K-feldspar (Fig. 8e,f). Taylor *et al.* (2014) showed this type of leucosomes is the result of the simplified reaction  $Bt + Pl + Qtz = Melt + Opx \pm Grt$ . They form patches of accumulated material that crosscut the main foliation. Therefore, their formation is interpreted to postdate the main deformation event.

The more complex shape of the discordant leucosomes (L2) does not allow the same kind of investigations than for the stromatic leucosome (L1). Nevertheless, we analyzed L2 leucosomes "core" and the associated wall rocks (Fig. 7f). The P-XRF analyzes indicate a K content (0.003–0.012 mol) equivalent to the one found in the stromatic leucosomes for the same maficity (0–0.9 mol). Analyzes of their hosting rocks show a slightly bigger variability in K and Fe+Mg than the L1 selvages (Fig. 7f).

Mineral in L2 leucosomes are unzoned. The garnet has a composition similar to the one in L1 leucosomes ( $X_{alm}$  0.52–0.55,  $X_{pyr}$  0.37–0.40,  $X_{spss}$   $\sim$  0.02,  $X_{grs}$  0.04–0.06). The orthopyroxene crystal does not display any core/rim zoning (Mg#: 0.65–0.68). Plagioclase in the L2 structure displays the same chemical pattern than plagioclase in the cm- to -dm L1 leucosomes ( $X_{an}$  0.33–0.38,  $X_{ab}$  0.65–0.71,  $X_{or}$   $\sim$  0.02) (Fig. 10c,d).

## 5. Chemical modeling

### 5.1 Model setup

In this study, we aim to understand how the leucosomes acquire their chemical signature and how anatectic features can crystallize while along the prograde path. In order to solve those two issues we attended to model the formation of the leucosomes using phase relation calculations on a three-step process as suggested by Taylor *et al.* (2014): (1) Melting of a portion of the source to produce a magma (melt + variable proportion of entrained peritectic garnet); (2) Segregation of the magma at peak metamorphic conditions and reequilibration of the magma in the melt transfer site; (3) extraction of a fraction of the melt and reequilibration of the left over (i.e. felsic residuum). A variable proportion of garnet (0% to 50%) is taken along with the melt from a step to another to show the influence of entrained peritectic phases (Stevens *et al.*, 2007). The modeling is performed using the thermodynamically constrained software *Perple\_X* (version 6.6.9, April 2014) (Connolly, 1990; Connolly & Pettrini, 2002). The thermodynamic datafile used is hp04ver.dat. Solid solution models contained

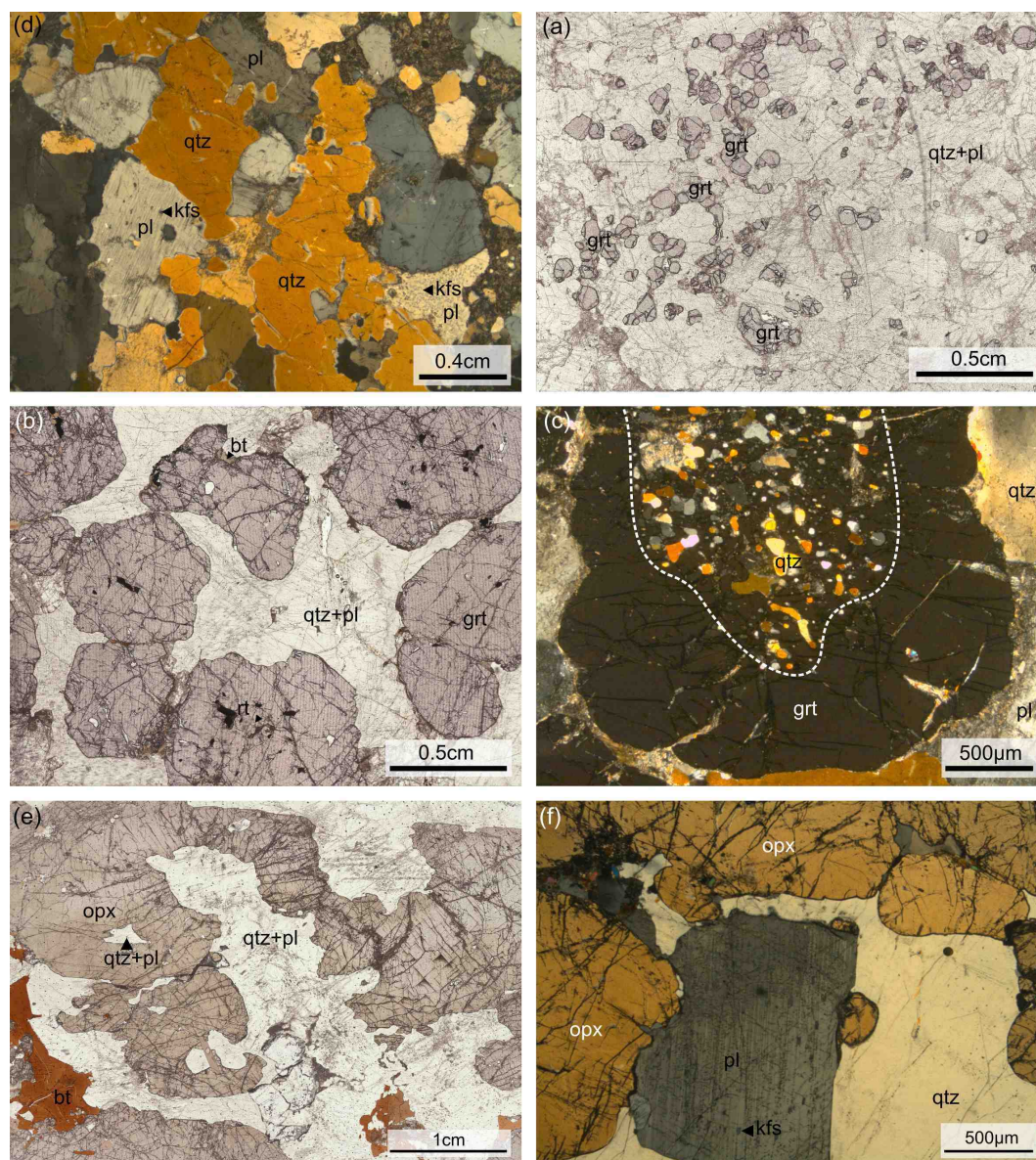


Figure 8: Petrography of the Brakspruit quarry leucosomes. (a) Detail of the plagioclase in the L1 structures. Kfs occurs as exsolution in large Pl minerals. (b) Small L1 leucosome characterized by small inclusion-free garnet. (c) Large L1 leucosome mainly dominated by garnet porphyroblasts. (d) Detail of garnet porphyroblast in L1 leucosomes. The garnet displays an inclusion-rich (Qtz + Bt + Pl) core and a large rim free of inclusion. (e) Large orthopyroxene in L2 leucosome. (f) Detail of the plagioclase in the L2 structure.

in solut\_09.dat are: Mica (CHA) (Cognon & Powell, 2002; Auzanneau *et al.*, 2005); Bio(TCC) (Tajčmanová *et al.*, 2009), Gt(WPH) (White *et al.*, 2007); Opx(HP), melt(HP) (Holland & Powell, 2001; White *et al.*, 2001); hCrd (Thompson & Hovis, 1979), feldspar (Fuhrman & Lindsley, 1988), Ilm (WPH) (White *et al.*, 2000). Previous study by Nicoli *et al.* (2014a) provides a well-constrained prograde heating *P-T* path for the Brakspruit quarry rocks. This *P-T* path can be modeled by the following equation:  $P = 0.02T - 6.5$  with *P* the pressure in kbar and *T* the temperature in °C and with boundary conditions of 650 °C-6.50 kbar and 900 °C-11.5 kbar. The magma (melt or melt + variable proportion of peritectic garnets) is extracted from the source to the accumulation site or melt transfer site when the melt in the source reaches the melt connectivity transition at 7 vol.% (Rosenberg & Handy, 2005; Yakymchuk & Brown, 2014).

The role of two main parameters were investigated: (1) the proportion of the source involved in the melting reaction (i.e. full-rock vs. sub-rock system), and (2) the behavior of the water.



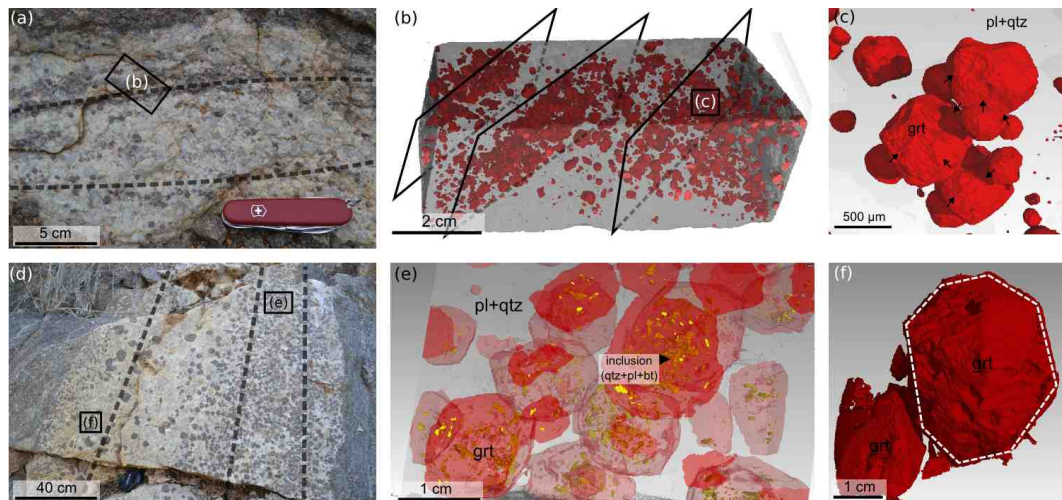


Figure 9: Detail of the garnet organization and the garnet shape in small L1 leucosomes (a–c) and large L1 leucosomes (d–f). (a) Field photo of a small L1 leucosome (DT09 sample). (b) Tomography image of a slab of DT09. The garnets are distributed along planes parallel to the edge of the leucosomes (c) Detail of the slab. The garnets organize themselves in cluster. (d) Field photo of a large garnet-bearing L1 leucosome (DT06 sample). The garnets are organized along planes parallel to the edge of the leucosomes (e) Tomography image of a slab of DT06. The garnets display a inclusion-rich core. (f) Detail of one single garnet from DT06. The porphyroblastic garnet is perfectly euhedral.

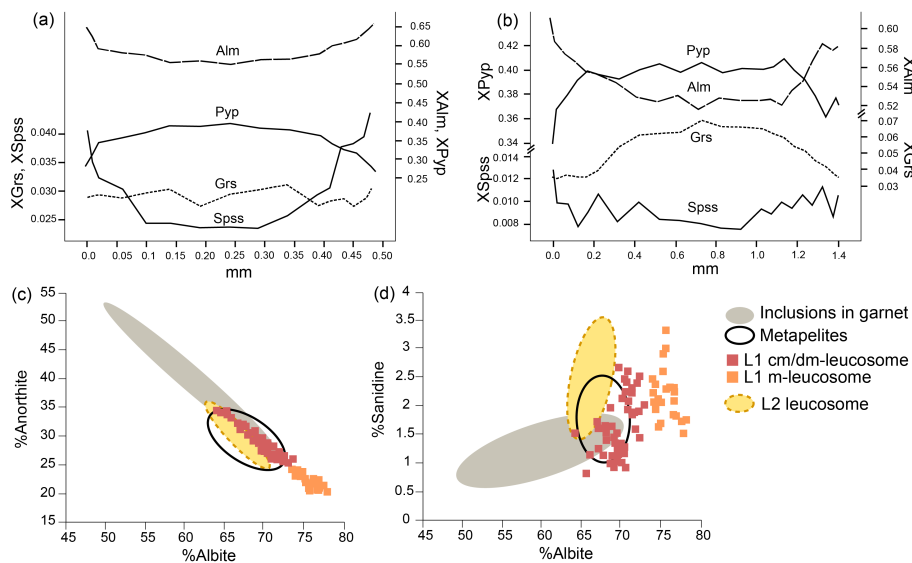


Figure 10: (a,b) Geochemical profiles through garnets from the small and large L1 leucosomes. (a) The garnet in small anatectic feature does not display any significant chemical zoning. (b) The garnet in the large anatectic feature displays a Ca-rich core richer. (c,d) Plagioclase composition in leucosomes (L1 and L2), residual metapelitic rocks and in inclusions in garnet.

## 5.2 Source

Two different setups are used for the source. In full-rock system (FRS) scenarios, we model melting of the whole source (hand-size sample) in which distribution of individual grains does not matter. As we see heterogeneities within the quarry metasedimentary rocks organization, such setup reflects equilibrium processes at the scale of an individual layer, but a disequilibrium processes at the scale of the outcrop.

In the sub-rock system (SRS) scenarios, we model melting of a portion of the source, i.e. we selected minerals from one sample and mix them in proportions that do not represent the mode of the source. Such

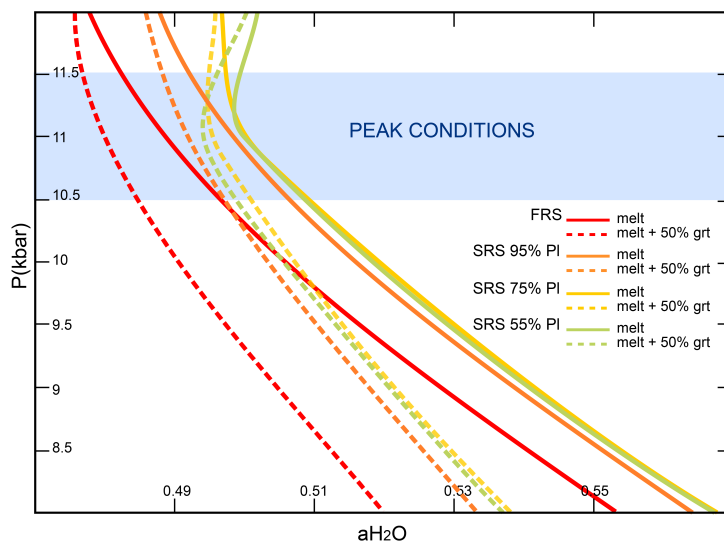


Figure 11: Evolution of the water activity ( $a_{H_2O}$ ) as a function of the pressure for different scenarios (FRS and SRS) and for different proportions of garnet entrained (0 or 50%). As the amount of plagioclase in the starting material decreases,  $a_{H_2O}$  in the melt column increases towards pressure higher than peak metamorphic conditions ( $\sim 870$  °C and 10.5-11.5 kbar).  $a_{H_2O}$  inflection occurs for the SRS75% scenario.

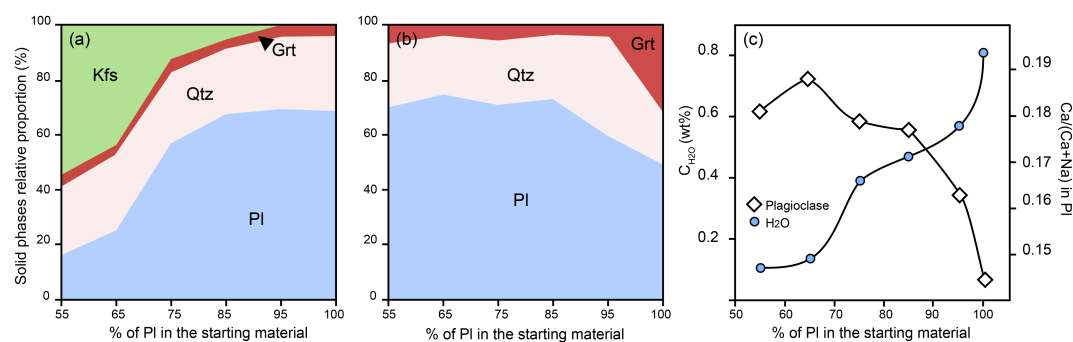


Figure 12: Influence of water diffusivity on the products of crystallization in the melt transfer site. (a) Phases crystallizing from the magma in the melt transfer site at peak conditions ( $\sim 870$  °C and  $\sim 10.5$  kbar) after diffusion of 0.5 wt% water for different scenarios (i.e. % of plagioclase involved). (b) Phases crystallizing from the magma in the melt transfer site at peak conditions after diffusion of water up to point Kfs crystallizes as a separated phase for different scenarios (i.e. % of plagioclase involved). (c) Proportion of water diffusing ( $C_{H_2O}$  in wt.%) and Ca/(Ca+Na) ratio in the plagioclase precipitated from the melt for different scenarios (i.e. % of plagioclase involved).

setup reflects equilibrium processes at the scale of an individual textural assemblage, but a disequilibrium process at the scale of the hand-sized rock sample.

The source used in FRS scenario is the melt reintegrated composition calculated after White *et al.* (2004) by Nicoli *et al.* (2014a) on a metapelite from the Brakspruit quarry in the NCKFMASHT system: SiO<sub>2</sub>: 65.41, TiO<sub>2</sub>: 1.50, Al<sub>2</sub>O<sub>3</sub>: 14.46, FeO: 5.28, MgO: 4.71, CaO: 1.14, Na<sub>2</sub>O: 2.60, K<sub>2</sub>O: 3.70, H<sub>2</sub>O: 1.9. The pre-melting assemblage is defined by 28% plagioclase, 35% biotite, 1% sillimanite, 35% quartz and 1% ilmenite. As the melt  $a-x$  model does not allow titanium in its composition, the calculated composition for the starting material using melt reintegration method might be different from the one used in experimental petrology (Grant, 2009). To solve this problem, the TiO<sub>2</sub> oxide concentration has been increased to 1.5 wt.% to avoid Ti-undersaturated scenario. Bartoli *et al.* (2013) also showed that FeO, MgO and CaO content are underestimated in the calculated melt at temperature  $< 700$  °C. Therefore, a best fit would be to reintegrate a certain percentage of S-type granite composition into the depleted source. However, this technique necessitates good knowledge of the amount S-type granite produced, which is in many cases very difficult to estimate. Consequently, White *et al.* (2004) melt reintegrated model is so far the more reliable method.

In SRS scenario, the proportion of minerals involved is such that all the biotite, all the quartz, all the sillimanite, all the ilmenite and a fraction of the plagioclase are involved in melting. We constrained the plagioclase fraction involved as follows: as the plagioclase percentage decreases, K-feldspar becomes part of the peak assemblage as a product of the partial melting reaction. In thin section, K-feldspar was not observed as being part of the

peak assemblage (Nicoli *et al.*, 2014a). Therefore, for less than 55% of the original plagioclase participating to the reaction, K-feldspar will be part of the products. Consequently, the models were ran with  $X_{plag}$  ranging between 55% and 95% (i.e. 5 % to 45 % of the plagioclase does not take part in the melting reaction).

### 5.3 Water behavior

Once the magma is segregated to the melt transfer site and once the melt pathway established, water might diffuse through the melt prior or coupled with melt loss. Experimental studies on H<sub>2</sub>O behavior in silica melt at high  $P$ - $T$  conditions (Nowak & Behrens, 1997; Zhang, 1999) showed the diffusivity of water is high compared to other elements. The diffusivity increases with H<sub>2</sub>O concentration in melt during crystallization and the energy needed to activate H<sub>2</sub>O diffusion is low. For water content in the melt (5 to 6 wt%) at peak condition, the diffusivity coefficient of H<sub>2</sub>O is  $>10^{-4} \text{ cm}^2 \cdot \text{s}^{-1}$  (Nowak & Behrens, 1997). Thermodynamic calculation of water activity ( $a_{H_2O}$ ) in the melt transfer site from peak conditions to upper crustal level for different scenarios (FRS, SRS95%, SRS75% , SRS55%) shows that  $a_{H_2O}$  in the melt column is highly dependent of the quantity of plagioclase involved the melting reaction (fig. 11).

To control how much water might diffuse, the water concentration in the ( $C_{H_2O}$  in wt.%) is modified to create a gradient that mimics the diffusion of H<sub>2</sub>O in the melt transfer site. We investigated two possibilities: (1) in the first case  $C_{H_2O}$  is fixed in all the scenarios for a low value of 0.5 wt% (Fig. 12a). As the plagioclase proportion decreases, the proportion on K-feldspar that precipitates in the melt transfer site increases. As no primary K-feldspar has been observed in the leucosomes, the maximum of  $C_{H_2O}$  is chosen to model a H<sub>2</sub>O gradient that does not trigger co-precipitation of K-feldspar with the plagioclase in the melt transfer site. (2) As a result  $C_{H_2O}$  in the melt decreases along with the plagioclase proportion involved in the melting reaction (Fig. 12b,c). Moreover, the plagioclase that precipitates from the melt sees its Ca/(Ca+Na) ratio increasing which in good correlation with the presence of Ca-rich plagioclase in garnet (Fig.12c).

### 5.4 Results

The different scenarios (FRS, SRS95%, SRS75%, SRS55%) were ran a first time in closed system (no melt extraction) and second time in a open system (melt extracted subsequent to magma reequilibration in the melt transfer site) with diffusion of water in the melt transfer site at maximum of  $C_{H_2O}$ .

In the closed system situation, the resulting felsic residuum composition does not match the leucosome chemistry of the Brakspruit leucosome even with different proportion of entrained peritectic garnet (Fig.13). K and Si correlated positively and the concentration of potassium [K] is 4 times higher than [K] in the leucosomes (Fig. 13a). This mechanism fails to precipitate plagioclase and quartz from the melt and fails to explain the high Ca/(Ca+Na) ratio (Fig.13b) and the low maficity (Fig.13c,d) of the leucosomes. Moreover, it necessitates an important episode of cooling to crystallize the melt fraction.

In open system, the different scenarios (FRS, SRS95%, SRS75% , SRS55%) provide a large range of compositions that cover the chemical signature of the Brakspruit quarry leucosome. K and Si correlated positively (Fig. 14a) but the different scenarios explain the chemistry of the leucosome with the higher K<sub>2</sub>O content. As the leucosome are build by repetitive batches of magma (Bons *et al.*, 2009), the discharge of peritectic phases and the diffusion of water in the melt transfer site would *in fine* drive the composition to slightly higher Si and lower K content. This is in good correlation with the presence of garnet ditribution plane inside the leucosomes. The crystallization of more calcic plagioclase in the SRS scenarios creates felsic residuum with Ca/(Ca+Na) ratios similar to ones measured in the natural leucosomes (Fig. 14b). Figure 14c,d shows the influence of peritectic garnet entrainment (25%) on the leucosome chemistry.

The lack of CaO, Feo and MgO into the melt composition (Bartoli *et al.*, 2013) does not considerably affect the chemical modeling. On the contrary, as these values are underestimates in the melt a-x model, our calculations generated leucosome of minimum composition. Increasing CaO, FeO and MgO content in the starting material would have driven the modelled leucosome composition towards an even better fit.

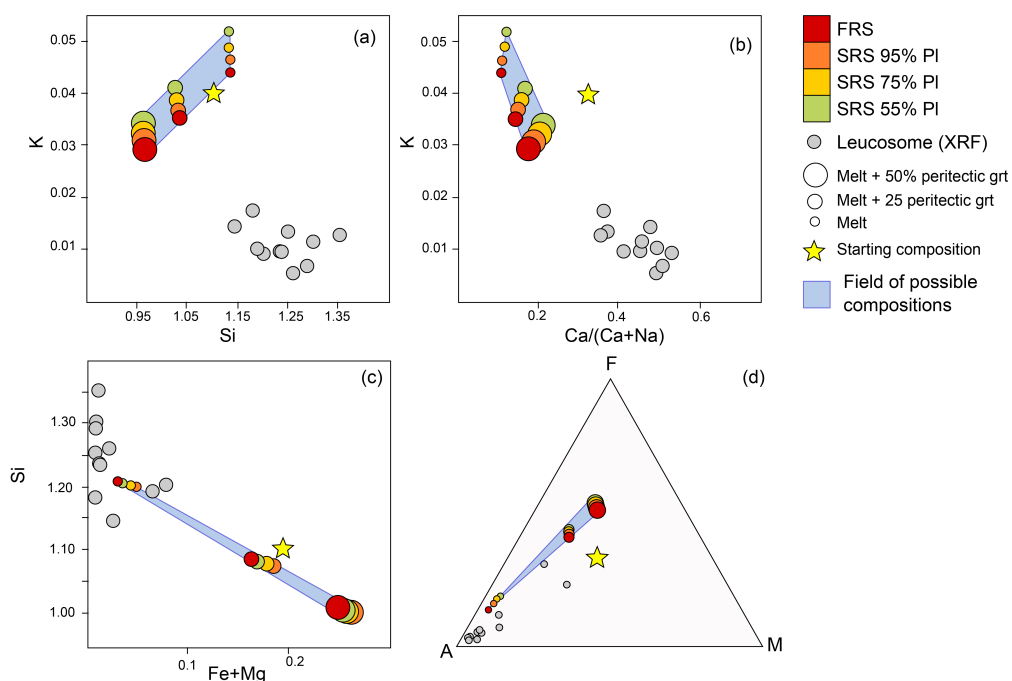


Figure 13: (a-d) Composition of the leucosomes obtained with FRS scenario and SRS scenarios (SRS95%, SRS75% , SRS55%) in a closed system compared to the leucosome chemistry from Brakspruit quarry. The field of possible compositions covers the hypothetical leucosome chemistry generated following FRS and SRS approaches.

## 6. Discussion

### 6.1 Scale of chemical heterogeneities

This study highlights the important issue of “equilibrium” v. “disequilibrium” mechanisms in migmatites. The investigation of partial melting processes is strongly dependant of the choice of the volume of equilibration. In migmatitic terrains, the leucosomes follow fractal power-law distribution (Bons *et al.*, 2004; Soesoo *et al.*, 2004). The more leucosomes are found in metatectic terrains, the less efficient the crustal differentiation was (Bons *et al.*, 2004). Ideally, full crustal differentiation will be achieved when the number of leucocratic features will tend towards 1. In the Bandelierkop formation anatexites, all sizes of leucosomes are found, from micro-felsic pockets in the metapelites to larger felsic dykes. This may indicate that the partial melting of the lower crust did not reach its full equilibrium state. Moreover, incomplete crustal differentiation is in good agreement with the preservation of some of the peak metamorphic biotite in the SMZ lithologies (Nicoli *et al.*, 2014a,b).

At the scale of the outcrop, this chemical heterogeneity is found in the metamorphic layering inherited from the sedimentary bedding (Nicoli *et al.*, 2014a, Taylor *et al.*, 2014). These different metasedimentary rocks possess different fertility degrees, and a rock from the metapelitic layer is in disequilibrium with a rock of the semipelitic layer. At the scale of the sample, bulk-rock analyzes give an average composition of the main textural assemblage, however it does not take into account the textural heterogeneities within the sample. The modeling presented in this paper takes in consideration this last aspect.

### 6.2 Partial melting, melt pathway and leucosome chemistry

The leucosomes from the Bandelierkop formation have been identified for being the result of the partial melting of the surrounding metasedimentary rocks under fluid absent melting conditions (Stevens & Van Reenen 1992; Taylor *et al.*, 2014; this study). In the Brakspruit quarry the partial melting reactions would have produced up to 15 to 35 vol.% of melt along with a significant amount of peritectic phases during the

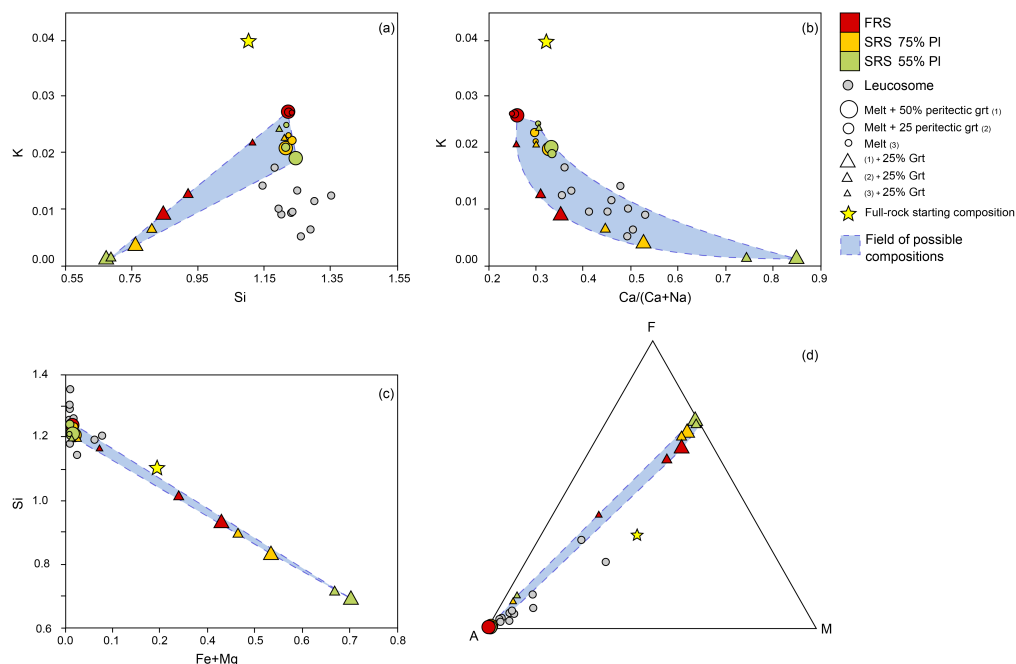


Figure 14: (a-d) Composition of the leucosomes obtained with the FRS scenario and the SRS scenarios (SRS75% and SRS55%) and water diffusivity inside the melt transfer site in an open system, compared to the leucosome chemistry from Brakspruit quarry. The field of possible compositions covers the hypothetical leucosome chemistry generated following FRS and SRS approaches. Despite some differences in K and Si content, the disequilibrium and water diffusivity mechanism is able to explain the formation of K<sub>2</sub>O-poor leucosomes.

prograde history of the rock (Nicoli *et al.*, 2014a). The diversity in size, shape and proportion of the peritectic garnet in the leucocratic features suggests that the outcrop displays several steps in the evolution of the leucosomes and highlights melt flow features (Taylor & Stevens, 2010) (Fig. 15). In cm-sized leucosomes, the peritectic garnet entrained with the melt amalgamates in clusters along segregation planes. In larger leucosomes, the environment is dominantly magmatic and allows the growth of thick inclusion-free rims by garnet/melt dissolution-precipitation mechanisms and the preservation of quartz inclusions-rich core (Waters 2001, Taylor & Stevens, 2010; Ward *et al.*, 2008). Based on similar anatectic features in the Namaqualand Metamorphic Complex, Waters (2001) argues the formation of quartz inclusion-rich garnet bearing leucosomes is achieved by the melt loss from the structure coupled with H<sub>2</sub>O diffusion in the melt pathway. The existence of garnet segregation planes inside the large leucocratic features (Fig. 9) as well as the chemistry of the peritectic phases support the hypothesis that leucosomes acted as melt transfer sites and built up over time, fed by repetitive batches of magma from a nearby source (Bons *et al.*, 2009).

In some case, the accumulation of peritectic garnet and/or orthopyroxene along the edge of the leucosome makes the maficity in the selvage more important than the host rock. Image analyzes of thin sections in the wall rock show that more than ~ 95 vol% of biotite (Fig. 4c,d) is part of the granulitic assemblage. Biotite associated with the retrogressed assemblage represents less than 5 vol.% of the total of biotite and is associated with orthoamphibole and kyanite. Consequently, the potassium in the selvage is mainly contained in the peak metamorphic biotite. In the selvage, the garnet and the orthopyroxene do not display evidence of significant rehydrated back reaction. Therefore, redistribution of K<sub>2</sub>O and H<sub>2</sub>O back to the wall rock is an incompatible mechanism to accommodate the lack of potassium in L1 leucosomes. The other potential reservoir for K<sub>2</sub>O is the plagioclase and the K-feldspar. In thin section, K-feldspar in the leucosome and the wall rock occurs as exsolution in the plagioclase (Nicoli *et al.*, 2014a; this study). The plagioclase in the L1 leucosome ( $X_{ab}$ : 0.6–0.8%;  $X_{an}$ : 0.2–0.35;  $X_{or}$ : 0.01–0.03) has a composition slightly different from the plagioclase in the residuum ( $X_{ab}$ : 0.62–0.72;  $X_{an}$ : 0.22–0.35;  $X_{or}$ : 0.01–0.25). The difference in potassium

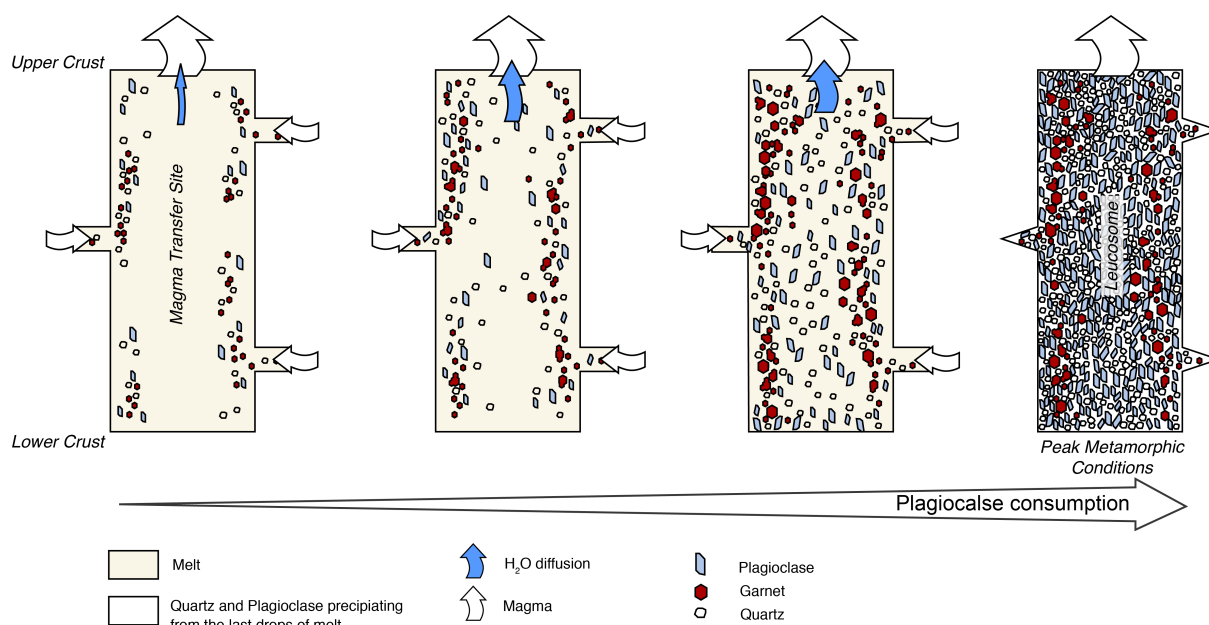


Figure 15: Formation and evolution of L1 stromatic and deformed leucosomes along the prograde path with consumption of plagioclase and water diffusivity in the melt transfer site. The load of plagioclase, quartz and garnet precipitating from the melt increases with time. The garnet also has a peritectic origin and a fraction of this phase directly comes from the partial melting reaction in the adjacent protolith. At the last stage of its evolution, i.e. peak metamorphic conditions, quartz + plagioclase + k-feldspar will crystallize from the small fraction of melt that failed to escape and the leucosome achieves its final chemistry.

content in the plagioclase from the source and the plagioclase from the leucosomes indicates the plagioclase in the leucosomes is not the one entrained from the source. Moreover, plagioclase inclusions in garnet are Ca-rich ( $X_{ab}$ : 0.5–0.7;  $X_{an}$ : 0.30–0.55;  $X_{or}$ : 0.01–0.02). This illustrates the formation of Ca-rich peritectic plagioclase during fluid-absent partial melting (Johannes & Koepke, 2001; Acosta-Vigil & London, 2006). L2 plagioclase possesses the same composition than the plagioclase in the mafic residuum and the cm-scale L1 leucosomes but has a higher K content, similar to the one in plagioclases from the m-size L1 leucosomes. This could be explained by the concurrent crystallization of two feldspars, i.e. K-feldspar exsolution in plagioclase, during the crystallization at lower  $P$ - $T$  conditions of the last granitic melt fraction that failed to escape. All these observations confirm previous findings in the area (Taylor *et al.*, 2014) and support the hypothesis that these anatectic features have achieved their chemical signature via melt loss before cooling of the terrain (Fig. 16).

### 6.3 K<sub>2</sub>O-poor Leucosome formation mechanism

Many studies (Sawyer, 1987; Brown, 2002; Kriegsman & Hensen, 1988; Fourcade *et al.*, 1992; Kriegsman, 2001) state K<sub>2</sub>O-poor leucosome chemistry is achieved during the retrograde history of the rock via melt loss and H<sub>2</sub>O-K<sub>2</sub>O diffusion back to the residuum. This study, previous work in the area (Taylor *et al.*, 2014) and works on similar anatectic terrains (Waters, 2001, Del Moro *et al.* 2000, Ward *et al.*, 2008) presented field evidence that discredits these mechanisms. In many cases, melt loss occurs during the prograde history of the rock leaving in the source a high-grade low K<sub>2</sub>O felsic residuum. Taylor *et al.* (2014) demonstrated that the full-rock system failed to explain the formation of K<sub>2</sub>O-poor leucosomes at peak metamorphic conditions (~ 870 °C and ~ 10.5 kbar). In the Bandelierkop formation anatectites the presence of the Ca-rich plagioclase inclusions in the garnet argues for melting of the plagioclase being a key process in the formation of the K<sub>2</sub>O-poor leucosomes (Johannes & Koepke, 2001; Acosta-Vigil & London, 2006; Taylor *et al.*, 2014).

Chemical modeling shows that leucosome chemistry can be achieved by the melting reaction happening in sub-rock system. In this particular case, it involves dissolution of the outer rim of the plagioclase followed by magma segregation to the melt transfer site, diffusion of water and melt loss.  $C_{H_2O}$  is highly dependant of the degree of “disequilibrium” (Fig. 12c). The presence of preserved garnet, orthopyroxene and prograde

biotite (Nicoli *et al.*, 2014a) in the wall rock of the leucosomes rules out the hypothesis of diffusion back to the residuum as the main mechanism for water loss.  $a_{H_2O}$  increases towards lower pressure conditions (Fig. 11). Consequently the water is likely to diffuse vertically into the melt pathway while the melt is extracted towards the shallower levels. As more plagioclase core is dissolved into the melt (i.e. from SRS55% scenario to the FRS scenario)  $a_{H_2O}$  gradient increases and water will diffuse more efficiently in the magma column. The formation of K<sub>2</sub>O-poor leucosomes has a direct consequence on the processes that shape crustal differentiation. After initiation of the melting reaction by the breakdown of biotite and the development of melt transfer site networks, water starts to diffuse in the magma column.  $C_{H_2O}$  increases coinjointly with the consumption of plagioclase. Consequently, the precipitation of plagioclase, quartz and in some case garnet from the melt is enhanced. From this mechanism results the formation of a solid state felsic-rich residuum at peak metamorphic conditions. Therefore, efficient plagioclase consumption coupled with water diffusivity may lead to the formation of K<sub>2</sub>O-poor leucosome during the heating of the whole terrain and magma extraction towards the middle crust to form the granite.

## 7. Conclusion

Field observations and chemical modeling strongly argue for K<sub>2</sub>O-poor and CaO-rich leucosomes representing the felsic residue left over in the plumbing system through which the melt was transferred to crustal upper levels. Therefore, major melt production and draining out of the source would have occurred priori decompression along the prograde path. In that system, large deformed and stromatic leucosomes correspond to a more evolved version of cm-scale L1 leucosome from a deeper source level of similar composition. L2 is the produce of late melting reaction during decompression and finishes to dry out the residuum. The chemical signature of the leucosome is directly linked to the crustal differentiation. Their formation reveals that the melting of the lower crust is likely to be controlled by different volumes of equilibrium at the scale of the sample and water diffusivity in the melt transfer site. The system tends to reach its full efficiency when all the sub-system evolves towards near “equilibrium” system (i.e. full-rock).

## Acknowledgments

The authors acknowledge the owner of the Brakspruit quarry for allowing us access to his property and thank Laubser Pepler for his help with the P-XRF on the field. This work was carried out as part of the France-South Africa scientific collaboration and was supported by a National Research Foundation (South Africa) grant and Centre National de la Recherche Scientifique (France) funding. Gary Stevens and Gautier Nicoli acknowledge PhD bursary support to Gautier Nicoli via the SARChI programme. JFM was also supported by the European Research Council (project MASE, ERC StG 279828 to J. van Hunen).

## Supporting information

Additional Supporting Information may be found in the online version of this article at the publisher's web site (see appendix D: Mineral Chemistry) Table S1. Mineral chemistry.

## REFERENCES

- Acosta-Vigil, A., London, D. & Morgan VI, G.B., 2006. Experiments on the kinetics of partial melting of a leucogranite at 200 MPa H<sub>2</sub>O and 690-800C: compositional variability of melt during the onset of H<sub>2</sub>O-saturated crustal anatexis. *Contribution to Mineralogy and Petrology*, **151**, 539-557.
- Bartoli, O., Tajčmanová, L., Cesare, B., & AcostaVigil, A., 2013. Phase equilibria constraints on melting of stromatic migmatites from Ronda (S. Spain): insights on the formation of peritectic garnet. *Journal of Metamorphic Geology*, **31**, 775-789.
- Bons, P. D., Arnold, J., Elburg, M. A., Kalda, J., Soesoo, A. & van Milligen, B. P., 2004. Melt extraction and accumulation from partially molten rocks. *Lithos*, **78**, 25-42.
- Bons, P. D., Becker, J. K., Elburg, M. A. & Urtson, K., 2009. Granite formation: Stepwise accumulation of melt or connected networks?. *Earth and Environmental Science Transactions of the Royal Society of Edinburgh*, **100**, 105-115.
- Boyle, J.F., 2000. Rapid elemental analysis of sediments by isotope source XRF. *Journal of Paleolimnology*, **23**, 213-221
- Brown, M., 2002. Retrograde processes in migmatites and granulites revisited. *Journal of Metamorphic Geology*, **20**, 25-40.
- Cesare, B., Ferrero, S., Salvioli-Mariani, E., Pedron & Cavallo, A. 2009. "Nanogranite" and glassy inclusions: The anatectic melt in migmatites and granulites. *Geology*, **37**, 627-630.
- Clemens, J. D. & Vielzeuf, D., 1987. Constraints on melting and magma production in the crust. *Earth and Planetary Science Letters*, **86**, 287-306.
- Connolly, J.A.D., 1990. Multivariable phase-diagrams – an algorithm based on generalized thermodynamics. *American Mineralogical Journal of Science*, **290**, 666-718.
- Connolly J.A.D. & Petrini, K., 2002. An automated strategy for

calculation of phase diagram sections and retrieval of rock properties as a function of physical conditions. *Journal of Metamorphic Petrology*, **20**, 697-708.

Del Moro, A., Fornelli, A. & Piccareta, G., 2000. Disequilibrium melting in granulite-facies metasedimentary rocks of the Northern Serre (Calabria-Southern Italy). *Mineralogy and Petrology*, **70**, 89-104.

Droop, G.T.R., 1987. A general equation for Fe<sup>3+</sup> concentrations in ferromagnesian silicates and oxides from microprobe analyses, using stoichiometric criteria. *Mineralogical Magazine*, **51**, 431-435.

Fourcade, S., Martin, H. & de Brémond d'Ars, J., 1992. Chemical exchange in migmatites during cooling. *Lithos*, **28**, 43-53.

Fuhrman, M.L. & Lindsley, J.G., 1988. Ternary-Feldspar Modeling and Thermometry. *American Mineralogy and Petrology*, **126**, 137-51.

Grant, J. A., 2009. Thermocalc and experimental modelling of melting of pelite, Morton Pass, Wyoming. *Journal of Metamorphic Geology*, **27**, 571-578.

Guernina, S. & Sawyer, E.W., 2003. Large-scale melt-depletion in granulite terranes: an example from the Archean Ashuanipi Subprovince of Quebec. *Journal of Metamorphic Geology*, **21**, 181-201.

Hasalová, P., Schulmann, K., Lexa, O., Štípská, P., Hrouda, F., Ulrich, S. & Týcová, P., 2008. Origin of migmatites by deformation-enhanced melt infiltration of orthogneiss: A new model based on quantitative microstructural analysis. *Journal of Metamorphic Geology*, **26**, 29-53.

Holland, T.J.B., & Powell, R., 1998. An internally consistent thermodynamic data set for phases of petrological interest. *Journal of Metamorphic Geology*, **16**, 309-343.

Holland, T.J.B. & Powell, R., 2001. Calculation of phase relations involving haplogranitic melts using an internally consistent thermodynamic dataset. *Journal of Petrology*, **42**, 673-683.

Johannes, W., 1988. What controls partial melting in migmatites? *Journal of Metamorphic Geology*, **6**, 451-465.

Johannes, W., Ehlers, C., Kriegsman, L. M. & Mengel, K., 2003. The link between migmatites and S-type granites in the Turku area, southern Finland. *Lithos*, **68**, 69-90.

Johannes, W. & Koepke, J., 2001. Incomplete reaction of plagioclase in experimental dehydration melting of amphibolite. *Australian Journal of Earth Sciences*, **48**, 581-590.

Joseph, C. S. A., 2013. The petrogenesis of the ignimbrites and quartz porphyritic granites exposed along the coast at Saldanha, South Africa. University thesis, Stellenbosch University.

Ketcham, R. A., & Carlson, W. D., 2001. Acquisition, optimization and interpretation of X-ray computed tomographic imagery: applications to the geosciences. *Computers & Geosciences*, **27**, 381-400.

Kisters, A. F. M., Ward, R. A., Anthonissen, C. J. & Vietze, M. E., 2009. Melt segregation and far-field melt transfer in the mid-crust. *Journal of the Geological Society*, **166**, 905-918.

Korhonen, F. J., Saito, S., Brown, M., Siddoway, C. S. & Day, J. M. D., 2010. Multiple generations of granite in the Fosdick Mountains, Marie Byrd Land, West Antarctica: implications for polyphase intracrustal differentiation in a continental margin setting. *Journal of Petrology*, **51**, 627-670.

Kreissig, K., Holzer, L., Frei, R., Villa, I.M., Kramers, J.D., Kröner, A., Smit, C.A. & Van Reenen, D.D., 2001. Geochronology of the Hout River Shear Zone and the metamorphism in the Southern Marginal Zone of the Limpopo Belt, Southern Africa. *Precambrian Research*, **109**, 145-173.

Kretz, R., 1983., Symbols for rock-forming minerals. *American Mineralogist*, **68**, 277-279.

Kriegsman, L. M., 2001. Partial melting, partial melt extraction and partial back reaction in anatectic migmatites. *Lithos*, **56**, 75-96.

Kriegsman, L.M. & Hensen, B.J., 1998. Back reaction between restite and melt: implications for geothermobarometry and pressure-temperature paths. *Geology*, **26**, 1111-1114. Laurent, O., Paquette, J-L., Martin, H., Doucelance, R. & Moyen, J-F, 2013., LA-ICP-MS dating of zircon from Meso- and Neoproterozoic granitoids of the Pietersburg block (South Africa): Crustal evolution at the northern margin of the Kaapvaal craton. *Precambrian Research*, **230**, 209-226.

Le Breton, N. & Thompson, A. B., 1988. Fluid-absent

(dehydration) melting of biotite in metapelites in the early stages of crustal anatexis. *Contributions to Mineralogy and Petrology*, **99**, 226-237.

Ledru, P., Courrioux, G., Dallain, C., Lardeaux, J. M., Montel, J. M., Vanderhaeghe, O. & Vitel, G., 2001. The Velay dome (French Massif Central): melt generation and granite emplacement during orogenic evolution. *Tectonophysics*, **342**, 207-237.

Martignole, J. & Martelat J-E., 2003. Regional-scale Grenvillian-age UHT metamorphism in the Mollendo-Camana block (basement of the Peruvian Andes). *Journal of Metamorphic Geology*, **21**, 99-120.

Mehnert, K. R., 1968. Migmatites and the origin of granitic rocks (p. 393). Amsterdam: Elsevier.

Mengel, K., Richter, M. & Johannes, W., 2001. Leucosome-forming small-scale geochemical processes in the metapelitic migmatites of the Turku area, Finland. *Lithos*, **5**, 47-73.

Montel, J. M., Marignac, C., Barbey, P. & Pichavant, M., 1992. Thermobarometry and granite genesis: the Hercynian lowP, highT Velay anatectic dome (French Massif Central). *Journal of Metamorphic Geology*, **10**, 1-15.

Montel, J.M. & Vielzeuf, D., 1997. Partial melting of metagreywackes. 2. Compositions of minerals and melts. *Contribution to Mineral and Petrology*, **128**, 176-196.

Nicoli, G., Stevens, G., Buick, I.S. & Moyen J-F, 2014b. A comment on Ultrahigh-temperature metamorphism from an unusual corundum+orthopyroxene intergrowth bearing Al-Mg granulite from the Southern Marginal Zone, Limpopo Complex, South Africa by Belyanin et al. *Contribution to Mineralogy and Petrology*, 167:1022.

Nicoli, G., Stevens, G., Moyen, J-F & Frei, D., 2014a. Rapid evolution from sediment to anatectic granulite in an Archean continental collision zone: The example of the Bandelierkop Formation metapelites, South Marginal Zone, Limpopo Belt, South Africa. *Journal of Metamorphic Geology*, DOI: 10.1111/jmg.12116.

Nowak, M. & Behrens, H., 1997. An experimental investigation on diffusion of water in haplogranitic melts. *Contributions to Mineralogy and Petrology*, **126**, 365-376.

Patiño Douce, A.E. & Beard, J. S., 1996. Effects of P, f (O<sub>2</sub>) and Mg/Fe ratio on dehydration melting of model metagreywackes. *Journal of Petrology*, **37**, 999-1024.

Patiño Douce, A.E. & Johnston, A.D., 1991. Phase equilibria and melt productivity in the pelitic system: implications for the origin of peraluminous granitoids and aluminous granites. *Contribution to Mineralogy and Petrology*, **107**, 202-218.

Patiño Douce, A.E. Harris, N., 1998. Experimental constraints on Himalayan anatexis. *Journal of Petrology*, **39**, 689-710.

Pickering, J.M. & Johnston, A.D., 1998. Fluid-absent melting behavior of two-mica metapelite: experimental constraints on the origin of black hills granite. *Journal of Petrology*, **39**, 1797-1894.

Potts, P.J., Williams-Thorpe, O., & Webb, P.C. 1997. The bulk Analysis of Silicate Rocks by Portable X-Ray Fluorescence: Effect of Sample Mineralogy in Relation to the Size of the Excited Volume. *Geostandards Newsletter*, **21**, 29-41.

Powell, R. & Holland, T., 1999. Relating formulations of the thermodynamics of mineral solid solutions: Activity modeling of pyroxenes, amphiboles, and micas. *American Mineralogist*, **84**, 1-14.

Racek, M., Štípská, P. & Powell, R., 2008. Garnet-clinopyroxene intermediate granulites in the St. Leonhard massif of the Bohemian Massif: ultrahigh-temperature metamorphism at high pressure or not? *Journal of Metamorphic Geology*, **26**, 253-271.

Rasband, W.S., ImageJ, U.S. National Institutes of Health, Bethesda, Maryland, USA, <http://imagej.nih.gov/ij/>, 1997-2012.

Rosenberg, C. L. & Handy, M. R., 2005. Experimental deformation of partially melted granite revisited: implications for the continental crust. *Journal of Metamorphic Geology*, **23**, 19-28.

Sawyer, E. W., 1999. Criteria for the recognition of partial melting. *Physics and Chemistry of the Earth*, **24**, 269 - 279.

Sawyer, E.W., 1987. The role of partial melting and fractional crystallization in determining discordant migmatite leucosome compositions. *Journal of Petrology*, **28**, 445-473.

Sawyer, E. W., Cesare, B. & Brown, M., 2011. When the continental crust melts. *Elements*, **7**, 229-234.

Sederholm, J. J., 1967. Selected works: granites and migmatites. Edinburgh: Oliver & Boyd.

Skjerlie, K. P., Douce, A. E. P. & Johnston, A. D., 1993. Fluid



- absent melting of a layered crustal protolith: implications for the generation of anatectic granites. *Contributions to Mineralogy and Petrology*, **114**, 365-378.
- Soesoo, A., Kalda, J., Bons, P., Urtson, K. & Kalm, V., 2004. Fractality in geology: a possible use of fractals in the studies of partial melting processes. In *Proceedings of the Estonian Academy of Sciences, Geology*, **53**, 13-27
- Stevens, G., Clemens, J.D. & Droop, G.T.R., 1997. Melt production during granulite-facies anatexis: experimental data from primitive metasedimentary protoliths. *Contribution to Mineralogy and Petrology*, **128**, 352-370 .
- Stevens, G. & Clemens, J. D., 1993. Fluid-absent melting and the roles of fluids in the lithosphere: a slanted summary? *Chemical Geology*, **108**, 1-17.
- Stevens, G. & Van Reenen, D.D., 1992a. Partial melting and the origin of metapelitic granulites in the Southern Marginal Zone of the Limpopo Belt, South Africa. *Precambrian Research*, **55**, 303-319 .
- Stevens, G. & Van Reenen, D.D., 1992b. Constraints on the form of the P-T loop in the Southern Marginal Zone of the Limpopo Belt, South Africa. *Precambrian Research*, **55**, 279-296.
- Stevens, G., Villaros, A. & Moyén, J-F., 2007. Selective peritectic garnet entrainment as the origin of geochemical diversity in S-type granites. *Geology*, **35**, 9-12.
- Taylor, J., Nicoli, G., Stevens, G., Frei, D., & Moyén, J-F., 2014. The processes that control leucosome compositions in metasedimentary granulites: Perspectives from the Southern Marginal Zone migmatites, Limpopo Belt, South Africa. *Journal of Metamorphic Geology*, **32**, 713-742.
- Taylor, J. & Stevens, G., 2010. Selective entrainment of peritectic garnet into S-type granitic magmas: Evidence from Archaean mid-crustal anatectites. *Lithos*, **120**, 277-292.
- Tindle, A.G. & Webb, P.C., 1994. Probe-AMPH-A spreadsheet program to classify microprobe-derived amphibole analyses. *Computer and Geosciences*, **20**, 1201-1228.
- Tajčmanová, L., Connolly, J. A. D. Cesare, B., 2009. A thermodynamic model for titanium and ferric iron solution in biotite. *Journal of Metamorphic Geology*, **27**, 153-165.
- Thompson, J.B. & Hovis, G.L., 1979. Entropy of Mixing in Sanidine. *American Mineralogist*, **64**, 57-65.
- Vanderhaeghe, O., 2009. Migmatites, granites and orogeny: flow modes of partially-molten rocks and magmas associated with melt/solid segregation in orogenic belts. *Tectonophysics*, **477**, 119-134.
- Vielzeuf, D., Clemens, J. D., Pin, C. & Moinet, E., 1990. Granites, granulites, and crustal differentiation. In *Granulites and crustal evolution* pp. 59-85. Springer Netherlands.
- Vielzeuf, D. & Holloway, J.R., 1988. Experimental determination of the fluid-absent melting reactions in the pelitic system. *Contribution to Mineralogy and Petrology*, **98**, 257-276.
- Villaseca, C., Downes, H., Pin, H., & Barbero, L. 1999. Nature and Composition of the Lower Continental Crust in Central Spain and the Granulite-Granite Linkage: Inference from Granulitic Xenoliths. *Journal of Petrology*, **40**, 1465-1496.
- Van Reenen, D.D., Roering, C., Ashwal L.D., & de Wit, M.J., 1992. Regional geological setting of the Limpopo Belt. *Precambrian Research*, **55**, 1-5.
- Ward, R., Stevens, G. & Kisters, A., 2008. Fluid and deformation induced partial melting and melt volumes in low-temperature granulite-facies metasediments, Damara Belt, Namibia. *Lithos*, **105**, 253-271.
- Waters, D. J., 2001. The significance of prograde and retrograde quartz-bearing intergrowth microstructures in partially melted granulite-facies rocks. *Lithos*, **56**, 97-110.
- Waters, D.J., 1988. Partial melting and the formation of granulite-facies assemblages in Namaqualand, South Africa. *Journal of Metamorphic Geology*, **6**, 387-404.
- White, R.W., Pomroy, N.E. & Powell, R., 2005. An in situ metatexite-diatexite transition in upper amphibolite facies rocks from Broken Hill, Australia. *Journal of Metamorphic Geology*, **23**, 579-602.
- White, R.W., Powell, R., Holland, T.J.B. & Worley, B.A., 2000. The effect of TiO<sub>2</sub> and Fe<sub>2</sub>O<sub>3</sub> on metapelitic assemblages at greenschist and amphibolite facies conditions: mineral equilibria calculations in the system K<sub>2</sub>O-FeO-MgO-Al<sub>2</sub>O<sub>3</sub>-SiO<sub>2</sub>-H<sub>2</sub>O-TiO<sub>2</sub>-Fe<sub>2</sub>O<sub>3</sub>. *Journal of Metamorphic Geology*, **18**, 497-511.
- White, R.W., Powell, R., & Clarke, G.L., 2004. Prograde Metamorphic Assemblage Evolution during Partial Melting of Metasedimentary Rocks at Low Pressures: Migmatites from Mt Stafford, Central Australia. *Journal of Petrology*, **44**, 1937-1960.
- White, R.W., Powell, R., & Holland, T.J.B., 2007. Progress relating to calculation of partial melting equilibria for metapelites. *Journal of Metamorphic Geology*, **25**, 511-527.
- White, R.W., Powell, R., & Holland, T.J.B. 2001. Calculation of partial melting equilibria in the system Na<sub>2</sub>O-CaO-FeO-MgO-Al<sub>2</sub>O<sub>3</sub>-SiO<sub>2</sub>-H<sub>2</sub>O (NCFMASH). *Journal of Metamorphic Geology*, **19**, 139-53.
- White, R.W., Powell, R., Holland, T.J.B., & Worley, B.A. 2001. The effect of TiO<sub>2</sub> and Fe<sub>2</sub>O<sub>3</sub> on metapelitic assemblages at greenschist and amphibolite facies conditions: mineral equilibria calculations in the system K<sub>2</sub>O-Na<sub>2</sub>O-CaO-FeO-MgO-Al<sub>2</sub>O<sub>3</sub>-SiO<sub>2</sub>-H<sub>2</sub>O-TiO<sub>2</sub>-Fe<sub>2</sub>O<sub>3</sub>. *Journal of Metamorphic Geology*, **18**, 497-511.
- Whitney, D. L. & Irving, A. J., 1994. Origin of K-poor leucosomes in a metasedimentary migmatite complex by ultrametamorphism, syn-metamorphic magmatism and subsolidus processes. *Lithos*, **32**, 173-192.
- Yakymchuk, C. & Brown, M., 2014. Consequences of open-system melting in tectonics. *Journal of Geological Society*, **171**, 21-40.
- Yakymchuk, C., Brown, M., Ivanic, T. J. & Korhonen, F. J., 2013. Leucosome distribution in migmatitic paragneisses and orthogneisses: A record of self-organized melt migration and entrapment in a heterogeneous partially-molten crust. *Tectonophysics*, **603**, 136-154.
- Zhang, Y., 1999. H<sub>2</sub>O in rhyolitic glasses and melts: measurement, speciation, solubility, and diffusion. *Reviews of Geophysics*, **37**, 493-516.
- Zurfluh, F.J., Beda, Hofmann, B.A., Gnos, E. & Eggenberger, U., 2011. Evaluation of the utility of handheld XRF in meteoritics. *X-ray Spectrometry*, **40**, 449-463.

## Appendix

### A.1 Portable X-ray (P-XRF)

Sample on the field have been analyzed with Niton XL3t (Thermo Fisher Scientific, Billerica, MA, USA) energy-dispersive P-XRF analyzer calibrated for geological sample. It is equipped with a miniature X-ray tube with an Au anode (max 50kV, 2W and 40 A), three primary beam filters and a silicon p-i-n diode detector (PIN). The size of the analyzed spot is 8 mm and penetrates the rock through few millimetres.

Standard calibrations have been determined using correlations between XRF analyzes for the whole rock in the laboratory and average P-XRF analyzes on the same sample in (Fig. 16). The estimated measurement error are Si:  $\pm 0.3$  mol; Al:  $\pm 0.04$  mol; Fe:  $\pm 0.03$  mol; Mg:  $\pm 0.05$  mol; Ca:  $\pm 0.01$  mol; K:  $\pm 0.005$  mol. Equations of the trend line for each element can be upload in the device to modified the standards of detection (Fig. 16).

### A.2 Whole-rock geochemistry

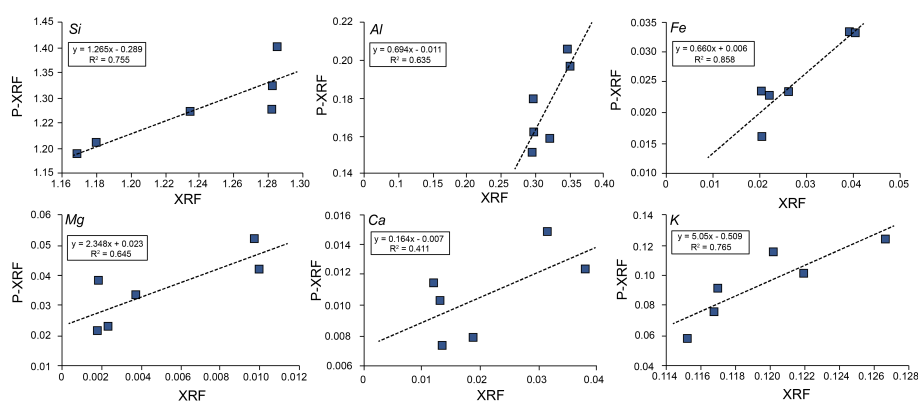


Figure 16: Comparison of P-XRF data and XRF data from the same set of samples (Joshep, 2013) the regression lines are used to set the standards calibration.

Rocks were crushed to a fine powder using a jaw crusher and tungsten swing mill prior to the preparation of a fused disc for major element and trace analysis. Glass disks were prepared for XRF analysis using 10 g of high purity trace element and REE element free flux (LiBO<sub>2</sub> = 32.83%, Li<sub>2</sub>B<sub>4</sub>O<sub>7</sub> = 66.67%, LiI = 0.50%) mixed with 1g of the rock sample. Whole-rock major element compositions were determined by XRF spectrometry on a PANalytical Axios Wavelength Dispersive spectrometer. The spectrometer is fitted with an Rh tube and with the following analyzing crystals: LIF200, LIF220, LIF420, PE, and PX1. The instrument is fitted with a gas-flow proportional counter and a scintillation detector. The gas-flow proportional counter uses a 90% Argon, 10% methane gas mixture. Major elements were analyzed on a fused glass disk at 50 kV and 50 mA tube operating conditions. Matrix effects in the samples were corrected for by applying theoretical alpha factors and measured line overlap factors to the raw intensities measured with the SuperQ PANalytical software. Control standards that were used in the calibration procedures for major element analyzes were NIM-G (Granite from the Council for Mineral Technology, South Africa) and BHVO-1 (Basalt from the United States Geological Survey, Reston).

### A.3 Mineral chemistry

Mineral major element compositions were analyzed using Leo<sup>®</sup> 1430VP Scanning Electron Microscope (SEM). Textures were studied in backscattered electron (BSE) mode and mineral compositions quantified by EDX (Energy Dispersive X-ray) analysis using an Oxford Instruments<sup>®</sup> 133 keV ED X-ray detector and Oxford INCA software. Beam conditions during the quantitative analyzes were 20 kV accelerating voltage and 1.5 nA probe current, with a working distance of 15mm and specimen beam current of -4.0nA. X-ray counts were typically  $\sim 7000$  cps, and the counting time was 50s live-time. Analyzes were quantified using natural mineral standards.

Rock Type sample	SM M5	GM1 DT04B	OM Ogn	L1 DT09	L1 DT01A	L12 DT06A	L12 DT02A	L12 DT07A	L3 DT03A
SiO <sub>2</sub>	65.80	55.77	54.74	74.29	72.91	70.10	79.21	74.02	70.52
TiO <sub>2</sub>	0.59	0.85	0.86	0.02	0.03	0.03	0.02	0.02	0.25
Al <sub>2</sub> O <sub>3</sub>	14.65	15.11	12.69	15.00	16.16	16.18	11.82	15.72	15.25
FeO <sub>T</sub>	7.87	11.82	12.20	0.65	0.36	2.53	0.25	0.24	1.88
MnO	0.10	0.11	0.12	0.03	0.01	0.04	0.01	0.01	0.03
MgO	4.55	11.35	10.99	0.41	0.27	1.06	0.27	0.15	1.97
CaO	1.82	2.05	3.03	3.44	3.37	3.32	1.63	2.52	3.57
Na <sub>2</sub> O	2.41	1.26	2.05	3.81	4.38	3.64	3.23	4.57	3.42
K <sub>2</sub> O	1.39	1.33	1.02	0.48	0.89	0.94	1.15	1.24	0.83
P <sub>2</sub> O <sub>5</sub>	0.06	0.02	0.05	0.03	0.02	0.05	0.05	0.01	0.06
LOI	0.06	0.40	0.00	0.42	0.73	0.60	0.76	0.49	0.77
Total	99.34	99.26	97.75	98.59	99.13	98.50	98.40	98.99	98.55
Mg#	0.31	0.43	0.41	0.30	0.34	0.22	0.43	0.30	0.42
A/CNK	2.07	2.78	1.73	1.49	1.41	1.59	1.45	1.38	1.54
V	127.35	215.71	215.55	6.19	6.08	12.99	5.41	7.32	43.74
Cr	316.57	1178.38	1479.83	23.06	16.67	115.78	13.71	17.78	288.18
Co	190.32	125.99	134.73	138.54	132.79	118.53	149.72	110.24	96.13
Ni	167.07	585.22	656.10	30.42	11.14	132.23	11.13	17.38	109.41
Cu	51.20	38.69	96.75	8.16	5.34	40.77	3.82	5.52	22.86
Zn	73.47	118.71	151.78	23.52	10.42	23.25	8.01	11.25	36.09
Rb	42.46	64.99	40.33	4.32	11.04	8.80	24.11	5.63	17.39
Sr	132.79	164.00	111.20	293.91	305.75	292.07	295.99	463.46	182.76
Y	16.58	19.66	17.71	6.34	1.21	5.39	0.27	0.32	2.44
Zr	146.87	99.58	95.52	9.65	23.33	11.49	14.11	25.68	57.55
Nb	4.87	4.58	4.64	0.10	0.03	0.38	0.07	0.06	1.67
Cs	0.26	1.36	0.70	0.10	0.11	0.07	0.21	0.13	0.60
Ba	360.11	283.32	252.89	100.96	141.71	196.49	946.96	112.23	127.25
Hf	3.77	2.72	2.64	0.34	0.59	0.30	0.37	1.08	1.45
Pb	8.02	5.45	6.89	19.87	9.96	15.46	8.98	20.18	12.69
Th	4.17	0.94	0.32	0.08	0.17	0.31	0.06	0.06	2.06
U	0.52	0.19	0.27	0.21	0.07	0.09	0.03	2.11	0.26
Sc	19.41	37.58	33.60	5.16	1.76	6.60	1.70	1.69	6.49
La	27.82	11.24	6.02	5.87	13.15	10.06	9.23	1.65	13.43
Ce	54.19	22.54	16.62	12.70	27.49	21.14	17.16	3.27	28.93
Pr	6.00	2.54	2.61	1.25	2.64	2.16	1.59	0.33	3.06
Nd	22.49	10.60	12.78	4.27	9.70	7.31	5.27	1.12	11.96
Sm	4.01	2.06	3.81	0.76	1.27	1.60	0.69	0.23	1.90
Eu	1.20	0.79	1.02	0.93	1.20	1.20	1.04	0.43	1.14
Gd	3.54	2.49	3.65	0.83	0.55	1.04	0.41	0.18	1.09
Tb	0.54	0.43	0.53	0.16	0.04	0.14	0.03	0.01	0.10
Dy	3.06	3.38	3.47	1.10	0.24	0.97	0.09	0.09	0.54
Ho	0.63	0.73	0.73	0.24	0.05	0.19	0.01	0.02	0.10
Er	1.77	2.29	2.04	0.72	0.15	0.55	0.02	0.02	0.24
Tm	0.25	0.32	0.30	0.11	0.02	0.08	0.00	0.01	0.04
Yb	1.67	2.25	2.03	0.88	0.15	0.57	0.01	0.06	0.22
Lu	0.24	0.31	0.31	0.12	0.02	0.08	0.00	0.01	0.03

Table I: Bulk-rock major compositions of leucosomes and metasedimentary rocks from the Brakspruit Quarry expressed in weight % oxide. Total iron as FeO.

Rock type Sample	L1 <sup>1</sup>		L1 <sup>2</sup>		L1 <sup>2</sup>		L1 <sup>2</sup>		L1 <sup>2</sup>		L2		SM		SM		GM		GM					
	DT09	Grt <sub>core</sub>	DT06A	Grt <sub>rim</sub>	DT06A	Grt <sub>core</sub>	DT02A	Grt <sub>rim</sub>	DT02A	Grt <sub>core</sub>	DT15	Grt <sub>rim</sub>	M5	Grt <sub>core</sub>	M5	Grt <sub>rim</sub>	DT04B	Grt <sub>rim</sub>	DT04B	Grt <sub>core</sub>	DT04B	Grt <sub>core</sub>	DT04B	Grt <sub>core</sub>
n	11	11	12	12	12	4	4	4	4	9	9	9	9	9	9	9	8	8	8	8	8	8	6	6
SiO <sub>2</sub>	37.51	39.17	39.46	39.28	39.35	38.61	38.61	39.35	39.57	40.21	40.02	39.00	39.30	38.84	39.50	39.77	38.84	39.50	39.77	38.84	39.50	39.77	38.84	39.77
TiO <sub>2</sub>	0.00	0.00	0.00	0.00	0.00	0.00	0.00	0.00	0.00	0.00	0.00	0.00	0.00	0.00	0.00	0.00	0.00	0.00	0.00	0.00	0.00	0.00	0.00	0.00
Al <sub>2</sub> O <sub>3</sub>	21.49	22.88	22.42	22.10	22.39	22.21	22.21	22.39	22.22	22.61	22.84	22.09	22.26	22.33	22.59	22.80	22.33	22.59	22.80	22.33	22.59	22.80	22.33	22.80
Cr <sub>2</sub> O <sub>3</sub>	0.12	0.00	0.12	0.19	0.00	0.19	0.19	0.00	0.28	0.21	0.00	0.00	0.00	0.00	0.00	0.00	0.00	0.00	0.00	0.00	0.00	0.00	0.00	0.00
FeO <sub>T</sub>	32.09	26.93	29.91	27.07	25.23	28.70	28.70	25.23	25.74	25.09	25.55	25.38	27.77	28.64	27.42	27.02	28.64	27.42	27.02	28.64	27.42	27.02	28.64	27.02
MnO	2.08	1.15	0.50	0.37	0.60	1.00	1.00	0.60	0.93	1.06	0.49	0.36	0.56	0.57	0.42	0.72	0.57	0.42	0.72	0.57	0.42	0.72	0.57	0.72
MgO	6.40	10.63	8.49	9.88	11.33	9.43	9.43	11.33	9.65	10.49	12.15	11.77	9.90	9.05	10.50	10.67	9.05	10.50	10.67	9.05	10.50	10.67	9.05	10.67
CaO	1.09	1.07	1.27	2.27	1.16	0.92	0.92	1.16	2.32	1.82	1.06	0.68	1.77	1.59	1.33	1.36	1.59	1.33	1.36	1.59	1.33	1.36	1.59	1.36
Na <sub>2</sub> O	-	-	-	-	-	-	-	-	-	-	-	-	-	-	-	-	-	-	-	-	-	-	-	-
K <sub>2</sub> O	-	-	-	-	-	-	-	-	-	-	-	-	-	-	-	-	-	-	-	-	-	-	-	-
total	100.79	101.84	102.16	101.16	100.05	101.06	101.06	100.05	100.70	101.49	102.10	99.30	101.57	101.02	101.75	102.34	101.02	101.75	102.34	101.02	101.75	102.34	101.02	102.34
ox	12.00	12.00	12.00	12.00	12.00	12.00	12.00	12.00	12.00	12.00	12.00	12.00	12.00	12.00	12.00	12.00	12.00	12.00	12.00	12.00	12.00	12.00	12.00	12.00
Si	2.93	2.94	2.97	2.98	2.98	2.95	2.95	2.98	3.01	2.98	2.97	2.98	2.93	2.93	2.97	2.94	2.93	2.97	2.94	2.93	2.97	2.94	2.93	2.94
Ti	0.00	0.00	0.00	0.00	0.00	0.00	0.00	0.00	0.00	0.00	0.00	0.00	0.00	0.00	0.00	0.00	0.00	0.00	0.00	0.00	0.00	0.00	0.00	0.00
Al	1.98	2.02	1.99	1.97	2.00	2.00	2.00	2.00	1.99	1.98	1.99	1.99	1.96	1.99	2.00	1.99	1.99	2.00	1.99	1.99	2.00	1.99	1.99	1.99
Cr	0.01	0.00	0.01	0.01	0.00	0.01	0.01	0.00	0.02	0.01	0.00	0.00	0.00	0.00	0.00	0.00	0.00	0.00	0.00	0.00	0.00	0.00	0.00	0.00
Fe <sup>3+</sup>	0.14	0.10	0.06	0.06	0.03	0.10	0.10	0.03	0.00	0.04	0.07	0.06	0.18	0.15	0.06	0.13	0.15	0.06	0.13	0.15	0.06	0.13	0.15	0.13
Fe <sup>2+</sup>	1.96	1.59	1.88	1.65	1.57	1.73	1.73	1.57	1.64	1.51	1.51	1.56	1.56	1.66	1.66	1.54	1.66	1.66	1.54	1.66	1.66	1.54	1.66	1.54
Mn <sup>2+</sup>	0.14	0.07	0.03	0.02	0.04	0.06	0.06	0.04	0.06	0.07	0.03	0.02	0.04	0.04	0.03	0.05	0.04	0.03	0.05	0.04	0.03	0.05	0.04	0.05
Mg	0.75	1.19	0.95	1.12	1.28	1.07	1.07	1.28	1.09	1.16	1.34	1.34	1.10	1.02	1.18	1.18	1.02	1.18	1.18	1.02	1.18	1.18	1.02	1.18
Ca	0.09	0.09	0.10	0.18	0.09	0.08	0.08	0.09	0.19	0.14	0.08	0.06	0.14	0.13	0.11	0.11	0.13	0.11	0.11	0.13	0.11	0.11	0.13	0.11
Na	-	-	-	-	-	-	-	-	-	-	0.00	0.00	0.00	-	-	-	-	-	-	-	-	-	-	-
K	-	-	-	-	-	-	-	-	-	-	0.00	0.00	0.00	-	-	-	-	-	-	-	-	-	-	-
total	8.00	8.00	8.00	8.00	8.00	8.00	8.00	8.00	8.00	7.90	8.00	8.00	7.90	7.91	8.00	7.93	7.91	8.00	7.93	7.91	8.00	7.93	7.91	7.93
X <sub>alm</sub>	0.67	0.54	0.63	0.56	0.53	0.59	0.59	0.53	0.55	0.52	0.51	0.52	0.55	0.58	0.56	0.54	0.58	0.56	0.54	0.58	0.56	0.54	0.58	0.54
X <sub>pyr</sub>	0.25	0.40	0.32	0.38	0.43	0.36	0.36	0.43	0.37	0.40	0.45	0.45	0.39	0.36	0.40	0.41	0.36	0.40	0.41	0.36	0.40	0.41	0.36	0.41
X <sub>spss</sub>	0.05	0.02	0.01	0.01	0.01	0.02	0.02	0.01	0.02	0.02	0.01	0.01	0.01	0.01	0.01	0.02	0.01	0.01	0.02	0.01	0.01	0.02	0.01	0.02
X <sub>grs</sub>	0.03	0.03	0.03	0.06	0.03	0.03	0.03	0.03	0.06	0.05	0.03	0.02	0.05	0.05	0.04	0.04	0.05	0.04	0.04	0.05	0.04	0.04	0.05	0.04

Table II: Representative scanning electron microscopy data for the garnets. Cation compositions include a stoichiometric estimate of Fe<sup>3+</sup> after Droop (1987). Mean values given, n = number of analyzes used to define the mean, L1<sup>1</sup>: small size L1 leucosome, L1<sup>2</sup>: large size (~ 1m) L1 leucosome.

Rock type Sample	L1		L1 <sup>2</sup>		L1 <sup>2</sup>		L1 <sup>2</sup>		L2		GM		SM		SM		OM	
	DT09 Pl <sub>rim</sub> 6	DT09 Pl <sub>core</sub> 6	DT06A Pl <sub>rim</sub> 6	DT06A Pl <sub>core</sub> 6	DT02A Pl <sub>rim</sub> 10	DT02A Pl <sub>core</sub> 10	DT03A Pl <sub>rim</sub> 8	DT03A Pl <sub>core</sub> 8	DT04B Pl <sub>inclusion</sub> 5	DT04B Pl <sub>core</sub> 6	DT03A Pl <sub>rim</sub> 8	DT03A Pl <sub>core</sub> 8	DT04B Pl <sub>inclusion</sub> 5	DT04B Pl <sub>core</sub> 6	M5 Pl <sub>inclusion</sub> 5	M5 Pl <sub>core</sub> 6	Ogn Pl <sub>core</sub> 10	Ogn Pl <sub>core</sub> 10
n	60.12	61.78	60.97	61.83	61.38	62.71	60.11	61.83	58.34	60.82	62.19	62.19	60.82	63.31	63.31	63.31	57.11	57.11
SiO <sub>2</sub>	-	-	-	-	-	-	-	-	-	-	-	-	-	-	-	-	-	-
TiO <sub>2</sub>	24.36	24.33	24.26	23.47	24.45	23.51	24.58	24.10	26.44	24.18	23.82	23.82	24.18	23.14	23.14	23.14	27.02	27.02
Al <sub>2</sub> O <sub>3</sub>	0.00	0.00	0.00	0.00	0.00	0.00	0.00	0.00	0.00	0.00	0.00	0.00	0.00	0.00	0.00	0.00	0.00	0.00
FeO <sub>T</sub>	7.12	6.65	6.54	6.05	6.46	5.54	6.97	5.87	8.88	6.53	5.91	5.91	6.53	5.23	5.23	5.23	9.76	9.76
CaO	7.36	6.99	7.68	8.15	8.02	8.44	7.56	8.26	6.28	7.41	7.95	7.95	7.41	8.39	8.39	8.39	5.73	5.73
Na <sub>2</sub> O	0.27	1.23	0.12	0.21	0.18	0.36	0.33	0.29	0.19	0.32	0.30	0.30	0.32	0.21	0.21	0.21	0.32	0.32
K <sub>2</sub> O	99.23	100.97	99.58	99.71	100.49	100.56	99.56	100.35	100.12	99.27	100.49	100.49	99.27	100.28	100.28	100.28	99.94	99.94
Total	8.00	8.00	8.00	8.00	8.00	8.00	8.00	8.00	8.00	8.00	8.00	8.00	8.00	8.00	8.00	8.00	17.00	17.00
ox	2.70	2.73	2.72	2.75	2.61	2.67	2.69	2.69	2.61	2.72	2.76	2.76	2.72	2.81	2.81	2.81	2.57	2.57
Si	-	-	-	-	-	-	-	-	-	-	-	-	-	-	-	-	-	-
Ti	1.29	1.27	1.28	1.23	1.22	1.18	1.30	1.21	1.39	1.28	1.25	1.25	1.28	1.21	1.21	1.21	1.44	1.44
Al	-	-	-	-	-	-	-	-	-	-	-	-	-	-	-	-	-	-
Cr	0.00	0.00	0.00	0.00	0.00	0.00	0.00	0.00	0.00	0.00	0.01	0.01	0.00	0.00	0.00	0.00	0.00	0.00
Fe <sup>2+</sup>	0.34	0.31	0.31	0.29	0.29	0.25	0.33	0.27	0.42	0.31	0.28	0.28	0.31	0.25	0.25	0.25	0.47	0.47
Ca	0.64	0.60	0.66	0.70	0.66	0.70	0.66	0.68	0.54	0.64	0.68	0.68	0.64	0.72	0.72	0.72	0.50	0.50
Na	0.02	0.07	0.01	0.01	0.01	0.02	0.02	0.02	0.01	0.02	0.02	0.02	0.02	0.01	0.01	0.01	0.02	0.02
K	4.98	4.97	4.98	4.99	4.80	4.83	5.00	4.87	4.98	4.97	5.00	4.98	4.97	5.00	5.00	5.00	5.00	5.00
total	0.34	0.32	0.32	0.29	0.30	0.26	0.33	0.28	0.43	0.32	0.29	0.43	0.32	0.25	0.25	0.25	0.48	0.48
X <sub>an</sub>	0.64	0.61	0.68	0.70	0.68	0.72	0.65	0.71	0.56	0.66	0.70	0.56	0.66	0.73	0.73	0.73	0.51	0.51
X <sub>ab</sub>	0.02	0.07	0.01	0.01	0.01	0.02	0.02	0.02	0.01	0.02	0.02	0.01	0.02	0.01	0.01	0.01	0.02	0.02
X <sub>or</sub>	-	-	-	-	-	-	-	-	-	-	-	-	-	-	-	-	-	-

Table III: Representative scanning electron microscopy data for the plagioclases. Cation compositions after Droop (1987). Mean values given, n = number of analyzes used to define the mean, L1<sup>1</sup>: small size L1 leucosome, L1<sup>2</sup>: large size (~ 1m) L1 leucosome.

# Chapter 5

## Synthesis, discussion and conclusion

### 5.1 Metamorphic study on the Bandelierkop Formation metapelites

#### 5.1.1 *P-T-t* history of the Bandelierkop Formation metapelites

In this thesis I have documented the metamorphic and anatexis history of the metasedimentary granulites from the Bandelierkop Formation in the Southern Marginal Zone (SMZ) of the Limpopo Belt, South Africa. The granulites, which have undergone a single metamorphic event at *c.* 2.71 Ga, provide insight into the evolution of the northern margin of the Kaapvaal Craton during the Neoproterozoic. The results drawn from this work, presented in Chapter 2 and Chapter 3, can be summarized as follows:

(I) Over the years, many different interpretations have been made concerning the origin of the SMZ and what geodynamic processes it highlights. In the early 90's, the SMZ was the focus of the geology group from the University of Johannesburg (previously Rand Afrikaans University). In their research, they set the metamorphic and geodynamic background for the Limpopo Belt (Du Toit, 1983; van Reenen *et al.*, 1992). Since then, the general consensus is that the SMZ is a reworked segment of greenstone belt and Kaapvaal Craton lithologies that has undergone a single granulitic event at 2.7 Ga and which is physically separated from the Kaapvaal craton by the Hout River Shear Zone. However, recent studies in the area (Rapopo, 2011; Laurent *et al.*, 2013, 2014, Laurent, 2012) and field investigations in the SMZ and the adjacent Kaapvaal craton revealed the current geological setting and the nature of the processes identified in the SMZ are not in total agreement with previous published information in the area.

In order to establish a solid background on which we can build arguments for anatexis processes, I proved that UHT metamorphism (Belyanin *et al.*, 2012) in the SMZ was an actual misinterpretation of the textural assemblages and the methods used for the *P-T* estimates predicated excess in temperature of 200 °C to 300 °C. This has been more or less acknowledged in the reply by the original authors, as they now say that the peak metamorphic conditions reached at least 900 °C. On the other hand, interpretation on the origin and the timing of emplacement of the Matok Igneous Complex (Rajesh *et al.*, 2014) are in complete disagreement with previously published geochronological and geochemical data (Laurent *et al.*, 2013, 2014).

As a consequence, the supposedly “new” geodynamic setting of the SMZ suggested by Rajesh *et al.* (2014)

using UHT metamorphism and data from the Matok Igneous Complex is unreasonable and/or equivocal.

(II) The application of phase equilibria modelling on metasedimentary rocks of the Bandelierkop Formation provides strong constraints on the prograde path followed by the metapelites. This path can be modelled by the following equation:  $P = 0.02T - 6.5$ ; with  $P$  the pressure in kbar and  $T$  the temperature in °C. Peak metamorphic conditions were attained at  $852.5 \pm 7.5$  °C and  $11.1 \pm 1.3$  kbar, followed by a near isothermal decompression to  $6.7 \pm 0.5$  kbar and isobaric cooling to  $T < 640$  °C. These  $P$ - $T$  conditions have been estimated by coupling several rocks from the same outcrop. Partial melting of the metasedimentary rocks produced two types of leucosomes: ante- to syn- peak metamorphism stromatic and deformed leucosomes (L1) and syn-decompression undeformed nebulitic leucosomes (L2). Petrographic evidence shows that the whole terrain has retained its textural granulitic assemblage. In the wall rock of the leucosomes, only a small proportion of the textural assemblage ( $< 5$  %) has been rehydrated to amphibolitic conditions. This  $P$ - $T$  path provides good support for further investigations on partial melting processes.

(III) LA-ICP-MS U-Pb dating of zircon from metasedimentary rocks and anatectic leucosomes indicate a tight time window for the whole metamorphic/anatectic event. Detrital ages on metapelites produce a range of concordant ages from *c.* 3.2 Ga to *c.* 2.7 Ga with a maximum deposit age of  $2733 \pm 11$  Ma. Metamorphic ages have been determined using the overgrowth in zircons from the leucosome and give a peak metamorphic age of  $2713 \pm 8$  Ma. Lastly, a fabric-crosscutting biotite and muscovite bearing pegmatite gave an age of  $2690 \pm 8$  Ma, which is consistent with the ages on Matok Igneous Complex ( $2689 \pm 6$  Ma) (Laurent *et al.*, 2013).

(IV) Combination of  $P$ - $T$  estimates and geochronological information unraveled a fast burial of the sediments ( $> 0.17$  cm.y<sup>-1</sup>), the whole metamorphic event lasting less than  $\sim 50$  Ma. As a comparison the burial rate for the Variscan orogen in the Bohemian massif is  $\sim 0.25$  cm.y<sup>-1</sup> (Schulmann *et al.*, 2002, 2005). In the Great Himalaya, Vance & Harris (1999) calculated a burial rate of 0.12 to 0.24 cm.y<sup>-1</sup>. In the Alps, a metamorphic study on garnet growth along the prograde path (Lapen *et al.*, 2003) showed the UHP unit of the Lago di Cignano, Italy, was buried at a speed of 0.23-0.47 cm.y<sup>-1</sup>. In those settings, lateral tectonic acts as the main mechanism responsible for burial of the sedimentary units and crustal thickening. On the other hand, François *et al.* (2014) found similar burial rate and  $P$ - $T$  path in the Pilbara Craton (Australia). They argue, based on numerical modelling ground that such metamorphic record can be explained by vertical tectonic via sagduction processes. However, the boundary conditions they chose do not allow any other type of tectonic process. Further work is required to investigate the impact of gravitational instabilities.

Consequently, because of the shape, the duration of the  $P$ - $T$ - $t$  path and analogies with late Paleozoic and present geodynamic settings, I suggest that horizontal shortening is more than likely responsible for the formation of the SMZ as an active margin in an orogenic system. These findings support the hypothesis of continental collision during the Neoproterozoic. To date, the SMZ of the Limpopo Belt is now one of the best-constrained Neoproterozoic geodynamic settings.

### 5.1.2 Consequences on the evolution of the Kaapvaal craton

The origin of the SMZ is one of the main focuses of the Centre for Crustal Petrology Research Group in Stellenbosch University, South Africa. Investigation on the SMZ formation was carried on after publication of the manuscripts contained in Chapters 2 and 3. In this section, I extend the interpretative model of the evolution of the northern margin of the Kaapvaal craton using previous published results and new hypotheses.

The well-constrained P-T-t loop strongly support lateral tectonic during the Neoproterozoic. However, the chaotic distribution pattern of the Bandelierkop Formation metasedimentary unit (Fig. 1.6) and the structural framework of the SMZ (Smit *et al.*, 1992) argue for gravitational redistribution inputs (Gerya *et al.*, 2000). The diapiric rise of partially melted, hot granulite upward in the crust might cause the formation of local convection cells that allow the movement of some of the ascending granulite blocks near the Hout River Shear Zone. By combination of the data presented in this thesis and the data collected by Laurent (2012) on the granitic intrusions, I propose the following evolution for the northern edge of the Kaapvaal craton (Fig. 5.1):

**2800 Ma - 2750 Ma:** Following the accretion of the 3.0-2.9 Ga Kaapvaal Craton basement with volcanic/continental arcs (Poujol *et al.*, 2003; Laurent, 2012), the North-South lateral shortening kept on going with the south-vergent subduction of the Paleo-ocean separating the Witwatersrand block (present day South) from an exotic block (present day North). Contemporary to such event, products of erosion (Witwatersrand group) filled up the foreland basins forming in the southern and eastern part of the orogeny, covering the cratonic basement ( $> 3000$  Ma) and the Dominion Supergroup deposit ( $3074 \pm 6$  Ma to  $2970$  Ma) (Johnson *et al.*, 2006). Like in any convergence zone, sediments from the erosion of the different units of the Kaapvaal Craton and the exotic block deposited along the active margin to form an accretionary wedge (Simpson, 2010). Magmatism within this period produced fabric-parallel large batholiths such as the Turfloop and Lekkersmaak intrusions, which are interpreted to be the results of the partial melting of recycled metasediments and TTG from previously accreted small volcanic/continental arcs (Laurent 2012, Henderson *et al.*, 2000). The possible presence of a subducting slab may have been responsible for metasomatism of the mantle wedge and a volcanic activity at surface from which the Pietersburg, Rhenosterkoppies and Giyani greenstone belt might be related. In the case of the Kaapvaal craton, we can assume an important part of the lithospheric mantle under the Kaapvaal craton was metasomatised due to the previous volcanic/continental-arc accretion (Poujol *et al.*, 2003; Laurent, 2012).

**2750 Ma - 2700 Ma:** The end of the sedimentation in the accretionary wedge at  $2733 \pm 11$  Ma indicates the beginning of the continental collision between the Kaapvaal Craton and the exotic craton. During the shortening, the Pietersburg block (i.e. accreted small continental/volcanic arcs) was trapped and deformed between the two cratonic blocks colliding. Lava flow from back-arc volcanism, i.e. the Ventersdorp Supergroup, started covering the Witwatersrand Central Group at  $2714 \pm 8$  Ma in the foreland basin (Eriksson *et al.*, 2006). Lateral motion led to the burial and partial melting of the sediments accumulated in the accretionary wedge to 35 km depth at  $2713 \pm 8$  Ma. The compression phase probably triggered the exhumation of allochthonous volcanic arc relic in the Pietersburg block such as the Pietersburg, Rhenosterkoppies and Giyani greenstone belt (de Wit *et al.*, 1992; Brandl *et al.*, 2006; Laurent, 2012; Kramer *et al.*, 2014).



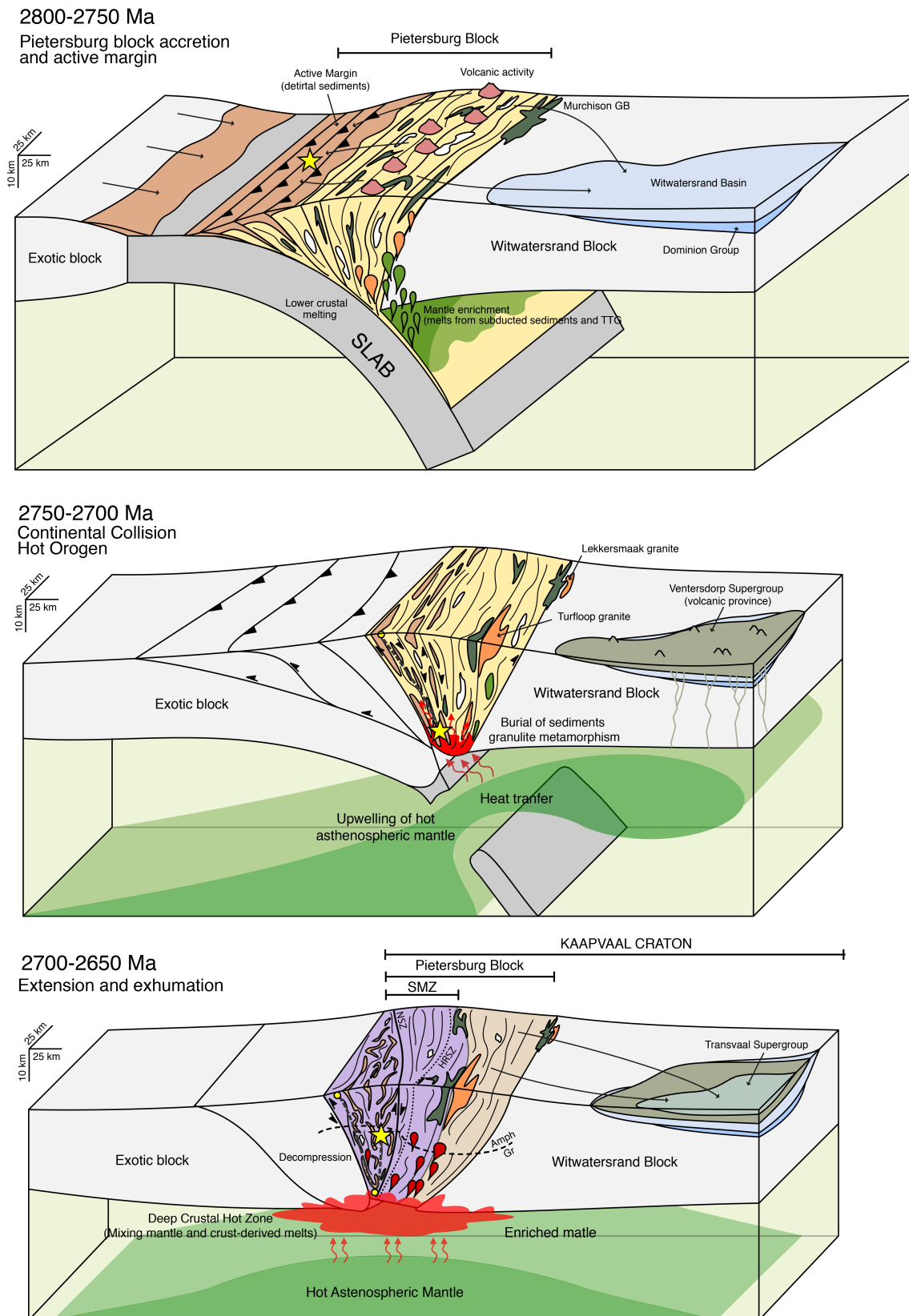


Figure 5.1: Conceptual model of the evolution of the northern margin of the Kaapvaal craton (Pietersburg Block) between 2800 Ma and 2650 Ma (based on metamorphic information and studies of the igneous activity). Modified after Laurent 2012. See text for details. Structures have been verticalised to correspond with today structural framework but do not necessarily represent the Neoproterozoic structural setting. The bottom sketch shows a geodynamic environment close to the present day situation. NSZ: N'tablala Shear Zone, HRSZ: Hout River Shear Zone.

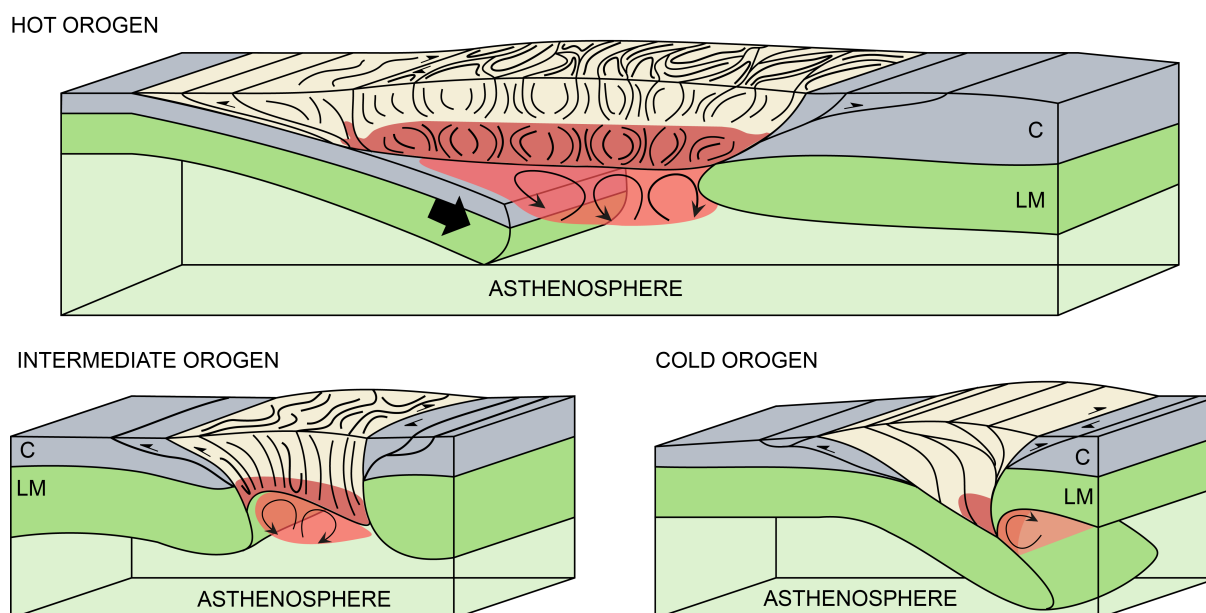


Figure 5.2: Example of different orogenic settings in time and space from hot to cold. In the case of the Pietersburg block, Hot to intermediate orogen is the most likely scenario to explain the origin of the SMZ. C: crust; LM: Lithospheric mantle. After Chardon *et al.*(2009).

**2700 Ma - 2650 Ma:** The Ventersdorp volcanism spreaded all over the Kaapvaal Craton, covering the basement and the sedimentary deposits (Armstrong *et al.*, 1991; Burke *et al.*, 1985). A series of undeformed plutons syn- to post- Hout River Shear Zone activity, intruded both the SMZ and the Kaapvaal craton at 2670-2700 Ma (Laurent *et al.*, 2013). These intrusions, as well as the  $2680 \pm 6$  Ma undeformed pegmatites in the Brakspruit quarry indicate the end of the collision. Because the chemical signature of the intrusions possesses a strong mantle-derived component (Laurent, 2013), I suggest the trigger mechanism for the genesis of such magmatic and volcanic activity (Ventersdorp Supergroup) to be an asthenospheric upwelling generated by a slab window subsequent to the collision in the mantle wedge or the Kaapvaal Craton in general (Lobach-Zhuchenko *et al.*, 2008; Heilimo *et al.*, 2010, Laurent *et al.*, 2014).

Contemporaneous of the magmatic and volcanic activity, the granulitic zone of the SMZ was exhumed with the combination of lateral motion (extension post-collision) and possible gravitational redistribution (Geyra *et al.*, 2000) as it is observable in present continental-collision settings (Whittington & Treolar, 2002; Beaumont *et al.*, 2006). It could have brought close to each other blocks of different ages and the granulite rocks next to the amphibolite. This episode is accompanied by the deposition of the Transavaal Supergroup in the foreland basin (Eriksson *et al.*, 2006).

In this scenario, the Limpopo orogeny, or at least the formation of the so-called SMZ, can be regarded as taking place in a hot to intermediate orogen setting (Chardon *et al.*, 2009; Cagnard *et al.*, 2011) (Fig. 5.2). Similar  $P$ - $T$ - $t$  path and structural pattern are found in other locations such as the Abitibi-Opatika sub-province, Superior Province - Neoproterozoic (Valli *et al.*, 2006); the Calos Chaga batholith, Braziliano orogeny - Neoproterozoic (Cavalcante *et al.*, 2013), the Bohemian massif - Variscan orogeny (Schulmann *et al.*, 2002, 2005) and in modern mountain range, Central Himalaya (Whittington & Treolar, 2002; Beaumont *et al.*, 2006). This implies lateral tectonic was efficient at the end of the Archean with additional

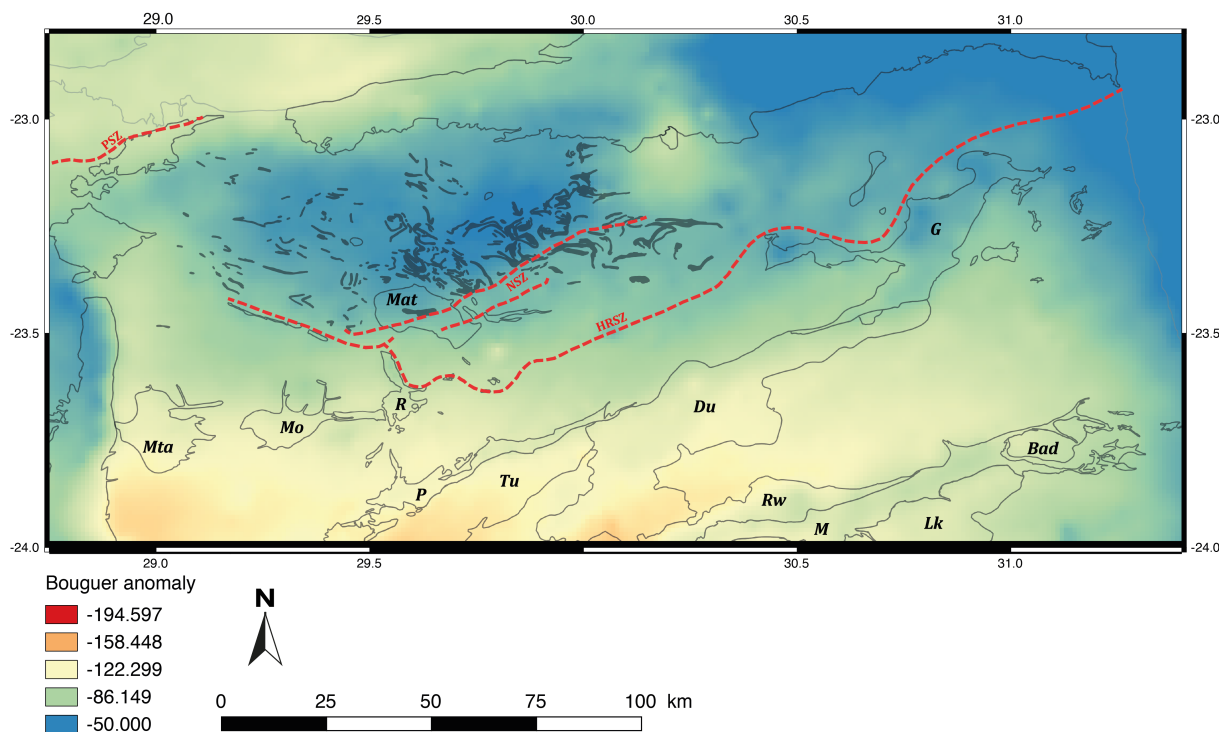


Figure 5.3: Gravimetric map of the Pietersburg block area. The metasedimentary unit north to the N'Tabalala Shear Zone (NSZ) has a strong negative Bouguer anomaly. The NSZ separates the granulitic rocks from the amphibolitic rocks. The Hout River Shear Zone (HRSZ) does not appear to be a relevant limit. PSZ: Palala Shear Zone. Source: Council for Geoscience.

post-continental collision gravitational redistribution within the lower and middle crust.

It seems more appropriate, regarding these new findings, to consider the SMZ as part of the northern margin of the Kaapvaal craton rather than an actual section of the 3-part Limpopo Belt. The area between the Letaba Shear Zone and the Palala Shear Zone (a.k.a. the Pietersburg block) (Fig.1.6, 5.1) formed by continuous accretion of small volcanic and continental arcs along the northern margin of the Kaapvaal craton. Moreover, the boundaries of the SMZ have been recently reconsidered (Kramer *et al.*, 2014). The South African Council of Geosciences performed a survey aiming to measure the gravimetric anomalies in the whole South Africa. In the SMZ, the gravimetry data does not show evidence of a sudden change in Bouguer anomaly close to the HRSZ (Fig. 5.3). The transition from the N'Tabalala Shear Zone (NSZ) to the Duiwelskloof intrusion is gradual. The NSZ seems to be a more important structure than the HRSZ (Fig.1.6, 5.1). Therefore, the definition "SMZ" is obsolete. The SMZ could represent only the granulitic portion of the Pietersburg block or the entire Pietersburg block itself (Fig. 1.5). In both cases, the denomination Southern Marginal Zone should not be used anymore. This area represents the last episode of Pietersburg block formation event and documents the continental collision between two large blocks in hot to intermediate orogenic settings.

## 5.2 Partial melting processes and crustal differentiation

### 5.2.1 Chemical investigation of the Bandelierkop formation anatectites

A second contribution to this work, presented in Chapter 4, includes a detailed investigation of  $K_2O$ -poor leucosome formation of the SMZ metapelites, with important implications for crustal differentiation mechanisms. This was done by documenting field evidence using new analytical techniques and modelling the influence of peritectic assemblages, volume of equilibrium and water diffusivity on the magma composition during incongruent melting of biotite in a reconstructed pelitic source. Key insights into these processes are summarized as follows:

(I) The study of the anatectic features of the Bandelierkop Formation shows there is a chemical mismatch between the leucosome, the melt and the granite. Leucosomes are low in potassium and high in calcium compared to the melt and the S-type granite. In the case of fluid-absent anatexis under granulite facies conditions, I argue, based on petrographic grounds that the melt or magma (melt + peritectic phases) must segregate from the source and leaves the system during the prograde history of the rock. Melt-reintegrated pseudosection showed the volume of melt produced during the anatexis is larger than the actual volume of the leucosomes. The preservation of granulitic textural assemblages in the wall rock of the leucosomes and the poorly defined  $K_2O$ -enriched selvage argue for melt loss towards upper crustal level and no diffusion back to the melanosome. Therefore, the leucosomes most likely represent melt transfer sites and are not magma cumulates crystallizing during the retrograde history of the terrain. Consequently, the leucosome can be defined as follows: at the scale of the macroscopic sample, the leucosome is a quartzo-feldspathic rock derived from segregated melts but is neither only a melt-depleted protolith nor a crystallized magma. At the scale of the outcrop, leucosome and melanosome represent what is left over in the crust after extraction of the magmatic batches, but both objects are not necessarily related. However, at the scale of the crust, the leucosome is part of the residuum, which is in agreement with efficient crustal differentiation, the melt being present only for a short period in the source. Based on these observations, I attempted to model leucosome chemistry through classic “equilibrium” (i.e. full-rock system) partial melting process. This kind of mechanism failed to explain the positive Eu anomaly in the crystallized anatectic feature and required significant cooling to reach solid state.

(II) One aspect of this PhD project was to develop new analytical techniques that could be used to investigate anatectic features from the outcrop scale to the mineral scale. The portable X-ray fluorescence (P-XRF) analyzer helped to quantify the repartition of major elements at the scale of the outcrop. This technique provides an instantaneous map of Fe, Mg, Ca, Si, Al, K abundances in the analysed rock section. Results obtained through this technique are in good agreement with the results obtained with the classic XRF analyses on whole rock samples. This technique brings new opportunities for the study of complex geological terrains and could be applied to other migmatitic outcrops and magma mingling features. In this study, P-XRF mapping revealed  $K_2O$  content in the wall rock of the leucosome cannot counterbalance the lack of potassium in the anatectic features.

At the scale of the macroscopic sample, small volumes of leucosomes have been scanned to unravel their

internal organization and the distribution of peritectic phases (i.e. garnet and orthopyroxene). This showed flow structures inside the leucosome and documents the maturation degree of the garnet (Taylor *et al.*, 2010). Thanks to this technique I showed that several steps of leucosome formation can be found in the same outcrop. These observations are consistent with the model suggested by Bons *et al.* (2004, 2009) who argued leucosomes are built by successive magma batches from the same or a nearby source and follow power-law distribution (Soesoo *et al.*, 2004).

(III) Processes involving full-rock system (i.e. whole rock composition) failed to explain the formation of leucosomes at peak metamorphic conditions ( $\sim 870$  °C and  $\sim 11.0$  kbar). The main chemical characteristic of the leucosomes lies in its low  $K_2O$  and high  $CaO$  content. Thus, I modelled the anatectic structures formed by melting in a sub-rock system in which the amount plagioclase in the starting assemblage is reduced compared to the full-rock system (Johannes & Koepke, 2001; Acosta-Vigil & London, 2006). From a theoretical point of view, I proposed only a part of the plagioclase is available for the melting reactions, which leaves a variable proportion of the core of the mineral untouched. The melt produced through this process will have a composition different from the full-rock system melt, which will induce co-precipitation of quartz, plagioclase and in less proportion garnet from the melt. The melt leaves the source entraining a variable amount of ferromagnesian peritectic minerals towards the melt transfer site and dumps plagioclase and quartz while being extracted towards the surface. From this process will result the formation of a  $K_2O$ -poor, Eu-enriched, quartz + plagioclase + garnet residue.

This study shows leucosome chemistry can be achieved by considering partial melting of a sub-textural assemblage, in which plagioclase is the limiting component; peritectic entrainment, melt loss and water diffusivity within the melt transfer site on the prograde path. Forcing the dissolution of the outer rim of the plagioclase into the melt in the starting material has direct consequences on the water activity ( $a_{H_2O}$ ) in the melt transfer site. Water gradient coupled with melt loss from the melt transfer site will trigger precipitation of plagioclase, quartz and in less proportion garnet from the melt. The maficity of the leucosome is mainly controlled by the amount of peritectic garnet entrained. Such mechanism produces solid-state quartz + plagioclase + garnet objects at peak metamorphic conditions and there is a good correlation between chemistry of leucosomes from the modelling and the chemistry of natural  $K_2O$ -poor leucosomes.

## 5.2.2 Consequence of partial melting of sub-rock systems and water diffusivity on crustal differentiation

The lack of S-type granite in the SMZ keeps the investigation of the final product of crustal differentiation difficult. Because of erosion processes, especially in these types of Precambrian terrains, the access to the full SLG (source - leucosome - granite) system is nearly impossible. Nevertheless, the preservation of  $K_2O$ -poor leucosomes into the lower crust highlights processes that may have a strong control on crustal differentiation mechanisms. Field evidence and numerical modelling suggest the whole system is articulated around changes in volume of equilibration. After the interconnection of the magma pockets and the development of melt transfer site network, water diffuses in the magma column. The consumption of plagioclase and water diffusivity in the melt transfer site increase conjointly. Consequently, the precipitation of plagioclase, quartz and minor garnet from the melt is enhanced. When all the plagioclase is available for the reaction (i.e. the core has been consumed), the system reaches its full efficiency. From this process results the formation of near-dry felsic residuum at peak metamorphism conditions (i.e. L1 leucosomes).

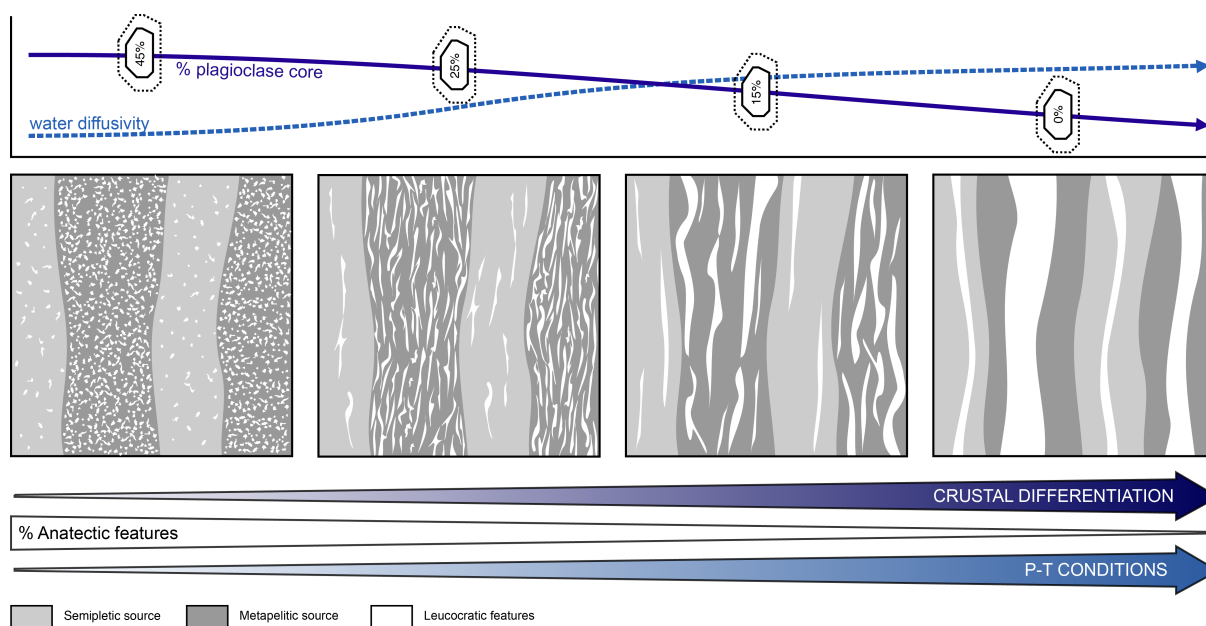


Figure 5.4: Ideal scenario of crustal differentiation through partial melting of a heterogeneous source: alternation of metapelite (ultra fertile source) semipelite (less fertile source). The leucocratic features are formed in situ and follow a fractal law of distribution. Along the prograde path, the consumption of plagioclase increases (i.e. % of remaining plagioclase core decreases), interconnectivity between the different leucocratic pockets augments over time to form melt transfer site. Water diffusivity within the “plumbing system” increases as the plagioclase is consumed. Consequently, the percentage of anatectic features in the whole volume tends towards 1 as crustal differentiation reaches its fully efficiency.

The water might also diffuse to the middle crust. This could be responsible for the amphibolite isograd observed south of the granulitic zone in the SMZ.

The presence of peak metamorphic biotite in the mafic residuum and difference in plagioclase chemistry between the leucosome and the restite indicate the melting reactions did not reach its full capacity. Moreover, the rock was still fertile enough after formation of the L1 leucosomes to produce L2 nebulitic leucosomes during the decompression episode.

In the particular case of the SMZ anatectites, there is a strong link between the amounts and the nature of leucosomes, the diffusion of water and the degree of crustal differentiation. As suggested by Soesoo *et al.* (2004), the leucosomes follow a fractal-law of distribution: the more they are, the less efficient the crustal differentiation was. In the model I present,  $K_2O$ -poor leucosomes crystallize more efficiently during the prograde path when water diffusivity in the melt transfer site augments (Fig. 5.4). Consequently, as the melting of the source increases, the source evolves from a sub-rock system to a full-rock system. The partial melting reaction produces a larger amount of melt (bigger magma batches). Therefore, building large leucosomes requires less magma batches accumulation and leaves the mafic residuum near-total depletion. Ideally, the system evolves towards a state of complete equilibrium from the sample to the whole terrain. In such scenario, the number of leucosomes in the outcrop should tend towards 1. As such observations have not been made in the SMZ, we can argue crustal differentiation did not reach its full efficiency. Further work is required on different migmatitic terrains to confirm this hypothesis.

### 5.3 General conclusion

This thesis presents detailed aspects of  $K_2O$ -poor leucosome formation in a Neoproterozoic continental collision zone. Results drawn from this study have strong impacts on two important geological issues: when did lateral tectonic start? And what are the mechanisms that control crustal differentiation?

The late history of the Pietersburg block formation along the northern margin of Kaapvaal craton documents one of the oldest examples of continental collision. This study demonstrates the chronometamorphic record in geological samples is a very powerful tool to understand paleo-geodynamic settings. The metamorphic record combined to geochronological information strongly suggests this orogenic episode occurred in hot to intermediate orogenic setting involving both lateral motion and gravitational redistribution. Therefore, horizontal tectonic was already an active process at *c.* 2.7 Ga in the Kaapvaal craton.

The 2.7 tectometamorphic event exhumed the granulitic lower crust, which offers the possibility to investigate partial melting processes in the source. Partial melting occurred in fluid-absent condition through muscovite and biotite breakdown and generates S-type related magmas. It produces through “disequilibrium” mechanisms, magma (melt + peritectic) batches that segregate and escape the source. This leaves a residuum made of melt-depleted metapelites and  $K_2O$ -poor / CaO-rich leucosomes. The leucosomes represent the fossilized print of the plumbing system through which the magma was transferred to crustal upper levels to build large magma accumulation structures. This specific composition of the leucosome may have direct consequences on crustal differentiation mechanisms.

In light of this study it seems that the process that generates  $K_2O$ -poor leucosomes is articulated around the behaviour of water. Its concentration in the melt has a direct influence on the chemistry of the residuum and consequently on the chemistry of the granitoid intrusions. It also indicates that crustal differentiation may not be fully achieved. This process will be fully efficient when the different volumes (terrain, outcrop, sample, mineral) will all be in state of “equilibrium”.

## REFERENCES

- Acosta-Vigil, A., London, D. & Morgan VI, G.B. 2006. Experiments on the kinetics of partial melting of a leucogranite at 200 MPa H<sub>2</sub>O and 690-800°C: compositional variability of melt during the onset of H<sub>2</sub>O-saturated crustal anatexis. *Contributions to Mineralogy and Petrology*, **151**, 539-557.
- Beaumont, C., Nguyen, M. H., Jamieson, R. A. & Ellis, S. 2006. Crustal flow modes in large hot orogens. *Geological Society, London, Special Publications*, **268**, 91-145.
- Belyanin, G.A., Rajesh, H.M., Sajeev, K. & Van Reenen, D.D., 2012. Ultrahigh-temperature metamorphism from an unusual corundum+orthopyroxene intergrowth bearing Al-Mg granulite from the Southern Marginal Zone, Limpopo Complex, South Africa. *Contributions to Mineralogy and Petrology*, **164s**, 457-475.
- Brandl, G., Cloete, M., & Anhaeusser, C. R. 2006. Archaean greenstone belts. *The Geology of South Africa*, 9-56.
- Bons, P. D., Arnold, J., Elburg, M. A., Kalda, J., Soesoo, A. & van Milligen, B. P., 2004. Melt extraction and accumulation from partially molten rocks. *Lithos*, **78**, 25-42.
- Bons, P. D., Becker, J. K., Elburg, M. A. & Urtson, K., 2009. Granite formation: Stepwise accumulation of melt or connected networks?. *Earth and Environmental Science Transactions of the Royal Society of Edinburgh*, **100**, 105-115.
- Cagnard, F., Barbey, P. & Gapais, D., 2011. Transition between Archaean-type and modern-type tectonics: Insights from the Finnish Lapland Granulite Belt. *Precambrian Research*, **187**, 127-142.
- Cavalcante, G.C.G., Egydio-Silva, M., Vauchez, A., Camps, P. & Oliveira, E., 2013. Strain distribution across a partially molten middle crust: Insights from the AMS mapping of the Carlos Chagas Anatexite, Araçuaí belt (East Brazil). *Journal of Structural Geology*, **55**, 79-100.
- Chardon, D., Gapais, D. & Cagnard, F., 2009. Flow of ultra-hot orogens: A view from the Precambrian, clues for the Phanerozoic. *Tectonophysics*, **477**, 105-118.
- South African Council for Geoscience, [www.geoscience.org.za](http://www.geoscience.org.za)
- De Wit, M.J., Van Reenen, D.D. & Roering, C., 1992. Geologic observations across a tectono-metamorphic boundary in the Babangu area, Giyani (Sutherland) greenstone belt, South Africa. *Precambrian Research*, **55**, 111-122.
- Du Toit, M.C., Van Reenen, D.D. & Roering, C., 1983. Some aspects of the geology, structure and metamorphism of the Southern Marginal Zone of the Limpopo metamorphic complex. *Geological Society of South Africa, Special Publications*, **8**, 121-142.
- Eriksson, P.G., Mazumder, R., Catuneanu, O., Bumby, A.J. & Ountsché Ilondo, B. Precambrian continental freeboard and geological evolution: A time perspective. *Earth-Science Reviews*, **79**, 165-204.
- François, C., Philippot, P., Rey, P. & Rubatto, D., 2014. Burial and exhumation during Archean sagduction in the East Pilbara Granite-Greenstone Terrane. *Earth and Planetary Sciences Letters*, **215**, 57-72.
- Gerya, T.V., Perchuck, L.L., Van Reenen, D.D. & Smit, C.A., 2000. Two-dimensional numerical modelling of pressure-temperature-time paths for the exhumation of some granulite facies terrains in the Precambrian. *Journal of Geodynamics*, **30**, 17-35.
- Heilimo, E., Halla, J. & Holtta, P., 2010. Discrimination and origin of the sanukitoid series: geochemical constraints from the Neoproterozoic western Karelian Province (Finland). *Lithos*, **115**, 27-39.
- Henderson, D.R., Long, L.E. & Barton Jr., J.M., 2000. Isotopic ages and chemical and isotopic composition of the Archaean Turfloop Batholith, Pietersburg granite-greenstone terrane, Kaapvaal Craton, South Africa. *South African Journal of Geology*, **103**, 38-46.



Johannes, W. & Koepke, J., 2001. Incomplete reaction of plagioclase in experimental dehydration melting of amphibolite. *Australian Journal of Earth Sciences*, **48**, 581-590.

Johnson, M.R., Anhaeusser, C.R. Thomas, R.J., 2006. The geology of South Africa, Geological Society of South Africa, Council for Geoscience, Pretoria 0001, South Africa, British Geological Survey, 691pp.

Kramers, J.D., Henzen, M. & Steidle, L. 2014. Greenstone belts at the northernmost edge of the Kaapvaal Craton: Timing of tectonic events and a possible crustal fluid source. *Precambrian Research*, **253**, 96-113.

Lapen, T.J., Johnson, C.M., Baumgartner, L.P., Mahlen, N.J., Beard, B.L. & Amato, J.M., 2003. Burial rates during prograde metamorphism of an ultra-high-pressure terrane: an example from Lago di Cignana, western Alps, Italy. *Earth and Planetary Sciences Letters*, **215**, 57-72.

Laurent, O., 2012. Les changements géodynamiques à la transition Archeen-Proterozoïque: étude des granitoides de la marge Nord du Craton du Kaapvaal (Afrique du Sud). University Thesis Université Blaise Pascal, Clermont Ferrand.

Laurent, O., Paquette, JâL., Martin, H., Doucelance, R. & Moyen, J-F, 2013. LA-ICP-MS dating of zircon from Mesoâ and Neoproterozoic granitoids of the Pietersburg block (South Africa): Crustal evolution at the northern margin of the Kaapvaal craton. *Precambrian Research*, **230**, 209-226.

Laurent, O., Rapopo, M., Stevens, G., Moyen, J-F., Martin, H., Doucelance, R. & Bosq, A. 2014. Constraining petrogenesis of Mg-K and Fe-K granitoids and implications for post-collisional magmatism: Case study from the late-Archean Matok pluton (Pietersburg, South Africa). *Lithos*, **197**, 131-149.

Lobach-Zhuchenko, S. B., Rollinson, H., Chekulaev, V. P., Savatkov, V. M., Kovalenko, A. V., Martin, H. & Arestova, N. A., 2008. Petrology of a Late Archean, highly potassic, sanukitoid pluton from the Baltic Shield: insights into Late Archean mantle metasomatism. *Journal of Petrology*, **49**, 393-420.

Poujol, M., Robb, L.J., Anhaeusser, C.R. & Gericke, B., 2003. A review of the geochronological constraints on the evolution of the Kaapvaal Craton, South Africa. *Precambrian Research*, **127**, 181-213.

Rajesh, H.M., Santosh, M., Wan, Y., Lui, D., Lui, S.J. & Belyanin, G.A., 2014. Ultrahigh temperature granulites and magnesian charnockites: Evidence for Neoproterozoic accretion along the northern margin of the Kaapvaal Craton. *Precambrian Research*, **246**, 150-159.

Rapopo, M., 2012. Petrogenesis of the syntectonic Matok Pluton in the Limpopo Belt (South Africa) and its implications of the geodynamic environment. University thesis, Stellenbosch University.

Schulmann, K., Kroner, A., Hegner, E., Wendt, I., Konopasek, J., Lexa, O. & Stipska, P., 2005. Chronological constraints on the pre-orogenic history, burial and exhumation of deep-seated rocks along the eastern margin of the Variscan Orogen, Bohemian Massif, Czech Republic. *American Journal of Science*, **305**, 407-448.

Schulmann, K., Schaltegger, U., Josef, J., Thompson, A.B. & Edel, J-B., 2002. Rapid burial and exhumation during orogeny: Thickening and synconvergent exhumation of thermally weakened and thinned crust (Variscan orogen in Western Europe). *American Journal of Science*, **302**, 856-879.

Simpson, G.D.H., 2010. Formation of accretionary prisms influenced by sediment subduction and supplied by sediments from adjacent continents. *Geology*, **38**, 131-134.

Smit, C. A., Roering, C. & Van Reenen, D. D., 1992. The structural framework of the southern margin of the Limpopo Belt, South Africa. *Precambrian Research*, **55**, 51-67. Soesoo, A., Kalda, J.,

Bons, P., Urtson, K. & Kalm, V., 2004. Fractality in geology: a possible use of fractals in the studies of partial melting processes. *In Proceedings of the Estonian Academy of Sciences, Geology*, **53**, 13-27

Taylor, J. & Stevens, G., 2010. Selective entrainment of peritectic garnet into S-type granitic mag-

mas: Evidence from Archaean mid-crustal anatexites. *Lithos*, **120**, 277-292.

Valli, F., Guillot, S. & Hattori, K.H., 2004. Source and tectono-metamorphic evolution of mafic and pelitic metasedimentary rocks from the central Quetico metasedimentary belt, Archean Superior Province of Canada. *Precambrian Research*, **132**, 155-177.

Vance, D. & Harris, N., 1999. Timing of prograde metamorphism in the Zaskar Himalaya. *Geology*, **27**, 395-398.

Van Reenen, D.D., Roering, C., Ashwal L.D. & de Wit, M.J., 1992. Regional geological setting of the Limpopo Belt. *Precambrian Research*, **55**, 1-5.

Whittington, A. G. & Treloar, P. J., 2002. Crustal anatexis and its relation to the exhumation of collisional orogenic belts, with particular reference to the Himalaya. *Mineralogical Magazine*, **66**, 53-91.

# Appendices

# Appendix A

## Glossary

**Anatexis:** It describes partial melting of the continental crust. It is generally accompanied by deformation, which enables other processes to occur, such as segregation of the melt from the solid, migration of the melt, fractional crystallization and magma flow.

**Diatexite migmatites:** A migmatite of liquid-dominated behaviour. Pre-partial melting structures are absent and are commonly replaced by anatectic flow structures. The newly formed rocks can range from predominantly leucocratic to predominantly mesocratic, to predominantly melanocratic. Unmelted parts (i.e. starting material) occur as schollen and enclaves.

**Granites:** Cf. granite classification Fig A.1.

GRANITOID TYPES			ORIGIN	GEODYNAMIC ENVIRONMENT
	<i>Barbarin (1999)</i>	<i>Chapell &amp; White (1974, 1983)</i>		
Muscovite-bearing Peraluminous granitoids	MPG	S	CRUSTAL ORIGIN Peraluminous granitoids	CONTINENTAL COLLISION
Cordierite-bearing Peraluminous granitoids	CPG	S		
K-rich calc-alkaline granitoids (high K - low Ca)	KCG	I	MIXED ORIGIN Metaluminous and calc-alkaline granitoids	TRANSITIONAL REGIMES
Amphibole-bearing calc-alkaline granitoids (low K - high Ca)	ACG	I		SUBDUCTION
Arc tholeiitic granitoids	ATG	M		
Mid-oceanic ridge Tholeiitic granitoids	RTG	M		
Peralkaline and alkaline granitoids	PAG	A	MANTLE ORIGIN Tholeiitic, alkaline and peralkaline granitoids	OCEANIC SPREADING OR CONTINENTAL DOMING AND RIFTING

Figure A.1: Synthetic table showing the relationships between petrogenetic types of granites, their origins and chemistry, and the geodynamic environment; modified after Barbarin (1999) and Clemens *et al.* (2011).

**Leucosome:** General term for the lighter-colored part in a migmatite. It dominantly consists of feldspar and quartz. The leucosome derives from segregated melt but does not necessarily have the composition of an anatectic melt. Leucosome can occur in situ or intrude upper levels.

**Melanosome:** A residuum that is composed predominantly of dark-colored minerals (biotite, garnet, cordierite, orthopyroxene, hornblende, clinopyroxene). The melanosome is the solid, residual fraction left after the melt fraction has been extracted.

**Mesosome:** A part of migmatite that is intermediate in colour between leucosome and melanosome generally taken as a non-molten portion.

**Metatexite migmatite:** A migmatite that is heterogenous at the outcrop scale, and in which coherent pre-partial melting structures are widely preserved. The products of partial melting are generally segregated into leucosome and melanosome and the deformation has a solid-dominated behaviour.

**Migmatite:** A rock formed by partial melting (synonym: anatexite). A rock found in medium- and high-grade metamorphic terrains that can be heterogeneous at the microscopic to macroscopic scale, which consists of two or more petrographically different parts. One of these parts must have formed by partial melting processes.

**Nebulitic migmatites:** A type of metatexite migmatite in which the leucosome occur as discontinuous patches overprinting the fabric of the rock.

**Peritectic Phases:** The breakdown of a hydrous phases is commonly accompanied by the formation of solid peritectic mineral phases (incongruent melting). The nature of the peritectic phases depends on the hydrous mineral that is breaking down. In the case of biotite melting the peritectic phases are typically ferromagnesian minerals (garnet, orthopyroxene and/or cordierite).

**Residuum:** The solid fraction left after partial melting and the extraction of a fraction of the melt. In the context of this study case, the term residuum indicates the melt-depleted protolith. At different scale (outcrop or terrain), the residuum can be considered as a combination of the melanosome and the leucosome.

**Segregation:** Term used to describe the overall process in which anatectic melt is separated from the residuum in a leucosome.

**Selvedge:** General term for a rim, or border zone, that is not residuum and is compositionally, mineralogically, or microstructurally different from the host and that occurs around a component of migmatite.

**Stromatic migmatites:** A type of metatexite migmatites in which the leucosome and melanosome or just the leucosome occur as laterally continuous, parallel layers oriented along the compositional layering (e.g. bedding) or fabric.

**Xenolith:** An inclusion (mineral or rock) in igneous rock during magma emplacement and eruption. A xenolith can be related to the source material or the country rock extracted during magma ascent.

## REFERENCES

- Barbarin, B., 1999. A review of the relationships between granitoid types, their origins and their geodynamic environments. *Lithos*, **46**, 605-626.
- Chappell, B.W. & White, A. J. R., 1974. Two contrasting granite types, *Pacific Geology*, **8**, 173-174.
- Clemens, J.D., Stevens G. & Farina, F., 2011. The enigmatic sources of I-type granites: The peritectonic connexion. *Lithos*, **126**, 174-181.
- Sawyer, E.W. 2008. Atlas of Migmatites. *The Canadian Mineralogist, Special Publication 9*. NRC Research Press, Ottawa, Ontario, Canada. 371 pp.
- Vielzeuf, D. & Holloway, J.R., 1988. Experimental determination of the fluid-absent melting reactions in the pelitic system. *Contribution to Mineralogy and Petrology*, **98**, 257-276.
- White, A. J. R. & Chappell, B. W., 1983. Granitoid types and their distribution in the Lachlan Fold Belt, southeastern Australia. *Geological Society of America*, 21-34.

# Appendix B

## Analytical techniques and numerical modelling

### B.1 Analytical techniques

All analyses reported in this manuscript were conducted in the Central Analytical Facility at Stellenbosch University. Additional details of equipment and standard operating conditions are available at [www.sun.ac.za/caf](http://www.sun.ac.za/caf).

#### Whole rock analyses

Samples were crushed to a fine powder using a jaw crusher and tungsten swing mill prior to the preparation of a fused disc for major element and trace analysis. Glass disks were prepared for XRF analysis using 10 g of high purity trace element and REE element free flux (LiBO<sub>2</sub>: 32.83%, Li<sub>2</sub>B<sub>4</sub>O<sub>7</sub>: 66.67%, LiI: 0.50%) mixed with 1g of the rock sample. Whole-rock major element compositions were determined by XRF spectrometry on a PANalytical Axios Wavelength Dispersive spectrometer. The spectrometer is fitted with an Rh tube and with the following analyzing crystals: LIF200, LIF220, LIF420, PE, and PX1. The instrument is fitted with a gas-flow proportional counter and a scintillation detector. The gas-flow proportional counter uses a 90% Argon, 10% methane gas mixture. Major elements were analysed on a fused glass disk at 50 kV and 50 mA tube operating conditions. Matrix effects in the samples were corrected for by applying theoretical alpha factors and measured line overlap factors to the raw intensities measured with the SuperQ PANalytical software. Control standards that were used in the calibration procedures for major element analyses were NIM-G (Granite from the Council for Mineral Technology, South Africa) and BHVO-1 (Basalt from the United States Geological Survey, Reston).

#### SEM mineral chemistry

Mineral major element compositions were analysed using Leo 1430VP Scanning Electron Microscope (SEM). Textures were studied in backscattered electron (BSE) mode and mineral compositions quantified by EDX (Energy Dispersive X-ray) analysis using an Oxford Instruments 133 keV ED X-ray detector and Oxford INCA software. Beam conditions during the quantitative analyses were 20 kV accelerating voltage and 1.5 nA probe current, with a working distance of 15mm and specimen beam current of 4

nA. X-ray counts were typically  $\sim 7000$  cps, and the counting time was 50s live-time. Analyses were quantified using natural mineral standards.

## Zircon dating

All U–Pb age data were acquired by laser ablation – single collector – magnetic sectorfield – inductively coupled plasma – mass spectrometry (LA–SF–ICP–MS) employing a Thermo Finnigan Element2 mass spectrometer coupled to a NewWave UP213 laser ablation system. All age data presented here were obtained by single spot analyses with a spot diameter of 30  $\mu\text{m}$  and a crater depth of approximately 15–20  $\mu\text{m}$ . The methods employed for analysis and data processing are described in detail by Gerdes & Zeh (2006) and Frei & Gerdes (2009). For quality control, the Pleovice (Sláma et al., 2008) and M127 (Nasdala et al., 2008) zircon reference materials were analysed, and the results were consistently in excellent agreement with the published ID–TIMS ages. The calculation of weighted mean and concordia ages, as well as plotting of concordia diagrams were performed using Isoplot/Ex 3.0 (Ludwig, 2003).

## Tomography

Some of the rock samples collected in the field have been cut in a 3x3x5  $\text{cm}^3$  volume in order to be analyzed with the Phoenix VTOMEX L240 CT scanner. This method a 3D and 2D tomography model of the rock highlights the density of the different phases. The resulting data are then reconstructed to create a cross-sectional image of the object in a plane or a 3D environment. A more detailed summary of CT and its application to geological materials is provided by Ketcham & Carlson (2001). At the same time, the technique is entirely nondestructive, leaving samples available for other analyses after scanning. NF180 x-ray inspection of the sample generates a series of files, which are assembled with Volume Graphics VGStudio Max 2.1 to generate a 3D view.

## Portable XRF

Sample on the field have been analysed with Niton XL3t (Thermo Fisher Scientific, Billerica, MA, USA) energy-dispersive P-XRF analyzer calibrated for geological sample. It is equipped with a miniature X-ray tube with an Au anode (max 50 kV, 2 W and 40  $\mu\text{A}$ ), three primary beam filters and a silicon p–i–n diode detector (PIN). The size of the analyzed spot is 8 mm and penetrates the rock through few millimetres. Standard calibrations have been determined using correlations between XRF analyses for the whole rock in the laboratory and average P-XRF analyses on the same sample (Fig. B.1). The estimated measurement error are Si:  $\pm 0.3$  mol; Al:  $\pm 0.04$  mol; Fe:  $\pm 0.03$  mol; Mg:  $\pm 0.05$  mol; Ca:  $\pm 0.01$  mol; K:  $\pm 0.005$  mol. Regression line for each element can be upload in the device to modified the standards of detection (Fig. B.1).

## B.2 Thermodynamic modelling

### THERIAK-DOMINO

Phase equilibria modelling in Chapter 2,3 and 4 was undertaken in the chemical system MnO–Na<sub>2</sub>O–CaO–K<sub>2</sub>O–FeO–MgO–Al<sub>2</sub>O<sub>3</sub>–SiO<sub>2</sub>–H<sub>2</sub>O–TiO<sub>2</sub>–O<sub>2</sub> (MnNCKFMASHTO) using THERIAK-DOMINO soft-



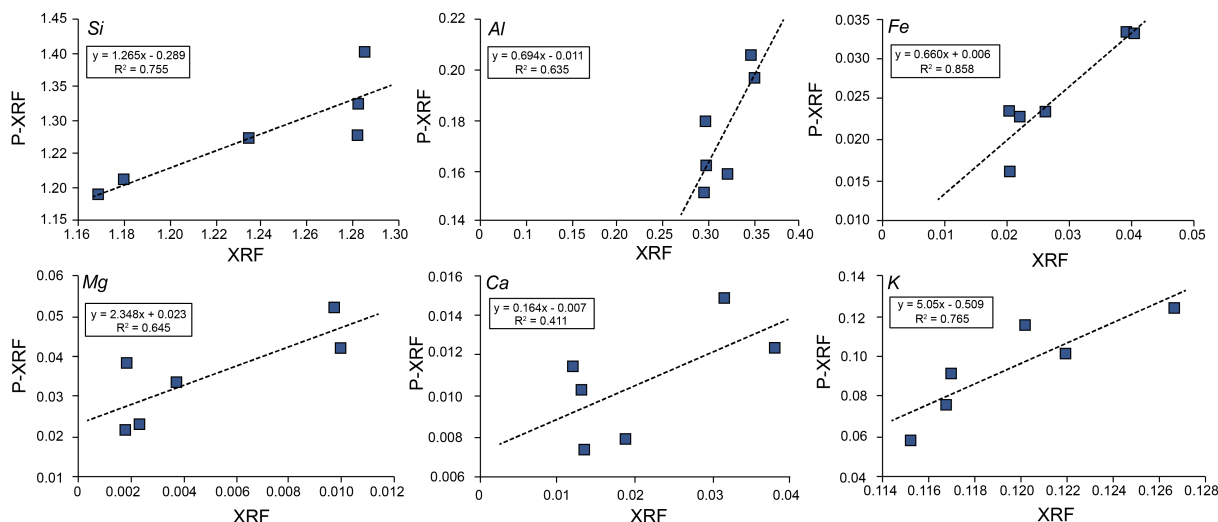


Figure B.1: Comparison of P-XRF data and XRF data from the same set of samples (Joshep, 2013) the regression line are used to set the standards calibration.

ware (de Capitani & Petrakakis, 2010), in combination with the updated Holland Powell (1998) dataset that includes silicate melt. The following  $a-x$  models were used: garnet, biotite (White et al., 2005), feldspar (Holland & Powell, 2003), orthopyroxene (White et al., 2002), cordierite, chlorite (Holland & Powell, 1998), ilmenite (White et al., 2000; 2005), muscovite (Coggon & Holland, 2002), orthoamphibole (Diener & Powell, 2012), spinel (White et al., 2000), melt (White et al., 2007).

## Perple<sub>X</sub>

Phase equilibria modelling in Chapter 2 and 4 was undertaken in the chemical system MnO-Na<sub>2</sub>O-CaO-K<sub>2</sub>O-FeO-MgO-Al<sub>2</sub>O<sub>3</sub>-SiO<sub>2</sub>-H<sub>2</sub>O-TiO<sub>2</sub>-O<sub>2</sub> (MnNCKFMASHTO) and Na<sub>2</sub>O-CaO-K<sub>2</sub>O-FeO-MgO-Al<sub>2</sub>O<sub>3</sub>-SiO<sub>2</sub>-H<sub>2</sub>O-TiO<sub>2</sub> (NCKFMASHT) using Perple<sub>X</sub> software (version 6.6.9 - April 2014) (Connolly, 1990; Connolly and Petrini, 2002). The thermodynamic datafile used is hp04ver.dat. Solid solution models contained in solut\_09.dat are: Mica (CHA) (Coggon & Holland, 2002; Auzanneau et al., 2005); Bio(TCC) (Tajmanova et al., 2009), Gt(WPH) (White et al., 2007); Opx(HP), melt(HP) (Holland & Powell, 2001; White et al., 2001); hCrđ (Thompson & Hovis, 1979), feldspar (Fuhrman & Lindsley, 1988), Ilm (WPH) (White et al., 2000), Opx(stx) and Grt(stx) (Stixrude & Lithgow-Bertelloni, 2005).

## REFERENCES

- Auzanneau, E., Vielzeuf, D., Schmidt, M. W., 2006. Experimental evidence of decompression melting during exhumation of subducted continental crust. *Contributions to Mineralogy and Petrology*, **152**, 125-148.
- Coggon, R. & Holland, T.J.B., 2002. Mixing properties of phengitic micas and revised garnet-phengite thermobarometers. *Journal of Metamorphic Geology*, **20**, 683-696.
- Connolly, J.A.D. 1990. Multivariable phase-diagrams - an algorithm based on generalized thermodynamics. *American Mineralogical Journal of Science*, **290**, 666-718.
- Connolly J.A.D. & Petrini, K. 2002. An automated strategy for calculation of phase diagram sections and retrieval of rock properties as a function of physical conditions. *Journal of Metamorphic Petrology*, **20**, 697-708.
- De Capitani, C. & Petrakakis, K., 2010. The computation of equilibrium assemblage diagrams with Theriak/Domino software. *American Mineralogist*, **95**, 1006-1016.
- Diener, J.F.A. & Powell, R., 2012. Revised activity-composition models for clinopyroxene and amphibole. *Journal Metamorphic Geology*, **20**, 131-142.
- Frei, D. & Gerdes, A., 2009. Precise and accurate in situ U-Pb dating of zircon with high sample throughput by automated LA-SF-ICP-MS. *Chemical Geology*, **261**, 261-270.
- Fuhrman, M.L. & Lindsley, J.G. 1988. Ternary-Feldspar Modeling and Thermometry. *American Mineralogist and Petrologist*, **126**, 137-51.
- Gerdes, A. & Zeh, A., 2006. Combined U-Pb and Hf isotope LA-MC-ICP-MS analyse of detrital zircons: comparison with SHRIMP and new constraints for the provenance and age of an Armorican metasediment in Central Germany. *Earth and Planetary Science Letter*, **249**, 47-61.
- Joseph, C. S. A., 2013. The petrogenesis of the ignimbrites and quartz porphyritic granites exposed along the coast at Saldanha, South Africa. University thesis, Stellenbosch University.
- Holland, T.J.B. & Powell, R., 1998. An internally consistent thermodynamic data set for phases of petrological interest. *Journal of Metamorphic Geology*, **16**, 309-343.
- Ketchum, R. A. Carlson, W. D., 2001. Acquisition, optimization and interpretation of X-ray computed tomographic imagery: applications to the geosciences. *Computers & Geosciences*, **27**, 381-400.
- Ludwig, K.R., 2003. Isoplot/Ex version 3.00: a Geochronological Toolkit for Microsoft Excel. Berkeley Geochronology Center, Berkeley, CA.
- Nasdala, L., Hofmeister, W., Norberg, N., Martinson, J.M., Corfu, F., Dorr, W., Kamo, S.L., Kennedy, A.K., Frei, D., Kosler, J., Wan, Y., Gotze, J., Hager, T., Kroner, A. & Valley, J.W., 2008. Zircon M257 - a Homogeneous Natural Reference Material for the Ion Microprobe U-Pb Analysis of Zircon. *Geostandards and Geoanalytical Research*, **32**, 247-265.
- Sláma, J., Kosler, J., Condon, D.J., Crowley, J.L., Gerdes, A., Hanchar, J.M., Horstwood, M.S.A., Morris, G.A., Nasdala, L., Noberg, N., Schaltegger, U., Schoene, B., Tubrett, M.N. & Whitehouse, M.J., 2008. Plešovič zircon - A new natural reference material for U-Pb and Hf isotopic microanalysis. *Chemical Geology*, **249**, 1-35.
- Stixrude, L. Lithgow-Bertelloni, C. 2005. Mineralogy and elasticity of the oceanic upper mantle: Origin of the low-velocity zone. *Journal of Geophysical Research: Solid Earth* (1978-2012), 110 B3.
- Tajčmanová, L., Connolly, J. A. D. Cesare, B., 2009. A thermodynamic model for titanium and ferric iron solution in biotite. *Journal of Metamorphic Geology*, **27**, 153-165.
- Thompson, J.B.
- Hovis, G.L. 1979. Entropy of Mixing in Sanidine. *American Mineralogist*, **64**, 57-65.

White, R.W., Pomroy, N.E. & Powell, R., 2005. An in situ metatexite-diatexite transition in upper amphibolite facies rocks from Broken Hill, Australia. *Journal of Metamorphic Geology*, **23**, 579-602.

White, R.W., Powell, R., & Holland, T.J.B., 2007. Progress relating to calculation of partial melting equilibria for metapelites. *Journal of Metamorphic Geology*, **25**, 511-527.

White, R.W., Powell, R. & Holland, T.J.B. 2001. Calculation of partial melting equilibria in the system  $\text{Na}_2\text{O}-\text{CaO}-\text{FeO}-\text{MgO}-\text{Al}_2\text{O}_3-\text{SiO}_2-\text{H}_2\text{O}$  (NCFMASH). *Journal of Metamorphic Geology*, **19**, 139-53.

White, R.W., Powell, R., Holland, T.J.B. & Worley, B.A., 2000. The effect of  $\text{TiO}_2$  and  $\text{Fe}_2\text{O}_3$  on metapelitic assemblages at greenschist and amphibolite facies conditions: mineral equilibria calculations in the system  $\text{K}_2\text{O}-\text{Na}_2\text{O}-\text{CaO}-\text{FeO}-\text{MgO}-\text{Al}_2\text{O}_3-\text{SiO}_2-\text{H}_2\text{O}-\text{TiO}_2-\text{Fe}_2\text{O}_3$ . *Journal of Metamorphic Geology*, **18**, 497-511.

## Appendix C

### Whole rock and trace elements chemistry



Type	L1	L1	L2	L2	L3	L3	L3	L3	L3	GDM	GDM	GM	SM	OM
Sample	l2a	l2b	L3a	l3d	L5a	L5b	L5c	BD-03	GR1A	Gcgn50	Ggn51	Ogn50		
Sc	4.95	6.53	6.59	6.05	37.44	27.63	53.40	34.59	31.33	43.17	14.79	36.11		
La	9.78	8.89	8.57	11.52	26.25	18.47	10.37	7.23	10.82	12.83	21.39	12.48		
Ce	19.78	19.73	17.94	24.85	58.28	39.14	21.51	15.41	24.42	24.88	43.02	25.83		
Pr	1.85	2.06	1.78	2.50	7.27	4.79	2.76	1.95	3.05	2.91	5.45	3.12		
Nd	6.51	7.39	6.15	8.68	29.96	20.48	10.90	8.52	12.38	11.20	21.81	12.33		
Sm	1.14	1.29	1.06	1.60	5.46	3.93	2.25	2.88	3.01	2.17	3.94	2.69		
Eu	1.14	0.94	0.67	0.67	0.84	1.01	0.64	0.74	0.33	0.93	1.33	0.94		
Gd	0.77	0.83	0.71	0.97	3.59	3.13	3.19	3.16	3.04	2.90	3.19	2.85		
Tb	0.08	0.08	0.09	0.10	0.44	0.39	0.68	0.48	0.48	0.51	0.44	0.44		
Dy	0.45	0.37	0.38	0.37	2.81	2.39	4.49	3.00	3.02	3.50	2.62	3.08		
Ho	0.08	0.08	0.07	0.05	0.66	0.54	0.94	0.63	0.63	0.79	0.46	0.65		
Er	0.21	0.23	0.23	0.13	2.06	1.52	2.82	1.63	1.79	2.31	1.27	2.10		
Tm	0.03	0.04	0.02	0.02	0.28	0.23	0.40	0.25	0.25	0.38	0.19	0.27		
Yb	0.20	0.25	0.17	0.09	2.21	1.44	2.93	1.83	1.71	2.56	1.07	2.02		
Lu	0.02	0.03	0.02	0.02	0.36	0.23	0.46	0.26	0.25	0.41	0.15	0.30		

Table C.1: Bulk-rock major and trace element compositions of leucosomes and metasedimentary rocks from the Bandelierkop Quarry (BP) expressed in weight % and ppm. Total iron as FeO. L1: Stromatic leucosome; L2: Deformed leucosomes; L3: Nebulitic leucosome; GM: Garnet-metapelite; GDM: Garnet-dominated metapelite; SM: Semipelite; OM: Orthopyroxene-metapelite.

Type	L1	L1	L1	L1	L1	L1	L2	L2	L2	L2	L2	L2	L2	L2
Sample	DT-01A	DT-04A	DT-05A	DT-06A	DT-09	DT-02A	DT-02A2	DT-07A	DT-08	DT-10A	L2a	L2	L2	DT-03A
SiO <sub>2</sub>	72.91	66.87	76.04	70.10	74.29	79.21	79.13	74.02	75.82	73.02	69.42	73.02	75.82	70.52
TiO <sub>2</sub>	0.03	0.02	0.01	0.03	0.02	0.02	0.02	0.02	0.04	0.03	0.01	0.03	0.04	0.25
Al <sub>2</sub> O <sub>3</sub>	16.16	19.54	13.52	16.18	15.00	11.82	11.83	15.72	14.20	15.79	17.85	15.79	14.20	15.25
FeO <sub>T</sub>	0.36	0.49	0.13	2.53	0.65	0.25	0.25	0.24	0.11	0.33	0.26	0.33	0.11	1.88
MnO	0.01	0.02	0.01	0.04	0.03	0.01	0.00	0.01	0.00	0.01	0.01	0.01	0.00	0.03
MgO	0.27	0.72	0.26	1.06	0.41	0.27	0.27	0.15	0.12	0.25	0.16	0.25	0.12	1.97
CaO	3.37	3.82	2.72	3.32	3.44	1.63	1.63	2.52	3.37	3.10	2.90	3.10	3.37	3.57
Na <sub>2</sub> O	4.38	4.48	3.45	3.64	3.81	3.23	3.19	4.57	3.54	4.79	5.55	4.79	3.54	3.42
K <sub>2</sub> O	0.89	1.31	1.04	0.94	0.48	1.15	1.15	1.24	0.61	0.89	1.61	0.89	0.61	0.83
P <sub>2</sub> O <sub>5</sub>	0.02	0.03	0.03	0.05	0.03	0.05	0.04	0.01	0.04	0.04	0.02	0.04	0.04	0.06
Total	98.40	97.31	97.22	97.90	98.17	97.64	97.51	98.50	97.85	98.26	97.77	98.26	97.85	97.78
V	6.08	5.23	4.44	12.99	6.19	5.09	5.41	7.32	6.00	10.16	14.50	10.16	6.00	43.74
Cr	16.67	20.39	11.78	115.78	23.06	19.61	13.71	17.78	23.45	21.03	23.49	21.03	23.45	288.18
Co	132.79	97.96	97.28	118.53	138.54	205.74	149.72	110.24	177.00	100.51	94.60	100.51	177.00	96.13
Ni	11.14	17.51	12.86	132.23	30.42	9.07	11.13	17.38	6.68	14.24	14.78	14.24	6.68	109.41
Cu	5.34	4.97	1.99	40.77	8.16	5.21	3.82	5.52	1.98	4.49	5.38	4.49	1.98	22.86
Zn	10.42	11.02	8.64	23.25	23.52	9.40	8.01	11.25	10.62	9.01	18.76	9.01	10.62	36.09
Rb	11.04	24.28	19.19	8.80	4.32	1.39	24.11	5.63	4.66	5.83	23.57	5.83	4.66	17.39
Sr	305.75	471.79	450.20	292.07	293.91	60.08	295.99	463.46	324.97	297.80	661.66	297.80	324.97	182.76
Y	1.21	0.87	0.40	5.39	6.34	0.73	0.27	0.32	0.85	0.97	0.76	0.97	0.85	2.44
Zr	23.33	2.21	79.36	11.49	9.65	21.08	14.11	25.68	115.50	15.80	50.67	15.80	115.50	57.55
Nb	0.03	0.07	0.06	0.38	0.10	0.05	0.07	0.06	0.14	0.45	0.07	0.45	0.14	1.67
Cs	0.11	0.34	0.21	0.07	0.10	0.02	0.21	0.13	0.11	0.03	0.40	0.03	0.11	0.60
Ba	141.71	229.05	138.61	196.49	100.96	47.62	946.96	112.23	105.15	162.14	368.04	162.14	105.15	127.25
Hf	0.59	0.08	2.35	0.30	0.34	0.59	0.37	1.08	3.19	0.54	1.52	0.54	3.19	1.45
Pb	9.96	13.73	8.38	15.46	19.87	2.50	8.98	20.18	9.47	18.93	21.39	18.93	9.47	12.69
Th	0.17	0.04	0.03	0.31	0.08	1.03	0.06	0.06	0.13	0.19	0.07	0.19	0.13	2.06
U	0.07	0.04	0.34	0.09	0.21	0.04	0.03	2.11	0.30	0.34	0.14	0.34	0.30	0.26

Type	L1	L1	L1	L1	L1	L1	L2	L2	L2	L2	L2	L2	L2	L2
Sample	DT-01A	DT-04A	DT-05A	DT-06A	DT-09	DT-02A	DT-02A2	DT-07A	DT-08	DT-10A	L2a	DT-03A	L2	DT-03A
Sc	1.76	2.25	2.23	6.60	5.16	2.53	1.70	1.69	2.20	3.04	8.78	6.49	L2	DT-03A
La	13.15	8.74	6.42	10.06	5.87	4.03	9.23	1.65	7.43	11.47	6.40	13.43	L2	DT-03A
Ce	27.49	17.94	12.87	21.14	12.70	9.37	17.16	3.27	15.69	25.47	12.60	28.93	L2	DT-03A
Pr	2.64	1.77	1.21	2.16	1.25	1.03	1.59	0.33	1.64	2.65	1.32	3.06	L2	DT-03A
Nd	9.70	6.17	4.39	7.31	4.27	4.13	5.27	1.12	5.74	9.03	4.23	11.96	L2	DT-03A
Sm	1.27	0.83	0.58	1.60	0.76	0.80	0.69	0.23	0.90	1.38	0.70	1.90	L2	DT-03A
Eu	1.20	1.78	1.49	1.20	0.93	0.30	1.04	0.43	1.01	0.95	1.46	1.14	L2	DT-03A
Gd	0.55	0.54	0.34	1.04	0.83	0.49	0.41	0.18	0.53	0.73	0.46	1.09	L2	DT-03A
Tb	0.04	0.05	0.03	0.14	0.16	0.06	0.03	0.01	0.06	0.07	0.05	0.10	L2	DT-03A
Dy	0.24	0.21	0.10	0.97	1.10	0.21	0.09	0.09	0.27	0.27	0.23	0.54	L2	DT-03A
Ho	0.05	0.03	0.01	0.19	0.24	0.03	0.01	0.02	0.03	0.05	0.03	0.10	L2	DT-03A
Er	0.15	0.06	0.02	0.55	0.72	0.05	0.02	0.02	0.06	0.10	0.10	0.24	L2	DT-03A
Tm	0.02	0.01	0.00	0.08	0.11	0.00	0.00	0.01	0.01	0.01	0.02	0.04	L2	DT-03A
Yb	0.15	0.04	0.04	0.57	0.88	0.03	0.01	0.06	0.04	0.05	0.07	0.22	L2	DT-03A
Lu	0.02	0.01	0.00	0.08	0.12	0.00	0.00	0.01	0.00	0.01	0.01	0.03	L2	DT-03A

Table C.2: Bulk-rock major and trace element compositions of leucosomes from the Brakspruit Quarry (BT) expressed in weight % and ppm. Total iron as FeO. L1: Stromatic leucosome; L2: Nebulitic leucosome.



## APPENDIX C. WHOLE ROCK AND TRACE ELEMENTS CHEMISTRY

142

Type	GM	GM	GM	GM	GM	GM	GM	GDM	SM	SM	SM	SM	SM	SM	SM	SM	OM
Sample	DT-01B	DT-04B	DT-05B	DT-07B	DT-10B	DT-11B	GRT1	M1B	M2	M3B	M4	M5	M6	M6	OGN	OGN	
SiO <sub>2</sub>	61.45	55.56	55.37	54.72	50.87	60.03	41.12	67.33	65.90	58.77	66.73	66.38	63.93	63.93	55.46	55.46	
TiO <sub>2</sub>	0.84	0.85	0.82	1.04	0.83	1.15	1.49	0.53	0.63	0.79	0.55	0.60	0.78	0.78	0.87	0.87	
Al <sub>2</sub> O <sub>3</sub>	12.05	15.33	15.75	15.39	16.38	9.86	19.24	14.58	12.95	15.04	13.48	14.78	12.82	12.82	12.86	12.86	
FeO <sub>T</sub>	9.40	10.56	13.74	13.53	12.43	11.94	20.41	5.75	6.64	8.52	6.92	6.99	9.06	9.06	10.88	10.88	
MnO	0.12	0.11	0.17	0.09	0.22	0.15	0.23	0.08	0.09	0.10	0.09	0.10	0.13	0.13	0.12	0.12	
MgO	9.86	11.51	10.80	11.54	11.86	11.98	11.91	4.19	6.19	8.16	4.26	4.59	6.67	6.67	11.13	11.13	
CaO	2.13	2.08	0.86	0.79	2.20	1.20	1.12	1.92	2.14	4.29	2.73	1.84	2.04	2.04	3.07	3.07	
Na <sub>2</sub> O	1.56	1.28	0.00	0.14	2.17	1.00	0.23	2.84	2.18	2.78	2.78	2.43	2.10	2.10	2.08	2.08	
K <sub>2</sub> O	1.34	1.35	1.12	1.39	1.57	1.23	2.36	1.39	1.58	0.41	1.13	1.40	1.36	1.36	1.03	1.03	
P <sub>2</sub> O <sub>5</sub>	0.03	0.02	0.02	0.01	0.05	0.03	GRT1 <sub>1</sub>	M1B <sub>1</sub>	M2 <sub>1</sub>	M3B <sub>1</sub>	M4 <sub>1</sub>	M5 <sub>1</sub>	M6 <sub>1</sub>	M6 <sub>1</sub>	OGN <sub>1</sub>	OGN <sub>1</sub>	
Total	98.78	98.66	98.64	98.65	98.57	98.58	98.10	98.61	98.29	98.85	98.67	99.10	98.90	98.90	97.49	97.49	
V	185.96	215.71	231.62	268.90	256.02	264.21	399.10	118.74	137.01	192.05	135.93	127.35	178.94	178.94	215.55	215.55	
Cr	1477.67	1178.38	1183.67	1353.05	1222.63	1412.75	1038.52	294.82	653.87	1032.59	420.31	316.57	474.87	474.87	1479.83	1479.83	
Co	160.58	125.99	205.96	182.49	150.31	154.15	163.53	138.44	92.25	108.42	130.12	190.32	132.22	132.22	134.73	134.73	
Ni	590.31	585.22	593.53	966.59	592.37	603.46	506.66	113.53	299.66	556.22	209.61	167.07	178.63	178.63	656.10	656.10	
Cu	93.66	38.69	48.37	84.24	84.21	71.40	157.81	56.23	68.63	55.83	91.99	51.20	115.49	115.49	96.75	96.75	
Zn	120.97	118.71	121.11	122.76	111.72	131.27	145.73	83.12	95.19	109.84	81.50	73.47	96.46	96.46	151.78	151.78	
Rb	57.51	64.99	72.04	81.54	68.57	54.48	112.03	39.01	52.94	3.58	44.36	42.46	45.51	45.51	40.33	40.33	
Sr	111.82	164.00	50.29	26.68	175.59	107.42	23.62	154.38	190.60	132.86	267.92	132.79	164.44	164.44	111.20	111.20	
Y	15.90	19.66	28.37	5.04	25.17	16.20	41.95	14.71	15.24	20.22	13.61	16.58	18.03	18.03	17.71	17.71	
Zr	106.24	99.58	124.53	121.50	115.66	175.11	176.68	140.88	106.17	94.06	126.52	146.87	172.50	172.50	95.52	95.52	
Nb	4.95	4.58	8.11	9.31	5.33	7.55	8.35	4.32	3.98	5.05	4.07	4.87	3.23	3.23	4.64	4.64	
Cs	0.93	1.36	2.01	2.08	1.74	0.65	1.65	0.19	0.62	0.07	0.45	0.26	0.34	0.34	0.70	0.70	
Ba	345.13	283.32	462.43	713.22	318.20	325.58	698.26	362.76	253.61	39.63	445.87	360.11	327.09	327.09	252.89	252.89	
Hf	2.75	2.72	3.57	3.27	3.21	4.47	4.72	3.70	2.80	2.65	3.43	3.77	4.41	4.41	2.64	2.64	
Pb	4.56	5.45	3.20	2.63	8.81	4.18	6.80	92.78	7.78	85.21	9.26	8.02	7.47	7.47	6.89	6.89	
Th	4.11	0.94	3.49	0.17	1.74	1.92	5.19	4.40	1.73	1.84	3.49	4.17	5.18	5.18	0.32	0.32	
U	0.78	0.19	0.72	0.14	0.42	0.33	0.52	0.67	0.35	0.82	0.53	0.52	0.36	0.36	0.27	0.27	



# Appendix D

## Mineral Chemistry

Sample	Gcgn50					Grt1a					Ggn51					
	Grt1c	Grt1r	Grt2c	Grt2r	Grt3c	Grt3r	Grt1c	Grt1r	Grt2c	Grt2r	Grt3c	Grt3r	Grt1c	Grt1r	Grt2c	Grt2r
SiO <sub>2</sub>	39.1	38.6	38.5	39.2	38.2	37.9	38.7	38.3	38.7	38.6	38.5	38.5	38.7	38.6	39.1	38.1
Al <sub>2</sub> O <sub>3</sub>	21.7	21.6	21.5	21.8	21.2	20.8	21.4	21.6	21.4	21.4	21.6	21.3	21.4	21.4	21.6	21.2
Fe <sub>2</sub> O <sub>3</sub>	0.9	1.6	1.8	1.6	1.5	1.5	0.8	0.9	0.8	0.9	1.4	1.0	1.1	1.2	1.2	1.2
FeO	26.1	26.0	25.4	26.4	26.3	26.6	26.0	25.2	26.0	25.2	25.5	25.5	25.1	25.2	26.2	26.0
MnO	0.7	0.7	0.7	0.6	0.8	0.7	0.5	0.3	0.6	0.4	0.5	0.5	0.6	0.5	0.8	0.7
MgO	10.2	9.9	10.2	10.1	9.1	8.9	10.2	10.0	10.2	10.6	10.4	10.2	10.3	10.1	10.1	9.5
CaO	1.3	1.4	1.4	1.4	1.9	1.6	1.3	1.9	1.2	1.3	1.3	1.4	1.7	1.9	1.3	1.5
Totals	100.0	99.8	99.5	101.1	99.0	98.0	98.8	98.2	98.9	98.4	99.1	98.4	98.8	99.0	100.4	98.1
Si	2.99	2.97	2.97	2.98	2.98	2.99	3.00	2.98	3.00	3.00	2.98	2.99	2.99	2.99	2.99	2.99
IVAl	0.01	0.03	0.03	0.02	0.02	0.01	0.00	0.02	0.00	0.00	0.02	0.01	0.01	0.01	0.01	0.01
VIAl	1.96	1.94	1.92	1.93	1.93	1.92	1.96	1.97	1.96	1.95	1.94	1.95	1.94	1.94	1.94	1.94
Fe <sup>3+</sup>	0.05	0.09	0.11	0.09	0.09	0.09	0.05	0.05	0.05	0.05	0.08	0.06	0.06	0.07	0.07	0.07
Fe <sup>2+</sup>	1.67	1.67	1.64	1.68	1.71	1.75	1.68	1.64	1.68	1.63	1.65	1.66	1.62	1.63	1.68	1.70
Mn	0.04	0.04	0.04	0.04	0.05	0.05	0.03	0.02	0.04	0.03	0.03	0.03	0.04	0.04	0.05	0.05
Mg	1.17	1.14	1.17	1.15	1.06	1.05	1.18	1.16	1.18	1.23	1.19	1.19	1.19	1.17	1.15	1.11
Ca	0.11	0.12	0.12	0.11	0.16	0.14	0.10	0.16	0.10	0.10	0.11	0.12	0.14	0.16	0.11	0.12
Totals	8.00	8.00	8.00	8.00	8.00	8.00	8.00	8.00	8.00	8.00	8.00	8.00	8.00	8.00	8.00	8.00
Mg#	0.41	0.41	0.42	0.41	0.38	0.37	0.41	0.41	0.41	0.43	0.42	0.42	0.42	0.42	0.41	0.39
X <sub>Spss</sub>	0.01	0.01	0.01	0.01	0.02	0.02	0.01	0.01	0.01	0.01	0.01	0.01	0.01	0.01	0.02	0.02
X <sub>Grs</sub>	0.04	0.04	0.04	0.04	0.05	0.05	0.03	0.05	0.03	0.03	0.04	0.04	0.05	0.05	0.04	0.04

Table D.1: Garnet chemistry in the metasedimentary rocks in the Bandelierkop Quarry. Grt = garnet; c = core analysis; r = rim analysis; Mg# = Mg/(Mg + Fe<sup>2+</sup>), X<sub>Spss</sub> = Mn/(Fe<sup>2+</sup> + Mn + Mg + Ca), X<sub>Grs</sub> = Ca/(Fe<sup>2+</sup> + Mn + Mg + Ca).

Sample	L2a						L2b						L2-t2						Gr1b						L3					
	Gntc	Gntr	Gnt2c	Gnt2r	Grt3c	Grt3r	Gntc	Gntr	Gnt2c	Gnt2r	Grt3c	Grt3r	Gntc	Gntr	Gnt2c	Gnt2r	Grt3c	Grt3r	Gntc	Gntr	Gnt2c	Gnt2r	Grt3c	Grt3r	Gntc	Gntr	Gnt2c	Gnt2r	Grt3c	Grt3r
SiO <sub>2</sub>	39.2	39.4	39.1	39.1	39.8	39.8	39.3	39.4	38.9	39.0	38.9	38.8	37.8	37.8	38.1	38.8	38.3	38.1	38.9	38.9	38.3	38.3	38.3	38.3	38.3	38.3	38.5	38.4	38.3	38.3
Al <sub>2</sub> O <sub>3</sub>	21.9	21.9	21.6	21.5	22.2	22.2	22.0	21.6	21.7	21.6	21.9	21.8	21.6	21.6	21.3	21.8	21.4	21.3	21.6	21.6	21.4	21.5	21.4	21.5	21.4	21.4	21.4	21.6	21.5	21.5
Fe <sub>2</sub> O <sub>3</sub>	1.0	1.0	1.4	0.6	1.5	0.8	0.9	0.5	1.8	1.0	1.4	1.3	0.7	0.7	0.4	0.1	0.7	0.4	0.1	0.1	0.4	0.6	0.0	0.6	0.0	0.0	0.0	0.6	0.0	0.0
FeO	26.1	26.0	26.4	26.6	26.4	26.7	26.7	26.2	26.0	26.3	26.3	25.9	27.9	27.9	27.6	27.6	28.3	27.6	25.4	24.4	24.4	25.5	29.2	29.2	29.8	29.3	29.3	32.0	32.0	32.0
MnO	1.1	1.0	1.1	1.0	1.0	1.1	1.2	1.2	1.2	1.2	1.2	1.3	0.8	0.7	0.8	0.7	0.6	0.6	0.5	0.4	0.5	0.7	0.6	0.7	0.6	0.2	0.1	0.1	0.1	0.1
MgO	10.0	10.3	9.9	9.6	10.4	10.6	9.8	9.3	9.9	9.6	9.7	9.7	8.7	8.9	8.7	8.9	8.7	8.7	10.7	11.2	11.1	10.2	8.4	8.3	8.8	8.8	7.1	7.1	7.1	7.1
CaO	1.5	1.4	1.2	1.6	1.3	0.7	1.3	2.4	1.4	1.5	1.4	1.5	0.8	1.3	0.8	1.3	0.8	1.5	1.1	1.4	1.4	1.9	0.7	0.7	0.7	0.6	0.6	0.6	0.6	0.6
Totals	100.8	101.1	100.7	99.9	102.6	101.8	101.0	100.6	100.9	100.3	100.7	100.3	98.3	99.3	98.5	99.9	99.0	98.2	98.3	98.0	98.6	99.1	99.4	99.2	99.4	99.4	99.7	99.7	99.7	99.7
Si	2.99	2.99	2.99	3.01	2.98	2.99	2.99	3.01	2.97	2.99	2.97	2.98	2.98	3.02	2.99	2.99	2.99	3.00	3.01	3.00	3.00	3.02	2.99	3.01	2.99	3.01	2.99	3.01	2.99	3.01
IVAl	0.01	0.01	0.01	0.00	0.02	0.01	0.01	0.00	0.03	0.01	0.03	0.02	0.02	0.00	0.01	0.01	0.01	0.00	0.00	0.00	0.00	0.00	0.01	0.00	0.01	0.00	0.01	0.00	0.01	0.00
VIAl	1.95	1.95	1.94	1.95	1.94	1.96	1.96	1.95	1.92	1.95	1.95	1.95	1.98	2.01	1.98	1.98	1.96	1.98	1.97	1.99	1.98	1.98	1.97	1.98	1.97	1.98	1.97	1.99	1.99	1.99
Fe <sup>3+</sup>	0.06	0.06	0.08	0.04	0.08	0.04	0.05	0.03	0.10	0.06	0.08	0.07	0.04	0.00	0.03	0.02	0.04	0.02	0.01	0.01	0.03	0.00	0.04	0.00	0.03	0.00	0.03	0.00	0.00	0.00
Fe <sup>2+</sup>	1.66	1.65	1.69	1.71	1.66	1.68	1.70	1.68	1.66	1.69	1.68	1.66	1.84	1.79	1.85	1.80	1.85	1.81	1.65	1.58	1.57	1.64	1.91	1.95	1.91	1.91	2.10	2.10	2.10	2.10
Mn	0.07	0.07	0.07	0.07	0.07	0.07	0.08	0.08	0.07	0.08	0.07	0.09	0.05	0.05	0.05	0.05	0.04	0.04	0.03	0.03	0.03	0.03	0.04	0.04	0.04	0.04	0.01	0.01	0.01	0.01
Mg	1.13	1.16	1.13	1.10	1.16	1.19	1.11	1.05	1.12	1.10	1.11	1.11	1.02	1.03	1.02	1.04	1.03	1.02	1.24	1.29	1.28	1.17	0.98	0.97	1.02	1.02	0.83	0.83	0.83	0.83
Ca	0.12	0.12	0.10	0.13	0.10	0.06	0.11	0.20	0.11	0.13	0.11	0.12	0.07	0.11	0.07	0.10	0.07	0.13	0.09	0.10	0.11	0.16	0.06	0.05	0.05	0.05	0.05	0.05	0.05	0.05
Totals	8.00	8.00	8.00	8.00	8.00	8.00	8.00	8.00	8.00	8.00	8.00	8.00	8.00	8.00	8.00	8.00	8.00	8.00	8.00	8.00	8.00	8.00	8.00	8.00	8.00	8.00	8.00	8.00	8.00	8.00
Mg#	0.41	0.41	0.40	0.39	0.41	0.41	0.39	0.39	0.40	0.40	0.40	0.40	0.36	0.37	0.36	0.37	0.36	0.36	0.43	0.45	0.45	0.42	0.34	0.33	0.35	0.35	0.28	0.28	0.28	0.28
X <sub>Spss</sub>	0.02	0.02	0.02	0.02	0.02	0.02	0.03	0.03	0.03	0.03	0.03	0.03	0.02	0.02	0.02	0.02	0.01	0.01	0.01	0.01	0.01	0.01	0.02	0.01	0.00	0.00	0.00	0.00	0.00	0.00
X <sub>Gr-s</sub>	0.04	0.04	0.03	0.04	0.03	0.02	0.04	0.07	0.04	0.04	0.04	0.04	0.02	0.04	0.02	0.03	0.02	0.04	0.03	0.03	0.04	0.05	0.02	0.02	0.02	0.02	0.02	0.02	0.02	0.02

Table D.2: Garnet chemistry in the stromatolite (L2-a, L2-b, L2-t2, Gr1b) and deformed leucosome (L3) of the Bandelierkop Quarry. Grt = garnet; c = core analysis; r = rim; Mg = Mg/(Mg + Fe<sup>2+</sup>), X<sub>Spss</sub> = Mn/(Fe<sup>2+</sup> + Mn + Mg + Ca), X<sub>Gr-s</sub> = Ca/(Fe<sup>2+</sup> + Mn + Mg + Ca).



Sample	L3										L5a										L5b																																																																																																																																																																																																																																																																																																																																																																																						
	Pl1c	Pl1r	Pl2c	Pl2r	Pl3c	Pl3r	Pl4c	Pl4r	Pl1c	Pl1r	Pl2c	Pl2r	Pl3c	Pl3r	Pl4c	Pl4r	Pl1c	Pl1r	Pl2c	Pl2r	Pl3c	Pl3r	Pliopx	Pliopx	Pl1c	Pl1r	Pl2c	Pl2r	Pl3c	Pl3r	Pliopx	Pliopx	Pl1c	Pl1r	Pl2c	Pl2r	Pl3c	Pl3r	Pliopx	Pliopx	Pl1c	Pl1r																																																																																																																																																																																																																																																																																																																																																																	
SiO <sub>2</sub>	64.7	64.4	64.9	64.9	64.9	66.0	64.9	66.6	61.9	60.9	62.0	61.0	61.7	60.9	60.9	61.2	60.2	59.2	60.3	59.7	Al <sub>2</sub> O <sub>3</sub>	22.1	22.4	21.6	21.5	21.5	20.6	21.5	20.5	23.9	24.5	24.0	24.7	24.0	24.7	24.5	24.8	24.2	24.9	24.4	24.6	FeO	0.0	0.0	0.0	0.0	0.0	0.0	0.0	0.0	0.0	0.0	0.0	0.0	0.0	0.0	0.2	0.2	0.4	0.0	0.0	CaO	3.5	3.8	3.4	3.2	3.3	2.3	3.3	2.2	6.0	6.8	6.4	7.1	6.2	7.0	6.8	6.8	6.5	7.3	6.5	6.9	Na <sub>2</sub> O	10.0	9.7	9.7	9.7	9.5	10.0	9.5	9.8	8.2	7.7	7.9	7.7	8.1	7.5	7.8	7.8	8.1	7.7	8.1	7.7	K <sub>2</sub> O	0.5	0.3	0.3	0.2	0.3	0.4	0.4	1.1	0.1	0.1	0.1	0.0	0.1	0.0	0.1	0.0	0.0	0.0	0.0	BaO	0.0	0.0	0.0	0.0	0.0	0.0	0.0	0.0	0.0	0.0	0.0	0.0	0.0	0.0	0.0	0.0	0.0	0.0	0.0	Totals	100.7	100.6	99.8	99.5	99.5	99.3	99.6	100.2	100.1	100.1	100.5	100.6	100.1	100.2	100.3	100.8	99.0	99.5	99.3	98.9	Si	2.84	2.83	2.87	2.87	2.87	2.92	2.87	2.93	2.75	2.71	2.74	2.70	2.74	2.70	2.70	2.70	2.71	2.66	2.70	2.69	Al	1.15	1.16	1.12	1.12	1.12	1.07	1.12	1.06	1.25	1.29	1.25	1.29	1.26	1.29	1.28	1.29	1.28	1.32	1.29	1.31	Fe <sup>2+</sup>	0.00	0.00	0.00	0.00	0.00	0.00	0.00	0.00	0.00	0.00	0.00	0.00	0.00	0.00	0.01	0.01	0.00	0.01	0.00	0.00	Ca	0.16	0.18	0.16	0.15	0.15	0.11	0.16	0.10	0.28	0.33	0.30	0.34	0.29	0.33	0.32	0.32	0.31	0.35	0.31	0.33	Na	0.85	0.83	0.83	0.83	0.82	0.86	0.82	0.83	0.70	0.67	0.68	0.66	0.70	0.65	0.67	0.67	0.71	0.67	0.71	0.67	K	0.03	0.02	0.02	0.01	0.02	0.02	0.02	0.06	0.01	0.00	0.01	0.00	0.00	0.00	0.01	0.00	0.00	0.00	0.00	0.00	Ba	0.00	0.00	0.00	0.00	0.00	0.00	0.00	0.00	0.00	0.00	0.00	0.00	0.00	0.00	0.00	0.00	0.00	0.00	0.00	0.00	Totals	5.02	5.01	5.00	4.99	4.98	4.98	4.99	4.99	4.98	4.99	4.98	4.99	4.99	4.98	4.99	4.99	5.01	5.01	5.01	5.00	X <sub>Ab</sub>	0.82	0.81	0.82	0.84	0.83	0.87	0.82	0.84	0.71	0.67	0.69	0.66	0.70	0.66	0.67	0.68	0.69	0.66	0.69	0.67	X <sub>An</sub>	0.16	0.17	0.16	0.15	0.16	0.11	0.16	0.10	0.29	0.33	0.31	0.34	0.29	0.34	0.32	0.32	0.31	0.34	0.31	0.33	X <sub>S<sub>an</sub></sub>	0.02	0.02	0.02	0.01	0.02	0.02	0.02	0.06	0.01	0.00	0.01	0.00	0.00	0.00	0.01	0.00	0.00	0.00	0.00	0.00
Al <sub>2</sub> O <sub>3</sub>	22.1	22.4	21.6	21.5	21.5	20.6	21.5	20.5	23.9	24.5	24.0	24.7	24.0	24.7	24.5	24.8	24.2	24.9	24.4	24.6	FeO	0.0	0.0	0.0	0.0	0.0	0.0	0.0	0.0	0.0	0.0	0.0	0.0	0.0	0.0	0.2	0.2	0.4	0.0	0.0	CaO	3.5	3.8	3.4	3.2	3.3	2.3	3.3	2.2	6.0	6.8	6.4	7.1	6.2	7.0	6.8	6.8	6.5	7.3	6.5	6.9	Na <sub>2</sub> O	10.0	9.7	9.7	9.7	9.5	10.0	9.5	9.8	8.2	7.7	7.9	7.7	8.1	7.5	7.8	7.8	8.1	7.7	8.1	7.7	K <sub>2</sub> O	0.5	0.3	0.3	0.2	0.3	0.4	0.4	1.1	0.1	0.1	0.1	0.0	0.1	0.0	0.1	0.0	0.0	0.0	0.0	BaO	0.0	0.0	0.0	0.0	0.0	0.0	0.0	0.0	0.0	0.0	0.0	0.0	0.0	0.0	0.0	0.0	0.0	0.0	0.0	Totals	100.7	100.6	99.8	99.5	99.5	99.3	99.6	100.2	100.1	100.1	100.5	100.6	100.1	100.2	100.3	100.8	99.0	99.5	99.3	98.9	Si	2.84	2.83	2.87	2.87	2.87	2.92	2.87	2.93	2.75	2.71	2.74	2.70	2.74	2.70	2.70	2.70	2.71	2.66	2.70	2.69	Al	1.15	1.16	1.12	1.12	1.12	1.07	1.12	1.06	1.25	1.29	1.25	1.29	1.26	1.29	1.28	1.29	1.28	1.32	1.29	1.31	Fe <sup>2+</sup>	0.00	0.00	0.00	0.00	0.00	0.00	0.00	0.00	0.00	0.00	0.00	0.00	0.00	0.00	0.01	0.01	0.00	0.01	0.00	0.00	Ca	0.16	0.18	0.16	0.15	0.15	0.11	0.16	0.10	0.28	0.33	0.30	0.34	0.29	0.33	0.32	0.32	0.31	0.35	0.31	0.33	Na	0.85	0.83	0.83	0.83	0.82	0.86	0.82	0.83	0.70	0.67	0.68	0.66	0.70	0.65	0.67	0.67	0.71	0.67	0.71	0.67	K	0.03	0.02	0.02	0.01	0.02	0.02	0.02	0.06	0.01	0.00	0.01	0.00	0.00	0.00	0.01	0.00	0.00	0.00	0.00	0.00	Ba	0.00	0.00	0.00	0.00	0.00	0.00	0.00	0.00	0.00	0.00	0.00	0.00	0.00	0.00	0.00	0.00	0.00	0.00	0.00	0.00	Totals	5.02	5.01	5.00	4.99	4.98	4.98	4.99	4.99	4.98	4.99	4.98	4.99	4.99	4.98	4.99	4.99	5.01	5.01	5.01	5.00	X <sub>Ab</sub>	0.82	0.81	0.82	0.84	0.83	0.87	0.82	0.84	0.71	0.67	0.69	0.66	0.70	0.66	0.67	0.68	0.69	0.66	0.69	0.67	X <sub>An</sub>	0.16	0.17	0.16	0.15	0.16	0.11	0.16	0.10	0.29	0.33	0.31	0.34	0.29	0.34	0.32	0.32	0.31	0.34	0.31	0.33	X <sub>S<sub>an</sub></sub>	0.02	0.02	0.02	0.01	0.02	0.02	0.02	0.06	0.01	0.00	0.01	0.00	0.00	0.00	0.01	0.00	0.00	0.00	0.00	0.00																					
FeO	0.0	0.0	0.0	0.0	0.0	0.0	0.0	0.0	0.0	0.0	0.0	0.0	0.0	0.0	0.2	0.2	0.4	0.0	0.0	CaO	3.5	3.8	3.4	3.2	3.3	2.3	3.3	2.2	6.0	6.8	6.4	7.1	6.2	7.0	6.8	6.8	6.5	7.3	6.5	6.9	Na <sub>2</sub> O	10.0	9.7	9.7	9.7	9.5	10.0	9.5	9.8	8.2	7.7	7.9	7.7	8.1	7.5	7.8	7.8	8.1	7.7	8.1	7.7	K <sub>2</sub> O	0.5	0.3	0.3	0.2	0.3	0.4	0.4	1.1	0.1	0.1	0.1	0.0	0.1	0.0	0.1	0.0	0.0	0.0	0.0	BaO	0.0	0.0	0.0	0.0	0.0	0.0	0.0	0.0	0.0	0.0	0.0	0.0	0.0	0.0	0.0	0.0	0.0	0.0	0.0	Totals	100.7	100.6	99.8	99.5	99.5	99.3	99.6	100.2	100.1	100.1	100.5	100.6	100.1	100.2	100.3	100.8	99.0	99.5	99.3	98.9	Si	2.84	2.83	2.87	2.87	2.87	2.92	2.87	2.93	2.75	2.71	2.74	2.70	2.74	2.70	2.70	2.70	2.71	2.66	2.70	2.69	Al	1.15	1.16	1.12	1.12	1.12	1.07	1.12	1.06	1.25	1.29	1.25	1.29	1.26	1.29	1.28	1.29	1.28	1.32	1.29	1.31	Fe <sup>2+</sup>	0.00	0.00	0.00	0.00	0.00	0.00	0.00	0.00	0.00	0.00	0.00	0.00	0.00	0.00	0.01	0.01	0.00	0.01	0.00	0.00	Ca	0.16	0.18	0.16	0.15	0.15	0.11	0.16	0.10	0.28	0.33	0.30	0.34	0.29	0.33	0.32	0.32	0.31	0.35	0.31	0.33	Na	0.85	0.83	0.83	0.83	0.82	0.86	0.82	0.83	0.70	0.67	0.68	0.66	0.70	0.65	0.67	0.67	0.71	0.67	0.71	0.67	K	0.03	0.02	0.02	0.01	0.02	0.02	0.02	0.06	0.01	0.00	0.01	0.00	0.00	0.00	0.01	0.00	0.00	0.00	0.00	0.00	Ba	0.00	0.00	0.00	0.00	0.00	0.00	0.00	0.00	0.00	0.00	0.00	0.00	0.00	0.00	0.00	0.00	0.00	0.00	0.00	0.00	Totals	5.02	5.01	5.00	4.99	4.98	4.98	4.99	4.99	4.98	4.99	4.98	4.99	4.99	4.98	4.99	4.99	5.01	5.01	5.01	5.00	X <sub>Ab</sub>	0.82	0.81	0.82	0.84	0.83	0.87	0.82	0.84	0.71	0.67	0.69	0.66	0.70	0.66	0.67	0.68	0.69	0.66	0.69	0.67	X <sub>An</sub>	0.16	0.17	0.16	0.15	0.16	0.11	0.16	0.10	0.29	0.33	0.31	0.34	0.29	0.34	0.32	0.32	0.31	0.34	0.31	0.33	X <sub>S<sub>an</sub></sub>	0.02	0.02	0.02	0.01	0.02	0.02	0.02	0.06	0.01	0.00	0.01	0.00	0.00	0.00	0.01	0.00	0.00	0.00	0.00	0.00																																										
CaO	3.5	3.8	3.4	3.2	3.3	2.3	3.3	2.2	6.0	6.8	6.4	7.1	6.2	7.0	6.8	6.8	6.5	7.3	6.5	6.9	Na <sub>2</sub> O	10.0	9.7	9.7	9.7	9.5	10.0	9.5	9.8	8.2	7.7	7.9	7.7	8.1	7.5	7.8	7.8	8.1	7.7	8.1	7.7	K <sub>2</sub> O	0.5	0.3	0.3	0.2	0.3	0.4	0.4	1.1	0.1	0.1	0.1	0.0	0.1	0.0	0.1	0.0	0.0	0.0	0.0	BaO	0.0	0.0	0.0	0.0	0.0	0.0	0.0	0.0	0.0	0.0	0.0	0.0	0.0	0.0	0.0	0.0	0.0	0.0	0.0	Totals	100.7	100.6	99.8	99.5	99.5	99.3	99.6	100.2	100.1	100.1	100.5	100.6	100.1	100.2	100.3	100.8	99.0	99.5	99.3	98.9	Si	2.84	2.83	2.87	2.87	2.87	2.92	2.87	2.93	2.75	2.71	2.74	2.70	2.74	2.70	2.70	2.70	2.71	2.66	2.70	2.69	Al	1.15	1.16	1.12	1.12	1.12	1.07	1.12	1.06	1.25	1.29	1.25	1.29	1.26	1.29	1.28	1.29	1.28	1.32	1.29	1.31	Fe <sup>2+</sup>	0.00	0.00	0.00	0.00	0.00	0.00	0.00	0.00	0.00	0.00	0.00	0.00	0.00	0.00	0.01	0.01	0.00	0.01	0.00	0.00	Ca	0.16	0.18	0.16	0.15	0.15	0.11	0.16	0.10	0.28	0.33	0.30	0.34	0.29	0.33	0.32	0.32	0.31	0.35	0.31	0.33	Na	0.85	0.83	0.83	0.83	0.82	0.86	0.82	0.83	0.70	0.67	0.68	0.66	0.70	0.65	0.67	0.67	0.71	0.67	0.71	0.67	K	0.03	0.02	0.02	0.01	0.02	0.02	0.02	0.06	0.01	0.00	0.01	0.00	0.00	0.00	0.01	0.00	0.00	0.00	0.00	0.00	Ba	0.00	0.00	0.00	0.00	0.00	0.00	0.00	0.00	0.00	0.00	0.00	0.00	0.00	0.00	0.00	0.00	0.00	0.00	0.00	0.00	Totals	5.02	5.01	5.00	4.99	4.98	4.98	4.99	4.99	4.98	4.99	4.98	4.99	4.99	4.98	4.99	4.99	5.01	5.01	5.01	5.00	X <sub>Ab</sub>	0.82	0.81	0.82	0.84	0.83	0.87	0.82	0.84	0.71	0.67	0.69	0.66	0.70	0.66	0.67	0.68	0.69	0.66	0.69	0.67	X <sub>An</sub>	0.16	0.17	0.16	0.15	0.16	0.11	0.16	0.10	0.29	0.33	0.31	0.34	0.29	0.34	0.32	0.32	0.31	0.34	0.31	0.33	X <sub>S<sub>an</sub></sub>	0.02	0.02	0.02	0.01	0.02	0.02	0.02	0.06	0.01	0.00	0.01	0.00	0.00	0.00	0.01	0.00	0.00	0.00	0.00	0.00																																																														
Na <sub>2</sub> O	10.0	9.7	9.7	9.7	9.5	10.0	9.5	9.8	8.2	7.7	7.9	7.7	8.1	7.5	7.8	7.8	8.1	7.7	8.1	7.7	K <sub>2</sub> O	0.5	0.3	0.3	0.2	0.3	0.4	0.4	1.1	0.1	0.1	0.1	0.0	0.1	0.0	0.1	0.0	0.0	0.0	0.0	BaO	0.0	0.0	0.0	0.0	0.0	0.0	0.0	0.0	0.0	0.0	0.0	0.0	0.0	0.0	0.0	0.0	0.0	0.0	0.0	Totals	100.7	100.6	99.8	99.5	99.5	99.3	99.6	100.2	100.1	100.1	100.5	100.6	100.1	100.2	100.3	100.8	99.0	99.5	99.3	98.9	Si	2.84	2.83	2.87	2.87	2.87	2.92	2.87	2.93	2.75	2.71	2.74	2.70	2.74	2.70	2.70	2.70	2.71	2.66	2.70	2.69	Al	1.15	1.16	1.12	1.12	1.12	1.07	1.12	1.06	1.25	1.29	1.25	1.29	1.26	1.29	1.28	1.29	1.28	1.32	1.29	1.31	Fe <sup>2+</sup>	0.00	0.00	0.00	0.00	0.00	0.00	0.00	0.00	0.00	0.00	0.00	0.00	0.00	0.00	0.01	0.01	0.00	0.01	0.00	0.00	Ca	0.16	0.18	0.16	0.15	0.15	0.11	0.16	0.10	0.28	0.33	0.30	0.34	0.29	0.33	0.32	0.32	0.31	0.35	0.31	0.33	Na	0.85	0.83	0.83	0.83	0.82	0.86	0.82	0.83	0.70	0.67	0.68	0.66	0.70	0.65	0.67	0.67	0.71	0.67	0.71	0.67	K	0.03	0.02	0.02	0.01	0.02	0.02	0.02	0.06	0.01	0.00	0.01	0.00	0.00	0.00	0.01	0.00	0.00	0.00	0.00	0.00	Ba	0.00	0.00	0.00	0.00	0.00	0.00	0.00	0.00	0.00	0.00	0.00	0.00	0.00	0.00	0.00	0.00	0.00	0.00	0.00	0.00	Totals	5.02	5.01	5.00	4.99	4.98	4.98	4.99	4.99	4.98	4.99	4.98	4.99	4.99	4.98	4.99	4.99	5.01	5.01	5.01	5.00	X <sub>Ab</sub>	0.82	0.81	0.82	0.84	0.83	0.87	0.82	0.84	0.71	0.67	0.69	0.66	0.70	0.66	0.67	0.68	0.69	0.66	0.69	0.67	X <sub>An</sub>	0.16	0.17	0.16	0.15	0.16	0.11	0.16	0.10	0.29	0.33	0.31	0.34	0.29	0.34	0.32	0.32	0.31	0.34	0.31	0.33	X <sub>S<sub>an</sub></sub>	0.02	0.02	0.02	0.01	0.02	0.02	0.02	0.06	0.01	0.00	0.01	0.00	0.00	0.00	0.01	0.00	0.00	0.00	0.00	0.00																																																																																			
K <sub>2</sub> O	0.5	0.3	0.3	0.2	0.3	0.4	0.4	1.1	0.1	0.1	0.1	0.0	0.1	0.0	0.1	0.0	0.0	0.0	0.0	BaO	0.0	0.0	0.0	0.0	0.0	0.0	0.0	0.0	0.0	0.0	0.0	0.0	0.0	0.0	0.0	0.0	0.0	0.0	0.0	Totals	100.7	100.6	99.8	99.5	99.5	99.3	99.6	100.2	100.1	100.1	100.5	100.6	100.1	100.2	100.3	100.8	99.0	99.5	99.3	98.9	Si	2.84	2.83	2.87	2.87	2.87	2.92	2.87	2.93	2.75	2.71	2.74	2.70	2.74	2.70	2.70	2.70	2.71	2.66	2.70	2.69	Al	1.15	1.16	1.12	1.12	1.12	1.07	1.12	1.06	1.25	1.29	1.25	1.29	1.26	1.29	1.28	1.29	1.28	1.32	1.29	1.31	Fe <sup>2+</sup>	0.00	0.00	0.00	0.00	0.00	0.00	0.00	0.00	0.00	0.00	0.00	0.00	0.00	0.00	0.01	0.01	0.00	0.01	0.00	0.00	Ca	0.16	0.18	0.16	0.15	0.15	0.11	0.16	0.10	0.28	0.33	0.30	0.34	0.29	0.33	0.32	0.32	0.31	0.35	0.31	0.33	Na	0.85	0.83	0.83	0.83	0.82	0.86	0.82	0.83	0.70	0.67	0.68	0.66	0.70	0.65	0.67	0.67	0.71	0.67	0.71	0.67	K	0.03	0.02	0.02	0.01	0.02	0.02	0.02	0.06	0.01	0.00	0.01	0.00	0.00	0.00	0.01	0.00	0.00	0.00	0.00	0.00	Ba	0.00	0.00	0.00	0.00	0.00	0.00	0.00	0.00	0.00	0.00	0.00	0.00	0.00	0.00	0.00	0.00	0.00	0.00	0.00	0.00	Totals	5.02	5.01	5.00	4.99	4.98	4.98	4.99	4.99	4.98	4.99	4.98	4.99	4.99	4.98	4.99	4.99	5.01	5.01	5.01	5.00	X <sub>Ab</sub>	0.82	0.81	0.82	0.84	0.83	0.87	0.82	0.84	0.71	0.67	0.69	0.66	0.70	0.66	0.67	0.68	0.69	0.66	0.69	0.67	X <sub>An</sub>	0.16	0.17	0.16	0.15	0.16	0.11	0.16	0.10	0.29	0.33	0.31	0.34	0.29	0.34	0.32	0.32	0.31	0.34	0.31	0.33	X <sub>S<sub>an</sub></sub>	0.02	0.02	0.02	0.01	0.02	0.02	0.02	0.06	0.01	0.00	0.01	0.00	0.00	0.00	0.01	0.00	0.00	0.00	0.00	0.00																																																																																																								
BaO	0.0	0.0	0.0	0.0	0.0	0.0	0.0	0.0	0.0	0.0	0.0	0.0	0.0	0.0	0.0	0.0	0.0	0.0	0.0	Totals	100.7	100.6	99.8	99.5	99.5	99.3	99.6	100.2	100.1	100.1	100.5	100.6	100.1	100.2	100.3	100.8	99.0	99.5	99.3	98.9	Si	2.84	2.83	2.87	2.87	2.87	2.92	2.87	2.93	2.75	2.71	2.74	2.70	2.74	2.70	2.70	2.70	2.71	2.66	2.70	2.69	Al	1.15	1.16	1.12	1.12	1.12	1.07	1.12	1.06	1.25	1.29	1.25	1.29	1.26	1.29	1.28	1.29	1.28	1.32	1.29	1.31	Fe <sup>2+</sup>	0.00	0.00	0.00	0.00	0.00	0.00	0.00	0.00	0.00	0.00	0.00	0.00	0.00	0.00	0.01	0.01	0.00	0.01	0.00	0.00	Ca	0.16	0.18	0.16	0.15	0.15	0.11	0.16	0.10	0.28	0.33	0.30	0.34	0.29	0.33	0.32	0.32	0.31	0.35	0.31	0.33	Na	0.85	0.83	0.83	0.83	0.82	0.86	0.82	0.83	0.70	0.67	0.68	0.66	0.70	0.65	0.67	0.67	0.71	0.67	0.71	0.67	K	0.03	0.02	0.02	0.01	0.02	0.02	0.02	0.06	0.01	0.00	0.01	0.00	0.00	0.00	0.01	0.00	0.00	0.00	0.00	0.00	Ba	0.00	0.00	0.00	0.00	0.00	0.00	0.00	0.00	0.00	0.00	0.00	0.00	0.00	0.00	0.00	0.00	0.00	0.00	0.00	0.00	Totals	5.02	5.01	5.00	4.99	4.98	4.98	4.99	4.99	4.98	4.99	4.98	4.99	4.99	4.98	4.99	4.99	5.01	5.01	5.01	5.00	X <sub>Ab</sub>	0.82	0.81	0.82	0.84	0.83	0.87	0.82	0.84	0.71	0.67	0.69	0.66	0.70	0.66	0.67	0.68	0.69	0.66	0.69	0.67	X <sub>An</sub>	0.16	0.17	0.16	0.15	0.16	0.11	0.16	0.10	0.29	0.33	0.31	0.34	0.29	0.34	0.32	0.32	0.31	0.34	0.31	0.33	X <sub>S<sub>an</sub></sub>	0.02	0.02	0.02	0.01	0.02	0.02	0.02	0.06	0.01	0.00	0.01	0.00	0.00	0.00	0.01	0.00	0.00	0.00	0.00	0.00																																																																																																																												
Totals	100.7	100.6	99.8	99.5	99.5	99.3	99.6	100.2	100.1	100.1	100.5	100.6	100.1	100.2	100.3	100.8	99.0	99.5	99.3	98.9	Si	2.84	2.83	2.87	2.87	2.87	2.92	2.87	2.93	2.75	2.71	2.74	2.70	2.74	2.70	2.70	2.70	2.71	2.66	2.70	2.69	Al	1.15	1.16	1.12	1.12	1.12	1.07	1.12	1.06	1.25	1.29	1.25	1.29	1.26	1.29	1.28	1.29	1.28	1.32	1.29	1.31	Fe <sup>2+</sup>	0.00	0.00	0.00	0.00	0.00	0.00	0.00	0.00	0.00	0.00	0.00	0.00	0.00	0.00	0.01	0.01	0.00	0.01	0.00	0.00	Ca	0.16	0.18	0.16	0.15	0.15	0.11	0.16	0.10	0.28	0.33	0.30	0.34	0.29	0.33	0.32	0.32	0.31	0.35	0.31	0.33	Na	0.85	0.83	0.83	0.83	0.82	0.86	0.82	0.83	0.70	0.67	0.68	0.66	0.70	0.65	0.67	0.67	0.71	0.67	0.71	0.67	K	0.03	0.02	0.02	0.01	0.02	0.02	0.02	0.06	0.01	0.00	0.01	0.00	0.00	0.00	0.01	0.00	0.00	0.00	0.00	0.00	Ba	0.00	0.00	0.00	0.00	0.00	0.00	0.00	0.00	0.00	0.00	0.00	0.00	0.00	0.00	0.00	0.00	0.00	0.00	0.00	0.00	Totals	5.02	5.01	5.00	4.99	4.98	4.98	4.99	4.99	4.98	4.99	4.98	4.99	4.99	4.98	4.99	4.99	5.01	5.01	5.01	5.00	X <sub>Ab</sub>	0.82	0.81	0.82	0.84	0.83	0.87	0.82	0.84	0.71	0.67	0.69	0.66	0.70	0.66	0.67	0.68	0.69	0.66	0.69	0.67	X <sub>An</sub>	0.16	0.17	0.16	0.15	0.16	0.11	0.16	0.10	0.29	0.33	0.31	0.34	0.29	0.34	0.32	0.32	0.31	0.34	0.31	0.33	X <sub>S<sub>an</sub></sub>	0.02	0.02	0.02	0.01	0.02	0.02	0.02	0.06	0.01	0.00	0.01	0.00	0.00	0.00	0.01	0.00	0.00	0.00	0.00	0.00																																																																																																																																																
Si	2.84	2.83	2.87	2.87	2.87	2.92	2.87	2.93	2.75	2.71	2.74	2.70	2.74	2.70	2.70	2.70	2.71	2.66	2.70	2.69	Al	1.15	1.16	1.12	1.12	1.12	1.07	1.12	1.06	1.25	1.29	1.25	1.29	1.26	1.29	1.28	1.29	1.28	1.32	1.29	1.31	Fe <sup>2+</sup>	0.00	0.00	0.00	0.00	0.00	0.00	0.00	0.00	0.00	0.00	0.00	0.00	0.00	0.00	0.01	0.01	0.00	0.01	0.00	0.00	Ca	0.16	0.18	0.16	0.15	0.15	0.11	0.16	0.10	0.28	0.33	0.30	0.34	0.29	0.33	0.32	0.32	0.31	0.35	0.31	0.33	Na	0.85	0.83	0.83	0.83	0.82	0.86	0.82	0.83	0.70	0.67	0.68	0.66	0.70	0.65	0.67	0.67	0.71	0.67	0.71	0.67	K	0.03	0.02	0.02	0.01	0.02	0.02	0.02	0.06	0.01	0.00	0.01	0.00	0.00	0.00	0.01	0.00	0.00	0.00	0.00	0.00	Ba	0.00	0.00	0.00	0.00	0.00	0.00	0.00	0.00	0.00	0.00	0.00	0.00	0.00	0.00	0.00	0.00	0.00	0.00	0.00	0.00	Totals	5.02	5.01	5.00	4.99	4.98	4.98	4.99	4.99	4.98	4.99	4.98	4.99	4.99	4.98	4.99	4.99	5.01	5.01	5.01	5.00	X <sub>Ab</sub>	0.82	0.81	0.82	0.84	0.83	0.87	0.82	0.84	0.71	0.67	0.69	0.66	0.70	0.66	0.67	0.68	0.69	0.66	0.69	0.67	X <sub>An</sub>	0.16	0.17	0.16	0.15	0.16	0.11	0.16	0.10	0.29	0.33	0.31	0.34	0.29	0.34	0.32	0.32	0.31	0.34	0.31	0.33	X <sub>S<sub>an</sub></sub>	0.02	0.02	0.02	0.01	0.02	0.02	0.02	0.06	0.01	0.00	0.01	0.00	0.00	0.00	0.01	0.00	0.00	0.00	0.00	0.00																																																																																																																																																																					
Al	1.15	1.16	1.12	1.12	1.12	1.07	1.12	1.06	1.25	1.29	1.25	1.29	1.26	1.29	1.28	1.29	1.28	1.32	1.29	1.31	Fe <sup>2+</sup>	0.00	0.00	0.00	0.00	0.00	0.00	0.00	0.00	0.00	0.00	0.00	0.00	0.00	0.00	0.01	0.01	0.00	0.01	0.00	0.00	Ca	0.16	0.18	0.16	0.15	0.15	0.11	0.16	0.10	0.28	0.33	0.30	0.34	0.29	0.33	0.32	0.32	0.31	0.35	0.31	0.33	Na	0.85	0.83	0.83	0.83	0.82	0.86	0.82	0.83	0.70	0.67	0.68	0.66	0.70	0.65	0.67	0.67	0.71	0.67	0.71	0.67	K	0.03	0.02	0.02	0.01	0.02	0.02	0.02	0.06	0.01	0.00	0.01	0.00	0.00	0.00	0.01	0.00	0.00	0.00	0.00	0.00	Ba	0.00	0.00	0.00	0.00	0.00	0.00	0.00	0.00	0.00	0.00	0.00	0.00	0.00	0.00	0.00	0.00	0.00	0.00	0.00	0.00	Totals	5.02	5.01	5.00	4.99	4.98	4.98	4.99	4.99	4.98	4.99	4.98	4.99	4.99	4.98	4.99	4.99	5.01	5.01	5.01	5.00	X <sub>Ab</sub>	0.82	0.81	0.82	0.84	0.83	0.87	0.82	0.84	0.71	0.67	0.69	0.66	0.70	0.66	0.67	0.68	0.69	0.66	0.69	0.67	X <sub>An</sub>	0.16	0.17	0.16	0.15	0.16	0.11	0.16	0.10	0.29	0.33	0.31	0.34	0.29	0.34	0.32	0.32	0.31	0.34	0.31	0.33	X <sub>S<sub>an</sub></sub>	0.02	0.02	0.02	0.01	0.02	0.02	0.02	0.06	0.01	0.00	0.01	0.00	0.00	0.00	0.01	0.00	0.00	0.00	0.00	0.00																																																																																																																																																																																										
Fe <sup>2+</sup>	0.00	0.00	0.00	0.00	0.00	0.00	0.00	0.00	0.00	0.00	0.00	0.00	0.00	0.00	0.01	0.01	0.00	0.01	0.00	0.00	Ca	0.16	0.18	0.16	0.15	0.15	0.11	0.16	0.10	0.28	0.33	0.30	0.34	0.29	0.33	0.32	0.32	0.31	0.35	0.31	0.33	Na	0.85	0.83	0.83	0.83	0.82	0.86	0.82	0.83	0.70	0.67	0.68	0.66	0.70	0.65	0.67	0.67	0.71	0.67	0.71	0.67	K	0.03	0.02	0.02	0.01	0.02	0.02	0.02	0.06	0.01	0.00	0.01	0.00	0.00	0.00	0.01	0.00	0.00	0.00	0.00	0.00	Ba	0.00	0.00	0.00	0.00	0.00	0.00	0.00	0.00	0.00	0.00	0.00	0.00	0.00	0.00	0.00	0.00	0.00	0.00	0.00	0.00	Totals	5.02	5.01	5.00	4.99	4.98	4.98	4.99	4.99	4.98	4.99	4.98	4.99	4.99	4.98	4.99	4.99	5.01	5.01	5.01	5.00	X <sub>Ab</sub>	0.82	0.81	0.82	0.84	0.83	0.87	0.82	0.84	0.71	0.67	0.69	0.66	0.70	0.66	0.67	0.68	0.69	0.66	0.69	0.67	X <sub>An</sub>	0.16	0.17	0.16	0.15	0.16	0.11	0.16	0.10	0.29	0.33	0.31	0.34	0.29	0.34	0.32	0.32	0.31	0.34	0.31	0.33	X <sub>S<sub>an</sub></sub>	0.02	0.02	0.02	0.01	0.02	0.02	0.02	0.06	0.01	0.00	0.01	0.00	0.00	0.00	0.01	0.00	0.00	0.00	0.00	0.00																																																																																																																																																																																																															
Ca	0.16	0.18	0.16	0.15	0.15	0.11	0.16	0.10	0.28	0.33	0.30	0.34	0.29	0.33	0.32	0.32	0.31	0.35	0.31	0.33	Na	0.85	0.83	0.83	0.83	0.82	0.86	0.82	0.83	0.70	0.67	0.68	0.66	0.70	0.65	0.67	0.67	0.71	0.67	0.71	0.67	K	0.03	0.02	0.02	0.01	0.02	0.02	0.02	0.06	0.01	0.00	0.01	0.00	0.00	0.00	0.01	0.00	0.00	0.00	0.00	0.00	Ba	0.00	0.00	0.00	0.00	0.00	0.00	0.00	0.00	0.00	0.00	0.00	0.00	0.00	0.00	0.00	0.00	0.00	0.00	0.00	0.00	Totals	5.02	5.01	5.00	4.99	4.98	4.98	4.99	4.99	4.98	4.99	4.98	4.99	4.99	4.98	4.99	4.99	5.01	5.01	5.01	5.00	X <sub>Ab</sub>	0.82	0.81	0.82	0.84	0.83	0.87	0.82	0.84	0.71	0.67	0.69	0.66	0.70	0.66	0.67	0.68	0.69	0.66	0.69	0.67	X <sub>An</sub>	0.16	0.17	0.16	0.15	0.16	0.11	0.16	0.10	0.29	0.33	0.31	0.34	0.29	0.34	0.32	0.32	0.31	0.34	0.31	0.33	X <sub>S<sub>an</sub></sub>	0.02	0.02	0.02	0.01	0.02	0.02	0.02	0.06	0.01	0.00	0.01	0.00	0.00	0.00	0.01	0.00	0.00	0.00	0.00	0.00																																																																																																																																																																																																																																				
Na	0.85	0.83	0.83	0.83	0.82	0.86	0.82	0.83	0.70	0.67	0.68	0.66	0.70	0.65	0.67	0.67	0.71	0.67	0.71	0.67	K	0.03	0.02	0.02	0.01	0.02	0.02	0.02	0.06	0.01	0.00	0.01	0.00	0.00	0.00	0.01	0.00	0.00	0.00	0.00	0.00	Ba	0.00	0.00	0.00	0.00	0.00	0.00	0.00	0.00	0.00	0.00	0.00	0.00	0.00	0.00	0.00	0.00	0.00	0.00	0.00	0.00	Totals	5.02	5.01	5.00	4.99	4.98	4.98	4.99	4.99	4.98	4.99	4.98	4.99	4.99	4.98	4.99	4.99	5.01	5.01	5.01	5.00	X <sub>Ab</sub>	0.82	0.81	0.82	0.84	0.83	0.87	0.82	0.84	0.71	0.67	0.69	0.66	0.70	0.66	0.67	0.68	0.69	0.66	0.69	0.67	X <sub>An</sub>	0.16	0.17	0.16	0.15	0.16	0.11	0.16	0.10	0.29	0.33	0.31	0.34	0.29	0.34	0.32	0.32	0.31	0.34	0.31	0.33	X <sub>S<sub>an</sub></sub>	0.02	0.02	0.02	0.01	0.02	0.02	0.02	0.06	0.01	0.00	0.01	0.00	0.00	0.00	0.01	0.00	0.00	0.00	0.00	0.00																																																																																																																																																																																																																																																									
K	0.03	0.02	0.02	0.01	0.02	0.02	0.02	0.06	0.01	0.00	0.01	0.00	0.00	0.00	0.01	0.00	0.00	0.00	0.00	0.00	Ba	0.00	0.00	0.00	0.00	0.00	0.00	0.00	0.00	0.00	0.00	0.00	0.00	0.00	0.00	0.00	0.00	0.00	0.00	0.00	0.00	Totals	5.02	5.01	5.00	4.99	4.98	4.98	4.99	4.99	4.98	4.99	4.98	4.99	4.99	4.98	4.99	4.99	5.01	5.01	5.01	5.00	X <sub>Ab</sub>	0.82	0.81	0.82	0.84	0.83	0.87	0.82	0.84	0.71	0.67	0.69	0.66	0.70	0.66	0.67	0.68	0.69	0.66	0.69	0.67	X <sub>An</sub>	0.16	0.17	0.16	0.15	0.16	0.11	0.16	0.10	0.29	0.33	0.31	0.34	0.29	0.34	0.32	0.32	0.31	0.34	0.31	0.33	X <sub>S<sub>an</sub></sub>	0.02	0.02	0.02	0.01	0.02	0.02	0.02	0.06	0.01	0.00	0.01	0.00	0.00	0.00	0.01	0.00	0.00	0.00	0.00	0.00																																																																																																																																																																																																																																																																														
Ba	0.00	0.00	0.00	0.00	0.00	0.00	0.00	0.00	0.00	0.00	0.00	0.00	0.00	0.00	0.00	0.00	0.00	0.00	0.00	0.00	Totals	5.02	5.01	5.00	4.99	4.98	4.98	4.99	4.99	4.98	4.99	4.98	4.99	4.99	4.98	4.99	4.99	5.01	5.01	5.01	5.00	X <sub>Ab</sub>	0.82	0.81	0.82	0.84	0.83	0.87	0.82	0.84	0.71	0.67	0.69	0.66	0.70	0.66	0.67	0.68	0.69	0.66	0.69	0.67	X <sub>An</sub>	0.16	0.17	0.16	0.15	0.16	0.11	0.16	0.10	0.29	0.33	0.31	0.34	0.29	0.34	0.32	0.32	0.31	0.34	0.31	0.33	X <sub>S<sub>an</sub></sub>	0.02	0.02	0.02	0.01	0.02	0.02	0.02	0.06	0.01	0.00	0.01	0.00	0.00	0.00	0.01	0.00	0.00	0.00	0.00	0.00																																																																																																																																																																																																																																																																																																			
Totals	5.02	5.01	5.00	4.99	4.98	4.98	4.99	4.99	4.98	4.99	4.98	4.99	4.99	4.98	4.99	4.99	5.01	5.01	5.01	5.00	X <sub>Ab</sub>	0.82	0.81	0.82	0.84	0.83	0.87	0.82	0.84	0.71	0.67	0.69	0.66	0.70	0.66	0.67	0.68	0.69	0.66	0.69	0.67	X <sub>An</sub>	0.16	0.17	0.16	0.15	0.16	0.11	0.16	0.10	0.29	0.33	0.31	0.34	0.29	0.34	0.32	0.32	0.31	0.34	0.31	0.33	X <sub>S<sub>an</sub></sub>	0.02	0.02	0.02	0.01	0.02	0.02	0.02	0.06	0.01	0.00	0.01	0.00	0.00	0.00	0.01	0.00	0.00	0.00	0.00	0.00																																																																																																																																																																																																																																																																																																																								
X <sub>Ab</sub>	0.82	0.81	0.82	0.84	0.83	0.87	0.82	0.84	0.71	0.67	0.69	0.66	0.70	0.66	0.67	0.68	0.69	0.66	0.69	0.67	X <sub>An</sub>	0.16	0.17	0.16	0.15	0.16	0.11	0.16	0.10	0.29	0.33	0.31	0.34	0.29	0.34	0.32	0.32	0.31	0.34	0.31	0.33	X <sub>S<sub>an</sub></sub>	0.02	0.02	0.02	0.01	0.02	0.02	0.02	0.06	0.01	0.00	0.01	0.00	0.00	0.00	0.01	0.00	0.00	0.00	0.00	0.00																																																																																																																																																																																																																																																																																																																																													
X <sub>An</sub>	0.16	0.17	0.16	0.15	0.16	0.11	0.16	0.10	0.29	0.33	0.31	0.34	0.29	0.34	0.32	0.32	0.31	0.34	0.31	0.33	X <sub>S<sub>an</sub></sub>	0.02	0.02	0.02	0.01	0.02	0.02	0.02	0.06	0.01	0.00	0.01	0.00	0.00	0.00	0.01	0.00	0.00	0.00	0.00	0.00																																																																																																																																																																																																																																																																																																																																																																		
X <sub>S<sub>an</sub></sub>	0.02	0.02	0.02	0.01	0.02	0.02	0.02	0.06	0.01	0.00	0.01	0.00	0.00	0.00	0.01	0.00	0.00	0.00	0.00	0.00																																																																																																																																																																																																																																																																																																																																																																																							

Table D.4: Plagioclase chemistry in deformed leucosome of the Bandelierkop Quarry. Pl = Plagioclase; c = core analysis; r = rim analysis; iopx = inclusion in orthopyroxene;  $X_{Ab} = \text{Na}/(\text{Na}+\text{Ca}+\text{K})$ ;  $X_{An} = \text{Ca}/(\text{Na}+\text{Ca}+\text{K})$ ;  $X_{San} = \text{K}/(\text{Na}+\text{Ca}+\text{K})$ .

Sample	Geg50					Geg51					Geg50					Plopx														
	Pl1c	Pl1r	Pl2c	Pl2r	Pligt	Pl1c	Pl1r	Pl2c	Pl2r	Pligt	Pl1c	Pl1r	Pl2c	Pl2r	Pligt	Pl1c	Pl1r	Pl2c	Pl2r	Pligt	Pl1c	Pl1r	Pl2c	Pl2r	Pligt	Pl1c	Pl1r	Pl2c	Pl2r	Pligt
SiO <sub>2</sub>	60.0	59.0	60.7	59.1	59.6	57.3	60.4	59.0	59.7	58.6	59.5	60.1	59.0	58.4	58.3	58.7	58.5	58.4	57.8	57.8	61.3	59.4	60.6	59.2	61.0	59.6	59.8	59.6	59.8	59.6
Al <sub>2</sub> O <sub>3</sub>	24.2	25.2	24.0	25.2	25.3	27.1	24.7	25.4	24.8	24.8	24.7	24.7	25.9	25.9	25.8	25.8	26.0	25.6	25.8	25.8	24.3	25.2	24.4	24.7	23.9	25.2	25.0	24.9	24.9	24.9
FeO	0.0	0.0	0.0	0.0	0.0	0.0	0.0	0.0	0.0	0.0	0.2	0.4	0.0	0.0	0.0	0.0	0.0	0.0	0.0	0.0	0.0	0.0	0.0	0.0	0.0	0.0	0.3	0.4	0.4	0.4
CaO	6.4	7.3	6.1	7.3	7.4	9.4	7.1	7.7	7.4	8.2	7.4	7.2	8.1	7.9	8.0	8.2	8.0	7.9	8.0	8.0	6.3	7.3	6.5	7.2	6.0	7.2	7.0	6.9	6.9	6.9
Na <sub>2</sub> O	8.1	7.5	8.3	7.4	7.5	6.1	7.6	7.3	7.3	6.9	7.1	7.6	7.0	7.2	7.1	7.0	7.2	7.2	7.4	7.4	8.4	7.7	8.1	7.7	8.3	7.9	7.9	7.7	7.7	7.7
K <sub>2</sub> O	0.2	0.0	0.0	0.2	0.3	0.4	0.1	0.1	0.1	0.0	0.3	0.1	0.0	0.3	0.2	0.0	0.2	0.3	0.3	0.3	0.0	0.0	0.0	0.0	0.2	0.1	0.0	0.4	0.4	0.4
BaO	0.0	0.0	0.0	0.0	0.0	0.0	0.0	0.0	0.0	0.0	0.0	0.0	0.0	0.0	0.0	0.0	0.0	0.0	0.0	0.0	0.0	0.0	0.0	0.0	0.0	0.0	0.0	0.0	0.0	0.0
Totals	98.8	98.9	99.2	99.2	100.1	100.3	99.9	99.4	99.3	99.3	99.3	100.1	100.0	99.7	99.4	99.7	99.9	99.3	99.2	100.3	99.6	99.7	98.8	99.2	100.0	100.0	100.0	100.0	100.0	100.0
Si	2.70	2.66	2.72	2.66	2.66	2.66	2.69	2.65	2.68	2.63	2.67	2.68	2.64	2.62	2.62	2.63	2.62	2.63	2.61	2.72	2.66	2.70	2.67	2.73	2.66	2.67	2.67	2.67	2.67	2.67
Al	1.28	1.34	1.27	1.34	1.33	1.43	1.30	1.35	1.31	1.36	1.31	1.30	1.36	1.37	1.37	1.36	1.37	1.36	1.37	1.27	1.33	1.29	1.31	1.26	1.33	1.31	1.31	1.31	1.31	1.31
Fe <sup>2+</sup>	0.00	0.00	0.00	0.00	0.00	0.00	0.00	0.00	0.00	0.00	0.01	0.01	0.00	0.00	0.00	0.00	0.00	0.00	0.00	0.00	0.00	0.00	0.00	0.00	0.00	0.01	0.01	0.02	0.02	0.02
Ca	0.31	0.35	0.30	0.35	0.35	0.45	0.34	0.37	0.35	0.39	0.36	0.34	0.39	0.38	0.38	0.39	0.39	0.38	0.39	0.30	0.35	0.31	0.35	0.29	0.34	0.34	0.33	0.33	0.33	0.33
Na	0.71	0.65	0.72	0.64	0.65	0.53	0.65	0.63	0.64	0.60	0.62	0.66	0.60	0.63	0.62	0.61	0.62	0.63	0.65	0.72	0.67	0.70	0.68	0.72	0.68	0.69	0.67	0.67	0.67	0.67
K	0.01	0.00	0.00	0.01	0.01	0.02	0.01	0.00	0.01	0.00	0.02	0.01	0.00	0.02	0.01	0.00	0.01	0.01	0.02	0.00	0.00	0.00	0.00	0.01	0.01	0.00	0.00	0.02	0.02	0.02
Ba	0.00	0.00	0.00	0.00	0.00	0.00	0.00	0.00	0.00	0.00	0.00	0.00	0.00	0.00	0.00	0.00	0.00	0.00	0.00	0.00	0.00	0.00	0.00	0.00	0.00	0.00	0.00	0.00	0.00	0.00
Totals	5.01	5.00	5.01	5.00	5.01	5.00	4.99	5.00	4.99	4.99	4.99	5.00	4.99	5.01	5.01	4.99	5.01	5.01	5.03	5.01	5.01	5.00	5.01	5.00	5.02	5.02	5.02	5.02	5.02	5.02
X <sub>Ab</sub>	0.69	0.65	0.71	0.64	0.64	0.53	0.65	0.63	0.64	0.61	0.62	0.65	0.61	0.61	0.61	0.61	0.61	0.61	0.62	0.71	0.65	0.69	0.66	0.71	0.66	0.67	0.65	0.65	0.65	0.65
X <sub>An</sub>	0.30	0.35	0.29	0.35	0.35	0.45	0.34	0.37	0.35	0.39	0.36	0.34	0.39	0.37	0.38	0.39	0.38	0.37	0.37	0.29	0.35	0.31	0.34	0.28	0.33	0.33	0.32	0.32	0.32	0.32
X <sub>San</sub>	0.01	0.00	0.00	0.01	0.01	0.02	0.01	0.00	0.01	0.00	0.02	0.01	0.00	0.02	0.01	0.00	0.01	0.01	0.02	0.00	0.00	0.00	0.00	0.01	0.01	0.00	0.00	0.02	0.02	0.02

Table D.5: Plagioclase chemistry in the metasedimentary rocks of the Bandelierkop Quarry.  $Pl = \text{Plagioclase}$ ;  $c = \text{core analysis}$ ;  $r = \text{rim analysis}$ ;  $igt = \text{inclusion in garnet}$ ;  $iopx = \text{inclusion in orthopyroxene}$ ;  $X_{Ab} = \text{Na}/(\text{Na}+\text{Ca}+\text{K})$ ;  $X_{An} = \text{Ca}/(\text{Na}+\text{Ca}+\text{K})$ ;  $X_{San} = \text{K}/(\text{Na}+\text{Ca}+\text{K})$ .



Sample	L2a		L2b		L2-t2		L2-t5		Gr1b		L3		Gcgn50				
	Kfs	Kfs	Kfs	Kfs	Kfs	Kfs	Kfs	Kfs	Kfs	Kfs	Kfs	Kfs	Kfs	Kfs			
SiO <sub>2</sub>	63.7	64.1	63.9	64.4	63.5	64.3	63.4	64.2	64.9	64.5	65.1	64.3	66.2	64.9	65.7	64.5	63.6
Al <sub>2</sub> O <sub>3</sub>	18.0	17.9	17.8	18.3	18.3	18.5	18.6	18.4	18.3	18.4	18.4	18.7	18.4	18.4	18.1	18.2	18.2
FeO	0.0	0.0	0.0	0.0	0.0	0.0	0.0	0.0	0.0	0.0	0.0	0.0	0.0	0.0	0.0	0.0	0.0
CaO	0.0	0.0	0.0	0.0	0.1	0.0	0.0	0.0	0.0	0.1	0.2	0.1	0.0	0.0	0.0	0.0	0.0
Na <sub>2</sub> O	0.9	0.9	0.7	0.8	0.6	0.9	1.2	1.1	0.7	0.9	1.3	1.9	1.8	1.4	0.9	0.8	1.0
K <sub>2</sub> O	15.2	15.7	15.9	15.6	15.3	14.9	14.5	15.4	15.1	14.8	13.9	14.6	14.6	15.1	15.1	14.7	15.3
BaO	0.7	0.0	0.0	0.8	1.3	0.0	1.2	1.8	1.2	0.0	0.9	0.0	0.0	0.0	0.0	0.9	0.0
Totals	98.5	98.6	98.2	99.8	99.2	100.0	99.4	99.9	99.2	99.9	99.5	100.4	100.0	99.0	98.4	100.7	99.5
Si	3.00	3.00	3.01	2.99	2.99	3.01	2.97	2.99	3.01	2.99	3.01	3.01	3.02	3.02	3.02	3.01	2.98
Al	1.00	0.99	0.99	1.00	1.01	0.99	1.03	1.01	1.00	1.01	0.98	0.98	0.98	0.97	0.98	0.98	1.01
Fe <sup>2+</sup>	0.00	0.00	0.00	0.00	0.00	0.00	0.00	0.00	0.00	0.00	0.00	0.00	0.00	0.00	0.00	0.00	0.00
Ca	0.00	0.00	0.00	0.00	0.00	0.00	0.00	0.00	0.00	0.00	0.00	0.00	0.00	0.00	0.00	0.00	0.00
Na	0.09	0.08	0.06	0.07	0.05	0.08	0.10	0.10	0.06	0.08	0.11	0.17	0.16	0.12	0.08	0.07	0.10
K	0.91	0.94	0.96	0.92	0.94	0.90	0.88	0.87	0.91	0.89	0.88	0.82	0.85	0.85	0.89	0.90	0.86
Ba	0.01	0.00	0.00	0.01	0.02	0.00	0.03	0.02	0.00	0.02	0.00	0.00	0.00	0.00	0.00	0.03	0.04
Totals	5.01	5.01	5.01	5.00	5.00	4.99	5.00	4.99	4.98	5.00	4.99	5.00	4.98	4.98	4.98	5.01	4.99
X <sub>Ab</sub>	0.09	0.08	0.06	0.07	0.05	0.09	0.11	0.10	0.06	0.08	0.11	0.17	0.16	0.12	0.08	0.07	0.10
X <sub>An</sub>	0.00	0.00	0.00	0.00	0.00	0.00	0.00	0.00	0.00	0.00	0.00	0.00	0.00	0.00	0.00	0.00	0.00
X <sub>San</sub>	0.91	0.92	0.94	0.93	0.95	0.91	0.89	0.90	0.94	0.92	0.89	0.82	0.84	0.87	0.91	0.92	0.90

Table D.6: K-feldspar chemistry in the metasedimentary rocks (Gcgn50), the stromatic leucosomes (L2a, L2b, L2t2, Gr1b) and nebular leucosomes (L3) of the Bandelierkop Quarry. Kfs = K-feldspar; int = Kfs interstitial around plagioclase and quartz; per = Kfs in perthite; X<sub>Ab</sub> = Na/(Na+Ca+K) ; X<sub>An</sub> = Ca/(Na+Ca+K) ; X<sub>San</sub> = K/(Na+Ca+K).

Sample	L2a		Gr1b		L5b		Crdm		Crdm		Gegn50		Gr1a		Ogn50					
	Crdgrt	Crdgrt	Crdgrt	Crdgrt	Crdm	Crdm	Crdm	Crdm	Crdm	Crdm	Crdm	Crdm	Crdm	Crdm	Crdm	Crdm				
SiO <sub>2</sub>	50.2	50.6	50.1	50.4	50.4	50.4	50.3	50.3	50.3	50.4	50.1	49.4	50.2	49.9	50.1	50.2	50.6	50.7	50.4	
Al <sub>2</sub> O <sub>3</sub>	33.6	33.8	33.8	34.2	33.7	34.2	34.2	34.2	34.3	34.1	33.9	33.9	33.7	34.0	34.4	33.9	34.1	34.1	33.8	34.1
FeO	3.6	3.7	3.8	2.8	2.8	3.0	3.0	3.0	2.7	2.6	2.7	3.8	3.7	3.5	3.8	3.0	2.8	2.8	2.9	2.7
MnO	0.0	0.0	0.0	0.0	0.0	0.0	0.0	0.0	0.0	0.0	0.0	0.0	0.0	0.0	0.0	0.0	0.0	0.0	0.0	0.0
MgO	11.5	11.3	11.3	12.0	11.9	12.2	11.8	11.7	11.9	12.1	12.0	11.5	11.4	11.5	11.8	11.9	11.9	11.9	12.1	11.9
CaO	0.0	0.0	0.0	0.0	0.0	0.0	0.0	0.0	0.0	0.0	0.0	0.0	0.0	0.0	0.0	0.0	0.0	0.0	0.0	0.0
Ni <sub>2</sub> O	0.0	0.0	0.0	0.0	0.0	0.0	0.0	0.0	0.0	0.0	0.0	0.0	0.0	0.0	0.0	0.0	0.0	0.0	0.0	0.0
K <sub>2</sub> O	0.0	0.0	0.0	0.0	0.0	0.0	0.0	0.0	0.0	0.0	0.0	0.0	0.0	0.0	0.0	0.0	0.0	0.0	0.0	0.0
Totals	98.0	97.3	97.0	98.4	97.9	98.7	97.6	98.2	97.1	97.3	97.1	97.7	97.6	97.2	97.8	97.8	98.1	96.3	97.5	97.2
Si	5.02	5.04	5.01	5.00	5.02	4.99	5.01	5.01	5.00	5.01	5.01	4.96	4.98	5.01	4.99	5.00	5.00	5.02	5.03	5.01
Al	3.96	3.96	3.99	3.99	3.98	3.97	3.98	4.00	4.01	3.99	3.99	4.02	4.01	3.97	4.04	3.99	4.00	3.98	3.95	3.99
Fe <sup>2+</sup>	0.30	0.31	0.32	0.23	0.22	0.24	0.24	0.24	0.25	0.22	0.22	0.22	0.31	0.30	0.21	0.25	0.23	0.23	0.24	0.23
Mn	0.00	0.00	0.00	0.00	0.00	0.00	0.00	0.00	0.00	0.00	0.00	0.00	0.00	0.00	0.00	0.00	0.00	0.00	0.00	0.00
Mg	1.71	1.67	1.69	1.77	1.77	1.81	1.76	1.74	1.76	1.76	1.78	1.73	1.72	1.72	1.75	1.77	1.75	1.75	1.79	1.77
Ca	0.00	0.00	0.00	0.00	0.00	0.00	0.00	0.00	0.00	0.00	0.00	0.00	0.00	0.00	0.00	0.00	0.00	0.00	0.00	0.00
Na	0.00	0.00	0.00	0.00	0.00	0.00	0.00	0.00	0.00	0.00	0.00	0.00	0.00	0.00	0.00	0.00	0.00	0.00	0.00	0.00
K	0.00	0.00	0.00	0.00	0.00	0.00	0.00	0.00	0.00	0.00	0.00	0.00	0.00	0.00	0.00	0.00	0.00	0.00	0.00	0.00
Totals	11.00	10.98	11.00	11.00	10.99	11.02	11.00	10.99	11.00	11.00	11.00	11.03	11.02	11.00	11.01	11.01	11.00	10.99	11.00	11.00
Mg#	85	85	84	88	89	88	88	88	88	89	89	84	85	85	84	88	88	88	88	89

Table D.7: Cordierite chemistry in the metasedimentary rocks (Gegn50, Gr1a) and the leucosomes (L2a, Gr1b, L5b) of the Bandedierkop Quarry. Crd = Cordierite; grt = Garnet; m = Crd in the matrix; s = synplectite with orthopyroxene; Mg = Mg/(Mg + Fe<sup>2+</sup>).

Rock	L2	GM										GDM		SM		OM			
Sample	L5a	Gegn50										Grla		Ggn51		Ogn50			
	Opx1c	Opx1r	Opx2c	Opx2r	Opx1c	Opx1r	Opx2c	Opx2r	Opxs	Opxs	Opxs	Opxs	Opxs	Opxs	Opxs	Opxs	Opxs	Opxs	
SiO <sub>2</sub>	54.1	54.7	53.7	54.3	52.2	53.4	52.2	53.1	52.7	52.4	50.7	50.3	51.1	51.2	51.9	51.4	51.9	51.6	52.5
Al <sub>2</sub> O <sub>3</sub>	4.6	3.5	5.0	3.7	6.0	4.5	6.0	4.7	4.5	4.4	4.4	5.0	5.1	5.1	4.6	3.4	3.0	4.0	5.0
Cr <sub>2</sub> O <sub>3</sub>	0.0	0.0	0.0	0.0	0.0	0.0	0.0	0.0	0.7	0.6	0.3	0.3	0.4	0.4	0.4	0.0	0.0	0.0	0.4
Fe <sub>2</sub> O <sub>3</sub>	0.0	0.0	0.0	0.0	0.0	0.0	0.0	0.0	0.0	0.0	0.0	0.5	0.0	0.0	0.0	0.0	0.0	0.0	0.0
FeO	15.8	16.7	15.7	16.1	17.6	17.9	17.6	17.2	16.2	16.4	22.1	22.0	19.6	18.3	21.3	20.8	20.7	20.8	21.0
MnO	0.0	0.0	0.0	0.0	0.0	0.0	0.0	0.0	0.0	0.0	0.0	0.0	0.0	0.0	0.0	0.0	0.0	0.0	0.0
MgO	26.1	25.7	26.1	25.9	24.2	24.5	24.2	24.9	26.0	26.1	21.6	21.4	23.3	23.9	22.6	23.1	22.9	22.9	22.6
CaO	0.0	0.0	0.0	0.0	0.0	0.0	0.0	0.0	0.0	0.0	0.0	0.0	0.0	0.0	0.0	0.0	0.0	0.0	0.0
Totals	100.5	100.6	100.4	100.0	100.4	100.3	99.9	99.8	100.2	99.9	99.1	99.5	99.5	99.0	100.9	98.7	98.5	99.3	100.9
Si	1.94	1.97	1.92	1.96	1.93	1.94	1.90	1.93	1.90	1.90	1.90	1.88	1.88	1.89	1.90	1.92	1.94	1.91	1.92
IVAl	0.06	0.03	0.08	0.04	0.08	0.11	0.11	0.08	0.10	0.10	0.10	0.12	0.12	0.11	0.10	0.08	0.06	0.09	0.08
VIAl	0.13	0.11	0.13	0.11	0.13	0.13	0.15	0.12	0.09	0.08	0.10	0.10	0.10	0.11	0.10	0.07	0.07	0.09	0.13
Cr	0.00	0.00	0.00	0.00	0.00	0.00	0.00	0.00	0.02	0.02	0.01	0.01	0.01	0.01	0.01	0.00	0.00	0.00	0.01
Fe <sup>3+</sup>	0.00	0.00	0.00	0.00	0.00	0.00	0.00	0.00	0.00	0.00	0.00	0.01	0.00	0.00	0.00	0.00	0.00	0.00	0.00
Fe <sup>2+</sup>	0.47	0.50	0.47	0.49	0.57	0.54	0.53	0.52	0.49	0.49	0.69	0.69	0.60	0.57	0.65	0.65	0.65	0.65	0.63
Mn	0.00	0.00	0.00	0.00	0.00	0.00	0.00	0.00	0.00	0.00	0.00	0.00	0.00	0.00	0.00	0.00	0.00	0.00	0.00
Mg	1.39	1.38	1.39	1.40	1.29	1.32	1.31	1.35	1.40	1.41	1.21	1.19	1.28	1.31	1.23	1.28	1.27	1.27	1.23
Ca	0.00	0.00	0.00	0.00	0.00	0.00	0.00	0.00	0.00	0.00	0.00	0.00	0.00	0.00	0.00	0.00	0.00	0.00	0.00
Totals	4.00	4.00	4.00	4.00	4.00	4.00	4.00	4.00	4.00	4.00	4.00	4.00	4.00	4.00	4.00	4.00	3.99	4.00	4.00
Mg#	75	73	75	74	69	71	71	72	74	74	64	63	68	70	65	66	66	66	65

Table D.8: Orthopyroxene chemistry in the metasedimentary rocks (GM, GDM, SM, OM) and the nebular leucosomes (L2) of the Banderierkop Quarry. Opx = Orthopyroxene; r = rim; c = core; s = symplectite with cordierite; Mg = Mg/(Mg + Fe<sup>2+</sup>).

Rock Sample	L1		L2		GM		GDM		SM		OM								
	Oam	Oam	Oam	Oam	Oam	Oam	Oam	Oam	Oam	Oam	Oam	Oam							
SiO <sub>2</sub>	50.3	50.2	49.8	51.8	52.1	51.3	51.0	51.9	51.5	51.4	51.7	50.4	56.1	49.6	50.6	51.9	51.8	51.6	50.6
TiO <sub>2</sub>	0.0	0.0	0.0	0.0	0.0	0.0	0.0	0.0	0.0	0.4	0.0	0.0	0.0	0.0	0.0	0.0	0.0	0.0	0.0
Al <sub>2</sub> O <sub>3</sub>	4.6	4.6	4.8	3.4	3.3	3.9	2.9	2.9	3.6	2.8	3.3	4.6	2.1	6.6	6.5	5.8	3.8	3.9	4.1
Cr <sub>2</sub> O <sub>3</sub>	0.0	0.0	0.0	0.0	0.0	0.0	0.0	0.0	0.0	0.3	0.0	0.5	0.0	0.0	0.0	0.0	0.0	0.0	0.4
FeO	19.8	20.4	20.8	18.5	18.2	18.1	20.4	20.8	20.0	18.4	17.8	17.8	15.4	16.5	17.1	16.3	17.7	17.6	18.1
MnO	0.0	0.0	0.0	0.0	0.0	0.3	0.0	0.0	0.0	0.0	0.0	0.0	0.0	0.0	0.0	0.0	0.3	0.0	0.0
MgO	22.8	22.1	21.9	24.2	24.6	24.3	23.3	22.8	23.1	24.5	24.6	24.4	24.2	23.5	23.7	23.6	24.3	24.5	24.1
CaO	0.0	0.0	0.0	0.0	0.0	0.0	0.0	0.0	0.0	0.0	0.0	0.0	0.3	0.9	0.0	0.0	0.0	0.0	0.0
Na <sub>2</sub> O	0.0	0.0	0.0	0.0	0.0	0.0	0.0	0.0	0.0	0.0	0.0	0.0	0.0	0.0	0.0	0.0	0.0	0.0	0.0
K <sub>2</sub> O	0.0	0.0	0.0	0.0	0.0	0.0	0.0	0.0	0.0	0.0	0.0	0.0	0.0	0.0	0.0	0.0	0.0	0.0	0.0
Totals	99.5	99.2	99.3	98.9	101.2	100.9	100.6	99.4	100.2	100.8	99.4	99.7	98.1	88.9	88.9	90.5	99.9	100.5	99.2
Si	7.26	7.28	7.24	7.39	7.40	7.33	7.38	7.45	7.38	7.36	7.40	7.21	7.81	7.05	7.17	7.33	7.38	7.36	7.28
Ti	0.00	0.00	0.00	0.00	0.00	0.00	0.00	0.00	0.00	0.05	0.00	0.00	0.00	0.08	0.00	0.00	0.00	0.00	0.00
IVAl	0.74	0.72	0.76	0.58	0.56	0.65	0.50	0.48	0.60	0.47	0.56	0.77	0.19	0.95	0.83	0.67	0.62	0.64	0.70
VAl	0.05	0.08	0.06	0.00	0.00	0.00	0.00	0.00	0.00	0.00	0.00	0.00	0.16	0.15	0.26	0.30	0.01	0.01	0.00
Cr	0.00	0.00	0.00	0.00	0.00	0.00	0.00	0.00	0.00	0.03	0.00	0.05	0.00	0.00	0.00	0.00	0.00	0.00	0.04
Fe <sup>2+</sup>	2.39	2.47	2.54	2.20	2.16	2.17	2.47	2.50	2.40	2.20	2.13	2.13	1.80	1.97	2.02	1.92	2.10	2.10	2.18
Mn	0.00	0.00	0.00	0.00	0.00	0.04	0.00	0.00	0.00	0.00	0.00	0.00	0.00	0.00	0.00	0.00	0.04	0.00	0.00
Mg	4.91	4.77	4.76	5.14	5.20	5.16	5.03	4.87	4.94	5.24	5.24	5.21	5.02	4.99	5.01	4.97	5.16	5.20	5.16
Ca	0.00	0.00	0.00	0.00	0.00	0.00	0.00	0.00	0.00	0.00	0.00	0.00	0.04	0.13	0.00	0.00	0.00	0.00	0.00
Na	0.00	0.00	0.00	0.00	0.00	0.00	0.00	0.00	0.00	0.00	0.00	0.00	0.00	0.00	0.00	0.00	0.00	0.00	0.00
K	0.00	0.00	0.00	0.00	0.00	0.00	0.00	0.00	0.00	0.00	0.00	0.00	0.00	0.00	0.00	0.00	0.00	0.00	0.00
Totals	15.35	15.32	15.35	15.32	15.32	15.35	15.37	15.31	15.32	15.34	15.32	15.38	15.02	15.32	15.29	15.19	15.31	15.31	15.35
Mg#	67	66	65	70	71	70	67	66	67	70	71	71	74	72	71	72	71	71	70

Table D.9: Orthoamphibole chemistry in the metasedimentary rocks (GM, SM, OM) and the stromatic and nebulitic leucosomes (L1, L2) of the Bandelierkop Quarry. Oam = Orthoamphibole; Mg = Mg/(Mg + Fe<sup>2+</sup>).

Sample	L2a										L2-b										Gr1b																			
	Bigt	Bigt	Bigt	Bigt	Bigt	Bigt	Bigt	Birt	Birt	Birt	Bigt	Bigt	Bigt	Bigt	Bigt	Bigt	Bigt	Birt	Birt	Birt	Bigt	Bigt	Bigt	Bigt	Bigt	Bigt	Bigt	Birt	Birt	Birt										
SiO <sub>2</sub>	38.4	38.1	38.6	37.7	38.3	38.2	38.9	38.7	39.3	38.3	39.4	39.0	39.1	40.1	39.5	39.9	40.0	40.1	40.1	40.0	Bigt	Bigt	Bigt	Bigt	Bigt	Bigt	Bigt	Birt	Birt	Birt	Bigt	Bigt	Bigt	Bigt	Bigt	Bigt	Bigt	Birt	Birt	Birt
TiO <sub>2</sub>	3.9	4.1	4.0	4.6	4.4	4.4	0.0	0.0	0.0	0.0	0.0	0.0	0.0	0.0	0.0	0.0	0.0	0.0	0.0	0.0	Bigt	Bigt	Bigt	Bigt	Bigt	Bigt	Bigt	Birt	Birt	Birt	Bigt	Bigt	Bigt	Bigt	Bigt	Bigt	Bigt	Birt	Birt	Birt
Al <sub>2</sub> O <sub>3</sub>	16.7	16.7	16.7	15.9	16.1	16.3	18.9	18.8	18.8	19.1	19.0	18.6	19.0	18.1	18.7	18.5	18.7	18.0	18.0	18.3	Bigt	Bigt	Bigt	Bigt	Bigt	Bigt	Bigt	Birt	Birt	Birt	Bigt	Bigt	Bigt	Bigt	Bigt	Bigt	Bigt	Birt	Birt	Birt
Cr <sub>2</sub> O <sub>3</sub>	0.7	0.7	0.8	1.2	0.9	0.9	0.0	0.0	0.0	0.0	0.0	0.0	0.0	0.0	0.0	0.0	0.0	0.0	0.0	0.0	Bigt	Bigt	Bigt	Bigt	Bigt	Bigt	Bigt	Birt	Birt	Birt	Bigt	Bigt	Bigt	Bigt	Bigt	Bigt	Bigt	Birt	Birt	Birt
FeO	9.6	9.5	9.8	9.6	9.7	9.4	9.3	10.0	8.8	10.7	9.4	9.7	8.7	7.6	7.4	8.0	7.4	7.5	7.0	7.0	Bigt	Bigt	Bigt	Bigt	Bigt	Bigt	Bigt	Birt	Birt	Birt	Bigt	Bigt	Bigt	Bigt	Bigt	Bigt	Bigt	Birt	Birt	Birt
MnO	0.0	0.0	0.0	0.0	0.0	0.0	0.0	0.0	0.0	0.0	0.0	0.0	0.0	0.0	0.0	0.0	0.0	0.0	0.0	0.0	Bigt	Bigt	Bigt	Bigt	Bigt	Bigt	Bigt	Birt	Birt	Birt	Bigt	Bigt	Bigt	Bigt	Bigt	Bigt	Bigt	Birt	Birt	Birt
MgO	17.6	17.6	17.6	17.1	17.3	17.8	19.5	19.4	19.4	20.2	19.9	19.6	20.4	21.5	21.0	21.0	20.9	21.3	21.5	21.5	Bigt	Bigt	Bigt	Bigt	Bigt	Bigt	Bigt	Birt	Birt	Birt	Bigt	Bigt	Bigt	Bigt	Bigt	Bigt	Bigt	Birt	Birt	Birt
Ni <sub>2</sub> O	0.0	0.0	0.0	0.0	0.0	0.0	0.0	0.0	0.0	0.0	0.0	0.0	0.0	0.0	0.0	0.0	0.0	0.0	0.0	0.0	Bigt	Bigt	Bigt	Bigt	Bigt	Bigt	Bigt	Birt	Birt	Birt	Bigt	Bigt	Bigt	Bigt	Bigt	Bigt	Bigt	Birt	Birt	Birt
K <sub>2</sub> O	9.8	9.8	9.8	9.7	9.8	9.9	10.0	10.0	10.0	8.0	9.5	9.3	9.5	9.7	9.5	9.1	9.5	9.7	9.9	9.9	Bigt	Bigt	Bigt	Bigt	Bigt	Bigt	Bigt	Birt	Birt	Birt	Bigt	Bigt	Bigt	Bigt	Bigt	Bigt	Bigt	Birt	Birt	Birt
Totals	96.7	96.5	97.2	95.9	96.4	96.8	96.6	96.8	96.4	96.5	97.2	96.3	96.7	97.0	96.2	96.6	96.4	96.6	96.8	96.8	Bigt	Bigt	Bigt	Bigt	Bigt	Bigt	Bigt	Birt	Birt	Birt	Bigt	Bigt	Bigt	Bigt	Bigt	Bigt	Bigt	Birt	Birt	Birt
Si	5.51	5.47	5.50	5.47	5.51	5.47	5.54	5.52	5.59	5.45	5.56	5.57	5.53	5.62	5.59	5.62	5.63	5.65	5.62	5.62	Bigt	Bigt	Bigt	Bigt	Bigt	Bigt	Bigt	Birt	Birt	Birt	Bigt	Bigt	Bigt	Bigt	Bigt	Bigt	Bigt	Birt	Birt	Birt
Ti	0.42	0.44	0.42	0.50	0.48	0.47	0.00	0.00	0.00	0.00	0.00	0.00	0.00	0.00	0.00	0.00	0.00	0.00	0.00	0.00	Bigt	Bigt	Bigt	Bigt	Bigt	Bigt	Bigt	Birt	Birt	Birt	Bigt	Bigt	Bigt	Bigt	Bigt	Bigt	Bigt	Birt	Birt	Birt
IVAl	2.49	2.53	2.50	2.53	2.49	2.53	2.46	2.48	2.41	2.55	2.44	2.43	2.47	2.38	2.41	2.38	2.37	2.35	2.38	2.38	Bigt	Bigt	Bigt	Bigt	Bigt	Bigt	Bigt	Birt	Birt	Birt	Bigt	Bigt	Bigt	Bigt	Bigt	Bigt	Bigt	Birt	Birt	Birt
V1Al	0.33	0.30	0.31	0.19	0.24	0.23	0.72	0.68	0.75	0.65	0.71	0.69	0.69	0.62	0.70	0.69	0.72	0.64	0.65	0.65	Bigt	Bigt	Bigt	Bigt	Bigt	Bigt	Bigt	Birt	Birt	Birt	Bigt	Bigt	Bigt	Bigt	Bigt	Bigt	Bigt	Birt	Birt	Birt
Cr	0.08	0.08	0.09	0.14	0.10	0.10	0.00	0.00	0.00	0.00	0.00	0.00	0.00	0.00	0.00	0.00	0.00	0.00	0.00	0.00	Bigt	Bigt	Bigt	Bigt	Bigt	Bigt	Bigt	Birt	Birt	Birt	Bigt	Bigt	Bigt	Bigt	Bigt	Bigt	Bigt	Birt	Birt	Birt
Fe <sup>2+</sup>	1.15	1.14	1.17	1.17	1.13	1.13	1.11	1.19	1.05	1.28	1.11	1.15	1.03	0.90	0.88	0.94	0.87	0.88	0.83	0.83	Bigt	Bigt	Bigt	Bigt	Bigt	Bigt	Bigt	Birt	Birt	Birt	Bigt	Bigt	Bigt	Bigt	Bigt	Bigt	Bigt	Birt	Birt	Birt
Mn	0.00	0.00	0.00	0.00	0.00	0.00	0.00	0.00	0.00	0.00	0.00	0.00	0.00	0.00	0.00	0.00	0.00	0.00	0.00	0.00	Bigt	Bigt	Bigt	Bigt	Bigt	Bigt	Bigt	Birt	Birt	Birt	Bigt	Bigt	Bigt	Bigt	Bigt	Bigt	Bigt	Birt	Birt	Birt
Mg	3.75	3.77	3.75	3.70	3.71	3.80	4.13	4.12	4.12	4.29	4.19	4.17	4.31	4.50	4.41	4.40	4.38	4.47	4.50	4.50	Bigt	Bigt	Bigt	Bigt	Bigt	Bigt	Bigt	Birt	Birt	Birt	Bigt	Bigt	Bigt	Bigt	Bigt	Bigt	Bigt	Birt	Birt	Birt
Na	0.00	0.00	0.00	0.00	0.00	0.00	0.00	0.00	0.00	0.00	0.00	0.00	0.00	0.00	0.00	0.00	0.00	0.00	0.00	0.00	Bigt	Bigt	Bigt	Bigt	Bigt	Bigt	Bigt	Birt	Birt	Birt	Bigt	Bigt	Bigt	Bigt	Bigt	Bigt	Bigt	Birt	Birt	Birt
K	1.79	1.80	1.78	1.80	1.80	1.81	1.81	1.81	1.82	1.46	1.70	1.70	1.72	1.73	1.71	1.63	1.71	1.73	1.77	1.77	Bigt	Bigt	Bigt	Bigt	Bigt	Bigt	Bigt	Birt	Birt	Birt	Bigt	Bigt	Bigt	Bigt	Bigt	Bigt	Bigt	Birt	Birt	Birt
Totals	15.52	15.54	15.52	15.50	15.50	15.54	15.78	15.80	15.74	15.68	15.71	15.72	15.75	15.75	15.71	15.66	15.68	15.73	15.75	15.75	Bigt	Bigt	Bigt	Bigt	Bigt	Bigt	Bigt	Birt	Birt	Birt	Bigt	Bigt	Bigt	Bigt	Bigt	Bigt	Bigt	Birt	Birt	Birt
Mg#	77	77	76	76	76	77	79	78	80	77	79	78	81	83	83	82	83	83	84	84	Bigt	Bigt	Bigt	Bigt	Bigt	Bigt	Bigt	Birt	Birt	Birt	Bigt	Bigt	Bigt	Bigt	Bigt	Bigt	Bigt	Birt	Birt	Birt

Table D.10: Biotite chemistry in deformed leucosomes of the Bandlerkop Quarry. Bt = Biotite; igrt = inclusion in garnet; r = retrograde biotite associated with orthoamphibole and kyanite; rgrt = rimming garnet; Mg =  $Mg/(Mg + Fe^{2+})$ .

L5b									
	Btiopx	Btiox	Btiopx	Btiox	Btiox	Btiox	Btiox	Btiox	Btiox
SiO <sub>2</sub>	40.3	38.9	38.8	40.5	40.3	40.8	39.9	39.8	39.4
TiO <sub>2</sub>	2.9	3.1	3.1	2.5	2.7	2.2	3.1	3.1	3.0
Al <sub>2</sub> O <sub>3</sub>	17.5	17.2	17.1	17.0	16.9	15.6	16.7	16.8	16.9
Cr <sub>2</sub> O <sub>3</sub>	1.0	1.0	1.0	1.0	1.1	0.9	1.1	1.2	1.1
FeO	8.6	8.6	8.9	8.5	8.8	9.2	9.0	8.9	8.9
MnO	0.0	0.0	0.0	0.0	0.0	0.0	0.0	0.0	0.0
MgO	19.0	18.2	18.0	19.3	19.2	19.7	18.3	18.3	18.3
Na <sub>2</sub> O	0.0	0.0	0.0	0.0	0.0	0.0	0.0	0.0	0.0
K <sub>2</sub> O	9.3	9.0	9.3	9.2	9.3	8.4	9.5	9.5	9.5
Totals	98.5	96.1	96.4	98.0	98.3	96.8	97.8	97.6	97.2
Si	5.59	5.55	5.54	5.65	5.62	5.75	5.62	5.61	5.58
Ti	0.30	0.34	0.34	0.26	0.29	0.23	0.33	0.32	0.32
IVAl	2.41	2.45	2.46	2.35	2.38	2.25	2.38	2.39	2.42
VAl	0.46	0.45	0.42	0.45	0.39	0.35	0.39	0.40	0.39
Cr	0.11	0.11	0.12	0.11	0.12	0.10	0.13	0.13	0.13
Fe <sup>2+</sup>	1.00	1.03	1.06	1.00	1.02	1.09	1.06	1.04	1.05
Mn	0.00	0.00	0.00	0.00	0.00	0.00	0.00	0.00	0.00
Mg	3.93	3.87	3.83	4.00	3.99	4.14	3.83	3.85	3.87
Na	0.00	0.00	0.00	0.00	0.00	0.00	0.00	0.00	0.00
K	1.64	1.64	1.69	1.63	1.65	1.51	1.71	1.71	1.72
Totals	15.44	15.43	15.47	15.45	15.48	15.42	15.46	15.46	15.49
Mg#	80	79	78	80	80	79	78	79	79

Table D.11: Biotite chemistry in nebulitic leucosomes of the Bandelierkop Quarry. Bt = Biotite; iopx = inclusion in orthopyroxene; r = retrograde biotite associated with orthoamphibole and kyanite; ropx = rimming orthopyroxene; Mg = Mg/(Mg + Fe<sup>2+</sup>).

Sample	Cggn50										Grl1a																													
	Bgrt		Btr		Bgrt		Btr		Btm		Bgrt		Btr		Bgrt		Btr		Btm		Bgrt		Btr																	
SiO <sub>2</sub>	38.1	37.8	38.0	38.2	37.6	37.5	37.6	37.8	38.4	38.8	38.3	38.8	38.8	38.4	40.1	38.4	38.5	39.0	39.4	39.1	38.1	37.8	38.0	38.2	37.6	37.5	37.6	37.8	38.4	38.8	38.3	38.8	38.8	38.4	40.1	38.4	38.5	39.0	39.4	39.1
TiO <sub>2</sub>	4.7	4.8	4.2	5.0	5.0	4.7	5.2	5.3	4.6	4.6	4.8	4.1	4.1	4.0	2.1	4.0	3.5	3.4	3.4	3.3	4.7	4.8	4.2	5.0	5.0	4.7	5.2	5.3	4.6	4.6	4.8	4.1	4.1	4.0	3.5	3.4	3.4	3.4	3.3	
Al <sub>2</sub> O <sub>3</sub>	16.0	16.0	16.2	15.9	15.5	16.2	15.9	16.2	16.2	16.0	16.3	16.1	16.1	16.2	17.2	16.8	17.0	16.2	16.6	16.8	16.0	16.0	16.2	15.9	15.5	16.2	15.9	16.2	16.2	16.0	16.3	16.1	16.1	16.2	16.8	17.0	16.2	16.6	16.8	
Cr <sub>2</sub> O <sub>3</sub>	0.6	0.8	0.5	0.8	1.0	1.0	0.9	0.9	0.7	0.8	0.9	0.0	0.4	1.2	1.1	1.1	0.5	0.5	0.5	0.6	0.8	0.5	0.8	1.0	1.0	0.9	0.9	0.7	0.8	0.9	0.0	0.4	1.2	1.1	0.5	0.5	0.5			
FeO	11.1	11.1	9.5	11.3	11.3	11.2	11.6	11.2	11.2	10.4	10.3	11.1	7.0	8.1	7.9	7.9	9.1	8.9	8.4	11.1	11.1	9.5	11.3	11.3	11.2	11.6	11.2	11.2	10.4	10.3	11.1	7.0	8.1	7.9	9.1	8.9	8.4			
MnO	0.0	0.0	0.0	0.0	0.0	0.0	0.0	0.0	0.0	0.0	0.0	0.0	0.0	0.0	0.0	0.0	0.0	0.0	0.0	0.0	0.0	0.0	0.0	0.0	0.0	0.0	0.0	0.0	0.0	0.0	0.0	0.0	0.0	0.0	0.0	0.0	0.0			
MgO	16.2	16.2	17.6	16.0	15.9	16.1	15.8	16.0	16.6	17.0	16.8	17.0	20.9	18.6	19.0	18.8	18.7	19.4	19.4	16.2	16.2	17.6	16.0	15.9	16.1	15.8	16.0	16.6	17.0	16.8	17.0	20.9	18.6	19.0	18.8	18.7	19.4			
Na <sub>2</sub> O	0.0	0.0	0.0	0.0	0.0	0.0	0.0	0.0	0.0	0.0	0.0	0.0	0.0	0.4	0.4	0.0	0.0	0.0	0.0	0.0	0.0	0.0	0.0	0.0	0.0	0.0	0.0	0.0	0.0	0.0	0.0	0.4	0.4	0.0	0.0	0.0	0.0			
K <sub>2</sub> O	9.6	9.8	9.7	9.4	9.7	9.8	9.8	9.8	9.8	9.8	9.5	9.7	9.8	8.8	8.8	8.8	9.2	9.2	9.3	9.6	9.8	9.7	9.4	9.7	9.8	9.8	9.8	9.8	9.5	9.7	9.8	8.8	8.8	8.8	9.2	9.2	9.3			
Totals	96.3	96.5	95.7	96.7	95.9	96.4	96.9	97.3	97.3	97.3	97.1	97.0	96.5	96.4	96.2	96.2	96.7	96.8	96.3	96.5	95.7	96.7	95.9	96.4	96.9	97.3	97.3	97.1	97.0	96.5	96.4	96.2	96.2	96.7	96.8					
Si	5.52	5.48	5.51	5.52	5.50	5.45	5.45	5.44	5.51	5.54	5.48	5.57	5.63	5.47	5.48	5.58	5.59	5.54	5.52	5.48	5.51	5.52	5.50	5.45	5.45	5.44	5.51	5.54	5.48	5.57	5.63	5.47	5.48	5.58	5.59	5.54				
Ti	0.51	0.53	0.45	0.55	0.55	0.52	0.56	0.57	0.49	0.50	0.52	0.44	0.22	0.43	0.37	0.36	0.35	0.35	0.51	0.53	0.45	0.55	0.55	0.52	0.56	0.57	0.49	0.50	0.52	0.44	0.22	0.43	0.37	0.36	0.36	0.35				
IVAl	2.48	2.52	2.49	2.48	2.50	2.55	2.55	2.56	2.49	2.46	2.52	2.43	2.37	2.53	2.52	2.42	2.41	2.46	2.48	2.52	2.49	2.48	2.50	2.55	2.55	2.56	2.49	2.46	2.52	2.43	2.37	2.53	2.52	2.42	2.41	2.46				
VIAl	0.25	0.21	0.27	0.23	0.16	0.21	0.17	0.19	0.24	0.24	0.24	0.30	0.46	0.29	0.34	0.31	0.37	0.34	0.25	0.21	0.27	0.23	0.16	0.21	0.17	0.19	0.24	0.24	0.24	0.30	0.46	0.29	0.34	0.31	0.37	0.34				
Cr	0.07	0.09	0.06	0.09	0.11	0.11	0.11	0.11	0.08	0.10	0.10	0.00	0.04	0.13	0.13	0.06	0.05	0.05	0.07	0.09	0.06	0.09	0.11	0.11	0.11	0.11	0.08	0.10	0.10	0.00	0.04	0.13	0.13	0.06	0.06	0.05				
Fe <sup>2+</sup>	1.35	1.34	1.15	1.36	1.38	1.36	1.41	1.35	1.34	1.25	1.23	1.34	0.82	0.97	0.95	1.06	0.99	0.99	1.35	1.34	1.15	1.36	1.38	1.36	1.41	1.35	1.34	1.25	1.23	1.34	0.82	0.97	0.95	1.06	0.99					
Mn	0.00	0.00	0.00	0.00	0.00	0.00	0.00	0.00	0.00	0.00	0.00	0.00	0.00	0.00	0.00	0.00	0.00	0.00	0.00	0.00	0.00	0.00	0.00	0.00	0.00	0.00	0.00	0.00	0.00	0.00	0.00	0.00	0.00	0.00	0.00	0.00				
Mg	3.50	3.51	3.80	3.45	3.46	3.49	3.42	3.44	3.54	3.63	3.59	3.64	4.38	3.94	4.02	4.01	3.95	4.11	3.50	3.51	3.80	3.45	3.46	3.49	3.42	3.44	3.54	3.63	3.59	3.64	4.38	3.94	4.02	4.01	3.95	4.11				
Na	0.00	0.00	0.00	0.00	0.00	0.00	0.00	0.00	0.00	0.00	0.00	0.00	0.00	0.12	0.10	0.00	0.00	0.00	0.00	0.00	0.00	0.00	0.00	0.00	0.00	0.00	0.00	0.00	0.00	0.12	0.10	0.00	0.00	0.00	0.00					
K	1.78	1.81	1.79	1.73	1.81	1.81	1.81	1.81	1.80	1.72	1.78	1.79	1.58	1.60	1.60	1.69	1.66	1.68	1.78	1.81	1.79	1.73	1.81	1.81	1.81	1.81	1.80	1.72	1.78	1.79	1.58	1.60	1.60	1.69	1.66	1.68				
Totals	15.46	15.48	15.52	15.40	15.47	15.50	15.48	15.47	15.49	15.43	15.46	15.51	15.51	15.48	15.51	15.46	15.52	15.52	15.46	15.48	15.52	15.40	15.47	15.50	15.48	15.47	15.49	15.43	15.46	15.51	15.48	15.51	15.46	15.52	15.52					
Mg#	72	72	77	72	71	72	71	72	73	74	74	73	84	80	81	79	80	80	72	72	77	72	71	72	71	72	73	74	74	73	84	80	81	79	79	80				

Table D.12: Biotite chemistry in metasedimentary rocks of the Bandelierkop Quarry. Bt = Biotite; m = biotite in the matrix; igrt/iopx = inclusion in garnet/orthopyroxene; r = retrograde biotite associated with orthoamphibole and kyanite; ropx/rgt = rimming orthopyroxene/garnet; Mg = Mg/(Mg + Fe<sup>2+</sup>).

Sample	Ggn51						Ogn50					
	Btgrt	Btgrt	Btm	Btm	Btr	Btr	Btm	Btm	Btr	Btr	Btr	
SiO <sub>2</sub>	38.4	39.2	37.2	37.7	38.3	38.3	38.3	38.3	38.3	38.2	37.6	
TiO <sub>2</sub>	3.9	4.0	5.1	5.0	3.2	3.7	3.6	3.6	3.6	3.6	3.8	
Al <sub>2</sub> O <sub>3</sub>	17.0	16.5	16.2	16.4	16.3	16.9	16.9	16.9	16.9	16.9	16.7	
Cr <sub>2</sub> O <sub>3</sub>	0.0	0.0	0.0	0.0	0.6	0.8	1.0	1.0	1.0	1.0	1.0	
FeO	11.5	11.0	14.0	13.4	10.0	11.9	11.0	11.3	11.0	11.0	11.3	
MnO	0.0	0.0	0.0	0.0	0.0	0.0	0.0	0.0	0.0	0.0	0.0	
MgO	16.0	17.2	14.1	14.8	17.7	16.2	16.4	16.1	16.2	16.4	16.1	
Na <sub>2</sub> O	0.0	0.0	0.0	0.0	0.1	0.0	0.0	0.0	0.0	0.0	0.0	
K <sub>2</sub> O	8.2	8.9	9.8	10.0	9.2	9.5	9.4	9.5	9.4	9.4	9.5	
Totals	95.0	96.9	96.4	97.2	95.5	97.4	96.6	96.1	97.4	96.6	96.1	
Si	5.58	5.59	5.46	5.47	5.55	5.49	5.51	5.47	5.49	5.51	5.47	
Ti	0.42	0.43	0.57	0.55	0.35	0.40	0.39	0.41	0.40	0.39	0.41	
IVAl	2.42	2.41	2.54	2.53	2.45	2.51	2.49	2.53	2.51	2.49	2.53	
VAl	0.50	0.37	0.27	0.27	0.34	0.36	0.37	0.34	0.36	0.37	0.34	
Cr	0.00	0.00	0.00	0.00	0.07	0.09	0.12	0.12	0.09	0.12	0.12	
Fe <sup>2+</sup>	1.39	1.32	1.73	1.63	1.22	1.43	1.33	1.37	1.43	1.33	1.37	
Mn	0.00	0.00	0.00	0.00	0.00	0.00	0.00	0.00	0.00	0.00	0.00	
Mg	3.46	3.65	3.08	3.20	3.82	3.47	3.53	3.50	3.47	3.53	3.50	
Na	0.00	0.00	0.00	0.00	0.03	0.00	0.00	0.00	0.00	0.00	0.00	
K	1.53	1.62	1.84	1.85	1.71	1.74	1.74	1.76	1.74	1.74	1.76	
Totals	15.30	15.40	15.48	15.50	15.53	15.50	15.48	15.50	15.50	15.48	15.50	
Mg#	71	73	64	66	76	71	73	72	71	73	72	

Table D.13: Biotite chemistry in metasedimentary rocks of the Bandelierkop Quarry. Bt = Biotite; m = biotite in the matrix; r = retrograde biotite associated with orthoamphibole and kyanite; rgrt = rimming garnet; Mg =  $Mg/(Mg + Fe^{2+})$ .



Sample	DT04										M5										GRU1																				
	Grt1c	Grt2c	Grt3c	Grt4c	Grt1r	Grt2r	Grt3r	Grt4r	Grtc	Grt1c	Grt2c	Grt3c	Grt4c	Grt1r	Grt2r	Grt3r	Grt4r	Grtc	Grt1c	Grt2c	Grt3c	Grt4c	Grt1r	Grt2r	Grt3r	Grt4r	Grtc	Grt1c	Grt2c	Grt3c	Grt4c	Grt1r	Grt2r	Grt3r	Grt4r	Grtc					
SiO <sub>2</sub>	38.86	38.75	39.50	38.75	39.27	39.05	38.53	39.47	39.30	39.67	39.10	39.01	38.86	39.33	39.11	39.47	39.30	38.75	38.58	38.80	39.35	39.57	38.15	38.15	39.30	38.75	38.58	38.80	39.35	39.57	38.15	38.15	39.30	38.75	38.58	38.80	39.35	39.57	38.15	38.15	
Al <sub>2</sub> O <sub>3</sub>	22.26	22.32	22.14	22.59	22.24	22.43	22.08	22.71	22.26	22.63	22.31	22.32	22.32	22.62	22.37	22.71	22.26	21.98	22.23	22.01	22.46	22.78	21.97	21.97	22.26	21.98	22.23	22.01	22.46	22.78	21.97	21.97	22.26	21.98	22.23	22.01	22.46	22.78	21.97	21.97	
FeO <sub>T</sub>	27.89	28.36	28.82	27.42	28.51	29.46	27.85	27.18	27.77	26.38	24.89	25.15	25.43	25.09	25.27	27.18	27.77	27.51	27.62	26.67	27.54	28.28	27.55	27.55	27.77	27.51	27.62	26.67	27.54	28.28	27.55	27.55	27.77	27.51	27.62	26.67	27.54	28.28	27.55	27.55	
MnO	0.51	0.55	0.60	0.42	0.56	0.52	0.44	0.53	0.56	0.48	0.45	0.56	0.48	0.50	0.46	0.53	0.56	0.36	0.36	0.31	0.44	0.39	0.43	0.43	0.56	0.36	0.36	0.31	0.44	0.39	0.43	0.43	0.56	0.36	0.36	0.31	0.44	0.39	0.43	0.43	
MgO	9.80	9.43	9.20	10.50	9.04	8.90	9.11	10.40	9.90	11.87	11.93	12.09	12.09	12.25	11.66	10.40	9.90	10.64	10.27	10.31	9.23	9.05	9.04	9.04	10.40	10.64	10.27	10.31	9.23	9.05	9.04	9.04	10.40	10.64	10.27	10.31	9.23	9.05	9.04	9.04	
CaO	1.39	1.70	1.62	1.33	1.58	1.70	1.55	1.63	1.77	0.90	0.88	0.72	0.78	0.70	1.21	1.63	1.77	1.29	1.13	1.51	2.09	1.91	2.21	2.21	1.63	1.29	1.13	1.51	2.09	1.91	2.21	2.21	1.63	1.29	1.13	1.51	2.09	1.91	2.21	2.21	
Totals	100.72	101.11	101.41	101.75	100.68	100.88	101.88	99.55	101.91	101.57	99.57	99.84	99.96	100.49	100.07	101.91	101.57	100.53	100.20	99.61	101.10	101.98	99.36	99.36	101.57	100.53	100.20	99.61	101.10	101.98	99.36	99.36	101.57	100.53	100.20	99.61	101.10	101.98	99.36	99.36	
Si	2.96	2.94	2.96	2.97	2.97	3.00	2.96	2.98	2.93	2.93	2.97	2.95	2.94	2.95	2.96	2.93	2.93	2.93	2.95	2.97	2.99	2.99	2.95	2.95	2.96	2.93	2.95	2.97	2.99	2.99	2.95	2.95	2.93	2.93	2.95	2.97	2.99	2.99	2.95	2.95	
Al	2.00	2.00	1.98	2.00	2.01	1.97	2.01	2.01	1.99	1.96	2.00	1.99	1.99	2.00	2.00	1.99	1.96	1.97	2.00	1.99	2.01	2.03	2.00	2.00	2.00	1.99	2.00	1.99	2.01	2.03	2.00	2.00	1.99	1.96	1.97	2.00	1.99	2.01	2.03	2.00	2.00
Fe <sup>3+</sup>	0.08	0.10	0.08	0.06	0.06	0.03	0.07	0.03	0.16	0.18	0.11	0.06	0.10	0.13	0.08	0.16	0.18	0.14	0.10	0.06	0.00	0.00	0.08	0.08	0.08	0.08	0.10	0.06	0.00	0.00	0.00	0.08	0.10	0.06	0.00	0.00	0.00	0.00	0.08	0.08	
Fe <sup>2+</sup>	1.70	1.70	1.75	1.66	1.77	1.77	1.80	1.77	1.53	1.56	1.52	1.50	1.48	1.49	1.52	1.53	1.56	1.61	1.66	1.65	1.75	1.79	1.70	1.70	1.56	1.61	1.66	1.65	1.75	1.79	1.70	1.70	1.56	1.61	1.66	1.65	1.75	1.79	1.70	1.70	
Mn	0.03	0.04	0.04	0.03	0.04	0.03	0.03	0.03	0.03	0.04	0.03	0.04	0.03	0.03	0.03	0.03	0.04	0.02	0.02	0.02	0.03	0.03	0.03	0.03	0.03	0.03	0.02	0.02	0.03	0.03	0.03	0.03	0.02	0.02	0.02	0.02	0.03	0.03	0.03	0.03	
Mg	1.11	1.07	1.04	1.18	1.03	1.05	1.01	1.05	1.15	1.10	1.32	1.36	1.36	1.37	1.32	1.15	1.10	1.21	1.17	1.18	1.05	1.02	1.04	1.04	1.10	1.17	1.18	1.05	1.02	1.04	1.04	1.10	1.17	1.18	1.05	1.02	1.04	1.04	1.04		
Ca	0.11	0.14	0.13	0.11	0.13	0.14	0.12	0.13	0.13	0.14	0.07	0.06	0.06	0.06	0.10	0.13	0.14	0.10	0.09	0.12	0.17	0.15	0.18	0.18	0.10	0.14	0.10	0.09	0.12	0.17	0.15	0.18	0.10	0.09	0.12	0.17	0.15	0.18	0.18		
Totals	8.00	7.98	7.98	8.00	8.00	8.00	8.00	8.00	7.91	7.90	8.00	8.00	8.00	7.99	8.00	7.90	7.90	8.00	8.00	7.99	8.00	8.00	7.99	8.00	8.00	7.90	8.00	7.99	8.00	8.00	7.99	8.00	8.00	7.99	8.00	8.00	8.00	8.00	7.99	8.00	
Mg#	0.40	0.39	0.37	0.41	0.37	0.37	0.36	0.37	0.43	0.41	0.46	0.47	0.48	0.48	0.46	0.43	0.41	0.43	0.41	0.42	0.37	0.36	0.38	0.38	0.41	0.43	0.41	0.42	0.37	0.36	0.38	0.38	0.41	0.43	0.41	0.42	0.37	0.36	0.38	0.38	
X <sub>Spss</sub>	0.01	0.01	0.01	0.01	0.01	0.01	0.01	0.01	0.01	0.01	0.01	0.01	0.01	0.01	0.01	0.01	0.01	0.01	0.01	0.01	0.01	0.01	0.01	0.01	0.01	0.01	0.01	0.01	0.01	0.01	0.01	0.01	0.01	0.01	0.01	0.01	0.01	0.01	0.01	0.01	
X <sub>Grs</sub>	0.04	0.05	0.04	0.04	0.04	0.05	0.04	0.04	0.05	0.05	0.02	0.02	0.02	0.02	0.03	0.05	0.05	0.04	0.03	0.04	0.06	0.05	0.06	0.06	0.06	0.05	0.04	0.03	0.04	0.06	0.05	0.06	0.05	0.04	0.04	0.06	0.05	0.06	0.05	0.06	

Table D.14: Garnet chemistry in the metasedimentary rocks in the Brakspruit Quarry. Grt = garnet; c = core analysis; r = rim analysis; e = euhedral garnet; Mg# =  $\text{Mg}/(\text{Mg} + \text{Fe}^{2+})$ , X<sub>Spss</sub> =  $\text{Mn}/(\text{Fe}^{2+} + \text{Mn} + \text{Mg} + \text{Ca})$ , X<sub>Grs</sub> =  $\text{Ca}/(\text{Fe}^{2+} + \text{Mn} + \text{Mg} + \text{Ca})$ .

Sample	dt04										M5										GRT1										Ogn														
	Btm	Btm	Btm	Btopx	Btgrt	Btr	Btr	Btr	Btgrt	Btm	Btm	Btm	Btm	Btgrt	Btr	Btr	Btr	Btgrt	Btm	Btm	Btm	Btm	Btm	Btgrt	Btr	Btr	Btr	Btgrt	Btm	Btm	Btm	Btm	Btm	Btgrt	Btr	Btr	Btr	Btgrt	Btm	Btm					
SiO <sub>2</sub>	37.64	37.85	37.53	36.97	37.91	37.97	36.59	38.06	38.03	37.43	37.56	37.06	38.92	38.08	38.38	40.59	38.68	37.20	37.33	37.49	38.87	37.20	37.33	37.49	38.87	37.20	37.33	37.49	38.87	37.20	37.33	37.49	38.87	37.20	37.33	37.49	38.87	37.20	37.33	37.49	38.87	37.20	37.33	37.49	38.87
TiO <sub>2</sub>	5.02	5.04	4.71	4.92	4.81	5.14	5.51	5.61	5.45	5.80	5.90	5.62	0.62	0.61	5.35	5.24	5.61	6.60	6.62	6.34	6.12	6.60	6.62	6.34	6.12	6.60	6.62	6.34	6.12	6.60	6.62	6.34	6.12	6.60	6.62	6.34	6.12	6.60	6.62	6.34	6.12	6.60	6.62	6.34	6.12
Al <sub>2</sub> O <sub>3</sub>	15.59	15.49	15.64	15.40	15.89	16.31	15.10	15.81	16.40	16.06	15.82	16.42	17.92	19.36	17.21	15.48	16.44	15.21	15.13	15.39	14.80	15.21	15.13	15.39	14.80	15.21	15.13	15.39	14.80	15.21	15.13	15.39	14.80	15.21	15.13	15.39	14.80	15.21	15.13	15.39	14.80	15.21	15.13	15.39	14.80
Cr <sub>2</sub> O <sub>3</sub>	0.00	0.00	0.00	0.00	0.00	0.00	0.00	0.20	0.19	0.33	0.31	0.33	0.00	0.00	0.00	0.00	0.00	1.20	1.12	1.10	0.00	1.20	1.12	1.10	0.00	1.20	1.12	1.10	0.00	1.20	1.12	1.10	0.00	1.20	1.12	1.10	0.00	1.20	1.12	1.10	0.00				
FeO	11.35	11.71	10.79	11.97	11.03	11.35	11.54	9.60	9.57	12.54	12.55	12.65	8.22	9.01	11.52	11.45	11.98	13.72	14.32	14.14	12.77	13.72	14.32	14.14	12.77	13.72	14.32	14.14	12.77	13.72	14.32	14.14	12.77	13.72	14.32	14.14	12.77	13.72	14.32	14.14	12.77				
MnO	0.00	0.00	0.00	0.00	0.00	0.00	0.00	0.00	0.00	0.00	0.00	0.00	0.00	0.00	0.00	0.00	0.00	0.00	0.00	0.00	0.18	0.00	0.00	0.00	0.18	0.00	0.00	0.00	0.18	0.00	0.00	0.00	0.18	0.00	0.00	0.00	0.18	0.00	0.00	0.00	0.18				
MgO	15.88	15.57	15.98	15.18	15.83	15.80	14.84	16.79	16.52	14.96	14.99	14.49	19.53	20.05	15.91	14.75	15.76	13.41	13.64	13.71	14.42	13.41	13.64	13.71	14.42	13.41	13.64	13.71	14.42	13.41	13.64	13.71	14.42	13.41	13.64	13.71	14.42	13.41	13.64	13.71	14.42				
Na <sub>2</sub> O	0.18	0.00	0.00	0.00	0.00	0.00	0.00	0.00	0.00	0.16	0.00	0.00	0.55	0.00	0.00	0.00	0.00	0.00	0.00	0.00	0.00	0.00	0.00	0.00	0.00	0.00	0.00	0.00	0.00	0.00	0.00	0.00	0.00	0.00	0.00	0.00	0.00	0.00	0.00	0.00	0.00				
K <sub>2</sub> O	9.72	9.68	9.84	9.68	9.75	9.46	9.39	10.02	10.05	9.97	9.94	9.91	8.51	7.98	10.42	9.47	9.95	10.06	10.02	9.92	10.16	10.06	10.02	9.92	10.16	10.06	10.02	9.92	10.16	10.06	10.02	9.92	10.16	10.06	10.02	9.92	10.16	10.06	10.02	9.92	10.16				
Totals	95.38	95.34	94.48	94.10	95.22	96.01	92.97	96.09	96.21	97.26	97.07	96.48	94.27	95.08	98.80	96.98	98.41	97.41	98.19	98.08	97.32	97.41	98.19	98.08	97.32	97.41	98.19	98.08	97.32	97.41	98.19	98.08	97.32	97.41	98.19	98.08	97.32	97.41	98.19	98.08	97.32				
Si	6.03	6.06	6.05	6.02	6.06	6.01	6.02	6.00	5.98	5.92	5.95	5.91	6.13	5.94	5.93	6.32	6.00	5.93	5.92	5.93	6.04	5.93	5.92	5.93	6.04	5.93	5.92	5.93	6.04	5.93	5.92	5.93	6.04	5.93	5.92	5.93	6.04	5.93	5.92	5.93	6.04				
Ti	0.60	0.61	0.57	0.60	0.58	0.61	0.68	0.67	0.65	0.69	0.70	0.67	0.07	0.07	0.62	0.61	0.65	0.79	0.79	0.76	0.72	0.79	0.79	0.76	0.72	0.79	0.79	0.76	0.72	0.79	0.79	0.76	0.72	0.79	0.79	0.76	0.72								
Al	2.94	2.92	2.97	2.96	2.99	3.04	2.93	2.94	3.04	2.99	2.95	3.09	3.33	3.56	3.14	2.84	3.01	2.86	2.83	2.87	2.89	2.86	2.83	2.87	2.89	2.86	2.83	2.87	2.89	2.86	2.83	2.87	2.89	2.86	2.83	2.87	2.89								
Cr	0.00	0.00	0.00	0.00	0.00	0.00	0.00	0.02	0.02	0.04	0.04	0.04	0.00	0.00	0.00	0.00	0.00	0.15	0.14	0.14	0.00	0.15	0.14	0.14	0.00	0.15	0.14	0.14	0.00	0.15	0.14	0.14	0.00	0.15	0.14	0.14	0.00								
Fe <sup>2+</sup>	1.52	1.57	1.45	1.63	1.47	1.50	1.59	1.27	1.26	1.66	1.66	1.69	1.64	1.70	1.80	1.95	1.86	1.83	1.90	1.87	1.79	1.83	1.90	1.87	1.79	1.83	1.90	1.87	1.79	1.83	1.90	1.87	1.79	1.83	1.90	1.87	1.79								
Mn	0.00	0.00	0.00	0.00	0.00	0.00	0.00	0.00	0.00	0.00	0.00	0.00	0.00	0.00	0.00	0.00	0.00	0.00	0.00	0.00	0.02	0.00	0.00	0.00	0.02	0.00	0.00	0.00	0.02	0.00	0.00	0.00	0.02	0.00	0.00	0.00	0.02								
Mg	3.79	3.72	3.84	3.69	3.77	3.73	3.64	3.95	3.88	3.53	3.54	3.44	4.59	4.67	3.67	3.43	3.64	3.19	3.22	3.23	3.34	3.19	3.22	3.23	3.34	3.19	3.22	3.23	3.34	3.19	3.22	3.23	3.34	3.19	3.22	3.23	3.34								
Na	0.06	0.00	0.00	0.00	0.05	0.00	0.00	0.00	0.00	0.05	0.00	0.00	0.00	0.00	0.00	0.00	0.00	0.00	0.00	0.00	0.00	0.00	0.00	0.00	0.00	0.00	0.00	0.00	0.00	0.00	0.00	0.00	0.00	0.00	0.00	0.00	0.00								
K	1.98	1.98	2.02	2.01	1.99	1.91	1.97	2.02	2.02	2.01	2.01	2.02	0.00	0.00	0.00	0.00	0.00	2.05	2.03	2.00	2.01	2.05	2.03	2.00	2.01	2.05	2.03	2.00	2.01	2.05	2.03	2.00	2.01	2.05	2.03	2.00	2.01								
Totals	16.92	16.86	16.91	16.90	16.91	16.81	16.82	16.86	16.85	16.90	16.85	16.86	15.75	15.94	15.16	15.16	15.16	16.79	16.82	16.81	16.81	16.79	16.82	16.81	16.81	16.79	16.82	16.81	16.81	16.79	16.82	16.81	16.81	16.79	16.82	16.81	16.81								
Mg#	0.71	0.70	0.73	0.69	0.72	0.71	0.70	0.76	0.75	0.68	0.68	0.67	0.74	0.73	0.67	0.64	0.66	0.64	0.63	0.63	0.65	0.64	0.63	0.63	0.65	0.64	0.63	0.63	0.65	0.64	0.63	0.63	0.65	0.64	0.63	0.63	0.65								

Table D.15: Biotite chemistry in the metasedimentary rocks of the Brakspruit. Bt = Biotite; m = biotite in the matrix; iopx/igrt = inclusion in orthopyroxene/garnet; r = retrograde biotite; Mg# = Mg/(Mg + Fe<sup>2+</sup>).

sample	DT14		dt14	
	Crd	Crd	Crd	Oam
SiO <sub>2</sub>	50.77	51.60	51.39	50.07
TiO <sub>2</sub>	0.00	0.00	0.00	0.00
Al <sub>2</sub> O <sub>3</sub>	33.85	34.04	34.34	4.60
FeO <sub>T</sub>	2.94	3.03	2.99	19.22
MnO	0.00	0.00	0.00	0.16
MgO	11.44	11.45	11.60	22.45
CaO	0.00	0.00	0.00	0.20
Na <sub>2</sub> O	0.00	0.00	0.00	0.20
K <sub>2</sub> O	0.00	0.00	0.00	0.00
Totals	99.00	100.11	100.32	96.90
Si	5.07	5.10	5.06	7.13
Ti	0.00	0.00	0.00	0.77
Al	3.98	3.96	3.99	0.00
Fe <sup>3+</sup>	0.00	0.00	0.00	0.92
Fe <sup>2+</sup>	0.25	0.25	0.25	1.37
Mn	0.00	0.00	0.00	0.02
Mg	1.70	1.69	1.70	4.76
Ca	0.00	0.00	0.00	0.03
Na	0.00	0.00	0.00	0.06
K	0.00	0.00	0.00	0.00
Totals	11.00	11.00	11.00	15.06
Mg#	0.87	0.87	0.87	0.78

Table D.16: Cordierite and Orthoamphibole chemistry in the metasedimentary rocks of the Brakspuit. Crd = Cordierite; Oam = orthoamphibole; Mg# =  $Mg/(Mg + Fe^{2+})$ .

Sample	dt14										M5										Grt1										Ogn									
	Opx1c	Opx2c	Opx3c	Opx1r	Opx2r	Opx3r	Opx1c	Opx2c	Opx3c	Opx1r	Opx2r	Opx3r	Opx1c	Opx2c	Opx3c	Opx1r	Opx2r	Opx3r	Opx1c	Opx2c	Opx3c	Opx1r	Opx2r	Opx3r	Opx1c	Opx2c	Opx3c	Opx1r	Opx2r	Opx3r										
SiO <sub>2</sub>	50.06	50.43	50.42	50.80	51.10	55.48	50.28	49.76	49.86	50.10	49.98	49.50	49.96	50.17	49.66	50.90	51.19	51.47	52.37	51.47	52.37	51.47	51.26	50.90	51.19	51.47	52.37	51.47	51.26											
TiO <sub>2</sub>	0.13	0.00	0.15	0.00	0.00	0.00	0.00	0.00	0.00	0.00	0.00	0.00	0.00	0.00	0.23	0.20	0.12	0.20	0.00	0.00	0.00	0.00	0.00	0.20	0.12	0.20	0.00	0.00	0.00											
Al <sub>2</sub> O <sub>3</sub>	5.52	5.53	5.68	5.12	4.93	8.80	7.39	7.48	6.93	7.18	7.59	7.08	7.03	6.97	6.74	4.92	5.00	4.89	4.50	4.50	4.50	4.92	4.75	4.92	4.92	4.89	4.50	4.92	4.75											
Cr <sub>2</sub> O <sub>3</sub>	0.30	0.25	0.30	0.19	0.26	0.19	0.00	0.00	0.00	0.15	0.00	0.00	0.23	0.17	0.19	0.40	0.32	0.41	0.33	0.35	0.35	0.33	0.33	0.40	0.32	0.41	0.33	0.35	0.33											
FeO	21.62	21.60	21.77	20.84	20.43	16.53	20.36	20.39	20.46	19.86	19.53	20.42	22.41	22.01	22.33	22.03	21.78	21.76	21.56	21.85	21.85	21.51	21.51	22.03	21.78	21.76	21.56	21.85	21.51											
MnO	0.00	0.00	0.00	0.00	0.00	0.00	0.00	0.00	0.00	0.00	0.00	0.00	0.00	0.00	0.00	0.00	0.00	0.00	0.00	0.00	0.00	0.00	0.00	0.00	0.00	0.00	0.00	0.00	0.00											
MgO	21.45	21.64	21.59	22.21	22.62	18.91	22.24	22.35	21.95	22.80	22.83	22.21	21.12	21.22	21.32	21.73	21.94	21.93	22.04	21.98	21.98	21.77	21.77	21.73	21.94	21.93	22.04	21.98	21.77											
CaO	0.00	0.09	0.10	0.09	0.10	0.00	0.00	0.00	0.00	0.00	0.12	0.09	0.09	0.00	0.09	0.15	0.15	0.00	0.12	0.12	0.12	0.15	0.15	0.15	0.15	0.00	0.12	0.12	0.15											
Totals	99.07	99.53	100.00	99.25	99.45	99.91	100.27	99.99	99.20	100.08	100.05	99.30	100.84	100.54	100.56	100.33	100.50	100.66	100.92	100.69	100.69	99.78	99.78	100.33	100.50	100.66	100.92	100.69	99.78											
Si	1.87	1.88	1.87	1.89	1.89	2.05	1.84	1.83	1.85	1.83	1.83	1.83	1.84	1.85	1.83	1.88	1.89	1.90	1.93	1.89	1.89	1.90	1.90	1.88	1.89	1.90	1.93	1.89	1.90											
Ti	0.00	0.00	0.00	0.00	0.00	0.00	0.00	0.00	0.00	0.00	0.00	0.00	0.00	0.00	0.01	0.01	0.00	0.01	0.00	0.00	0.00	0.00	0.00	0.01	0.00	0.01	0.00	0.00	0.00											
Al	0.24	0.24	0.25	0.22	0.22	0.38	0.32	0.32	0.30	0.31	0.33	0.31	0.30	0.30	0.29	0.21	0.22	0.21	0.19	0.21	0.21	0.21	0.21	0.21	0.21	0.21	0.19	0.21	0.21											
Cr	0.01	0.01	0.01	0.01	0.01	0.01	0.00	0.00	0.00	0.00	0.00	0.00	0.01	0.01	0.01	0.01	0.01	0.01	0.01	0.01	0.01	0.01	0.01	0.01	0.01	0.01	0.01	0.01	0.01											
Fe <sup>2+</sup>	0.68	0.67	0.67	0.65	0.63	0.51	0.62	0.60	0.63	0.59	0.58	0.60	0.68	0.68	0.66	0.68	0.67	0.67	0.66	0.67	0.67	0.67	0.67	0.68	0.67	0.67	0.66	0.67	0.67											
Mn	0.00	0.00	0.00	0.00	0.00	0.00	0.00	0.00	0.00	0.00	0.00	0.00	0.00	0.00	0.00	0.00	0.00	0.00	0.00	0.00	0.00	0.00	0.00	0.00	0.00	0.00	0.00	0.00	0.00											
Mg	1.20	1.20	1.19	1.23	1.25	1.04	1.22	1.25	1.21	1.26	1.27	1.26	1.17	1.17	1.20	1.20	1.21	1.20	1.21	1.21	1.21	1.21	1.21	1.20	1.21	1.20	1.21	1.21	1.21											
Ca	0.00	0.00	0.00	0.00	0.00	0.00	0.00	0.00	0.00	0.00	0.00	0.00	0.00	0.00	0.00	0.00	0.00	0.00	0.00	0.00	0.00	0.00	0.00	0.00	0.00	0.00	0.00	0.00	0.00											
Totals	4.00	4.00	4.00	4.00	4.00	4.00	4.00	4.00	4.00	4.00	4.00	4.00	4.00	4.00	4.00	4.00	4.00	4.00	4.00	4.00	4.00	4.00	4.00	4.00	4.00	4.00	4.00	4.00	4.00											
Mg#	0.64	0.64	0.64	0.66	0.66	0.67	0.66	0.67	0.66	0.68	0.69	0.68	0.63	0.63	0.64	0.64	0.64	0.64	0.65	0.64	0.64	0.64	0.64	0.64	0.64	0.64	0.65	0.64	0.64											

Table D.17: Orthopyroxene chemistry in the metasedimentary rocks of the Brakspruit. Opx = Orthopyroxene; c = core analysis; r = rim analysis; Mg# =  $Mg/(Mg + Fe^{2+})$ .

sample	dtl4										M5										GRTI										Ogn																																																																																																																																																																																																																				
	Plc	Plc	Pli	Pli	Pl	Pl	Plc	Pli	Pli	Pl	Plc	Pli	Pli	Pl	Pl	Plc	Pli	Pli	Pl	Pl	Pli	Pli	Pli	Pl	Pl	Pli	Pli	Pli	Pl	Pl	Pli	Pli	Pli	Pl	Pl	Pli	Pli	Pli	Pl	Pl																																																																																																																																																																																																											
SiO <sub>2</sub>	60.82	61.48	58.34	57.94	64.24	63.94	63.91	65.63	58.92	57.82	57.82	65.98	58.92	62.54	61.51	61.93	57.60	57.10	57.75	56.67	56.92	57.62	24.18	24.26	26.44	26.30	22.57	22.89	22.91	18.12	18.42	25.76	25.35	23.78	23.79	23.78	23.65	26.67	27.19	26.89	27.68	27.95	0.00	0.00	0.00	0.00	0.00	0.00	0.00	0.31	0.49	0.18	0.27	0.00	0.00	0.00	0.00	0.00	0.00	0.00	0.00	0.00	0.00	0.00	6.53	6.55	8.88	8.98	4.71	4.75	4.80	0.29	0.31	8.75	8.07	1.88	6.43	8.07	7.77	8.00	5.95	6.04	5.84	5.47	5.72	5.91	7.41	7.78	6.28	6.44	8.80	8.64	8.60	1.71	1.88	6.43	6.68	1.71	6.43	8.07	7.77	8.00	5.95	6.04	5.84	5.47	5.72	5.91	0.32	0.31	0.19	0.25	0.32	0.30	0.35	14.08	13.66	0.12	0.10	0.42	0.44	0.38	0.35	0.32	0.32	0.32	0.32	0.37	0.29	0.26	0.00	0.00	0.00	0.00	0.00	0.00	0.00	0.00	0.00	0.00	0.00	0.00	0.00	0.00	0.00	0.00	0.00	0.00	0.00	0.00	0.00	0.00	99.27	100.55	100.12	99.90	100.63	100.51	100.57	100.15	100.73	99.07	99.40	99.40	100.73	99.40	100.72	99.60	99.91	99.99	100.15	100.23	100.53	100.82	101.87																																																																				
Totals	2.72	2.72	2.61	2.60	2.83	2.83	2.82	3.02	2.62	2.62	2.62	3.01	2.62	2.77	2.75	2.66	2.59	2.58	2.59	2.54	2.54	2.54	1.28	1.27	1.39	1.39	1.17	1.19	1.19	0.98	0.99	1.38	1.35	1.35	0.99	1.24	1.25	1.20	1.41	1.42	1.42	1.46	1.45	0.00	0.00	0.00	0.00	0.00	0.00	0.00	0.00	0.00	0.00	0.00	0.00	0.00	0.00	0.00	0.00	0.00	0.00	0.00	0.00	0.00	0.00	0.31	0.31	0.42	0.43	0.22	0.22	0.23	0.01	0.02	0.57	0.59	0.02	0.57	0.69	0.67	0.67	0.52	0.52	0.51	0.48	0.50	0.51	0.64	0.67	0.54	0.56	0.75	0.74	0.74	0.15	0.17	0.01	0.01	0.17	0.01	0.02	0.02	0.02	0.02	0.02	0.02	0.02	0.02	0.01	0.02	0.02	0.01	0.01	0.02	0.02	0.02	0.82	0.80	0.00	0.00	0.80	0.00	0.00	0.00	0.00	0.00	0.00	0.00	0.00	0.00	0.00	0.00	0.00	0.00	0.00	0.00	0.00	0.00	0.00	0.00	0.00	0.00	0.00	0.00	0.00	0.00	0.00	0.00	0.00	0.00	0.00	0.00	0.00	4.97	4.98	4.98	4.99	5.00	5.00	5.00	4.99	4.98	4.57	4.57	4.98	4.57	4.60	4.72	4.71	4.54	4.55	4.55	4.55	4.50	4.51	4.52	0.66	0.67	0.56	0.56	0.76	0.75	0.75	0.15	0.17	0.01	0.01	0.17	0.01	0.01	0.03	0.04	0.03	0.04	0.03	0.04	0.03	0.03	0.03	0.32	0.31	0.43	0.43	0.22	0.23	0.23	0.01	0.02	0.99	0.99	0.02	0.99	0.97	0.96	0.96	0.97	0.96	0.97	0.97	0.96	0.97	0.02	0.02	0.01	0.01	0.02	0.02	0.02	0.83	0.81	0.00	0.00	0.81	0.00	0.00	0.00	0.00	0.00	0.00	0.00	0.00	0.00	0.00

Table D.18: Plagioclase chemistry in the metasedimentary rocks the Brakspruit Quarry. Pl = Plagioclase; c = core analysis; r = rim analyses; i = inclusion in garnet/orthopyroxene;  $X_{Ab} = \text{Na}/(\text{Na}+\text{Ca}+\text{K})$ ;  $X_{An} = \text{Ca}/(\text{Na}+\text{Ca}+\text{K})$ ;  $X_{San} = \text{K}/(\text{Na}+\text{Ca}+\text{K})$ .

Sample	dt14		GRT1			Ogn	
	Kfs	Kfs	Kfs	Kfs	Kfs	Kfs	Kfs
SiO <sub>2</sub>	65.16	65.28	65.71	65.94	65.05	65.17	65.02
Al <sub>2</sub> O <sub>3</sub>	18.10	17.70	18.15	17.95	18.19	18.21	18.15
CaO	0.21	0.17	0.00	0.00	0.00	0.16	0.31
Na <sub>2</sub> O	1.10	0.63	0.78	0.89	0.66	1.04	0.37
K <sub>2</sub> O	14.37	15.45	15.20	15.24	15.26	14.32	16.23
BaO	0.00	0.00	0.00	0.00	0.00	0.00	0.00
Totals	98.93	99.23	99.84	100.02	99.16	98.91	100.08
Si	3.02	3.03	3.04	3.05	3.03	3.04	3.02
Al	0.99	0.97	0.99	0.98	1.00	1.00	0.98
Ca	0.01	0.01	0.00	0.00	0.00	0.00	0.00
Na	0.10	0.06	0.07	0.08	0.06	0.09	0.03
K	0.85	0.91	0.90	0.90	0.91	0.85	0.95
Totals	4.96	4.97	5.00	5.00	5.00	4.99	4.97
X <sub>Ab</sub>	0.10	0.06	0.07	0.08	0.06	0.10	0.03
X <sub>An</sub>	0.01	0.01	0.00	0.00	0.00	0.00	0.00
X <sub>S<sub>ann</sub></sub>	0.89	0.93	0.93	0.92	0.94	0.90	0.97

Table D.19: K-feldspar chemistry in the metasedimentary rocks the Brakspruit Quarry.  $Kfs = K\text{-feldspar}$ ;  $X_{Ab} = Na/(Na+Ca+K)$ ;  $X_{An} = Ca/(Na+Ca+K)$ ;  $X_{Sann} = K/(Na+Ca+K)$ .

Sample	dt14		M5		GRT1		Ogn	
	Rt	Rt	Rt	Ilm	Ilm	Ilm	Rt	Ilm
SiO <sub>2</sub>	0.50	0.21	0.47	0.34	0.85	1.50	0.23	
TiO <sub>2</sub>	98.04	97.86	96.05	54.50	49.63	96.62	49.90	
Al <sub>2</sub> O <sub>3</sub>	0.00	0.00	0.00	0.00	0.30	0.62	0.00	
Cr <sub>2</sub> O <sub>3</sub>	0.00	0.00	0.98	0.30	0.00	0.00	0.50	
FeO	0.68	0.47	1.67	44.22	49.10	1.27	47.24	
MnO	0.00	0.00	0.00	0.77	0.21	0.00	1.16	
MgO	0.00	0.00	0.00	0.00	0.52	0.83	0.00	
CaO	0.00	0.00	0.00	0.54	0.00	0.00	0.09	
K <sub>2</sub> O	0.00	0.00	0.00	0.00	0.00	0.34	0.00	
Totals	99.22	98.54	99.17	100.67	100.61	100.83	99.11	
Si	0.01	0.00	0.01	0.01	0.02	0.02	0.00	
Ti	0.99	0.99	0.96	1.03	0.92	0.96	0.82	
Al	0.00	0.00	0.00	0.00	0.01	0.01	0.00	
Cr	0.00	0.00	0.01	0.01	0.00	0.00	0.01	
Fe <sup>3+</sup>	0.00	0.00	0.00	0.00	0.10	0.00	0.61	
Fe <sup>2+</sup>	0.01	0.01	0.02	0.93	0.91	0.01	0.26	
Mn	0.00	0.00	0.00	0.02	0.00	0.00	0.02	
Mg	0.00	0.00	0.00	0.00	0.02	0.02	0.00	
Ca	0.00	0.00	0.00	0.01	0.00	0.00	0.00	
Na	0.00	0.00	0.00	0.00	0.00	0.00	0.02	
K	0.00	0.00	0.00	0.00	0.00	0.01	0.25	
Totals	1.00	1.00	1.00	2.00	2.00	1.02	2.00	

Table D.20: Rutile and ilmenite chemistry in the metasedimentary rocks of the Brakspruit Quarry. Rt = rutile; Ilm = ilmenite

Rock type Sample	L1 <sup>1</sup>		L1 <sup>2</sup>				L2				L2					
	DT09 Grtc	DT09 Grtc	DT06A Grtr	DT06A Grtc	DT02A Grtr	DT02A Grtc	DT15 Grtr	DT15 Grtc	DT15 Grtr	DT15 Grtc	DT15 Opx1r	DT15 Opx1c	DT15 Opx2r	DT15 Opx2c	DT03A Opx1r	DT03A Opx1c
SiO <sub>2</sub>	37.51	39.17	39.46	39.28	38.61	39.35	39.57	40.21	50.34	50.90	50.26	51.94	50.70	50.82		
TiO <sub>2</sub>	0.00	0.00	0.00	0.00	0.00	0.00	0.00	0.00	0.00	0.15	0.29	0.00	0.00	0.00		
Al <sub>2</sub> O <sub>3</sub>	21.49	22.88	22.42	22.10	22.21	22.39	22.22	22.61	6.08	5.47	6.62	4.72	6.01	5.92		
Cr <sub>2</sub> O <sub>3</sub>	0.12	0.00	0.12	0.19	0.19	0.00	0.28	0.21	0.21	0.19	0.27	0.24	0.38	0.29		
FeO <sub>T</sub>	32.09	26.93	29.91	27.07	28.70	25.23	25.74	25.09	20.74	19.98	19.96	19.97	19.98	19.49		
MnO	2.08	1.15	0.50	0.37	1.00	0.60	0.93	1.06	0.00	0.00	-	0.00	0.00	0.00		
MgO	6.40	10.63	8.49	9.88	9.43	11.33	9.65	10.49	21.88	22.95	21.98	23.01	22.28	22.79		
CaO	1.09	1.07	1.27	2.27	0.92	1.16	2.32	1.82	0.00	0.00	0.00	0.17	0.09	0.09		
Totals	100.79	101.84	102.16	101.16	101.06	100.05	100.70	101.49	99.25	99.64	99.38	100.05	99.43	99.39		
Si	2.93	2.94	2.97	2.98	2.95	2.98	3.01	2.98	1.87	1.88	1.86	1.91	1.86	1.88		
Ti	0.00	0.00	0.00	0.00	0.00	0.00	0.00	0.00	0.00	0.00	0.01	0.00	0.00	0.00		
Al	1.98	2.02	1.99	1.97	2.00	2.00	1.99	1.98	0.27	0.24	0.29	0.20	0.26	0.26		
Cr	0.01	0.00	0.01	0.01	0.01	0.00	0.02	0.01	0.01	0.01	0.01	0.01	0.01	0.01		
Fe <sup>3+</sup>	0.14	0.10	0.06	0.06	0.10	0.03	0.00	0.04	0.00	0.00	0.00	0.00	0.01	0.00		
Fe <sup>2+</sup>	1.96	1.59	1.88	1.65	1.73	1.57	1.64	1.51	0.64	0.62	0.62	0.61	0.61	0.60		
Mn	0.14	0.07	0.03	0.02	0.06	0.04	0.06	0.07	0.00	0.00	0.00	0.00	0.00	0.00		
Mg	0.75	1.19	0.95	1.12	1.07	1.28	1.09	1.16	1.21	1.26	1.21	1.26	1.24	1.25		
Ca	0.09	0.09	0.10	0.18	0.08	0.09	0.19	0.14	0.00	0.00	0.00	0.00	0.00	0.00		
Totals	8.00	8.00	8.00	8.00	8.00	8.00	8.00	7.90	4.00	4.00	4.00	3.99	4.00	4.00		
Mg#	0.28	0.43	0.34	0.40	0.38	0.45	0.40	0.43	0.65	0.67	0.66	0.67	0.67	0.68		
X <sub>Spss</sub>	0.05	0.02	0.01	0.01	0.02	0.01	0.02	0.02	0.00	0.00	0.00	0.00	0.00	0.00		
X <sub>GrS</sub>	0.03	0.03	0.03	0.06	0.03	0.03	0.06	0.05	0.00	0.00	0.00	0.00	0.00	0.00		

Table D.21: Garnet and orthopyroxene chemistry in the stromatic (L1) and nebulitic (L2) leucosomes of the Brakspruit Quarry.<sup>1</sup> centimetric leucosome; <sup>2</sup> metric leucosome; Grt = garnet; Opx = orthopyroxene c = core analysis; r = rim analysis; Mg# = Mg/(Mg + Fe<sup>2+</sup>), X<sub>Spss</sub> = Mn/(Fe<sup>2+</sup> + Mn + Mg + Ca), X<sub>GrS</sub> = Ca/(Fe<sup>2+</sup> + Mn + Mg + Ca).



Rock type Sample	L12			L2			L12			L2					
	DT06AI	DT06AII	DT06AI	Btr	Btr	DT06AII	DT15	Btm	DT15	Btm	DT03A	DT06A	Ilm	DT03A	Ilm
SiO <sub>2</sub>	38.46	37.55	37.87	38.26	36.78	36.63	37.71					0.18	0.00	6.83	4.05
TiO <sub>2</sub>	0.31	0.25	1.37	1.23	5.10	5.01	4.98					100.16	48.59	43.08	47.78
Al <sub>2</sub> O <sub>3</sub>	18.81	18.37	17.12	16.78	15.79	15.87	16.05					0.00	0.00	3.40	0.51
Cr <sub>2</sub> O <sub>3</sub>	0.13	0.13	0.12	0.16	0.59	0.53	0.66					0.36	0.32	0.14	0.00
FeO <sub>T</sub>	10.74	10.38	12.57	12.63	12.79	12.54	12.61					0.00	47.63	36.28	43.67
MnO	0.00	0.00	0.00	0.00	0.00	0.00	0.00					0.00	3.79	5.01	1.83
MgO	19.34	19.01	17.20	17.23	14.16	14.22	14.97					0.00	0.00	3.68	0.46
Na <sub>2</sub> O	0.17	0.00	0.19	0.23	0.20	0.00	0.00					-	-	-	-
K <sub>2</sub> O	9.03	8.31	9.45	9.24	9.71	9.33	9.51					0.00	0.00	1.54	0.36
Totals	96.98	93.99	95.90	95.76	95.11	94.14	96.49					100.71	100.33	99.95	98.66
Si	5.97	5.99	6.04	6.10	5.96	5.97	5.99					0.00	0.00	0.16	0.10
Ti	0.04	0.03	0.16	0.15	0.62	0.62	0.60					0.99	0.92	0.75	0.90
Al	3.44	3.45	3.22	3.15	3.02	3.05	3.01					0.00	0.00	0.09	0.01
Cr	0.02	0.02	0.01	0.02	0.08	0.07	0.08					0.00	0.01	0.00	0.00
Fe <sup>3+</sup>	0.00	0.00	0.00	0.00	0.00	0.00	0.00					0.00	0.16	0.13	0.00
Fe <sup>2+</sup>	1.39	1.38	1.68	1.68	1.73	1.71	1.68					0.00	0.84	0.59	0.92
Mn	0.00	0.00	0.00	0.00	0.00	0.00	0.00					0.00	0.08	0.10	0.04
Mg	4.48	4.52	4.09	4.09	3.42	3.46	3.55					0.00	0.00	0.13	0.02
Na	0.05	0.00	0.06	0.07	0.06	0.00	0.00					0.00	0.00	0.00	0.00
K	1.79	1.69	1.92	1.88	2.01	1.94	1.93					0.00	0.00	0.05	0.01
Totals	17.18	17.09	17.17	17.14	16.90	16.82	16.83					1.00	2.00	2.00	2.00
Mg#	0.76	0.77	0.71	0.71	0.66	0.67	0.68								

Table D.22: Biotite, rutile and ilmenite chemistry in the metasedimentary rocks of the Brakspruit. Bt = Biotite; Rt = rutile; Ilm = ilmenite; m = biotite in the matrix; i = inclusion in orthopyroxene/garnet; r = retrograde biotite; Mg# =  $\text{Mg}/(\text{Mg} + \text{Fe}^{2+})$ .

Rock type Sample	L1		L12		L2		L11		L12		L2			
	DT09 Plr	DT09 Plr	DT06A Plr	DT06A Plc	DT02A Plr	DT02A Plc	DT03A Plr	DT03A Plr	DT01A Kfs	DT01A Kfs	DT02A Kfs	DT02A Kfs	DT03A Kfs	DT03A Kfs
SiO <sub>2</sub>	60.12	61.78	60.97	61.83	61.38	62.71	60.11	61.83	65.81	65.68	65.59	65.78	65.89	66.66
Al <sub>2</sub> O <sub>3</sub>	24.36	24.33	24.26	23.47	24.45	23.51	24.58	24.10	18.24	17.86	17.62	17.84	17.78	18.17
CaO	7.12	6.65	6.54	6.05	6.46	5.54	6.97	5.87	0.15	0.19	0.22	0.12	0.14	0.13
Na <sub>2</sub> O	7.36	6.99	7.68	8.15	8.02	8.44	7.56	8.26	0.85	0.62	0.53	0.61	0.59	0.63
K <sub>2</sub> O	0.27	1.23	0.12	0.21	0.18	0.36	0.33	0.29	14.94	15.33	15.37	15.38	15.80	15.35
BaO	0.00	0.00	0.00	0.00	0.00	0.00	0.00	0.00	0.00	0.00	0.00	0.00	0.00	0.00
Total	99.23	100.97	99.58	99.71	100.49	100.56	99.56	100.35	99.98	99.68	99.32	99.74	100.20	100.95
Si	2.70	2.73	2.72	2.75	2.61	2.67	2.69	2.69	3.04	3.05	3.06	3.03	3.03	3.03
Al	1.29	1.27	1.28	1.23	1.22	1.18	1.30	1.21	0.99	0.98	0.97	0.97	0.96	0.97
Ca	0.34	0.31	0.31	0.29	0.29	0.25	0.33	0.27	0.01	0.01	0.01	0.01	0.01	0.01
Na	0.64	0.60	0.66	0.70	0.66	0.70	0.66	0.68	0.08	0.06	0.05	0.05	0.05	0.06
K	0.02	0.07	0.01	0.01	0.01	0.02	0.02	0.02	0.88	0.91	0.91	0.90	0.93	0.89
Ba	0.00	0.00	0.00	0.00	0.00	0.00	0.00	0.00	0.00	0.00	0.00	0.00	0.00	0.00
total	4.98	4.97	4.98	4.99	4.80	4.83	5.00	4.87	4.99	4.99	5.00	4.96	4.98	4.96
X <sub>Ab</sub>	0.64	0.61	0.68	0.70	0.68	0.72	0.65	0.71	0.08	0.06	0.05	0.63	0.69	0.06
X <sub>An</sub>	0.34	0.32	0.32	0.29	0.30	0.26	0.33	0.28	0.01	0.01	0.01	0.63	0.69	0.01
X <sub>Sann</sub>	0.02	0.07	0.01	0.01	0.01	0.02	0.02	0.02	0.91	0.93	0.94	93.70	93.97	0.93

Table D.23: Plagioclase and K-feldspar chemistry in the leucosomes of the Brakspruit. Pl = Plagioclase; Kfs = K-feldspar; c = core analysis; r = rim analysis; X<sub>Ab</sub> = Na/(Na+Ca+K); X<sub>An</sub> = Ca/(Na+Ca+K); X<sub>Sann</sub> = K/(Na+Ca+K).

# Appendix E

## U-Pb zircon analyses

## APPENDIX E. U-PB ZICON ANALYSES

169

Sample	Analysis	U[ppm] <sup>a</sup>	Pb[ppm] <sup>a</sup>	Th/U <sup>a</sup>	Ratios				Ages(Ma)				Conc. %				
					<sup>207</sup> Pb/ <sup>235</sup> U <sup>b</sup>	<sup>206</sup> Pb/ <sup>238</sup> U <sup>b</sup>	<sup>207</sup> Pb/ <sup>206</sup> Pb <sup>c</sup>	$2\sigma^d$	$2\sigma^d$	$2\sigma^d$	$2\sigma^d$	<sup>207</sup> Pb/ <sup>235</sup> U		<sup>206</sup> Pb/ <sup>238</sup> U	<sup>207</sup> Pb/ <sup>206</sup> Pb	$2\sigma$	
L2a	1	204	108	0.07	13.52	0.48	0.530	0.015	0.82	0.185	0.004	2716	2739	65	2699	33	101
L2a	2	225	117	0.11	13.23	0.45	0.522	0.015	0.82	0.184	0.004	2696	2708	62	2687	31	101
L2a	3	207	108	0.08	13.30	0.40	0.522	0.013	0.82	0.185	0.003	2701	2709	54	2696	28	100
L2a	4	251	131	0.08	13.40	0.38	0.524	0.012	0.82	0.186	0.003	2708	2714	51	2704	26	100
L2a	5	239	125	0.08	13.54	0.45	0.525	0.014	0.80	0.187	0.004	2718	2722	59	2715	33	100
L2a	6	166	88	0.06	13.72	0.42	0.528	0.013	0.82	0.188	0.003	2731	2734	57	2729	28	100
L2a	7	194	101	0.10	13.29	0.39	0.521	0.012	0.82	0.185	0.003	2701	2703	53	2699	27	100
L2a	8	325	170	0.07	13.52	0.45	0.525	0.014	0.82	0.187	0.004	2717	2718	61	2715	32	100
L2a	9	157	82	0.08	13.51	0.65	0.524	0.020	0.82	0.187	0.005	2716	2718	87	2715	45	100
L2a	10	283	147	0.10	13.23	0.37	0.519	0.012	0.82	0.185	0.003	2696	2697	50	2695	26	100
L2a	11	217	115	0.08	13.82	0.49	0.529	0.015	0.82	0.189	0.004	2737	2738	65	2737	33	100
L2a	12	221	115	0.09	13.38	0.38	0.522	0.012	0.82	0.186	0.003	2707	2707	51	2707	26	100
L2a	13	167	87	0.15	13.49	0.46	0.523	0.015	0.83	0.187	0.004	2714	2714	62	2715	31	100
L2a	14	138	73	0.19	13.85	0.57	0.529	0.018	0.82	0.190	0.004	2740	2739	75	2740	38	100
L2a	15	187	99	0.10	13.77	0.46	0.528	0.014	0.82	0.189	0.004	2734	2733	61	2735	31	100
L2a	16	216	112	0.09	13.15	0.44	0.518	0.014	0.82	0.184	0.004	2691	2689	59	2692	31	100
L2a	17	219	116	0.06	13.84	0.38	0.529	0.012	0.82	0.190	0.003	2739	2736	51	2741	26	100
L2a	18	130	69	0.09	13.63	0.47	0.525	0.015	0.80	0.188	0.004	2724	2720	62	2727	34	100
L2a	19	214	111	0.07	13.36	0.53	0.520	0.017	0.81	0.186	0.004	2705	2700	71	2709	37	100
L2a	20	309	165	0.02	14.17	0.39	0.533	0.012	0.81	0.193	0.003	2761	2755	49	2766	26	100
L2a	21	214	113	0.11	13.74	0.44	0.526	0.014	0.82	0.190	0.003	2732	2723	59	2739	30	99
L2a	22	205	107	0.07	13.42	0.47	0.520	0.015	0.82	0.187	0.004	2710	2698	63	2719	33	99
L2a	23	169	88	0.15	13.37	0.43	0.519	0.013	0.80	0.187	0.004	2706	2694	57	2716	32	99
L2a	24	129	67	0.18	13.39	0.50	0.518	0.016	0.80	0.187	0.004	2708	2693	66	2719	37	99
L2a	25	139	71	0.13	13.05	0.45	0.512	0.014	0.79	0.185	0.004	2683	2666	60	2696	35	99
L2a	26	130	67	0.11	13.54	0.52	0.519	0.016	0.82	0.189	0.004	2718	2696	70	2735	36	99
L2a	27	238	124	0.01	13.69	0.41	0.522	0.013	0.80	0.190	0.003	2729	2706	53	2746	30	99
L2a	28	95	48	0.12	12.54	0.47	0.502	0.015	0.80	0.181	0.004	2646	2623	65	2663	37	98
L2a	29	113	57	0.09	12.56	0.44	0.501	0.014	0.80	0.182	0.004	2647	2620	60	2669	34	98
L2a	30	162	81	0.10	12.60	0.42	0.500	0.013	0.79	0.183	0.004	2650	2613	57	2679	33	98
L2a	31	119	60	0.05	13.07	0.48	0.507	0.015	0.79	0.187	0.004	2685	2644	63	2716	36	97
L2a	32	150	76	0.08	13.09	0.44	0.507	0.014	0.80	0.187	0.004	2686	2643	58	2719	33	97
L2a	33	139	70	0.08	12.80	0.47	0.502	0.014	0.79	0.185	0.004	2665	2621	62	2699	36	97
L2a	34	141	71	0.11	12.97	0.45	0.504	0.014	0.79	0.187	0.004	2677	2631	59	2712	34	97
L2a	35	170	86	0.11	13.31	0.45	0.509	0.014	0.79	0.190	0.004	2702	2652	58	2740	34	97
L2a	36	149	74	0.09	12.67	0.44	0.497	0.014	0.79	0.185	0.004	2656	2602	59	2697	35	96
L2a	37	190	95	0.04	13.03	0.41	0.501	0.013	0.82	0.189	0.003	2682	2618	56	2730	30	96
L2a	38	83	41	0.06	12.74	0.51	0.494	0.016	0.80	0.187	0.005	2661	2587	69	2718	39	95
L2a	39	134	66	0.10	12.39	0.41	0.488	0.013	0.81	0.184	0.004	2634	2561	57	2692	32	95

Sample	Analysis	U[ppm] <sup>a</sup>	Pb[ppm] <sup>a</sup>	Th/U <sup>a</sup>	Ratios				Ages(Ma)				Conc.				
					<sup>207</sup> Pb/ <sup>235</sup> U <sup>b</sup>	<sup>206</sup> Pb/ <sup>238</sup> U <sup>b</sup>	<sup>207</sup> Pb/ <sup>206</sup> Pb <sup>e</sup>	<sup>207</sup> Pb/ <sup>235</sup> U	<sup>206</sup> Pb/ <sup>238</sup> U	<sup>207</sup> Pb/ <sup>206</sup> Pb	2σ	2σ	%				
L2a	40	100	50	0.06	13.07	0.46	0.498	0.014	0.81	0.190	0.004	2684	2607	62	2743	34	95
L2a	41	133	67	0.35	13.33	0.44	0.503	0.014	0.81	0.192	0.004	2703	2625	58	2763	31	95
L2a	42	128	61	0.09	12.16	0.40	0.476	0.013	0.81	0.185	0.004	2617	2510	56	2700	32	93
L2a	43	122	57	0.13	12.00	0.40	0.470	0.013	0.81	0.185	0.004	2605	2484	56	2701	32	92
L2a	44	604	278	0.01	11.47	0.28	0.460	0.009	0.81	0.181	0.003	2562	2441	40	2660	24	92
L2a	45	358	167	0.03	11.95	0.36	0.466	0.011	0.79	0.186	0.003	2600	2466	49	2707	30	91
L2a	46	467	216	0.04	11.82	0.33	0.461	0.010	0.79	0.186	0.003	2590	2445	45	2706	28	90
L2a	47	487	199	0.02	9.97	0.28	0.408	0.009	0.80	0.177	0.003	2432	2204	42	2629	28	84

Table E.1: U-Th-Pb geochronologic data for metamorphic zircon rim in stromatic leucosome in the Bandelierkop Quarry. <sup>a</sup> U and Pb concentrations and Th/U ratios are calculated relative to GJ-1 reference zircon; <sup>b</sup> Corrected for background and within-run Pb/U fractionation and normalised to reference zircon GJ-1 (ID-TIMS values/measured value); <sup>c</sup> 207Pb/235U calculated using (207Pb/206Pb)/(238U/206Pb\*1/137.88); <sup>d</sup> Rho is the error correlation defined as the quotient of the propagated errors of the 206Pb/238U and the 207/235U ratio; <sup>e</sup> Quadratic addition of within-run errors (2 SD) and daily reproducibility of GJ-1 (2 SD); <sup>f</sup> Corrected for mass-bias by normalising to GJ-1 reference zircon (~0.6 per atomic mass unit) and common Pb using the model Pb composition of Stacey & Kramers (1975)

## APPENDIX E. U-PB ZICON ANALYSES

171

Sample	Analysis	U[ppm] <sup>a</sup>	Pb[ppm] <sup>a</sup>	Th/U <sup>a</sup>	Ratios				Ages(Ma)				Conc. %					
					<sup>207</sup> Pb/ <sup>235</sup> U <sup>b</sup>	<sup>206</sup> Pb/ <sup>238</sup> U <sup>b</sup>	<sup>207</sup> Pb/ <sup>206</sup> Pb <sup>c</sup>	<sup>207</sup> Pb/ <sup>235</sup> U	<sup>206</sup> Pb/ <sup>238</sup> U	<sup>207</sup> Pb/ <sup>206</sup> Pb	<sup>207</sup> Pb/ <sup>235</sup> U	<sup>206</sup> Pb/ <sup>238</sup> U						
L5a	1	135	72	0.14	13.73	0.73	0.530	0.023	0.83	0.188	0.006	2731	145	2742	98	2724	48	101
L5a	2	202	106	0.02	13.39	0.40	0.524	0.013	0.81	0.185	0.003	2708	81	2715	53	2702	29	100
L5a	3	142	74	0.10	13.18	0.58	0.520	0.019	0.81	0.184	0.005	2693	118	2700	79	2687	42	100
L5a	4	221	116	0.02	13.38	0.44	0.523	0.013	0.77	0.185	0.004	2707	90	2714	57	2702	35	100
L5a	5	269	142	0.04	13.60	0.45	0.527	0.014	0.81	0.187	0.004	2722	90	2729	59	2718	31	100
L5a	6	212	111	0.04	13.49	0.50	0.525	0.016	0.82	0.186	0.004	2714	101	2720	68	2710	35	100
L5a	7	278	146	0.02	13.42	0.45	0.524	0.014	0.78	0.186	0.004	2710	91	2715	57	2706	34	100
L5a	8	137	73	0.10	14.01	0.56	0.533	0.017	0.79	0.190	0.005	2750	111	2756	71	2746	40	100
L5a	9	103	54	0.15	13.10	0.46	0.518	0.015	0.81	0.183	0.004	2687	94	2692	62	2683	34	100
L5a	10	92	48	0.21	13.34	0.48	0.522	0.015	0.80	0.185	0.004	2704	96	2709	63	2701	35	100
L5a	11	91	48	0.12	13.44	0.51	0.524	0.016	0.79	0.186	0.004	2711	103	2714	67	2708	38	100
L5a	12	104	54	0.18	13.47	0.50	0.524	0.016	0.81	0.186	0.004	2713	100	2717	67	2711	35	100
L5a	13	111	58	0.19	13.34	0.46	0.522	0.015	0.81	0.185	0.004	2704	94	2707	62	2702	33	100
L5a	14	109	57	0.18	13.46	0.47	0.524	0.015	0.82	0.186	0.004	2712	94	2715	63	2710	33	100
L5a	15	152	81	0.06	14.09	0.50	0.534	0.016	0.82	0.191	0.004	2756	98	2758	65	2755	33	100
L5a	16	104	55	0.21	13.39	0.51	0.522	0.016	0.80	0.186	0.004	2708	103	2709	68	2706	37	100
L5a	17	216	114	0.03	13.88	0.42	0.530	0.013	0.80	0.190	0.003	2742	83	2743	55	2741	30	100
L5a	18	131	69	0.16	13.75	0.54	0.528	0.017	0.82	0.189	0.004	2733	107	2733	72	2733	37	100
L5a	19	365	193	0.10	13.88	0.37	0.530	0.011	0.80	0.190	0.003	2741	73	2742	47	2741	26	100
L5a	20	124	65	0.15	13.44	0.46	0.523	0.014	0.80	0.186	0.004	2711	93	2711	61	2711	33	100
L5a	21	102	54	0.22	14.09	0.48	0.533	0.015	0.81	0.192	0.004	2756	95	2756	62	2756	33	100
L5a	22	155	81	0.05	13.22	0.42	0.519	0.013	0.81	0.185	0.003	2696	85	2696	56	2696	30	100
L5a	23	128	68	0.10	13.95	0.47	0.531	0.014	0.79	0.191	0.004	2747	92	2747	59	2747	33	100
L5a	24	101	52	0.19	13.05	0.64	0.516	0.021	0.83	0.183	0.005	2683	131	2683	89	2684	45	100
L5a	25	122	63	0.19	13.11	0.56	0.517	0.018	0.80	0.184	0.005	2688	114	2687	75	2688	41	100
L5a	26	161	83	0.00	12.96	0.42	0.515	0.013	0.79	0.183	0.004	2677	87	2676	56	2678	33	100
L5a	27	195	101	0.15	13.13	0.44	0.517	0.013	0.77	0.184	0.004	2689	89	2688	56	2690	35	100
L5a	28	139	73	0.06	13.65	0.50	0.526	0.016	0.82	0.188	0.004	2725	99	2724	66	2726	34	100
L5a	29	159	83	0.12	13.24	0.42	0.519	0.013	0.80	0.185	0.004	2697	86	2695	56	2698	31	100
L5a	30	115	60	0.19	13.63	0.51	0.526	0.016	0.82	0.188	0.004	2725	102	2723	68	2726	35	100
L5a	31	401	209	0.00	13.33	0.41	0.521	0.012	0.78	0.186	0.004	2703	83	2701	53	2705	32	100
L5a	32	229	123	0.01	14.16	0.40	0.534	0.012	0.81	0.192	0.003	2761	78	2758	51	2762	27	100
L5a	33	348	182	0.02	13.41	0.39	0.522	0.012	0.80	0.186	0.003	2709	80	2707	52	2711	29	100
L5a	34	128	68	0.18	14.17	0.51	0.534	0.016	0.81	0.192	0.004	2761	100	2759	65	2763	34	100
L5a	35	95	50	0.21	13.34	0.67	0.520	0.022	0.83	0.186	0.005	2704	135	2701	91	2706	46	100
L5a	36	333	174	0.01	13.50	0.39	0.523	0.012	0.81	0.187	0.003	2715	78	2711	51	2718	27	100
L5a	37	180	93	0.06	13.19	0.40	0.518	0.013	0.79	0.185	0.003	2693	82	2689	53	2696	30	100
L5a	38	409	211	0.19	13.05	0.35	0.515	0.011	0.78	0.184	0.003	2683	73	2679	47	2686	28	100
L5a	39	174	91	0.05	13.53	0.53	0.523	0.017	0.80	0.188	0.004	2717	107	2713	70	2720	38	100

## APPENDIX E. U-PB ZICON ANALYSES

172

Sample	Analysis	U[ppm] <sup>a</sup>	Pb[ppm] <sup>a</sup>	Th/U <sup>a</sup>	Ratios				Ages(Ma)				Conc. %				
					<sup>207</sup> Pb/ <sup>235</sup> U <sup>b</sup>	<sup>206</sup> Pb/ <sup>238</sup> U <sup>b</sup>	$2\sigma^d$	$\rho^c$	<sup>207</sup> Pb/ <sup>206</sup> Pb <sup>e</sup>	$2\sigma^d$	<sup>207</sup> Pb/ <sup>235</sup> U	$2\sigma$		<sup>206</sup> Pb/ <sup>238</sup> U	$2\sigma$	<sup>207</sup> Pb/ <sup>206</sup> Pb	$2\sigma$
L5a	40	112	60	0.12	13.97	0.530	0.016	0.79	0.191	0.004	2748	104	2743	67	2751	38	100
L5a	41	110	57	0.21	13.35	0.520	0.016	0.81	0.186	0.004	2705	102	2700	67	2708	36	100
L5a	42	129	68	0.20	13.48	0.522	0.017	0.82	0.187	0.004	2714	106	2709	71	2718	36	100
L5a	43	101	52	0.18	13.13	0.516	0.014	0.81	0.184	0.004	2689	92	2683	61	2693	33	100
L5a	44	119	63	0.13	13.89	0.528	0.018	0.82	0.191	0.005	2742	113	2735	75	2748	39	100
L5a	45	94	50	0.19	13.73	0.526	0.016	0.82	0.189	0.004	2731	103	2724	69	2737	35	100
L5a	46	222	117	0.04	13.78	0.526	0.015	0.82	0.190	0.004	2735	95	2726	63	2741	33	99
L5a	47	141	73	0.14	13.29	0.518	0.014	0.77	0.186	0.004	2700	92	2691	58	2707	35	99
L5a	48	543	280	0.02	13.15	0.516	0.011	0.76	0.185	0.003	2690	76	2681	47	2697	30	99
L5a	49	328	170	0.01	13.37	0.519	0.012	0.77	0.187	0.003	2706	78	2695	49	2714	30	99
L5a	50	133	68	0.08	13.03	0.54	0.017	0.82	0.184	0.004	2682	110	2671	74	2690	38	99
L5a	51	100	52	0.20	13.45	0.61	0.020	0.83	0.188	0.005	2712	124	2695	83	2725	42	99
L5a	52	123	63	0.08	13.15	0.513	0.014	0.79	0.186	0.004	2690	93	2671	59	2705	35	99
L5a	53	88	45	0.20	12.84	0.508	0.015	0.79	0.183	0.004	2668	100	2647	64	2684	37	99
L5a	54	248	127	0.02	13.14	0.512	0.012	0.78	0.186	0.004	2690	82	2666	52	2708	31	98
L5a	55	456	236	0.23	13.57	0.518	0.010	0.80	0.190	0.003	2720	87	2692	43	2742	24	98
L5a	56	189	95	0.02	12.61	0.501	0.012	0.78	0.183	0.003	2651	81	2617	52	2677	31	98
L5a	57	191	97	0.06	12.98	0.505	0.018	0.80	0.186	0.005	2678	119	2636	77	2710	43	97
L5a	58	123	62	0.12	12.99	0.51	0.016	0.79	0.187	0.004	2679	105	2633	67	2714	39	97
L5a	59	258	130	0.18	12.87	0.502	0.012	0.77	0.186	0.004	2670	84	2624	52	2706	33	97
L5a	60	506	253	0.02	12.71	0.499	0.010	0.80	0.185	0.003	2659	64	2610	42	2696	23	97
L5a	61	587	299	0.17	13.35	0.509	0.010	0.79	0.190	0.003	2704	65	2652	42	2744	24	97
L5a	62	108	53	0.19	12.58	0.490	0.020	0.82	0.186	0.005	2648	130	2570	85	2709	46	95
L5a	63	178	82	0.20	11.88	0.41	0.0458	0.81	0.188	0.004	2595	89	2431	56	2726	33	89
L5a	64	483	213	0.25	11.29	0.28	0.009	0.80	0.186	0.003	2547	63	2356	39	2703	24	87
L5a	65	587	246	0.03	10.55	0.31	0.009	0.76	0.182	0.003	2484	72	2259	42	2674	31	84

Table E.2: U-Th-Pb geochronologic data for metamorphic zircon rim in nebulitic leucosome in the Bandelierkop Quarry. <sup>a</sup> U and Pb concentrations and Th/U ratios are calculated relative to G-J-1 reference zircon; <sup>b</sup> Corrected for background and within-run Pb/U fractionation and normalised to reference zircon G-J-1 (ID-TIMS values/measured value); <sup>c</sup> Rho is the error correlation defined as the quotient of the propagated errors of the (207Pb/206Pb)/(238U/206Pb \* 1/137.88); <sup>d</sup> Quadratic addition of within-run errors (2 SD) and daily reproducibility of G-J-1 (2 SD); <sup>e</sup> Corrected for mass-bias by normalising to G-J-1 reference zircon (~0.6 per atomic mass unit) and common Pb using the model Pb composition of Stacey & Kramers (1975).

## APPENDIX E. U-PB ZICON ANALYSES

173

Sample	Analysis	U [ppm] <sup>a</sup>	Pb [ppm] <sup>a</sup>	Th/U <sup>a</sup>	Ratios			Ages (Ma)			Conc.							
					<sup>207</sup> Pb/ <sup>235</sup> U <sup>b</sup>	<sup>206</sup> Pb/ <sup>238</sup> U <sup>b</sup>	$2\sigma^d$	$2\sigma^d$	$2\sigma^d$	<sup>207</sup> Pb/ <sup>206</sup> Pb <sup>c</sup>	$2\sigma^d$	<sup>207</sup> Pb/ <sup>238</sup> U	$2\sigma$	%				
M2	A005	108	56	0.12	13.21	0.40	0.518	0.012	0.73	0.1850	0.0038	2695	82	2691	49	2698	34	100
M2	A006	127	62	0.12	12.36	0.37	0.492	0.011	0.73	0.1823	0.0038	2632	80	2579	47	2674	34	96
M2	A007	249	130	0.12	13.45	0.41	0.522	0.012	0.74	0.1868	0.0038	2712	82	2710	49	2714	33	100
M2	A008	1057	352	1.78	7.56	0.23	0.333	0.007	0.74	0.1646	0.0034	2180	66	1853	36	2503	34	74
M2	A009	1398	347	0.05	5.07	0.15	0.248	0.006	0.74	0.1480	0.0030	1831	55	1430	28	2323	35	62
M2	A010	157	81	0.16	12.96	0.39	0.515	0.011	0.73	0.1827	0.0038	2677	81	2676	49	2678	34	100
M2	A011	272	172	0.42	21.56	0.65	0.633	0.014	0.74	0.2471	0.0050	3164	95	3161	55	3166	32	100
M2	A012	1893	360	0.06	3.29	0.10	0.190	0.004	0.73	0.1254	0.0026	1478	44	1122	23	2035	36	55
M2	A016	262	133	0.13	12.55	0.38	0.507	0.011	0.73	0.1796	0.0037	2646	80	2642	48	2649	34	100
M2	A017	570	188	0.62	7.85	0.24	0.329	0.007	0.74	0.1728	0.0035	2214	67	1835	35	2585	34	71
M2	A019	100	57	0.73	16.67	0.51	0.572	0.013	0.73	0.2115	0.0044	2916	89	2915	52	2917	34	100
M2	A021	333	176	0.23	13.87	0.42	0.528	0.012	0.73	0.1904	0.0039	2741	82	2734	49	2745	33	100
M2	A022	184	95	0.15	12.94	0.39	0.516	0.011	0.73	0.1820	0.0037	2675	81	2680	48	2671	34	100
M2	A023	1252	350	0.01	5.59	0.17	0.279	0.006	0.73	0.1451	0.0030	1914	58	1588	31	2289	35	69
M2	A024	852	245	0.25	6.79	0.21	0.288	0.006	0.73	0.1710	0.0035	2085	63	1633	32	2567	35	64
M2	A025	1923	372	0.32	3.34	0.10	0.194	0.004	0.73	0.1251	0.0026	1491	45	1141	23	2030	36	56
M2	A031	58	38	0.40	23.95	0.73	0.660	0.015	0.73	0.2632	0.0055	3266	99	3266	57	3266	33	100
M2	A032	118	61	0.12	13.05	0.40	0.516	0.011	0.73	0.1834	0.0038	2683	81	2683	48	2684	34	100
M2	A033	188	99	0.14	13.68	0.42	0.526	0.012	0.73	0.1885	0.0040	2728	83	2725	49	2729	34	100
M2	A034	693	285	0.01	9.46	0.28	0.411	0.009	0.74	0.1669	0.0034	2384	71	2221	41	2527	34	88
M2	A035	657	137	0.04	5.32	0.18	0.209	0.005	0.69	0.1848	0.0044	1872	62	1223	25	2696	39	45
M2	A036	373	130	0.78	7.46	0.23	0.347	0.008	0.71	0.1558	0.0035	2168	68	1923	37	2410	38	80
M2	A037	749	262	0.29	8.94	0.27	0.349	0.008	0.72	0.1855	0.0039	2332	71	1932	37	2703	35	71
M2	A040	1218	352	0.38	7.40	0.22	0.289	0.006	0.73	0.1859	0.0038	2161	65	1635	32	2706	33	60
M2	A041	45	26	0.65	17.68	0.54	0.586	0.013	0.72	0.2187	0.0046	2972	91	2974	53	2971	34	100
M2	A042	1549	341	0.02	3.95	0.12	0.220	0.005	0.72	0.1304	0.0028	1624	50	1281	26	2103	37	61
M2	A043	284	132	0.79	13.94	0.42	0.465	0.010	0.73	0.2176	0.0045	2745	82	2460	45	2963	33	83
M2	A044	1135	347	0.09	6.48	0.19	0.306	0.007	0.73	0.1537	0.0031	2043	61	1720	33	2387	35	72
M2	A045	248	142	0.35	16.62	0.50	0.571	0.013	0.73	0.2112	0.0043	2913	87	2910	51	2915	33	100
M2	A046	757	232	0.06	7.68	0.24	0.307	0.007	0.72	0.1817	0.0039	2194	68	1724	33	2668	35	65
M2	A047	132	83	0.26	20.87	0.63	0.626	0.014	0.73	0.2419	0.0050	3133	94	3134	54	3132	32	100
M2	A051	72	43	0.74	18.48	0.57	0.596	0.013	0.72	0.2248	0.0049	3015	93	3014	53	3016	34	100
M2	A057	114	59	0.14	13.18	0.42	0.522	0.012	0.70	0.1831	0.0042	2692	86	2707	49	2681	38	101
M2	A058	144	75	0.15	13.05	0.39	0.518	0.011	0.73	0.1828	0.0038	2683	81	2689	48	2679	34	100
M2	A059	493	264	0.24	14.27	0.43	0.536	0.012	0.73	0.1931	0.0039	2768	83	2767	49	2769	33	100
M2	A060	190	98	0.09	13.15	0.39	0.518	0.011	0.73	0.1840	0.0038	2690	81	2692	48	2689	34	100
M2	A061	747	218	0.22	7.42	0.22	0.292	0.006	0.73	0.1844	0.0038	2164	65	1651	32	2693	33	61
M2	A062	167	97	0.75	17.24	0.52	0.580	0.013	0.72	0.2155	0.0045	2949	89	2951	52	2947	34	100
M2	A063	1380	248	0.45	3.84	0.12	0.180	0.004	0.70	0.1549	0.0035	1602	51	1067	22	2401	38	44



## APPENDIX E. U-PB ZICON ANALYSES

174

Sample	Analysis	U [ppm] <sup>a</sup>	Pb [ppm] <sup>a</sup>	Th/U <sup>a</sup>	Ratios			Ages (Ma)			Conc.					
					<sup>207</sup> Pb/ <sup>235</sup> U <sup>b</sup>	<sup>206</sup> Pb/ <sup>238</sup> U <sup>b</sup>	$2\sigma^d$	$207\text{Pb}/^{206}\text{Pb}^c$	$2\sigma^d$	$207\text{Pb}/^{238}\text{U}$	$2\sigma$	$207\text{Pb}/^{206}\text{Pb}$	$2\sigma$	%		
M2	A064	127	75	1.38	18.11	0.591	0.013	0.2222	0.0046	2995	90	2993	52	2997	33	100
M2	A065	95	45	0.81	15.87	0.474	0.011	0.2426	0.0061	2869	98	2503	48	3137	40	80
M2	A066	282	132	0.11	11.88	0.467	0.010	0.1843	0.0038	2595	78	2472	45	2692	34	92
M2	A067	116	60	0.67	15.12	0.46	0.011	0.2109	0.0044	2823	86	2699	48	2912	34	93
M2	A068	445	192	0.03	10.91	0.432	0.009	0.1832	0.0038	2515	75	2314	42	2682	34	86
M2	A069	583	242	0.16	10.24	0.415	0.009	0.1788	0.0037	2457	73	2240	41	2642	34	85
M2	A070	568	298	0.02	13.77	0.41	0.011	0.1900	0.0039	2734	82	2723	48	2742	33	99
M2	A071	371	195	0.26	13.64	0.41	0.011	0.1886	0.0039	2725	81	2720	48	2730	33	100
M2	A074	84	39	0.20	15.77	0.470	0.011	0.2430	0.0066	2863	103	2486	49	3140	43	79
M2	A075	200	104	0.14	13.12	0.39	0.011	0.1839	0.0038	2688	80	2689	48	2688	34	100
M2	A076	559	219	0.31	10.54	0.32	0.009	0.1954	0.0041	2483	76	2129	40	2788	35	76
M2	A077	672	266	0.15	10.12	0.30	0.009	0.1857	0.0038	2446	73	2148	40	2704	34	79
M2	A078	395	227	1.28	16.73	0.50	0.012	0.2115	0.0043	2919	87	2923	51	2917	33	100
M2	A079	440	227	0.39	13.04	0.39	0.011	0.1835	0.0037	2683	80	2681	47	2684	34	100
M2	A080	45	30	0.55	24.33	0.76	0.015	0.2667	0.0058	3282	102	3273	57	3287	34	100
M2	A081	192	105	0.63	15.10	0.45	0.012	0.2000	0.0041	2821	84	2815	49	2826	33	100
M2	A082	422	154	0.04	8.68	0.26	0.008	0.1725	0.0035	2305	69	2007	37	2582	34	78
M2	A083	569	294	0.00	13.09	0.39	0.011	0.1834	0.0037	2686	80	2689	48	2684	34	100
M2	A084	317	134	0.18	11.15	0.35	0.009	0.1909	0.0042	2536	79	2277	42	2750	36	83
M2	A085	163	84	0.13	12.89	0.39	0.011	0.1819	0.0038	2672	81	2675	48	2670	35	100
M2	A086	382	194	0.07	13.02	0.39	0.011	0.1858	0.0038	2681	80	2650	47	2705	34	98
M2	A087	974	322	0.29	8.30	0.25	0.007	0.1823	0.0038	2265	68	1840	35	2674	34	69
M2	A088	234	116	0.34	12.70	0.38	0.011	0.1861	0.0039	2657	80	2591	46	2708	34	96
M2	A091	1563	328	0.01	3.80	0.12	0.005	0.1315	0.0028	1593	48	1226	24	2119	37	58
M2	A092	1254	285	0.28	4.52	0.14	0.005	0.1441	0.0031	1734	53	1320	26	2277	36	58
M2	A093	457	208	0.38	11.66	0.35	0.010	0.1859	0.0038	2578	77	2417	43	2707	34	89
M2	A094	216	121	1.11	15.85	0.47	0.012	0.2050	0.0042	2868	86	2870	50	2867	33	100
M2	A095	265	147	0.60	15.44	0.46	0.012	0.2024	0.0042	2843	85	2838	50	2846	33	100
M2	A096	701	264	0.02	8.87	0.26	0.008	0.1706	0.0035	2325	69	2062	38	2564	34	80
M2	A097	318	177	0.40	15.50	0.46	0.012	0.2018	0.0042	2847	85	2855	50	2841	33	100
M2	A098	295	169	0.66	16.80	0.50	0.012	0.2124	0.0044	2923	87	2922	51	2924	33	100
M2	A100	509	185	0.13	8.33	0.25	0.008	0.1668	0.0035	2268	68	1993	37	2526	35	79
M2	A101	256	116	0.47	11.66	0.35	0.010	0.1857	0.0039	2577	77	2419	44	2704	34	89
M2	A102	206	107	0.13	13.16	0.39	0.011	0.1840	0.0038	2691	80	2695	47	2689	34	100
M2	A108	1164	292	0.93	5.02	0.15	0.005	0.1448	0.0031	1822	55	1445	28	2286	36	63
M2	A109	224	86	0.36	12.57	0.43	0.009	0.2381	0.0061	2648	91	2091	41	3107	40	67
M2	A110	179	104	0.32	17.14	0.51	0.012	0.2146	0.0044	2943	88	2946	51	2941	33	100
M2	A111	357	189	0.32	13.78	0.41	0.011	0.1894	0.0040	2735	82	2732	48	2737	34	100
M2	A112	378	221	0.32	17.60	0.52	0.013	0.2182	0.0045	2968	88	2969	51	2967	33	100

## APPENDIX E. U-PB ZICON ANALYSES

175

Sample	Analysis	U [ppm] <sup>a</sup>	Pb [ppm] <sup>a</sup>	Th/U <sup>a</sup>	Ratios			Ages (Ma)			Conc.						
					<sup>207</sup> Pb/ <sup>235</sup> U <sup>b</sup>	<sup>206</sup> Pb/ <sup>238</sup> U <sup>b</sup>	$2\sigma^d$	$\rho^{c,e}$	<sup>207</sup> Pb/ <sup>206</sup> Pb <sup>e</sup>	$2\sigma^d$	<sup>207</sup> Pb/ <sup>235</sup> U	$2\sigma$	<sup>206</sup> Pb/ <sup>238</sup> U	$2\sigma$	%		
M2	Al13	405	150	0.14	9.54	0.28	0.371	0.008	0.1864	0.0039	2392	71	2035	37	2711	34	75
M2	Al14	298	132	0.04	11.24	0.34	0.445	0.010	0.1834	0.0038	2543	76	2371	43	2684	34	88
M2	Al15	127	77	0.98	19.35	0.58	0.606	0.013	0.2317	0.0048	3060	92	3053	52	3064	33	100
M2	Al16	99	57	0.81	17.00	0.51	0.577	0.012	0.2137	0.0045	2935	88	2936	51	2934	34	100
M2	Al18	219	94	0.59	12.62	0.38	0.427	0.009	0.2142	0.0044	2652	79	2294	41	2937	33	78
M2	Al19	195	115	0.56	18.19	0.54	0.593	0.013	0.2223	0.0046	3000	90	3003	51	2998	33	100
M2	Al25	356	199	0.40	15.79	0.47	0.559	0.012	0.2047	0.0042	2864	85	2863	49	2864	33	100
M2	Al26	632	206	0.33	8.33	0.25	0.326	0.007	0.1854	0.0039	2267	68	1818	34	2702	35	67
M2	Al27	61	34	0.63	15.92	0.48	0.560	0.012	0.2062	0.0044	2872	87	2866	50	2876	34	100
M2	Al28	801	330	0.27	10.54	0.31	0.412	0.009	0.1857	0.0038	2483	74	2223	40	2704	34	82
M2	Al29	186	97	0.15	13.20	0.40	0.521	0.011	0.1838	0.0039	2694	81	2703	47	2688	34	101
M2	Al30	755	359	0.01	12.86	0.38	0.475	0.010	0.1964	0.0041	2670	80	2506	44	2796	34	90
M2	Al31	540	223	0.10	11.17	0.33	0.414	0.009	0.1958	0.0041	2538	76	2233	40	2791	34	80
M2	Al32	363	200	0.35	15.21	0.45	0.552	0.012	0.2000	0.0041	2829	84	2832	49	2826	34	100
M2	Al33	285	159	0.26	15.81	0.47	0.558	0.012	0.2056	0.0043	2865	86	2857	49	2871	34	100
M2	Al34	835	321	0.34	9.87	0.29	0.385	0.008	0.1861	0.0039	2423	72	2098	38	2708	34	77
M2	Al35	231	107	0.81	13.59	0.41	0.463	0.010	0.2131	0.0045	2722	82	2451	44	2930	34	84
M2	Al36	120	69	0.33	17.07	0.51	0.578	0.012	0.2144	0.0045	2939	88	2939	50	2939	34	100
M2	Al37	276	161	0.67	17.59	0.52	0.584	0.012	0.2183	0.0045	2967	88	2966	51	2968	33	100
M2	Al38	166	102	0.56	20.38	0.61	0.619	0.013	0.2389	0.0050	3110	93	3105	52	3113	33	100
M2	Al39	144	74	0.15	13.00	0.39	0.516	0.011	0.1827	0.0038	2679	80	2682	47	2678	35	100
M2	Al42	243	139	0.47	16.75	0.50	0.572	0.012	0.2125	0.0044	2921	87	2916	50	2924	33	100
M2	Al43	523	254	2.58	13.83	0.41	0.486	0.010	0.2064	0.0043	2738	81	2553	45	2878	34	89
M2	Al44	199	81	0.12	10.37	0.32	0.407	0.009	0.1849	0.0041	2469	76	2201	40	2698	36	82
M2	Al45	1014	359	0.02	9.10	0.27	0.355	0.008	0.1863	0.0039	2349	70	1956	36	2709	34	72
M2	Al46	54	33	0.60	20.36	0.62	0.620	0.013	0.2382	0.0051	3109	94	3110	53	3108	34	100
M2	Al47	232	121	0.10	13.42	0.40	0.522	0.011	0.1863	0.0039	2710	81	2709	47	2710	34	100
M2	Al48	148	71	0.16	12.23	0.38	0.479	0.010	0.1853	0.0041	2622	81	2522	45	2701	36	93
M2	Al49	151	79	0.13	13.25	0.40	0.522	0.011	0.1842	0.0039	2698	81	2706	47	2691	35	101
M2	Al50	329	193	1.26	17.78	0.53	0.587	0.012	0.2198	0.0046	2978	88	2976	50	2979	33	100
M2	Al51	306	146	0.07	12.20	0.36	0.478	0.010	0.1852	0.0039	2620	78	2518	44	2700	34	93
M2	Al52	255	86	0.09	8.44	0.25	0.339	0.007	0.1809	0.0038	2280	68	1880	35	2662	35	71
M2	Al53	241	105	0.22	12.37	0.37	0.438	0.009	0.2049	0.0043	2633	78	2341	42	2866	34	82
M2	Al54	942	227	0.14	5.19	0.15	0.241	0.005	0.1560	0.0032	1851	55	1394	26	2413	35	58
M2	Al55	380	216	1.62	16.14	0.48	0.567	0.012	0.2065	0.0044	2885	86	2895	49	2878	34	101
M2	Al56	352	202	0.47	16.82	0.50	0.573	0.012	0.2128	0.0044	2925	87	2922	50	2927	33	100
M2	Al59	63	39	0.35	21.44	0.66	0.628	0.013	0.2477	0.0054	3159	97	3141	53	3170	34	99
M2	Al60	752	249	0.20	7.07	0.21	0.332	0.007	0.1547	0.0032	2120	63	1846	34	2398	35	77
M2	Al61	250	128	0.08	12.75	0.38	0.511	0.011	0.1811	0.0038	2661	79	2660	46	2663	34	100

Sample	Analysis	U [ppm] <sup>a</sup>	Pb [ppm] <sup>a</sup>	Th/U <sup>a</sup>	Ratios			rho <sup>c</sup>	207Pb/206Pb <sup>e</sup>	2σ <sup>d</sup>	Ages (Ma)			2σ	Conc. %			
					207Pb/235U <sup>b</sup>	2σ <sup>d</sup>	206Pb/238U <sup>b</sup>				2σ <sup>d</sup>	207Pb/235U	2σ			206Pb/238U	2σ	
M2	A162	324	147	0.48	13.20	0.39	0.454	0.010	0.71	0.2108	0.0044	2694	80	2413	42	2912	34	83
M2	A163	369	156	0.04	11.46	0.34	0.423	0.009	0.71	0.1966	0.0041	2561	76	2273	40	2798	34	81
M2	A164	292	106	0.45	9.33	0.28	0.365	0.008	0.71	0.1852	0.0039	2371	71	2007	36	2700	35	74
M2	A165	1335	283	0.32	4.27	0.13	0.212	0.004	0.71	0.1462	0.0031	1687	50	1238	24	2302	36	54
M2	A166	299	196	0.69	23.31	0.69	0.656	0.014	0.71	0.2578	0.0054	3240	96	3251	54	3233	33	101
M2	A167	162	78	0.14	11.71	0.35	0.480	0.010	0.71	0.1771	0.0037	2582	77	2525	44	2626	35	96
M2	A168	321	118	0.15	9.30	0.28	0.368	0.008	0.71	0.1835	0.0039	2368	70	2018	37	2685	35	75
M2	A169	166	99	0.93	21.02	0.62	0.598	0.013	0.71	0.2548	0.0053	3139	93	3023	51	3215	33	94
M2	A170	1811	264	1.21	2.36	0.07	0.146	0.003	0.69	0.1176	0.0026	1231	38	877	17	1920	39	46
M2	A171	222	94	0.56	10.80	0.33	0.422	0.009	0.69	0.1858	0.0041	2506	77	2268	41	2705	36	84
M2	A176	339	162	0.68	13.30	0.40	0.478	0.010	0.70	0.2016	0.0043	2701	81	2521	44	2839	34	89
M2	A177	581	252	0.01	11.08	0.33	0.434	0.009	0.71	0.1853	0.0039	2530	75	2323	41	2701	34	86
M2	A178	924	328	0.15	9.07	0.27	0.355	0.007	0.71	0.1854	0.0039	2345	69	1958	35	2701	34	72
M2	A179	91	42	0.12	11.82	0.36	0.464	0.010	0.70	0.1845	0.0040	2590	79	2459	43	2694	36	91
M2	A180	253	139	0.83	14.90	0.44	0.548	0.012	0.71	0.1971	0.0041	2809	83	2819	48	2802	34	101
M2	A181	339	159	0.74	14.93	0.45	0.468	0.010	0.70	0.2313	0.0050	2811	85	2475	43	3061	34	81
M2	A182	275	174	0.67	21.65	0.64	0.634	0.013	0.71	0.2477	0.0052	3168	94	3165	53	3170	33	100
M2	A183	182	88	0.44	12.41	0.37	0.484	0.010	0.70	0.1859	0.0040	2636	79	2546	44	2706	35	94
M2	A185	71	41	0.47	17.36	0.53	0.582	0.012	0.70	0.2165	0.0047	2955	89	2956	50	2955	35	100
M2	A186	131	68	0.14	13.07	0.39	0.517	0.011	0.70	0.1833	0.0039	2685	80	2687	46	2683	35	100
M2	A187	248	129	0.05	13.32	0.40	0.521	0.011	0.71	0.1853	0.0039	2703	80	2705	46	2701	35	100
M2	A188	894	291	1.01	8.34	0.25	0.325	0.007	0.71	0.1860	0.0039	2269	67	1816	33	2707	34	67
M2	A189	552	262	0.63	13.05	0.39	0.475	0.010	0.71	0.1993	0.0042	2683	80	2505	43	2820	34	89
M2	A190	287	157	0.51	18.00	0.54	0.545	0.011	0.70	0.2394	0.0051	2990	89	2806	48	3116	33	90

Table E.3: U-Th-Pb geochronologic data for detrital zircon in metapelite in the Brakspruit Quarry. <sup>a</sup> U and Pb concentrations and Th/U ratios are calculated relative to GJ-1 reference zircon; <sup>b</sup> Corrected for background and within-run Pb/U fractionation and normalised to reference zircon GJ-1 (ID-TIMS values/measured value); <sup>c</sup> 207Pb/235U calculated using (207Pb/206Pb)/(238U/206Pb \* 1/137.88); <sup>d</sup> Rho is the error correlation defined as the quotient of the propagated errors of the 206Pb/238U and the 207/235U ratio; <sup>e</sup> Quadratic addition of within-run errors (2 SD) and daily reproducibility of GJ-1 (2 SD); <sup>f</sup> Corrected for mass-bias by normalising to GJ-1 reference zircon (~0.6 per atomic mass unit) and common Pb composition of Stacey & Kramers (1975).

## APPENDIX E. U-PB ZICON ANALYSES

Sample	Analysis	U[ppm] <sup>a</sup>	Pb[ppm] <sup>a</sup>	Th/U <sup>a</sup>	<sup>207</sup> Pb/ <sup>235</sup> U <sup>b</sup>	Ratios			<sup>207</sup> Pb/ <sup>206</sup> Pb <sup>e</sup>	$2\sigma^d$	rho <sup>c</sup>	Ages(Ma)			$2\sigma$	Conc. %		
						<sup>207</sup> Pb/ <sup>235</sup> U <sup>b</sup>	$2\sigma^d$	<sup>206</sup> Pb/ <sup>238</sup> U <sup>b</sup>				$2\sigma^d$	<sup>207</sup> Pb/ <sup>235</sup> U	$2\sigma$			<sup>206</sup> Pb/ <sup>238</sup> U	$2\sigma$
L2b	A093	287	153	0.03	14.01	0.46	0.531	0.014	0.78	0.191	0.004	2751	91	2746	57	2754	34	100
L2b	A094	139	74	0.06	13.86	0.46	0.530	0.014	0.77	0.190	0.004	2740	92	2740	57	2740	35	100
L2b	A095	331	176	0.02	13.83	0.46	0.531	0.014	0.78	0.189	0.004	2738	90	2747	57	2732	34	101
L2b	A096	268	142	0.03	13.84	0.46	0.531	0.014	0.78	0.189	0.004	2739	91	2746	57	2733	34	100
L2b	A098	566	286	0.04	13.23	0.44	0.504	0.013	0.78	0.190	0.004	2696	89	2633	56	2744	34	96
L2b	A099	239	133	0.04	15.52	0.52	0.556	0.014	0.77	0.203	0.004	2848	95	2849	59	2848	34	100
L2b	A101	343	182	0.02	14.07	0.47	0.533	0.014	0.78	0.192	0.004	2755	91	2753	58	2756	34	100
L2b	A102	241	128	0.04	13.91	0.46	0.532	0.014	0.78	0.190	0.004	2744	91	2749	58	2740	34	100
L2b	A104	702	372	0.08	13.90	0.46	0.530	0.014	0.78	0.190	0.004	2743	91	2743	57	2743	34	100
L2b	A105	221	117	0.04	13.92	0.46	0.531	0.014	0.78	0.190	0.004	2744	91	2747	58	2743	34	100
L2b	A108	164	87	0.05	13.90	0.47	0.529	0.014	0.76	0.191	0.004	2743	94	2739	58	2747	36	100
L2b	A109	275	146	0.08	14.05	0.47	0.532	0.014	0.78	0.191	0.004	2753	92	2752	58	2754	34	100
L2b	A110	214	113	0.04	13.85	0.47	0.529	0.014	0.76	0.190	0.004	2739	94	2739	58	2740	37	100
L2b	A111	347	184	0.02	13.99	0.47	0.532	0.014	0.78	0.191	0.004	2749	91	2748	58	2750	34	100
L2b	A113	349	186	0.02	13.85	0.46	0.532	0.014	0.77	0.189	0.004	2739	92	2752	58	2730	35	101
L2b	A115	281	148	0.03	13.55	0.45	0.525	0.014	0.77	0.187	0.004	2719	91	2722	57	2717	35	100
L2b	A116	139	74	0.05	14.19	0.48	0.533	0.014	0.77	0.193	0.004	2762	93	2752	58	2769	35	99
L2b	A119	325	173	0.02	13.89	0.46	0.532	0.014	0.78	0.190	0.004	2743	91	2749	58	2738	34	100
L2b	A120	197	105	0.04	13.94	0.47	0.532	0.014	0.77	0.190	0.004	2746	92	2748	58	2744	35	100
L2b	A121	246	131	0.05	13.99	0.49	0.532	0.014	0.74	0.191	0.005	2749	97	2751	58	2747	39	100
L2b	A122	302	160	0.03	13.86	0.47	0.531	0.014	0.77	0.189	0.004	2740	92	2746	58	2736	35	100
L2b	A129	335	178	0.03	13.94	0.47	0.531	0.014	0.77	0.190	0.004	2745	92	2746	58	2746	35	100
L2b	A130	270	143	0.03	13.94	0.47	0.530	0.014	0.77	0.191	0.004	2745	92	2742	58	2748	35	100
L2b	A131	275	146	0.03	13.95	0.47	0.531	0.014	0.77	0.191	0.004	2747	92	2746	58	2747	35	100
L2b	A132	330	176	0.03	14.01	0.47	0.531	0.014	0.77	0.191	0.004	2750	92	2748	58	2752	35	100
L2b	A133	339	177	0.02	13.36	0.45	0.522	0.014	0.77	0.186	0.004	2705	91	2707	57	2704	35	100
L2b	A134	303	158	0.03	13.42	0.45	0.522	0.014	0.77	0.187	0.004	2710	91	2707	58	2712	35	100
L2b	A135	189	99	0.08	13.60	0.47	0.523	0.014	0.76	0.189	0.004	2722	93	2710	58	2732	36	99
L2b	A137	287	149	0.04	13.48	0.46	0.520	0.014	0.76	0.188	0.004	2714	93	2700	58	2724	36	99
L2b	A138	216	113	0.04	13.47	0.46	0.523	0.014	0.76	0.187	0.004	2713	93	2710	58	2715	37	100
L2b	A142	223	119	0.04	14.04	0.48	0.532	0.014	0.77	0.191	0.004	2752	93	2751	58	2754	35	100
L2b	A143	124	65	0.07	13.45	0.47	0.522	0.014	0.75	0.187	0.004	2712	94	2708	58	2715	38	100
L2b	A144	350	184	0.02	13.43	0.45	0.524	0.014	0.77	0.186	0.004	2710	92	2715	58	2706	35	100
L2b	A145	195	104	0.03	14.04	0.48	0.532	0.014	0.76	0.191	0.004	2752	95	2750	59	2754	37	100
L2b	A146	414	202	0.30	12.61	0.43	0.489	0.013	0.77	0.187	0.004	2651	90	2565	55	2717	35	94
L2b	A148	146	76	0.05	13.42	0.46	0.523	0.014	0.77	0.186	0.004	2710	93	2710	58	2709	36	100
L2b	A149	287	150	0.04	13.46	0.46	0.523	0.014	0.77	0.187	0.004	2712	92	2712	58	2712	36	100
L2b	A150	277	133	0.02	12.25	0.42	0.482	0.013	0.77	0.184	0.004	2624	90	2536	55	2693	36	94
L2b	A151	336	163	0.03	12.65	0.43	0.484	0.013	0.77	0.189	0.004	2654	91	2546	55	2737	36	93

Sample	Analysis	U[ppm] <sup>a</sup>	Pb[ppm] <sup>a</sup>	Th/U <sup>a</sup>	Ratios				Ages(Ma)				Conc.					
					<sup>207</sup> Pb/ <sup>235</sup> U <sup>b</sup>	<sup>206</sup> Pb/ <sup>238</sup> U <sup>b</sup>	$2\sigma^d$	$\rho^c$	<sup>207</sup> Pb/ <sup>206</sup> Pb <sup>e</sup>	$2\sigma^d$	<sup>207</sup> Pb/ <sup>235</sup> U	$2\sigma$	<sup>206</sup> Pb/ <sup>238</sup> U	$2\sigma$	<sup>207</sup> Pb/ <sup>206</sup> Pb	$2\sigma$	%	
L2b	A154	260	138	0.03	14.02	0.48	0.532	0.014	0.77	0.191	0.004	2751	94	2749	59	2752	36	100
L2b	A155	274	142	0.03	13.28	0.45	0.519	0.014	0.77	0.186	0.004	2699	92	2695	58	2703	36	100
L2b	A156	216	113	0.03	13.35	0.46	0.522	0.014	0.76	0.186	0.004	2705	93	2706	58	2704	37	100
L2b	A160	249	131	0.03	13.54	0.47	0.525	0.014	0.76	0.187	0.004	2718	94	2720	58	2717	37	100
L2b	A161	467	244	0.02	13.47	0.46	0.523	0.014	0.76	0.187	0.004	2713	93	2712	58	2715	36	100
L2b	A162	255	134	0.03	13.47	0.46	0.523	0.014	0.76	0.190	0.004	2713	93	2713	58	2714	36	100
L2b	A163	389	206	0.02	13.87	0.48	0.531	0.014	0.76	0.189	0.004	2741	94	2744	59	2738	36	100
L2b	A164	267	141	0.03	13.75	0.47	0.528	0.014	0.76	0.189	0.004	2733	94	2733	59	2732	36	100
L2b	A167	147	77	0.06	13.54	0.48	0.523	0.014	0.74	0.188	0.005	2718	97	2712	58	2723	39	100

Table E.4: U-Th-Pb geochronologic data for metamorphic zircon in leucosomes in the Brakspruit Quarry. <sup>a</sup> U and Pb concentrations and Th/U ratios are calculated relative to GJ-1 reference zircon; <sup>b</sup> Corrected for background and within-run Pb/U fractionation and normalised to reference zircon GJ-1 (ID-TIMS values/measured value); <sup>c</sup> 207Pb/235U calculated using (207Pb/206Pb)/(238U/206Pb \* 1/137.88); <sup>d</sup> Rho is the error correlation defined as the quotient of the propagated errors of the 206Pb/238U and the 207/235U ratio; <sup>e</sup> Quadratic addition of within-run errors (2 SD) and daily reproducibility of GJ-1 (2 SD); <sup>f</sup> Corrected for mass-bias by normalising to GJ-1 reference zircon (~0.6 per atomic mass unit) and common Pb using the model Pb composition of Stacey & Kramers (1975).

## APPENDIX E. U-PB ZICON ANALYSES

179

Sample	Analysis	U[ppm] <sup>a</sup>	Pb[ppm] <sup>a</sup>	Th/U <sup>a</sup>	Ratios				Ages(Ma)				Conc. %					
					<sup>207</sup> Pb/ <sup>235</sup> U <sup>b</sup>	2σ <sup>d</sup>	<sup>206</sup> Pb/ <sup>238</sup> U <sup>b</sup>	2σ <sup>d</sup>	rho <sup>c</sup>	<sup>207</sup> Pb/ <sup>206</sup> Pb <sup>e</sup>	2σ <sup>d</sup>	<sup>207</sup> Pb/ <sup>235</sup> U		2σ	<sup>206</sup> Pb/ <sup>238</sup> U	2σ		
Peg A004		57	30	0.63	13.19	0.46	0.518	0.014	0.76	0.185	0.004	2693	94	2691	58	2695	37	100
Peg A005		73	38	0.30	12.95	0.45	0.515	0.013	0.75	0.182	0.004	2676	93	2680	57	2673	38	100
Peg A006		78	40	0.44	12.92	0.44	0.512	0.013	0.76	0.183	0.004	2674	91	2666	57	2680	37	99
Peg A007		86	40	0.19	11.85	0.40	0.469	0.012	0.76	0.183	0.004	2592	88	2481	54	2681	36	93
Peg A008		44	20	0.90	11.33	0.40	0.447	0.012	0.74	0.184	0.004	2551	90	2380	52	2690	39	88
Peg A009		37	15	0.75	10.03	0.39	0.396	0.010	0.67	0.183	0.005	2437	95	2152	48	2685	47	80
Peg A010		70	34	0.36	12.30	0.42	0.487	0.013	0.76	0.183	0.004	2627	90	2557	55	2682	37	95
Peg A011		55	27	0.39	12.20	0.42	0.486	0.013	0.76	0.182	0.004	2620	90	2554	55	2671	37	96
Peg A012		55	27	0.45	12.57	0.43	0.496	0.013	0.75	0.184	0.004	2648	92	2598	56	2686	37	97
Peg A013		81	40	0.42	12.39	0.42	0.488	0.013	0.76	0.184	0.004	2634	90	2564	55	2689	36	95
Peg A016		80	42	0.41	13.06	0.45	0.517	0.013	0.76	0.183	0.004	2684	92	2685	57	2683	37	100
Peg A017		52	27	0.80	13.02	0.45	0.514	0.013	0.75	0.184	0.004	2681	93	2675	57	2686	37	100
Peg A018		50	25	0.38	12.63	0.45	0.498	0.013	0.72	0.184	0.005	2653	95	2605	56	2689	41	97
Peg A019		84	42	0.42	12.79	0.44	0.503	0.013	0.76	0.184	0.004	2664	91	2628	56	2692	36	98
Peg A020		84	42	0.36	12.72	0.44	0.500	0.013	0.74	0.185	0.004	2659	92	2614	56	2694	38	97
Peg A028		52	27	0.37	13.10	0.45	0.516	0.013	0.75	0.184	0.004	2687	92	2684	57	2689	37	100
Peg A029		55	27	0.32	12.47	0.44	0.493	0.013	0.73	0.184	0.005	2641	94	2582	55	2686	40	96
Peg A031		39	20	0.43	12.81	0.47	0.504	0.013	0.71	0.184	0.005	2666	97	2633	56	2691	42	98
Peg A032		85	44	0.40	13.00	0.44	0.516	0.013	0.76	0.183	0.004	2680	91	2680	56	2679	36	100
Peg A033		71	37	0.88	13.11	0.45	0.517	0.013	0.76	0.184	0.004	2688	91	2687	57	2689	36	100
Peg A034		63	32	0.43	13.06	0.45	0.517	0.013	0.75	0.183	0.004	2684	92	2685	57	2683	37	100
Peg A035		64	33	0.39	12.93	0.44	0.516	0.013	0.76	0.182	0.004	2675	91	2681	56	2670	37	100
Peg A036		84	43	0.38	13.07	0.44	0.516	0.013	0.76	0.184	0.004	2685	91	2680	56	2689	36	100
Peg A037		49	26	0.37	13.10	0.45	0.518	0.013	0.75	0.184	0.004	2687	92	2690	57	2685	37	100
Peg A041		84	40	0.42	12.07	0.41	0.478	0.012	0.76	0.183	0.004	2610	88	2520	53	2680	36	94
Peg A042		69	34	0.40	12.50	0.43	0.495	0.013	0.75	0.183	0.004	2643	90	2591	55	2683	37	97
Peg A043		70	30	0.32	10.67	0.36	0.425	0.011	0.75	0.182	0.004	2495	85	2282	49	2672	37	85
Peg A044		87	44	0.32	12.75	0.43	0.509	0.013	0.76	0.182	0.004	2661	90	2651	56	2669	36	99
Peg A045		91	46	0.33	12.82	0.43	0.510	0.013	0.76	0.182	0.004	2667	90	2655	56	2676	36	99
Peg A046		56	28	0.32	12.63	0.44	0.502	0.013	0.74	0.182	0.004	2653	91	2623	55	2675	38	98
Peg A047		130	63	0.20	12.16	0.41	0.486	0.012	0.76	0.181	0.004	2617	88	2554	54	2665	36	96
Peg A048		60	29	0.34	12.40	0.43	0.494	0.013	0.74	0.182	0.004	2635	91	2587	55	2672	38	97
Peg A049		87	45	0.13	12.92	0.44	0.513	0.013	0.75	0.183	0.004	2674	91	2667	56	2679	37	100
Peg A050		51	27	0.32	13.08	0.45	0.515	0.013	0.74	0.184	0.004	2686	93	2680	56	2690	38	100
Peg A051		271	139	0.02	12.69	0.42	0.515	0.013	0.76	0.179	0.004	2657	89	2678	56	2642	36	101
Peg A052		57	29	0.35	12.66	0.44	0.501	0.013	0.74	0.183	0.004	2655	92	2617	55	2683	38	98
Peg A053		55	28	0.34	12.65	0.44	0.500	0.013	0.74	0.183	0.004	2654	92	2616	55	2683	38	97
Peg A054		70	36	0.29	13.12	0.45	0.518	0.013	0.75	0.184	0.004	2688	92	2690	56	2687	37	100
Peg A057		42	22	0.36	13.03	0.46	0.514	0.013	0.73	0.184	0.004	2682	95	2675	57	2687	40	100

Sample	Analysis	U[ppm] <sup>a</sup>	Pb[ppm] <sup>a</sup>	Th/U <sup>a</sup>	<sup>207</sup> Pb/ <sup>235</sup> U <sup>b</sup>	2 $\sigma^d$	Ratios			Ages(Ma)			Conc.			
							<sup>206</sup> Pb/ <sup>238</sup> U <sup>b</sup>	2 $\sigma^d$	rho <sup>c</sup>	<sup>207</sup> Pb/ <sup>206</sup> Pb <sup>e</sup>	2 $\sigma^d$	<sup>207</sup> Pb/ <sup>235</sup> U	2 $\sigma$	<sup>206</sup> Pb/ <sup>238</sup> U	2 $\sigma$	2 $\sigma$
Peg	A058	49	25	0.35	12.96	0.45	0.515	0.013	0.74	0.183	0.004	2677	56	2677	38	100
Peg	A059	91	44	0.52	12.18	0.41	0.485	0.012	0.75	0.182	0.004	2618	89	2673	37	95
Peg	A060	136	70	0.18	12.93	0.44	0.517	0.013	0.75	0.181	0.004	2675	90	2666	37	101
Peg	A061	57	29	0.37	13.00	0.45	0.516	0.013	0.74	0.183	0.004	2680	92	2683	38	100
Peg	A062	57	29	0.39	12.86	0.44	0.510	0.013	0.74	0.183	0.004	2670	92	2657	38	99
Peg	A063	285	147	0.06	12.88	0.44	0.515	0.013	0.75	0.181	0.004	2671	90	2679	37	101
Peg	A064	81	39	0.45	12.37	0.42	0.489	0.012	0.74	0.183	0.004	2633	90	2566	54	96
Peg	A066	86	44	0.29	13.03	0.45	0.515	0.013	0.74	0.183	0.004	2682	92	2679	56	100
Peg	A067	72	37	0.30	12.82	0.44	0.507	0.013	0.74	0.184	0.004	2666	91	2642	55	98
Peg	A068	206	106	0.08	12.99	0.44	0.517	0.013	0.75	0.182	0.004	2679	90	2685	55	100
Peg	A069	55	26	0.35	11.86	0.41	0.477	0.012	0.73	0.180	0.004	2593	90	2514	53	95
Peg	A070	36	19	0.60	13.03	0.51	0.515	0.013	0.65	0.183	0.005	2682	105	2684	49	100
Peg	A071	61	31	0.32	13.00	0.45	0.516	0.013	0.74	0.183	0.004	2680	92	2682	56	100
Peg	A074	77	38	0.39	12.57	0.43	0.497	0.013	0.74	0.183	0.004	2648	91	2603	54	97
Peg	A075	58	29	0.51	12.41	0.43	0.493	0.013	0.74	0.182	0.004	2636	91	2586	54	97
Peg	A076	54	27	0.36	12.40	0.43	0.492	0.012	0.73	0.183	0.004	2635	91	2578	54	96
Peg	A078	63	31	0.40	12.12	0.42	0.484	0.012	0.73	0.181	0.004	2614	90	2546	53	96
Peg	A079	55	26	0.31	11.95	0.41	0.473	0.012	0.73	0.183	0.004	2600	90	2498	52	93
Peg	A080	60	28	0.35	11.82	0.41	0.470	0.012	0.73	0.182	0.004	2590	90	2483	52	93
Peg	A081	48	23	0.31	12.04	0.42	0.480	0.012	0.73	0.182	0.004	2607	91	2527	53	95
Peg	A082	60	29	0.32	12.38	0.43	0.491	0.012	0.73	0.183	0.004	2634	91	2577	54	96
Peg	A083	112	55	0.28	12.35	0.42	0.491	0.012	0.74	0.182	0.004	2632	90	2575	53	96
Peg	A084	135	67	0.17	12.50	0.43	0.496	0.012	0.74	0.183	0.004	2643	90	2598	54	97

Table E.5: U-Th-Pb geochronologic data for zircon in the pegmatite in the Brakspruit Quarry. <sup>a</sup> U and Pb concentrations and Th/U ratios are calculated relative to GJ-1 reference zircon; <sup>b</sup> Corrected for background and within-run Pb/U fractionation and normalised to reference zircon GJ-1 (ID-TIMS values/measured value); <sup>c</sup> 207Pb/<sup>235</sup>U calculated using (207Pb/<sup>206</sup>Pb)/((<sup>238</sup>U/<sup>206</sup>Pb) \* 1/137.88); <sup>d</sup> Rho is the error correlation defined as the quotient of the propagated errors of the 206Pb/<sup>238</sup>U and the 207/<sup>235</sup>U ratio; <sup>e</sup> Quadratic addition of within-run errors (2 SD) and daily reproducibility of GJ-1 (2 SD); <sup>f</sup> Corrected for mass-bias by normalising to GJ-1 reference zircon (~0.6 per atomic mass unit) and common Pb using the model Pb composition of Stacey & Kramers (1975).

# Appendix F

## Abstracts to conferences

List of communications:

(I) Nicoli G., Taylor J., Stevens, G. Frei D. (2013) Leucosome formation by disequilibrium melting and melt loss: Limpopo Belt. 5th Igneous and Metamorphic Study Group 2013, Bloemfontein, South Africa. (presentation)

(II) Nicoli, G., Stevens, G., Moyen, J-F. Taylor, J. (2013) Leucosome formation by disequilibrium melting and melt loss: perspectives from the South Marginal Zone (SMZ) of the Limpopo Belt, South Africa. Goldschmidt 2013, Florence, Italy. (presentation)

(III) Nicoli G., Stevens G., Moyen J-F. (2014) Rapid evolution from sediment to anatexitic granulite in Archean continental collision zone: the example of the Bandelierkop Formation metapelites, South Marginal Zone, Limpopo Belt, South Africa. 6th Igneous and Metamorphic Study Group 2014, Rhodes, South Africa. (presentation)

(IV) Vezinet A., Nicoli G., Moyen J-F., Laurent O. Stevens G. (2014) Localized collision vs regional heating: the paradoxical aspects of 2720-2670 Ma geological evolution in the Kaapvaal craton, southern Africa. EGU 2014, Vienna, Austria (poster)

(V) Nicoli G., Vezinet A., Moyen J-F., Stevens G. Laurent O. (2014) 2.7 Ga heating event and P-T evolution of the southern marginal belt of the Limpopo belt, south Africa : consequences for neoproterozoic continental accretion. RST 2014, Pau, France. (presentation)



## LEUCOSOME FORMATION BY DISEQUILIBRIUM MELTING AND MELT LOSS: LIMPOPO BELT

Nicoli, G., Taylor, J., Stevens, G., Frei, D.

Centre for Crustal Petrology, Department of Earth Sciences, Stellenbosch University, Private Bag X1, Matieland 7602, South Africa

**Keywords:** Limpopo Belt, granulite, fluid-absent partial melting, disequilibrium melting

In many granulite facies metamorphic belts, the biotite fluid-absent melting reactions which produced the leucosomes in metapelitic migmatites are well constrained by the assemblage of peritectic minerals produced within the residua from which the melts separated. The melt compositions produced by these reactions are well documented from experimental studies and from melt inclusions within garnet from metapelitic granulites. Leucosome compositions typically depart markedly from those of melts. The main areas of major-element compositional mismatch involve  $K_2O$ ,  $Na_2O$  and  $CaO$ , with the leucosomes commonly having lower  $K_2O$  and lower  $Na_2O:CaO$  ratios than the melts, although examples of anomalously high  $K_2O$  also exist. As the leucosomes form as a consequence of segregation of melt or magma, this compositional miss-match has been interpreted to reflect processes affecting the leucosomes after their formation. Fractional crystallization of plagioclase in the leucosomes and/or  $K_2O$  and  $H_2O$  migration out of the leucosomes are the most commonly invoked mechanisms. The leucosomes produced within metapelitic granulites of the South Marginal Zone of the Limpopo Belt are markedly low in  $K_2O$  and have  $Na_2O:CaO$  ratios similar to their source rocks. Anatexis of these rocks has occurred via two biotite breakdown reactions which can be modelled as: 1.  $Bt + Sil + Qtz + Pl^1 = Grt + Pl^2 + Melt$ ; and at higher temperature, 2.  $Bt + Qtz + Pl^1 = Opx + Pl^2 + Melt$ . The lower temperature reaction produces stromatic leucosomes which underwent solid-state deformation before the formation of nebulitic patch leucosomes by the nominally higher temperature, lower pressure reaction which destroyed the earlier formed fabric. The zircon U:Pb ages for both leucosomes,  $2714 \pm 6.4$  Ma and  $2713 \pm 5.4$  Ma respectively, are within error identical and there is no evidence for poly metamorphism of these rocks. Thus, the magma formed by reaction 1. appears to have segregated and formed the mechanically solid stromatic veins whilst temperature was increasing and pressure possibly decreasing. As a consequence, an explanation is required for how the magma solidified during PT evolution of the rocks that should have resulted in increasing magma volume. As the leucosomes predominantly consist of quartz, plagioclase and minor garnet, the process that forms the solid leucosomes at high temperature cannot simply be entrainment of the peritectic plagioclase ( $Pl^1$ ) and garnet produced by reaction 1. and the precipitation of these crystals from the magma following segregation and prior to melt escape from the structure. In this scenario, the quartz in the leucosomes is the consequence of crystallization from the melt on cooling. Thus, quartz mode should correlate positively with  $K_2O$  content and  $Na_2O/CaO$  ratio in the leucosomes. No such correlations exist necessitating a mechanism to precipitate quartz and plagioclase without cooling. The trace element compositions of the leucosomes and residua appear to hold the key to identifying this process. Leucosome REE compositions are characterised by marked positive Eu anomalies, whilst their residua show no significant Eu anomaly. Modelling of trace element behaviour under equilibrium melting followed by precipitation of peritectic plagioclase produces leucosomes that have smaller positive Eu anomalies and residua with slight positive Eu anomalies. Consequently, we suggest a disequilibrium melting process that was characterised by a lack of incongruity in the plagioclase behaviour in the source. We suggest that the outer zones of plagioclase crystals melts completely in the source, with no production of a more calcic peritectic plagioclase. This produces a higher than equilibrium amount of Anorthite molecule in the melt and recovery from this state occurs after melt has segregated into the leucosomes. This process is characterised by a lack of Eu fractionation on melt formation and segregation (batch melting of plagioclase in the source), with the crystallization of relatively An-rich plagioclase in the leucosome structures coupled with co-precipitation of quartz due to the influence of plagioclase precipitation of melt  $SiO_2$  content. These findings argue that the melt leaves the source instantaneously. The leucosome volumes significantly underestimate the volume of melt lost from the rocks. Individual leucosome volumes do not represent the volume of melt or magma present at any one time in the locality occupied the leucosome. Rather they form incrementally as melt leaving the source dump its disequilibrium plagioclase load, as well as quartz and entrained ferromagnesian peritectic minerals, in sites of melt transfer.

## Leucosome formation by disequilibrium melting and melt loss: Perspectives from the South Marginal Zone (SMZ) of the Limpopo Belt, South Africa

G. NICOLI<sup>1\*</sup>, G. STEVENS<sup>1</sup>, J-F MOYEN<sup>2</sup>, AND J. TAYLOR<sup>1</sup>

<sup>1</sup>Stellenbosch University, PB X1, Matieland 7602, South Africa (\*correspondence: gnicoli@sun.ac.za)

<sup>2</sup>UMR 6524 CNRS, Université Jean Monnet, 23 rue du Dr Michelon, 42023 Saint-Etienne, France

This study investigates the details of the anatexis process which result in the formation of dm- to m-scale, markedly low K<sub>2</sub>O content leucosomes during biotite incongruent melting.

Two hypotheses exist for the origin of such leucosomes: that they represent the products of fractional crystallization of plagioclase and quartz [1]; and, the redistribution of K<sub>2</sub>O and H<sub>2</sub>O from the segregated melt back into the residuum [2]. Evidences from metapelites in the SMZ do not support either hypothesis. The peritectic assemblage is well preserved in zones of residua adjacent to leucosomes [3]; leucosomes are characterised by strong positive Eu anomalies, whilst the gneisses from which they were derived have insignificant Eu anomalies; Na:Ca ratios in the leucosomes are similar to those in their source rocks; field-based XRF profiles of K<sub>2</sub>O content across leucosomes and their hosting gneisses does not show substantial K<sub>2</sub>O enrichment in the gneisses adjacent to the leucosomes. In addition, leucosomes formed by biotite + sillimanite melting are shown to have become rheologically solid prior to the occurrence of biotite melting in the absence of sillimanite at higher temperature.

These findings suggest that the leucosomes formed by biotite fluid-absent melting involving disequilibrium behaviour of plagioclase. Such a mechanism fits with the entire spectrum of field, textural and chemical data from the SMZ and open new perspectives on the role played by disequilibrium processes during S-type granite genesis. The results argue that the melt leaves the source instantaneously, that individual leucosomes are constructed incrementally; that leucosome volumes do not represent the volume of melt present at any time; and the leucosomes in such granulites constitute part of the residuum after partial melting.

[1] Brown (2002), *J. metamorphic Geol.*, **20**, 25-40. [2] Kreisman (2001), *Lithos*, **56**, 75-96. [3] Stevens and van Reenen. (1992) *Precambrian. Research*, **55**, 303-319.

## Changes of magma geochemistry at Mt. Etna during the last 45ka due to sampling of a variegated mantle

EUGENIO NICOTRA<sup>1,2\*</sup>, MARCO VICCARO<sup>2</sup>, RENATO CRISTOFOLINI<sup>2</sup> AND SANDRO CONTICELLI<sup>3</sup>

<sup>1</sup>Università della Calabria, Via P. Bucci 15/B, 87036, Arcavacata di Rende (CS), Italy, (eugenio.nicotra@unict.it)

<sup>2</sup>Università di Catania, Corso Italia 57, 95129 Catania, Italy

<sup>3</sup>Università di Firenze, Via G. La Pira 4, 50121, Firenze, Italy

Mt. Etna magmas show long- and short-term variations especially for K contents, some LILEs and HFSEs as well as Sr-Nd-Pb-Hf isotope ratios, a feature increasingly more evident during the last four decades of activity. Nonetheless, magma source characteristics are still debated. Contributions to this discussion arise from focusing the attention on volcanic products of Etna of the last 45 ka of activity, belonging to the “*Ellittico*” and “*Recent Mongibello*” volcanic successions. Incompatible trace elements for mantle-equilibrated compositions of the most basic products reveal that the Etnean magmas under consideration can be produced by rather low partial melting degrees of a peridotite variably enriched by metasomatic phases such as amphibole and/or phlogopite. Sr-Nd-Pb-Hf isotopes suggest that recycled and altered oceanic lithosphere is a dominant component in the Etnean mantle source. A dominant FOZO reservoir has been inferred [1], although not sufficient to satisfactorily explain the observed isotopic variations. Addition of variable proportions of an EM1-type component (up to 10%) has been then suggested. Hf isotopes provide further evidence that the enriching component at Mt. Etna could be related to the metasomatizing action of high-T fluids (i.e., silicate melts), which may be frozen in the form of pyroxenite veins at mantle conditions. Our calculations confirm that involvement of variable amounts of this enriched component in magma genesis is able to explain the long- and short-term geochemical and isotopic variations observed throughout the last 45 ka.

[1] Viccaro M., Nicotra E., Cristofolini R., Millar I.L. (2011), *Chemical Geology* 281, 343-351.

RAPID EVOLUTION FROM SEDIMENT TO ANATECTIC GRANULITE IN AN ARCHEAN CONTINENTAL COLLISION ZONE: THE EXAMPLE OF THE BANDELIERKOP FORMATION METAPELITES, SOUTHERN MARGINAL ZONE, LIMPOPO BELT, SOUTH AFRICA

G. Nicoli<sup>1</sup>, G. Stevens<sup>1</sup>, J-F. Moyen<sup>2</sup> & D. Frei<sup>1</sup>

<sup>1</sup> Centre for Crustal Petrology, Department of Earth Sciences, Stellenbosch University, Private Bag X1, Matieland 7602, South Africa; telephone (+27) 21 808 3219; fax (+27) 21 808 3129, [gnicoli@sun.ac.za](mailto:gnicoli@sun.ac.za), [gs@sun.ac.za](mailto:gs@sun.ac.za), [dfreigs@sun.ac.za](mailto:dfreigs@sun.ac.za)

<sup>2</sup> UMR 6524 CNRS & Université Jean-Monnet, 23 rue du Dr Michelon, 42023 Saint-Etienne, France, [jean.francois.moyen@univ-st-etienne.fr](mailto:jean.francois.moyen@univ-st-etienne.fr)

The Southern Marginal Zone (SMZ) of the Limpopo Belt, South Africa, is regarded as the reworked equivalent of the Kaapvaal craton basement, consisting of granitoid gneisses (Baviaanskloof gneiss (BG)) and infolded greenstone belt lithologies (Bandelierkopp formation (BF)). The BF includes clastic sediments and along with all other SMZ rocks these metapelites underwent granulite facies metamorphism at approximately 2700 Ma. This study aims to better constrain the P-T-t evolution of the granulites by using the combined metamorphic constraints provided by five different metasedimentary compositions from a single large quarry. In addition, detrital zircon ages, as well as the ages of zircon from leucosomes within partially melted metapelites provide constraints on the maximum duration of the metamorphic episode, from burial to anatexis under conditions of peak metamorphism. Results of this study reveal a large range of detrital zircon ages in the metasediments, from 3300 Ma to ~2720 Ma, with a minimum age at  $2719 \pm 10$  Ma. This implies that the sediments from the Bandelierkopp formation are not the equivalent of any of the greenstone belt sedimentary successions on the Kaapvaal craton. Rather, they post-date formation of the major sedimentary successions of the Witwatersrand basin on the Kaapvaal craton. These sediments appear to have been sourced from both the Zimbabwe and the Kaapvaal cratons. Consequently, at approximately 2720 Ma, the BG most likely acted as basement onto which the sedimentary succession represented by the BF metapelites was deposited. Peak condition,  $890 \pm 10^\circ\text{C}$  and  $10.5 \pm 0.2$  kbar, was reached at  $2713 \pm 8$  Ma. This was followed by an isothermal decompression to  $850 \pm 30^\circ\text{C}$  and  $7.1 \pm 0.3$  kbar and isobaric cooling to amphibolite facies conditions,  $665 \pm 15^\circ\text{C}$  and  $6.5 \pm 0.3$  kbar. At  $2680 \pm 6$  Ma crosscutting, undeformed pegmatites, that are consistent with the age of the crosscutting Matok intrusion ( $2686 \pm 7$  Ma), mark the end of the high grade metamorphic event. The age of sedimentation relative to metamorphism; the burial rate of the sediments (0.17 to  $>4\text{cm/y}$ ) as well as the shape of the P-T path, argue strongly that the SMZ contains sediments deposited in an active margin during convergence, and metamorphosed as a consequence of continental collision along the northern margin of the Kaapvaal Craton at ~2700 Ma. In this context, the SMZ is proposed to have behaved in a manner similar to a Himalayan crustal channel or taper. These findings make a strong case for the presence of modern tectonic process at the end of the Archean.

Keywords: Phase equilibria modelling, Zircon dating, P-T-t path, Archean orogen, Southern Marginal Zone



## **Localized collision vs regional heating: the paradoxical aspects of 2720-2670 Ma geological evolution in the Kaapvaal craton, southern Africa.**

Adrien Vezinet (1,2,3), Gautier Nicoli (1,2,3), Jean-François Moyen (1,2), Oscar Laurent (4), and Gary Stevens (3)

(1) Laboratoire Magmas et Volcans, UMR 6524 CNRS, Université Blaise Pascal, Rue Kessler, 63038 Clermont-Ferrand, France, (2) Université Jean Monnet, 23 rue du Dr Paul Michelon, 42023 Saint-Étienne, France, (3) Department of Geology, Stellenbosch University, Matieland 7602, South Africa, (4) Institut für Geowissenschaften, Fachinheit Mineralogie, Goethe Universität Frankfurt, Abt. Petrologie und Geochemie, Altenhöferallee 1, D-60438 Frankfurt, Germany

The Kaapvaal craton (KC) in South Africa, one of the oldest cratonic nuclei on Earth, is bounded to the North by the Limpopo belt, whose Southern Marginal Zone (SMZ) is regarded as a ca. 2.7Ga collisional orogeny. This is substantiated by structural data, such as the south verging thrust system that bounds the SMZ to the South (HRSZ); metamorphic data, demonstrating that metapelites from the SMZ underwent a very fast ( $\sim 40$ Ma) clockwise PTt loop at ca. 2.7Ga, with a peak of metamorphism dated at  $2713 \pm 8$ Ma. The SMZ is therefore interpreted as representing a partially molten orogenic channel behaving like modern Himalaya. However, a review of geochronological data of Limpopo Belt, KC and Zimbabwean Craton shows that geological activity at around 2.7Ga was not restricted to the Limpopo belt, but was instead scattered throughout the KC. That is not in agreement with a Himalayan model but could be a response to a general thermal event, which is recorded by:

- 1) The massive flood basalts of the Vendersdorp Supergroup in central South Africa. This supergroup crops out from Johannesburg in the North to Prieska in the South and records the most widespread sequence of volcanic rocks of the KC. This massive basaltic extrusion occurs between  $2714 \pm 8$ Ma (Klipriviersberg Group) and  $\sim 2650$ Ma (Transvaal Supergroup lower limit).
- 2) A series of granitic plutons immediately south of the HRSZ, emplaced at 2670-2680Ma; all of them include a mantle-derived component whose composition is similar to the Vendersdorp basalts. A similar and synchronous pluton, the Mashishimale, emplaces South-East of the HRSZ.
- 3) Further afield, in the Eastern KC, slightly older plutons (I-type (high-Ca) granitoids) emplace in Swaziland between 2720 and 2700Ma.
- 4) Granulite-facies metamorphism in Swaziland at ca. 2.7Ga.
- 5) Finally, in the Zimbabwe Craton intermediate to felsic lavas erupted at the same time as well as gneisses and granitoids from northern Botswana. However, interactions of Zimbabwe craton with Limpopo Complex and KC are still vague.

Collectively, the data demonstrate that during the evolution of the SMZ, the whole of the KC crust underwent significant heating, permitting partial melting and extraction of granitic melts even far away from the main collision. The crustal heating is linked to mantle activity, as mafic, mantle-derived melts also form and emplace at the same time.

The coexistence of both an Himalayan-style belt, and the far-field heating (apparently not related to any plate boundary), can be interpreted in different ways: (i) Coexistence of a mantle hotspot and a collision orogeny in close vicinity; (ii) Small-scale convections in the asthenospheric mantle, driven by differences in thickness of the lithosphere and resulting in heating of the foreland; (iii) Alternatively, the combination of apparently distinct events can actually reflect specificities of neo-Archaean orogenic style and could be the response of a hot, possibly molten or near-melting crust to regional convergence, permitting generation or extraction of melt over a zone much wider than in typical modern orogens.

3.8.1 Keynote communication : Orogenesis and metamorphism : state of the art and perspectives from the Western Alps and the French Massif Central

Jean-Marc Lardeaux<sup>1</sup>

<sup>1</sup>GEOAZUR, Sophia Antipolis

Since pioneering works of Suess (1875, 1904-1909), Bertrand (1894), Termier (1903), Franchi et al. (1908), Argand (1911), Heim (1919-1922), Demay (1931), Stille (1936) and summarized by the assertion of Bertrand « Chaque chaîne a ses gneiss », the spatial-temporal link between metamorphism and orogeny has been clearly established in both Alpine and Variscan belts. In this presentation, we review and discuss, in a synthetic historical way, the main results obtained on the metamorphic evolutions of both Western Alps and French Massif Central.

First, for the Western Alps we portray the progressive metamorphic evolution through time and space with the presentation of 5 metamorphic maps corresponding to critical orogenic periods, namely 85-65 Ma, 60-50 Ma, 48-40 Ma, 38-33 Ma and 30-20 Ma. Second, for the French Massif Central we present 6 metamorphic maps corresponding to critical orogenic periods, namely 430-400 Ma, 400-370 Ma, 370-360 Ma, 360-345 Ma, 340-325 Ma and 320-290 Ma.

In both orogenic systems, we emphasize the lack of temporal data on high-pressure metamorphic rocks as well as the uncertainties on the sizes of rock units that have recorded the same metamorphic history (i.e. coherent P-T-t/deformation trajectories).

We discuss the role of subduction-driven metamorphism in ocean-derived protoliths and the conflicting models that account for the diachrony of continental subductions in the Western Alps, as well as the role of multiple subductions in orogeny and the metamorphic effects of continental collision in the French Massif Central.

Finally, we underline the main differences and similarities between the metamorphic evolutions of the western Alps and the French Massif Central.

3.8.2 (o) Quelques mécanismes orogéniques illustrés par la chaîne des Maghrébides

Dominique Frizon De Lamotte<sup>1</sup>

<sup>1</sup>GEC, Cergy Pontoise

La structure de la chaîne des Maghrébides (Tell, Rif) est apparemment très simple. On y décrit un empilement où l'on distingue de bas en haut :

(1) des zones externes correspondant à la marge nord-africaine inversée, (2) une « zone des flyschs » associée à de rares témoins ophiolitiques et représentant l'ancien bassin profond (Téthys maghrébine) qui sépare l'Europe de l'Afrique et (3) des zones internes interprétées comme l'ancienne marge européenne de la Téthys maghrébine. Certaines caractéristiques de premier ordre restent néanmoins mal comprises et interrogent sur les mécanismes orogéniques à l'œuvre dans cette chaîne. Trois questions principales seront abordées :

Quel mécanisme de transfert permet d'expliquer que le métamorphisme alpin HP-BT soit exclusivement présent dans les zones internes, c'est-à-dire dans la plaque supérieure, alors qu'il trouve forcément son origine dans l'évolution de la plaque inférieure ?

Quelle est la signification du métamorphisme qui affecte certaines unités externes ? Est-il lié à la compression miocène ou à un amincissement crustal antérieur et dans ce cas de quel âge ?

Comment expliquer que les panneaux lithosphériques plongeants observés aux deux extrémités du système (Arcs de Gibraltar et Siculo-Calabrais) soient déconnectés des sutures océaniques et pourquoi l'histoire de ces panneaux semble contrôler les taux de déformation en surface ?

3.8.3 (o) 2.7 Ga heating event and P-T-T evolution of the southern marginal belt of the Limpopo belt, south Africa : consequences for neoproterozoic continental accretion

Gautier Nicoli<sup>1</sup>, Adrien Vézinet<sup>2</sup>, Jean-François Moyen<sup>2</sup>, Gary Stevens<sup>1</sup>

<sup>1</sup>Stellenbosch University, Centre for Crustal Petrology, Department of Earth Sciences, Stellenbosch University, Afrique du Sud  
<sup>2</sup>LMV, Saint-Etienne

The Kaapvaal craton (KC) in South Africa is bounded to the North by the Southern Marginal Zone (SMZ) of the Limpopo belt, which has been regarded as the reworked equivalent of the Kaapvaal craton basement, consisting of TTG granitoid gneisses (Baviaanskloof gneiss) and infolded metasediments (Bandelierkop formation) both of which were metamorphosed and deformed during 2.7 Ga orogeny. Metamorphic and geochronologic data collected in metapelites, demonstrates that sediments from the SMZ underwent a very fast (40Ma) clockwise P-T-t loop at ca. 2.7Ga, with burial rate of (0.17 to >4cm/y) to achieve peak metamorphic conditions at 2713 ± 8 Ma.

Phase equilibria modeling constrains peak conditions to 845 ± 15°C and 10.8 ± 1.6 kbar. This was followed by isothermal decompression to 805 ± 10°C and 6.6 ± 0.63kbar, with subsequent isobaric cooling to amphibolite facies conditions, below 610°C, prior to 2680 ± 6 Ma. This evidence argues strongly that the SMZ contains sediments deposited in an active margin during convergence, and that the metapelites were metamorphosed and underwent anatexis as a consequence of continental collision along the northern margin of the KC at 2.7 Ga.

Several simultaneous high-temperature geological events occurred in the KC at this time : (1) widespread Ventersdorp Supergroup mafic to intermediate volcanism ; (2) local plutonic activity both north and south (Swaziland) of the edges of the KC (2670-2680Ma) with mantle component signature ; (3) granulite-facies metamorphism in Swaziland at 2.7 Ga due to crustal thinning. Collectively, the data demonstrate that at 2.7 Ga, the portions of the lower and mid-crust of the KC, underwent a significant heating event. The combination of information from these different rocks has the potential to provide detailed information on neo-Archaeon orogenic style.

3.8.4 (o) Imaging late-collisional slab retreat in the Variscan Eastern French Massif Central : a coupled U-Pb and Lu-Hf isotope study of granites and high-K mafic intrusives

Simon Couzinié<sup>1</sup>, Oscar Laurent<sup>1</sup>, Jean-François Moyen<sup>1</sup>, Armin Zeh<sup>2</sup>, Olivier Vanderhaeghe<sup>3</sup>, Véronique Gardien<sup>4</sup>, Adrien Vézinet<sup>1</sup>

<sup>1</sup>LMV, Saint-Etienne

<sup>2</sup>J.W. Goethe Universität, Institut für Geowissenschaften, Frankfurt, Allemagne

<sup>3</sup>GeoRessources, Nancy

<sup>3</sup>LGLTPE, Lyon

The Variscan nappe pile of the Eastern French Massif Central was built up during the Devonian and Carboniferous as a result of subduction and subsequent collision between Gondwana and Laurussia. During the late-to post-collisional stage associated with orogen collapse (330-290 Ma), the nappe pile was intruded by numerous granite plutons and reworked by the rise of a migmatite-granite dome, the Velay complex.

Granites in the area belong to two main suites, namely : (i) peraluminous two-micas or cordierite-bearing leuco- and monzogranites (MPG